ISBN : 978-9924-9047-3-1

Techno-Science Research Journal Volume 12, Special Issue on Earth Resources and Geo-Environment Technology

ORGANIZED & HOSTED BY
FACULTY OF GEO-RESOURCES AND GEOTECHNICAL ENGINEERING, INSTITUTE OF TECHNOLOGY OF CAMBODIA

PARTNERED WITH:

- 14th RCGeoE, AUN/SEED-Net, JICA
- KYUSHU UNIVERSITY, JAPAN
- THE 50TH YEAR OF ASEAN-JAPAN FRIENDSHIP AND COOPERATION

INSTITUTE OF TECHNOLOGY OF CAMBODIA
PHNOM PENH, CAMBODIA
2023

Table of Contents

Techno-Science Research Journal 12 (Special Issue) 1-8

Content list available at ITC

Techno-Science Research Journal

Journal Homepage: www.ric.itc.edu.kh

Techno-Science Research Journal

Petrochemistry of Granitic Rocks in the Kyaikhto Gold District, Mon State, southern Myanmar

Myo Kyaw Hlaing[1*], Kotaro Yonezu[2], May Thwe Aye[1], Koichiro Watanabe[2], Seang Sirisokha[3]

[1]*Department of Geology, University of Yangon, Yangon, Kamayut 11041, Myanmar*
[2]*Department of Earth Resources Engineering, Faculty of Engineering, Kyushu University, Fukuoka 819-0395, Japan*
[3]*Faculty of Geo-resources and Geotechnical Engineering, Institute of Technology of Cambodia, Russian Federation Blvd., P.O. Box 86, Phnom Penh, Cambodia*

Received: 7 July 2023; Accepted: 15 May 2024; Available online: August 2024

Abstract: *Petrochemical experiments have been performed on granitoids in the Kyaikhto Gold District of southern Myanmar. In Kyaikhto Gold District, there are a variety of gold events in Myanmar within the Mergui Belt as well as in the Mogok Metamorphic Belt. Four gold and sulfide occurrences have been reported in the Kyaikhto District: Kunzeik in the north, Zibyaung and Thae Phyu Chaung in the center, and Meyon in the south. The Kyaikhto Gold District comprises the Carboniferous metasedimentary rocks of the Mergui Belt and intrusive igneous rocks. Biotite granite and granodiorite are the predominant igneous rocks. Biotite granite is the most common igneous rock, made up of alkali feldspar, quartz, plagioclase, biotite, muscovite, and opaque. Geochemical data suggest that granites are peraluminous and extremely fractional and classified as having high SiO_2 and high A/CNK [molecular $Al_2O_3/(CaO+Na_2O+K_2O)$] values (> 1.1). At Kunzeik, ore-bearing granites and granodiorite include elevated concentrations of silica and alkali. It is metaluminous to weakly peraluminous and has A/CNK values of 0.90–1.1. Granitoids in Kyaikhto reveal a trend from pre-plate collision to the post-orogenic setting. Granodiorite is spatially associated with Cu-Mo mineralization at Kunzeik. The Kyaikhto Gold District is structurally located to the north of the Papun Fault. The mineralized zone occurs in the vicinity of the major NNW-SSE trending structure, probably formed in conjunction with the activity of this fault.*

Keywords: Cu-Mo Mineralization; Intrusive Igneous Rocks; Kyaikhto Gold District

1. INTRODUCTION

The Kyaikhto Gold District (KGD), located in the Mergui Belt (MB) as well as in the Mogok Metamorphic Belt (MMB) [1, 2], is one of the largest gold-producing belts in Myanmar (Fig. 1). The belts contain varying amounts of Au, Ag, Cu, Pb, Zn, Mo, antimony, and tin / tungsten deposits. The KGD was affected by episodic granitoid plutonism throughout the formation of the district orogen, with many episodes of plutonic activity during the Cretaceous to the Eocene that are now well defined by a wide body of geochemical and geochronological evidence [3, 4, 5]. However, the Kunzeik, Zibyaung, and Thae Phyu Chaung granitoids in the KGD have been poorly documented. Chemical and mineral (modal) compositions are the two most widely used numerical and effective criteria for the classification and description of granitoid rocks [6, 7, 8, 9]. These properties have relatively similar relationships, but the mineral composition is not specifically consistent with the chemical composition of granitoids. For example, the A / CNK values used to discriminate I-and S-type granitoids do not have a direct relationship to the modal composition of the rock. However, the chemical composition of granitoids could be used to establish genetic links between spatially related granitoid rocks. This article describes key geological characteristics, from continental to regional scales, that make it possible to view the tectonic setting of the KGD. This includes a summary of the MB and MMB as well as a description of the KGD. It discusses whole-rock geochemical results, including the classification of igneous rocks.

*Corresponding author: Myo Kyaw Hlaing
E-mail: myokyawhlaing@uy.edu.mm; Tel: +959-776-571-577; Fax:+95 (0)1 510721.

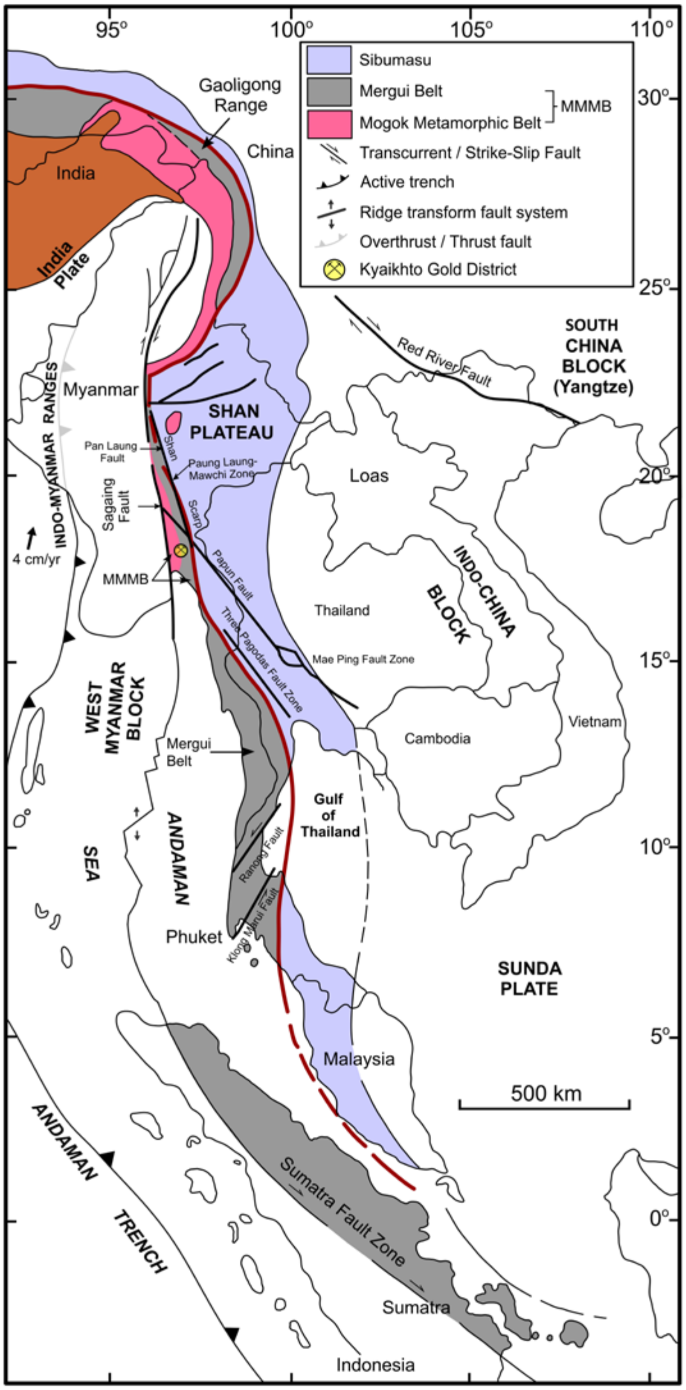

Fig. 1. Regional tectonic setting of Myanmar and distribution of the Mergui Belt and Mogok Metamorphic Belt (Gaoligong Range and its southeastward continuation through Thailand into Indonesia). The red line at the eastern margin of the Mergui Belt is the Medial Myanmar suture zone (Modified after [5]), MMMB, Mogok-Mandalay-Mergui belt.

2. GEOLOGIC SETTING

The KGD is situated between the southeastern part of the Indo-Burma Range (Burma Plate) and the southwestern part of the Indo-China Block (the southern part of the Eastern Highlands) (Fig. 1). In the Cretaceous to Eocene, the rocks of the MB and the MMB underwent greenschist to amphibolite facies metamorphism [3, 4]. The MB and MMB are intruded by several granitic rocks as part of the Western Granite Province, with an extension into peninsular Thailand. These granites form a part of the Southeast Asian Tin Belts and are also known as the Central Granitoids Belt of Myanmar ([10,11,12]; Fig. 1). The structure of the KGD is controlled by NNE-SSW- and NW-SE-trending faults, and the intrusive igneous rocks belong mostly to the late Mesozoic Mokpalin quartz diorites, whereas Eocene Kyaikhtiyo granites also occur, notably east of the KGD ([3]; Figs. 1 and 2). Geological structures at the southwestern margin of the Eastern Highlands are complicated due to the presence of older and some younger active strike-slip faults [13, 14]. The KGD is accompanied by metasedimentary rocks and later granitic rocks. Metasedimentary rocks belong to the Mergui Group of Carboniferous to Lower Permian Age [15], along with the southwestern portion of the Eastern Highlands, which strikes the N-S. In addition to the large volume of heat from the batholiths to the east, KGD seems to have been subjected to complex deformation and conjugate local faults [16]. The age of mineralization is proposed as Late Cretaceous to Paleogene and may have been consistent with deformation and metamorphism along the Papun Fault Zone (e.g., [17, 18]; Fig. 1).

3. GEOLOGY OF THE KYAIKHTO GOLD DISTRICT

Four mineralized zones from south to north have been defined as Kunzeik, Zibyaung, Thae Phyu Chaung, and Meyon (Fig. 2). Gold mineralization in the KGD occurred as massive veins, network veinlets, stockworks, and dissemination. The general trend of quartz veins is NNE-SSW, with some veins trending NW-SE. In the KGD, gold mineralization is mainly hosted by biotite granite, granodiorite, and metasedimentary rocks (Fig. 2). The MB and MMB consist of slate, phyllite, and schist. Greenschist facies are distinguished by a mineral assemblage of epidote, biotite, muscovite, and chlorite, which is the metamorphic grade of these rocks. Locally, fine-grained pyrite crystals are distributed in granite, phyllite, and slate. Mokpalin Quartz Diorites and Kyaikhtiyo Granites, which have LA-ICP-MS zircon U-Pb ages of 90.8 ± 0.8 Ma and 63.3 ± 0.6 Ma, respectively, can be linked to the granitic rocks in this district ([3]; Fig. 2). In the study area, 2 km^2 of pyroxenite bodies were mapped by [16], within the sericite schist belonging to the MB and intruded by granitic rocks. Approximately 10 km southwest, many secondary and alluvial gold explorations are carried out near the serpentinite bodies which is exposed under the lateritic cover. Metasedimentary rocks of the MB expanded the whole KGD and were composed of black slate, slaty phyllite, and schist. The black slate of the MB reveals lepidoblastic to granolepidoblastic textures, which are characterized by the orientation of biotite and chlorite. Black slate and phyllite with an outcrop blocky form are very fine-grained with a black to pale green texture. Black slate is controlled by sericitic and chlorite. Black slate and phyllite are characterized by the mineral assemblage of greenschist facies such as epidote, chlorite, and sericite. Locally, the black slate is interbedded with and/or gradationally changes to slaty phyllite. The grains are up to 10 µm in size with varying amounts of sericite, and chlorite. Schist is mainly composed of quartz, biotite, and chlorite. Mineral grains are typically affected by chloritization, which modifies the shapes of minerals and obscures their primary character in some cases. The matrix of black slate comprises 30 to 70% carbonaceous materials (graphite) and very fine quartz particles [1].

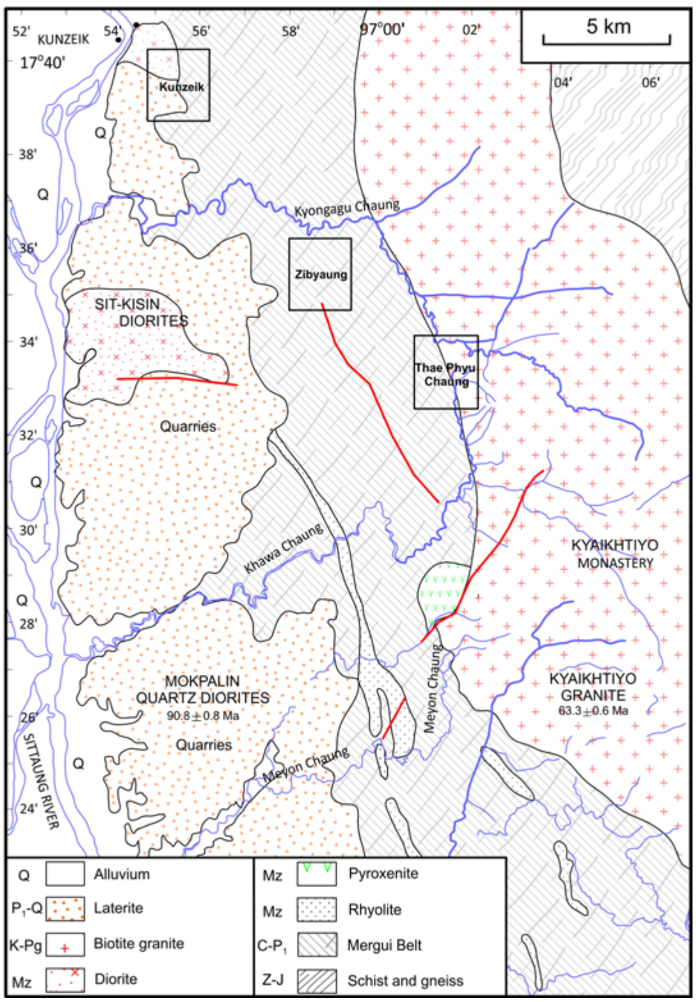

Fig.2. Geological map of the Kyaikhto Gold district. The red lines are faults (Modified after [1,3,16]). Abbreviations: Q = Quaternary, P1-Q = Lower Pliocene to Quaternary; K-Pg = Cretaceous to Paleogene; Mz = Mesozoic; C-P1=Carboniferous to Lower Permian; Z-J = Late Proterozoic to partly Jurassic.

4. ANALYTICAL METHODS

Petrography analyses were carried out on thin and polished sections using a transmitted and reflected light optical microscope. Eleven rock samples for geochemical analysis were prepared by crushing them into small pieces with a hammer and then powdering them to 200 mesh with an agate ball mill. Concentrations of major and trace elements were determined by X-ray fluorescence spectroscopy (XRF) on the RIGAKU RIX-3100 under conditions of 30 kV and 70 mA. Loss-on-ignition (LOI) was estimated at 1000 °C for each sample, and the essential concentrations were determined from the results of both analyses. The standard JA-3 was repeatedly analyzed to monitor precision, yielding an error of less than ± 5%. Both analyses were performed at the Earth Resources Engineering Department, Kyushu University.

5. RESULTS AND DISCUSSION

5.1 Granitic Rocks

On the basis of textural and mineralogical characteristics, the granitic rocks exposed in the KGD are classified into biotite granite and granodiorite.

5.1.1 Biotite Granite

Biotite granite is exposed in the vicinity of Kunzeik and Thae Phyu Chaung. It is generally medium-to coarse-grained, massive, and equigranular (Fig. 3a). At the Kunzeik, biotite granite at some exposures is highly mineralized, containing disseminated grains of molybdenite, chalcopyrite, and pyrite. In thin section, the quartz crystals are generally anhedral, although some have wavy edges that are relatively large (2–5 mm). Petrographically, biotite granite is mainly composed of plagioclase and K-feldspar. Elongated and subhedral biotites occur as accessory phases (Fig. 3b). Biotite granite in the Thae Phyu Chaung has textures similar to the Kyaikhtiyo granite, with a zircon U-Pb age of 63.3 ± 0.6 Ma [3] (Fig. 2).

5.1.2 Granodiorite

Granodiorite is exposed at Kunzeik. It is medium-to-coarse-grained with an equigranular texture (Fig. 3c, d) and consists of quartz, plagioclase, K-feldspar, and biotite. Biotite occurs as fresh vitreous flakes or highly chloritized patches. Pyrite and chalcopyrite are dispersed in the granodiorite exposed at Kunzeik (Fig. 3c). Plagioclase ranges from 100 to 400 µm in diameter (Fig. 3d). The grain size of all minerals is roughly equal. Both untwined and simple contact twined orthoclase are the most common minerals in granodiorite. Orthoclase, plagioclase, biotite, and quartz are major constituents of the granodiorite. Quartz generally occurs as anhedral grains and interstitial crystals, among other rock-forming minerals. Some quartz grains show undulatory extinction. Euhedral to subhedral plagioclase is partially intergrown with the orthoclase.

5.2 Modal Composition

The modal analysis of granites was conducted using the point counter and applying the normal approach of petrological studies that can be seen elsewhere. Modal percentages were obtained by point counting in thin sections (Table 1). At least two thin sections of each granitoid type shall be counted (cf. Table 1). The KGD granitoids are more broadly distributed within the three ranges of the Streckeisen diagram (Fig. 4a). Granitoids from the Thae Phyu Chaung and Kunzeik are mostly syeno-granites to monzogranite ([6]; Fig. 4a).

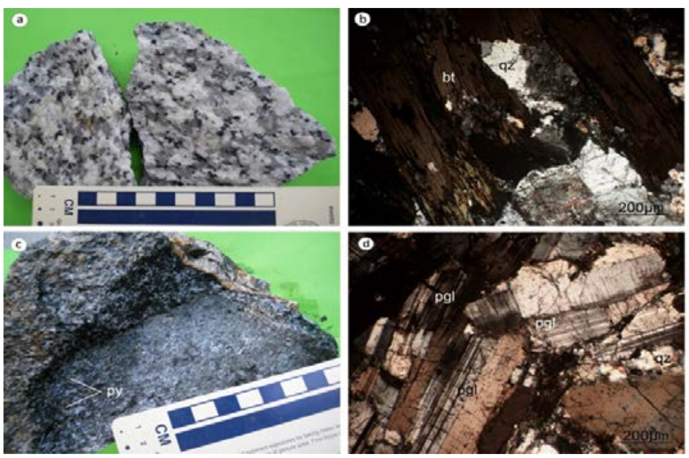

Fig.3. (a) Photograph of a hand specimen of biotite granite at the Thae Phyu Chaung; (b) Photomicrograph of biotite granite at the Thae Phyu Chaung consisting of quartz (qz), orthoclase (or), and biotite (bt); (c) Hand specimen of granodiorite at the Kunzeik; and (d) Photomicrograph of granodiorite at the Kunzeik consisting of quartz (qz), orthoclase (or), plagioclase (pgl), and biotite (bt).

5.3. Chemical Composition

5.3.1. Major and Trace Element

The major element concentrations of the granitic rocks from the KGD are listed in Table 2, and the trace element data are listed in Table 3. Loss on ignition (LOI) ranges from 0.7 to 1.1 wt%, representing the low effect of hydrothermal activity. The SiO_2 abundances of biotite granite are variable (53.6 – 75.9 wt%). The FeO concentrations of biotite granite are low (1.5 –2.0 wt%) at the Thae Phyu Chaung, but are higher at the Kunzeik (4.2 – 7.7 wt%). The MgO concentration of biotite granite ranges from 0.4 to 0.7 wt% in the Thae Phyu Chaung and is 1.7 wt% at the Kunzeik. The Al_2O_3 concentrations of biotite granite are similar in all deposits (12.8 – 14.7 wt%). The biotite granites in Kunziek and The Phyu Chaung are silicious (SiO_2 = 72.3 – 75.9 wt.%) with 12.7 – 14.7 wt.% Al_2O_3, 2.6 – 3.3 wt.% Na_2O, and 1.3 – 4.7 wt.% K_2O. Intrusive rocks in the KGD fall in the granite to diorite fields in the total alkali versus SiO_2 composition [19] (Fig. 4b).

The biotite granites are classified as high-K calc-alkaline series on a SiO_2–K_2O diagram [20] (Fig. 4c) and are classified as peraluminous (S-type) on an A/CNK–A/NK diagram [21] (Fig. 4d). The granodiorite samples from the Kunzeik prospect contain 58.6 wt.% SiO_2, 16.9 wt.% Al_2O_3, 3.3 wt.% Na_2O, and 1.31wt.% K_2O. The K_2O versus SiO_2 discrimination diagram indicates that the granodiorite from the Kunzeik is medium K calc-alkaline [20] (Fig. 4c). Classification of rocks based on the ASI (alumina saturation index = A/CNK [Al_2O_3 / (CaO + Na_2O + K_2O) molar]) indicates that granodiorite in the Kunzeik is metaluminous (I-type) [21] (Fig. 4d). The granodiorite is enriched in Ni, Sr, and V, and depleted in Nb, Zr, and Ba compared to the biotite granite. Regarding the tectonic environment, the Kyaikhto granitoids are positioned on the diagram R_1 vs. R_2 [22], forming a trend from pre-plate collision to the post-orogenic setting (Fig. 4e).

Table 1. The modal composition of the Kyaikhto granitoids

Deposit/ Prospect	Rock type	Quartz	Plagioclase	Biotite	K-feldspar vol%	Others	Total
Thae Phyu Chaung	Biotite granite	39.5	21.7	3.4	35.3	0.1	100.0
	Biotite granite	40.5	13.0	9.2	37.2	0.1	100.0
	Biotite granite	35.1	13.2	2.8	48.8	0.1	100.0
	Biotite granite	39.3	19.4	5.9	35.3	0.1	100.0
	Biotite granite	35.6	23.9	4.5	35.9	0.1	100.0
	Biotite granite	38.2	18.0	4.5	39.3	-	100.0
	Biotite granite	36.2	25.9	4.3	33.6	-	100.0
	Biotite granite	37.4	19.8	4.3	38.4	0.1	100.0
	Biotite granite	35.6	25.2	4.8	34.3	0.1	100.0
Kunzeik	Biotite granite	33.9	24.1	3.3	38.6	0.1	100.0
	Granodiorite	32.4	41.1	5.2	19.0	2.3	100.0

Note: - = not detected and 'Others' refers to opaque, chlorite etc.

Table 2. Representative major element analyses of intrusive rocks in the Kyaikhto Gold District

Deposit/ Prospect	Rock type	SiO_2	TiO_2	Al_2O_3	FeO	MnO	MgO	CaO wt%	Na_2O	K_2O	P_2O_5	LOI	Total
Thae Phyu Chaung	Biotite granite	75.9	0.18	12.7	1.50	0.14	0.54	0.80	2.60	4.25	0.03	1.12	99.9
	Biotite granite	75.1	0.19	13.5	1.71	0.09	0.63	1.36	3.16	3.14	0.04	0.97	99.8
	Biotite granite	73.0	0.22	14.5	1.88	0.14	0.65	1.36	3.36	3.74	0.04	0.87	99.8
	Biotite granite	75.8	0.17	12.6	1.47	0.08	0.57	1.21	2.64	4.40	0.03	0.84	99.8
	Biotite granite	72.8	0.20	14.4	1.70	0.12	0.60	1.46	3.06	4.72	0.05	0.70	99.8
	Biotite granite	72.3	0.21	14.6	1.82	0.16	0.62	1.61	3.12	4.35	0.04	0.97	99.8
	Biotite granite	74.4	0.21	13.6	1.74	0.09	0.62	1.54	3.03	3.82	0.44	0.75	100.3
	Biotite granite	72.4	0.23	14.7	2.04	0.20	0.68	1.33	3.13	4.32	0.04	0.72	99.8
	Biotite granite	73.5	0.17	14.0	1.53	0.12	0.57	1.32	2.93	4.64	0.04	0.96	99.7
Kunzeik	Biotite granite	71.8	0.61	12.8	4.28	0.08	1.74	3.08	2.69	1.35	0.13	1.14	99.7
	Granodiorite	58.6	1.33	16.9	7.73	0.14	2.55	6.62	3.32	1.31	0.35	0.84	99.7

LOI= loss on ignition

Table 3. Representative trace element analyses of intrusive rocks in the Kyaikhto Gold District

Deposit/ Prospect	Rock type	S	V	Co	Ni	Cu	Mo	Sn	W	Rb ppm	Sr	Ba	Y	Zr	Nb	Th	U
Thae Phyu Chaung	Biotite granite	116	12	34	8	19	13	16	27	126	130	632	36	102	11	9	8
	Biotite granite	146	21	36	8	bdl	13	19	27	111	160	331	38	120	12	9	3
	Biotite granite	224	22	45	9	2	14	19	33	126	161	368	40	109	13	10	3
	Biotite granite	149	20	18	7	bdl	13	25	19	133	137	561	32	87	11	11	3
	Biotite granite	175	18	34	7	12	13	26	41	146	159	455	47	114	12	11	3
	Biotite granite	146	18	37	9	8	16	29	15	139	180	730	42	188	12	13	2
	Biotite granite	17	20	37	11	bdl	14	20	22	127	157	458	40	93	13	11	2
	Biotite granite	152	19	62	9	bdl	15	23	41	142	160	447	40	100	14	11	10
	Biotite granite	657	22	31	9	9	1	16	20	132	142	502	32	88	10	6	3
Kunzeik	Biotite granite	501	80	25	8	19	7	13	20	51	362	300	16	133	6	5	5
	Granodiorite	408	221	13	9	12	8	14	40	30	912	344	12	117	3	4	5

bdl=below detection limit

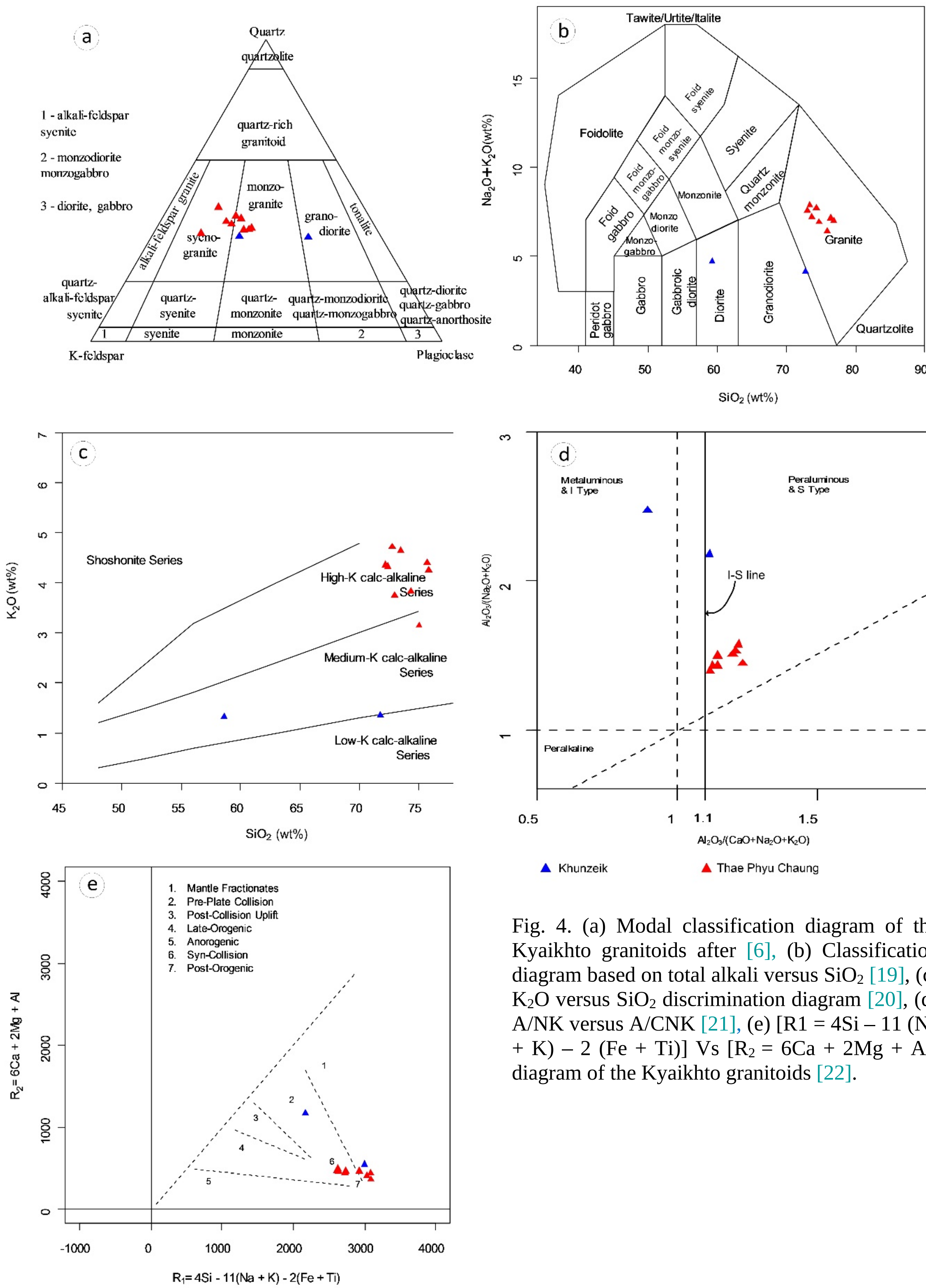

Fig. 4. (a) Modal classification diagram of the Kyaikhto granitoids after [6], (b) Classification diagram based on total alkali versus SiO_2 [19], (c) K_2O versus SiO_2 discrimination diagram [20], (d) A/NK versus A/CNK [21], (e) [R1 = 4Si – 11 (Na + K) – 2 (Fe + Ti)] Vs [R_2 = 6Ca + 2Mg + Al] diagram of the Kyaikhto granitoids [22].

6. CONCLUSIONS

The Kyaikhto Gold District is dominated by metasedimentary rocks and intrusive rocks. Schist, phyllite, and slate are metasedimentary rocks, and biotite granite and granodiorite are intrusive rocks. Gold mineralization in the Kyaikhto Gold District developed as massive veins, network veinlets, stockworks, and dissemination. The general trend of quartz veins is NNE-SSW, with some NW-SE trending veins. The chemical and modal compositions found in the Kunziek and Thae Phyu Chaung granitoid complexes of the major rock types support the hypotheses of a different source for the rocks. The granitic rocks in the Kyaikhto Gold District are medium-K calc-alkaline and high-K calc-alkaline. The Kunziek and Thae Phyu Chaung biotite granites are peraluminous (S-type) (A/CNK > 1.1), although the Kunziek granodiorite is metaluminous (I-type) (A/CNK < 1.1). Low A/CNK values (< 1.1) suggest mafic source rocks for intermediate igneous composition or infracrustal derivation, but high A/CNK values (> 1.1) suggest sedimentary or supracrustal protolith source rocks [23]. Granitoids in the Kyaikhto Gold District represent a trend from pre-plate collision to post-orogenic setting in the geochemical discrimination diagram. I-type granitoid is commonly linked with Cu-Mo mineralization at Kunzeik.

ACKNOWLEDGMENTS

This research was funded by the SHIGEN NO KIZUNA program of the Japan International Cooperation Agency (JICA), which is greatly appreciated.

REFERENCES

[1] Myo Kyaw Hlaing., Aung Zaw Myint., Tindell, T., & May Thwe Aye. (2019). Gold mineralization in the Kyaikhto District, Mon State, southern Myanmar. Open Journal Geology, 9, 29-42. https://doi.org/10.4236/ojg.2019.91003

[2] Myo Kyaw Hlaing., Yonezu. K, Khin Zaw., Aung Zaw Myint., May Thwe Aye., & Watanabe.K. (2021). Origin and Characteristics of the Shwetagun deposit, Modi Taung-Nankwe Gold District and the Kunzeik and Zibyaung deposits, Kyaikhto Gold District in Mergui Belt, Myanmar: Implications for fluid source and orogenic gold mineralization. Front. Earth Sci. 9, 1-24. https://doi.org/10.3389/feart.2021.772083

[3] Mitchell, A.H.G., Chung, S.-L., Oo, T., Lin, T.-H., & Hung, C.-H. (2012). Zircon U-Pb ages in Myanmar: Magmatic–metamorphic events and the closure of a Neo-Tethys ocean? Journal Asian Earth Science, 56, 1-23.

[4] Gardiner, N.J., Searle, M.P., Robb, L.J., & Morley, C.K. (2015). Neo-Tethyan magmatism and metallogeny in Myanmar – An Andean analogue? Journal of Asian Earth Sciences, 106, 197-215.

[5] Mitchell, A.H.G. (2018). Geological Belts, Plate Boundaries, and Mineral Deposits in Myanmar. Elsevier.

[6] Streckeisen, A. (1976). To each plutonic rock its proper name. Earth Science Reviews, 12, 1-33.

[7] Streckeisen, A., & Lemaitre, R.W. (1979). A chemical approximation to the modal QAPF classification of the igneous rocks. Neues Jahrbuch für Mineralogie, Abhandlungen 136, 169-206.

[8] Pearce, J.A., Harris, N.B. & Tindle, A.G. (1984). Trace element discrimination diagrams for the tectonic interpretation of granitic rocks. Journal of Petrology 25, 956-983.

[9] Barbarin, B. (1990). Granitoids: main petrogenetic classifications in relation to origin and tectonic setting. Geological Journal, 25, 227-238.

[10] Cobbing, E.J., Pitfield, P.E.J., Darbyshire, D., & Mallick, D.I.J. (1992). The granites of the Southeast Asian Tin Belt. British Geological Survey, Overseas Memoirs 10.

[11] Khin Zaw. (1990). Geological, petrological and geochemical characteristics of granitoid rocks in Burma: with special reference to the associated W-Sn mineralization and their tectonic setting. Journal of Southeast Asian Earth Sciences, 4, 293-335.

[12] Schwartz, M.O., Rajah, S.S., Askury, A.K., Putthapiban, P., & Djaswadi, S. (1995). The Southeast Asian tin belt. Earth Science Reviews, 38, 95–293.

[13] Zaw Naing oo., & Khin Zaw. (2009). Geology and mineralization characteristics of Meyon gold deposit, Mon State, southern Myanmar. Proceedings of 11th Regional Congress on Geology, Mineral and Energy Resources of Southeast Asia (GEOSEA), 8-10 June, Kuala Lumpur, Malaysia, 32.

[14] Zaw Naing oo., Khin Zaw., & Mernagh, T. (2010). Geological setting and nature of mineralization at Meyon gold deposit, Mon State, Myanmar. 13th Quadrennial International Association on Genesis of Ore Deposits (IAGOD) Symposium, Adelaide, 6-9 April 2010 CD-ROM.

[15] Mitchell, A.H.G., Ausa, C., Deiparine, L., Hlaing, T., Htay, N. & Khine, A. (2004). The Modi Taung-Nankwe gold district, Slate Belt, Central Myanmar: mesothermal veins in a Mesozoic orogen. Journal Asian Earth Science, 23, 321-341.

[16] Mackenzie, M.J. (1999). Report on the Exploration Progress in block 3/13 for the Period January 1998 to

December 1998. Palmer Resources Ltd. Myanmar (Burma) Project, (Unpublished), 1-67p.

[17] Barber, A., Khin Zaw., & Crow, M. (2017). Myanmar: Geology, Resources and Tectonics, Memoirs. The Geological Society, Memoir 48.

[18] Khin Zaw, & Meffre, S. (2014). Tectonics and metallogeny of mainland SE Asia - a review and contribution. Special Issue on Tectonics and Metallogeny of Mainland SE Asia. Gondwana Research, 26, 5-30.

[19] Middlemost, E.A.K. (1985). Magmas, and Magmatic Rocks. An Introduction to Igneous Petrology. Longman Group, UK, 73-87.

[20] Maniar, P. D., & Piccoli, P. M. (1989). Tectonic discrimination of granitoids. Geological Society of American Bulletin, 101, 635-643.

[21] Peccerillo, R., & Taylor, S.R. (1976). Geochemistry of Eocene Calc-Alkaline Volcanic Rocks from the Kastamonu Area, Northern Turkey. Contributions to Mineralogy and Petrology, 58, 63-81.

[22] Batchelor, R.A., & Bowden, P. (1985). Petrogenetic interpretation of granitoid rock series using multicationic parameters. Chemical Geology, 48, 45-55.

[23] Chappell, B. W., & White, A.J.R. (1974). Two contrasting granite types. Pacific Geology 8, 173-174.

Techno-Science Research Journal 12 (Special Issue) 9-16

Content list available at ITC

Techno-Science Research Journal

Journal Homepage: www.ric.itc.edu.kh

Techno-Science Research Journal

Hydrothermal Alteration, Ore Mineralization, and Geochemical Characteristics for Gold and Copper Exploration in Area 5, Phnom Sro Ngam, Kampot Province, Southwest Cambodia

Rothana Kheng[1*], Sirisokha Seang[1,2], Kakda Kret[1,3] Kimhouy Oy[1], Panhavong Ly[1], Kotaro Yonezu[4], Koichiro Watanabe[4]

[1]*Faculty of Geo-Resources and Geotechnical Engineering, Institute of Technology of Cambodia, Russian Federation Blvd., P.O. Box 86, Phnom Penh, Cambodia*
[2]*Materials Science and Structure Unit, Research and Innovation Center, Institute of Technology of Cambodia*
[3]*Energy Technology and Management Unit, Research and Innovation Center, Institute of Technology of Cambodia*
[4]*Department of Earth Resources Engineering, Kyushu University, Fukuoka, Japan*

Received: 22 August 2023; Accepted: 15 May 2024; Available online: August 2024

Abstract: The research area is located in Taken Commune, Kampot Province, within the Loei Fold Belt, represents a geologically significant region with rich history and resource potential. The purpose of this research is to understand hydrothermal alteration, ore mineralization of the deposit, and geochemistry characteristics of intrusive rocks. The analysis methods for the precise collection of this information are hand specimen description, petrographic thin section, X-ray diffraction, and X-ray fluorescence. The lithology in the research area are classified into quartzite, schist, granite, diorite, andesite,rhyolite, and old alluvium. According to petrography and XRD analysis, the alteration of mineral patterns can be classified as phyllic alteration, which contains sericite, chlorite, and quartz, formed by hydrothermal fluids at temperatures ranging from 200°C to 350°C. The mineralization consists of pyrite, chalcopyrite, sphalerite, covellite, and arsenopyrite. Arsenopyrite is the mineral most frequently linked with hydrothermal gold in high-temperature hydrothermal deposits. Mineralization ia mainly associated with phyllic alteration. Geological characteristics indicate that the intrusive rocks in Area 5 formed in a volcanic arc setting. Furthermore, the aluminum saturation index classifies these intrusive rocks as I-type granites. Based on the findings from this study, the specific area of interest for gold prospect lies to the southwest of zone 5.

Keywords: Hydrothermal alteration, Ore mineralization, Geochemical characteristics, Area 5, Kampot, Cambodia.

1. INTRODUCTION

Cambodia is an agriculture country that has many natural resources, both surface and underground. There are many types of mineral resources that have not been explored yet, such as copper, gold, iron ore, zinc, lead, tin, and bauxite. Exploration licenses in Cambodia granted to both foreign and local companies increased. Metallic minerals like gold, iron, and copper are still the main resources in Cambodia. And also, gold is still trading at a significant price in the world market. Minerals exploration projects in Cambodia are divided into four parts, such as metallic minerals, non-metallic minerals, gemstones, and coal [1].

Many foreign companies are interested in exploring the mineral resources in Cambodia. Samnang Angkor Development Ltd., one of the mining exploration companies in Cambodia, has been granted an exploration license by the Cambodia Development Council (CDC) [2], has explored the economical mineral resources such as gold and copper in Koh Sla prospect, Chhouk district of Kampot province .

The study area is located in Koh Sla, Chhouk District, Kampot Province and south Cambodia within the Loei Fold Belt (LFB) of the western periphery of Indochina Terrane Fig. 1. The Loei Fold Belt (LFB) is one of the meltallogenic belts of Indochina Terrane, which occupies the region from northern Laos to western Cambodia through northeastern Thailand [3]. Based on geochemical studies, most of the

* Corresponding author: Kheng Rothana
E-mail: khengrothana20001907@gmail.com
Tel: +855 11 642 681

granitoids of this belt are I-type, consistent with the abundance in Cu-Au mineralization in the belt [3].

The prospect area of Koh Sla is dominated by metamorphics such as quartzite, metasandstone, phyllite, and schist. The gold-bearing veins in Area 5 of the Koh Sla Prospect are hosted by quartzite and schist that have been invaded by magmatically derived auriferous sulfide fluids. Furthermore, prospect areas have the potential for valuable mineralization, which is indicated as vein-type gold mineralization. Ore mineralization veins are generally northwest and west-northwest trending, which dip generally to the northeast, whereas southwest dips are also noted. The gold in the research is highly associated with the silver. However, the ore type is not yet sufficient for the characteristic. The primary indication may be epithermal or an organic deposit. Skarn mineralization was also observed on the property but is yet to be explored thoroughly. The company covers 159.50 km^2 [2]. Although this area has gold and copper minerals, the detailed rock types, geochemistry of igneous rocks, and hydrothermal alteration have not worked out. Therefore, this research is carried out to better understand the detailed rock types, geochemistry characteristics of igneous rocks, and hydrothermal alteration as well.

1.1 Regional Geology

The central zone of Cambodia is defined by a thick condensate sedimentary layer from the Quaternary period and a little mountain. In the southwest part, Mesozoic sedimentary rock units (mainly Triassic-Cretaceous) with anticlinorial and synclinorial zones in Indosinian fold belts are present. In the north-east part, Mesozoic sedimentary units (upper Triassic–Cretaceous) with Precambrian–Early sedimentary granites and high-grade metamorphic rocks are present. There are also synclinorial zones in Indosinian fold belts (mainly Carbaoniferous-Triassic) [4].

The LFB extends from northern Laos to Sra Kaeo in Thailand and western Cambodia. It contains Late Permian to Triassic andesitic-rhyolitic volcanic rocks, but older Devonian-Carboniferous and Silurian magmatic rocks have also been reported. It also hosts a variety of mineral deposits, including Cu-Au skarn deposits, Au skarn deposits, epithermal Au deposits, and epithermal Sb-Au deposits.

In those provinces occur mineral deposits such as the Pu Thap Fah Au skarn deposit [5]. the Chatree epithermal Au deposit; the Phu Lon Cu-Au skarn deposit; the Kusa Cu-Au deposit, and the Anlong Au Deposit (Rovieng, Preah Vihear in Cambodia) [5].

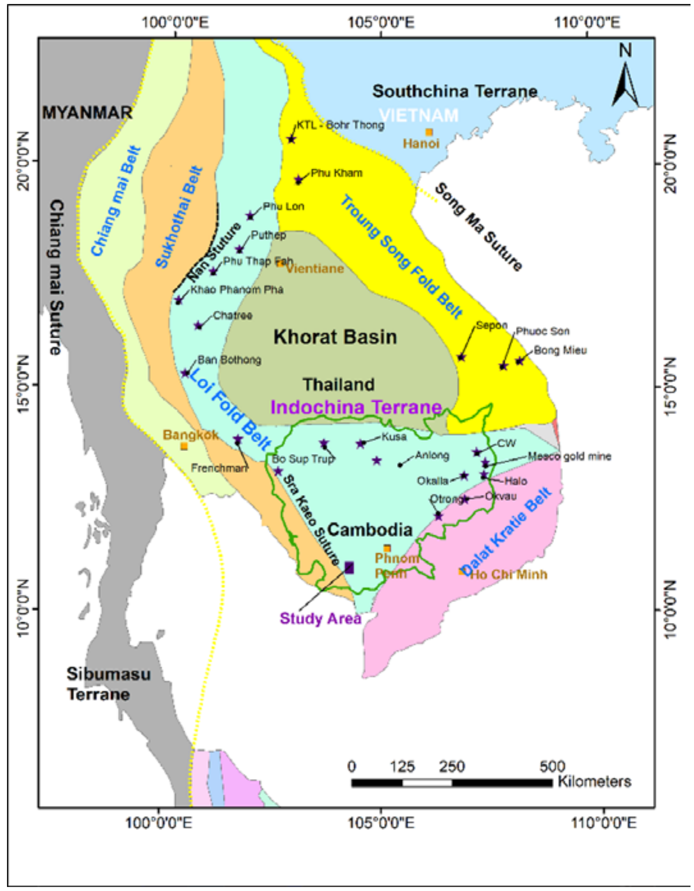

Fig. 1. Map showing tectonic divisions of the SE Asian Terrane including mineralized belt of Cambodia, Vietnamese, Laos, and Thailand [6].

1.2 Geology of Study Area

Phnom Sro Ngam region is located in Kampot province, SW Cambodia, and is a possible target for investigating porphyry, epithermal, and skarn-related gold deposits. Since the majority of the surface area is covered by Cambrian to Silurian metamorphic rocks (quartzite, metasandstone, phyllite, and schist), multiple intrusions are located in the region, some of which are buried, as demonstrated by shallow diggings that are assumed to have mineralization. Quartzite and other metamorphic strata that have been invaded by magmatically generated auriferous, sulfide-bearing fluids contain gold-bearing veins [7].

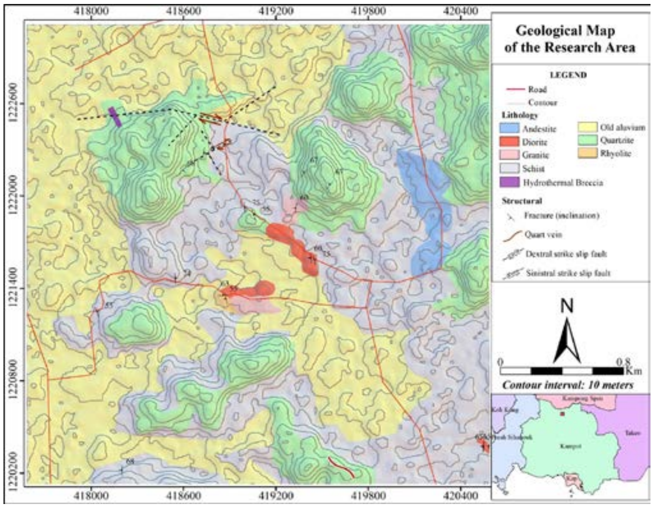

Fig. 2.The geological map of the research area.

2. METHODOLOGY

Six thin sections, three polished sections, and one SEM analysis to determine the textural features of the rocks, alteration minerals, and accompanying ore minerals Additionally, bulk and clay fraction X-ray diffraction (XRD) analyses were conducted to identify the altered mineral assemblage. To further study the alteration of mineral assemblages, we utilized a combination of hand specimens, petrographic, X-ray diffraction (XRD) analyses, and analytical spectral devices (ASD). Three samples were collected for the Inductively Coupled Plasma-Mass Spectrometry (ICP-MS) method at the Laboratory of ALS Geochemistry Analysis in Australia. All of these experiments, except XRD analysis and Inductively Coupled Plasma-Mass Spectrometry (ICP-MS) methods, were carried out at the Institute of Technology of Cambodia's faculty of geo-resources and geotechnical engineering. XRD analysis was conducted at Kyushu University.

3. RESULTS AND DISCUSSION

3.1 Petrography

The types of rocks found in a specific region serve as reliable indicators of the locations and formation processes of mineral deposits.Therefore, it is important to characterize different rock types and determine their origin which is related to mineralization. Based on the detailed geological mapping, physical properties, petrographic:

Physical properties of rhyolite, the sample A5-10.1 has yellowish grey to orange in color, fine-grained rhyolite with porphyritic texture by phenocrysts of quartz Fig. 3A. Under the microscope, it could be identified that the rhyolite is composed of fine-grained quartz and sericite. It contained silica rich mineral assemblage of fine-grained quartz with other minerals and groundmass that contains felsic microcrystalline mineral formed by rapid cooling during crystallization, with sizes between 0.02 mm and 0.1 mm Fig. 3a.

Schist sample A5-03 has medium-sized, plate-shaped mineral grains and is a strongly oxidized greyish pink color Fig. 3B. Under the microscope, schist is appeared to be consisted of foliation as dark brown color in plane polarized light view and light brown color in cross-polarized light view. Quartz in microscope can be appear to be large up to 0.01mm Fig. 3b.

The quartzite has a fine-grained grayish-reddish-brown grain as indicated by its physical characteristics. It is also acknowledged to have a non-foliated texture Fig. 3C. This sample primarily comprises of quartz grains that are interlocked and have considerable oxidation. Under a microscope, it is clear that quartz, which appeared white to gray in the cross-polarized light view and colorless in the plane polarized light view, dominates the quartzite. The majority of the quartz grains are monocrystalline, with sizes between 0.09 mm and 0.2 mm Fig. 3c.

According to the hand specimen properties of diorite, sample A5-10 is dark grey to green in color, medium-grained, and has a phaneritic texture with strong chlorite alteration. Moreover, the sample contains fractures that were later filled with calcite Fig. 3D. Under the microscope, the clinopyroxene phenocryst showed an irregular shape with sizes ranging from approximately 0.1 to 0.8 mm. The plagioclase phenocryst is euhedral to subhedral, with sizes ranging from 0.1 to 0.3 mm. Some plagioclases were slightly altered to sericite, and biotite was altered to chlorite Fig. 3d.

The physical properties, the andesite sample A5-12 has green-grey color, fine to medium-grained size and porphyritic texture. It consists of chlorite altered and slightly oxidation Fig. 3E. Under the microscope, andesite consists mainly of plagioclase feldspar, chlorite, hornblende, and opaque minerals. It is identified as having a porphyritic texture due to the presence of phenocrysts of plagioclase and a felsic groundmass. Plagioclase is the most abundant mineral, showing a grey color in XPL and appearing colorless in PPL, with twinning observed in its crystals with shapes up to 0.02mmFig. 3e.

In hand specimen, sample A5-32 is greenish-grey in color, medium-grained, and exhibits a porphyritic texture typical of granitic rocks. The rock consists of alkali feldspar, chlorite, with quartz grains approximately 0.01mm in size, and biotite-chlorite alteration minerals are commonly observed Fig. 3F. Under the microscope, quartz is observed as phenocrysts, while alkali feldspar is the predominant mineral, with grains ranging in size from 0.04 to 0.09mm Fig. 3f.

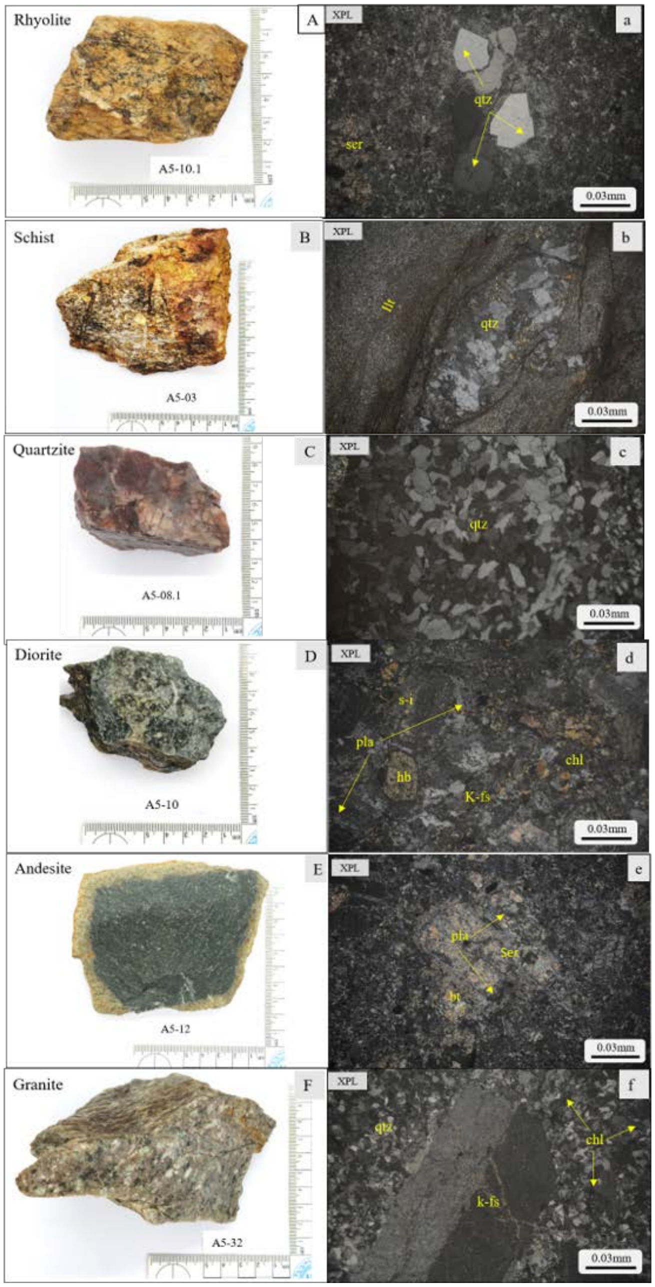

Fig. 3. Photomicrographs (A) & (a): rhyolite, (B) & (b): schist, (C) & (c): quartzite, (D) & (d). diorite, (E) & (e): andesite, and (F) & (f): granite. Abbreviation: Qtz=quartz,Pl=plagioclase feldspars, Hb=hornblende, K-fs=alkali feldspar, Bt=biotite, Chl=chlorite, S-i=smectite-illite, Ser=sericite and Cpx=clinopyroxene.

3.2. Whole-rock geochemistry

The major elements of the igneous rocks in study area have been analyze by X-ray Fluorescence (XRF). The result from the analysis is all summary in the Table 1. The percentage of major chemical composition are plotted in TAS diagram for identification and classification of plutonic rock and volcanic rock by using the percentage of total alkalis and silica in each igneous rock.

Table 1. Major elements analyses of intrusive and volcanic rocks from Area 5, Phnom Sro Ngam.

Rock Type	Diorite	Rhyolite	Granite	Basaltic tranchy -Andesite
Sample ID	A5-10	A5-10.1	A5-32	A5-12
SiO2 (%)	63.8	75.2	72.5	53.04
TiO2	0.53	0.28	0.22	0.89
Al2O3	16.35	13.2	14.05	17.04
Fe2O3	6.07	2.38	2.56	7.72
MnO	0.11	0.06	0.04	0.11
MgO	2.92	0.49	0.73	3.16
CaO	4.38	0.71	1.02	6.05
Na2O	3.17	2.8	4.21	1.82
K2O	1.79	3.02	2.76	4.29
P2O5	0.1	0.06	0.05	0.23
LOI	2.67	2.36	1.16	7.60
Total	101.97	100.63	99.4	101.95
Y (ppm)	16.9	20.8	17.9	-
Rb	70.3	120	86.6	-
Nb	6	9.5	9.6	-

The SiO_2 concentrations of volcanic rocks in the given region vary from 58.04 to 71.77 wt.%. Based on the (Na_2O+K_2O) versus SiO_2 diagram, The intrusive rocks are classified as diorite and granite and volcanic rocks are classified as rhyolite and andesite.

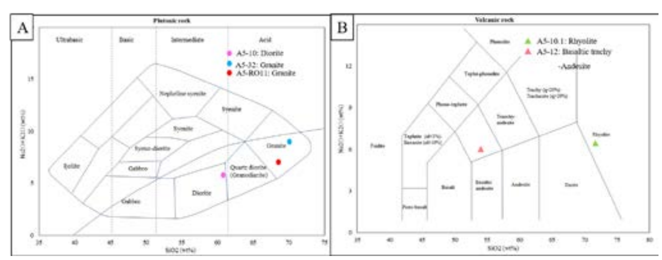

Fig. 4. Classification diagram based on total alkali versus SiO_2. A). TAS plutonic rock classification diagram [8]. B). TAS volcanic rock classification diagram [9].

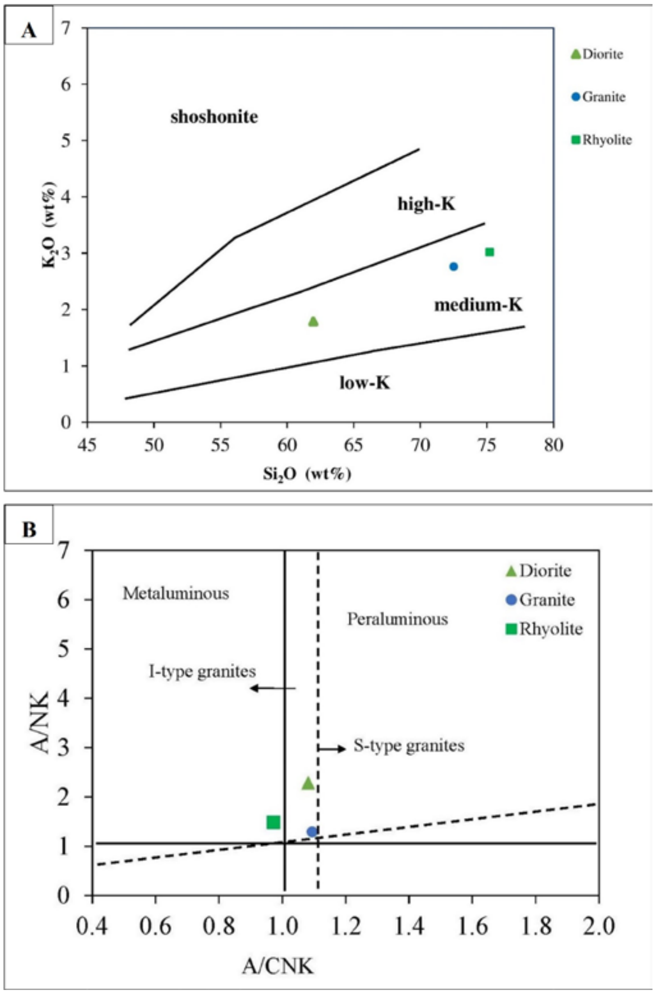

Fig. 5.A) Diagrams showing the magma composition of intrusive rock [10]. (B) A/CNK [= molar Al2O3/ (CaO+K2O+Na2O)] versus A/NK [=molar Al2O3/ (K2O+Na2O)] diagram [11,12].

Trace element analyses were used in this study to investigate the tectonic origins of intrusive rocks in the study area. On the tectonic discrimination Y+Nb vs Rb and Y vs. Nb diagram [13], the intrusive rocks from the research area were plotted on the volcanic arc setting.

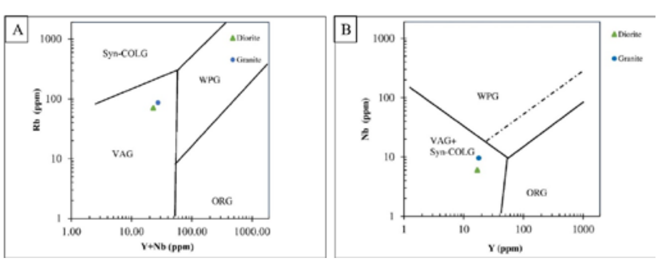

Fig. 6. (A).Y+Nb vs Rb and (B).Y vs. Nb diagram [13].

3.3. Wall rock alteration

The hydrothermal alteration that occurred at the research area (Area 5) was conducted through an investigation of the host rock samples. The combination of properties of hand specimen, petrographic, and XRD analysis were applied to discuss the alteration mineral assemblages.

Chlorite is commonly associated with alteration and metamorphism, the mineral displays absorption feature in the 2200 nm and 2400 nm region due to the hydroxy molecule, the wavelength of these absorption shift with differing proportions of the Mg and Fe elements. The green coloration of chlorite is attribution to the properties of Fe in the crystal lattice, which affect the spectral feature in the VNIR region [14].

Goethite is formed under oxidizing condition from weathering of iron bearing minerals and is often found mixed with hematite. The mineral displays trans opaque behavior. Both the Fe^{3+} ion and Fe^{2+} occur, creating features at 550 nm and 900 nm respectively. Goethite displays no hydroxyl band features despite the 'traditional formula (FeO-OH) possessing OH. Hydrated goethite ($2Fe_2O_3.3H_2O$) has been identified as limonite in much of the older [15].

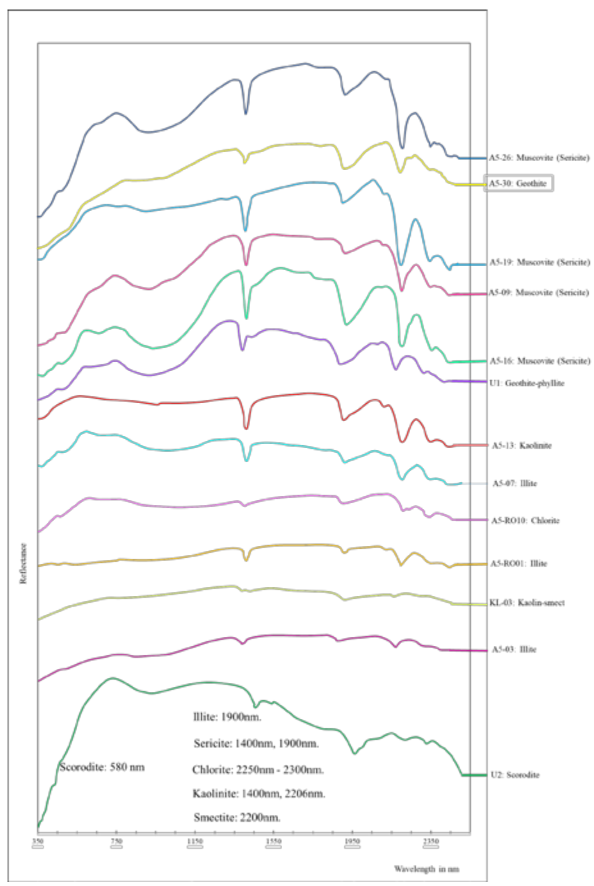

Fig. 7.Results of handheld XRD analysis.

Muscovite (sericite,$KAl_3Si_3O_{10}$-$(OH)_3$) is commonly associated with igneous rocks. Muscovite is characterized by absorption features in the 1400nm and 2200nm regions [9]. In addition, a wavelength of muscovite showed 1900nm which is shallower than illite. The Illite alteration (K, H_3O) (Al, Mg, Fe)$_2$(Si, Al) 4O 10[$(OH)_2$, (H_2O)] is formed in the early stages of the weathering of muscovite. Illite has similar properties to muscovite and is differentiated by the lesser abundance of interlayer K. The main difference with illite is found only at the 1990nm absorption feature which is much shallower in the muscovite. The scorodite shows faintly greenish color with the hardness around 2-4 on mohs scale. Base on spectral analysis ASD, the scorodite are identified from the absorption at wavelength 580 nm [15].

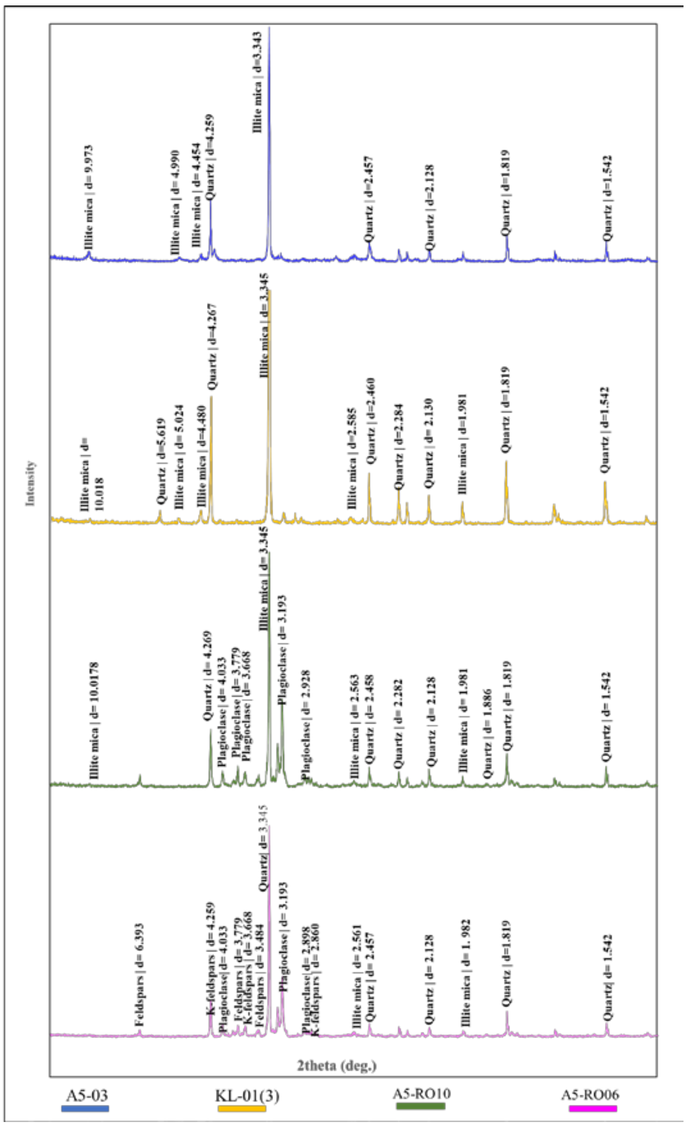

Fig. 8.Peak of XRD analysis of samples.

Based on X-ray diffraction analysis, the primary minerals and alteration minerals in study area are quartz k-feldspars, plagioclase, illite-mica (sericite) (Fig.8). The pH and temperature ranges of the mineral phase are presented in Fig. 10. The alteration assemblage of Area 5 indicates that the ore-forming fluid varied from slightly acidic to slightly alkaline. The hydrothermal alteration in Area 5 consists of quartz, sericite (illite mica), chlorite, and scorodite, which are classified as phyllic alteration zones. Phyllic alteration forms at temperatures ranging from 200°C to 350°C under pH 4.5-7 and is associated with many mineral deposits [16].

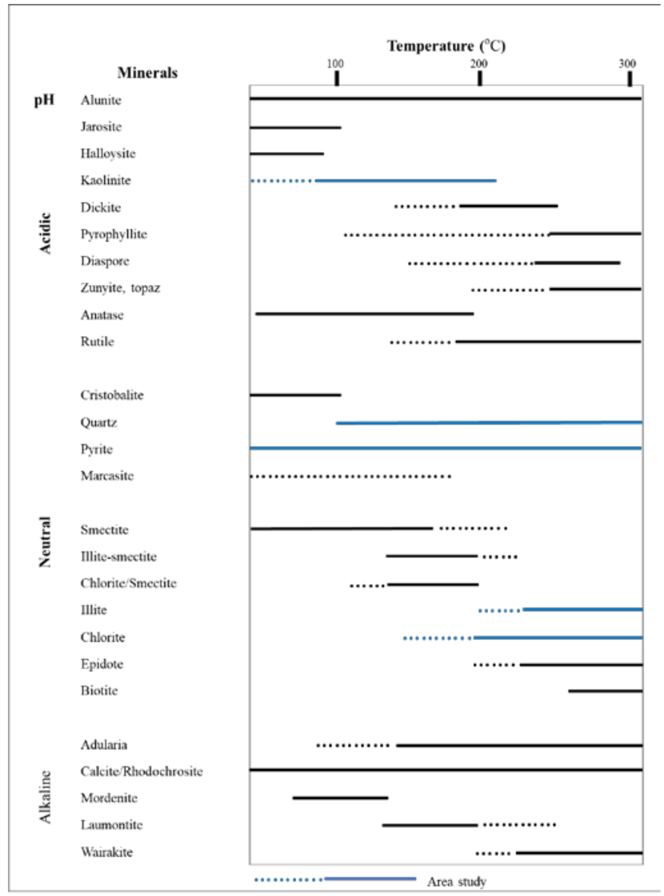

Fig. 9. pH and temperature ranges of alteration minerals (Modified after [16]). Dark blue line are alteration minerals in study area

3.2 Ore mineral assemblages

The ores mineralization identification under reflected-light microscope are pyrite, chalcopyrite, covellite, sphalerite, and arsenopyrite.

Pyrite in study area occurs disseminated with diorite and quartz vein. Further, chalcopyrite, covellite and pyrite is associated with arsenopyrite Fig. 10C,D & 11B. Under microscopic view, pyrite is a common opaque mineral in all mineralization stage and euhedral cubic shape. Pyrite is the most commonly found sulfide mineral in the present area. Chalcopyrite is a form of goldy-yellow mineral with irregular shapes, anhedral shape, and medium relief. In plan-polarized light, it has the interference color is brown and weakly non-isotropic, while in cross polarize light it is bright yellow and anhedral in shape. Under a microscope, sphalerite appears blackish-gray, showing isotopism Fig. 10C & 10B.

Covellite has a characteristic deep indigo-blue color, often with a purple iridescence. Some aggregate specimens exhibit deformation and recrystallization structures. Covellite shows a greenish-blue color in reflected light. It has moderate reflectivity and is extremely anisotropic. Covellite occurs as irregular laths or veins within chalcopyrite and pyrite Fig. 10B,C & 11C,D.

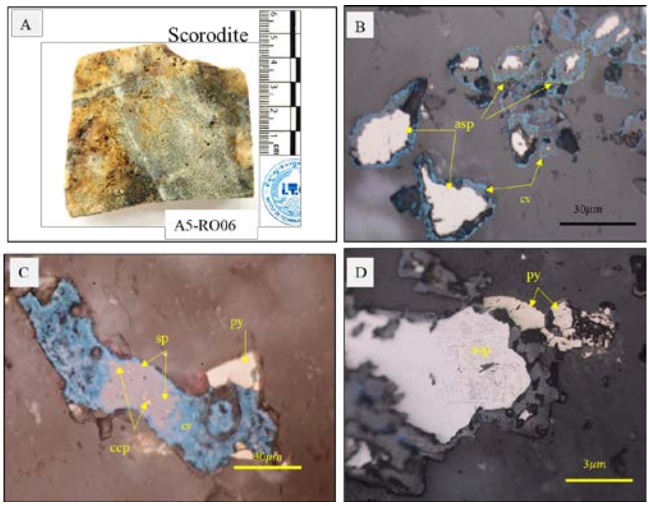

Fig. 10. Photographs of ore minerals sample (ID: A5-RO06). (A). Hand specimen. B, C, D). Arsenopyrite (asp), Covellite (cv), Pyrite (py), Sphalerite (sp), Chalcopyrite (ccp).

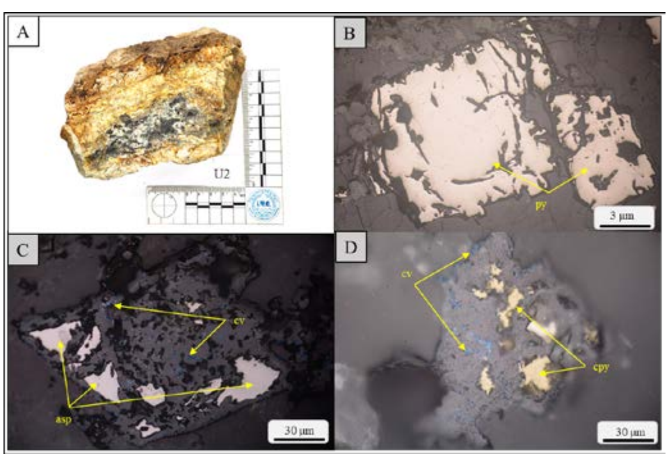

Fig. 11.Photographs of ore minerals of sample ID: U2. A). Hand specimen. B, C, D). Arsenopyrite (asp), Covellite (cv), Pyrite (py), Sphalerite (sp), Chalcopyrite (ccp).

Under the microscope arsenopyrite is white, and shows strong shades of blue, green, and brownish-yellow anisotropic colors Fig. 10B,D & 11C. Based on the results of Scanning Electron Microscope (SEM) and EDX analysis, the mineral is mainly composed of As and Fe, which agrees with the chemical formula of arsenopyrite (FeAsS), Fig. 12. Arsenopyrite is commonly associated with hydrothermal gold and also with vein ores of Sn and W in high-temperature hydrothermal deposits [17]. Sample (U2) was at the west-northern part of study area.

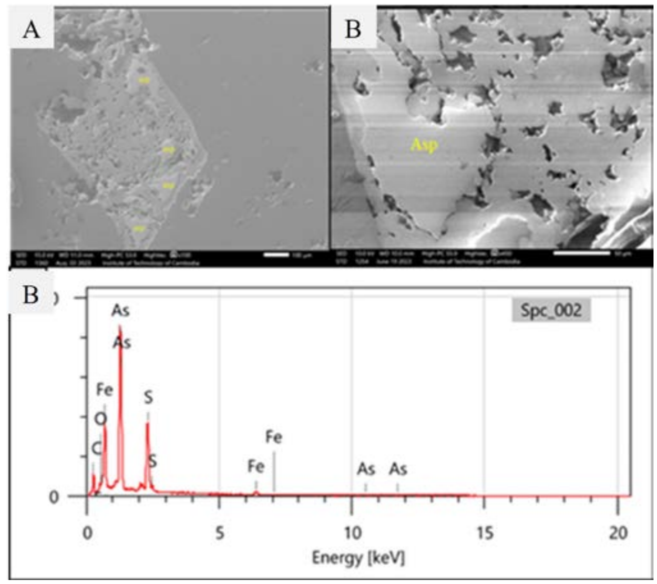

Fig. 12.(A and B) Back-scattered scanning electron microscopy images of quartz of arsenopyrite, (C) Energy dispersive spectroscopy spectra showing the composition of As and Fe composition. Abbreviations: Asp=Arsenopyrite.

4. CONCLUSIONS

- There are six main lithologies of unit rocks identified, such as the oldest alluvium, contact metamorphism (quartzite), regional metamorphism (schist), and later diorite, granite, rhyolite, and andesite.
- The intrusive and volcanic rocks belong to medium-K, volcanic arcs, and I-type granite.
- The hydrothermal alteration in Area 5 consists of quartz, sericite, and scorodite, classified into the phyllic alteration zone.This alteration zone mainly associated with mineralization. The mineralization in this study area are pyrite, chalcopyrite, covellite, sphalerite, and arsenopyrite.
- The study offers valuable insights for mineral exploration and resource assessment in the region. It enhances understanding of geological processes and mineralization, aiding geologists and miners in targeting gold and copper exploration areas.

ACKNOWLEDGMENTS

We gratefully acknowledge the support of the Laboratory-Based Education (LBE) promoted by the Project for Strengthening Engineering Education and Research for Industrial Development in Cambodia, as well as the Faculty of Geo-Resources and Geotechnical Engineering Institute of Technology of Cambodia (ITC), and Department of Geology, Ministry of Mines and Energy, Cambodia. Our heartfelt gratitude extends to His Excellency Kong Samnang, Chairman of Samnang Angkor Development Co. Ltd., for generously permitting and facilitating our field research in Phnom Sro Ngam, Chhouk District, Kampot, Cambodia.

REFERENCES

[1] Chrea, V., (2013). The Current Situation of Mining Industry in Cambodia. Ministry of Mine and Energy, MME.

[2] Inres, researcher, (2017). New Areas Open for Mineral Exploration Licenses. integrity cambodia.

[3] Tum, S., Puotinen, M.L., Copeman, D.B., 2004. A geographic information systems model for mapping risk of fasciolosis in cattle and buffaloes in Cambodia. Vet. Parasitol. 122, 141–149.

[4] ESCAP, (1993). Atlas of Mineral Resources of the ESCAP region: Geological map of Cambodia; Mineral resources map of Cambodia. vol.10. United Nations, New York.

[5] Phan, C. T. (1992). Geology of Cambodia, Laos, and Vietnam: explanatory note to the Geological map of Cambodia, Laos and Vietnam at 1: 1,000,000 scale. Geological Survey of Vietnam.

[6] Zaw, K., Meffre, S., Lai, C. K., Burrett, C., Santosh, M., Graham, I., ... & Cromie, P. (2014). Tectonics and metallogeny of mainland Southeast Asia—A review and contribution. Gondwana Research, 26(1), 5-30.

[7] Samnang Angkor, (2020). SEMI-ANNUAL EXPLORATION REPORT. SAMNANG ANGKOR DEVELOPMENT LTD. Phnom Sro Ngam Exploration License Chhouk District, Kampot Province, Kingdom of Cambodia.

[8] Cox, K. G. (Ed.). (2013). The interpretation of igneous rocks. Springer Science & Business Media.

[9] Bas, M. L., Maitre, R. L., Streckeisen, A., Zanettin, B., & IUGS Subcommission on the Systematics of Igneous Rocks. (1986). A chemical classification of volcanic rocks based on the total alkali-silica diagram. Journal of petrology, 27(3), 745-750.

[10] Peccerillo, A., & Taylor, S. R. (1976). Geochemistry of Eocene calc-alkaline volcanic rocks from the Kastamonu area, northern Turkey. Contributions to mineralogy and petrology, 58, 63-81.

[11] Chappell, B. W., & White, A. J. R. (1992). I-and S-type granites in the Lachlan Fold Belt. Earth and Environmental Science Transactions of the Royal Society of Edinburgh, 83(1-2), 1-26.

[12] Maniar, P. D., & Piccoli, P. M. (1989). Tectonic discrimination of granitoids. Geological society of America bulletin, 101(5), 635-643.

[13] Pearce, J. A., Harris, N. B., & Tindle, A. G. (1984). Trace element discrimination diagrams for the tectonic interpretation of granitic rocks. Journal of petrology, 25(4), 956-983.

[14] Hunt, W. A., Barnett, L. W., & Branch, L. G. (1971). Relapse rates in addiction programs. Journal of clinical psychology, 27(4).

[15] Pirajno, F. (2008). Hydrothermal processes and mineral systems. Springer Science & Business Media.

[16] Hedenquist, J. W., Arribas, A. N. T. O. N. I. O., & Gonzalez-Urien, E. (2000). Exploration for epithermal gold deposits.

[17] MacKenzie, W. S., & Guilford, C. (2014). Atlas of the rock-forming minerals in thin section. Routledge.

Techno-Science Research Journal 12 (Special Issue) 17-22

Content list available at ITC

Techno-Science Research Journal

Journal Homepage: www.ric.itc.edu.kh

Techno-Science Research Journal

Assessment of Relative Permeability Modification During Low Salinity Waterflooding in Shaly-Sandstone

Tina Tharn[1*], Falan Srisuriyachai [2], Chandoeun Eng [3]

[1] *Department of Mining and Petroleum Engineering, Faculty of Engineering, Chulalongkorn University, Bangkok 10330, Thailand*
[2] *Department of Mining and Petroleum Engineering, Faculty of Engineering, Chulalongkorn University, Bangkok 10330, Thailand*
[3] *Faculty of Geo-resources and Geotechnical Engineering, Institute of Technology of Cambodia, Russian Federation Blvd., P.O. Box 86, Phnom Penh, Cambodia*

Received: 22 August 2023; Accepted: 15 May 2024; Available online: August 2024

Abstract: *This study assesses changes in relative permeability curves during low salinity waterflooding (LSWF) in shaly-sandstone, employing the Johnson, Bossler, & Naumans (JBN) method. Coreflood experiments were performed to obtain several data points, including the oil recovery factor, fluid production rates, and differential pressure. Data was transformed into relative permeability data by an unsteady-state relative permeability method called JBN, and relative permeability curves were generated by Corey's correlation to match the data. The Corey's exponent from the best-fit curves was used for investigation. Ion compositions in effluents from coreflood and the turbidity of the fluid were utilized in the analysis of the oil recovery mechanism. From the experiments, it can be observed that relative permeability curves insignificantly change their curvature, which can be explained by the fact that oil recovery mechanisms may occur without changing rock preference from oil to water wetness. Supporting this result, the observation of calcium and magnesium ions in the effluents of high oil recovery cases confirms the occurrence of multi-component ion exchange. The turbidity of effluent during the transition from formation water injection to low salinity waterflooding also supports the oil recovery mechanism by means of fine migration.*

Keywords: Low-salinity Waterflooding; Relative permeability cuvers; Un-steady state relative permeability; Corey's correlation, JBN method.

1 INTRODUCTION

Petroleum production, crucial for meeting energy demands, encompasses primary, secondary, and tertiary recovery phases. Enhanced Oil Recovery (EOR) methods like low-salinity waterflooding (LSWF) have gained prominence. For several decades, several investigators discovered benefits from LSWF. Smith (1942) [1] used low-salinity brine over fresh water for fluid injection, resulting in an increase of 15% in oil production in sandstone rocks. Reiter (1961) [2] found that clay hydration improved oil recovery by 21.3% compared to using oil-high salinity water. Zhang et al. (2007) [3] demonstrated that sodium chloride solution at 1,500 ppm was adequate to improve oil recovery, while Webb et al. (2005) [4] suggested an optimal range of low-salinity water around 1,000-2,000 ppm salinity to obtain positive effects in enhancing oil recovery. Nevertheless, the salinity threshold for LSWF is typically considered to be in the 4000-5000 ppm range, as supported by various researchers [3, 5-9]. Low-salinity water can yield benefits through several oil recovery mechanisms, such as 1) generating multi-component ion exchange (MIE), resulting in a change in rock wettability; 2) raising the pH value, favoring the generation of in-situ surfactant; and 3) provoking the liberation of clay particles together with oil drops. Nevertheless, it is nowadays difficult to confirm the contribution of each mechanism. Assessing the petrophysical properties of rock before and after the process could then be evidence for confirmation. In this study, the change of relative permeability curves comprising relative permeability to oil and to water is observed. Relative permeability data is obtained from an unsteady state technique known as the Johnson-Bossler-Nauman (JBN) technique. The data is matched with generated curves using Corey's correlation,

* Corresponding author: Tina Tharn
E-mail: 6570802121@student.chula.ac.th; Tel: +66-98-570-5213

and the best matching curves with Corey's exponents are used for discussion. The assessment is also performed by measuring the concentration of ions in the effluent from the coreflood experiment. As shaly sandstone is enriched by illite and kaolinite, the detection of ions in water is mainly based on calcium and magnesium ions, which are ions that can create interactions with organic acid in the oil phase, causing the shaly sand surface to be more oil-wet.

Identifying oil recovery mechanisms from low-salinity waterflooding would be important for future studies, especially for creating water formulations to fit specific reservoir characteristics. Moreover, the obtained relative permeability curves will be useful for studies at the macroscopic scale, such as those using reservoir simulation, which is an important step prior to field implementation.

2 METHODOLOGY

2.1 Coreflood Experiment

Coreflood experiments were performed using Coreflood apparatus. Shaly-sandstone core sample from Sirikit oilfield, located in the north of Thailand, was used to represent reservoir rock in this study. Two core samples were utilized in this study. Core A has 17% porosity, 106 mDarcy in absolute permeability, and 31% clay content. Core B had 18.5% porosity, 107 mDarcy, and a 42% clay content. The clay contents of both cores were mainly illite, followed by kaolinite. Crude oil from the Sirikit oilfield was mixed with dodecane at a ratio of 3:7 (crude oil to dodecane) to avoid the formation of internal wax during the experiment. Formation water was synthesized using the water formation of the Sirikit oilfield with a total dissolved solid of 14,098 ppm. Two experiments were selected to be performed using low salinity water at 5,000 and 1,000 ppm. A water formulation was prepared to consist of potassium ions, calcium ions and magnesium ions, using a mass ratio of chloride salt of 1:2:2. Core A was selected to perform with a low-salinity water formulation of 5,000 ppm, whereas Core B was used for low salinity water at 1,000 ppm. Figure 1 illustrates the laboratory setup for this experiment. Coreflooding was performed using an injection rate of 0.5 cc/min under a confining pressure of 2,500 psi and a reservoir temperature of 50 Celsius. Produced oil was collected to calculate oil recovery, and differential pressure was detected for the relative permeability curves. Portions of effluent were collected for the observation of fine migration and the detection of liberated ions during the process. The detection of calcium ion and magnesium ion was conducted by color titration using Ethylene Diamine Tetraacetic Acid as a titrant using

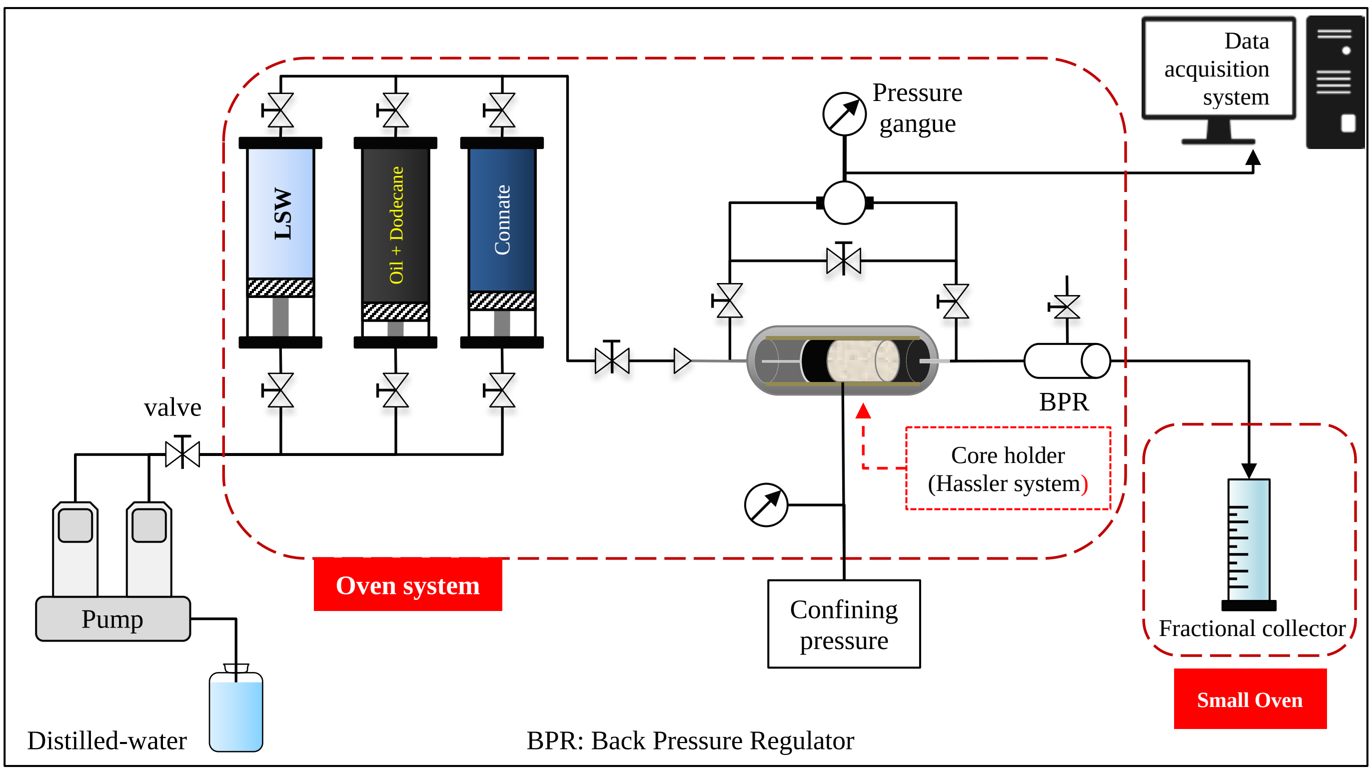

Figure 1. An illustration of the coreflooding laboratory setup includes three chambers filled with low-salinity water, oil, and connate water. Core holder ais typically manufactured using the Hassler system. Back pressure regulators (BPR) must be used to diminish the effect of pressure shock. The pressure for injection must be maintained at 300 psi lower than the pressure for confining.

Eriochrome Black T (EBT) and Hydroxy Naphthol Blue (HNB) as color indicators.

2.2 Johnson–Bossler–Naumann (JBN)

The collected data from coreflood experiments is crucial for the scientific analysis of the relative permeability characteristics. The most suitable analysis for unsteady-state was called Johnson, Bossler, & Naumans (JBN), which is better for two-phase flow through porous media [10]. It plays a vital role in understanding how fluids flow within underground formations, particularly in the context of the oil and gas industry. To obtain the relative permeability of each phase at a specific water saturation, which is calculated from JBN analysis, experimental data from the core flood must be recorded for instant

- Q_i : Quantity of displacing phase injected

$$Q_i = \frac{Q_t}{V_P} \tag{1}$$

where:

Q_t	: Volume of liquid produced	(ml)
V_P	: Volume of pore space	(ml)

- ΔP : Pressure differential (psi)
- ΔP_i : Pressure differential at initial conditions (psi)
- Q_o : Volume of oil produced (ml)
- Q_w : Volume of water produced (ml)

To evaluate the relative permeability curve from JBN analysis, there are several calculation stages are involved such as:

- The value of S_{wav} after breakthrough will be calculated from eq (2)
- The value of k_{ro} & k_{rw}

the fractional flow will be calculated from the equation above:

$$f_o = \frac{dS_{wav}}{dQ_i} = \frac{Q_o}{Q_t} = \frac{Q_o}{Q_{w,inj}} = \frac{1}{1+{k_{rw}\mu_o}/{k_{ro}\mu_w}} \tag{2}$$

where:

S_{wav}	: Average water saturation	
μ_o, μ_w	: Oil viscosity and water viscosity	(cp)

The relative permeability value will be calculated from the ratio of effective permeability and absolute permeability (from the coreflooding experiment).

$$k_{r,n} = \frac{k_{eff,n}}{k_a} \tag{3}$$

Darcy equation

$$k_{eff,n} = \frac{q \times \mu_n \times L}{A \times \Delta P} \tag{4}$$

Where:

k_a	: Absolute permeability	(md)
n	: fluid phase	(oil, water)
q	: fluid flow rate	(cc/mn)
A	: Cross area of core	(cc)
ΔP	: Pressure drop	(psi)

2.3 Data Extrapolation

Since most of the actual data (k_{rw} and k_{ro}) were accumulated at the end-point, Corey-correlation must be the preferred approach in this circumstance. However, the Corey-exponent number must be adequate and representative of actual data. The results from Corey-correlation (k_{ro} and k_{rw}), which are calculated in a range similar to actual saturation data, are considered predicted data. Additionally, the root mean square error (RSME) is used in numerical regression techniques. The Corey-exponent with the best match will be iterated until the RSME is the minimum value.

Corey-correlation

$$k_{rw}(S_w) = k_{rw,or}\left(\frac{S_w - S_{cw}}{1 - S_{cw} - S_{or}}\right)^{n_w} \tag{5}$$

$$k_{ro}(S_w) = k_{ro,cw}\left(\frac{1 - S_w - S_{or}}{1 - S_{cw} - S_{or}}\right)^{n_o} \tag{6}$$

Where:

$k_{rw,or}$	: relative water permeability at S_{or}
$k_{ro,cw}$	: relative oil permeability at S_{cw}
S_{cw}	: connate water saturation
S_w	: water saturation
S_{or}	: irreducible oil saturation
n_w, n_o	: Corey exponent for water, oil

Root means square error (RSME):

$$RSME = \sqrt{\frac{1}{N}\sum_{i=1}^{N}(\hat{y}_i - y_i)^2} \tag{7}$$

N	: The total amount of data
$\hat{y}_i$	: Predicted $k_{r,n}$ from Corey-correlation
y_i	: Actual $k_{r,n}$ from JBN analysis

3 RESULTS AND DISCUSSION

Production data, including recovery factor and differential pressure across the core sample throughout the experiment of case no. 1 (core A), is illustrated in Figure 2. As mentioned in the methodology, this experiment was conducted by injecting formation water first at a salinity of 14,098 ppm and switching to low-salinity water at 5,000 ppm once the pressure difference was constant. Due to the gradual increment of oil recovery during 0.25 to 1.0 and 2.5 to 3.5 injected pore volumes of water, relative permeability to oil and to water data can be generated using the JBN technique. Corey's correlation was then used to generate the relative permeability curves, and the best-fitting curves were identified using Root Mean Square Error (RSME).

Figure 3 depicts the relative permeability to oil and water during injection of formation water and low salinity water, respectively.

From Figure 3, it can be observed that there are two major appearances that obviously changed: 1) reduction of end point relative permeability to water, and 2) increment of end point water saturation. From these two major changes, it can be explained that the effects provided by low-salinity water result in the liberation of oil, which causes flow paths in the aqueous phase. At the end of the process, differential pressure was reduced compared to the period of injection of formation water, and hence, the end-point relative permeability to water was relatively smaller during low salinity waterflooding. The Corey's exponent for oil is changed from 2.1 to 2.4, and the Corey's exponent for water is changed from 1.3 to 1.6. The magnitude of the change is relatively small, and this can be

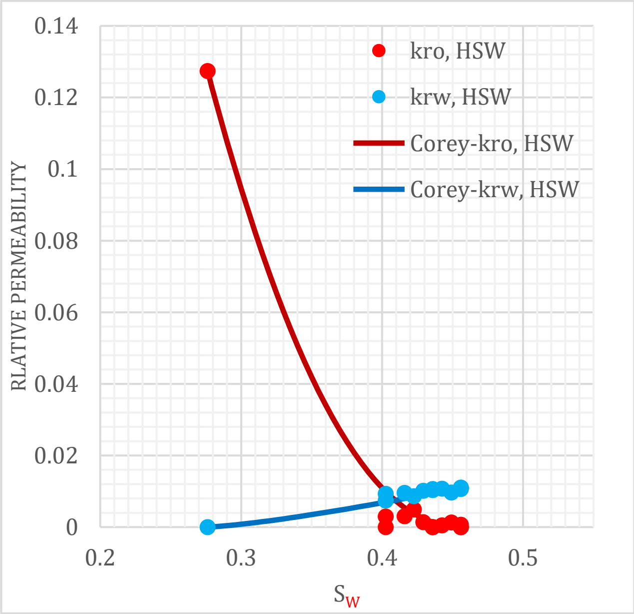

Figure 2. Recovery factor and differential pressure as a function of injected pore volume of water from case no.1 (Core A)

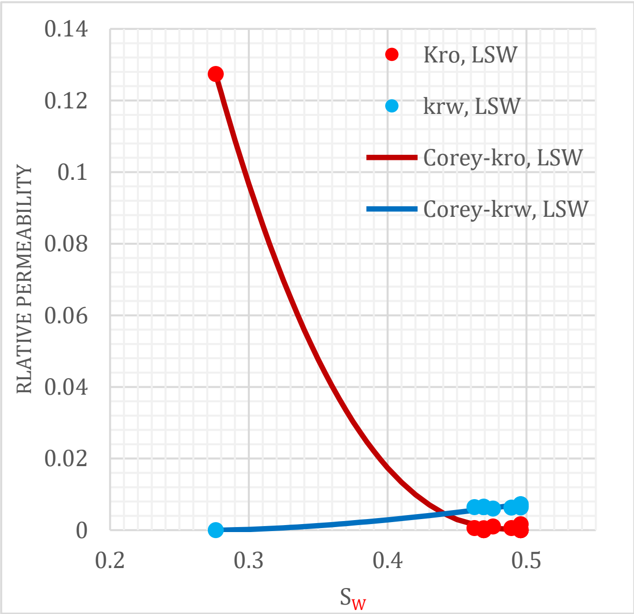

Figure 3. Relative permeability to oil and to water obtained from (left) injection of formation water (right) low salinity waterflooding from case no.1 (Core A)

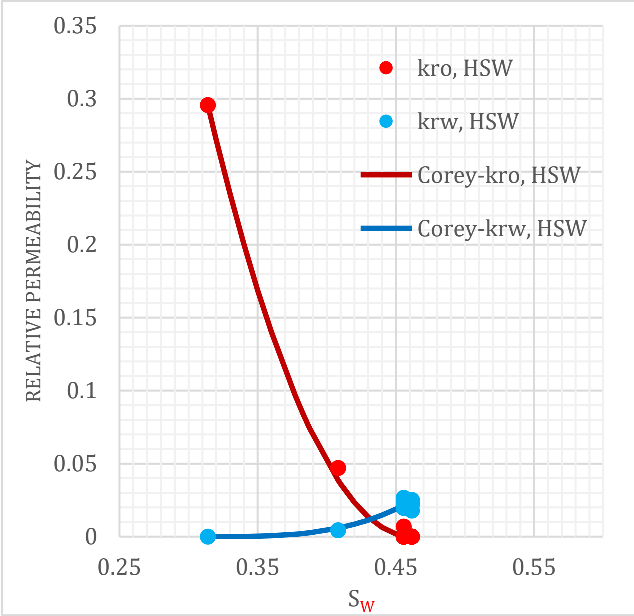

Figure 4. Recovery factor and differential pressure as a function of injected pore volume of water from case no.2 (Core B)

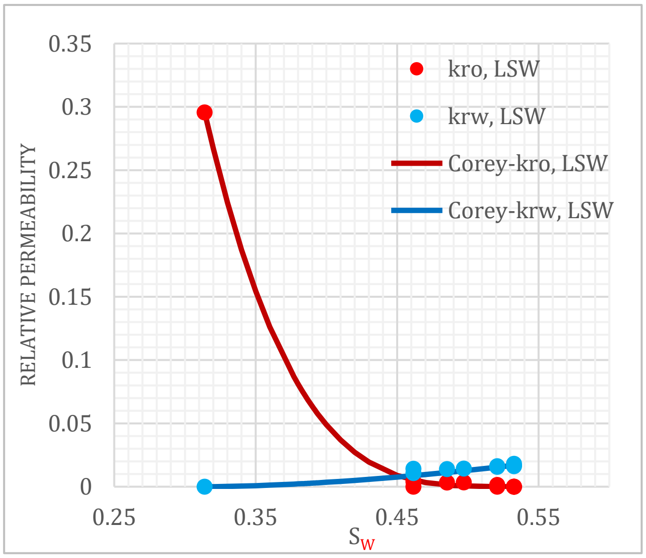

Figure 5. Relative permeability to oil and to water obtained from (left) injection of formation water (right) low salinity waterflooding from case no.2 (Core B)

explained by the fact that additional production of oil may come from oil recovery mechanisms that do not involve the changing of rock preference. The incremental oil recovery in this case is 4.6.

For case no. 2, which was conducted on core B, the recovery factor and differential pressure across the core sample are shown in Figure 4. Similar to the previous case, the gradual increment of oil recovery during injection of formation water and low-salinity water allows the construction of relative permeability curves using the JBN technique. Figure 5 illustrates the relative permeability of oil and water during injection of formation water and low salinity water, respectively.

From Figure 5, it can be observed that two major appearances, as explained for case no. 1 also appear in this case. However, Corey's exponent to oil is changed from 2.0 to 3.6, whereas Corey's exponent to water is remarkably changed from 3.2 to 1.7. The magnitude of changing is larger in these cases for both oil and water. For oil, the increment in curvaceous could be explained by combining the relative permeability to oil during injection of formation water and low salinity water injection together, as shown in Figure 6.

From the figure, the curvaceous of relative permeability to oil is slightly change to extension of data near the end point of relative permeability to water. Similar to relative permeability to oil, the reduction of relative permeability to water is due to the extension of the data, and hence, the alteration of curvaceous is not obvious. Even though the incremental of oil recovery in this

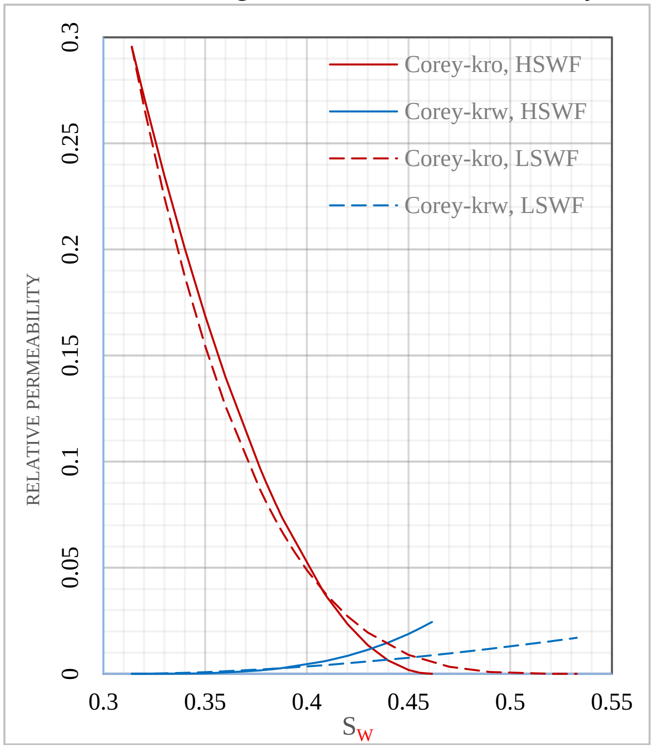

Figure 6. Comparison of relative permeability to oil and to water obtained from injection of formation water and low salinity waterflooding from case no.2 (Core B)

case is 10.4 which is much larger compared to the previous case, the cause of improvement may not be involved with changing of rock preference. Table 1 summarizes important data from case 01 and case 02.

Table 1. Summary of important parameters from coreflood tests and assessment of relative permeability curves

	Case 01	Case 02
Water formulation (ppm)	5,000	1,000
Incremental RF (%)	4.6	10.4
Corey's exponent oil (formation water/LSW)	2.1/2.4	2.0/3.6
Corey's exponent water (Formation water/LSW)	1.3/1.6	3.2/1.7

The results from ion titration from effluents are summarized in Table 2. Observation fluid turbidity is also included.

Table 2. Summary of ion concentrations and observation of fluids from the tests.

Observation	Case 01	Case 02
Calcium ion during formation water injection (ppm)	27.05	27.39
Calcium ion during LSW (ppm)	9.05	27.39
Magnesium ion during formation water injection (ppm)	21.27	16.05
Magnesium ion during LSW (ppm)	3.65	53.07
Appearance of turbidity	Yes	Yes

From the table, it can be observed that during low-salinity flooding using 5,000 ppm, reduction of calcium and magnesium ions can be observed. As these two ions are important in linking oil droplets and rock surfaces, the smaller amount of liberated ion can be related to the smaller rate of ion exchange. For case 02, where a water formulation of 1,000 ppm is utilized, the presence of potential ions important for oil recovery mechanisms, together with low salinity conditions, helps the mechanism occur. Higher amounts of calcium and magnesium ions, together with a higher oil recovery factor, conclude that multi-component ion exchange may occur. Moreover, the appearance of turbidity in the water was observed in both cases during the change from formation water injection to low salinity water flooding. This supports the idea that not only MIE but also fine migration may occur at the same time.

4 CONCLUSIONS

From the assessment of the curvature of relative permeability curves, it can be observed that the changing of Corey's exponents is due to the extension of fluid saturation, resulting in an adjustment of the curvature. Lacking the distribution of data throughout water saturation is still a problem with the unsteady state technique to estimate the curvature of the whole line. Nevertheless, physical observation reveals that the curves are insignificantly changed, which can be due to the fact that rock may not change the wetting preference from oil to water.

Results from titration and observation of the turbidity of effluents support the theory that oil recovery is improved by the liberation of oil due to multi-component ion exchange and fine migration. With the better improvement of oil recovery, the amount of calcium and magnesium ions in the effluent has increased.

The future study will aim for an analytical study of rock composition before and after contact with low-salinity water. Determination of elemental change and observation of pore surface structure would confirm the oil recovery mechanisms during the process.

ACKNOWLEDGMENTS

The authors would like to thank PTT Exploration and Production Public Company Limited for providing rock samples, oil samples, and information on formation water.

REFERENCES

[1] Smith, K.W. *Brines as Flooding Liquids. Seventh Annual Technical Meeting*. in *Seventh Annual Technical Meeting*. 1942. Mineral Industries Experiment Station: Pennsylvania State College.

[2] Reiter, P.K., *A water-sensitive sandstone flood using low salinity water*. 1961, University of Oklahoma.

[3] Zhang , Y., X. Xie , and N.R. Morrow *Waterflood Performance by Injection of Brine with different Salinity for Reservoir Cores*, in *SPE Annual Technical Conference and Exhibition*. 2007: Anaheim, California, USA.

[4] Webb, K.J., C.J.J. Black, and G. Tjetland, *A Laboratory Study Investigating Methods for Improving Oil Recovery in Carbonates.*, in *SPE International Petroleum Technology Conference,*. 2005: Doha, Qatar.

[5] Al-Shalabi, E.W. and K. Sepehrnoori, *A comprehensive review of low salinity/engineered water injections and their applications in sandstone and carbonate rocks.* Journal of Petroleum Science and Engineering, 2016. **139**: p. 137-161.

[6] Boussour, S., et al. *Oil recovery by low salinity brine injection: Laboratory results on outcrop and reservoir cores*. in *SPE Annual Technical Conference and Exhibition*. 2009. OnePetro.

[7] Lager, A., et al., *Low salinity oil recovery-an experimental investigation1*. Petrophysics-The SPWLA Journal of Formation Evaluation and Reservoir Description, 2008. 49(01).

[8] Ligthelm, D.J., et al. *Novel waterflooding strategy by manipulation of injection brine composition*. in *EUROPEC/EAGE conference and exhibition*. 2009. OnePetro.

[9] McGuire, P., et al. *Low salinity oil recovery: An exciting new EOR opportunity for Alaska's North Slope*. in *SPE wesstern regional meeting*. 2005. SPE.

[10] Apostolos, K., J. Bryan, and S. Taheri, *Fundamentals of Fluid Flow in Porous Media.* PERM Inc TIPM laboratory, 2016.

Techno-Science Research Journal 12 (Special Issue) 23-31

Content list available at ITC

Techno-Science Research Journal

Journal Homepage: www.ric.itc.edu.kh

Techno-Science Research Journal

Geology and Mineralization at Okvau Gold Deposit, Keo Seima District, Mondulkiri Province, Cambodia

Ni Sokmeng[1*], Oy Kimhouy[1,2], Him Daravichet[1], Pich Bunchoeun[1], Chea Monyneath[1], Bo Malis[1], Kotaro Yonezu[2], Seang Sirisokha[1], Sio Sreymean[1], Thim Sethi [1]

[1]*Faculty of Geo-Resources and Geotechnical Engineering, Institute of Technology of Cambodia, Phnom Penh, Cambodia*
[2] *Department of Earth resources Engineering, Kyushu University, Japan*

Received: 22 August 2023; Accepted: 15 May 2024; Available online: August 2024

Abstract: *Australian Renaissance Minerals (Cambodia) Limited, a 100%-owned company, has discovered gold mineralization in the Okvau gold deposit in the Keo Seima district of Mondulkiri province. This study aims to determine petrographic characteristics and ore mineralization at Okvau Gold Deposit, as an initial guide for further exploration stages. Handspecimen, ore microscopy and scanning electron microscope (SEM) and energy Dispersive X-ray Spectroscopy (EDS) and previous analysis of petrographic and X-ray Fluorescence (XRF), are conducted in this study. The hand specimen, previous petrographic analysis shows the three main rock units such as diorite,* hornfels, *and mafic dyke. Major elements results from previous analysis XRF analysis suggest that intrusive rocks in the study area is diorite, which classify into medium calc alkaline nature. Moreover, the intrusive in the area are predominantly I-type granite. The intrusive rock plot within the volcanic-arc granites and syn-collisional granite field (VAG+Syn-COLG). The "Okvau Gold Deposit" contains with the association of sulfide minerals such as arsenopyrite, pyrrhotite, and pyrite that have been found associated during the complex intrusion process of the hydrothermal fluid exsolved by crystallizing magma. Gold mineralization is concentrated along a network of brittle/ductile shears and arsenopyrite-rich sulphide veins. The Okvau gold deposit area and other gold occurrences within the exploration licenses are directly associated with diorite intrusions and are best classed as Intrusive Related Gold mineralization.*

Keywords: Okvau gold deposit, Ore mineralization, Petrographic, Scanning Electron Microscope (SEM), Energy Dispersive X-ray spectroscopy (EDS), Intrusion Related Gold Deposit (IRGD), X-Ray Fluorescence (XRF), Renaissance Minerals Limited (RNS)

1. INTRODUCTION

Australian Renaissance Minerals (Cambodia) Limited (RNS), which located in the Okvau gold deposit of the Keo Seima district, southwest of Mondulkiri province, has intersected ore mineralization associated with gold. Gold at the Okvau deposit is concentrated along a network of brittle shears and arsenopyrite-rich sulphide veins [7] It is dedicated to the exploration, development and operation of the Cambodian Gold Project. The company is 100% owned by Emerald Resources NL, an ASX-listed company established with international capital. Furthermore, "Okvau Gold Deposit" in which the sulfide minerals have found during the complex intrusion process of the hydrothermal fluid exsolved by crystallizing magma and typically, it was found associated with felsic and intermediate igneous rocks such as diorite, granodiorite, hornfels rock and dike, often occurring with the layered complexes of stocks [7]. Intrusion Related Gold deposits, encompassing various deposit styles, including skarns, mineralized breccia, sheeted veins, and disseminations within or peripheral to the intrusion [1], [2] & [3] And in some case, RNS has been granted a license by the Ministry of Mines and Energy of Cambodia to conduct a pre-feasibility study on the potential for gold mineralization in the Okvau gold deposit area, which is closely related to the IRGD and represents a significant class of gold mineralization. This present research aims to interpret petrographic characteristics using a transmitted light microscope, analyze ore mineralization using a reflected light microscope and SEM analysis, and perform X-ray fluorescence (XRF) analysis for comprehensive whole rock geochemical analysis, all of which are related to the conditions of Intrusion-Related Gold Deposits (IRGD).

2. GEOLOGICAL FRAMEWORK

2.1 Regional Geology

Southeast Asia's Indochina Terrane includes Cambodia in its southernmost region. During the middle Carboniferous to the late Triassic, the Indosinian Orogeny created the Indochina Terrane. Cambodia is located in the south-central SE Asia, a

* Corresponding author:Kimhouy Oy
E-mail:oykimhouyitc@gmail.com

region characterized by a prominent geotectonic framework comprising five magmatic belts: the Loei Fold Belt, Truong Son Belt, Central Belt, Dalat-Kratie Belt, and Wuntho PoPa Belt (Fig 1) [22]. Each of these belts is endowed with Cu-Au and Au mineralization that was generated in plate subduction-related settings.

Gold mineralization is confined in a north-east-trending fracture, primarily hosted within a small diorite apophysis. However, it also extends into the metasediments beyond the diorite contact. Beneath Indo-China, western Laos, Cambodia, and southern Vietnam lies the extensive Kontum Metamorphic Complex or Kontum Massif. This vast region comprises Permo-Carboniferous metamorphosed shallow marine to upper arc volcanic rocks. Following the Indo-Sinean collision in the Carboniferous, this metamorphic complex was created in rifting settings. Okvau is located in the central part of the Dalat-Kratie Belt, an area characterized by Cretaceous subduction zone activity. This belt is associated with Au-systems featuring quartz–sulphide veins. The deposits in this region are strongly indicative of being related to intrusive-related gold, primarily hosted within granitic rock formations. This geological context is notable in eastern Cambodia and Tien Thuan in southern Vietnam [7].

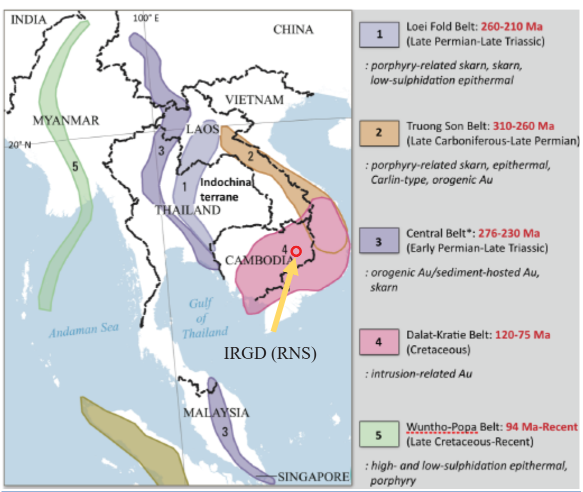

Fig.1. Metallogenic Belts of SE Asia, where the Okvau Gold Deposit was found in Dalat-Kratie Belt in Mondulkiri province [22]

2.1. Previous study of Geology and Ore Mineralization at Okvau Gold Deposit, Renaissance Mineral (Cambodia) Limited

Previous exploration endeavors within the Okvau Gold Deposit area, along with other gold occurrences within exploration licenses, have consistently shown a direct association with diorite intrusions, classifying them as Intrusive Related Gold mineralization. Exploration to date has demonstrated the potential for large scale gold deposits with the geology and geochemistry analogous to other world-class Intrusive Related Gold districts [22]. There are numerous high priority exploration prospects based on anomalous geochemistry, geology, and geophysics which remain untested with drilling. These targets are all located within close proximity to the Okvau gold deposit area [8]. Gold mineralization is concentrated along a network of brittle/ductile shears and arsenopyrite-rich sulfide veins (Fig 2).

The greater width of the alteration haloes around the shears and textural evidence of movement along the shears implies they, rather than the narrow veins, were the principal fluid conduits within the Okvau gold deposit area. Gold-bearing fluids presumably accessed the fractured mesh, which hosts the auriferous sulfide veins, via the more strongly altered shears. The Okvau gold deposit area and other gold occurrences within the exploration licenses are directly associated with diorite intrusions and are best classed as intrusive-related gold mineralization (Fig 2) [8].

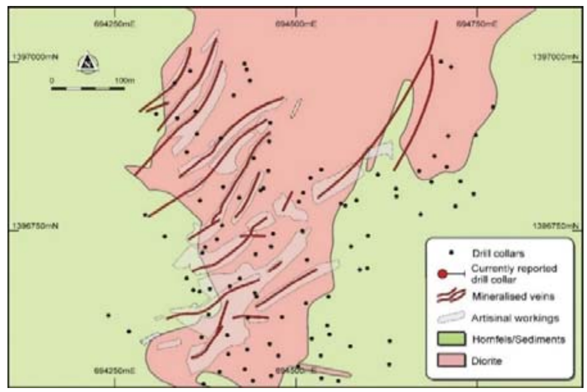

Fig.2. The principal controls on the mineralization are interpreted to be parallel to the western diorite contact with the Hornfels/Sediments. However, the low angle dipping planar shears (hornfels/sediments bedding parallel) also exert influence on the 3D distribution of the mineralization. Consequently, gold grade continuity is best defined as parallel to low dipping shears within the diorite, which have a shallow to moderately dipping orientation to the southeast [8]

2.2. Previous study of whole-rocks geochemistry

Sample GC136286 and GC138288 were known to be "Diorite", which is plotted into medium Calc-alkaline by using element percentage of silica and potassium oxide; [23], the diorite was plotted into I-type granite [24]. Additionally, the classification of rock is based on the ASI values. The ASI values less than 1.1 suggest that intrusive in the area predominantly exhibit I-type granite affinity [24]. The tectonic discrimination diagram for granite (after Piearce et al., 1984) shows the fields of syn-collisional granites (syn-COLG), within-plate granites (WPG), volcanic-arc granites (VAG), and ocean-ridge granites (ORG). The rock from the study area plot within the VAG granite field, and using the Y and Nb diagram, the result is ploted in VAG+Syn-COLG (volcanic-arc granites and syn-collisional granite field) [25].

3. METODOLOGY

The study involved Petrographic and Ore Microscopy analyses. The rock samples were examined using a transmitted-light microscope and X-ray Fluorescence (XRF) to identify the rock units and rock geochemistry characteristics, respectively. Additionally, samples associated with ore mineralization were analyzed using a reflected-light microscope and Scanning Electron Microscope with Energy-Dispersive X-ray Spectroscopy (SEM-EDX) to describe the mineralogy of the gold-bearing samples. These analyses were conducted at the laboratory of the Faculty of Geo-resources and Geotechnical Engineering, Institute of Technology of Cambodia, Cambodia. In addition, there are 3 samples were used in Petrographic-Thin Section and 2 of intrusion sample were used in XRF and the other 3 massive ore samples were used in Petrographic-Polished Section and SEM-EDS.

4. RESULTS AND DISCUSION

4.1. Rock units' characterization

Eight (8) representation samples were selected for hand specimen analysis (Fig. 4), petrographic, and ore microscopy analyses. According to hand specimen inspection, the samples with the codes of GC136289 (Fig. 4A), GC136287 (Fig. 4D), GC136291 (Fig. 4G) and RNS01 (Fig. 4H) were identified as having ore mineralization associated with diorite. These rocks are characterized by the presence of quartz-pyrite and large arsenopyrite veins, as well as substantial ore content within the quartz veins. On the other hand, samples GC136286 (Fig.4B) and GC136288 (Fig. 4C) exhibit medium-gray hues and an overall medium-grained, phaneritic texture, indicating diorite rock in terms of its physical properties. The samples of GC136283 (Fig. 4E), GC136285 (Fig. 4F) are dark color, fine-grained hornfels rock. Due to the hydrothermal fluid injection, some part of rock units was changed its original form.

Diorite unit

Igneous rocks "Diorite" in the area have undergone weak to moderate pervasive alteration. This alteration has resulted in the replacement of primary igneous minerals by secondary phases, including secondary mineral of sericite, and ore mineralization. In rocks displaying propylitic alteration, minor veining is observed, featuring assemblages containing K-feldspar, quartz, carbonate, pyrrhotite, arsenopyrite, chalcopyrite, and pyrite, as confirmed as in the documented by [8]. A subset of the igneous rocks exhibits more pronounced hydrothermal alteration, characterized by the replacement of primary minerals with secondary assemblages that may include K-feldspar, biotite, quartz, and sulfides. Notably, locally, K-feldspar displays a habit characteristic of adularia. These extensively altered igneous rocks are interpreted as potential examples of endoskarn replacement.

Fig.4. Photographs of representative wall rocks and ore veins in Okvau Gold Deposit. A, B, and C are diorite, and cut by mineralized vein (A). E and F are fine-grained hornfels, D, G, and H are massive ore veins within diorite wall rock. Abbreviation: As= Arsenopyrite; Cpy= Chalcopyrite; Py= Pyrite; Po= Pyrrhotite.

Within these rocks, localized veins are present, featuring assemblages comprising quartz, and arsenopyrite (fig 4 (B&C)).

Diorite units of GC136286 and GC136288 are composed primarily of the quartz and a few accessory minerals, such as hornblende. Quartz, hornblende, and plagioclase were the principal component minerals. Furthermore, some part of the minerals was altered to secondary minerals. Plagioclase feldspar is slightly replaced by the slightly secondary mineral's Sericite. Sericite is an abundance of alteration minerals observed under the microscope. The major elements of the igneous rocks in the research area have been analyzed by X-ray Fluorescence (XRF). The percentage of major chemical composition is plotted in the TAS diagram for classifying the igneous rocks encountered in the research area by using the percentage of total alkalis and silica in each sample. Intrusive rock from the Okvau gold project is plotted on the Total Alkalis versus Silica (TAS) diagram for chemical classification of igneous rock [26]. Major element data suggest that intrusive rocks in the study area is diorite [25].

Hornfels unit

The rocks with sedimentary protoliths are identified as having originated from a calcareous protolith, which has subsequently undergone recrystallization into fine-grained contact metamorphic rocks known as hornfels, occasionally displaying a strongly porphyroblastic calc-silicate assemblage Hornfels units (Fig.4 (E&F)).

These rocks have been recrystallized to form biotite-bearing quartz-feldspathic hornfels, although some also contain carbonate, actinolite, and sulfides. Minor veining observed in these rocks includes K-feldspar, carbonate, and actinolite. Metamorphic grade in the metasedimentary rocks may have achieved hornblende hornfels facies, although some assemblages are not diagnostic of grade (Fig.4 (E&F)).

Mafic Dyke Unit

The hand specimen was applied. The mafic dyke of the sample of GC136284 is dark-grey-green in color with fine to medium grain size (fig. 5).

Fig.5. Mafic dike at Okvau gold deposit.

Based on [8] reported by King, the various dykes at Okvau and commented as follows: The diorite and sedimentary country rocks are cut by dykes and sills of differing styles, but the most common are massive mafic dykes. The intrusion of the mafic dyke spans (but largely postdates) faulting on "mylonitic"-style faults and shears, and post-dates arsenopyrite mineralization which was not found in structures deforming the dykes. Many examples of passive mafic dykes can be found with unfaulted contacts and no internal deformation or veining. A significant number of dykes intrude pre-existing, often mineralized, faults. Dykes can therefore mask significant fault zones, which may not be logged as such (as a consequence). There are many examples where alteration or deformation levels change significantly across an undeformed dyke. There are no obvious examples of strongly sheared dykes but some are clearly intruded into active fault zones and have faulted contacts – commonly formed by carbonate laminated shears and sometimes "mylonitic" structures. The mafic dyke event is thought to span the waning phases of significant fault movements. Other dykes are intruded into fault zones, post movement, and have undeformed margins. Examples of porphyritic dykes are occasionally present but are much less common than the aphyric mafic dykes. They are interpreted to have been intruded in the early stages of the dyke event as they are commonly more altered and have faulted margins. Porphyritic margins can be found to aphyric dykes. An even earlier dyke phase has been recognized but is uncommon. These are grey, altered, porphyritic dykes which contain blebs of pyrrhotite or pyrrhotite and arsenopyrite.

4.2. Ore Mineralization

Based on the hand specimen analysis, ore mineralization was discovered in the research region, which includes arsenopyrite, pyrrhotite pyrite, chalcopyrite and covellite (Fig.7). These minerals occur in the form of quartz veins was found of containing with small amount of gold and other type of metals during the processing process and geochemistry process. They are also disseminated within the wall rocks surrounding the vein, and are associated with massive ore related to both vein and intrusive rocks. The quartz vein is commonly segmented with massive, brecciated and fracture textures (Fig 6A – Fig. 6D).

The goal of ore microscopic analysis is to identify the ore minerals present in the samples of RNS01, GC136289, and GC136291. Polished sections of specimens, following the methodology outlined by Hughes (1971), were examined under a polarizing microscope, to determine the ore minerals and their paragenetic sequences. In this study, a polarizing microscope was utilized in conjunction with a camera and screen to capture photomicrographs of ore minerals. This analysis used different type of light compared to petrographic analysis, employing reflected light, plane-polarized light (PPL), and cross-polarized light (XPL) interchangeably to produce distinct optical characteristics. Under PPL, recognized attributes include color, bi-reflectance, pleochroism, and cleavage, while under XPL, other features such as isotropic/anisotropic behavior, polarization color, and internal reflection can be detected. Intergrowth patterns among ore minerals are also studied under both lighting conditions. The ore minerals identified include arsenopyrite, pyrrhotite pyrite, chalcopyrite, and covellite (Fig.7), which are closely associated with Intrusion-Related Gold Deposit (IRGD) based on the metal mineralization.

Scanning Electron Microscopy (SEM) and Energy Dispersive X-ray Spectroscopy (EDS) Analyses

Automated determination of mineralogy, based on a Scanning Electron Microscope (SEM), involves the use of an electron beam. Accurate textural analysis and the associated distribution of minerals within the rock texture are key to accurately describe the physical and chemical aspects of a rock system. SEM functions by intensely concentrating on assessing the presence of ore minerals. The EDS detector is the tool utilized for measuring the energy of the emitted photons in the X-ray electromagnetic spectrum. Depending on the surface topography, secondary electrons are released when a beam electron contacts a sample. These electrons are used to detect the ore minerals and can be presented as images (Fig 8).

Mineralization such as arsenopyrite, pyrrhotite, pyrite, chalcopyrite and covellite can be detected in SEM-EDS based on their chemical components, which help clarify the formation of ore mineralization in the samples (Fig 7). The EDS detector uses X-ray electromagnetic spectrum on the ore's surface, detecting elements such as As, Fe, S (arsenopyrite), Fe, S (pyrite), Cu, Fe, S (chalcopyrite), and Cu, Fe, S (covellite), as well as Fe, S (iron component). SEM can provide a detailed interpretation and clarification of the ore through imaging, which is consistent with observations under reflected light microscope (Fig.8).

The main ore minerals consist of arsenopyrite, pyrite, pyrrhotite, and a minor amount of chalcopyrite and covellite. Gangue minerals present include quartz, calcite.

Fig.6. Selection part of samples for polished analyses were represented ore mineralization at Okvau gold deposit. **Abbreviation:** Arsenopyrite (As); Chalcopyrite (Cpy); Pyrite (Py), Pyrrhotite (Po) and Quartz (Qtz).

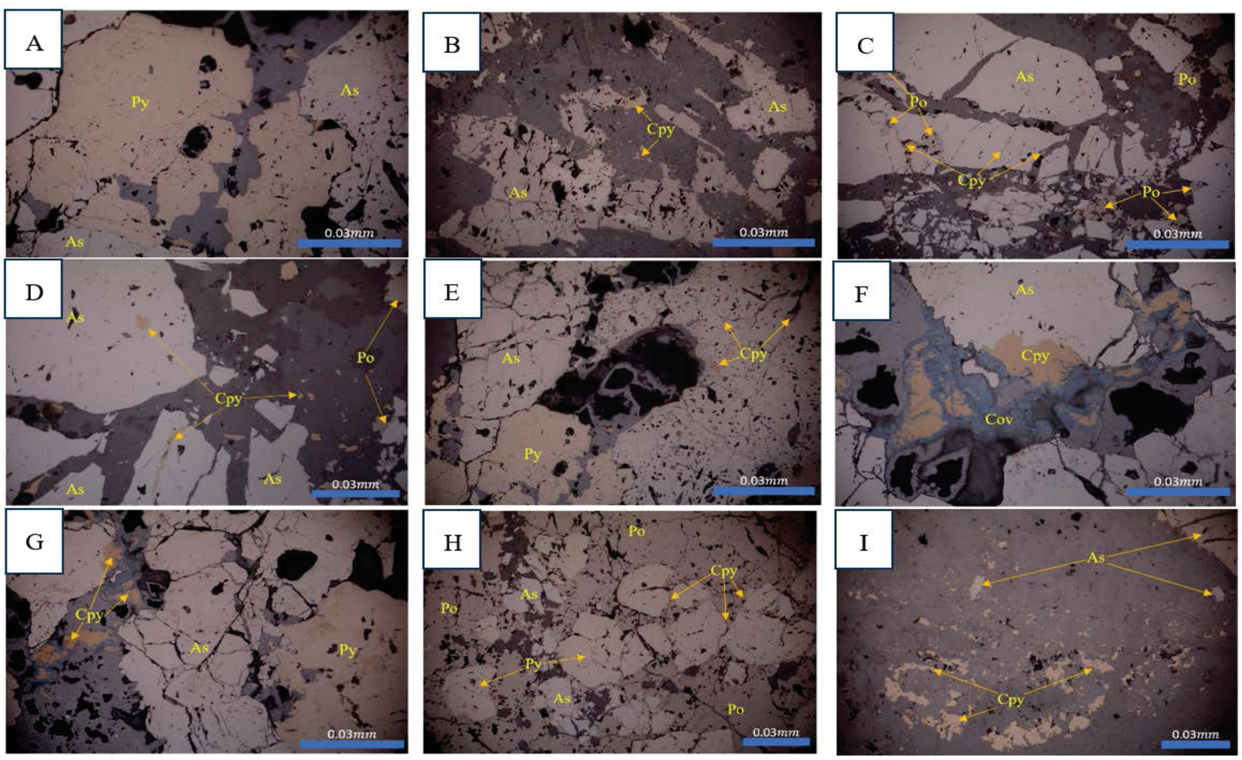

Fig.7. Reflected light photomicrographs taken during the petrography analysis of selected samples from GC136289, GC136291, and RNS01 reveal the presence of sulfide minerals, including arsenopyrite (creamy-white), chalcopyrite (yellowish), pyrite (brassy-yellow), pyrrhotite (brownish-pink), and covellite. Based on the RNS, these sulfide minerals are currently associated with gold mineralization, and they are abbreviated as follows: arsenopyrite (As), chalcopyrite (Cpy), pyrite (Py), pyrrhotite (Po), and covellite (Cv).

Images of Scanning Electron Microscope (SEM-EDX) Analysis

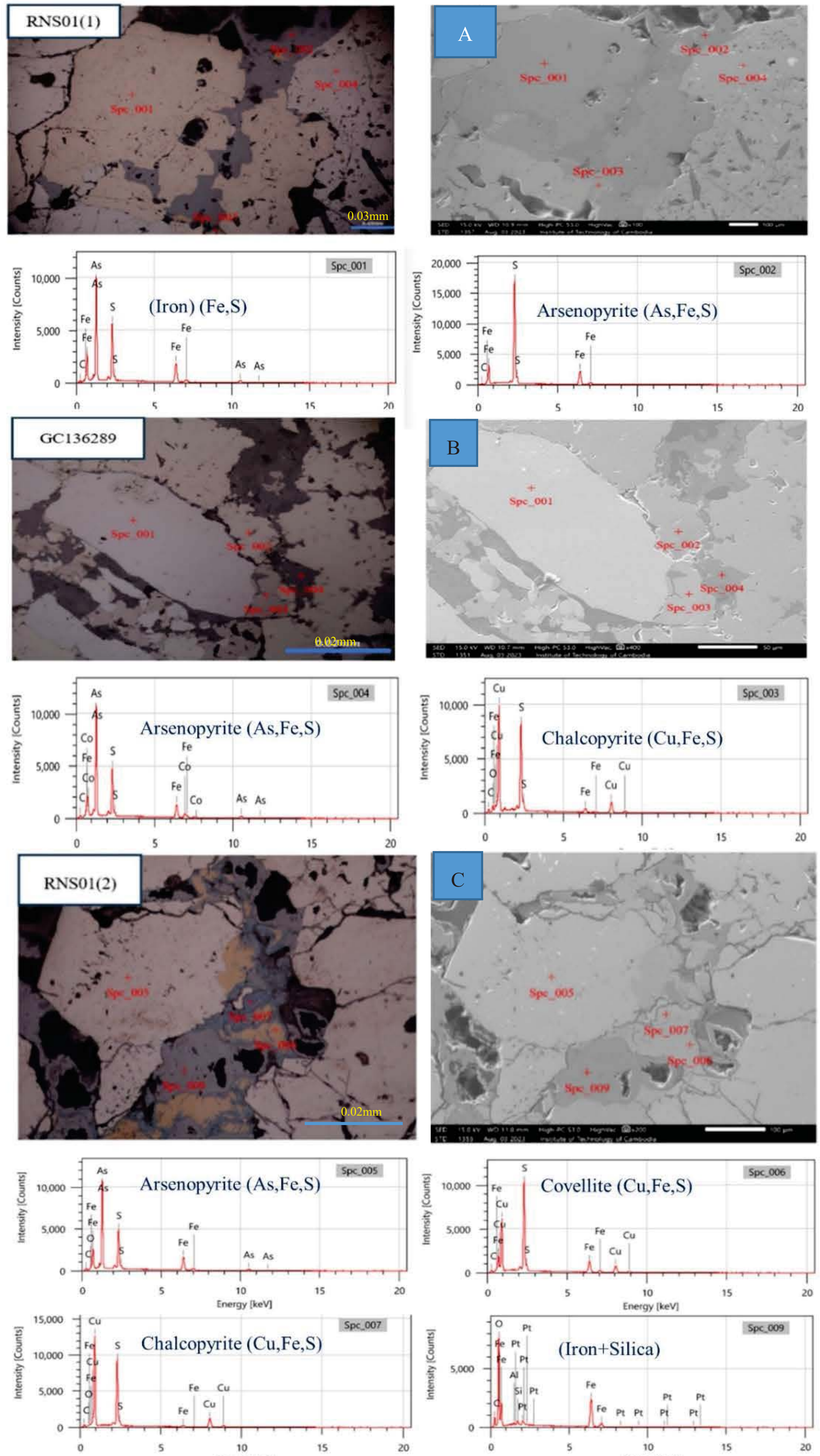

Arsenopyrite in the study area is associated with pyrrhotite and pyrite, and is replaced by fine-grained chalcopyrite. This mineral is easily distinguishable by its texture, typically appearing creamy white-grey, with sizes ranging from 0.01 to 0.1 mm (Fig. 6A - 6I & Fig. 7). The textures suggest that arsenopyrite tends to form in close association with pyrrhotite and pyrite. Arsenopyrite is replaced by chalcopyrite, and replaces some part of pyrrhotite. Chalcopyrite is usually identified as inclusion in arsenopyrite (Fig. 6B - 6I & Fig. 7). Pyrite, a prevalent sulfide mineral, is found in all samples and exhibits euhedral to subhedral forms, typically ranging from 0.01 to 0.1mm (Fig. 6A, E, G, H & Fig. 7). Pyrrhotite, appearing greyish-pink in color, tends to closely associate with arsenopyrite. Covellite, on the other hand, undergoes oxidation from chalcopyrite due to weathering condition. Some occurrences show coexistence with pyrite and chalcopyrite, with size ranging from 0.001 mm to 0.03 mm (Fig 7 F&G & Fig 8). These findings are indicative of gold occurrence in association with base-metal-bearing minerals, including arsenopyrite, pyrite, pyrrhotite, chalcopyrite, and covellite, within mineralized veins, shear zones, fault structures, and their relationship to diorite rock

Structural Control and Ores Mineralization at Okvau Gold Deposit.

Gold at the Okvau deposit is concentrated along a network of brittle shears and arsenopyrite-rich sulfide veins [7] & [8]. Arsenopyrite-rich sulfide veins are generally a few mms to cms wide, although occasionally up to a dm wide.

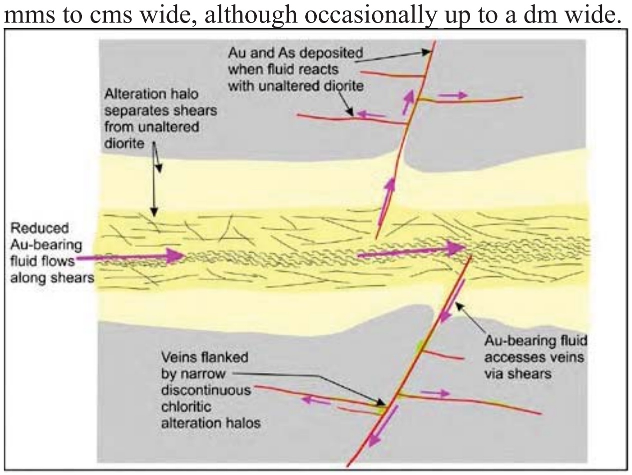

Fig.9. Schematic illustration of the inferred relationships between shears, veins, alteration, and Au deposition at Okvau [7] & [8]. Reduced metal-bearing fluid is inferred to access the fracture mesh which hosts the auriferous veins via the wider more intensely altered shears. Both Au and as are deposited in the veins where reduced metal-bearing fluids react with magnetite in unaltered or partially altered diorite.

The previous study by [7] & [8] mentioned that mineralized shears typically comprise a 1 - 5 dm wide core of strongly altered, fractured, and/or sheared rock, with locally a weak planar fabric, surrounded by 0.5-2 m wide less intensely altered halos that retain the relict diorite texture. Variably deformed pyrrhotite, arsenopyrite and/or pyrite-rich layers up to a dm wide also commonly occur in the core of the brittle shears (Fig. 9). Alteration haloes around the veins are typically less than 2 Cm wide, unlike the more extensive alteration halos around the shears. The veins are located along extensional fractures with little or no sign of any fabric development (Fig. 9) [8].

Cambodian IRGS (Intrusion-related gold system) contain stockwork auriferous quartz veins (Au±Bi±W±Te). The intrusion-hosted ore assemblage contains high fineness gold intergrown with bismuth- and tellurium-bearing phases, which locally are associated with scheelite. Skarns are present in contact zones adjacent to the intrusions (Au±W, Cu±Bi±Te); proximal, thermal aureole-hosted replacement, disseminated, and fracture-controlled mineralization occurs in metasedimentary rocks (Au-As±Sb); and fissure veins vary outward from Au-As to Au-As-Sb to Pb-Zn-Ag [1], [2] & [3]. These deposits typically exhibit an evolutionary sequence from early, high-temperature magmatic stages to lower temperature hydrothermal veins. The spatial relationships and metal assemblages of these occurrences are zoned with respect to a central mineralizing pluton in response to steep temperature and fluid chemical gradients away from the causative pluton.

IRGD (Intrusion-related gold deposit) mineralization is located within the intrusion and its fractured thermal aureole. The intrusions display weak deformation characteristics, as they postdate regional ductile shearing and peak metamorphism. The exposed intrusions from one to 2 km-wide stocks may correspond to apices or cupolas of an underlying larger plutonic body. Intrusion-related and orogenic gold deposits share a large number of common characteristics (Fig. 10) [1], [2] & [3]. The gold occurrences have direct associations with diorite intrusion and are best classed as intrusion-related gold systems. The gold occurrences so far discovered are parts of broader mineralizing systems that form within and a central causative pluton [6], [7] & [8].

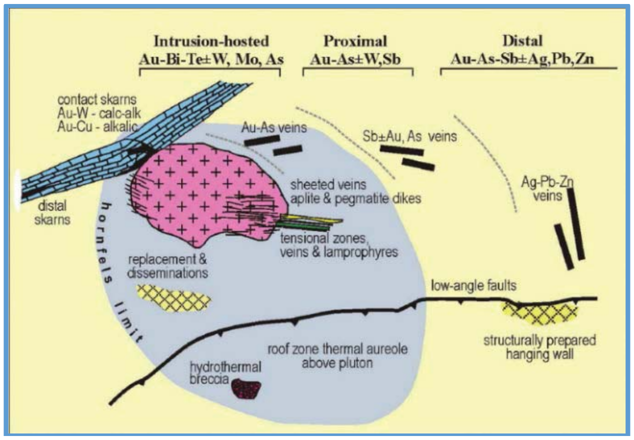

Fig.10. Illustration of the general zonation and styles of mineralization that may be associated with an IRGS Style orebody [2]

[27] mention that a world expert on this style of mineralization, visited the Okvau Project in 2008 and confirmed that the Okvau Deposit was indeed an intrusion-related gold system (Fig 10).

5. CONCLUSIONS

Based on the hand specimen and previous petrogrpahic characterization [25], the rock units consist of intrusive diorite that have undergone weak to moderate selective alteration. Another unit is hornfels, which formed from sedimentary protolith including calcareous rocks. Those sedimentary rocks have recrystallized into a fine grained hornfels by later intrusive diorite. The diorite and sedimentary country rocks are cut by dykes and sills of differing styles, but the most common are massive mafic dykes. Major element data suggest that intrusive rocks in the study area are diorite. The intrusive diorite shows the medium calc-alkaline nature. The ASI values less than 1.1 suggest that intrusive in the area are predominantly I-type granite. The rock from the study area plot within the volcanic-arc granites and syn-collisional granite field (VAG+Syn-COLG) [25]. Mineralization discovered in the Okvau gold deposit consist of arsenopyrite, pyrrhotite pyrite, chalcopyrite and covellite are occurred in the form of quartz veins containing gold and other metals, and disseminated in wall rocks around the vein and massive ore related to vein and intrusive rock. Compare to report [6], [7] & [8]., the gold at the Okvau deposit is concentrated along a network of brittle shears and arsenopyrite-rich sulphide veins. The arsenopyrite-rich sulphide veins are generally a few millimeters to centimeters wide and some veins are up to a dm wide. The quartz vein is commonly massive, brecciated and fracture textures, the style of mineralization visited the Okvau Project in 2008 and confirmed that the Okvau Deposit was indeed an intrusion-related gold system.

ACKNOWLEDGEMENTS

This study was funded by Learning-Based Education (LBE), JICA, and the research grant 2023-2024 awarded to the second and fourth authors. The research was partly supported by Australian Renaissance (Mineral) Cambodia Limited (RNS). The authors would like to thank Learning-Based Education (LBE) for the award of the project, JICA, the project coordinators of the LBE project, for their best coordination to make our research go smoothly, RNS for their good cooperation for the research location, the Faculty of Geo-resources and Geotechnical Engineering (GGE) for proving us the laboratories, and the Centre of Research and Innovation in Science, Engineering, at Technology at the Institute of Technology of Cambodia (ITC).

REFERENCES

[1] J. F. H. Thompson á R. H. Sillitoe á T. Baker, J. R. Lang á J. K. Mortensen., 1999, Intrusion-related gold deposits associated with tungsten-tin provinces.

[2] Lang and Baker., 2000, Intrusion-related gold systems: The present level of understanding.

[3] Hart et al., 2000, Reduce intrusive related gold.

[4] Barton P.B. Jr. and Bethke P.M.,1987, Chalcopyrite disease in sphalerite; pathology and epidemiology. American Mineralogist, v. 72, p. 451-467.

[5] Bortnikov N.S., Genkin A.D., Dobrovol M.G., Muravitskaya G.N. and Filimonova A.A.,1991, The nature of chalcopyrite inclusions in sphalerite; exsolution, coprecipitation, or "disease"? Economic Geology, v. 86, p. 1070-1082.

[6] Australian Rennaissance (Mineral) Cambododia Limited (2016)https://s3.amazonaws.com/rgidocuments/5409dd754c881b02187169d48d79122461c5f8fc

[7] Australian Rennaissance (Mineral) Cambododia Limited- Emerald Resources(2015), https://www.emeraldresources.com.au/renaissance-minerals-cambodia-limited

[8] Australian Rennaissance (Mineral) Cambododia Limited- Emerald Resources (2015), https://www.emeraldresources.com.au/okvau-gold-deposit

[9] Eldursi, Khalifa, et al.,2018 "Intrusion-Related Gold Deposits: New insights from gravity and hydrothermal integrated 3D modeling applied to the Tighza gold mineralization (Central Morocco)." Journal of African Earth Sciences 140: 199-211.

[10] Hein K.A.A. (2003) The Batman and Quigleys gold deposits of the Mt. Todd (Yimuyn Manjerr) Mine, Australia: structural, petrographic and

mineralogical investigations of coeval quartz sulphide vein and lode/stockwork systems. Ore Geology Reviews, v. 23, p. 3-33.

[11] Hallbauer, D.K., 1986, The mineralogy and geochemistry of the Witwa- 1995, Development of the tersrand pyrite, gold, uraninite and carbonaceous matter, in Anhaeusser, C.R., Maske, S., ed., Mineral deposits of Southern Africa: Johannesburg, Geological Society of South Africa, p. 731-752.

[12] Kumarapeli P.S., Kheang L., Höy L. and Pintson H. (1999) Chalcopyrite-bornite and chalcopyrite-bornite- barite in the Acton Vale Limestone, southeastern Quebec; mineralized shelf-margin slivers in a Taconian nappe. Canadian Journal of Earth Sciences, v. 27, p. 27-39.

[13] Kelly D.P. and Vaughan D.J. (1983) Pyrrhotite-pentlandite ore textures: A mechanistic approach. Mineralogical Magazinev. 47, p. 453-463.

[14] Kretschmar U. and Scott S.D. (1976) Phase relations involving arsenopyrite in the system Fe-As-S and their application. Canadian Mineralogist, v. 14, p. 364-386.

[15] Lentz D.R. (2002) Sphalerite and arsenopyrite at the Brunswick No. 12 massive-sulfide deposit, Bathurst Camp, New Brunswick; constraints on P-T evolution. Canadian Mineralogist, v. 40, p. 19-31.

[16] Lynch G. and Mengel F. (1995) Metamorphism of arsenopyrite-pyrite-sphalerite-pyrrhotite lenses, Western Cape Breton Island, Nova Scotia. Canadian Mineralogist, v. 33, p. 105-114.

[17] Morimoto N. and Clark L.A. (1961) Arsenopyrite crystal- chemical relations. American Mineralogist, v. 46, p. 1448-1469.

[18] Mizuta T. and Scott S.D. (1997) Kinetics of iron depletion near pyrrhotite and chalcopyrite inclusions in sphalerite; the spha- lerite speedometer. Economic Geology, v. 92, p. 772-783.

[19] O'Reilly W., Hoffmann V., Chouker A.C., Soffel H.C. and Menyeh A. (2000) Magnetic properties of synthetic analogues of pyrrhotite ore in the grain size range 1- 24 μm. Geophysical Journal International, v. 142, p. 669-683.

[20] Schulz, B.,2017, Polymetamorphism in garnet micaschists of the Saualpe Eclogite Unit (Eastern Alps, Austria), resolved by automated SEM methods and EMP-Th- U-Pb monazite dating. J. Metamorph. Geol., 35, 141–163.

[21] Utter, T., 1978, Morphology and geochemistry of different pyrite types from the upper Witwatersrand system of the Klerksdorp Goldfield, South Africa ansactions of the Geological Geologische Rundschau, v. 67, p. 774-8

[22] Kyi Khin, Sakai, T., Khin Zaw, 2014. Neogene sedimentation in the Arakan-Bengal Basins, and its implication on the India-Asia collision in Western Myanmar. Gondwana Research. http://dx.doi.org/10.1016/j.gr.2013.04.012.

[23] Peccerillo, A. and Taylor, S.R. (1976) Geochemistry of Eocene Calc Alkaline Volcanic Rocks from Kastamonu Area, Northern Turkey. Contribution to Mineralogy and Petrology, 58, 63-81. http://dx.doi.org/10.1007/BF00384745

[24] Chappell and White, 1974. B.W. Chappell, A.J.R. ... Maniar and Piccoli, 1989 Geochemistry of Granitoid.

[25] Malis, et al (2022), Thesis, Faculty of Geo-resources and Geotechnical Engineering (GGE_ITC).

[26] Cox et al. (1979), Total Alkalis versus Silica (TAS) diagram for chemical classification of igneous rock

[27] Hart et al., 2008, Okvau project, intrusive related gold

Techno-Science Research Journal 12 (Special Issue) 32-39

Content list available at ITC

Techno-Science Research Journal

Journal Homepage: www.ric.itc.edu.kh

Techno-Science Research Journal

Environmentally Friendly Green Surfactants for Soil Washing: A Review

Kyu Kyu Tin[1], and Wirach Taweepreda[2]*

[1]*Environmental Management, Faculty of Environmental Management, Prince of Songkla University, Hat-Yai, Songkhla 90110, Thailand*

[2]*Polymer Science Program, Division of Physical Science, Faculty of Science, Prince of Songkla University, Hat-Yai, Songkhla 90110, Thailand*

Received: 18 August 2023; Accepted: 15 May 2024; Available online: August 2024

Abstract: *An interesting restoration methodology as surfactant soil remediation can handle the soil treatment of soil contaminated with hydrophobic as well as other oil derivatives and hydrocarbon contaminants. Therefore, the potential remediation techniques as surfactant addition combined with soil washing can energetically discard contaminants from soil briefly. Nevertheless, as additives, commonly employ synthetic surfactants induce other obstacles because of their accretion of by-products, leading to ruin other aquatic life and fish, devastate aquatic microbial, hostile waste-water treatment mechanisms and then bring down photochemical energy conversion competence of plants. For above reasons, undoubtedly, this literature reviews assurance to grant to improvement of green technologies of surfactants for the treatment of soil pollution with economic profits and also supports researchers to select and consider proper surfactants for soil remediation. Mainly, in different types of soils, applying biosurfactants can enhance the contaminant's biodegrading but the process of services to market or bringing new products, is still circumscribed.*

Keywords: green surfactants; soil contamination; biodegradation; environmental protection; soil remediation.

1. INTRODUCTION

In the Earth's ecosystem, soil is an essential part of human life. Healthy soil can handle climate change storing carbon dioxide, support to get nutrients for food security, maintain groundwater quality acting as buffer, gives vital antibiotics against diseases, habitat for living organisms, distribute the plant nutrition, cover flooding and remove rainwater [1].Therefore, among all pollution, soil pollution mentioned as an emergency case to solve because of its toxicities from hydrocarbon, greenhouse gases, pesticides, heavy metals and nuclear waste leading to soil infertility, decrease the productivity and harm humans health [2]. Nevertheless, The scrubbing soils is regarded as oil washing which applies mechanical process and liquids but sometimes water as liquid collaborative with chemical constitutes.The huge amount of soil is clean and non toxic and also can be introduced as backfill [50].

Moreover,surface active agents (SAAS, surfactants) (Fig 1.) can able to cooperate in solution and appearing micelles that adsorbed at boundary phases to emit hydrophilic sector from water to minimize energy systems [33]. Surfactant molecules demonstrates one tail or two tails. Two tails can regards as double chained. Normally, structure of the tails of most surfactants looks similar comprised of an apolar carbon chain that could be branched or linear or aromatic rings. Based on the polarity of surfactants, the surfactants can be noted as nonionic (no charge), anionic (-), cationic (+) and ampholytic/zwitterionic (both charge) [2].

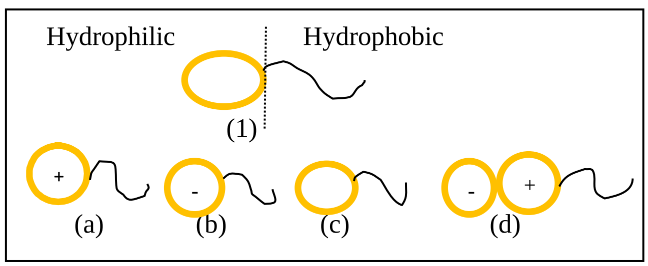

Figure 1. Surfactants (a) cationic (b) anionic (c) nonionic (d) ampholytic/zwitterionic (created by authors)

* Corresponding author: Wirach Taweepreda
E-mail: wirach.t@psu.ac.th; Tel: 0-7428-8007

Currently, the green surfactants in apply derived from two different sources: oleo surfactants and biosurfactants (Table 1.). In addition, there are two types of biosurfactant: high molecular weight and low molecular weight. Especially, in contaminated soil, modern bioremediation including biosurfactants, serving in ex situ and in situ methods, can keep a high biodegradation rate that become eco-friendly alternative to synthetic surfactants [29].

Table 1. Sources of surfactant and its properties [29]

Synthetic surfactants	Biosurfactants
1. Reduce cost of production 2. In the manufacturing, no need microorganisms 3. Hazardous to environment 4. Enhance toxicity 5. Rejecting biodegradation	1. In various industries, a useful tool functioning 2. Comparison between its analogues and its effective 3. Simple production process 4. Positive impacts to human health 5. Good views from environmental sides

However, applying surfactants, the successful remediation of contaminated soil should be considered the following: the elution/solubilization capacity of the surfactant correlate to the target contaminant, the biodegradability, toxicity, adsorption behavior of the surfactants, and then , amount of soil contaminated and surfactants expense as economic factor must also be counted.

2. Soil

2.1 Soil contamination

As a global threat, soil pollution, is devastating and growing more and more compelling in Asia, Northe Africa and Europe based on Food and Agricultural Organization of the United Nations (FAO) data and also confirmed that both moderate and intense deterioration leading to affecting on third of the world's soil, besides, to become a few centimetres layer as arable soil, it takes 1,000 years if rehabilitation goes slowly [49]. Actually, in the natural soil environment, soil pollution is largely happened (Fig.2) by improper disposal of waste, agricultural chemicals, industrial activity and so on [35].

soil contaminants

1. Heavy Metals (lead, chromium, cadmium, silver, selenium, mercury,barium and arsenic)
2. Solvents (heterocyclic, aromatic and aliphatic)
3. Agrochemicals (fungicides,herbicides,insecticides,nematicides,pesticides)
4. Polycyclic (garbage, organic substances and fuels)
5. Petroleum hydrocarbons (oil and natural gas)

Figure 2. Main types of soil contaminants [35]

Consequences of soil pollution finds that economic impact, deforestation, complete annihilation,climate change, air and water pollution, crop failure, population rearrangement and adverse health [32].

2.2 Types of soil remediation

The selection of technology for soil remediation rely on category and type of contamination, soil type (soil organic matter, soil texture-type of clay, soil pH), spatial constribution of contamination (volume and location of contamination- the proximity of surface /ground water), defined legal frame work and future land apply based on requirement of remediation in a specific area and also an exposure duration of contamination [45]. Treatment options for contaminated soil are regarded are as follow (Table 2) [1].

Table 2. Soil remediation techquies [1]

Remediation methods	
Physical	soil vapor extraction,electrokinetic extraction,surface capping
Chemical	solidification,stabilization, nanoremediation, soil washing
Thermal	thermal desorption,vitrification
Biological	phytoremediaiton, nermiremediation,biostimulating, bioinventing,bioaugmentation
Combinative	nanoremediation

Ex situ technology needs soil excavation that moves to special landfill for remediation, on the other hands, At sites, on situ have to contact soil digging but in situ can solve the soil remediation without soil burrowing that no impacting the soil structure. Nonetheless, based on the various factors including public health, environmentally friendly and expense of remediation and so on, in situ or on situ methods are more attractive compared with ex situ [5]. A prospective outlook toward the future of soil remediation are biochar (adsorption of heavy metal), phytoremediation (development of transgenic plants), electrokinetic remediation (use of bacteria for bioelectrokinetic remediation), and finally nanoparticles (polyelectrolytes, different matierials for nanoparticles) [14].

3. Soil Washing

Soil washing (Fig.3) introduced in the matter of soil contamination due to pesticides, hydrocarbons and heavy metals. Removal of contaminants noted in one of three methods: physical, chemical , or physical- chemical which chemical separation is washing solution (chemical agent with water) with pollutant solubilization reacting with soil particles into washing solution and physical method plans to divide polluted particles from bulk soil decreasing with volume of contaminated soil that will get coarse-grained particles and then physical-chemical method, in the form of suspened particle, eventually and concentration dispersion of the pollutants in the extraction liquid [8].

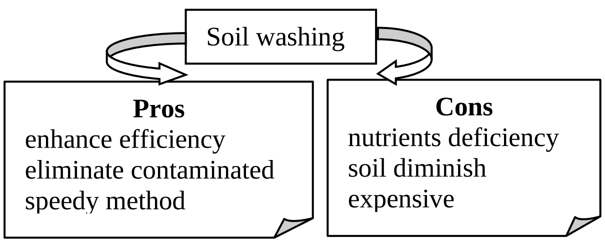

Figure 3. advantages and disadvantages of soil washing

At a site, the process of soil washing predominantly decrease the volume of polluted soil as a pretreatment step. Afterward, soil washing can be ruined in six ways, they are pretreatment, separation, coarse grained and fine grained treatments, process water treatment and residuals management [30]. However, specific factors impression types of soil washing: cosolvent soil washing, alkali soil washing, surfactant soil washing and ground water and water flooding extraction [52], among them, soil contamination for washing methods using surfactants, such as an ex situ treatment, soil washing and an in situ treatment,soil flushing have described good results especially in hydrocarbon contamination.

Determination of the effectiveness of soil washing, site characterization is an essential part to reduce cost with the best yield. Therefore, hydrogeology and site geology, soil chemistry, depth vs composition, soil type, organic carbon content, grain size distribution, hydraulic conductivity of soil, horizontal and vertical and total amount soil contamination profiles could be considered [31].

3.1 *Soil Washing with Surfactants*

Nowadays, in the world, fossil fuel as petroleum is currently caused critical soil pollution because of petrochemical contamination and petroleum extraction waste from improper management as well as underground oil tanks beyond its capacity happened large oil spills and oil leakage leading to groundwater and soil contamination [20].

Soil remediation technique as soil washing with surfactant represent good data without using a lot of money process and one of the most promising for hydrocarbon contaminated samples, mainly, the choosing surfactants and doses is the primary steps of soil washing [19]. Removal of soil contamination by surfactants reply on properties of soil including soil organic matter content, soil composition, etc., and following soil age, surfactant types and concentration, washing time and temperature [4].

The critical micelle concentration(CMC)(Fig 4.) is regarded the surfactants required to receive the minimum possible surface tension that needed to carry a molecule from the bulk phase to the surface to measure the surface free energy per unit area [38].

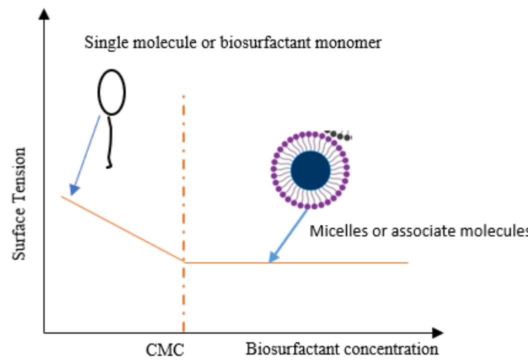

Figure 4. micelle formation of biosurfactant monomers and critical micelle concentration (CMC) adopted from Kumar, et al.(2021)

Surfactants start to form micelles and surface tension resides consistent after CMC is accomplished [51]. Hydrocarbon chain length, salinity and surfactant impact on the CMC that biosurfactants mainly between 1–200 mg/L. The concentration where micelles form in aqueous phase is many times lower than micelles form in soil [40].At sorption of saponin critical micelle concentration in soil texture (clay loam, clay, sandy clay loam) was more advanced than sorption of rhamnolipids [41].

In order to biological activities of surfactants, after soil washing, the residual surfactants arrives surfactants toxicity that disturb the pore/soil water sysem (Table 3) [9].

Table 3. Surfactants and its ecological behavior [9]

Surfactants	Properties
nonionic	utilize antimicrobial activity by combinding to various phospholipid and proteins
cationic	influence the cytoplasmic membrane of bacteria
anionic	attach to bioactive macromolecules including enzymes, DNA, peptides, altering the biological function of microorganisms

A surface active agent, perfluorooctanoic acid (PFOA) unveils carcinogenic and toxic effects in animal and perseveres endlessly in soil [53].

Apparently, most synthetic surfactants applied in soil remediation remain undegraded via the soil microbes lead to toxic adverse impacts on the soil ecosystem [56]. Evidently, instead of using conventional ionic surfactants, gemini surfactants stand as enhanced surface activity (C20), hard water resistance effect, superior wetting agent, increase aggregation and reduce the concentration requirement for solubilizing lower concentration requirement for solubilizing hydrophobic organic contaminants (HOCs) but nonionic surfactants hold most cost-effectiveness, low toxicity, susceptibility and low CMC to aggregate clay minerals and then more biodegradable compared to ionic surfactants[55].For example, surfactants SDS (sodium dodecyl sulfate) and CTAB (cetyltrimethylammonium bromide) as ionic surfactants exhibits high toxicity than biosurfactant and Tween as nonionic surfactant.The high toxicity surfactants can disturb the functioning of endocrine mechanism in human beings and wildlife [57].

4. Green Surfactants for Soil Washing

Green surfactants, biosurfactants as microbial surfactants are noted the most ecologically safe and biocompatible from living cells especially yeast and bacteria that no need to apply organic synthesis but biobased surfactants are synthesized by chemical methods, comprising sugars, fats or amino acid from renewable sources according to their structure and they have intermediate biocompatibility [3].

Polymeric biosurfactants and Particulate biosurfactants serve as high molecular polymer, polymeric biosurfactants comprised of three to four repeating sugar with fatty acids attached to them, such as liposan, emulsan, alasan producting microorganisms from candida liplytica, acinethobacter calcoaceticus, on the other hand, particulated biosurfactants could be whole microbial cell and extracellular vesicles, microorganisms from cyanobacteria, pseudomonas marginalis, Acinetobacter calcoaceticus[48].

Low molecular weight biosurfactants are phospholipids, neutral acids and fatty acids, lipoproteins and lipopeptides, glycolipids[18]. Anyhow, based on green surfactants, the evaluation of new formulations should be critically considered because it could happen hinder effects on pollutant degrading bacteria, delay or restrain biodegradation[17].

Interestingly, their application has been applied more attention in hydrocarbon and oil contaminated soil compared with metal contaminated soils[27].All over the world, weathered crude oil contaminated soils (Fig.5) from many other chemical industries and refineries, aren't easy to handle to remediate compared with freshly contaminated soil.

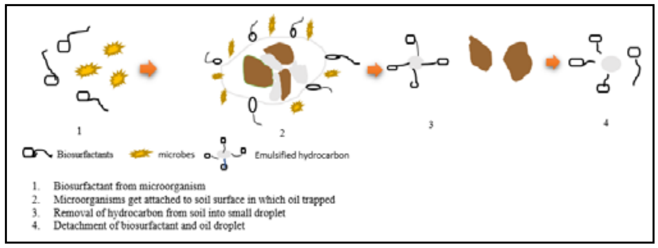

Figure 5. Mechanism of biosurfant with hydrocarbon modified and adopted from Rizvi, et al. (2021)

A biosurfactant, Pseudomonas aeruginosa UCP 0992 showed the removal of oil conatminats in soil about 80% and 90%[39].Pseudomonas cepacia CCT6659, glycolipid nature,can reduce cost and recovered 75% oil from sand and replaced 81% oil in water[7].Candida sphaerica UCP0995 and Bacillus sp. described 10–20% raise oil decomposition [43]. Nonionic surfactants, alkyl polyglucoside(APGs) comes from natural renewable resources, 1.5% APG1214 serves as 81.0% crude oil was terminated, removal efficiency of deionized water was only 30.1% and the addition of inorganic salts of removal efficiency 97.4% and then The BET surface area of soil enhanced (0.79 to 4.16 m^2g^{-1})[16]. The produced methyl ester sulphoate (MES) surfactant from groundnut oil, triglyceride might be able to recure 96.0 % polycyclic aromatic hydrocarbon (PAH) and 61.7% total petroleum hydrocarbon (TPH), this ecofriendly synthesis surfactant for petroleum spill remediation [24] . Under statistic condition, the commercial, as biosurfactant, the yeast Starmerella bombicola ATCC 2214 described high capacity to disperse and emulsify hydrophobic compound, free toxicity, decrease water tension and remove motor oil with excellent effectiveness for contaminated beach sand(65.0 ± 0.14%) and sandy soil (80.0 ± 0.46%).For biodegration test on motor oil contaminated soil with sugarcane molassess,oil removal yield 90% after 60days, shouldnot exceed 20% for only S.bombicola cells, that data will take advantages to oil industries for treatement of hydrophobic contaminats[25].

Heavy metals(cadmium (Cd), copper (Cu), lead (Pb), arsenic(As),chromium(Cr),and mercury (Hg))contamination in soil lead to unbiodegradable, toxicant and persistent, therefore, Heavy metals has introduced global attention to keep sustainable improvement, if it exceeds the maximum value, causing human unhealthy, food chain imporper function, microorganisms and plants function damage [46]. Pseudomonas aeruginosa PTCC 1340, rhamnolipid biosurfactant, at an optimum condition (concentration: 0.8 g/l, pH 11 and temperature: 25◦C), heavy metals (cadmium: 52.81%, chromium: 34.73%, and nickel: 43.05%,) was successfully removed[22].The yeast Candida tropicalis, a biosurfactant, under static condition, can shed Zn and Cu ranged from 45 to 65% but Pb was not kick off, on the other hand, under dynamic conditions, Cu and Zn at rates ranging from 30 to 80%.

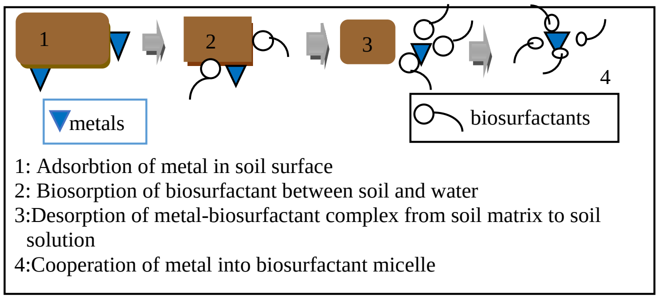

Figure 6.Mechanism of metal-biosurfactant in soil. modified and adopted from Pacwa-Plociniczak et al. (2011)

The yeast Candida guilliermondii UCP 0992 as the crude biosurfactant, removal of heavy metals were (Zn:98.9%, Pb:89.1% and Fe:89.3%) respectively[42].An unidentified bacterium clone JX981747 (CMS) and Odoribacter splanchnicus DSM 20712 (WBS1) from waste metal dumpsite soil, Heavy metals (lead: 97.68%,copper:95.73% and zinc: 98.98%) cut out[34].

In Poland, in the remediation of a soil from a smelter, removal of Cu was the highest 87.4% and 0.40 following Pb from 0.25 to 0.55 by using sequential washing with saponin, rhamnolipid and tannic acid [13].Combination of saponin and rhamnolipid with triple washing of sewage sludge described the stability of Pb from 0.25 to 0.55 and Cu from 0.23 to 0.47 due to easy remove from exchangeable and reducible fractions, whereas residual and oxidizable, did not easy to discard[44].Highly heavy metals contaminated with bath washing of soil, for microbial rhamnolipids (RAM) 24% (Cu) to 62% (Cd) and 61% (Zn) to 89% (Cd) for tannic acid but tannic acid followed by humic-like substances (HLS) or HLS followed by tannic acid can get low ecological risk[21].From artificially contaminated soil , The elimination of (cadmium: 69.07, copper:64.72% , lead:62%, Zn: 68.54%) for a saponin (soapnut) and (cadmium: 63.08, copper: 61.58%, lead: 59.65%, Zn: 62.65%)for microbial (rhamnolipid), afterwards, in- situ soil remediation could be applied alternative to exsitu method[47].

After 24 h washing time, arsenic (As) removal showed 38% after single and 63% after double washings using 4% tannic acid[15].Arsenic from brownfield soils, saponin (SAP), a glycoside and Tannic acid (TA), a polyphenol, was reduced by 37%–73%[12].The surfactin, Bacillus subtilis, a biodegradable surfactant, Heavy metals(6 and 25% of the zinc, 25 and 70% of the copper and 5 and 15% of the cadmium)from contaminated soil after one and five batch washing and then after a single washing 6% of the zinc and 15% of the copper could be deleted[28].

Biosurfactant enhanced soil washing (BESW), under the optimal conditions, removal rated of phenanthrene and cadmium hit 87.8% and 72.4%[54].In soil washing sequences, using a combination of various types of biosurfactant, might certainly affect metal removal, basically reliability of soil organic carbon and residul metals.After soil washing, soil organic carbon can see abundantly because of biosurfactant sorption[11].

Based on the biosurfactants for soil washing with tannic, saponin and rhamnolipids to discard heavy metals contaminations, tannic acid and saponin are the highest removal efficiency (Zn, Cu, Ni) while rhamnolipid stands as the highest lead removal activity. Heavy metals (Mn, Cr and Ni) in soil, have successfully mentioned by the soapnut fruit pericarp and soapberry (Sapindus mukorossi L)[26].

Accordingly to literature review,all biosurfactants effectively discarded the heavy metals. Specifically, microbial (rhamnolipids) and plant (tannic acid, saponin) biosurfactants cannot remove heavy metals in soil due to enhance their stability by changing their distribution in soil. For contaminated with lead (Pb) case, sequential washing or single washing using the same biosurfactants in individual step couldn't remove metals efficiently than sequential soil washing with plants and then microbial biosurfactants [58].In soil, green surfactants are the best choose to progess the biodegradation rate of hydrophobic contaminats, at the same time, it must be reminded that it did not effect on the degradation of hydrocarbon or delay. The good points of biosurfactants from microorganisms and plants in soil washing can increase the activity of heavy metals ions by creating micelles, decrease interfacial and surface tension to weaken adhesion between the soil and metal ions and then improve the separation of metals ions from the soil and their complexation with the biosurfactant itself, increasing soil fertility that develop the plant growth[10].

In soil remediation practices, as environmentally friendly green surfactants for soil washing, statistical analysis must describe to promote sustainable application definitely. Plus, future research should focus on the environmental impact of soil washing with biosurfactants, social life cycle assessment, life cycle costing and /or techno-economic must be introduced to understand and showed most sustainable and the greenest soil washing with biosurfactants strategies.

5. CONCLUSIONS

Physically or chemically, hazardous contaminants intent to bind clay and silt that can cover to gravel and sand particles again, however, from coarse soil (gravel and sand), soil washing can divide the contaminated fine soil (clay and silt). Soil washing with surfactants has described satisfactory results especially anionic and/or nonionic surfactants are interested compared with cationic surfactants that are strongly adsorbed by clay minerals (soil organic matter and aluminosilicates) but their biodegradability of the surfactants and toxicity shouldn't neglect. Using synthetic surfactants including their high levels of poor biodegradability and toxicity carry on many negative environmental consequences.The key to long term competitive advantage, the surfactant industries are concentrating on greener chemical constitutes and eco innovation with moving towards sustainability, nevertheless, a welcome package of green surfactants is still struggling stage. Therefore, using biosurfactants for soil washing are also facing challenges, even though, the use of green surfactants for contaminated soil remediation has the benefits for environmental sector and can halt environmental-anxiety. Remarkables are the exceptation of the commercial production and the developent of merge surfactants with low CMC boasting additives lead to decrease remediation expense and enhance remediation process. Furthermore, with plant extracts, the operational costs of soil remediation are substantially lower than those with commercial biosurfactants.

ACKNOWLEDGMENTS

We would like to acknowledge Faculty of Environmental Management (Prince of Songkla University, Hatyai, Thailand) for constant support.

REFERENCES

[1] Asim Hussain, Fazeelat Rehman, HamzaRafeeq, Muhammad Waqas, Asma Asghar, Nadia Afsheen, Abbas Rahdar, Muhammad Bilal, Hafiz M.N. Iqbal, 2022.In-situ, Ex-situ, and nano-remediation strategies to treat polluted soil, water, and air -a review, Chemosphere, Volume 289,133252,ISSN 0045-6535.

[2] Abbot, V., Paliwal, D., Sharma, A., & Sharma, P. (2022). A review on the physicochemical and biological applications of biosurfactants in biotechnology and pharmaceuticals. Heliyon, 8(8), e10149.

[3] Abdullahi Adekilekun Jimoh, Johnson Lin,(2019). Biosurfactant: A new frontier for greener technology and environmental sustainability,Ecotoxicology and Environmental Safety, 184,109607,ISSN 0147-6513

[4] Bhatt, Jayesh & Rai, Avinash & Gupta, Meghavi & Vyas, Shubang & Ameta, Rakshit & Ameta, Suresh & Chavoshani, Afsane & Hashemi, Majid. (2020). Surfactants: an emerging face of pollution.

[5] Bhadani, A.; Kafle, A.; Ogura, T.; Akamatsu, M.; Sakai, K.;Sakai, H.; Abe, M. Current perspective of sustainable surfactants based on renewable building blocks. Curr. Opin. Colloid Interface Sci. 2020, 45, 124– 135.

[6] Chu, W., & Kwan, C. Y. (2003). Remediation of contaminated soil by a solvent/surfactant system. Chemosphere, 53(1), 9–15.

[7] Cássia, R. & Silva, F.S. & Rufino, Raquel & Luna, Juliana & Farias, Charles & Hilario, F. & Santos, Valdemir Alexandre & Sarubbo,Leonie. (2013). Enhancement of Biosurfactant Production from Pseudomonas cepacia CCT6659 Through Optimisation of Nutritional Parameters Using Response Surface Methodology. Tenside, Surfactants, Detergents.

[8] Cho K, Kim H, Purev O, Choi N, Lee J.(2022) Physical Separation of Contaminated Soil Using a Washing Ejector Based on Hydrodynamic Cavitation. Sustainability.14(1):252.

[9] Durval, Italo & Rufino, Raquel & Sarubbo, Leonie. (2022). Biosurfactant as an Environmental Remediation Agent: Toxicity, Formulation, and Application in the Removal of Petroderivate in Sand and Rock Walls. Biointerface Research in Applied Chemistry. 12. 34-48.

[10]Gayathiri E, Prakash P, Karmegam N, Varjani S, Awasthi MK, Ravindran B.(2022).Biosurfactants: Potential and Eco-Friendly Material for Sustainable Agriculture and Environmental Safety—A Review. Agronomy. 2022; 12(3):662.

[11] Gusiatin, Mariusz & Radziemska, Maja & Żochowska, Alicja. (2019). Sequential soil washing with mixed biosurfactants is suitable for simultaneous removal of multi-metals from soils with different properties, pollution levels and ages. Environmental Earth Sciences.

[12]Gusiatin Z. M. (2014). Tannic acid and saponin for removing arsenic from brownfield soils: Mobilization, distribution and speciation. Journal of environmental sciences (China), 26(4), 855–864.

[13]Gusiatin, Z. M., Kumpiene, J., Carabante, I., Radziemska, M., & Brtnicky, M. (2021). Remediation of Smelter Contaminated Soil by Sequential Washing Using Biosurfactants. International journal of environmental research and public health, 18(24), 12875.

[14]Gogoi, Lina & Narzari, Rumi & Chutia, Rahul & Borkotoki, Bikram & Gogoi, Nirmali & Kataki, Rupam. (2021). Remediation of heavy metal contaminated soil: Role of biochar. 10.1016/bs.apmp.2021.08.002.

[15] Gusiatin, Z. M., Klik, B., & Kulikowska, D. (2019). Tannic acid for remediation of historically arsenic-contaminated soils. Environmental technology, 40(8), 1050–1061.

[16] Han, M., Ji, G., & Ni, J. (2009). Washing of field weathered crude oil contaminated soil with an environmentally compatible surfactant, alkyl polyglucoside. Chemosphere, 76(5), 579–586.

[17] Hosaka T, Tsuji H, Tamaoka A. Biomolecular Modifications Linked to Oxidative Stress in Amyotrophic Lateral Sclerosis: Determining Promising Biomarkers Related to Oxidative Stress. Processes. 2021; 9(9):1667.

[18] Hamidreza Bagheri, Ali Mohebbi, Fereshteh S. Amani, Mina Naderi,(2022).Chapter 1 - Application of low molecular weight and high molecular weight biosurfactant in medicine/biomedical/pharmaceutical industries,Editor(s): Inamuddin, Charles Oluwaseun Adetunji, Mohd Imran Ahamed,Green Sustainable Process for Chemical and Environmental Engineering and Science,Academic Press,Pages 1-60,ISBN 9780323851466,

[19]Hao Ling, Jinyu Hou, Mingjun Du, Yun Zhang, Wuxing Liu, Peter Christie, Yongming Luo,(2023).Surfactant-enhanced bioremediation of petroleum-contaminated soil and microbial community response: A field study,Chemosphere,Volume 322,2023,138225,ISSN 0045-6535

[20] Ivica, Kisic, Zeljka, Zgorelec and Aleksandra, Percin. "Soil treatment engineering" Physical Sciences Reviews, vol. 2, no. 11, 2017, pp. 20160124.

[21]Klik, Barbara & Gusiatin, Mariusz & Kulikowska, Dorota. (2019). Simultaneous Multi-metal Removal from Soil with Washing Agents of Waste, Plant and Microbial Origin. Soil and Sediment Contamination: An International Journal. 28. 1-19.

[22] Kholghi, N., Amani, H., Malek mahmoudi, S., & Amiri, A. (2019). The removal of heavy metals (Ni, Cr, Cd) from soil contamination with crude oil using rhamanolipid biosurfactant. Journal of Microbial World, 12(1), 62-72.

[23] Kumar, Ajay & Singh, Sandeep & Kant, Chandra & Verma, Hariom & Kumar, Dharmendra & Singh, Prem & Modi, Arpan & Droby, Samir & Kesawat, Mahipal & Alavilli, Hemasundar & Bhatia, Shashi & Saratale, Ganesh & Saratale, Rijuta & Chung, Sang-Min & Kumar, Manu. (2021). Microbial Biosurfactant: A New Frontier for Sustainable Agriculture and Pharmaceutical Industries. Antioxidants. 10. 10091472.

[24] Liping Huang, Jiangyu Ye, Kemei Jiang, Yichao Wang, Yunyi Li,(2021).Oil contamination drives the transformation of soil microbial communities: Co-occurrence pattern, metabolic enzymes and culturable hydrocarbon-degrading bacteria,Ecotoxicology and Environmental Safety,Volume 225,112740,ISSN 0147-6513,

[25] Lopes, C. & Teixeira, D. & Braz, Bernardo & Santelli, Ricardo & Castilho, L. & Gomez, J. & Castro, R. & Seldin, Lucy & Freire, D.. (2020). Application of rhamnolipid surfactant for remediation of toxic metals of long- and short-term contamination sites. International Journal of Environmental Science and Technology.

[26] Mukhopadhyay, Soumyadeep & Mukherjee, Sumona & Hashim, Mohd & Sahu, Jaya & Martínez-Villegas, Nadia & Sen Gupta, Bhaskar. (2018). Zinc Removal from Soil by Washing with Saponin Obtained from Sapindus mukorossi. Journal of Environmental Analytical Chemistry.

[27] Maceiras, R., Alfonsin, V., Martinez, J. et al. (2018). Remediation of Diesel-Contaminated Soil by Ultrasonic Solvent Extraction. Int J Environ Res 12, 651–659.

[28]Mulligan, Catherine & Yong, Raymond & Gibbs, Bernard. (1999). Removal of Heavy Metals from Contaminated Soil and Sediments Using the Biosurfactant Surfactin. Soil and Sediment Contamination. 8. 231-254.

[29] Moldes, A. B., Rodríguez-López, L., Rincón-Fontán, M., López-Prieto, A., Vecino, X., & Cruz, J. M. (2021). Synthetic and Bio-Derived Surfactants Versus Microbial Biosurfactants in the Cosmetic Industry: An Overview. International journal of molecular sciences, 22(5), 2371.

[30] Marschalko M, Kempa T, Popielarczyk D, Cernik M, Vicherkova M, Vicherek P, Niemiec D. Analysis of the Remediation of Coal Tar-Contaminated Groundwater Using Ex Situ Remediation. Water. 2022; 14(14):2182.

[31] Nam S, Gutierrez M, Diplas P, Petrie J. Laboratory and In Situ Determination of Hydraulic Conductivity and Their Validity in Transient Seepage Analysis. Water. 2021; 13(8):1131.

[32] Oliver, M. & Gregory, Peter. (2014). Soil, food security and human health: A review. European Journal of Soil Science. 66. 10.1111/ejss.12216.

[33]Olkowska,E.,Ruman,M.,Kowalska,A.& Polkowska,Ż. (2013).Determination of Surfactants in Environmental Samples. Part II. Anionic Compounds. Ecological Chemistry and Engineering S,20(2) 331-342.

[34] Ogbulie, Toochukwu & Okore, Chioma & Ejele, Agunna. (2020). Comparative Heavy Metal Removal Efficiencies of Biosurfactants Produced by Odoribacter Splanchnicus DSM 20712, Bacterium Clone JX981747 and Soil Washing Agents.

[35] Perfumo, A., Rudden, M., Marchant, R., Banat, I.M. (2018). Biodiversity of Biosurfactants and Roles in Enhancing the (Bio)availability of Hydrophobic Substrates. In: Krell, T. (eds) Cellular Ecophysiology of Microbe: Hydrocarbon and Lipid Interactions. Handbook of Hydrocarbon and Lipid Microbiology . Springer, Cham.

[36]Pacwa-Plociniczak PGA, Piotrowska-Seget Z, Cameotra SS.(2011).Environmental applications of biosurfactants: recent advances. Int J Mol Sci. 2011;12:633–654.

[37] Rizvi, H., Verma, J.S., Ashish (2021). Biosurfactants for Oil Pollution Remediation. In: Inamuddin, Ahamed, M.I., Prasad, R. (eds) Microbial Biosurfactants. Environmental and Microbial Biotechnology. Springer, Singapore.

[38] Ruths, M. (2013). Surface Forces, Surface Tension, and Adhesion. In: Wang, Q.J., Chung, YW. (eds) Encyclopedia of Tribology. Springer, Boston, MA.

[39] Sui X, Wang X, Li Y, Ji H. (2021).Remediation of Petroleum-Contaminated Soils with Microbial and Microbial Combined Methods: Advances, Mechanisms, and Challenges. Sustainability. 13(16):9267.

[40]Santos, D. K., Rufino, R. D., Luna, J. M., Santos, V. A., & Sarubbo, L. A. (2016). Biosurfactants: Multifunctional Biomolecules of the 21st Century. International journal of molecular sciences, 17(3), 401.

[41]Souza, Lilian & Pomarolli, Luiza & Veiga, Márcia. (2020). From classic methodologies to application of nanomaterials for soil remediation: an integrated view of methods for decontamination of toxic metal(oid)s. Environmental Science and Pollution Research. 27.

[42] Sarubbo, Leonie & Brasileiro, Pedro & Silveira, Gabriel & Luna, Juliana & Rufino, Raquel & Santos, Valdemir Alexandre. (2018). Application of a Low Cost Biosurfactant in the Removal of Heavy Metals in Soil. Chemical Engineering Transactions.

[43] Silva, Ivison & Helena, Ana & Resende, Mendonça & Silva, Maria & Pinto, Pedro & Brasileiro, Ferreira & Didier, Júlia & Amorim, P & Luna, Juliana & Rufino, Raquel & Alexandre, Valdemir & Santos, Dos & Sarubbo, Leonie. (2018). Aplication of Biosurfactants Produced by Bacillus cereus and Candida sphaerica in the Bioremediation of Petroleum Derivative in Soil and Water. Chemical Engineering Transactions.

[44]Tang, Jian & He, Junguo & Qiu, Zhongping & Xin, Xiaodong. (2019). Metal removal effectiveness, fractions, and binding intensity in the sludge during the multiple washing steps using the combined rhamnolipid and saponin. Journal of Soils and Sediments.

[45]Thomé, Antônio & Reginatto, Cleomar & Vanzetto, Guilherme & Braun, Adeli. (2018). Remediation Technologies Applied in Polluted Soils: New Perspectives in This Field.

[46]Tchounwou, P. B., Yedjou, C. G., Patlolla, A. K., & Sutton, D. J. (2012). Heavy metal toxicity and the environment. Experientia supplementum (2012), 101, 133–164.

[47] Ugwu, E., Sen Gupta, B., Adeloye, A. J., & Martínez-Villegas, N. (2021). Column Experiment for the Removal of Cadmium, Copper, Lead and Zinc from Artificially Contaminated Soil using EDTA, Rhamnolipids, and Soapnut. European Journal of Environment and Earth Sciences, 2(2).

[48] Uzoigwe, C., Burgess, J. G., Ennis, C. J., & Rahman, P. K. (2015). Bioemulsifiers are not biosurfactants and require different screening approaches. Frontiers in microbiology, 6, 245.

[49] Verma, A. (2022). Bioremediation Techniques for Soil Pollution: An Introduction. IntechOpen. doi: 10.5772/intechopen.99028

[50] Vaishnavi S. Nagtode, Clive Cardoza, Haya Khader Ahmad Yasin, Suraj N. Mali, Srushti M. Tambe, Pritish Roy, Kartikeya Singh, Antriksh Goel, Purnima D. Amin, Bapu R. Thorat, Jorddy N. Cruz, and Amit P. PratapACS Omega 2023 8 (13), 11674-11699.DOI: 10.1021/acsomega.3c00591

[51]Vincent, Akpoveta & Osakwe, S. & Egharevba, F. & Medjor, W.O. & Imohimi, Asia & Ize-Iyamu, Osaro. (2012). Surfactant enhanced soil washing technique and its kinetics on the remediation of crude oil contaminated soil. PJST. 13. 443-456.

[52]Volkering, Frank & Breure, Anton & Rulkens, Wim. (1997). Microbiological Aspects of Surfactant Use for Biological Soil Remediation. Biodegradation. 8. 401-17.

[53]Zhou, Y. T., Li, R., Li, S. H., Ma, X., Liu, L., Niu, D., & Duan, X. (2022). Perfluorooctanoic acid (PFOA) exposure affects early embryonic development and offspring oocyte quality via inducing mitochondrial dysfunction. Environment international, 167, 107413.

[54] Zhang, Xu & Zhang, Xiaodong & Wang, Shuguang & Zhao, Shan. (2022). Improved remediation of co-contaminated soils by heavy metals and PAHs with biosurfactant-enhanced soil washing. Scientific Reports.

[55] Ivey, G. A., & Beaudoin, M. (2010). Case study: In-situ surfactant enhanced DNAPL recovery pilot project, Refinery site. Montreal Canada. In FCS 2010: Federal Contaminated Sites National workshop., Montreal, Quebec, Canada.

[56]Ishiguro, M., & Koopal, L. K. (2016). Surfactant adsorption to soil components and soils. Advances in colloid and interface science, 231, 59-102.

[57] Ying, G. G., & Kookana, R. S. (2002). Endocrine disruption: an Australian perspective.

[58] Gusiatin, Z.M., Radziemska, M. & Żochowska, A. (2019).Sequential soil washing with mixed biosurfactants is suitable for simultaneous removal of multi-metals from soils with different properties, pollution levels and ages. Environ Earth Sci 78, 529.

Techno-Science Research Journal 12 (Special Issue) 40-48

Content list available at ITC

Techno-Science Research Journal

Journal Homepage: www.ric.itc.edu.kh

Techno-Science Research Journal

Performance Evaluation of Activated Carbon Prepared from Agricultural Waste for Indoor Air Purification

Yaowatat Boongla[1*], Thaneeya Chetiyanukornkul[2]

[1]*Faculty of Science and Technology, Thammasat University, Rangsit Campus, Pathumtani, 12120, Thailand*
[2]*Faculty of Science, Chiang Mai University, Muang, Chiang Mai, 50200, Thailand*

Received: 22 August 2023; Accepted: 15 May 2024; Available online: August 2024

Abstract: *An Indoor air pollution and its consequences harm human health. The purpose of this research is to assess the performance of activated carbon (AC) for indoor air cleaning. The experiment was carried out using activated carbon made from coconut shell. Activated carbon is a well-known adsorbent used in air filtration. Coconut shell was carbonized, and the best approach in this study was to use KOH treatment to produce activated carbon with a high yield%, high iodine number, and well-developed pores.The results showed that using the coconut shell activated carbon adsorbent boosted the performance of the air purifier, particularly in the room unit area. The maximum bacteria were found in the room unit area without coconut shell activated carbon. Because of its high microporous volume and adsorption kinetics, AC is favored. The primary outcome of the study was that carbon activated from coconut shell may be used to remove indoor air pollution (airborne microbes). Furthermore, activation and the addition of specific functional groups to the surfaces of the AC can improve the AC's ability to absorb smells and other indoor air contaminants.*

Keywords: Airborne microorganism removal; Air purifier; Activated carbon; Coconut shell; Agricultural waste management;

1. INTRODUCTION

Indoor air pollution is a major issue in modern society. Because of their presence in interior air, indoor air pollutants can cause substantial harm to human health (Prashant P. Bhave and Deepali Yeleswarap, 2020). In general, humans spend more than 80% of their waking hours indoors [Zewudu Andualem et al., 2019; Kuma et al., 2022]. The indoor microbiome is a complex community comprised of all living microorganisms found in an interior environment, as well as their fragments and by-products. The microbiome that surrounds us is diverse and constantly changing. Bacteria, viruses, fungi, and other single-celled creatures comprise it [US EPA, 2022]. Indoor air pollution is created by a variety of factors, including working and living indoors, home cooking, building materials, smoking, and burning activities such as household energy. Volatile organic compounds (VOC), formaldehyde, gaseous pollutants, air exchange rate, air movement, temperature, and humidity are all elements that influence indoor air quality [Model et al., 2021; Phuipanya et al., 2019]. In recent decades, research on indoormicrobial aerosols has primarily relied on bioaerosol sampling, which was carried out in accordance with the NIOSH 0800 standard for Bioaerosol Samplingan, such as the Anderson 6-stage sampler, to quantify and compare the concentrations of bacteria and fungi [Chen et al., 2020; Department of Health, Ministry of Public Health, Thailand, 2016]. Agricultural waste has emerged as one of the primary carbon sources for the manufacturing of activated carbon. Agricultural waste is typically waste or byproducts of agricultural activities. We provide another environmentally acceptable alternative to disposing of waste and by-products by reusing or recycling these low-cost materials to manufacture activated carbon. [Feng et al., 2020]. Several activated carbon (AC) are used for improving indoor air quality, AC might be shell-based such as coconut shell-based, pecan shell, and almond shell-based [Ma et al., 2019] or it might be activated charcoal, bamboo charcoal (BC) [Ponken et al., 2023]. Activated carbon has a high capacity to capture gaseous contaminants such as formaldehyde [Peng Lin et al., 2022; Ying et al., 2022; Ongwandee et al., 2018]. The purpose of this study was to use activated carbon derived from coconut shell to eliminate

* Corresponding author: Yaowatat Boongla
E-mail: yaowatat@tu.ac.th; Tel: +669-2-463-0064

airborne microorganisms in an indoor space. Furthermore, the proximate analysis and characteristics of coconut shell were studied. The current investigation additionally investigated the effect of various activities (living activities, room size and type) and conditions on activated carbon, such as activation duration and temperature.

2. METHODOLOGY

2.1 Raw material

The gathering procedure involved selecting dried coconut shell (CS) that was thick enough to shorten the cleaning process, save time, and be resistant to heat. The coconut shell was then extensively cleansed to remove any coconut fiber that had become stuck to the shell's surface.Coconut shells utilized in the present study were obtained from local comminity in southern province of Thailand. The starting materials were manually chosen, cleaned with deionized water, dried at 80 °C for 12h and ground using a roller mill and sieved to a size range of 212 µm and stored in sealed containers for experimentation. The proximate analysis was examined moisture content (MC), volatile matters and ash content (AC), which is in accordance with the American Society of Testing and Materials (ASTM) standard and calculated using the equation below [Sunardi et al., 2019]:

$$\text{MC (\%)} = \left(\frac{X1-X2}{X1} x\ 100\%\right) \qquad \text{(Eq. 1)}$$

where:
MC = Moisture content, stove at a temperature of 103 ± 2°C.
X1 = Weight of initial sample (gram)
X2 = Weight of the sample after drying (gram)

$$\text{VM (\%)} = \left(\frac{B-C}{W} x\ 100\%\right) \qquad \text{(Eq. 2)}$$

where:
VM = Volatile matterat
B = Weight of the sample after drying at temperatures of 105-110 ºC (gram)
W = Weight of initial sample (gram)
C = Specimen weight after heating (gram)

$$\text{Ash (\%)} = \left(\frac{F-G}{W} x\ 100\%\right) \qquad \text{(Eq. 3)}$$

where:
AC = Ash content
F = Weight of crucible and ash (gram)
G = Empty crucible weight (gram)
W = Initial weight of specimen (gram).

$$\text{FC (\%)} = 100 - (MC + VM + AC)\ \% \qquad \text{(Eq. 4)}$$

where:
FC = Fix carbon
MC = Moisture content (%)
VM = Volatile matter (%)
AC = Ash content (%)

2.2 Praparation of activated carbons (AC)

In this study, activated carbon from coconut shell residue was prepared in a two-step process: carbonization and chemical activation processes. The precursor chemical activator was potassium hydroxide (KOH) [Hu et a., 1999]. 10 grams of raw coconut shell were weighed and placed in an empty crucible. 10 grams of solid KOH were diluted in 20 milliliters of distilled water. The solution was poured to the weighted coconut shell in a 1:1 ratio and mixed uniformly. Later, the mixture was oven-dried for 24 hours. The raw material was then carbonized using an activating agent in a furnace. The furnace was set to a constant temperature of 700 °C, activation duration of 30 minutes, and rate of 5°C per minute. Following the carbonization process, the sample was washed with 3M of HCl, vacuum filtered, and rinsed with hot distilled water until it reached pH 7. The sample was then transferred to an empty petri dish and baked in an oven at 80°C for 24 hours. The dried sample was weighed and the percentage of yield was calculated using Equation (5) [Andas et al., 2017]. The dried sample was sieved (150 µm) and stored in a tight container for later use. The impregnation ratio was 1:5, and the activation temperature (800°C) was tuned in this study under KOH treatment to produce activated carbon with a high yield%, high iodine number, and well-developed pore structure. The prepared activated carbon was denoted as KOH-activated carbon. Figure 1 shows the framework of coconut shell activated carbon using chemical activation.

$$\text{Yield (\%)} = \left(\frac{Mass\ fianl}{Mass\ initial} x\ 100\%\right) \qquad \text{(Eq. 5)}$$

where, Mass final = Mass of product; Mass Initial = Mass of precursor used.

2.3 Surface area analysis (S_{BET})

The specific surface area, pore volume, and pore size distribution of the activated carbon were determined from the adsorption isotherms using the Brunauer-Emmett-eller (BET) equation and a Quantachrome Nova Win2 1994-2002 instrument (Quantachrome Instruments, Boynton Beach, FL, USA).The cross-sectional area of the nitrogen molecules was assumed to be 0.162 nm2. The Dubinin- Radushkevich (DR) equation was used to calculate the micropore volume. The total pore volume was estimated as the liquid volume of the adsorbate (N_2) at a relative pressure of 0.985. The pore size distribution was deter mined using the Barrett-Joyner-Halenda (BJH) model. The average pore diameter was calculated as four times the total pore volume over the BET surface area [Duangani et al., 2022].

2.4 Activated carbons Sampling

Activated carbon (AC) are carbonaceous adsorbents made from carbonaceous materials having a high carbon content, low ash content, and considerable volatile matter via physical, chemical, or a combination of both methods. Activated carbon is the most established and efficient technology available for removing most bioaerosal and certain microorganisms from air. The activated carbon employed in this investigation was 40g per area (Fig.2). In the first area, activated carbon is placed in the room, and in the second area, activated carbon is placed in the toilet in the room condomium to test the possibility of air removal in inddor air.

2.5 Total Bacteria

In this study, the Microbial Test Kit "Compact Dry TC" was employed.The number of colony forming units (cfu) generated on a plate count medium after a particular incubation time at mesophilic temperatures (approx. 30 - 37 °C) is indicated by the "aerobic mesophilic count. The aerobic count is a measure of the microbial status of the manufacturing process and the surrounding environment. Compact dry TC is a total viable mesophilic count test plate that includes a standard nutrition medium. Because of the redox indicator triphenyl tetrazolium chloride, the colonies produced on Compact Dry TC are red. As a result, they are simple to recognize and distinguish from potential food residues.

2.5 Total Bacteria

In this study, the Microbial Test Kit "Compact Dry TC" was employed.The number of colony forming units (cfu) generated on a plate count medium after a particular incubation time at mesophilic temperatures (approx. 30-37°C) is indicated by the "aerobic mesophilic count. The aerobic count is a measure of the microbial status of the manufacturing process and the surrounding environment. Compact dry TC is a total viable mesophilic count test plate that includes a standard nutrition medium. Because of the redox indicator triphenyl tetrazolium chloride, the colonies produced on Compact Dry TC are red. As a result, they are simple to recognize and distinguish from potential food residues.

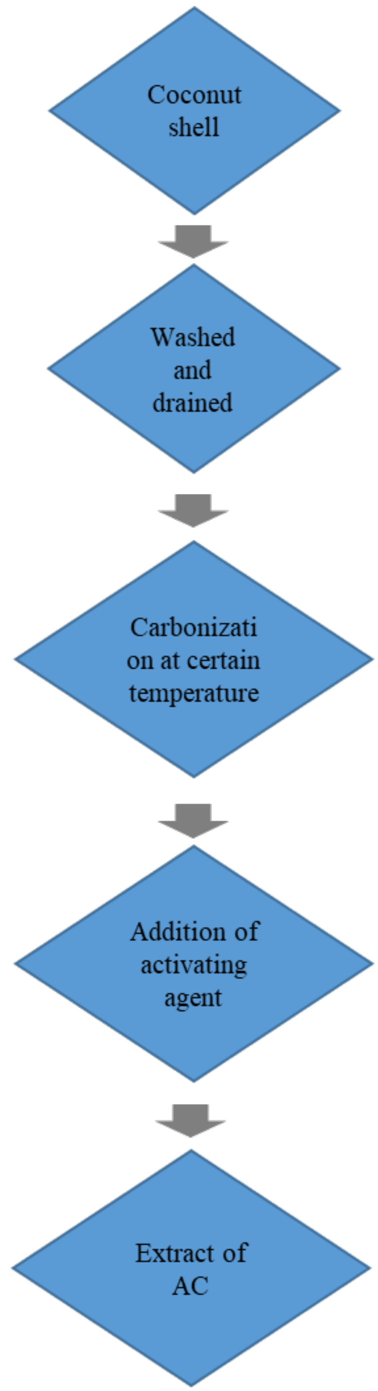

Fig.1 Framework of coconut shell activated carbon using chemical activation.

Fig.2. Coconut shell activated carbon powder for air removing.

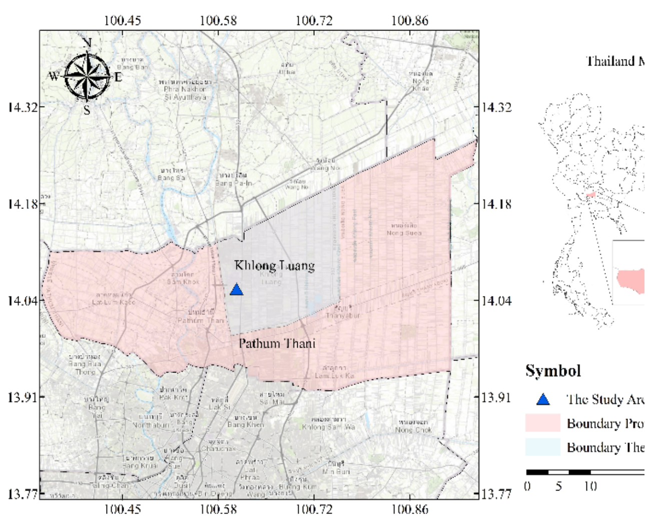

Fig.3. Study site.

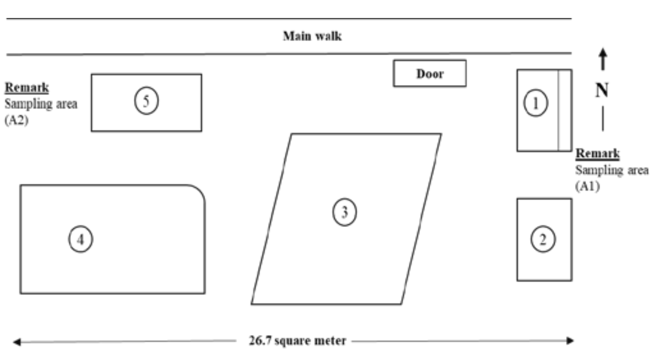

Fig.4. Lay out of the room condominium and sampling locations Whereas: No.1 = kitchen area; No. 2 = television; No. 3 = room center; No. 4 = bed; No.5 = toilet.

2.6 Study room

The interior samples were taken at the dcondo campus hideaway condominium in Bangkok. Chiangrak Road, Pathum Thani province, Thailand (14°03'39.3"N 100°36'37.0"E, 8 m above ground) (Fig.3). The sample room is approximately 28 m^2, with one kitchen, desks, chairs, televisions, and laptops; a two-person sofa; and a small restroom space. The room now has an air conditioning system. Indoor human activities usually involved no more than two or three people per day. Indoor sampling stations were used 24 hours a day, two days a week (from August 21 to July 23, 2023). Figure 4 shows lay out the room condominium and sampling locations while Table 1 shows the room characterization of this study. General information was similar, while the room floor and number of family members were different between rooms A and B.

Table 1. Room Characterization

General Information	Room A	Room B
Room size	26.7	26.7
Floor	7	1
Bathroom No.	1	1
Ventilation	air conditioner	air conditioner
Sunlight	sunshiny	sunshiny
Balcony	Yes	Yes
Dust in room	Yes	Yes
Musty smell	No	Yes
Cleanning (< 3 times/week)	No	Yes
(> 3 times/week)	Yes	No
Family Member	3	2

2.4 Statistical analysis

Descriptive analyses were performed in SPSS v.28. To evaluate test mean difference and performance with 95% confidence intervals (95% CI) were calculated. The correlation between microbial on Compact Dry and growth on activated carbon and without activated carbon was evaluated using Pearson’s correlation test.

3. RESULTS AND DISCUSSION

3.1 Characterization of activated carbons

The proximate analysis of the coconut shell is shown in Table 2. The activation temperature of 800 °C showed average yield of 30.0%. As a result, characteristics of the activated carbon produced from coconut shell found moisture 5.0%wt, iodine number 900 mg/m average pore diameters 2.3 nm, total pore volume 1.2 cm^3/g and BET surface area 950 m^2/g, respectively (Table 3). Coconut shell can use as an activated carbon because the moisture content is less than 8% and iodine numbers are above 600 mg/g which are the values considered by the Thai Industrial Standards Institute, TISI-900 (Thai Industrial Standards Institute, 2003). The activation step is critical in the production of activated carbon. Chemical or physical activation influences the form and size of pores in activated carbon. The chemical used in this study was KOH.
High-surface-area activated carbons were obtained by chemical activation of coconut shells with KOH. Commercially available activated carbon is typically derived from costly and finite resources such as petroleum, coal, wood, lignite, and peat. Ketwong et al., [2019] stated that coconut shell charcoal was used to make activated carbon (AC) for ammonia adsorption applications, with a good activation temperature of 700°C and H_2SO_4 impregnation in their investigation. BET surface area, pore size distribution study, and iodine number revealed good results at 900°C. The activation temperature for biomass raw materials is generally reliant on chemical reagents, reaching 400-800°C [Gratuito et al., 2008].

Table 2. results of coconut shell.

Material	Moisture (%)	Ash (%)	Volativle Matter (%)	Fix carbon (%)
CS	5	1	70	19

Remark: Coconut shell (CS)

Table 3. Iodine number and surface area of the coconut shell-based activated carbon.

Material	Iodine number (mg/m)	Pore diameter (nm)	Pore volume (cm^3/g)	BET surface area (m^2/g)
Coconut shell	900	2.3	1.2	950

Remark: Coconut shell (CS)

3.2 Exploration of the microbials from different indoor room condominium

As can be seen in Tabel 4 and 5, The results indicated that the concentrations of total viable mesophilic count test plates (TC) in rooms A and B were 595.0, 276.0, 1087.0, and 513.0, respectively. The results indicated that the total viable mesophilic count test plate in room condominium B was higher than in room condominium A. The viable mesophilic count test plate of area No.2 (toilet area) was higher than area No 1 (room area). Room A's character is bloated and always cooking, whereas Room B's character is less filled. This research takes place in the evening because the room owner is available at that time. As a result, their activity is always concentrated in the afternoon and evening. In most situations, it could be concluded that indoor concentrations of airborne bacteria were lower in the morning than in the afternoon.

3.3 Airbore microbial assessment by activated carbon adsorption

This section must summarize the key findings of the study and describe potential activated carbon for further research. The TC in rooms A and B showed high colony-forming units. The results indicated that the concentration of TC in the room condominiums A and B with activated carbon was 276.0 and 513.0, respectively. The concentration of TC in all rooms was lower than without activated carbon (Fig.5 and 6). It indicated that air is purified by activated carbon as presented in Table 4 and 5. In room A, the viable mesophilic count test plate of area No. 1 (toilet area) was lower than area No. 2 (room area), while room B, the viable mesophilic count test plate of area No. 2 (toilet area) was lower than area No. 1 (room area). In the toilet, the results indicated that the concentration of TC was high due to the fact that it is an area of microorganism contamination. It is less clean than the room area. This might be caused by the activity inside the room, which included boiling, frying, and cooking. Moreover, the compact dry TC was placed on a shelf above the cooking area. As can be seen figure 7 to 9, the colony-forming unit, found maximum value in room B with area No. 2 (toilet). The count on the test plate was 220, 249, and 219, for a total of 688. On the day with activated carbon, the count on the test plate was 344 (toilet area, room B). Room A: The family member always buys delivery food and sometimes eats outside. In the research report of Kuma, the results revealed the bacterial aerosol concentration was high, and *Staphylococcus*, *Streptobacillus*, and *Micrococcus* were the predominant bacteria in their report. A previous study found that exposure to–varied bacterial concentrations could have direct and indirect effects on human health [Kuma et al., 2022]. Semilar observation by others are agreement with these data [Ongwandee et al, 2018; Sasan et al., 2015; Hayleeyesus et al., 2014]. As a result, the most important way to minimize negative health impacts is to prevent (or reduce) prolonged wetness and microbial growth on interior surfaces and in building structures.

3.4 The influence of meteorological factors on microbial concentration

Wind speed, air condition, and relative humidity all had an effect on the concentration of TC in rooms condominium A and B, according to the meteorological results. Wind speed had an effect on TC concentration, according to the results. High wind speeds had a low TC concentration, whereas low wind speeds had a high TC concentration. Room B had a higher wind speed than Room A. The temperature in room A ranged from 25.1-27.5 °C, with the first day study showing a lower temperature than the second day research. Room B had a temperature range of 28.0-30.9 °C, with the first day study having a lower temperature than the second day research. This discovery demonstrated that temperature has a substantial impact on the indoor TC content in room condomium. The relative humidity in both rooms was low on the first day of the trial. The relative humidity in room A ranged from 42.0 to 42.7%, while it ranged from 52.1-52.7% in room B. The first day study revealed a lower temperature than the second day study, however the difference was not statistically significant. Tables 4 demonstrate the Pearson correlation. Tables 6 show the relationship between microbiological concentration and meteorological conditions in a room condominium. Correlations between meteorological parameters (wind speed, temperature, and relative humidity) and bacterial concentrations in this investigation were consistent with prior data but inconsistent with others. Microorganism concentrations in the air were found to be highly connected to meteorological parameters such as wind speed. Table 6 depicts the association between microbiological content and weather conditions in room A and B condominiums. High wind speed reduced microbiological concentrations due to dilution of the air from the wind, especially when the wind moved the air from a lower concentration of both relevant parameters. Because microorganisms are normally attached to dust in the air, dispersion of the dust at the sampling region led in dilution of microbial concentration, which was consistent with the findings of others (Phuipanya et al., 2019; Bragoszewska and Pastuszka, 2018). The correlation coefficient was 0.381, which agrees well with the findings of Bragoszewska and Pastuszka et al. In 2018, the connection between bacteria and wind speed was 0.266. Furthermore, Bragoszewska and Pastuszka et al. 2018 state that it is critical to assess the concentration of bacterial aerosol for wind speeds ranging from less than 1 km h-1 to more than 20 km h-1. We found a statistically significant negative connection between TC aerosol and temperature during the research periods, with values of - 0.212. As a result, airborne bacteria in condominiums are more likely to multiply and thrive at low temperatures, whereas high temperatures inhibit their growth. In our investigation, we discovered a negative relationship between RH and bacterial levels. Table 6 shows that the connection was statistically significant negative, with an R2 value of -0.404. In contrast to the findings of Jones and Harrison (2004), moisture in the air could change the integrity of cell walls and viral coatings, promoting the growth and release of germs. When temperature and relative humidity were compared, the opposite was observed. The capacity of ambient bacteria to survive was reduced as the temperature rose [Ali Abu Rub et al., 2021]. This reliance resulted from the significant relationship between temperature and relative humidity. Temperature and relative humidity had Pearson correlation values of 0.820. The obtained results could be used as a reference for future evaluations and contribute to policy reviews and agricultural waste management.

Table 4. The total of microorganisms and environmental conditions in room A

Sampling period	Room A	Wind speed	Temperature (°C)	Humidity (%)
1st day (without AC) Area No.1	245.0	1.6	25.1	42.7
Area No.2	350.0	1.4	25.1	42.0
Total	595.0	3.0	50.2	84.8
2nd day (with AC)				
Area No.1	141.0	1.5	27.3	51.8
Area No.2	135.0	1.5	27.5	55.1
Total	276.0	3.0	54.8	96.9

Remark: Wind speed (Wd), Temperature (T), Humidity (H)

Table 5. The total of microorganisms and environmental conditions in room B

Sampling period	Room B	Wd	T (°C)	H (%)
1st day (without AC)				
Area No.1	399.0	1.8	28.1	52.7
Area No.2	688.0	1.9	28.0	52.1
Total	1087.0	1.0	54.1	84.8
2nd day (with AC)				
Area No.1	169.0	1.8	30.9	58.8
Area No.2	344.0	1.8	28.5	59.1
Total	513.0	1.6	58.4	117.9

Remark: Wind speed (Wd), Temperature (T), Humidity (H)

Table 6. The correlation coefficient (R2) of microbial concentration and meteorological factors at room condominium.

R2	Microbial	Wd	T (°C)	H (%)
Microbial	1			
WS	.381	1		
Temp	-.212	.588	1	
RH	-.404	.528	.820*	1

Remark: *Correlation is significant at 0.05 level
Wind speed (Wd), Temperature (T), Humidity (H)

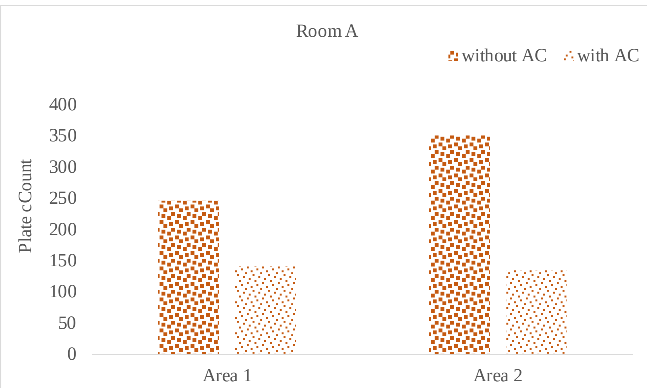

Fig.5. The amounts of microorganisms in room condominiums without activated carbon and with activated carbon (Room A).

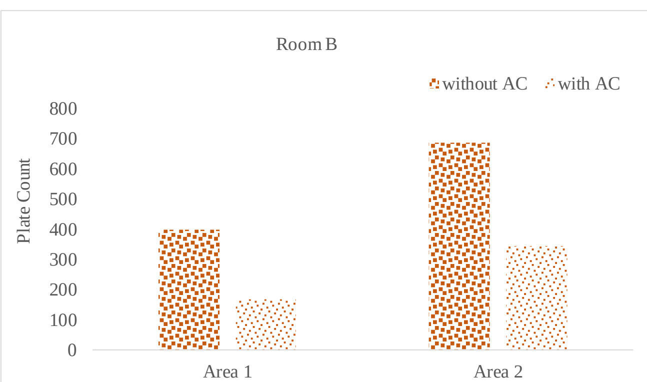

Fig.6. The amounts of microorganisms in room condominiums without activated carbon and with activated carbon (Room B)

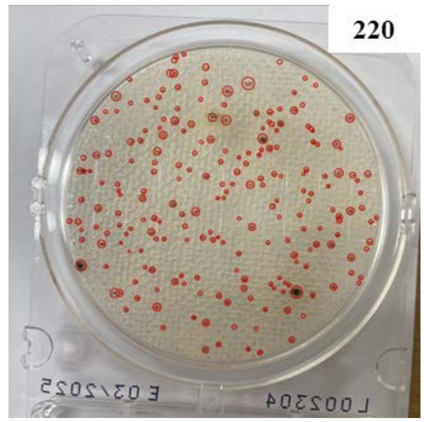

Fig.7. Colony forming units (The maximum colony forming units)

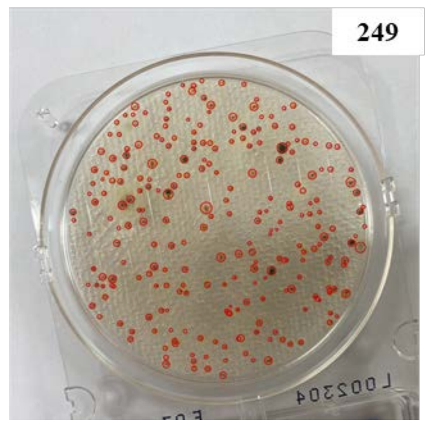

Fig.8. Colony forming units (The maximum colony forming units)

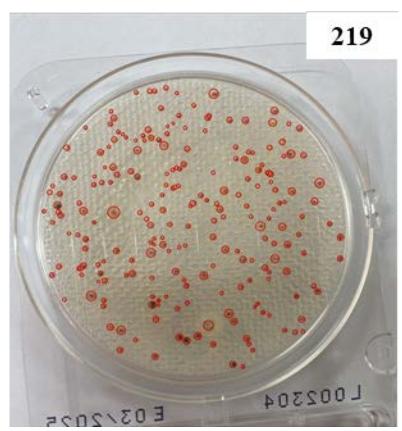

Fig.9. Colony forming units (The maximum colony forming units)

4. CONCLUSIONS

This paper presents the AC production from coconut shell. Under these conditions, coconut shell activated carbon performs well in terms of air removal. Microorganism contamination is significant in the room condominiums that do not use coconut shell activated carbon. Coconut shell activated carbon produced similar results to Thailand Industrial Standard. As a result, the coconut shell-derived AC could be employed as an airborne adsorptive bed material in condominiums.

A significant correlation between bioaerosols and relative humidity, temperature, demonstrated in this study suggested that these variables can be considered as the determinant factors of microorganism growth in the indoor environment of condominium facilities.

ACKNOWLEDGMENTS

The authors are grateful to Thammasat University for the financial support, condominium owners for providing access to the sampling points as well as to the Department of Sustainable Development Technology for providing lab facilities.

REFERENCES

[1] Bhave, P.P., Yeleswarap, D. (2020). Removal of Indoor Air Pollutants Using Activated Carbon-A Review. Global Challenges in Energy and Environment Select Proceedings of ICEE 2018, Springer Nature Singapore Pte Ltd, 65-75.

[2] Andualem, Z., Gizaw, Z. Bogale, L., Dagne, H. (2019). Indoor bacterial load and its correlation to physical indoor air quality parameters in public primary schools. Multidisciplinary Respiratory Medicine, 4:2 https://doi.org/10.1186/s40248-018-0167-y.

[3] United States Environment Protection Agency. (2022). Indoor Air Quality in Apartments. https://www.epa.gov/indoor-air-quality-iaq/indoor-air-quality-apartments.

[4] Modal, S., De, S., Saha, P. (2021). Removal of VOCs and Improvement of Indoor Air Quality Using Activated Carbon Air Filter. Advances in Structural Technologies Select Proceedings of CoAST 2019, Springer, 123-132.

[5] Phuipanya, T., Seeubon, W., Srinakara, S., Siriwat, S. (2019). Assessment of Respirable Dust and Bioaerosols in Dormitory Building: Case study of Kasetsart University Chalermphrakiat SakonNakhon Province Campus. Journal of Sakon Nakhon Hospital, 22(3), 77-85.

[6] Chen, H., Du, R., Ren, W., Zhang, S. Du, P., Zhang, Y. (2020). The Microbial Activity in $PM_{2.5}$ in Indoor Air: As an Index of Air Quality Level. Aeorosol and Air Quality Research. 21(2), 1-13.

[7] Department of Health, Ministry of Public Health, Thailand, (2016). Method for Evaluating Indoor Air Quality for Government Employees.

[8] Feng, P., Lee, J., Wang, H. Xu, Z. (2020). Biomass-Based Activated Carbon and Activators: Preparation of Activated Carbon from Corncob by Chemical Activation with Biomass Pyrolysis Liquids. ACS Omega, 5, 24064-24072.

[9] Ma, X., Smith, L.M., Cai, L., Shi, S.Q. Li, H., Fei, B. (2019). Preparation of High Performance Activeted Carbons Using Bamboo through One-Step Pyrolysis. BioResources, 14(1), 688–699.

[10] Ponken, T., Phumuen, T. Phosopa, N., Tangsin, P., Ponhan, W., Phakkhawan, A., Klangtakai, P. (2023). Activated Carbon Synthesized from Bamboo Shoots for Supercapacitor Application. Creative Science, 1 5(1) 2 4 70 5 1.

[11] Sasan, F., Mohammad, S.H., Kazem, N., Masud, Y., Ramin, N., Mohammad, H.S, Homa.K , Akbar, G, Sadegh, N., Ahad, Z., Shahrokh, N., Mahmood, A.. (2015). Indoor/outdoor relationships of bioaerosol concentrations in a retirement home and a school dormitory. Environ Sci Pollut Res, 22, 8190–200.

[12] Hayleeyesus, S.F., Manaye, A.M. (2014). Microbiological Quality of Indoor Air in University Libraries. Asian Pacific Journal of Tropical Biomedicine, 4(Suppl 1): S312-S317.

[13] Ongwandee, M., Chatsuvan, T., Pattiya, A. (2018). Technical Feasibility Study of Char from Fast-Pyrolysis as Adsorbent for Removing Indoor Air Pollutant, Journal of Engineering, RMUTT, 91-102.

[15] Djuanda, S., Mandra, M.A.S. (2019). Characteristics of Charcoal Briquettes from Agricultural Waste with Compaction Pressure and Particle Size Variation as Alternative Fuel. International Energy Journal, 19, 139-148.

[16] Andas, J., Rahman, M. L. A., Yahya, M. S. M. (2017). Preparation and Characterization of Activated Carbon from Palm Kernel Shell, Materials Science and Engineering, 226 012156.

[17] Hu, Z., Srinivasan, M. P. (1999). Preparation of high-surface-area activated carbons from co conut shell. Microporous and Mesoporous Materials, 27, 11-18.
[18] Duangani, R., Munawar, S.S., Karliati, T., Malik, J., Aditiawati, P., Sulistyono. (2022). Study of characterization of activated carbon from coconut shells on various particle scales as filler agent in composite materials. Journal of the Korean Wood Science and Technology, 50(4) 256-271.
[19] Bragoszewska, E., Pastuszka, J.F. (2018). Influence of meteorological factors on the leveland characteristics of culturable bacteria in the air in Gliwice, Upper Silesia (Poland). Aerobiologia, 34, 241-255.
[20] Jones, A. M., and Harrison, R. M. (2004). The effects of meteorological factors on atmospheric bioaerosol concentrations-A review. Science of the Total Environment, 326(1–3), 151–180. https://doi.org/10.1016/j.scitotenv. 2003.11.021.
[21] Ali Abu Rub, L.I., Gharbi, D., Saf, M., Eltai, N.O., Suhail, M., Kotb, M.M. Yigiterhan, O., Alfoldy, B. (2021). A preliminary study on microbial air contamination in select schools in Doha, Qatar. Arabian Journal of Geosciences, 14: 2707. https://doi.org/10.1007/s12517-021-08867
[22] Thai Industril Standard. (2007). Activated carbon standard. http://www.fio.co.th/web/tisi_fio/fulltext/TIS900-2547.pdf (access on 15 March 2024).
[23] Ketwong, T., Sitthiseree, S., Khembubpha, A., Areeprasert, C. (2019). Activated carbon production from coconut shell charcoal employing steam and chemical activation for ammonium adsorption application. Proceedings of the World Congress on Engineering and Computer Science 2019 WCECS 2019, October 22-24, 2019, San Francisco, USA.
[24] Gratuito, M.K.B., Panyathanmaporn, T., Chumnanklang, R. A., Sirinuntawittaya, N., Dutta, A. (2008). Production of activated carbon from coconut shell: Optimization using response surface methodology. Bioresource Technology, 99, 4887-4895.

Techno-Science Research Journal 12 (Special Issue) 49-56

I.T.C

Content list available at ITC

Techno-Science Research Journal

Journal Homepage: www.ric.itc.edu.kh

Techno-Science Research Journal

Assessment of e-commerce plastic waste management during the COVID-19 pandemic in Dasmariñas, Cavite

Noriza T. Sadie[1*], Sarah Pearl L. Falcutila[1], Audrey Arianne S.P. Florentino[1], Ma. Brida Lea D. Diola[1]

[1]Institute of Civil Engineering, University of the Philippines Diliman, Quezon City, Philippines 1101
[*]nrtibon@up.edu.ph; ORCID: 0000-0003-2773-9852

Received: 22 August 2023; Accepted: 15 May 2024; Available online: August 2024

Abstract: *The rapid development of e-commerce in the Philippines has led to an increase in the production of plastic waste. To estimate the city's e-commerce plastic waste generation, the factors affecting consumers' shopping habits, the awareness on e-commerce waste pollution, and household waste management practices, an online survey was conducted with 243 respondents from the city of Dasmariñas, Cavite. Utilizing a five-point Likert scale, the survey also assessed the frequency with which respondents encountered distinct plastic packaging types in their orders. The annual generation of e-commerce plastic waste was estimated by considering the total annual purchase of the city, the frequency of encountering distinct plastic packaging types, and the estimated weight of the plastic types. Secondary data pertaining to Dasmariñas' waste management policies were also gathered from official city reports and relevant literature sources. The results showed that the e-commerce plastic waste generated by the city's residents increased from 7,500 tons in 2019 to 24,600 tons in 2022. This e-commerce plastic waste is 11.2% of the projected waste generation of the city in 2022, with bubble wraps and plastic bags being the most frequently encountered. The majority of the respondents demonstrated awareness of the issue of excessive packaging in the country, possessed limited knowledge about green packaging concepts, and acknowledged the severity of environmental concerns related to plastic generation and disposal in e-commerce. With this, policies should be put in place to properly manage plastic waste, such as reducing plastic usage, investing in research on the use of alternatives to plastic, promoting social enterprises that collect and recycle plastic packaging waste, providing incentives to sellers and consumers to encourage eco-friendly packaging, and calling on e-commerce platforms to lessen their carbon footprint.*

Keywords: e-commerce; plastic waste; online shopping; packaging; solid waste management

1. INTRODUCTION

Electronic commerce (e-commerce) in the Philippines has seen an immense rise in popularity during the COVID-19 pandemic. The Department of Trade and Industry stated that the e-commerce adoption in the country has risen from 70% in 2019 to 80.2% in 2021 [2]. The top e-commerce platforms in the Philippines regularly organize double-digit monthly promotions and mega campaigns such as platform birthday, payday sale, 10.10, 11.11, and 12.12 events. In 2021, the country's e-commerce market sales reached $17 billion, which is estimated to reach $24 billion, with 17% growth through 2025 [4]. With the restrictions brought about by the pandemic, more and more Filipinos discovered new avenues for product purchase leading to the increase in e-commerce demand.

Due to the dramatic increase in volume of express delivery, a problem arose in the form of e-commerce packaging. According to a study by Pålsson [7], the e-commerce industry generally consumes more energy than traditional stores, with packaging contributing to most of the energy consumption difference. The type of packaging materials that cause the most damage to the environment are plastic bags, internal buffers, and other plastic products which are mostly non-recyclable or non-degradable materials [5]. There is conclusive data that plastic pollution negatively impacts marine and coastal ecosystems, wildlife, soil, and water resources, and poses a risk to human health [8].

[*] Corresponding author: Noriza T. Sadie
E-mail: nrtibon@up.edu.ph

Leading e-commerce companies like Shopee and Lazada have not officially released any numbers regarding not just their total number of sales but also the amount of plastic waste generated by their service. Both platforms have yet to add environmentally friendly packaging as an option for consumers in their purchases. There is also a lack of study on the consumer's awareness of the harmful effects of plastic pollution and their behavior towards e-commerce plastic waste disposal. A study conducted by Ren and Zhao [10], found that the improvement of regulations and raising public awareness can reduce environmental pollution caused by packaging.

Therefore, this study aims to assess the e-commerce plastic waste management of households during the COVID-19 pandemic in Dasmariñas, Cavite, particularly 1) estimate the e-commerce plastic waste generated from consumers residing in Dasmariñas, Cavite, 2) identify the factors affecting consumer's online shopping behavior, 3) identify household plastic waste management practices, and 4) determine consumers' awareness on overpackaging, green packaging, and e-commerce plastic waste pollution. These will be beneficial in assessing the severity of the plastic pollution brought about by online shopping in the Philippines and can aid in the creation of packaging regulations.

2.1 Study Area

The city of Dasmariñas, as shown in Figure 1, is a 1st class city located in the province of Cavite in Region 4A. It has a land area of 90.1 km^2, a population of 703,141 residents, and a population growth rate of 1.37% from 2015 [9]. According to the National Solid Waste Management Commission [6], the waste generation of the city steadily increased from 195,000 tons in 2019 to 220,000 tons in 2022.

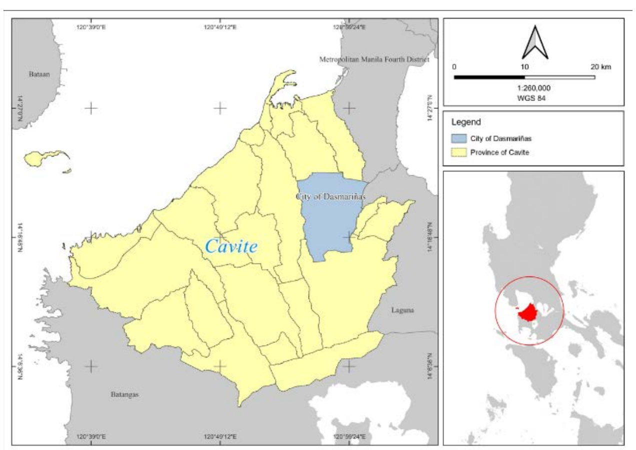

Fig.1. Location of Dasmariñas City

Policies that are specifically directed towards e-commerce plastic waste do not currently exist in the city and the country, in general, but there are a handful of existing policies regarding plastic use that the city of Dasmariñas have implemented. Provincial Ordinance No. 007-S-2012 entitled "The selective plastic ban and the use of eco-bag ordinance of the province of Cavite", is an ordinance regulating the various uses of plastics for goods and commodities that end up as residual wastes. The ordinance promotes the utilization of eco-bags and other environmentally friendly practices as an alternative. City Ordinance No. 03-S-2012 entitled "Ordinance regulating the use of plastic bags and styrofoam in the City of Dasmarinas", on the other hand, aims to reduce the volume of garbage specifically plastic waste that is generated in the daily operations and other activities around the city of Dasmariñas.

2. METHODOLOGY

In this study, primary data regarding participant demographics and the generation of plastic waste were acquired via an online survey. Furthermore, secondary data encompassing Dasmariñas' waste management policies were compiled from official city reports and relevant literature sources. Figure 2 illustrates the study's methodological framework.

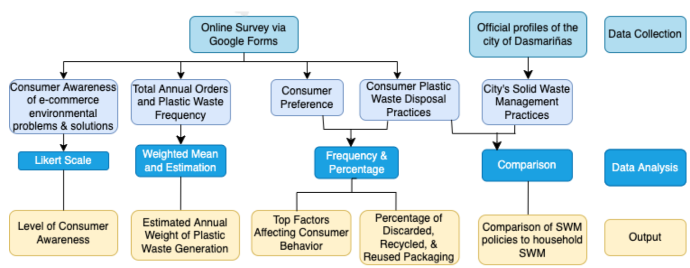

Fig.2. Methodological Framework

2.1 Online Survey

Due to the restrictions brought about by the COVID-19 pandemic, an online questionnaire survey was conducted via Google Forms to gather data on the participants for the study. The survey questionnaire is made up of four main sections: 1) characteristics of the consumers, 2) online shopping purchases, 3) online shopping behavior of consumers, and 4) online shopping packaging waste disposal.

The required number of respondents to sufficiently represent the population was determined using Slovin's formula. For this study, a 95% confidence interval and a precision level of ±7% were chosen. Consequently, a total of 243 participants were selected for the study, all of whom are residents of Dasmariñas, Cavite, possessing knowledge of online shopping platforms and prior experience in online purchases. The participant pool is restricted to individuals aged between 16 and 64 years old.

2.1 E-commerce Plastic Packaging Waste Generation

This study utilized the information given by the respondents regarding their annual purchases throughout a four-year period and produced the total annual purchase of the city. This value is obtained by getting the average annual purchase of a consumer using Equation 1. Note that a ceiling of 1200 is applied to the total number of orders per customer per year, as instances of orders surpassing this threshold were not observed in the dataset.

$$AAP_Y = \frac{\sum_{i=1}^{1200}(i \times x_i)}{\#_{TOTAL}} \quad \text{(Eq. 1)}$$

where:
AAP = average annual purchase of a consumer
Y = year evaluated: 2022, 2021, 2020, 2019
i = amount of orders purchased in a year
x_i = number of respondents who answered with amount of orders
$\#_{TOTAL}$ = total number of respondents

To determine the cumulative percentage of plastic packaging encountered for each plastic type, both the proportion of consumers who encountered each specific plastic and the frequency of those encounters were taken into account. Utilizing a five-point Likert scale, the frequency with which respondents came across distinct plastic packaging types in their orders was assessed. The descriptive ranges, corresponding descriptions, and equivalent frequency percentages for the five-point scale are detailed in Table 1.

Table 1. Five-Point Likert Scale Descriptive Range, Descriptive Equivalent, and Percentage of Frequency

Descriptive Range	Descriptive Equivalent	Percentage of Frequency (%)
1 - 1.8	Almost Never	20
1.9 - 2.6	Rarely	40
2.7 - 3.4	Sometimes	60
3.5 - 4.2	Often	80
4.3 - 5	Always	100

The total percentage of plastic packaging encounters for each plastic type was calculated using Equation 2.

$$T\%_k = E\%_k * LS\%_k \quad \text{(Eq. 2)}$$

where:
T% = total percentage plastic packaging is encountered
E% = percentage of consumers who have encountered each plastic
LS% = percentage equivalent of Likert scale
K = kind of plastic packaging

Table 2. Density, Thickness, and Estimated Weight of Plastic Packaging

Plastic Packaging Encountered	Density of Plastic (g/cc) [3]	Thickness (cm)	Estimated Weight of Plastic in One Order (g)
Plastic Bags (LDPE)	0.91	0.010	3.875
Bubble Wrap (LDPE)	0.91	0.020	7.750
Polystyrene Foam (PS)	1.07	0.050	22.781
Air Bubble (HDPE)	0.94	0.002	0.801
Packing Peanuts (PS)	1.07	0.038	17.313

Considering both the parcel's volume, in conjunction with the density of each plastic, this research adopted the dimensions of the smallest parcel accessible on Shopee's official website - a 6 in x 11 in pouch or 15.24 cm x 27.94 cm pouch, equating to a total area of 425.81 cm². Thickness measurements for individual plastic packaging types was sourced from various plastic manufacturers. The calculated weight of plastic packaging, determined by factoring in density and volume, is presented in Table 2.

Utilizing the results and data derived from the preceding procedures, Equation 3 is used to compute the annual generation of e-commerce plastic waste.

$$\mathrm{TPPG}_Y = TAP_Y[(T\%_{BW} * W_{BW}) + (T\%_{PB} * W_{PB}) + (T\%_{PF} * W_{PF}) + (T\%_{AP} * W_{AP}) + (T\%_{PP} * W_{PP})] \quad \text{(Eq. 3)}$$

where:
TPPG = total plastic packaging waste generated
TAP = total annual purchase of the city
Y = year evaluated: 2022, 2021, 2022, 2019
T% = total percentage plastic packaging is encountered
W = estimated weight of plastic type
BW = bubble wrap
PB = plastic bags
PF = polystyrene foam
AP = air pillow
PP = packing peanuts

3. RESULTS AND DISCUSSION

3.1 Demographics

Table 3 provides an overview of the demographic distribution among respondents. The collected data indicates a prevalent age group among e-commerce consumers within the city, with the majority falling between 25-34 years (51%), followed by the 16-24 age bracket (27%), 35-44 (14%), and 45-64 (8%). Notably, respondents aged 16-34 constitute 78% of the total participants, aligning with a survey conducted by Shopee, which disclosed that 71% of their shoppers fall within the 18-34 age range [1]. This concurrence underscores the prominence of younger generations in the online shopping consumer base.

Table 3. Summary of Respondent's Demographics (N=243)

		Frequency	Percentage
Age	16 - 24	65	27%
	25 - 34	125	51%
	35 - 44	34	14%
	45 - 64	20	8%
Education Level	Primary	5	2%
	Secondary	79	32.4%
	Tertiary	141	57.8%
	Vocational or Technical University	9	3.7%
	Post-Graduate	10	4.1%
Occupation	Employed	124	50.8%
	Student	77	31.6%
	Self Employed	31	12.7%
	Unemployed	8	3.3%
	Housekeeper	4	1.6%
Household Monthly Income (PhP)	< 11,000	43	18%
	11,000 - 22,000	47	19%
	22,001 - 44,000	69	28%
	44,001 - 77,000	47	19%
	77,001 - 131,000	20	8%
	131,001 - 219,000	8	3%
	> 219,000	10	4%
Household Type	Only adults	82	33.5%
	Family with children and older adults	58	23.8%
	Family with children	57	23.4%
	Family with older adults	41	16.8%
	Living alone	6	2.5%
Residence Type	Single Attached	108	44.3%
	Single Detached	95	39%
	Apartment	23	9.4%
	Shared House	14	5.7%
	Compound	2	0.8%
	Condominium	1	0.4%
	Dormitory	1	0.4%
Job Requires to Purchase or Sell on Online Shopping Platforms	No	177	72.5%
	Yes	67	27.5%

The typical income range for Filipino households falls within the bracket of Php 22,001 to Php 44,000 per month [9]. The data reveals that the largest segment of consumers falls within this middle-income category. Following closely are those earning between Php 11,001 and Php 22,000 and those with incomes ranging from Php 44,001 to Php 77,000. In contrast, the smallest proportion consists of individuals earning Php 219,000 or more. Meanwhile, the employment status of the consumers displayed that the majority of respondents are employed, followed by the students, and the self-employed. This signifies that a significant portion of the consumers, totaling 65.1%, are part of the working class. Notably, 27.5% of the consumers hold jobs that require them to make purchases or sales through online shopping platforms. This could potentially lead to an increased frequency of orders throughout the year for those whose professions necessitate the use of these platforms.

3.2 Online Shopping Purchases

As shown in Table 4, Shopee and Lazada emerge as the city's two dominant e-commerce platforms, with a percentage of 90.2% and 72.1%, respectively. The third spot is occupied by Facebook Marketplace, followed sequentially by ZALORA, Carousell, and Shein. It can be deduced that these prominent platforms stand at the forefront of e-commerce plastic packaging waste generation in the city.

Table 4. Frequently Used Online Shopping Platforms

Shopping Platform	Number of Responses	Percentage
Shopee	220	90.2%
Lazada	176	72.1%
FB Marketplace	92	37.7%
ZALORA	27	11.1%
Carousell	11	4.5%
Shein	6	2.5%

According to the respondents, the top five types of goods they purchase through online shopping are clothes (72.5%), mobile accessories (63.9%), accessories (54.9%), beauty products (46.7%), and electronic gadgets (32%). In light of these findings, it becomes evident that if e-commerce platforms aspire to reduce their plastic footprint and address environmental concerns, one effective strategy would be to implement stringent regulations and sustainable packaging practices within these particular product categories. Initiatives aimed at enhancing the eco-friendliness of packaging materials and practices for these products could have a substantial impact on overall plastic reduction efforts in the e-commerce sector.

3.3 Estimated Plastic Waste Generation of the City

Using Equation 1 and the information given by the respondents on their annual online shopping purchases, the total annual purchase of the city each year is calculated and shown in Table 5. Results show that the average monthly purchase of each consumer increased from 1.3 to 4.4 orders each month from 2019 to 2022, and the estimated total annual purchase of the city has increased from 5.7M orders in 2019 to 18.7M orders in 2022. It can also be seen that the purchases are in an upward trend that is showing continuous growth in e-commerce orders over the last four years and that 2022 has a 230% increase in total orders from the year 2019.

The results from the online survey for the percentage of consumers who have encountered each kind of plastic packaging in their online shopping orders, as presented in Figure 3, show that bubble wrap and plastic bags are the most encountered kind of plastic packaging, both being observed in more than 95.06% and 90.95% of total packages, respectively, followed by polystyrene foam (25.43%), air pillows (23.21%), and plastic peanuts (0.33%). A study done by Kao [5] stated that the role of packaging is shown in the safe transportation of goods. As e-commerce sellers want to guarantee that their products will survive the harsh conditions of express delivery, the results show that bubble wrap is seen as the best choice of packaging to protect their goods. This can be due to the fact that among all the types of packaging that provides cushion to the product, bubble wrap is one of the lightest.

Table 5. Annual Purchase of the City

Year	Average Annual Purchase of Consumer (orders)	Average Monthly Purchase of Consumer (orders)	Total Annual Purchase of the City (orders)
2019	16	1.3	4,408,880
2020	27	2.3	7,439,985
2021	39	3.3	10,746,645
2022	53	4.4	14,549,304

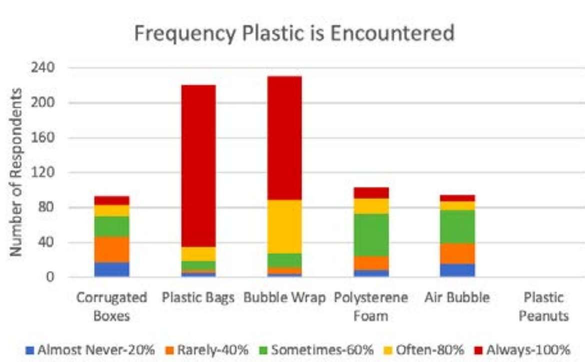

Fig.3. Distribution of Responses on Frequency that the Plastic Packaging is Encountered

Table 6. Estimated Total E-commerce Plastic Waste Generation

Year	Total Plastic Packaging Waste Generated (tons)	Dasmariñas Total Solid Waste (tons) [4]	Percentage of E-commerce Waste to Total Solid Waste
2019	7,462.92	195,934	3.8%
2020	12,593.68	203,500	6.19%
2021	18,190.88	211,359	8.60%
2022	24,627.65	219,521	11.22%

By utilizing the information presented in Table 2, along with the data derived from Figure 3 and Equation 3, the total annual e-commerce plastic waste generated was calculated. As shown in Table 6, an observable upward trend is apparent in both the annual e-commerce plastic waste generated and the percentage of e-commerce's contribution to the overall solid waste generation in Dasmariñas city. Notably, this percentage has experienced a significant rise, increasing from 3.8% in 2019 to an impressive 11.22% in 2022, as projected for the total solid waste generation. It can be inferred that without the prioritization of regulations concerning plastic packaging, this contribution is likely to continue its upward trajectory in the forthcoming years.

3.4 Factors Affecting E-commerce Consumer Behavior

An overwhelming 88.1% of consumers acknowledged that they increased their usage of e-commerce platforms during the pandemic, while 7.4% maintained their pre-pandemic usage levels. Conversely, 4.5% of users decreased their use of online shopping platforms during this period.

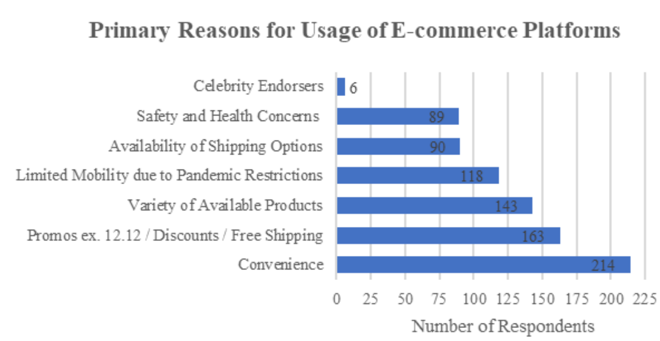

Fig.4. Distribution of Responses on the Primary Reasons for Usage of E-commerce Platforms

From Figure 4, consumers indicated that convenience, promos such as free shipping and monthly festival sales, and the platforms' variety of products were crucial to their usage of the platform. Users also pointed out that limited mobility due to pandemic restrictions affected their usage of the platform.

3.4 Awareness of E-Commerce Consumers on the Industry's Environmental Issues

As shown in Figure 5, e-commerce consumers residing in Dasmariñas exhibit awareness concerning the prevalent issue of overpackaging when it comes to their online orders. However, there exists a notable gap in their knowledge when it comes to the concept of green express packaging. This can be attributed, in part, to the fact that leading e-commerce platforms have yet to introduce green packaging options. The idea of eco-friendly packaging remains somewhat unfamiliar to the average consumer in Dasmariñas, indicating the need for greater education and eco-conscious initiatives within the e-commerce industry. Furthermore, the survey responses indicate a recognition among consumers of the potentially severe environmental repercussions associated with the e-commerce sector. This realization underscores a broader awareness of the industry's ecological footprint and its potential to contribute to environmental issues. It suggests that most consumers are mindful of the need for sustainable practices within the e-commerce sector to mitigate its impact on the environment.

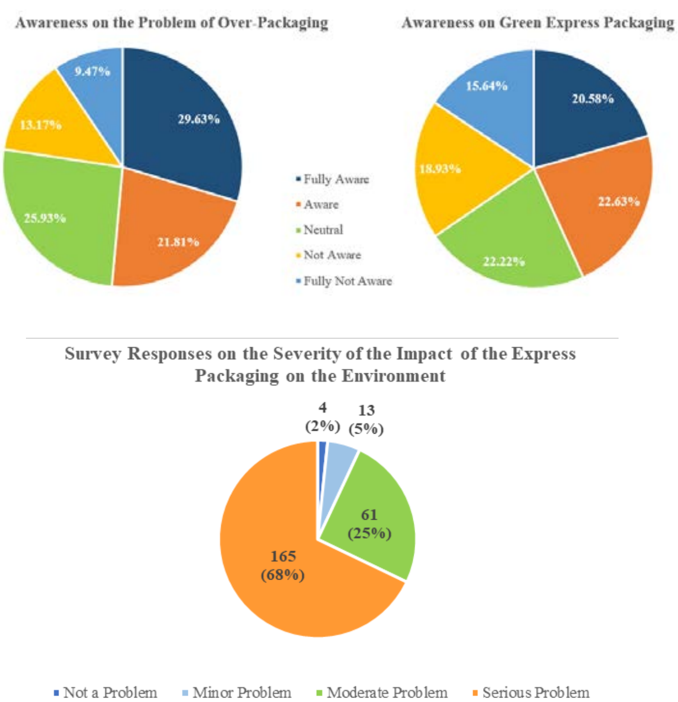

Fig.5. Summary of Respondents' Awareness of E-Commerce Environmental Issues

Table 7. Percentage of Consumers who are "Not Aware" or "Fully Not Aware" of Over-Packaging and Green Express Packaging

Age Bracket	Over-Packaging	Ranking	Green Express Packaging	Ranking
16 - 24	14%	4	26%	4
25 - 34	25%	2	31%	3
35 - 44	21%	3	50%	1
45 - 64	40%	1	45%	2

In Table 7, it is evident that individuals in the 45-64 age group are more likely to lack awareness about over-packaging, as 40% of respondents within this age bracket indicated 'Not Aware' or 'Fully Not Aware' of this issue. Furthermore, when examining knowledge about the concept of green express packaging across different age groups, it becomes apparent that approximately 25%-50% of respondents in each age category have insufficient knowledge, with the 35-44 and 45-64 age groups having the highest percentages at 50% and 45%, respectively. Younger individuals, specifically those aged 16-24, exhibit the highest levels of awareness on both topics. Consequently, it would be prudent to concentrate awareness-raising efforts on the older age groups in order to bridge the knowledge gap and promote greater understanding of these e-commerce-related issues.

3.5 Dasmarinas Household Waste Disposal Practices

Consumer responses on their household plastic waste disposal practices for each type of plastic is summarized in Figure 6. Results show that polystyrene plastics, such as polystyrene foam and plastic peanuts, are disposed of 63.4% of the time. LDPE bags, such as bubble wrap and courier plastic bags, are disposed of more than 52.3% of the time. In contrast, HDPE bags receive the lowest disposal rate at 10.3% while being reused 66.3% of the time.

Fig.6. Consumers Household Plastic Waste Disposal Practices

Regarding household solid waste collection, the majority (79%) of respondents reported that waste is collected once a week, with some areas having biweekly collections (13.2%), and daily pickups occurring for approximately 4.5% of households. Furthermore, the majority of respondents (70.5%) do not have separate collection systems for biodegradable and non-biodegradable waste in their households. The practice of mixed waste collection tends to discourage source segregation. Given that solid waste management ranks as the foremost environmental challenge in the province, it is imperative for local governments to prioritize comprehensive solid waste management solutions, beginning with waste segregation at source to its proper disposal.

4. CONCLUSIONS AND RECOMMENDATIONS

The study's findings indicate that the pandemic has significantly influenced consumers' shopping behaviors, leading to a notable increase in online shopping activity. The research reveals that consumers are drawn to online shopping platforms primarily due to factors such as convenience, enticing promotions, free shipping, and discounts. From the results, many of the respondents dispose of their online shopping plastic packaging waste immediately without segregation. Unfortunately, these discarded materials ultimately contribute to the accumulation of plastic waste in landfills, where it can take hundreds of years to decompose. This accumulation of plastic waste can also exacerbate the existing solid waste management challenges in Dasmariñas, Cavite and may add to the volume of solid waste that finds its way into the waterways, posing potential risks to both animals and humans. It is anticipated that unless express packaging regulations are implemented, there will be a continued rise in plastic waste generation, further contributing to the overall solid waste production in the coming years.

The results of the study also indicate that consumers exhibited awareness of the issue of excessive packaging within the nation. However, they displayed limited familiarity with the concept of environmentally friendly packaging. Furthermore, consumers expressed agreement regarding the potential for the industry to significantly affect the environment. The study also observed that older age groups exhibited the highest percentages of unawareness regarding these environmental concerns. These emphasize the importance of targeted educational efforts to inform consumers about sustainable packaging practices and encourage environmentally responsible choices, with a particular focus on older consumer demographics.

Based on the findings of this study, recommendations for the e-commerce industry include publicizing their plastic consumption data, regulating packaging for frequently purchased items, offering low-cost eco-friendly packaging options at checkout, and providing incentives for sellers adopting sustainable packaging. The government, on the other hand, should improve solid waste management through household segregation, collaborate with e-commerce platforms, express delivery companies, and packaging manufacturers to create and enforce policies for reducing plastic usage, hold the e-commerce sector accountable for its plastic waste contributions, and invest in research for alternative packaging materials to benefit both sellers and consumers. These measures can collectively contribute to reducing the environmental impact of plastic waste generated by the e-commerce industry.

Further studies are recommended to determine the actual average size of parcels delivered annually by the e-commerce industry. Waste analysis and characterization study is recommended to accurately account for the average weight of plastic packaging and the composition of plastic packaging waste produced in each household.

ACKNOWLEDGMENTS

The authors would like to thank the UP Diliman Office of the Vice Chancellor for Research and Development for the research dissemination grant.

REFERENCES

[1] Business Mirror. (2021). Shopee posts new record of over 2 billion items sold across 11.11 Big Christmas Sale. https://businessmirror.com.ph/2021/11/13/shopee-posts-new-record-of-over-2-billion-items-sold-across-11-11-big-christmas-sale/

[2] Department of Trade and Industry (2021), Keynote Speech of Secretary Ramon M. Lopez, Virtual Launch of Philippines E-Commerce Roadma 2022[Transcript]. Retrieved January 10, 2022, from Department of Trade and Industry Philippines website: https://www.dti.gov.ph/speeches/virtual-launch-of-philippines-e-commerce-roadmap-2022/DTI.html

[3] Emblem, A. (2012). Plastics properties for packaging materials. Packaging Technology, 287–309.

[4] International Trade Administration (2022). Philippines – Country Commercial Guide. Published on July 25, 2022 on https://www.trade.gov/country-commercial-guides/philippines-ecommerce

[5] Kao, C.K., Sun, M., Tang, Z.B., Luo, Y.P., & Zeng, F. (2020). Green manufacturing strategy of e-commerce

express packaging in China. The International Technology Management Review, 9(1), 11-26.

[6] National Solid Waste Management Commission. (n.d.). Projected waste generation from 2020 to 2025. https://nswmc.emb.gov.ph/

[7] Pålsson, H., Pettersson, F., & Winslott Hiselius, L. (2017). Energy consumption in e-commerce versus conventional trade channels - Insights into packaging, the last mile, unsold products and product returns. Journal of Cleaner Production,164,765–778.

[8] Phelan, A. (Anya), Meissner, K., Humphrey, J., & Ross, H. (2022). Plastic pollution and packaging: Corporate commitments and actions from the food and beverage sector. Journal of Cleaner Production, 331, 129827.

[9] Philippine Statistics Authority (2021). Highlights of the Region IV-A (CALABARZON) Population 2020 Census of Population and Housing. https://psa.gov.ph/population-and-housing/node/165019

[10] Ren, G. & Zhao, C. (2020). Research on the pollution of express plastic packaging based on system dynamics. Environmental Engineering, Pollution Control and Prevention, 165, 02011

Techno-Science Research Journal 12 (Special Issue) 57-62

I.T.C

Content list available at ITC

Techno-Science Research Journal

Journal Homepage: www.ric.itc.edu.kh

Techno-Science Research Journal

Study on Seismic Behaviors of Irrigation Dams by Changing their Heights

Kentaro Fukuda[1*], Sreng Sokkheang Suzuki[1], Hiroki Ishikawa[2], Seiichi Sato[1]

[1]*R&D Center, NIPPON KOEI, CO., LTD., 2304, Inahara, Tsukuba-shi, Ibaraki 300-1259, Japan*
[2]*Sapporo branch office, NIPPON KOEI, CO., LTD., Kita 5 Jyo Nishi 6-2, Chuo-Ku, Hokkaido 060-0005, Japan*

Received: 22 August 2023; Accepted: 15 May 2024; Available online: August 2024

Abstract: *There are approximately 0.15 million irrigation dams in Japan, and most of them were designed and constructed before the establishment of aseismic design. It is assumed that massive earthquakes, such as the Nankai Trough Mega earthquake, will occur in the future, and may cause considerable damage to irrigation dams. This study aimed to develop a seismic assessment method for irrigation dams. Several dynamic centrifuge model tests were conducted in which the heights of irrigation dams were changed in a 50G field. The material used for testing was "Edosaki sand", and the model ground was prepared under a degree of compaction of 95%. The dam heights were set at 15 m, 10 m and 5 m. The input wave was obtained by adjusting the strong motion earthquake record (NS component) observed at the Kobe Marine Meteorological Observatory of the Japan Meteorological Agency, considering the 1995 Hyogoken-Nanbu Earthquake at a maximum acceleration of approximately 6 m/s^2. Settlement, response acceleration, and deformation of the dams were compared to evaluate deformation characteristics of the dams during the shaking tests. From the test results, it was found that the settlement of the top of the dam was large in proportion to the dam height and that the deformation characteristics were almost the same in these cases, irrespective of the dam height. Important fundamental data were obtained in this study to investigate the seismic assessment of irrigation dams. In future studies, tests under different conditions and numerical analyses to simulate tests should be conducted to investigate the seismic behavior of irrigation dams.*

Keywords: irrigation dam; centrifuge model test; seismic behavior; dam height; deformation

1. INTRODUCTION

The 2011 earthquake off the Pacific coast of Tohoku caused considerable damage to irrigation dams. There are approximately 0.15 million irrigation dams in Japan, and most of them were designed and constructed before the establishment of aseismic design. Hence, the occurrence of massive earthquakes in the future, such as the Nankai Trough Mega Earthquake, can be assumed. Therefore, a seismic assessment method for irrigation dams is required. To develop a seismic assessment method for irrigation dams, the authors evaluated the seismic behavior of irrigation dams by conducting centrifuge model tests and numerical analysis [1,2,3].

This paper presents the results of dynamic centrifuge model tests in which the heights of irrigation dams were changed.

2. CENTRIFUGE MODEL TESTS

2.1 Test apparatus

The centrifuge model tests were performed at a centrifugal acceleration of 50G. The beam-type centrifuge with an effective radius of 2.6 m and the shaking table owned by Nippon Koei Co. Ltd. were used in the test (Figs. 1, 2). The shaking-table specifications are listed in Table 1.

[*] Corresponding author: Kentaro Fukuda
E-mail: a6621@n-koei.co.jp*; Tel: +81-29-871-2148*

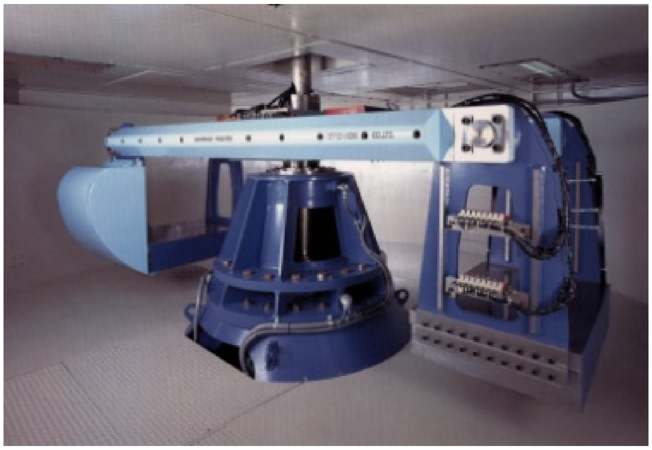

Fig. 1. Centrifuge of Nippon Koei

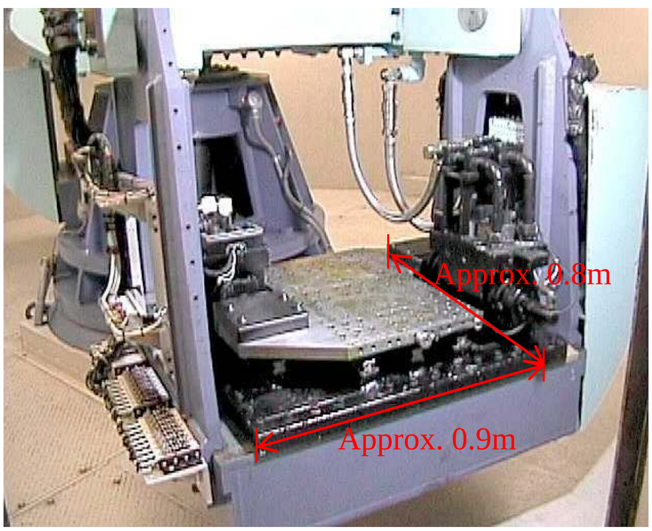

Fig. 2. Shaking table of Nippon Koei

Table 1. Specifications of the shaking-table

Item	Specification
Shaking control system	Electrohydraulic Servo control
Max. centrifuge acceleration	100G
Max. shaking acceleration	25G
Max. payload	250 kg
Max. displacement	±3.0 mm
Frequency range	10-400 Hz
Max. velocity	40 cm/s

2.2 Model preparation and measurements

The material used in the test was “Edosaki sand,” which was sampled from Ibaraki Prefecture, Japan. Fig. 3 shows the grain size distribution curve. Tables 2, 3, and 4 show the physical properties, compaction test results, and the results of the consolidated drained triaxial compression test of the material, respectively. The Edosaki sand had a small fine fraction content of 4.4% (Fig. 3).

Fig. 4 shows an outline of the centrifuge model tests (in model scale, 1:50), and Table 5 lists the test cases and conditions. In Case 1, Case 2, and Case 3, the heights of the dam were set at 15 m, 10 m, and 5 m, respectively (in prototype scale). The model ground was prepared by compacting the material in a rigid soil container with a 95% degree of compaction (ρ_d=1.622 g/cm^3) and a water content of 15% (optimum water content). During the model preparation process, colored sand layers and targets were installed to observe the deformation of the dam during shaking.

A methylcellulose solution (metolose), adjusted to a kinematic viscosity of 50 mm/s^2, was used for water storage in the dams. The input wave was obtained by adjusting the strong motion earthquake record (NS component) observed at the Kobe Marine Meteorological Observatory of the Japan Meteorological Agency, considering the 1995 Hyogoken-Nanbu Earthquake at a maximum acceleration of approximately 6 m/s^2.

Fig. 5 shows the seepage line observed after reaching 50G before shaking. The seepage line observed from the piezometer partially agrees with the theoretical line of Casagrande’s method [4].

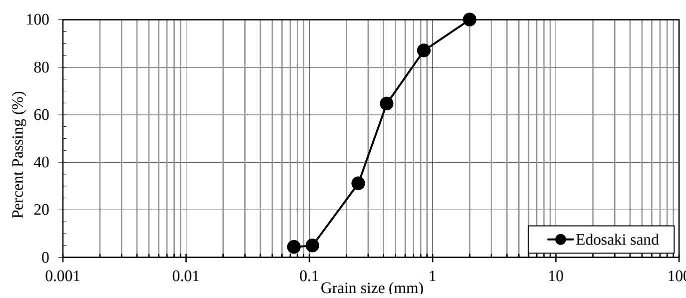

Fig. 3. Grain size distribution curve of the Edosaki sand.

Table 2. Physical properties

Maximum grain size, D_{max} (mm)	2.0
Mean grain size, D_{50} (mm)	0.335
Uniformity coefficient, U_c	2.56
Coefficient of curvature, U_c'	1.00
Fine fraction content (%)	4.4
Coarse sand fraction (%)	13.0
Medium sand fraction (%)	55.9
Fine sand fraction (%)	26.7
Density of soil particles, ρ_s (g/cm^3)	2.681

Table 3. Results of the compaction test

Maximum dry density, ρ_{dmax} (g/cm^3)	1.707
Optimum water content, w_{opt} (%)	15.0

Table 4. Results of the consolidated drained triaxial compression test

Degree of compaction, D_c (%)	95
Dry density, ρ_d (g/cm^3)	1.622
Water content, w (%)	15.0
Cohesion, c, (kN/m^2)	4.5
Friction angle, ϕ, (deg.)	36.3

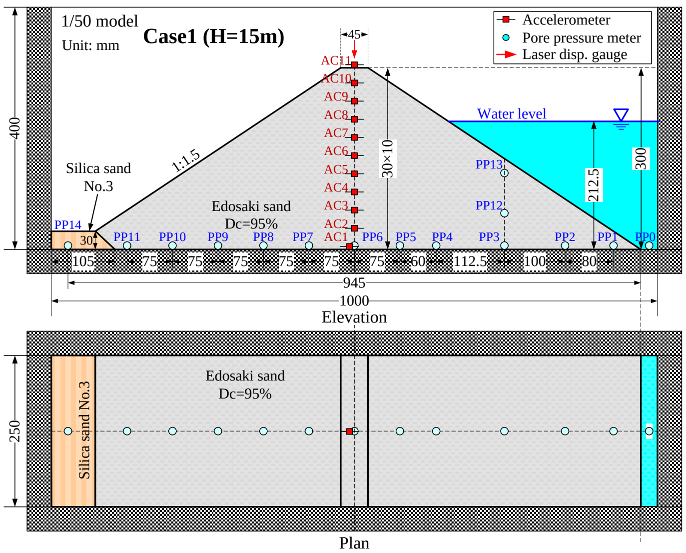

(a) Case 1 (H=15 m)

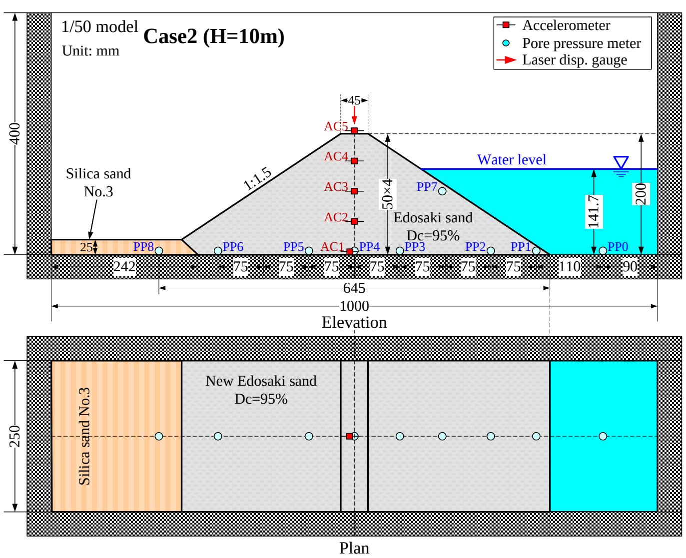

(b) Case 2 (H=10 m)

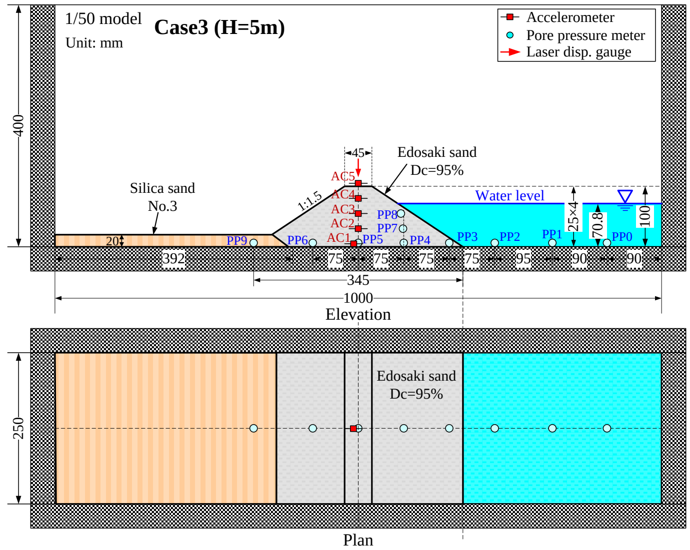

(c) Case 3 (H=5 m)

Fig. 4. Outline of the centrifuge model tests

Table 5. Test cases and conditions

Test cases	Dam height (H) Degree of compaction (D_c) Water level (Wl)	Input wave (Common condition)
Case 1	H=15 m ρ_d=1.622g/cm^3, D_c=95% Wl=10.625 m	A wave recorded by JMA Kobe Kaiyo station for the 1995 Hyogoken-Nanbu earthquake (Mj 7.3) by adjusting the wave amplitude to a maximum acceleration of approximately 6 m/s^2 Mj: Japan Meteorological Agency Magnitude
Case 2	H=10 m ρ_d=1.622g/cm^3, D_c=95% Wl=7.085 m	
Case 3	H=5 m ρ_d=1.622g/cm^3, D_c=95% Wl=3.540 m	

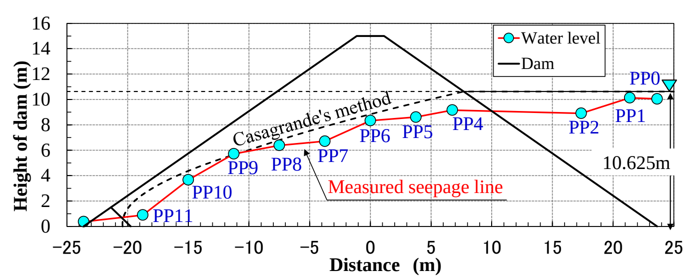

(a) Case 1 (H=15 m)

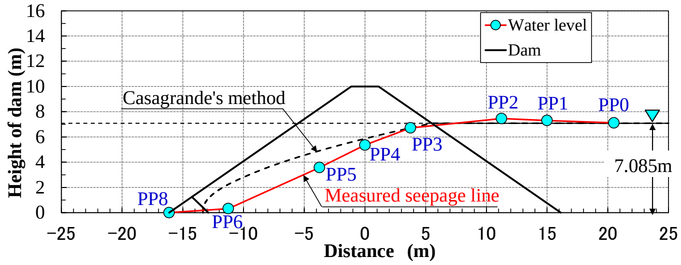

(b) Case 2 (H=10 m)

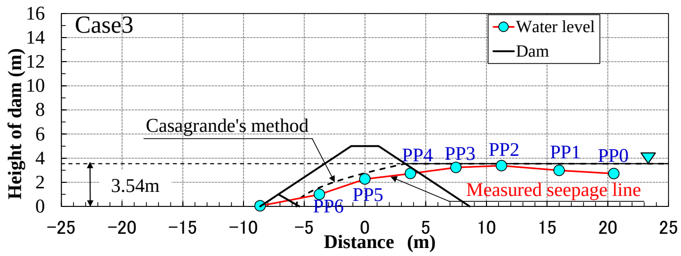

(c) Case 3 (H=5 m)

Fig. 5. Seepage line

3. RESULTS

3.1 Response acceleration and settlement

Fig. 6 shows a comparison of the relationship between settlement and time at the top of the dam. The maximum settlements of Case 1, Case 2, and Case 3 were -0.73 m, -0.21 m, and -0.14 m, respectively. In the comparison of the differences in dam height, the settlement of the top of the dam was large in proportion to the dam height. Fig. 7 shows a comparison of the relationship between the response acceleration and time at the top of the dam. The response acceleration at the top of the dam was the smallest in Case1 where the dam height was the largest. It was also found that the acceleration peak time was longer when the dam height was larger. This is thought to be due to the fact that acceleration energy is transmitted to the top of the dam in proportion to the dam height. Fig. 8 shows a comparison of the relationship between the amplification ratio of the maximum response acceleration to the base and the dam height. In these cases, the response acceleration increased at the top of the dam, and a similar tendency was observed. This is assumed to be because the model ground was prepared with D_c=95 %, which increased the rigidity of the entire ground. However, in Case1, it was confirmed that the amplification ratio of the maximum response acceleration was less than 1 when the dam height was between 1 m and 12 m, indicating that the response acceleration was attenuated. On the other hand, in Cases 2 and 3, the amplification ratio of the maximum acceleration is around 1 except for that of the top of the dam. Therefore, it is considered that the ground of the model in Case1 had a lower rigidity than in Cases 2 and 3, and consequently, the settlement at the top of the dam increased. Based on the above results, it is assumed that in the actual field, when the dam height is large, the acceleration will be attenuated due to the non-linearity of the ground, and the amount of settlement will increase even if the material is dense. If the amplification ratio of the maximum acceleration is around 1 except for the top of the dam and the material is dense, it is considered that the settlement of the top of the dam is small, and the effect on irrigation dams is small.

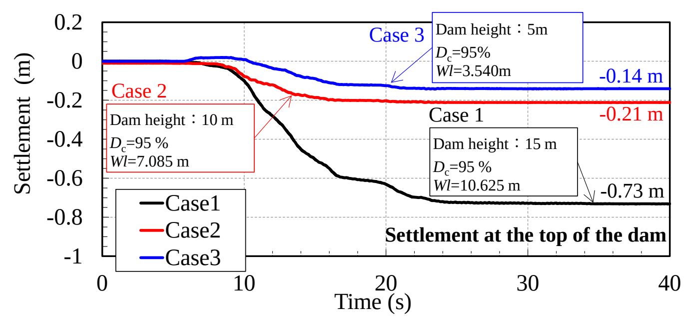

Fig. 6. Comparison of settlements at the top of the dam

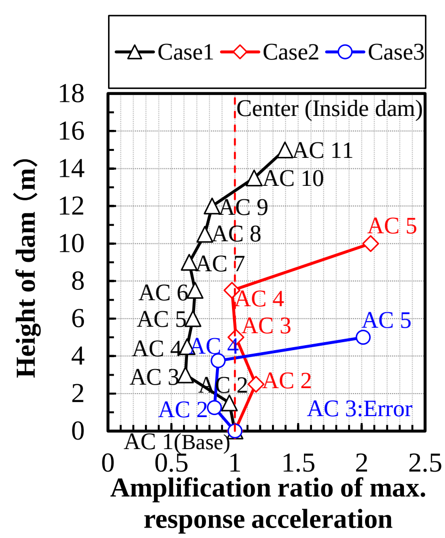

Fig. 8. Comparison of the amplification ratio of maximum response acceleration to the base (center).

Annotation: In each case, the location of the accelerometer is different.

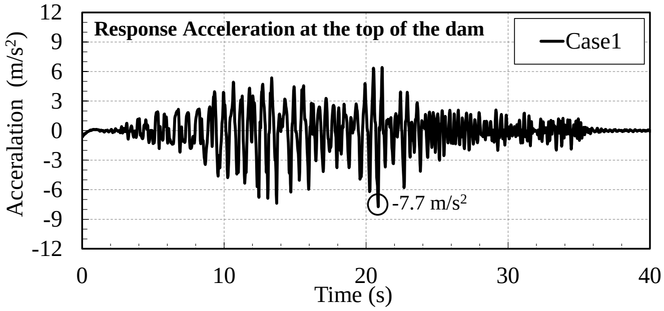

(a) Case 1 (H=15 m)

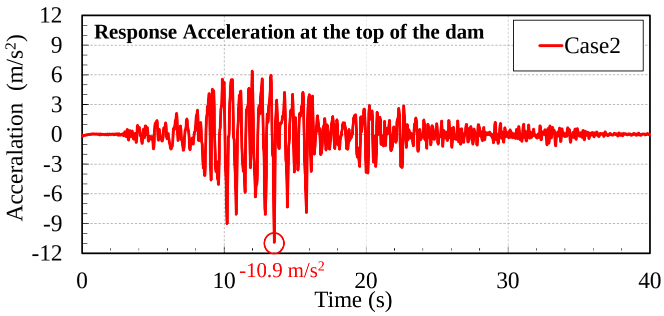

(b) Case 2 (H=10 m)

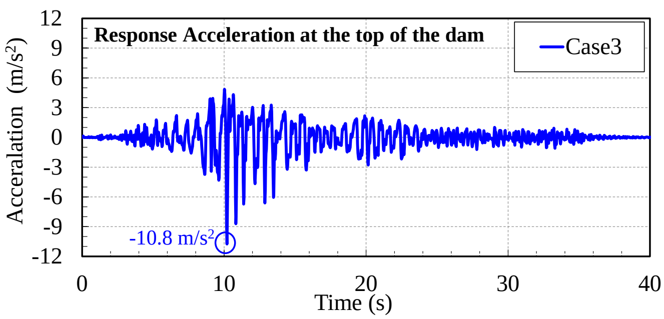

(c) Case 3 (H=5 m)

Fig. 7. Comparison of response accelerations at the top of the dam

3.2 Deformation mechanism

Fig. 9 compares the states of the irrigation dams after the shaking tests. Fig. 10 shows a comparison of the deformation distribution diagrams based on the sketches after testing. No slip line was observed. Instead, a small deformation occurred on the non-submerged side slope. Protrusions were observed near the toe slope on the submerged side slope. In Case 1, the settlement at the top of the dam, the deformation on the non-submerged side slope, and the protrusion near the toe slope of the submerged side slope were larger than those in Cases 2 and 3. However, in Cases 2 and 3, a similar tendency was observed.

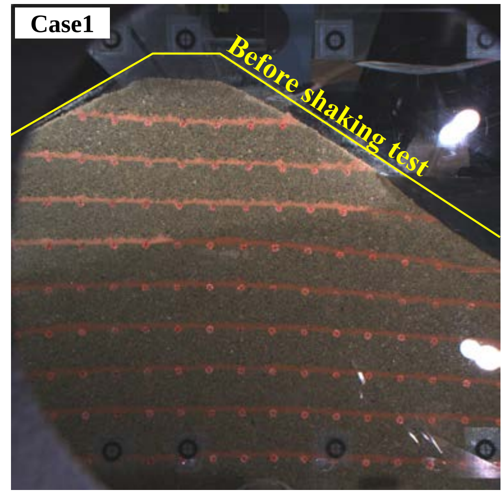

(a) Case 1 (H=15 m)

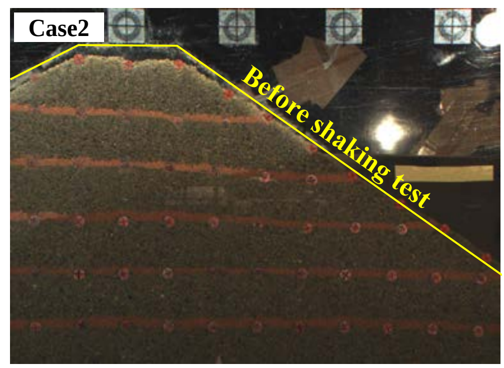

(b) Case 2 (H=10 m)

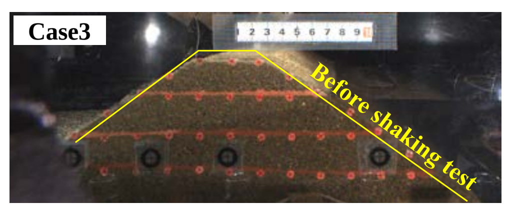

(c) Case 3 (H=5 m)

Fig.9. States after the shaking tests

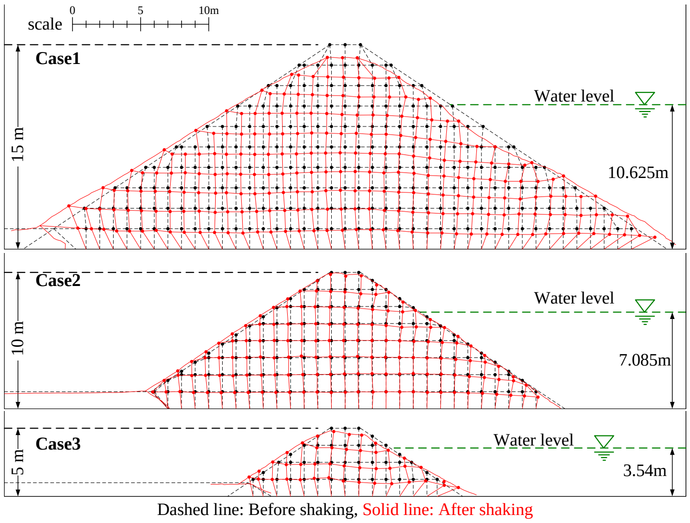

Fig. 10. Deformation sketch of the target markers before and after the shaking test

4. CONCLUSIONS

Three dynamic centrifuge model tests were performed on irrigation dams.

The results of the centrifuge model tests are summarized as follows.

(1) The slip line did not occur, a small deformation occurred on the non-submerged side slope during shaking, and protrusion occurred near the toe of the slope on the submerged side slope.

(2) The deformation characteristics were almost the same in these cases, irrespective of the dam height.

(3) The settlement of the top of the dam was large in proportion to the dam height.

(4) When the dam height is large, the acceleration is attenuated due to the non-linearity of the ground, and the amount of settlement increase even if the material is dense.

(5) Based on the test results, the effect of the difference in the dam height on the deformation behavior of an irrigation dam during an earthquake was clarified, and important fundamental data were obtained.

(6) In future studies, tests under different conditions and numerical analyses to simulate tests should be conducted to investigate the seismic behavior of irrigation dams.

REFERENCES

[1] Fukuda, K., Sreng, S., Sato, S., Ishikawa, K., & Kobayashi, K. (2017). Evaluation of seismic behavior of irrigation dam—Centrifuge model test and its analysis using LIQCA program. Annual Conference of Japan Geotechnical Society, 915–916 (in Japanese).

[2] Suzuki, S., Koyama, Y., Kobayashi, K., & Ishikawa, H. (2019). Dynamic behavior of irrigation dams under water storage condition by centrifuge model tests and their numerical simulations. 7th International Conference on Earthquake Geotechnical Engineering.

[3] Fukuda, K., Suzuki, S., & Ishikawa, H. (2022). Experimental study on dynamic behaviors of irrigation dams by changing their heights and degree of compactions. Physical Modelling in Geotechnics, 916–919.

[4] Casagrande, A. (1937). Seepage through Dams. Journal of New England Water Works Association, 52(2), 131–172.

Techno-Science Research Journal 12 (Special Issue) 63-68

Content list available at ITC

Techno-Science Research Journal

Journal Homepage: www.ric.itc.edu.kh

Numerical Analysis of Bearing Capacity of Defected Bored Piles

David Tung[1*], Keangse Pouv[2], Sambath Ky[3]

[1,2,3] *Faculty of Materials and Structural Engineering, Institute of Technology of Cambodia, Russian Federation Blvd., P.O. Box 86, Phnom Penh, Cambodia*

Received: 14 August 2023; Accepted: 15 May 2024; Available online: August 2024

Abstract: *Bored concrete pile is a very popular choice for supporting high rise buildings. Its bearing capacity depends on several parameters, such as properties of soil stratifications, the strength of materials and the geometry of pile. However, defects (e.g., voids, poor quality concrete, geometric errors, etc.) can occur at any point during the construction of bored piles. When a pile is defective, we usually question about its effective bearing capacity. Pile load testing is an expensive method, especially when there are many defected piles. So, the aim of this paper is to analyse the bearing capacity of defected bored piles using PLAXIS 2D. We study the effects of various defect sizes (i.e., thickness ranging from 0.5m to 2m and area ranging from 10% to 90%) at the toe and at the mid length as well as the effects of several concrete strengths (i.e., between 1MPa and 25MPa) for a defect section of 50% and thickness of 0.5m. We assume a bored pile of 24m length installed in an existing soil stratification. The results show that the pile has a much greater bearing capacity reduction when defects appear at the mid-length. In fact, for a defect thickness of 0.5m and defect area of 50%, there is a reduction of more than 60% for mid-length defect compared to a reduction of just below 15% for toe defect. When the concrete strength is reduced from 30MPa to 1MPa, the bearing capacity also reduces by more than 65%. So, the seriousness of defect can be defined by either the location and size of defects or the quality of concrete.*

Keywords: Bored pile, Bearing capacity, numerical method, structural defects, concrete strength

1. INTRODUCTION

The complexity of bored pile construction has been raising concerns in the field of geotechnical engineering. As the long length of bored pile embedded into the soil strata, it is very challenging to achieve its perfect shape. Imperfection or defect of bored pile usually arise after the construction. In order to locate the imperfection, standard practice testing tools can be used to detect these defects such as cross-hole ultra sonic test and pile integrity test. Figure 1 has shown different types of defects such as voids, weak area (poor concrete quality), necking and soft toe comparing to perfect design case where the perfect shape is assumed. It is necessary to perform pile testing in order to ensure the pile integrity as it is related to pile behavior and load transfer mechanism. More importantly, different shape, size and position of defect could impact bored pile in different manners. However, these testing tools could not answer the major concern of geotechnical engineering which is its bearing capacity. The current state of knowledge related to defected bored pile could not provide a general conclusion on its bearing capacity. The bearing capacity is very dependence on several parameters such as soil stratification, strength of material and geometry of pile. Since the parameters can be differed due to defects, especially concrete strength, the bearing capacity can also be varied. Thus, the current state of informations between defects and bearing capacity of bored pile need to be fullfiled.

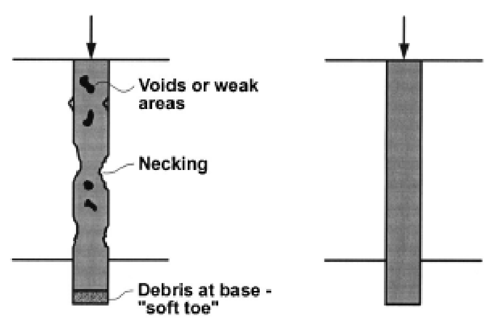

Fig.1. Imperfection vs Perfect design case

Previous studies has provided a great understanding related to defective bored pile. O'Neill [8] explained general informations on type of construction and catargories of defects

* Corresponding author: David Tung
E-mail: tungdavid9@gmail.com; *Tel: +855-11-76-45-76*

that arise from general construction problems, while Poulos [10] further detailed on cause of imperfection and possible effect on pile behaviour. One study by Kog [7] focus on how integrity problem due to defect (concrete bleeding) effect to structural performance. Severals other studies mainly focus the relationship between defective bored pile and bearing capacity. Petek et al [9] presents the analysis using PLAXIS 2D with three different locations of defect such as top, mid and toe defect. However, Iskander et al [6] perform the experiment by carrying out in situ (static load test and slow maintained load tests), and Albuquerque et al [2] perfrom the experiment in laboratory testing.

The objective of this research is going to estimate the bearing capacity of defected bored pile through numerical method (PLAXIS 2D) of differences thickness of defect such as 0.5m, 1.0m and 2.0m with differences area of defect ranging from 10% to 90%. Also, the variation of concrete strength from 1MPa to 25MPa are also considered in the analysis where the defective area is fixed at 50% of 0.5m defective thickness.

2. METHODOLOGY

In this research, we use PLAXIS 2D as a tool for modeling. A reinforced concrete bored pile is installed in seven soil layers that were investigated at a real site construction located in Phnom Penh city. The properties of soils such as dry unit weight (γ_d), saturated unit weight (γ_{sat}) Young modulus (E), cohesion (c_u) and internal friction angle (φ^o) are given in below in Table 1.

Table 1. Properties of soils at a site in Phnom Penh used for the study

	γ_d (kN/m^3)	γ_{sat} (kN/m^3)	E (kN/m^2)	c_u (kPa)	φ^o
Layer 1	18	18.5	5000	10	-
Layer 2	16.52	19.56	14850	177	-
Layer 3	15.05	19.13	7480	52	-
Layer 4	16	19.45	27500	-	34^o
Layer 5	19	21	80000	431	-
Layer 6	19	21.5	104621	337	-
Layer 7	19	21.45	80000	652	-

Mohr-Coulomb is used as the model for both soil and concrete. It is important to model concrete properties as Mohr-Coulomb in order to obtained failure at the defected area. Fine mesh is applied for this study to obtain the accurate result. The properties of concrete consisted of unit weight (γ_c), Young modulus (E_c), Poisson ratio (ν') and compressive strength (σ_c) as listed in Table 2 below.

Table 2. Properties of concrete materials

Concrete strength (MPa)	γ_c (kN/m^3)	E_c (kN/m^2)	σ_c (kN/m^2)	ν'
1		4700	1	
7		11465	2975	
10		13703	4250	
15	25	16782	6375	0.2
20		19379	8500	
25		21666	10625	
30		23734	12750	

Table 3. Condition for study

Case	Defective area (%)	Defect thickness (m)	Depth of defects (m)	Concrete strength of defects (MPa)
1	10,20,30,40, 50,60,70,80, and 90	0.5	23.5 (toe defects)	1
2	10,20,30,40, 50,60,70,80, and 90	1.0	23.0 (toe defects)	1
3	10,20,30,40, 50,60,70,80, and 90	2.0	22.0 (toe defects)	1
4	10,20,30,40, 50,60,70,80, and 90	0.5	12±0.25 (mid-length)	1
5	10,20,30,40, 50,60,70,80, and 90	1.0	12±0.50 (mid-length)	1
6	10,20,30,40, 50,60,70,80, and 90	2.0	12±1.0 (mid-length)	1
7	50	0.5	12±0.25 (mid-length)	1,7,10,15,20 and 25

The pile has a diameter of 1.0m with the length of 24m, as shown in figure 2 below, for modeling including toe and mid-length defected bored pile. The compressive strength of pile is 30MPa. According to ACI Standard (2011), the safety factor of 0.85 is used for concrete bored pile. With the existing soil data and the pile dimensions, we obtained the results from PLAXIS 2D with an ultimate bearing capacity of 20051kN for perfect bored pile.

The conditions of study involve the variation of sizes and thickness of defects as well as the concrete strength of defected area of bored pile as shown in Table 3 above.

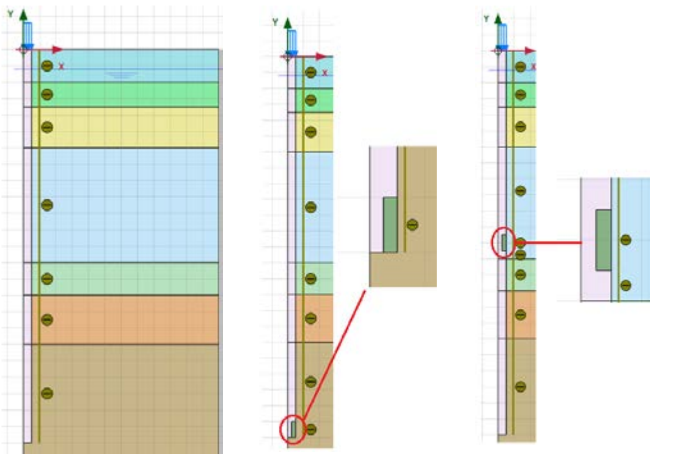

(a) (b) (c)

Fig.2. Models of pile and soil in PLAXIS 2D (a) perfect pile integrity, (b) pile with toe defect, (c) pile with mid-length defect

In this analysis, vertical loading are applied to the pile head with an increment of 5% of the total load, as shown in figure 3, with each loading increment is maintained for 10mn. Such loading stages are applied, according to ASTM International (2013). The results are analysed in terms of effective pile bearing capacity computed from the concrete strength and the soil data.

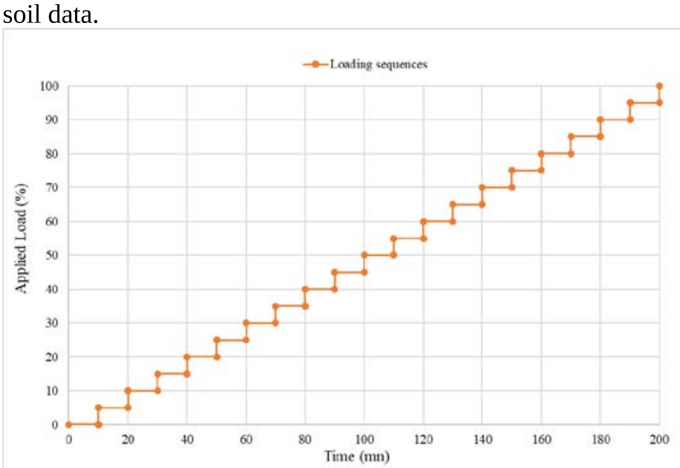

Fig.3. Loading sequences

3. RESULTS AND DISCUSSIONS

3.1 Toe defects

Figure 4 has shown the decreasing of ultimate bearing capacity due to the impact of toe defect.

For defective length 0.5m, the bearing capacity decreased for about 10% at 10% and 20% defective area. At the 30% defective area, the additional reduced in bearing capacity for 4.4% in which the remaining bearing capacity is about 85.5%. The bearing capacity further reduced at 50% defective area for about additional 4% and slightly reduce for about 1.2% more at 60% defective area. From 70% to 90% defective area, the bearing capacity remained the same that the total reduction in bearing capacity is 19.6%.

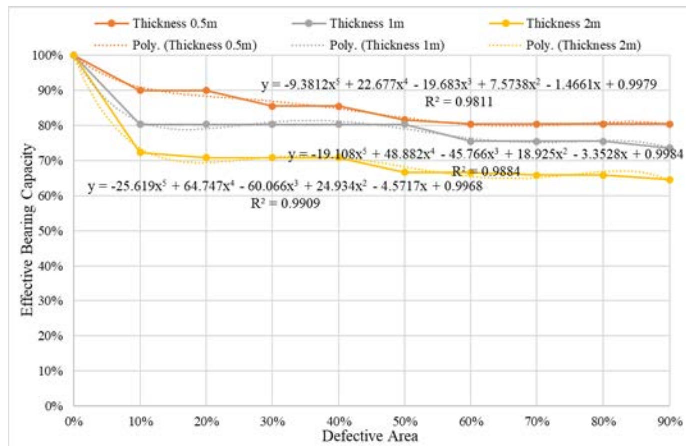

Fig.4. Effective bearing capacity of toe defected bored pile

Unlike defective thickness 0.5m, the ultimate bearing capacity of defective thickness of 1m started to drop at 10% defective area for 19.6%. The bearing capacity continues to stayed the same until 50% defective zone. At 60% defective area, the capacity lightly reduced for 4.8% and 2% for 90% defective area. Based on the results, the total reduction of bearing capacity of bored pile was about 26.4% with 73.6% remaining of total bearing capacity.

At defective thickness 2m, the bearing capacity significantly decreased at 10% defective area. It was about 27.0% of reduction in bearing capacity. It was further reduced for 1.4% at 20% defective area, and continue to remain the same until 40% defective area. As the increase of defective area to 50%, the bearing capacity reduced for 4.2%. The decrease of bearing capacity was continued to lightly reduce for about 0.1% and 0.7% for each 60% and 70% defective area, respectively. At 90% defective area, the total reduction in bearing capacity was 35.4% with 64.6% ultimate bearing capacity remaining.

The results can be observed that the length of defect had a significant impact to the bearing capacity of bored pile. As shown in figure 4, different thickness of defect led to different outcome in effective bearing capacity. The higher of defective thickness, the greater lost of bearing capacity at 10% defective area as the bearing capacity immediately decreased. According to figure 4, the capacity reduction about 10%, 20% and 30% for each defective thickness 0.5m, 1.0m and 2.0m, respectively. From 10% to 90% defective area of each defective thickness, the different between effective bearing capacity was not more than 10%. It shows that toe defect does not heavily impact to bearing capacity of bored pile, even the defective area was increased to 90%. Based on deformed shape in figure 5, it can be observed that the failure type of toe defect is punching shear failure.

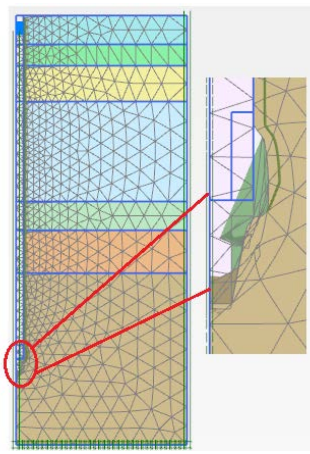

Fig.5. Deformed shape due to toe defect

3.2 Mid length defect

In the case of mid length defect, figure 6 has shown the effect of defective area related to effective bearing capacity. For defective thickness 0.5m, after the decreased 5.9% at 10% defective area, the bearing capacity was drastically declined at the rate about 17% from 10% to 40% defective area.

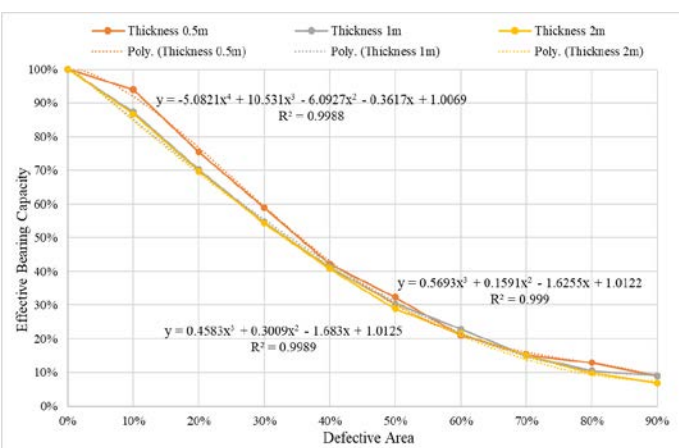

Fig.6. Effective bearing capacity of mid-length defected bored pile

At 50% defective area, the bearing capacity of bored pile could only produced for 32.4%. As the defective area increase, the bearing capacity constantly reduced until 90.9% at 90% defective area.

For 1.0m and 2.0m defective thickness, the effect of defective area to bearing capacity was quite similar. From 20% to 40% defective area, the differences of reduction in bearing capacity between these two cases was less than 1%. From 50% defective area, the results remain similar that the reduction in bearing capacity was 69.5% and 71.1% for each 1.0m and 2.0m defective thickness, respectively. For both defective thickness, the total ultimate bearing capacity continue to decreased to 9% and 6.9% at 90% defective area.

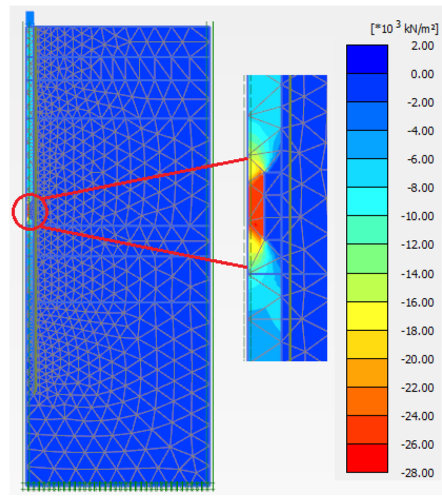

Fig.7. Stress concentration around mid-length defect

In the case of mid-length defect, the bearing capacity is significantly decreased from 10% until 90% defective area. For defective thickness 1.0m and 2.0m, the results are similar from the start of the analysis. It can be seen that from defective thickness 1.0m, the defects did not have any more influence to the bearing capacity. Comparison between 0.5m and 1.0m defective thickness, 0.5m defective thickness had higher bearing capacity from 10% to 30% defective area. However, the results appeared to be similar from 40% defective area onward. These results showed that the influence of defective thickness to bearing capacity are the same from 40% defective area. Comparison to toe defects, it also can be seen that the effect of mid-length defects is significantly higher than that of toe defect. In comparison between 10% to 90% defective thickness, it is about 80% different in effective bearing capacity. Unlike toe defect where it is only about 10% different in effective bearing capacity.

Based on the observation on the defective area, as shown in figure 7, stress development were found around the defective area during loading sequences. This phenomena caused the structural failure at the defective area due to the stress concentration.

3.3 *Effect of concrete strength*

Strength of concrete is also an importance factor contributed to the ultimate bearing capacity in defective area. Various of concrete strength would effect the effective bearing capacity in different manners. In this case, base on figure 8, the behavior of concrete strength effect to the capacity is in form of second degree of polynomial equation. It was a reduction in capacity about 65% for concrete strength 1MPa. For concrete strength 7MPa, bearing capacity had reduced 20% less than the case of concrete strength 1MPa. For concrete strength 10MPa and 15MPa, the bearing capacity reduced about 35% and 20%, respectively. As the concrete strength increase to 20MPa and 25MPa, the reduction in capacity is just about 10% and 4% respectively.

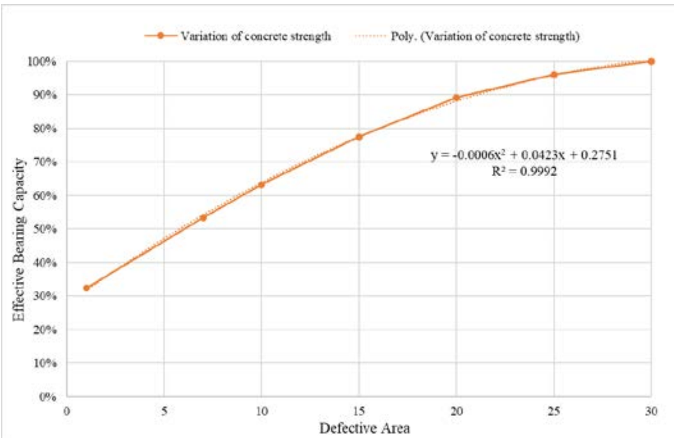

Fig.8. Effect of concrete strength of bearing capacity

It is clearly to see that concrete strength of the defective area has a strong influence to the effective bearing capacity of bored pile. It is important to consider the concrete strength of defected area in order to archieve better result when performing analysis. Comparing between 1MPa and 25MPa concrete, it was about 65% different in capacity reduction. Thus, strength of concrete is a strong factor in considering for defected bored pile at any location.

4. CONCLUSION

This paper has investigated the bearing capacity of defected bored pile through numerical method by modeling in PLAXIS 2D. Different factors were conducted in analysis such as defective thickness, defective area and various concrete strength in order to provide a deep understanding on its behaviour. Some conclusions can be made from this research:

1. The effect of defect at mid-length of bored pile is significantly greater than that of toe defect. Just 30% defective area of mid-length defects, the effective bearing capacity has reduced more than 90% defective area of toe defect.

2. Thickness of defects produced different results on toe defect, while the results are similar on mid-length defect. For 1.0m and 2.0m defective thickness of mid-length defect, it seem to have no more influences to effective bearing capacity. For 0.5m defective thickness, the results appeared to be the same as others when the defective area increased to 40%.

3. Concrete strength of the defective area played an important role in determining the effective bearing capacity of bored pile. Between concrete strength 1MPa and 25MPa, it was about 65% different in effective bearing capacity.

4. Failure type for toe defect is punching shear due to failure of the soil surrounded the toe of pile, while structural failure appears at mid-length defect as the stress developed around the defected area.

It is interesting to investigate the bearing capacity of bored pile, especially when there is defected. Future research should expand the area of related topic to different type of soil such as sand and rock, different types of defects and analysis in 3D modeling such as ABAQUS and PLAXIS 3D.

ACKNOWLEDGMENTS

The author would like to express deepest gratitude to Dr. KY Sambath for his guidance, effort, explanation and patient to make this paper completed. I also would like to express deepest gratitude to Dr. POUV Keangse for his effort, explanation and extra material which are essential tool for paving the way for this research.

REFERENCES

[1] A'amal, A., & Al-Shakarchi, Y. A.-S. (2021). Behavior of Defective Cast in Place Piles. Journal of Engineering, 27(4), 96-117.

[2] Albuquerque, P. J. R. d., Garcia, J. R., Freitas Neto, O. d., Cunha, R. P. d., & Santos Júnior, O. F. d. (2017). Behavioral evaluation of small-diameter defective and intact bored piles subjected to axial compression.

[3] Feng, S. L., Zhou, Y. M., Li, J., & Li, P. L. (2012). Finite Element Analysis of the Vertical Bearing Capacity of Single Piles in Tianjin Soft Soil Areas. Advanced Materials Research, 446, 1387-1390.

[4] Hao, F. S., Guo, Y., & Huang, Y. (2013). The bearing capacity of excavated pile under load test and finite element analysis. Applied Mechanics and Materials, 256, 388-393.

[5] International, A. (2013). Standard Test Method for Deep Foundations Under Static Axial Compressive Load. ASTM International.

[6] Iskander, M., Roy, D., Kelley, S., & Ealy, C. (2003). Drilled shaft defects: Detection, and effects on capacity in

varved clay. Journal of Geotechnical and Geoenvironmental engineering, 129(12), 1128-1137.
[7] Kog, Y. C. (2009). Integrity problem of large-diameter bored piles. Journal of Geotechnical and Geoenvironmental engineering, 135(2), 237-245.
[8] O'Neill, M. W. (1991). Construction practices and defects in drilled shafts. Transportation Research Record, 1331, 6-14.
[9] Petek, K., Felice, C. W., & Holtz, R. (2002). Capacity analysis of drilled shafts with defects. In Deep Foundations 2002: An International Perspective on Theory, Design, Construction, and Performance (pp. 1120-1135).
[10] Poulos, H. G. (2005). Pile behavior—Consequences of geological and construction imperfections. Journal of Geotechnical and Geoenvironmental engineering, 131(5), 538-563.
[11] Standard, A. (2011). Building code requirements for structural concrete (ACI 318-11). American Concrete Institute
[12] Thounaojam, S., & Sultana, P. (2014). Prediction of bearing capacity of bored cast-in situ pile. International Journal of Research in Science and Technology, 51.
[13] Wrana, B. (2015). Pile load capacity–calculation methods. Studia Geotechnica et Mechanica, 37(4), 83--93.
[14] Wu, J. J., Chen, J. J., Liu, S. J., & Wang, J. H. (2013). Numerical Analysis on the Bearing Capacity of Single Pile in Deep Excavation Area. Advanced Materials Research, 671, 226-229.
[15] Zhang, Q.-Q., Zhang, Z.-M., & Li, S.-C. (2013). Investigation into skin friction of bored pile including influence of soil strength at pile base. Marine Georesources & Geotechnology, 31(1), 1-16.
[16] Zhou, J.-j., Wang, K.-h., Gong, X.-n., & Zhang, R.-h. (2013). Bearing capacity and load transfer mechanism of a static drill rooted nodular pile in soft soil areas. Journal of Zhejiang University Science A, 14, 705-719.

Techno-Science Research Journal 12 (Special Issue) 69-77

Content list available at ITC

Techno-Science Research Journal

Journal Homepage: www.ric.itc.edu.kh

Techno-Science Research Journal

Study on influence of soil erosion on the collapse of Mekong Riverbank in Cambodia

Sreng Sokkheang SUZUKI [1*], Sopheap POR [2], Muoy Yi HENG [2], Sainglong KAING [2], and Seiichi SATO [1]

[1] R&D Center, NIPPON KOEI CO.,LTD., 2304, Inarihara, Tsukuba-shi, Ibaraki 300-1259, Japan
[2] Faculty of Geo-resources and Geotechnical Engineering, Institute of Technology of Cambodia, Russian Federation Blvd., P.O. Box 86, Phnom Penh, Cambodia

Received: 22 August 2023; Accepted: 15 May 2024; Available online: August 2024

Abstract: *Slope failure along Mekong riverbanks has been problematic since many years with severe consequences, such as the collapse of structures and homes with occasional human victims. Recently, slopes failures are occurring in wide areas, such as Kandal province, Kampong Cham province, Cambodia with a few kilometers along the river, and are responsible for the collapse of many houses, farms, and other structures. However, the main factors of the riverbank failure, collapse mechanism, and appropriate solution have not been investigated. This study was aimed at investigating the main factors of the slope failure along Mekong riverbank from the geotechnical engineering viewpoint. Hence, in this study, field investigation and a series of laboratory tests (physical properties, crumb test, and double hydrometer tests adhering to ASTM standard), centrifuge model test, and slope stability analysis were conducted to determine the cause of failure and collapse mechanism of the riverbank. The laboratory test results indicated that most of the soils, classified as dispersive soils (unusual soil), caused the riverbank failure. Results of field investigation and centrifuge model test (consideration of slope stability and failure mechanism due to the change of water level in dry and rainy seasons) were also analyzed and presented in the paper. The results of this study can be useful for other research on riverbank failure problem in other Mekong River countries, such as Lao and Vietnam.*

Keywords: Mekong Riverbank, slope failure, soil erosion, dispersive soil, Centrifuge model test

1. INTRODUCTION

Riverbank failure is a serious problem in all countries located along the Mekong River, including Thailand, Laos, Myanmar, Cambodia, and Vietnam. These problems have not only occurred in the past, but will continue to occur in the future. Slope failure can cause socioeconomic losses and threaten human life. Many factors cause riverbank failure, such as soil erosion, changes in water level and river flow during the dry and rainy seasons, and cut slopes. A few researchers, including Soksan et al. [6] and XUYEN et al. [5], have studied slope failure along the Mekong River.

In 2015, Soksan et al. [6] studied the stability of a river bank subjected to variations in the water level. They also reported a riverbank failure that occurred in April 2008 in the Reussey Keo district of Phnom Penh, Cambodia. The failure zone was approximately 50 m long and 30 m wide along the Tonle Sap River bank. Consequently, 38 houses were destroyed and more than 300 people were homeless. In March 2012, a 110-m long riverbank failure occurred along the Mekong River occurred in Long Xuyen town, An Giang province, Vietnam. Twenty-two houses were collapsed, and hundreds of people were evacuated [5, 6]. Recently, riverbank failure occurred in the Leuk Daek district, Kandal province, as shown in Figure 1.

According to local people, more than 70 houses collapsed into the river, and around 50 m of national roads collapsed due to riverbank failure.

In 2006, Xu et al. [4] investigated the magnitudes of runoff and soil loss from road embankments. Their results showed that engineering measures can be effective in the short term, whereas the revegetation of roadside slopes is effective when vegetation cover is established. Overall, the combination of the lattice and revegetation was the most effective. A few researchers studied the riverbank failure that occurred along the Mekong River. However, the main

[*] Corresponding author: Sreng Sokkheang SUZUKI
E-mail: sokkheang-sr@n-koei.jp*; Tel: +81-29-871-2065*

factors affecting riverbank failure, collapse mechanisms, and appropriate solutions have not been investigated.

This study was aimed at investigating the main factors of slope failure along the Mekong Riverbank from a geotechnical engineering perspective.

Hence, field investigations, laboratory tests (physical properties, crumb tests, and double hydrometer tests of ASTM standards), centrifuge model tests, and slope stability analyses were conducted to investigate the cause of the failure and collapse mechanism of the riverbank.

Fig. 1. Photograph of Mekong riverbank failure at Leuk Daek, Kandal province, Cambodia, 2017/06.

2. FIELD INVESTIGATIONS

Field investigations were conducted on the riverbank at two locations: Leuk Daek District (Kandal Province, coordinate: 11.076283, 105.189104) and Peam Chi Kang Commune (Kang Meas District, Kompong Cham Province, coordinate: 11.937572, 105.169105). A drone was used to capture photographs and measure the slopes of the collapsed riverbanks. Sampling for laboratory tests was conducted on a collapsed riverbank.

2.1 Surveying of collapsed slope

To assess the failure condition of the slope, a drone was used to capture photographs of the riverbank and generate accurate orthomosaic images and elevations of the riverbank. Consequently, the gradient of the slope was analyzed.

Fig. 2 and 3 show photographs of the large-scale collapse of riverbanks in Leuk Daek and Peam Chi Kang, respectively.

Fig. 4 shows the cross-sections (A-A, B-B, C-C, and D-D) of the failure slope in the Leuk Daek district surveyed by drone.

Fig. 5 shows the slope angles obtained from the drone survey, as shown in Fig. 4. The height of the slopes and slope angles were approximately 5 m and 62 °, respectively.

Fig. 6 shows the cross-sections (A-A, B-B, and C-C) of the failure slope at the Peam Chi Kang Commune. Fig. 7 shows the slope angles obtained from the drone survey in Fig. 6. The height of the slopes and slope angles were approximately 10 m and 51 °, respectively.

Fig. 2. Photograph of the Mekong Riverbank failure in Kandal province, Cambodia, 2018/08 (By Drone).

Fig. 3. Photograph of the Mekong Riverbank failure in Kampong Cham Province, Cambodia, 2019/11 (By Drone).

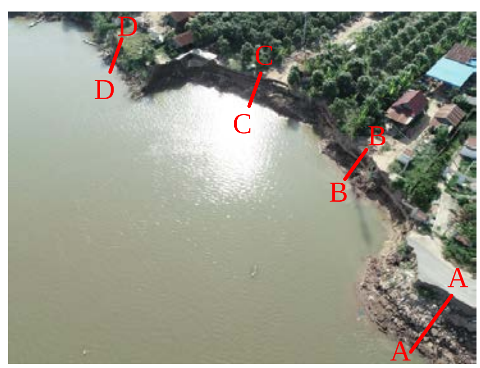

Fig. 4. Cross-sections obtained from the drone survey (Leuk Daek District).

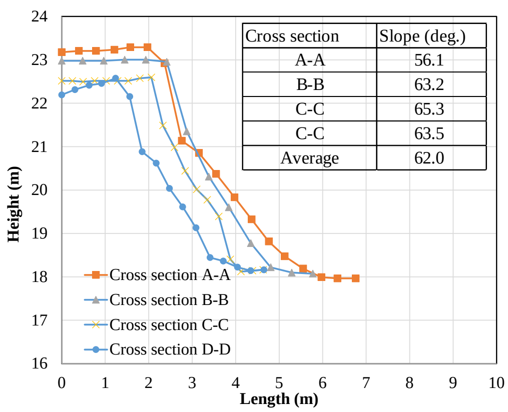

Fig. 5. Slope angles in Leuk Daek District.

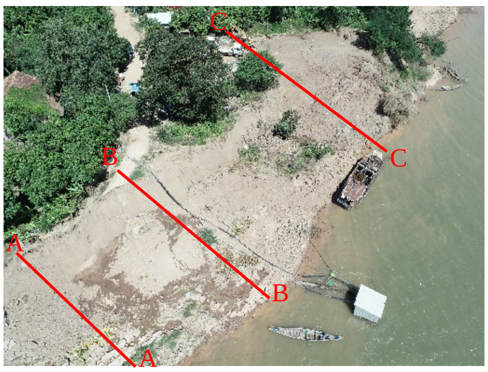

Fig. 6. Cross-sections obtained from drone survey (Peam Chi Kang Commune).

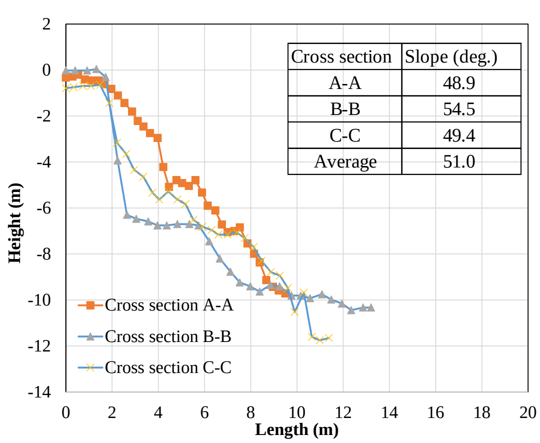

Fig. 7. Slope angle at Peam Chi Kang Commune.

2.2 Some considerations on failure mechanism of the Mekong riverbank

Based on the field investigation results, the failure mechanisms of the riverbank are as follows:

1) Soil erosion during rainy season

Visual confirmation of the field (Fig. 8) showed that soil erosion and slope failure occurred gradually on the riverbank owing to the rising water level caused by the impact of small river waves during rainy season. A decrease in the strength of the soil under saturated conditions during the rainy season could also be a factor causing slope failure.

2) Large-scale collapse during the dry season

In dry season, the water level of the river decreases, and a sudden decrease in water level can cause a large-scale slope failure (Fig. 9).

Slope stability analysis (modified Fellenius method) was performed to simulate slope failure due to the lowering of the water level. The parameters used in the analysis are listed in Table 1. The unit weight was obtained from the density test results; however, the internal friction angle and cohesion of the soil were set using the general value of the soil, whose physical properties were similar to those of the Mekong riverbank.

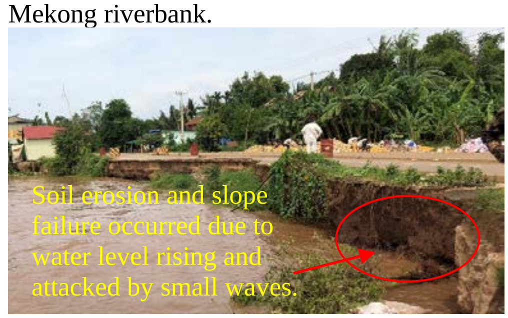

Fig. 8. Visual confirmation of the field (rainy season).

Fig. 9. Visual confirmation of the field (dry season).

Table 1. Parameters used in the slope stability analysis.

Saturated unit weight (kN/m^3)	Wet unit weight (kN/m^3)	Internal friction angle(deg.)	Cohesion (kN/m^2)
19.70	18.40	34.00	10.00

The slope stability analysis results, shown in Fig. 10, indicate that under full water conditions (rainy season), the slope did not collapse (Fsmin=1.373); however, under water-level lowering conditions (dry season), the slope collapsed (Fsmin=0.823). The slope collapse in the dry season can be attributed to the following factors:

1) Decrease in soil strength under saturated conditions during full water (rainy season).

2) Increase in the effective stress of the ground due to the lowering of the water level (increase in the sliding mass in the wet condition of the slope).

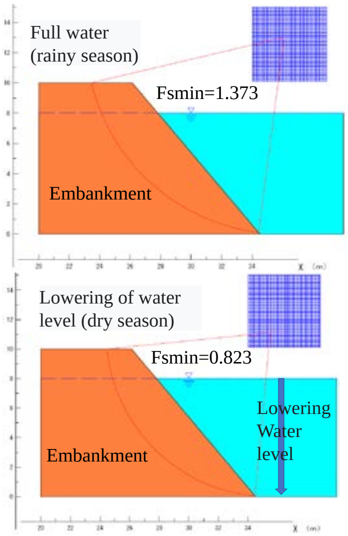

Fig. 10. Slope stability analysis under lower water levels (dry season).

3. LABORATORY TESTS

To confirm the basic properties and dispersive characteristics of the soil collected from the collapsed sites, physical property, density test, double hydrometer (ASTM D 4221), and crumb tests (ASTM D 6572) were conducted.

3.1 Test for Physical Properties of soil

The physical property and density test results of the (samples collected from the field investigation site at Luek Daek, PCK: Peam Chi Kang) are summarized in Table 2.

Table 2. Laboratory test results.

Physical properties	LD-1 3.5 m	LD-2 6 m	PCK-1 4 m
Water content (%)	4.3	26.3	19.5
Maximum grain size, (mm)	4.75	4.75	2
Fine fraction content (%)	74.3	98.3	93.5
Sand (%)	25.2	1.6	6.5
Silt (%)	55.8	29.0	47.8
Clay (%)	18.5	69.3	45.7
Dry density, ρ_d (g/cm^3)	1.528	1.510	1.545
Density of soil particles, ρ_s (g/cm^3)	2.741	2.759	2.758

LD: Luek Daek; PCK: Peam Chi Kang.

3.2 Double Hydrometer test (ASTM D 4221)

The dispersed soil causes soil erosion during rainy season. To investigate the characteristics of the dispersive soil, a series of double hydrometer tests of the soil samples acquired from the Mekong Riverbank (in Luek Daek District) were conducted. The following is a brief description of the test method [3]:

This test method determines the dispersive characteristics of a sample by comparing the amount of soil particles smaller than 5-µm obtained from the standard sedimentation analysis method with and without a dispersant.

The percentage dispersion of the soil is defined as follows [1]:

$$\text{Percentage Dispersion}(D_p) = \frac{A \times 100}{B} \qquad \text{(Eq. 1)}$$

A: % of particles smaller than 5-µm obtain from sedimentation analysis test using chemical dispersant.

B: % of particles smaller than 5-µm obtain from sedimentation analysis test without using chemical dispersant.

The dispersiveness of soil was determined as follows (Sherard et al. 1977).

Dp≦30%	Nondispersive
30%<Dp<50%	Intermediate
Dp≧50%	Dispersive

The double hydrometer test results of the samples collected from Mekong Riverbank are summarized in Table 3. The Dp values for most samples obtained by using Eq. (1) were greater than 50%, indicating dispersiveness of these soils. Therefore, the existence of dispersive soils may cause erosion of the Mekong Riverbank during the rainy season and is one of the factors responsible for the collapse of the riverbank.

Table 3. Double Hydrometer test results

Sample No.	Dp (%)	Judgement	Remark
Mekong Sample01	54.2	Dispersive	Leuk Daek, Depth 0.8 m
Mekong Sample02	57.6	Dispersive	Leuk Daek, Depth 1.2 m
Mekong Sample03	34.4	Intermediate	Leuk Daek, Depth 0.6 m
Mekong Sample04	65.8	Dispersive	Leuk Daek, Depth 1 m
Mekong Sample05	62.7	Dispersive	Leuk Daek
Mekong Sample06	55.3	Dispersive	Leuk Daek
Mekong Sample07	98.0	Dispersive	Leuk Daek, Depth 0.5 m
Mekong Sample08	28.0	Nondispersive	Leuk Daek, Depth 0.5 m

3.3 Crumb test (ASTM D 6572)

Crumb tests were also conducted to investigate the dispersive characteristics of the erosion soils.

The test method is as follows [2]: A cube of (approximately 15 mm a side) remolded soil (approximately the size of a single die in a pair of dice) or a natural soil crumb of approximately similar volume was placed on the bottom of a white porcelain dish containing 250 mL of distilled water. The temperature of the water was recorded, and visual determinations of the dispersion grade were made and recorded at 2 min, 1 h, and 6 h. Grade determination was based on the formation, extent, and turbidity of a dense cloud or halo of colloidal-sized particles extending from the soil crumb. The determination consisted of grades 1 (nondispersive), 2 (intermediate), 3 (dispersive), and 4 (highly dispersive).

The crumb test results of the materials obtained from the Mekong Riverbank are summarized in Table 4. The test results showed no clouds; therefore, the test samples may have been of grade 2 or 3. However, all the specimens collapsed owing to water saturation. This indicates that soil erosion is a cause of riverbank failure during the rainy season.

Table 4. Crumb test results.

Sample No.	Before test	Recorded at 1 h
LD-1 3.5 m		
LD-2 6 m		
PCK-1 4 m		

LD: Luek Daek; PCK: Peam Chi Kang.

4. CENTRIFUGE MODEL TEST

4.1 Outline of centrifuge

Centrifuge model test is a powerful experimental technique used in geotechnical engineering. It can be used to simulate the real phenomena of related geotechnical structures (such as slopes, embankments, foundations, and retaining walls) and verify practical designs or numerical analyses. The principle of centrifuge is illustrated in Fig. 11. By spinning a small model through a centrifuge loading system and applying centrifugal acceleration, the model can be subjected to the same stress conditions and behavior as the prototype. For example, if a 30 cm-high slope model is used to conduct the model test at 100G (G is the centrifugal acceleration), then the size of the slope will be 100 times of the model slope; thus, a 30 m-high prototype slope was simulated (see Figure 12).

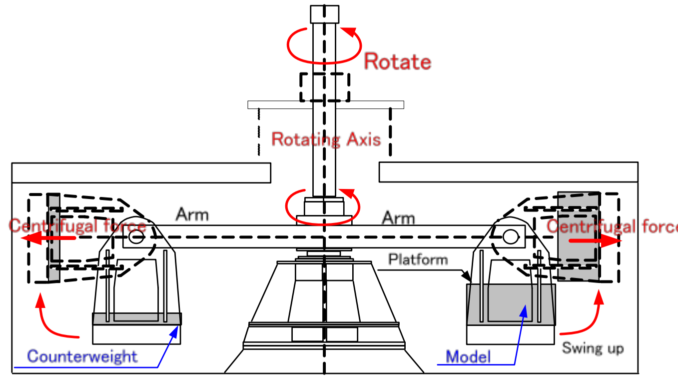

Fig. 11. Principle of centrifuge.

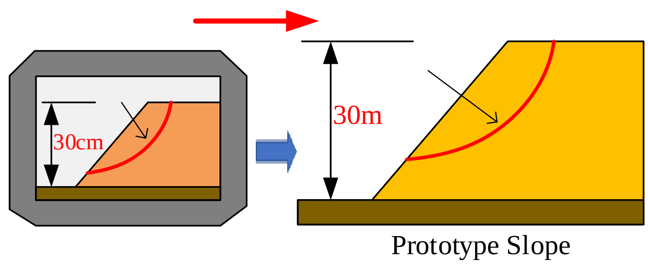

Fig. 12. Relationship between model and prototype.

The similarity law relationship between the model and prototype, when a 1/n geometrical similarity model of the prototype was made with exactly the same soil composition as the prototype, is summarized in Table 5, and the model was tested in a centrifugal acceleration field of nG.

Table 5. List of similarity laws (scaling laws).

Item	1/n Model	Prototype
Length	l_m	l_p/n
Area	A_m	A_p/n^2
Volume	V_m	V_p/n^3
Stress	σ_m	σ_p
Strain	ε_m	ε_p
Displacement	δ_m	δ_p/n
Load	F_m	F_p/n^2
Time (Permeability/Consolidation)	t_m	t_p/n^2
Time (Dynamic problem)	t_m	t_p/n
Acceleration	a_m	$a_p \cdot n$
Velocity	v_m	$v_p \cdot n$

m: model; p: prototype

4.2 Centrifuge used in this study

A centrifuge model test was conducted under a centrifugal force field of 50G. The centrifugal model test system (belonging to the Research and Development Center of Nippon Koei Co., Ltd., Japan) used in this study was a balanced beam-type apparatus with an effective radius of 2.6 m, as shown in Fig. 13.

Fig. 13. Centrifuge of Nippon Koei.

4.3 Model preparation and measurements

The material used in the tests was Edosaki sand (mountain sand) obtained from a mountain in Ibaraki Prefecture, Japan. The physical properties, compaction test results, and consolidated drained triaxial compression test results of the material are listed in Tables 6, 7, and 8, respectively.

Fig. 14 shows an outline of the centrifuge model test. The height of the slope was 200 mm (10 m on the prototype scale), angle of the slope was 50 °, and water level was 160 mm (8 m on the prototype scale). These slope dimensions were determined from the field investigation results of the Peam Chi Kang area (Fig. 7).

Table 6. Physical properties.

Physical properties	Edosaki sand
Maximum grain size, D_{max} (mm)	2.0
Mean grain size, D_{50} (mm)	0.335
Uniformity coefficient, U_c	2.56
Coefficient of curvature, U_c'	1.00
Fine fraction content (%)	4.4
Coarse sand fraction (%)	13.0
Medium sand fraction (%)	55.9
Fine sand fraction (%)	26.7
Density of soil particles, ρ_s (g/cm^3)	2.681

Table 7. Compaction test result.

Maximum dry density, ρ_{dmax} (g/cm^3)	1.707
Optimum water content, w_{opt} (%)	15.0

Table 8. Triaxial compression test results (CD).

Degree of compaction, D_c (%)	95
Dry density, ρ_d (g/cm^3)	1.622
Water content (%)	15.0
Cohesion, c (kN/m^2)	4.5
Friction angle (deg.)	36.3

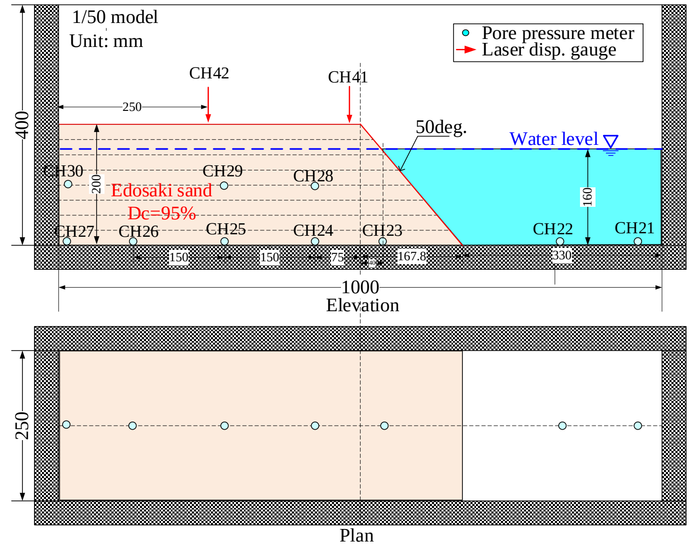

Fig. 14. Centrifuge model test.

The procedure for preparing the model embankment is as follows: First, a model with a degree of compaction of 95% (ρ_d=1.622 g/cm^3) and an optimum water content of 15% was prepared and compacted in a rigid soil container. Colored sand layers with 3 mm of thickness were installed in the model to observe the deformation of the embankment after testing.

A methylcellulose solution (metolose) with a kinematic viscosity of 50 mm^2/s was used as the substituted pore fluid for water storage.

The test procedure was as follows: (1) The centrifugal force acceleration was increased to 50G, (2) water was poured into the container up to a specified water level (8 m), and (3) the water level was lowered to the initial condition.

5. RESULT OF CENTRIFUGE MODEL TEST

5.1 Slope stability before water storage

Fig. 15 shows photographs of the slope failure at 50G before water storage (when the slope was 10-m high in the prototype).

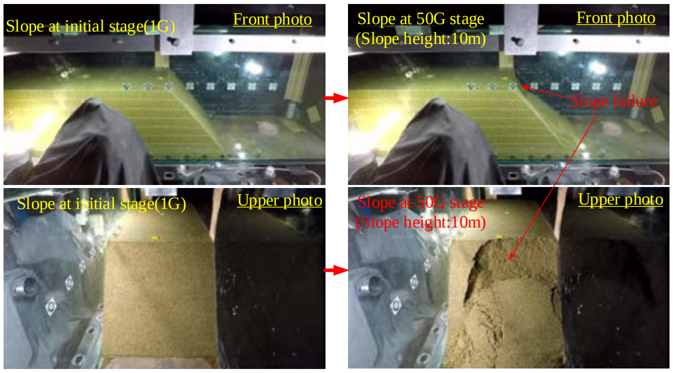

Fig. 15. Photographs of slope failure at 50G (before water storage).

This result indicates slope failure when the height and angle of the slope were 10 m and 50 °, respectively. Fig. 16 shows the results of the slope stability analysis of the centrifuge model before water storage. The analysis results showed that the slope failure was similar to that in the model test (Fsmin=0.996).

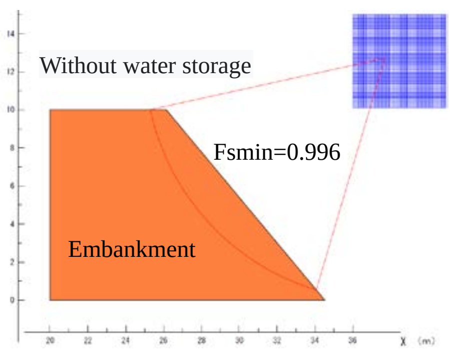

Fig. 16. Slope stability analysis of model test before water storage.

5.2 Slope failure during rising and lowering of water level

Fig. 17 and 18 show the pore water pressure and vertical displacement obtained from the centrifuge model test during the rising and lowering of the water level, respectively. A sudden change in the vertical displacement of the embankment (slope failure) occurred during the rising and lowering of water level.

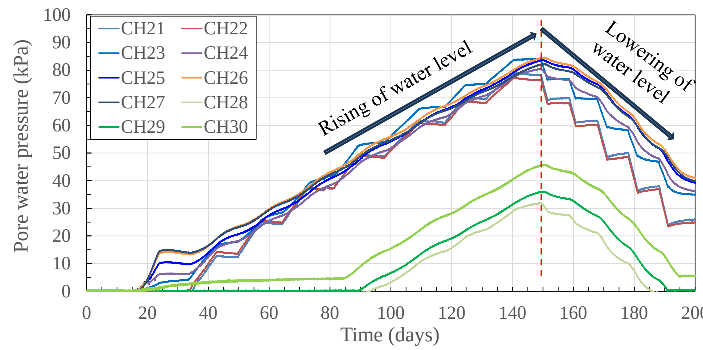

Fig. 17. Pore water pressure.

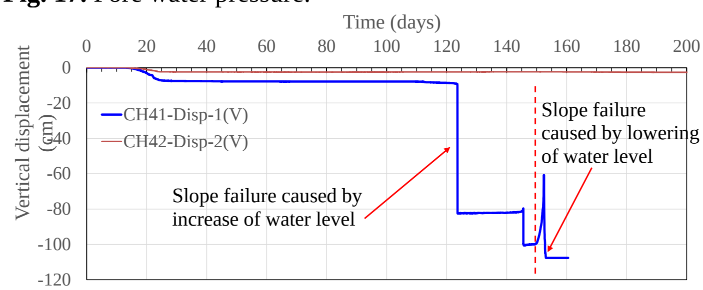

Fig. 18. Vertical displacement.

Fig. 19 shows photographs of slope failure during the rising and lowering of the water level. When the water level was increased to full water, part of the slope collapsed owing to soil erosion (the left photograph in Fig. 19). In the next step, when the water level lowered, another part of the slope collapsed owing to an increase in the effective stress of the ground (the right photograph in Fig. 19).

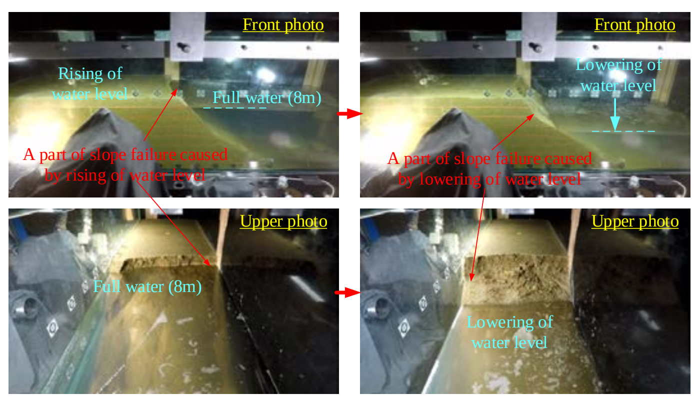

Fig. 19. Photographs of slope failure during increases and decreases in the water level

Fig. 20 shows a sketch of the deformation of the embankment before and after the centrifuge model test. The initial angle of the slope before the test was 50 °; however, after the slope failure, the slope angle was 34 °and became stable.

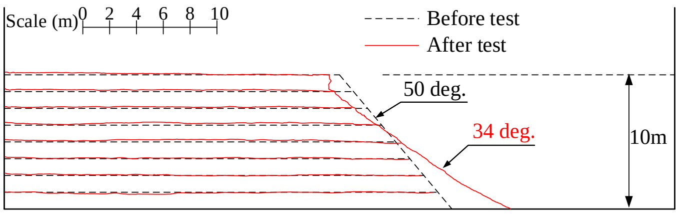

Fig. 20. Sketch of the embankment deformation after testing.

5.3 Slope failure process due to lowering of water level

To investigate the slope failure process during the lowering of the water level, image analysis was conducted using a high-resolution image captured using a high-speed camera [7]. Fig. 21 shows two example images (before and after dewatering) used for image analysis. Fig. 22 shows the maximum shear strain distribution of slope failure during the lowering of water level. The shear strain gradually increased with decreasing water level, indicating occurrence of progressive failure on the slope. Notably, the maximum shear strain developed from the point of water level reduction and was concentrated in the saturated zone.

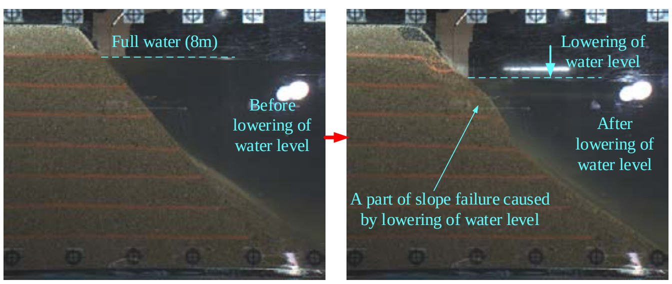

Fig. 21. Images used for image analysis were captured using a high-resolution camera.

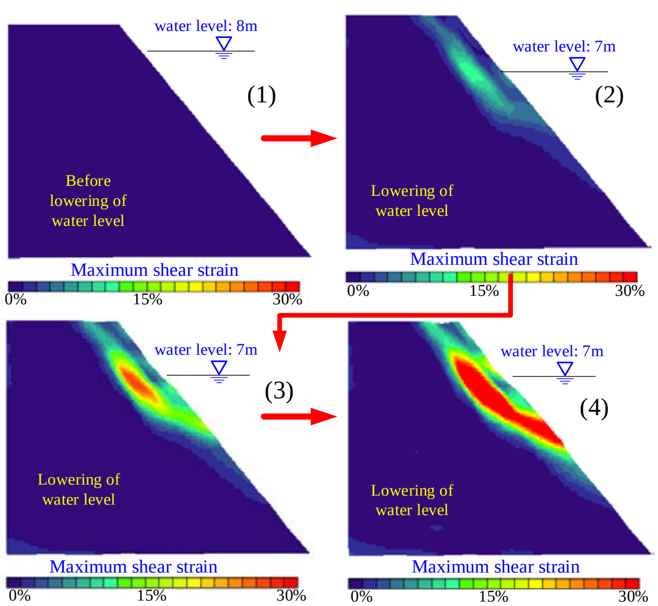

Fig. 22. Results of image analysis.

6. CONCLUSIONS

To investigate the main factors of slope failure along the Mekong Riverbank from a geotechnical engineering viewpoint, field investigations, soil laboratory tests, slope stability analyses, and a centrifuge model test were conducted. The results of this study are summarized as follows:

(1) A drone survey was used to capture photographs and measure the slope angles of riverbanks at two locations in Cambodia (Leuk Daek district and Peam Chi Kang commune). The photographs indicated occurrence of large-scale slope failures along the riverbank. The heights and angles of the collapsed slopes were approximated as follows:
- Leuk-Daek district: Height: 5 m, Angle: 62 °.
- Peam Chi Kang Commune: Height: 10 m, Angle: 51 °.

(2) Based on the field investigation results, the failure mechanisms of the riverbank were as follows:
- Soil erosion occurred during the rainy season. A decrease in the strength of the soil under saturated conditions during the rainy season could also be a factor causing slope failure.
- Lowering of the water level during the dry season can cause slope failure. A stability analysis of the slope under water-level-lowering conditions was conducted. The analysis results showed that slope failure occurred owing to the lowering of water level. The main reason for slope failure during the dry season is considered to be the increase in the effective stress of the ground caused by the lowering of the water level.

(3) Physical property tests revealed that the riverbank soil was sandy clay. According to the double hydrometer and crumb test results, most of the soils were classified as dispersive, which may cause the soil erosion during rainy season. This erosion phenomenon is one of the factors causing the collapse of the riverbank.

(4) A centrifuge model test was conducted to investigate the mechanism of slope failure during the rising and lowering of the water level. The slope failure mechanisms obtained from the centrifuge model test are as follows:
- Slope failure occurred before water storage at 50G of centrifugal acceleration (when the slope height was 10 m) and was well-simulated by the slope stability analysis (Fs=0.996). The reason for the slope failure in the model test is probably the larger slope gradient and height used in the experiment than those on the riverbank.

- Slope failure during the rise in water level was caused by soil erosion and a decrease in soil strength under saturated conditions.
- Slope failure occurred during the lowering of the water level owing to an increase in the effective stress of the ground. The slope failure process during the lowering of the water level was clearly observed using image analysis.

(5) Further experimental and analytical studies on the collapse mechanism of riverbanks and development of countermeasures should be conducted.

ACKNOWLEDGMENTS

The authors would like to express their gratitude to Dr. Kim Ngun Bun of the Institute of Technology of Cambodia for his support in sampling and discussions and Mr. Takuya Miki, Mr. Kentaro Fukuda, and Mr. Takeshi Nomura at Nippon Koei Co., Ltd. for their assistance during the analytical and experimental work.

REFERENCES

[1] Sherard, J. L., Dunnigan, L. P., and Decker, R. S. (1977). Some Engineering Problems with Dispersive Clays, Related Piping, and Erosion in Geotechnical Projects, ASTM STP 623, 3-12.

[2] ANNUAL BOOK OF ASTM STANDARDS 2002, Standard Test Methods for Determining the Dispersive Characteristics of Clayey Soils by the Crumb Test, ASTM D 6572-00, 907-910.

[3] ANNUAL BOOK OF ASTM STANDARDS 2005, Standard Test Method for Dispersive Characteristics of Clay Soil by Double Hydrometer, ASTM D 4221-99, 549-551.

[4] Xu, X., Zhang, K., Kong, Y., Chen, J., and Yu, B. (2006). Effectiveness of erosion control measures along Qinghai–Tibet Highway, Tibetan Plateau, China. Transportation Research Part D: Transport and Environment 11(4), 302-309.

[5] Xuyen, R. S. T. S. L., AN, R. T. P. S. I., Loss, I. O. P. S., COVER-BASED, E. O. L. (2011). AUN/SEED-Net ASEAN Engineering Journal.

[6] Soksan, C., Sambath, K., Juan, M., and Son, H. T. (2015). Prediction of mass landslides on riverbanks subjected to variations in water levels GMSARN International Journal, 9, 113 - 118.

[7] Uemura, K., Suzuki, S. S., and Tsuda, M. (2022). Experimental study of the dynamic behavior of ashlar masonry walls using centrifuge model tests. ICPMG 2022, Physical Modeling in Geotechnics, 648-651.

Techno-Science Research Journal 12 (Special Issue) 78-85

Content list available at ITC

Techno-Science Research Journal

Journal Homepage: www.ric.itc.edu.kh

Techno-Science Research Journal

The Chemical Speciation of the Contaminated Sediments from Olgoy Lake, Mongolia

Keo Tithya[1*], Heng Muoy Yi[1], Heng Hongchhay[1] Keisuke Fukushi[2], Baasansuren Gankhurel[3]

[1]*Faculty of Geo-resources and Geotechnical Engineering, Institute of Technology of Cambodia, Russian Federation Blvd., P.O. Box 86, Phnom Penh, Cambodia*

[2]*Institute of Nature and Environmental Technology, Kanazawa University, Kakuma-machi, Kanazawa, Ishikawa 920-1192, Japan*

[3]*Graduate School of Natural Science and Technology, Kanazawa University, Kakuma-machi, Kanazawa, Ishikawa 920-1192, Japan*

Received: 8 August 2023; Accepted: 15 May 2024; Available online: August 2024

Abstract: *The investigation was carried out with the naturally contaminated sediments from Olgoy Lake at the southern foothill of Khangai Mountain, Mongolia. This study aims to elucidate the mobility and solubility of the contaminated heavy metal elements such as As, Cd, and U by characterizing their chemical speciation from the contaminated lake sediments from various depths of the Olgoy Lake by using mineralogical analysis by X-ray diffraction combined with the soil analysis by the six steps of sequential extraction procedures(SEP) and pH adsorption. After that, chemical analysis of metal elemental from ICP-MS and major cation elemental from ICP-OES were identified. Next, twelve sediment samples sliced from an Olgoy Lake sediment core were investigated and sent for geochemistry laboratory analysis. The result of mineralogy found monohydrocalcite, calcite, quartz, feldspar, amphibole, plagioclase, illite, and chlorite as crystalline minerals while the result of chemical analysis of interesting elemental such as aluminum (Al), calcium (Ca), and iron (Fe), manganese (Mn), arsenic (As), cadmium (Cd), and uranium (U) were used to predict its behavior in the natural geological contaminated sediments between pH3 to pH 10 by adsorption. The sequential extraction procedures (SEP) illustrated the speciation of heavy metals such as As, Cd, and U of the lake sediment, respectively. In conclusion, Most of As was released from the dissolved ferrihydrite and monohydrocalcite. Cd may be adsorbed on the illite as clay minerals because of the cation exchange reaction which is consistently dissolved in exchangeable fraction while U concentrations are mainly associated with the carbonate fraction and adsorbed onto calcite mineral.*

Keywords: Adsorption; Heavy Metals; Olgoy Lake; Sequential extraction procedures(SEP); Speciation

1. INTRODUCTION

Heavy metals such as arsenic (As), cadmium (Cd), and uranium (U) were found in the surface soils of the natural geological environment, particularly in the crucial sources of natural lakes and places affected by agricultural practices, anthropogenic, radio-geochemical regions or naturally geology contamination. Moreover, the contamination and pollution of the water are considered a health concern due to its toxicity, and non-biodegradability. Fukushi & Gankhurel [**8,11,12**] said If these trace elements are mobile, they can become a threat to environmental and human health if they are transported downward through the soil and into plant roots while numerous studies on contaminated water found inorganic arsenic and other heavy metals affected the millions of people healthy [**19**].

Some techniques are available to identify the speciation of heavy metals in the soil. The sequential chemical extraction procedure (SEP) has traditionally been used to assess the contribution of various host phases throughout the soil while it can quantitatively separate different geochemical forms (e.g exchangeable, acid-soluble, reducible, oxidizable, or residual) based on the rational use of a series of selective reagents Fukushi & Sekine & Gankhurel [**8,11**]. Many studies have involved the use of SEP to examine the chemical speciation of heavy metals in the soils from contaminated lakes and rivers Gankhurel & Gleyzes [**11,12,14**]. This method can be used to determine operationally defined fractions in which the concentration of the leached element in each step depends on the selected reagents. The contaminated soils in this area provide good opportunities to enhance understanding of the relationship between the chemical speciation of heavy metals and their mobilities in natural conditions. To better understand the solubility of the contaminated heavy metal in the lake water and their mobility in soils, plants, and biota

* Corresponding author: Keo Tithya
E-mail:tithyakeo0008@gmail.com; Tel: +855-96-601-3111

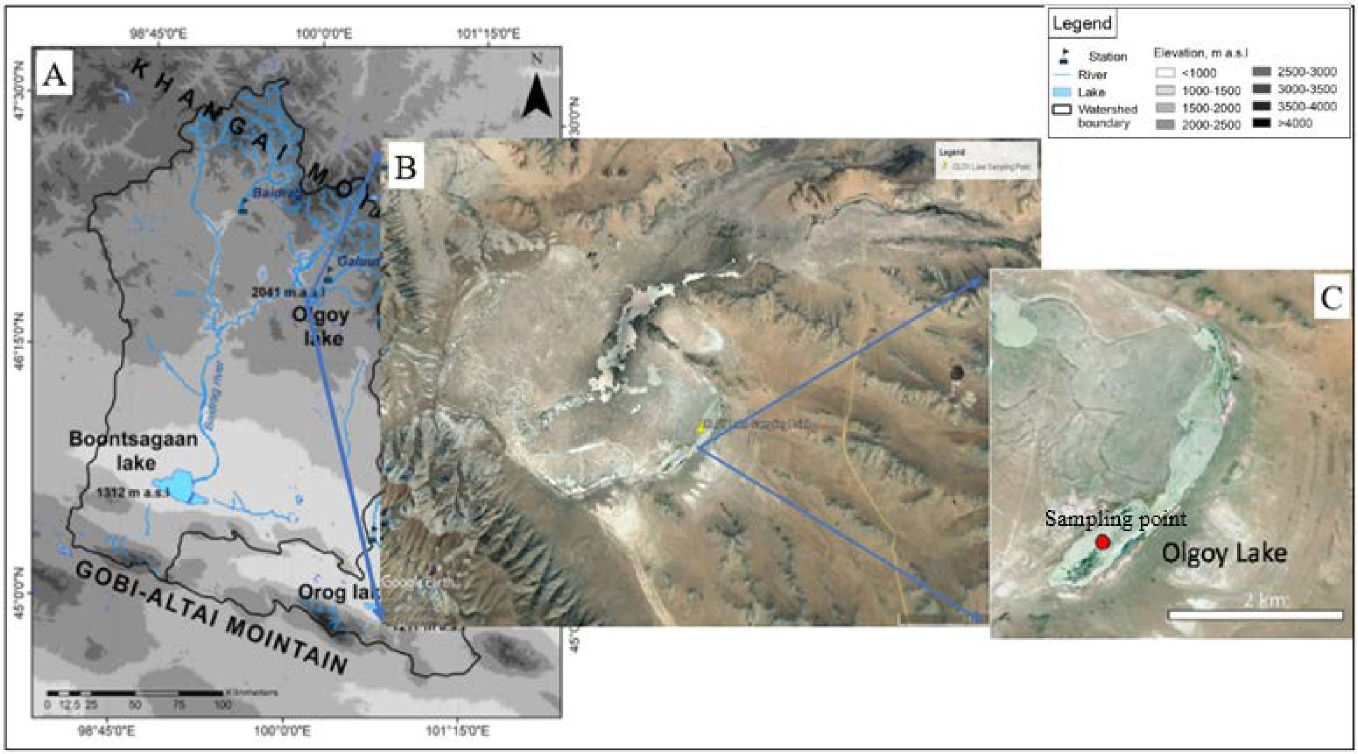

Fig. 1. Location of Study Area Modified from Udaanjargal et al. [**22**] (A). Natural zone map, (B). Olgoy Lake, (C). Sampling point.

are required to determine their chemical speciation while the six steps of the sequential extraction technique combined with mineralogy may illustrate better geochemical processes in the soil [**14,28**]. The main objective of the present study is to understand the mobility of heavy metals through the combination methods of SEP with mineralogy and adsorption from Olgoy Lake sediments in Mongolia.

1.1 Location of Study Area

Olgoy Lake lies in the northernmost part of the valley of the Gobi Lakes, where the surface area is 1.55 km^2, with a depth of 1m and there is no inflow and outflow inside this valley (Figure 1). This Valley is 500 km long and 150 km wide, with an average elevation between 100 and 1400m above sea level [**22,25**]. The Valley of Gobi Lakes is an elongated mountain depression formed between the Siberian Craton and the Tarim and Sino-Korean Cratons and a tectonically active foreland basin in Gobi-Altai and Khangai strike-slip regime by Lakshmipathiraj et al. 2006 [**19**].

2. MATERIAL AND METHODS

In this study, a total of 12 samples of approximately 39.5cm depth were sliced and classified as (OL-01, OL-03, OL-05, OL-10, OL-13, OL-15, OL-18, OL-20, OL-25, OL-30, OL-35, OL-40) was obtained by the gravity corer. These samplings were sent to the laboratory for soil analysis by the six fractions of the sequential extraction procedures and mineralogy by X-ray diffraction (XRD) after being dried. After that, pH adsorption experiments from pH 3 to pH 10 were investigated to understand the heavy metal remediation of lake-available minerals. Lastly, solutions from all fractions in SEP and each pH were done with chemical analysis by ICP-OES and ICP-MS to determine the major elements concentration (Al, Fe, Ca, Mn) and trace elements (As, Cd, U), respectively.

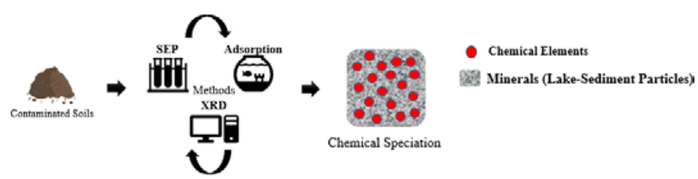

Fig. 2. Methodology

2.1 X-ray Diffraction(XRD)

The mineral compositions of the sieved samples were analyzed via XRD (Ultima IV; Rigaku Corp., Kanazawa Japan). A total of 6 samples (OL-03, OL-05, OL-10, OL-13, OL-15, OL-18) were done with XRD to examine the available minerals of the sediments before dissolving the minerals by using SEP main reagents of each fraction. Moreover, sediment samples from the residue in pH3, pH6, and pH9 were also investigated to understand the adsorption mechanism of each heavy metal into the mineral interiors.

2.2 Sequential Extraction Procedures(SEP)

A total of 12 samples were distributed from the lake-sediment core which was obtained from the gravity corer in 2014 and was sliced at the National University of Mongolia described by Udaanjargal et al. [**22**]. Numerous studies have involved the use of sequential extraction procedures(SEP) to examine the chemical speciation of the soil [**11,14,28**]. **Table 1** summarizes the reagents and the target materials in each step.

Table 1. Six Steps of Sequential Extraction Procedures

Fractions	Reagents	Phases
1	(1M) $MgCl_2$, pH 7	Exchangeable
2	**Morgan**: (1M) $CH_3COONa.3H_2O$ with CH_3COOH, pH 5	Carbonates
3	**TAO:** (0.2M) $C_2H_2O_4 + C_2H_8N_2O_4$, pH 3	Amorphous iron and Manganese oxide
4	**CDB**: (0.3M) $Na_3C_6H_5O_7$, (0.2M) $NaHCO_3$, $Na_2S_2O_4$ HCl, pH 6.7	Crystalline iron and manganese oxides
5	(8.8M) H_2O_2 with (1M) CH_3 $COONH_4$, pH 2	Organic matter and sulfides
6	(60%) HNO_3 with HF (48%), HCl (36%)	Residues

The first step (F1) target was the elements in the exchangeable (adsorbed) fraction. 1 g of a sample was treated with 20mL of 1 M magnesium chloride solution and mixed on the rotator for 1 h at room temperature. After that, the solids part was separated from the suspensions via centrifugation (Kubota 6200; Kubota Corp., Japan) at 15000 rounds per minute (rpm) for 10 min. Next, use the syringe and filter through a 0.20 µm filter. The filter solution samples were immediately acidified with ultrapure grade HNO_3 and then already to do analyses for F1. The solids in the centrifuge tube were then washed with deionized water and kept for the next step. The solids were repeated after each extraction step. The target of the second step (F2) was the elements in the carbonate fraction [**11,28**]. The residue from F1 was treated with 1 M sodium acetate adjusted to pH 5 with acetic acid on a mix rotator for 16h at room temperature. The same treatments were repeated after each extraction step. The target of the third step (F3) was the elements in amorphous iron and manganese oxides[**16**]. After the second 1 M sodium acetate extraction, the residue was treated with a 20mL solution of 0.2 M ammonium oxalate and adjusted to pH3 with oxalic acid on a mix rotator for 4 h at room temperature[**27**]. The fourth step (F4) was the elements in crystalline iron and manganese oxides [**28,29**]. The residue from F3 was treated with a mixture of 0.3M $Na_3C_6H_5O_7$, 0.2M $NaHCO_3$, and 1.125g of sodium dithionite (CDB solution) at pH 7.6 on a mix rotator for 8h at room temperature. The target of the fifth step F5 was the elements in organic matter and sulfide minerals [**11**]. The residue from F4 was extracted with 10mL of 8.8 M H_2O_2 on a mix rotator for 1h. Then vessels were heated at 85ºc, and 20ml of 1 M ammonium acetate adjusted to pH 2 with HNO3 was added to the residue for 16h on a mix rotator. The target of the sixth step (F6) was the partitioning of the residual. The residue from F5 was digested completely in a mixture of 48% HF, 60% HNO3, and 30% HCl, a ratio of 1:1:1.

Lastly, the extracted solutions from each step (12 bottles for a step) have to be diluted before being analyzed for major elements by using ICP-OES; 710-ES; Varian Inc, and trace elements by ICP-MS; X7, Thermo Inc, respectively.

2.3 Chemical Adsorption

These sediments were mixed with two both low and high sodium chloride ionic strength, respectively. These suspends were rotated before being centrifuged to separate the residue and solution while the residue needed to freeze in the refrigerator and then sent to the XRD section and the solutions were investigated with the chemical analysis by ICP-OES for major elements and ICP-MS for trace elements.

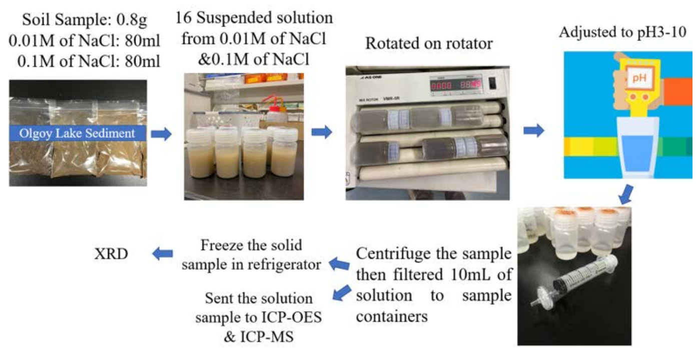

Fig. 2.1 Adsorption pH Experiments

3. RESULTS AND DISCUSSION

3.1 Result

3.1.1 Mineralogical Characterization

The major crystalline minerals, identified by XRD, found silicate minerals: were quartz, feldspar, amphibole, and plagioclase, carbonate minerals such as monohydrocalcite, and calcite, while there are also clay minerals such as illite and chlorite, were found in the sediment sample from the Olgoy lake from OL-03(2.5cm) to OL-18(17.5cm) (Fig.3). These six sediments samples from the surface seem not to show any significant differences in major mineral compositions.

Under the alkaline condition, XRD results showed the availability of major minerals such as illite, chlorite, quartz, plagioclase, feldspar, monohydrocalcite, and calcite in the sediments. Notably, monohydrocalcite started to disappear below pH 9 while quartz and clay minerals are increasing in pH 6 (Fig. 4A, B).

Despite this, the lake sediments in the mainly acidic condition pH 3 were reported the dissolved all carbonate minerals and other crystalline minerals (Fig.3.1 C). The disappearance of these minerals may cause the release of the important major elements and heavy metals which were adsorbed onto the found minerals in the alkaline pH.

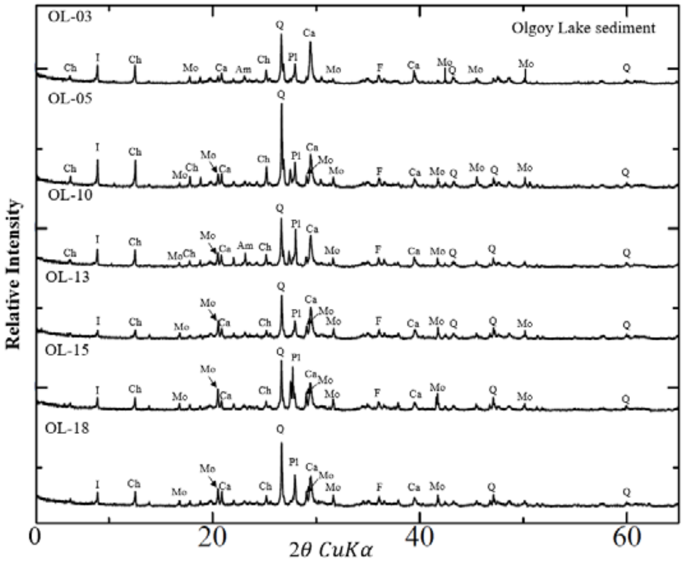

Fig. 3. Result of Mineral Identification by XRD Abbreviation: I: illite, Q: Quartz, F: Feldspar, Ch: Chlorite, Mo: Monohydrocalcite, Am: Amphibole, Pl: Plagioclase, Ca: Calcite, OL-xx: Olgoy Lake Sample ID

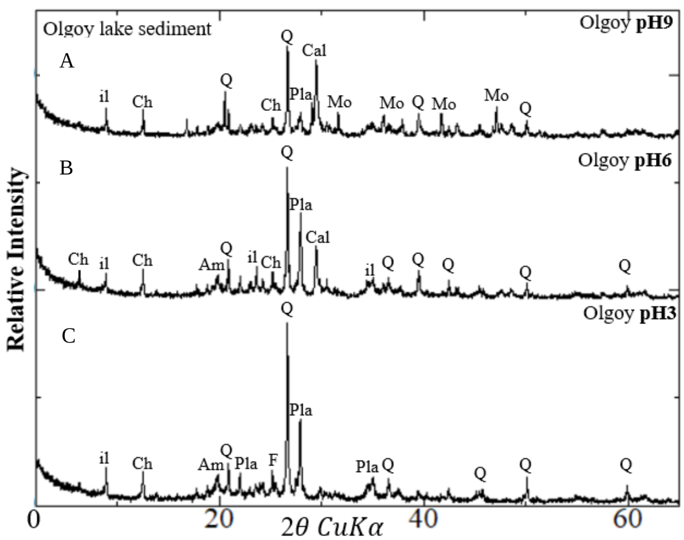

Fig. 3.1 Result of Mineral Identification by XRD Abbreviation: (I): illite, (Q): Quartz, (F): Feldspar, (Ch): Chlorite, (Mo): Monohydrocalcite, (Am): Amphibole, (Pl): Plagioclase, (Cal): Calcite, (OL-xx): Sample ID

3.1.3 Result of Sequential Fractionations

Al, Ca, Fe, Mn, and Mg were ubiquitous elements that constituted the major minerals. It should be noted that Mg concentrations were contaminated and cannot be used because $MgCl_2$ has been used as the main reagent in the exchangeable fraction(F1) described in the **SEP section**.

Ca was the most abundant major element in the soil samples, while the range of its concentrations was found up to 10.1 wt %. The highest Ca concentrations were mainly predominant in the F2 fraction where carbonate minerals such as monohydrocalcite, and calcite were detected in the XRD patterns and it should in accounted for the Ca in F2. The contributions to Ca from the F3, F4, and F5 fractions were negligible. The main reagent magnesium chloride used in F1 was aimed to extract the exchangeable fraction. This behavior may indicate soil samples containing clay minerals that possessed cation exchange capacities, such as illite and chlorite.

Fe most content was F6 in the range of its concentrations 1.9-5.4 wt%. The little Fe in the F3 fraction was most likely derived from amorphous iron oxide [**30**]. Silicate minerals detected in XRD patterns could have accounted for the Fe in F6 because the chemicals used in F6 were HCl and dilute HNO_3 with HF for the residue, which may have been released from the dissolving of silicate minerals.

Al was one of the most abundant major elements in samples, the range of its concentrations was 1.9-6.2 wt %. The Al contents of the fractions other than the F6 were negligible relative to the residue fraction (F6). The XRD patterns showed the presence of feldspar and clay minerals, which could not be dissolved by extractions in steps 1-5. Most of the Al was probably derived from primary minerals and clay minerals.

Mn concentrations were less than 1 wt%. The distribution of Mn concentrations among the samples was associated mainly with F6. The reagents used to collect the F6 fraction were designed to dissolve the residue. The Mn in the soil samples was most likely present in silicate minerals, although most host phases of Mn were negligible in the sediment.

Most of the As concentrations were associated with the F3 fraction followed by F2, F1, and F5 while the range of its concentration was (4.7-128.3 ppm), (11.1-95.4 ppm), (7-23.9ppm), (6.7-19.4ppm), respectively. The ratios of the concentrations from these four fractions are almost constant among the samples. The contributions from F4 and F6 were negligible. Cadmium was distributed mainly in F1 followed by (F2) carbonated fraction and (F5) organic matter bound fraction. The contributions from other fractions were negligible. In addition, Uranium concentrations seem to be partitioned with carbonate fractions followed by F6 and F3 fractions. The U content of the crystalline iron fraction (F4), and organic matter (F5) were negligible in the sediment sample.

3.2 Discussion

3.2.1 Chemical Speciation of the Heavy Metals

The result of SEP revealed that As was distributed primarily in the F3(amorphous iron and manganese oxide) and F2(carbonates phases) fractions. The XRD and the SEP of Ca from the lake sediment notify that MHC was associated as

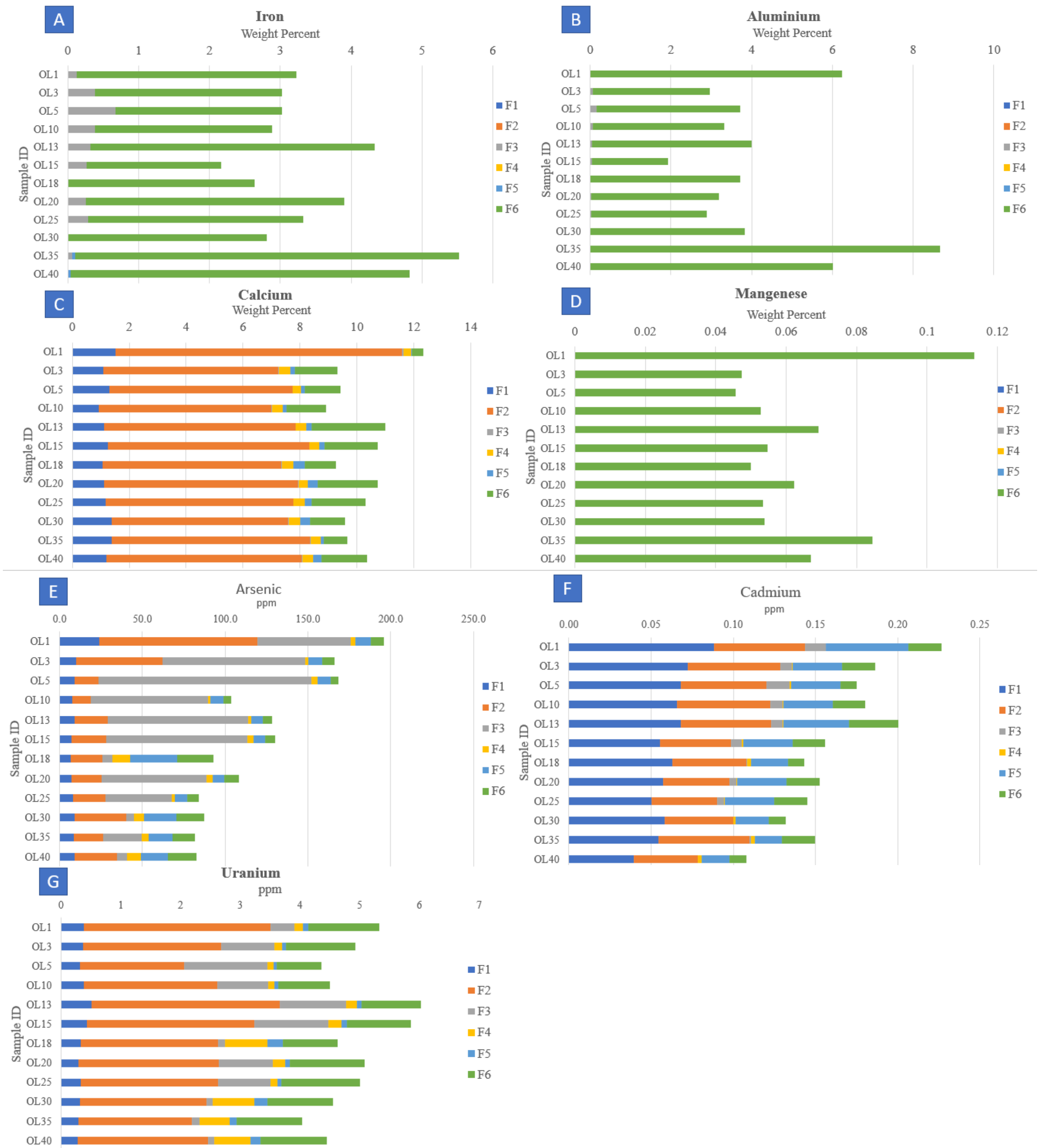

Fig. 3.2 The Result of the Sequential Fractionation: (A). Iron, (B). Aluminum, (C). Calcium, (D). Manganese, (E). Arsenic, (F). Cadmium, (G). Uranium

one of the most crystalline minerals in the lakes. Under carbonate fraction (F2), residue with sodium acetate solution in pH5 illustrated that arsenic adsorbed on the carbonates phase, particularly MHC[**6**]. Arsenic is coprecipitated and inhabits the MHC transformation[**6**]. Numerous studies reported that the sorption mechanism of As on amorphous iron oxides is a bidentate inner-sphere surface complexation and it has been well documented that the adsorption ability of As is higher on amorphous iron oxides than on carbonate[**15**]. Based on the result of SEP and the relationship between As and Fe in F3

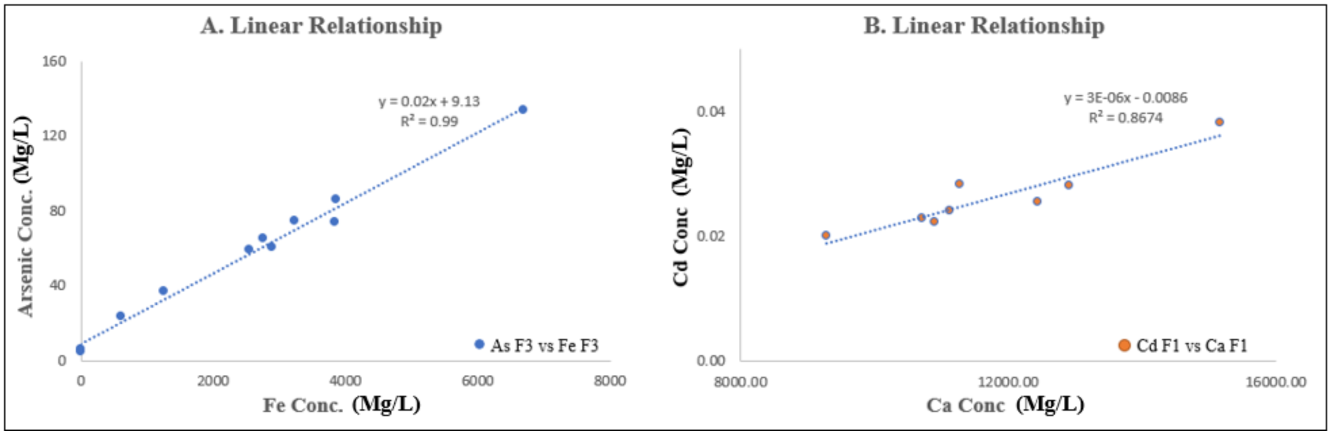

Fig. 3.3 Relationship and Correlation between major and heavy metal: (A). As F3 vs Fe F3, (B). Cd F1 vs Ca F1.

(Fig3.3 A), Most arsenic concentrations seem to be on account with the amorphous iron and manganese oxides (ferrihydrite), a common mineral in soil, and monohydrocalcite in F2 [**30,6**].

Cadmium was reported as a mobile element in soils and therefore more available to organic matter than other heavy metals [**1**]. The SEP indicated Cd was associated mostly with the F1, F2, and F5, respectively. It was bound to exchangeable, carbonates, and organic matter fractions. Clay minerals can adsorb heavy metal onto their interlayer through an ion exchange reaction while the target clay minerals for F1 are illite and chlorite[**23**]. Moreover, the Cd concentration may be associated with calcium in F1 (Fig 3.3 B) which indicates the bioaccumulation into clay minerals[**11**]. The Cd in the soil is adsorbed mainly on clay minerals and possesses a cation exchange capacity[**23**].

SEP showed that U concentrations were released in the carbonate phase while the solubility of U is controlled by sorption processes with carbonate [**18,12**]. The result of the soil analysis showed that U was mainly partitioned into carbonated minerals. The host phase of the F2 fraction in sequential extraction was expected to be calcite mineral because U has been shown to be effectively partitioned in calcite structure via coprecipitation[**12**] and U interacted very little(adsorbs) with pre-existing calcite.

3.2.3 Environmental Implication

Most of the As in the soil could be adsorbed by ferrihydrite, and carbonate, depending on the pH condition. Arsenic could be released under oxidizing conditions and then adsorbed onto ferrihydrite and carbonate. Numerous studies have concerned the arsenic behavior in acidic conditions, As(V) takes anionic oxidation to As (III) [**10**]. In the natural lakes, Mn concentrations will interact and help to promote the effectiveness of arsenic[**19**] while arsenate can coprecipitate from MHC in the alkaline lake was reported [**6**]. It is well noted that arsenic will remediate/adsorb under the acidity to alkaline pH of the solution due to the availability of MHC (Fig. 3.1 A&C) because the highest concentrations of As in pH3 (Fig. 3.4 A) were slightly dropped in alkalinity solution while the precipitation of MHC in Olgoy Lake reported being occurred when the pH is higher than 8 [**6,7,8,22**]. Consequently, Olgoy Lake is alkaline in both the fall and summer seasons could be illustrated that arsenic concentrations were being adsorbed with MHC because the precipitation of MHC occurs when the alkaline pH [**8,22**].

U was associated with carbonate minerals. The host mineral of U was expected to be calcite. In Olgoy Lake, calcite in sediments must have been formed in alkalinity during sedimentation [**8**] while U concentrations are effectively partitioned in calcite structure via coprecipitation whereas it adsorbs little with pre-existing calcite. Uranium was released in the acidic pH due to the dissolution of their speciation mainly, calcite while (Fig 3.1 and 3.4 C) were illustrated the adsorption of uranium into calcite in pH 6 and pH 9. Lastly, the high-ionic-strength solutions are associated with the desorption of U in the sediment. The contaminated uranium of Olgoy Lake is naturally remediated by the alkalinity [**22**].

4. CONCLUSIONS

According to the result and discussion could be indicated that:

- √ Speciation of major elements, were dissolved from major crystalline minerals respectively.
- √ Most of As associated with Fe was partitioned with ferrihydrite and monohydrocalcite (MHC).
- √ Cd with Ca suggests being accumulated in clay minerals after the death of the plants as organic matter on the lake.
- √ Uranium concentrations could be dissolved from calcite and other associated minerals.

The interaction of heavy metals and minerals could be clarified with X-ray Adsorption Fine Structure (XAFS) which leads to evaluating the potential environmental risk in the lake.

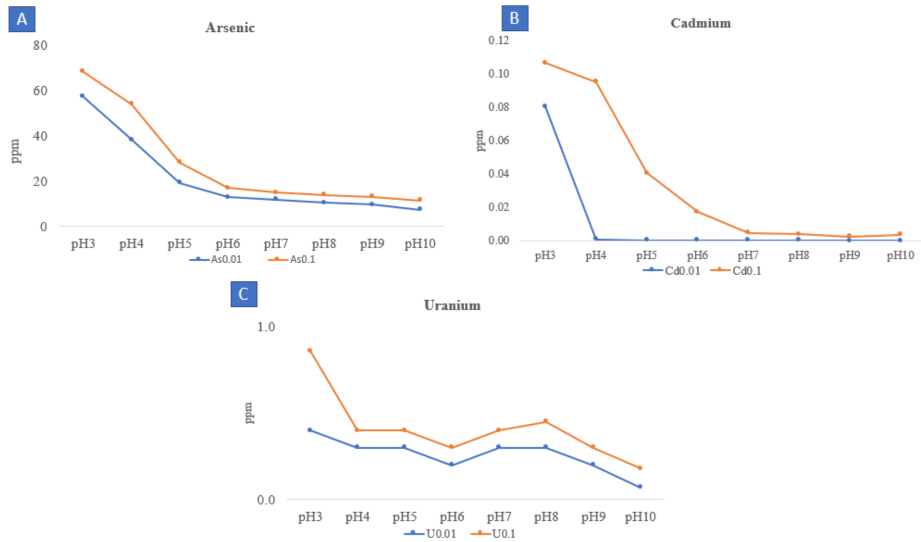

Fig. 3.4 Chemical Adsorption from acidic to alkaline pH: (A). Arsenic, (B), Cadmium, (C). Uranium.

ACKNOWLEDGMENTS

The author expresses sincere gratitude to the **Faculty of Geo-resources and Geotechnical Engineering** for organizing the Earth Resources and GEO-Environment Technology 2023 and encouraging local students and researchers. Appreciate Kanazawa University for providing laboratory analysis and JASSO for supporting funds.

REFERENCES

[1] Anju, M.; Banerjee, D. K. Comparison of Two Sequential Extraction Procedures for Heavy Metal Partitioning in Mine Tailings. Chemosphere 2010, 78 (11), 1393−1402.

[2] Chen, Coleman, M. L., & Katz, L. E. (2006). Bridging the gap between macroscopic and spectroscopic studies of metal ion sorption at the oxide/water interface: Sr (II), Co (II), and Pb (II) sorption to quartz. Environmental Science & Technology, 40(1), 142-148.

[3] Chrastný, V.; Vaněk, A.; Teper, L.; Cabala, J.; Procházka, J.; Pechar, L.; Drahota, P.; Penížek, V.; Komárek, M.; Novák, M. Geochemical Position of Pb, Zn and Cd in Soils near the Olkusz Mine/Smelter, South Poland: Effects of Land Use, Type of Contamination and Distance from Pollution Source. Environ. Monit. Assess. 2012, 184 (4), 2517−2536.

[4] Conesa, H. M.; Robinson, B. H.; Schulin, R.; Nowack, B. Metal Extractability in Acidic and Neutral Mine Tailings from the Cartagena-La Unión Mining District (SE Spain). Appl. Geochem. 2008, 23 (5), 1232−1240.

[5] Dixit, S., & Hering, J. G. (2003). Comparison of arsenic (V) and arsenic (III) sorption onto iron oxide minerals: implications for arsenic mobility. Environmental science & technology, 37(18), 4182-4189.

[6] Fukushi, K., Sakai, M., Munemoto, T., Yokoyama, Y., & Takahashi, Y. (2016). Arsenate sorption on monohydrocalcite by coprecipitation during transformation to aragonite. Journal of hazardous materials, 304, 110-117.

[7] Fukushi, K., & Matsumiya, H. (2018). Control of water chemistry in alkaline lakes: solubility of monohydrocalcite and amorphous magnesium carbonate in CaCl2–MgCl2–Na2CO3 solutions. ACS Earth and Space Chemistry, 2(7), 735-744.

[8] Fukushi, K., Imai, E., Sekine, Y., Kitajima, T., Gankhurel, B., Davaasuren, D., & Hasebe, N. (2020). In situ formation of monohydrocalcite in alkaline saline lakes of the valley of Gobi lakes: Prediction for Mg, Ca, and total dissolved carbonate concentrations in Enceladus' Ocean and alkaline-carbonate Ocean worlds. Minerals, 10(8), 669.

[9] Fytianos, K., & Lourantou, A. (2003, September). Chemical speciation of elements in sediment samples collected at lakes Volvi and Koronia, N. Greece. In Proceedings of the International Conference on Environmental Science and Technology (Vol. 2, pp. 208-215).

[10] Gamaletsos, P. N., Kalatha, S., Godelitsas, A., Economou-Eliopoulos, M., Göttlicher, J., & Steininger, R. (2018). Arsenic distribution and speciation in the bauxitic Fe-Ni-laterite ore deposit of the Patitira mine, Lokris area (Greece). Journal of Geochemical Exploration, 194, 189-197.

[11] Gankhurel, B., Fukushi, K., Akehi, A., Takahashi, Y., Zhao, X., & Kawasaki, K. (2020). Comparison of chemical speciation of lead, arsenic, and cadmium in contaminated soils from a historical mining site: Implications for different mobilities of heavy metals. ACS Earth and Space Chemistry, 4(7), 1064-1077. [5] Sfakianos, J., Coward, L., Kirk, M. & Barnes, S. (1997). Proceedings of the 3rd Conference on Biotechnology, 1134–1140, Frankfurt, Germany.

[12] Gankhurel, B., Fukushi, K., Davaasuren, D., Imai, E., Kitajima, T., Udaanjargal, U., ... & Hasebe, N. (2022). Arsenic and uranium contamination of Orog Lake in the Valley of Gobi Lakes, Mongolia: Field evidence of conservative accumulation of U in an alkaline, closed-basin lake during evaporation. Journal of Hazardous Materials, 436, 129017.

[13] Gaskova, O. L., Isupov, V. P., Vladimirov, A. G., Shvartsev, S. L., & Kolpakova, M. N. (2015, November). Thermodynamic modeling of the behavior of Uranium and Arsenic in mineralized Shaazgai-Nuur Lake (Northwest Mongolia). In Doklady Earth Sciences (Vol. 465, No. 1, pp. 1159-1163). Pleiades Publishing.

[14] GLEYZES, C. et al. Fractionation studies of trace elements in contaminated soils and sediments: a review of sequential extraction procedures. Trends in Analytical Chemistry, Netherlands, v.21, n.6, p.451-467, June, 2002.

[15] Goldberg, S., & Johnston, C. T. (2001). Mechanisms of arsenic adsorption on amorphous oxides evaluated using macroscopic measurements, vibrational spectroscopy, and surface complexation modeling. Journal of colloid and Interface Science, 234(1), 204-216.

[16] HALL, A.C. et al. Intestinal metallothionein and the mutual antagonism between copper and zinc in the rat. Journal of inorganic biochemistry, United States, v.11, p.57-66, 1979.

[17] Kralj, D., & Brečević, L. (1995). Dissolution kinetics and solubility of calcium carbonate monohydrate. Colloids and Surfaces A: Physicochemical and Engineering Aspects, 96(3), 287-293.

[18] Kobayashi, Y., Fukushi, K., Kosugi, S., 2020. A Robust Model for Prediction of U(VI) Adsorption onto Ferrihydrite Consistent with Spectroscopic Observations. Environ. Sci. Technol. 54, 2304–2313.

[19] Lakshmipathiraj, P., Narasimhan, B. R. V., Prabhakar, S., & Raju, G. B. (2006). Adsorption studies of arsenic on Mn-substituted iron oxyhydroxide. Journal of colloid and interface science, 304(2), 317-322.

[20] Li, M., Zang, S., Xiao, H., & Wu, C. (2014). Speciation and distribution characteristics of heavy metals and pollution assessments in the sediments of Nashina Lake, Heilongjiang, China. Ecotoxicology, 23, 681-688.

[21] Nordstrom, D. K. (2002). Worldwide occurrences of arsenic in ground water. Science, 296(5576), 2143-2145.

[22] Udaanjargal, U., Hasebe, N., Davaasuren, D., Fukushi, K., Tanaka, Y., Gankhurel, B., ... & Gerelmaa, T. (2021). Characteristics of Lake Sediment from Southwestern Mongolia and Comparison with Meteorological Data. Geosciences, 12(1), 7.

[23] Uddin, M. K. (2017). A review on the adsorption of heavy metals by clay minerals, with special focus on the past decade. Chemical Engineering Journal, 308, 438-462.

[24] Johnson, D. A., Sheehy, D. P., Miller, D., & Damiran, D. (2006). Mongolian rangelands in transition. Science et changements planétaires/Sécheresse, 17(1), 133-141.

[25] Sekine, Y., Kitajima, T., Fukushi, K., Gankhurel, B., Tsetsgee, S., Davaasuren, D., ... & Hasebe, N. (2020). Hydrogeochemical study on closed-basin lakes in cold and semi-arid climates of the valley of the Gobi lakes, Mongolia: Implications for hydrology and water chemistry of paleolakes on Mars. Minerals, 10(9), 792.

[26] Smedley, P. L., & Kinniburgh, D. G. (2001). Source and behavior of arsenic in natural waters. United Nations synthesis report on arsenic in drinking water. World Health Organization, Geneva, Switzerland. http://www. who. int/water_sanitation_health/dwq/arsenicun1. pdf, 1-61.

[27] Solongo, T.; Fukushi, K.; Altansukh, O.; Takahashi, Y.; Akehi, A.; Baasansuren, G.; Ariuntungalag, Y.; Enkhjin, O.; Davaajargal, B.; Davaadorj, D.; Hasebe, N. Distribution and Chemical Speciation of Molybdenum in River and Pond Sediments Affected by Mining Activity in Erdenet City, Mongolia. Minerals 2018, 8 (7), 288−304.

[28] Tessier, A.; Campbell, P. G. C.; Bisson, M. Sequential Extraction Procedure for the Speciation of Particulate Trace Metals. Anal. Chem. 1979, 51 (7), 844−851.

[29] Yanase, N.; Nightingale, T.; Payne, T.; Duerden, P. Uranium Distribution in Mineral Phases of Rock by Sequential Extraction Procedure. Radiochim. Acta 1991, 52−53 (2), 387−394.

Techno-Science Research Journal 12 (Special Issue) 86-92

Content list available at ITC

Techno-Science Research Journal

Journal Homepage: www.ric.itc.edu.kh

Techno-Science Research Journal

Paleotsunami Study at Cikembulan River, Pangandaran Area, West Java, Indonesia

Sreypich Run[1,2], Noriko Hasebe[2], Ridwan Januar[2], Ogawa Rinta[2], Muoy Yi Heng[1], Sokvireak Say[1]

[1]*Faculty of Geo-resources and Geotechnical Engineering, Institute of Technology of Cambodia, Russian Federation Blvd., P.O. Box 86, Phnom Penh, Cambodia*

[2]*School of Geosciences and Civil Engineering, College of Science and Engineering, Kanazawa University, Kakumamachi, Kanazawa, Ishikawa 920-1192, Japan*

Received: 21 August 2023; Accepted: 15 May 2024; Available online: August 2024

Abstract: *Indonesia is among the world's most earthquake-prone countries, with some resulting in catastrophic tsunamis. The earthquake that triggered the 2006 Pangandaran tsunami, resulting in the loss of many lives, had a magnitude of 6.1 and was accompanied by unusually high tsunami waves. This incident serves as a reminder to geoscientists that there is still much to learn about the features of tsunamis along Java's southern coast, which is also consistent with the scarcity of historical data on tsunami incidents in this region. The Cikembulan River in the Pangandaran Area was chosen to be the study area for this research instead of Pangandaran Beach, even though the beach was the most severe area whenever the tsunami happened, because it preserved tsunami sand deposits from the 2006 event better than any other area. In accordance with research conducted in 2010 by Amijaya, West Pangandaran Beach has morphologically flat topography, which caused the tsunami wave to move easily onshore and reach the Cikembulan River. It has also been recognized by previous paleotsunami investigators for its visible layers in the stratigraphy of the river. Hence, the Cikembulan River is essential for the study of paleotsunamis in West Java, Indonesia. This research primary objective is to identify layers that can be confirmed as tsunami deposits within the sequence and to comprehend the sedimentary systems and environmental shifts in the area. Utilizing grain-size analysis (Laser Particle Size Analyzer SALD-2200) and Biogenic Silica Analysis, this study investigates the characteristics of this sequence to offer a comprehensive understanding of the events related to the tsunami in this region. The CT scan and graph data from the core sample indicate that there are three tsunami deposit layers and one storm deposit layer dating back to the 16th century. Soil characteristics in the area indicate a shift towards a brackish environment as a result of the numerous natural disasters that have taken place in the region.*

Keywords: paleotsunami; cikembulan river; biogenic silica analysis; grain size analysis

1. INTRODUCTION

Tsunamis occur either before there is historical documentation or for which there are no documented observations. Paleotsunami study is essentially centered on the identification, mapping, and dating of tsunami deposits discovered in coastal locations, as well as their association with related strata discovered elsewhere locally, regionally, or across ocean basins. As research in this field continues, it may provide important new data on past tsunamis to aid in assessing the threat of future tsunamis. In addition, studying earthquakes is crucial when investigating tsunamis since they typically occur following an earthquake on the ocean floor.

Paleotsunami deposits offer vital hints for reconstructing earlier earthquake and tsunami-related sea intrusions [32]. Typically, the geological, sedimentological, and geochemical properties of tsunami deposits are used to identify them. According to Dawson et al., [6], descriptions of tsunami deposits demonstrate a vast variation of tsunami deposits. This covers changes in particle size composition, distribution pattern, and sedimentary facies. Since tsunamis promptly destroy coastal regions, resulting in the death of property and the lives of people as well as harm to ecosystems, they have received a great deal of

* Corresponding author: Sreypich Run
E-mail: sreypichrun@gmail.com; Tel: +855-12-622-304

social and scientific attention [29]. The different phases of uprush during coastal flooding and backwash when the tsunami water recedes are characteristics of tsunamis [27]. According to Minoura and Nakaya [20], tsunami deposits in sediments may preserve evidence of a tsunami invasion. It might be challenging to distinguish tsunami deposits from deposits left behind by other processes, such as storms. Insufficient observations of contemporary tsunamis and their deposits contribute to the problem. Despite significant advances over the past ten years, the published material is still insufficient to identify the diagnostic characteristics of tsunami deposits [3, 10, 22, 23, 27].

Indonesia is a country situated between the Indian and Pacific oceans off the coast of Southeast Asia. in the region, spanning up to 5,100 km from east to west and 1,800 km from north to south. Unfortunately, the country is prone to natural disasters such as floods, severe droughts, tsunamis, earthquakes, volcanic eruptions, and forest fires. Indonesia rests on the Pacific Ring of Fire's volatile fault lines, regularly experiencing seismic activity, volcanic eruptions, and earthquakes. Furthermore, Java, an island in Indonesia, serves as the home of more than half of the country's population. The fourth largest island in Indonesia, Java is located in the southeast of Sumatra and has a total size of 127,570 sq km including the offshore islands.

Figure 1. Location of the study area

Indonesia experienced tsunamis between 2004 and 2020, which took hundreds to thousands of lives. Numerous people died in the Pangandaran region in 2006 due to a tsunami that was triggered by an earthquake with a tsunami magnitude of 6.1 but a low frequency earthquake. The lack of historical data on tsunami events in this region corresponds with this incidence serving as a warning to geoscientists that much remains to be learned about the characteristics of tsunamis along Java's southern coast. This information gap can be filled by the paleo-tsunami research, which investigated historical tsunami events using a scientific methodology. These information and data can help the scientist to calculate the date of the tsunami events throughout history and to expect the next tsunami that might happen in the future. These lead to some questions that needed to discuss in this research.

- How many tsunami deposits are there?
- What is the sedimentary system/environment around the area?

Since the purpose of this research is to focus on the paleotsunami study, two objectives have been proposed:

- Confirming some layers as tsunami deposits among candidates in the sequence.
- Understanding of sedimentary systems and environmental changes

Tsunamis have occurred frequently in the area, prompting the investigation of sedimentary layers to differentiate between those from old and recent events. The identification of terrestrial versus seawater layers is crucial, hence two methods are utilized in this research. A sediment's grain size can be determined using a particle size analyzer, while the biogenic silica content in a soil sample may be determined using biogenic silica analysis.

Figure 2. Rip-up clasts of sediment showing the visible tsunami layers (A. rip-up clasts of sediment throughout layers of soil, B. visible dark tsunami layers)

2. METHODOLOGY

2.1 Grain Size Analysis

In the field of earth sciences, laser diffraction is commonly employed for particle size analysis. When properly executed, this approach can yield significant amounts of grain size data with high levels of precision and accuracy [4]. Earlier research indicates that laser diffraction provides a precise method for studying and comparing sediment, soil, and similar material samples, given that proper sample preparation and handling protocols are followed [4]. In this study, the SALD-2200 Laser Diffraction Particle Size Analyzer was used to perform the grain size analysis. Laser diffraction particle size analyzers are utilized to determine particle sizes in a material. Particle size is determined by measuring the angle of light that is scattered by the particles when they pass through a laser beam.

2.2 Biogenic Silica Analysis

A chemical estimation of the quantity of siliceous microfossils is provided by the measurement of the biogenic silica (BSi) content of sediments. Sediments are briefly leached with a weak base, often Na2CO3, for a period of time (generally 2 to 5 hours), and aliquots are gradually removed. In paleolimnology, siliceous microfossils, particularly diatoms, are frequently employed as proxies for research on regional hydrologic and climatic change, eutrophication, and acidification of surface waters [28]. Sediment amorphous silica concentration is measured by the chemically determined proxy known as "biogenic silica" (BSi). Biogenic silica analysis is used to identify biogenic silica content in soil samples from the Cikembulan River. Biogenic silica analysis is a really important method since it is one of the most important components in marine sediments.

3. RESULTS AND DISCUSSION

The result below showing the core sample pictures from CT scan, sediment grain size (mm), mineral grain size (mm), and biogenic silica content (%) from the wet and dried soil sample collected from Cikembulan River, Pangandaran area, West Java, Indonesia. Before collecting the soil sample in the study area, the geological investigation data also collected around the area in order to confirm the study area. This area was selected as the sample collection area since it preserves the better tsunami deposits than any other area in Pangandaran region [1] because of the morphologically flat topography of the Pangandaran beach.

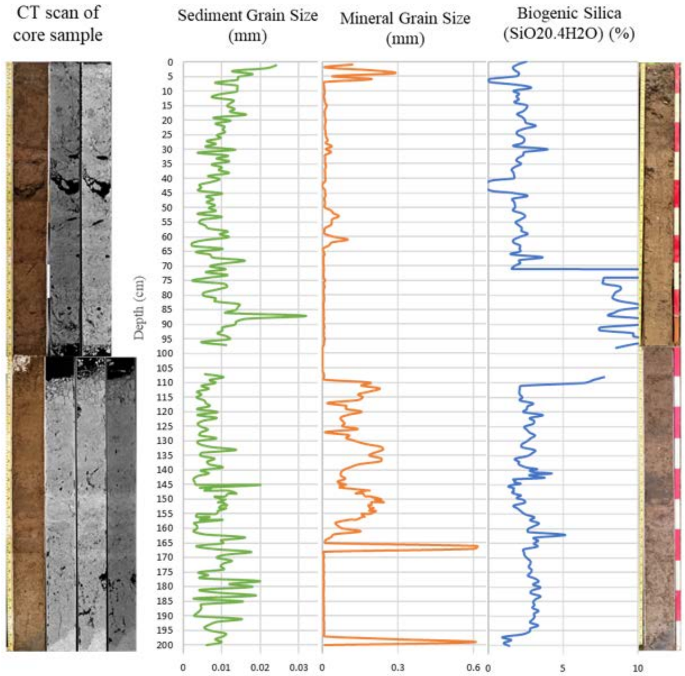

Table 1. Result from sediment grain size, mineral grain size, and biogenic silica (soil sample in the middle was damaged around 10cm while transported)

3.1 Results

3.1.1 Sediment Grain Size

The first 10cm from the surface is a fine to medium silt range from 0.008-0.025mm then fluctuates from clay to medium silt between 60-80cm (0.002-0.015mm). The changes started from 80cm and created a peak at 87cm between 0.002-0.03mm which is the coarsest layer among the candidate layers. The complicated layer of soil from 140-200cm varies from clay to medium silt (0.002-0.02mm). The result of the sediment grain size is very complicated ranging from mud-clay to silty-sand resulting from the force of waves from the tsunami and storm which happened in the area before. The comparison of CT scan pictures and sediment grain size shows visible layers that are fine grain and coarse grain. Meanwhile, the core samples pictures show the dark visible layers of soil that are abundant in organic matter.

3.1.2 Mineral Grain Size

The first 6cm from the surface shows the coarse grain of fine silt to medium sand (0.008-0.28mm) before staying stable and increasing steadily from fine silt to coarse sand (0.009-0.1mm) in 50-65cm. The graph increases again and starts to fluctuate with a complex layer of mixed soil from very fine silt to fine sand (0.006-0.24mm) in 110-168cm before peaking at the depth of 166 and 199cm in pebble size (0.6mm).

3.1.3 Biogenic Silica

The percentage of biogenic silica content seems to be normal with an average of 2%. It starts to have a peak at 71cm depth for more than 10% and fluctuated until 100cm depth before it drops dramatically to around 2% again. The percentage rises to 4% at 135cm then falls again and starts to rise until 5% at 165cm.

3.2 Discussion

3.2.1 Grain Size Analysis

There are 3 rip-up clasts as shown in the first picture of Figure 2 (around 20cm, 90cm, and 140cm depth) which are considered as the tsunami deposit candidate from the comparison of sediment grain size results and the core sample picture. Because of its flat topography and easy movement of tsunami waves, West Pangandaran Beach's morphology, the wave's height at Cikembulan River was about 3 meters [1]. Only 10 cm deep, the new tsunami layer is surrounded by older, darker-colored beach silt from an erosional surface (Figure 2; right picture). According to research conducted in 2015 by Amijaya et al. [1], the average grain size of a tsunami deposit in Cikembulan River ranges from medium to fine sand but it now ranges from clay to the size of pebble which show the depositional changes over time through the waterflow. Eroded soil was fragmented both during and after the erosion, and it was occasionally carried as rip-up clasts (Figure 2). These rip-up clasts, which were formed by the erosion of pre-tsunami soil during the run-up phase of the tsunami, were moved landward from their initial site [8, 31]

A tsunami deposit's depositional environment can be affected by adding sediment to the deposit or by changing the flow parameters. A recent study by Peters and Jaffe [24] found that sorting during transportation and deposition can cause a difference in grain size between the tsunami deposit and underlying sediments, often presenting as either coarser sand or a heavy mineral remaining at the base of the tsunami deposit. Sorting during transportation and deposition can cause a difference in grain size between the tsunami deposit and the underlying sediments, which often presents as either coarser sand or a heavy mineral delay at the base of the tsunami deposit. Mud frequently overlays the tsunami deposits in coastal marsh and lagoonal deposits [15, 16]. In the coastal marsh, lagoon, or tidal channel environments, mud is a frequent component of tsunami deposits, and crucial traits for identifying tsunami deposits, including mud rip-up clasts and mud caps, require a source for mud. Identification of tsunami deposits is made easier by the differences between the underlying mud and the sand that has been deposited by a tsunami above it. The tsunami deposit may be characterized by erosion contacts over the muddy soil or it may directly overlie a vegetative surface. Tsunami deposits can differ from fluvial sediments in terms of grain size, sedimentary structures, and chemical reactions where they overflow stream basins [17].

3.2.2 Biogenic Silica

The percentage of biogenic silica has a correlation with the sediment grain size. Even though it is not the same as the result from mineral grain size and the other two graphs of data, we can still say that 71-97cm of depth is the tsunami deposit that happened from the 19th century tsunami from the data that showing a huge amount of biogenic silica content in the soil sample. From 110-168cm depth, it should be the tsunami deposit from the 16th century tsunami which cover by paleosoil on top. Even silty muds with large concentrations of biogenic silica and calcareous nannoplankton, which provide little in the way of cohesion, have a significant potential for liquefaction.

4. CONCLUSIONS

As the result shown in the discussion, we can conclude that there are 3 layers of tsunami deposits. The date of the tsunami defines by the tsunami events happened in the past with records and the other research article that toke place in the Pangandaran area. All of these following soil layers will confirm by using the other research method.

- From the 16th century tsunami (138-168cm depth) which was covered by the paleosoil on the top layer (110-138cm depth). This soil layer is a complicated layer which consist of many types of soil from 140-200cm variety from clay to medium silt (0.002-0.02mm).
- From the 19th century tsunami starts from 71-95cm in the depth range from clay to medium silt (0.002-0.03mm) with a peak at 87cm depth which is the coarsest sediment layer among the candidate layers.
- From the 2006 tsunami starts at the first 6cm from the surface with a variety of soil from fine to medium silt range (0.008-0.025mm) then fluctuate from clay to medium silt between 60-80cm (0.002-0.015mm).

Even though there are 4 candidates of tsunami deposits, one of the candidates is from the storm deposit that creates the rip-up clast and erodes the sediment influencing the rise of carbonate, sediment, and mineral grain size in the core sample (almost 15cm depth) (Figure 2). Moreover, sediment grain size, organic matter, carbonate content, and biogenic silica content give more information to confirm the tsunami layers and differentiate the deposits apart from the terrestrial environment (Table 1). Since the waterflow of the river possibly flow in and out of the lagoon nearby, the environment around the study area is more like an estuary which is brackish water (a mixture of salinity and freshwater).

Criteria	Tsunami	Depth (cm)	Storm	Depth (cm)	References
Sedimentological	Basal erosion contact	-	Basal erosion contact	-	[18]
	One or more fining upward sequences, heterogenous sometimes homogeneous	0-8 70-82	Fining upward or homogeneous	55-60	
	Intraclasts from the underlying material	150-168	Not found	-	
	Sedimentary structures are very rarely found	-	Sediment structures are more common	-	
	Eroded clasts	80-95	Less erosional	-	[30]
	Wide range of materials from terrestrial to marine	-	Nearby sediment	-	
	Poorly sorted (particle size range from mud to coarse silt)	75-83	Relatively better sorted (particle size range from fine silt to medium silt)	-	
	Often chaotic beds sometimes graded, normally or reverse graded bed	130-170	Laminae with foreset or tabular bedding	-	
	Bi-directional imbrication	-	Unidirectional imbrication	-	[18, 30]

	Rare rip-up clasts	80-90	Rip-up clast	50-60	[5, 6, 11, 14]
Palaeontolo-gical	Marine fossils	-	Marine fossils	-	[9, 12, 13, 18, 30]
	Shells and debris are found	-	Shells and debris are found	-	[2, 5, 19, 21, 26]
	Increased diversity (mixture of marine and brackish fossils)	-	A mixture of marine and freshwater fossils	-	[18]

Table 2. Summary of the data result distinguish between tsunami and storm deposits

ACKNOWLEDGMENTS

I would like to thank JASSO and Kanazawa University for giving me a chance to do an exchange program in Japan and supporting me during my stay while also helping me with my research.

In addition, I would like to thank Prof. HASEBE Noriko, Mr. JANUAR Ridwan, Mr. SHUUKHAAZ Ganbat, and Mr. OGAWA Rinta for their help and guidance during my research. I am wholeheartedly appreciative of their sincerity and kindness. I would not get to do the sample preparation properly if there is no extra help and guidance from them.

Last but not least, I would like to thank my advisor, Mr. SAY Sokvireak, and my co-advisor Ms. HENG Muoy Yi, for their guidance, and explanation.

REFERENCES

[1] Amijaya, H., Ngisomuddin, N., & Akmaluddin, A. (2015). CHARACTERIZATION OF JULY 17, 2006 TSUNAMIITE AT SOUTH COAST OF WEST JAVA. Journal of Applied Geology. https://doi.org/10.22146/jag.7232

[2] Atwater, B. F., Nelson, A. R., Clague, J. J., Carver, G. A., Yamaguchi, D. K., Bobrowsky, P. T., Bourgeois, J., Darienzo, M.E., Grant, W.C., Hemphill-Haley, E., Kelsey, H.M., Jacoby, G.C., Nishenko, A.P., Palmer, S.P., Peterson, C.D., & Reinhart, M. A. (1995). Summary of coastal geologic evidence for past great earthquakes at the Cascadia subduction zone. Earthquake spectra, 11(1), 1-18.

[3] Benson, B. E., Grimm, K. A., & Clague, J. J. (1997). Tsunami deposits beneath tidal marshes on northwestern Vancouver Island, British Columbia. Quaternary Research, 48(2), 192-204.

[4] Blott, S. J., & Pye, K. (2006). Particle size distribution analysis of sand-sized particles by laser diffraction: an experimental investigation of instrument sensitivity and the effects of particle shape. Sedimentology, 53(3), 671–685. https://doi.org/10.1111/j.1365-3091.2006.00786.x

[5] Clague, J. J., Bobrowsky, P. T., & Hutchinson, I. (2000). A review of geological records of large tsunamis at Vancouver Island, British Columbia, and implications for hazard. Quaternary Science Reviews, 19(9), 849-863.

[6] Dawson, A. G., Long, D., & Smith, D. E. (1988). The Storegga slides: evidence from eastern Scotland for a possible tsunami. Marine geology, 82(3-4), 271-276.

[7] Faiqoh, I., Gaol, J. L., & Ling, M. M. (2014, April 11). VULNERABILITY LEVEL MAP OF TSUNAMI DISASTER IN PANGANDARAN BEACH, WEST JAVA. International Journal of Remote Sensing and Earth Sciences (IJReSES), 10(2). https://doi.org/10.30536/j.ijreses.2013.v10.a1848

[8] Fujiwara, O., & Tanigawa, K. (2014). Bedforms record the flow conditions of the 2011 Tohoku-Oki tsunami on the Sendai Plain, northeast Japan. Marine Geology, 358, 79-88.

[9] Fullagar, R., Head, L., Bryant, E. A., & Beaman, S. (1999). Tsunami disturbance on coastal middens: McCauleys Beach. New South Wales, In J. Hall & I. McNiven (Eds.), Australian coastal archaeology, 235-238.

[10] Gelfenbaum, G., & Jaffe, B. (2003). Erosion and sedimentation from the 17 July, 1998 Papua New Guinea tsunami. Pure and Applied Geophysics, 160(10), 1969-1999.

[11] Goff, J. R., & Chagué-Goff, C. (1999). A late Holocene record of environmental changes from coastal wetlands: Abel Tasman National Park, New Zealand. Quaternary International, 56(1), 39-51.

[12] Goff, J. R., & McFadgen, B. G. (2001). Catastrophic seismic-related events and their impact on prehistoric human occupation, coastal New Zealand. Antiquity, 75(287), 155-162.

[13] Goff, J. R., & McFadgen, B. G. (2001). Nationwide tsunami during prehistoric Maori occupation, New Zealand. In Proceedings of International Tsunami Symposium (pp. 469-476).

[14] Goff, J. R., Crozier, M., Sutherland, V., Cochran, U., & Shane, P. (1999). Possible tsunami deposits from the 1855 earthquake, North Island, New Zealand. Geological Society, London, Special Publications, 146(1), 353-374.

[15] Higman, B., & Bourgeois, J. (2021). Deposits of the 1992 Nicaragua tsunami. In Tsunamiites (pp. 85-107). Elsevier.

[16] Jackson, K. L. (2008). Paleotsunami history recorded in Holocene coastal lagoon sediments, southeastern Sri Lanka (Doctoral dissertation, University of Miami).

[17] Jaffe, B., Gelfenbaum, G., Rubin, D., Peters, R., Anima, R., Swensson, M., ... & Riega, P. C. (2003). Identification and interpretation of tsunami deposits from the June 23, 2001 Peru tsunami. In Proceedings of the international conference on coastal sediments (p. 13).

[18] Kortekaas, S. (2002). Tsunamis, storms and earthquakes: distinguishing coastal flooding events (Doctoral dissertation, Coventry University).

[19] Liu, K. B., & Fearn, M. L. (2000). Reconstruction of prehistoric landfall frequencies of catastrophic hurricanes in northwestern Florida from lake sediment records. Quaternary Research, 54(2), 238-245.

[20] Minoura, K., & Nakaya, S. (1991). Traces of tsunami preserved in inter-tidal lacustrine and marsh deposits: some examples from northeast Japan. The Journal of Geology, 99(2), 265-287.

[21] Minoura, K., Imamura, F., Takahashi, T., & Shuto, N. (1997). Sequence of sedimentation processes caused by the 1992 Flores tsunami: evidence from Babi Island. Geology, 25(6), 523-526.

[22] Nanayama, F., Shigeno, K., Satake, K., Shimokawa, K., Koitabashi, S., Miyasaka, S., & Ishii, M. (2000). Sedimentary differences between the 1993 Hokkaido-nansei-oki tsunami and the 1959 Miyakojima typhoon at Taisei, southwestern Hokkaido, northern Japan. Sedimentary Geology, 135(1-4), 255-264.

[23] Nishimura, Y., & Miyaji, N. (1995). Tsunami deposits from the 1993 southwest Hokkaido earthquake and the 1640 Hokkaido Komagatake eruption, northern Japan. In Tsunamis: 1992–1994 (pp. 719-733). Birkhäuser Basel.

[24] Peters, R., & Jaffe, B. (2010). Identification of tsunami deposits in the geologic record; developing criteria using recent tsunami deposits. US Geological Survey Open-File Report, 1239(2010), 39.

[25] Semeniuk, V. (1996). Coastal forms and Quaternary processes along the arid Pilbara coast of northwestern Australia. Palaeogeography, Palaeoclimatology, Palaeoecology, 123(1-4), 49-84.

[26] Shi, S., Dawson, A. G., & Smith, D. E. (1995). Coastal sedimentation associated with the December 12th, 1992 tsunami in Flores, Indonesia. In Tsunamis: 1992–1994 (pp. 525-536). Birkhäuser Basel.

[27] Slootman, A., Simpson, G., Castelltort, S., & de Boer, P. L. (2018). Geological record of marine tsunami backwash: The role of the hydraulic jump. The Depositional Record, 4(1), 59-77.

[28] Smol, J. P., & Stoermer, E. F. (Eds.). (1999). The diatoms: applications for the environmental and earth sciences. Cambridge University Press.

[29] Sugawara, D., Minoura, K., & Imamura, F. (2008). Tsunamis and tsunami sedimentology. In Tsunamiites (pp. 9-49). Elsevier.

[30] Switzer, A. D. (2005). Depositional characteristics of recent and late Holocene overwash sandsheets in coastal embayments from southeast Australia.

[31] Tappin, D. R., Evans, H. M., Jordan, C. J., Richmond, B., Sugawara, D., & Goto, K. (2012). Coastal changes in the Sendai area from the impact of the 2011 Tōhoku-Oki tsunami: Interpretations of time series satellite images, helicopter-borne video footage, and field observations. Sedimentary Geology, 282, 151-174.

[32] Watanabe, T., Kagami, S., & Niwa, M. (2021). Geochemical and heavy mineral signatures of marine incursions by a paleotsunami on the Miyazaki plain along the Nankai–Suruga trough, the Pacific coast of southwest Japan. Marine Geology, 444, 106704. https://doi.org/10.1016/j.margeo.2021.106704

Techno-Science Research Journal 12 (Special Issue) 93-97

Content list available at ITC

Techno-Science Research Journal

Journal Homepage: www.ric.itc.edu.kh

Techno-Science Research Journal

The contamination of surface soil in Myanmar: A brief review

Mang Sial Thang[1], Hnin Wutyi Phoo[2], Kyu Kyu Tin[3], and Wirach Taweepreda[4]*

[1,2]*Chemistry, Department of Chemistry, University of Yangon, Yangon, Kamayut Township 11041, MYANMAR*
[3]*Environmental Management, Faculty of Environmental Management, Prince of Songkla University, Hat-Yai, Songkhla 90110, THAILAND*
[4]*Polymer Science Program, Division of Physical Science, Faculty of Science, Prince of Songkla University, Hat-Yai, Songkhla 90110, THAILAND*

Received: 22 August 2023; Accepted: 15 May 2024; Available online: August 2024

Abstract: *Currently, environmental challenges pose urgent and significant problems worldwide. In response, Myanmar, the largest mainland Southeast Asian country, is taking steps to improve measures to combat pollution. It is worth noting that soil contamination has a detrimental impact on both the environment and human health worldwide. Anthropogenic activities such as agriculture, mining, and industry can cause soil pollution. Remediation of contaminated soil is necessary to meet acceptable international standards. A healthy soil ecosystem can improve ecosystem services and biological productivity due to beneficial components in the soil. This literature review presents findings on the prevalence of contaminated soil areas in Myanmar and highlights research conducted by local scientists. It also acknowledges the promising potential of bioremediation processes in mitigating soil contamination. The review suggests that Myanmar faces significant environmental challenges due to human-induced soil pollution and must prioritize remediation efforts.*

Keywords: soil contamination; Myanmar; heavy metals; bacteria; healthy soil.

1. INTRODUCTION

As a Southeast Asian country, Myanmar is well-known for its natural beauty and unexplored cultural and natural heritage, making it one of the top tourist destinations in Asia [15].Myanmar's climate is significantly influenced by its geographic location within the monsoon region of Asia. In the lowland regions of Myanmar, alluvial soil consisting of clay and silt is common, resulting in the depletion of organic matter and nutrients. However, fertilizers can enhance the productivity of these soils. Conversely, Myanmar's highland regions are characterized by iron-rich reddish-brown soils that are dark red and leached but prone to rapid erosion during heavy rainfall. Red-brown soils rich in magnesium and calcium are observed in the dry central region. If the soil has low clay content, it becomes saline due to high evaporation, which can appear as brown or yellow in color. [1].

2. Soil Pollution

2.1 Overview of Soil Contamination

Soil contamination is defined as the occurrence of contaminants in soil that cause deterioration of one or more soil functions beyond a certain level. This can be categorized as point pollution, particularly from ex-industrial sites, or diffuse pollution from agricultural use of pesticides, herbicides, or heavy metals. Diffuse pollution acts as a sink due to low levels of contaminants distribute and lodge in the soil that hard to track and analyze, on the other hands, point pollution happen at a particular place, understood and well mapped[11]. The greatest threats of soil contamination come from unsustainable human activities, including deforestation, overuse of pesticides and fertilizers, littering, and industrial waste disposal [10]. Soil contaminants can be absorbed by humans through ingestion of soil, inhalation of dust and volatiles, dermal absorption of dust and volatiles, and consumption of contaminated food. Soil pollution can have long-term impacts on our health, potentially causing diseases. However, the lack of adequate indicators for soil pollution results in complex health outcomes [12].

2.2 Myanmar's Soil Contamination

* Corresponding author: Wirach Taweepreda
E-mail: wirach.t@psu.ac.th; Tel: 0-7428-8007

Myanmar is a geologically diverse country with abundant mineral resources, including gemstones, zinc, jade, tin, copper, tungsten, silver, and gold. Despite the potential of gold mining, which is a pillar of the industry, it has been struggling due to poor exploration efforts[23]. The gold mining industries especially Sagaing region, Kachin region in Myanmar, display an crucial sector in economy of Myanmar and its people. Copper and gold mineralization is widely noted and related with sulfide minerals in Mandalay region, Myanmar. There is estimated to be around 186,700 tons of gold still in the ground. To extract gold, people can use two main methods: finding it in the rivers (placer mining) and rocks (hard rock mining). People pan for gold in river or use machines to dig it up from rocks. In some places, they use a chemical called cyanide to help get gold our of rocks. They mix it with ground-up rock, and then they can separate the gold from the rest. They also use activated carbon to help. Gold panning is a simple way to find gold, but it is not good for getting lots of gold out. Gold mining is important for a country's economy, but it needs a lot of money to start[6]. Gold mining sites in Myanmar have high levels of heavy metals such as cadmium, arsenic, lead, and mercury in the soil, and failure to properly remediate the soil results in adverse health effects for the miners[15]. In the amalgamation stage, the maximum heavy metal concentration were 210.000mg.kg $^{-1}$ for Pb, 77.440 mg.kg-1 for Hg,22.170 mg.kg -1 for As,3.070mg.kg-1 for Cd[3]. Mercury(Hg) will release the geosphere,atmosphere and hydrosphere that source from Artisanal and small scale gold mining (ASGM) industries including Thailand, Laos, Malaysia, Myanmar, Cambodia, Indonesia,and the Philippines. Around ASGM area in Mandalay region, Myanmar, 16% of miners suffered from Hg poisoning. During soil ore processing, panning stages (gold-amalgamation stage), and sluicing were 0.68,4.86,0.51 μg/g respectively. A small scale gold mining township in Pyin Oo Lwin District in Mandalay reigion, 0.33–6.51 ug/g and 0.02 ug/g of Hg reported [21]. United States Environmental Protection Agency (US EPA) generic soil guidelines value (0–0.2 μg/g) but the Philippines, Myanmar and Thailand descried the higher Hg levels.Clear cutting surface soil erosion, water pollution, soil, air and noise griners, whatever channels face sedimentation cases due to open-pit mining underground mining (inlones) and amalgam and cyanide happened the nearest river water and streams are becoming extensively polluted. The natural environmental occurrence of heavy metal and arsenic accumulation is due to the oxidation, weathering, and erosion of sulfide minerals. According to the CEIC database report, Myanmar produced 1692 kg of gold in 2015 and 1700 kg in 2016 [5]. In Myanmar, there are still struggling to study the impacts of gold mining. Systematic operation of gold mining intent to decrease the risk of the environmental impacts and economically sustainable mining activities for the long- term improvement of the sector. For the greenification of Myanmar's mining industry, it is crucial to implement continuous monitoring, efficient protocols, and life cycle assessment (LCA). The use of fertilizers to cultivate vegetables and plants has resulted in heavy metal contamination and environmental pollution, with the consumption of such crops leading to health risks[6-9]. The products from Ngazun Township, Mandalay Division are used for soil heavy metal analysis, and according to the Geoaccumulation Index (Igeo) evaluation, the levels of heavy metals (Pb, Cr, As, Cu, Co) are below zero, which indicates a safe level for agricultural activities in this area. Nevertheless, a field survey conducted in the melon-cultivated areas of Myitthar, Kyaukse, and Tada U Township in Mandalay Division of Myanmar revealed soil degradation caused by improper use of pesticides and their residues. Undoubtedly, Many pesticides residues of above study area described as unauthorised pesticides because farmers would like to reduce cost without noticing harmful for them, to meet or solve ever enhancing requirement of food and other agricultural commodities for the rapid increasement of world population. Actually, registered pesticides can beat higher deleterious effect on soil fertility and environment[22]. Heavy meatals Cd, Pb, Zn, Cu and Fe in soil is higher than in rice sample in Min Ywa, Nyaung Bin Zauk, and Inn Gone due to the capability to migrate heavy metals from soil to plants[4].Under a humid subtropical climate,Two sites from apple and tea growing site from Nine Mile village and pyay village, was followed and mentioned both soils deprivate potassium but tea growing soil need potassium and phosphorous content. Both soils of heavy metals content was detected the order: : Fe (iron) > Cu (copper) >Zn (zinc) > Pb (lead) > Cr (chromium) that was lower than maximum allowed concentration(MAC), afterwards, Fe, Al and Si for apple and tea was favourable, In addition toxic element As, Ag, Hg should be neglected. Potentially toxic element levels should be monitored if it is necessary to apply pesticides and fertilizers in order to recover pollutants of apple and tea plantation in Myanmar[8].The vicinity of soil samples of Mandalay Industrial Zone II,the rice grown on the soil and soils described iron, copper,zinc, cadmium and lead in soil and then transferring soil to rice 0.371-0.658 for zinc, 0.001-0.004 for iron, 0.282-0.577 for copper, fortunately, lead and cadmium are lower than detectable permission[18].

Burkholderia pseudomallei has been found in soil in Myanmar, marking the first instance of environmental research of the states and regions of the country. The research shows that Burkholderia pseudomallei is significantly distributed in central parts of Myanmar, particularly in rice fields of agricultural land. These observations should encourage clinicians in Myanmar to consider melioidosis as a priority, especially for patients who regularly handle soil or have underlying risk factors such as diabetes. Improving the timeliness and accuracy of melioidosis diagnosis and treatment is critical to saving lives[17].The range of protozoa, bacteria, viruses and helminths in soil in Yangon, Myanmar, are detected to follow environmental pathogen loads. It describes viral gene counts correlates with the sanitation facilities between 50 m of the collection point (RR = 0.96, 95% CI 0.93, 0.99) compared with bacterial pathogen gene counts relates with drainage ditches and elevation (RR = 1.70, 95% CI 1.18, 2.45, RR = 0.96, 95% CI 0.93, 0.99 respectively) and vital contamination can enhance because of presence of a latrine within 50m of the sample collection.Following life cycle assessment of 8 cement plants in Myanmar, it was observed that 68% reduction in climate change, 83% reduction in acidification, 96% reduction in eutrophication if fuel shifting from the coal dominating mix to 100% natural gas especially 89% of the total climate change came from the calcination stage, therefore, current cement manufacturing in Myanmar, must seek to change to a green economy sector.In addition, there is welcome for research about impacts and potential of other options for thermal energy including municipal solid waste, bimass) and altermative raw constitutes to decrease the clinker ration in cement manufacturation, afterwards, economic feasibility of enhanced natural gas apply for cement production[20].

2.3 *Garbage Pollution and Management in Myanmar*

Garbage pollution is caused by improper disposal and management of waste. It can include littering, inadequate waste collection and disposal systems, open dumping, and insufficient recycling. Garbage pollution can adversely affect the environment, public health, and residents' quality of life. In order to manage it effectively, we can take certain measures. Encourage recycling in our community and follow proper recycling guidelines. Additionally, non-recyclable waste can be converted into energy through processes such as gasification, reducing landfill use and generating power. Another important aspect is to raise awareness about the significance of responsible waste management, including promoting appropriate disposal methods. Lastly, it is crucial to support government policies that promote waste reduction, recycling, and responsible disposal.Many regions have regulations in place to manage waste. The most important effective waste management is to combine of individual efforts, community engagement, government support, and technological advancements.Nowadays, along with growing population, increasing per capita waste generation and improper waste collection and treatment system, solid waste management in developing countries has a great impact on environment and public health. Myanmar is a developing country in Asia. Municipal solid waste generation rate in Myanmar amounted to 5,616 tons per day in 2012, trending around 21,012 tons per day in 2025. Open dumping is a major waste disposal method and recycling is at an early development stage. Currently, the most immediate economic and environmental issues related to the wastes have accelerated the need for a sustainable approach to waste management in major cities of Myanmar. Approximately 55% of the country’s total waste is produced from the country’s three major cities. Those cities are Yangon (1,981 tons/day), Nay Pyi Taw (955 tons/day), and Mandalay (160 tons/day). In Myanmar’s municipal waste proportion are households (60%), markets (15%), commercial producers (10%), hotels (2%), gardens (5%) and others (8%). For organic materials waste, (77%) while the remainder comprises plastic (13%), paper (7%), and others (3%). In 2015, Yangon Municipality employed 4220 workers for waste collection and disposal. Waste collection and disposal is the first priority of the municipality, and reuse (i.e., recycling) is also an important aspect[3-5]. In Myanmar, recycling activities are carried out as small-scales industries in many cities, which includes scavengers, waste collectors, and waste dealers. Recyclable materials such as newspaper, plastic bottles, metal, tin and glass are collected from households, communal depots, streets, commercial areas and final disposal sites and in turn sell them to waste dealers by these scavengers and waste collectors. The waste is cleaned, sorted, and stored by waste dealers and then sold by traders to both domestic and foreign recycling industries.The exact volume of recycling, ratios, and number of recycling factories in Myanmar are currently difficult to determine. However, a sample survey carried out in Yangon City about 86 tonnes of recyclable materials are being sold everyday. In addition, they received as a direct revenues from the collection of user charges for waste management services. Waste collection charges are based on the amount of waste and the location to disposed for household or domestic waste. The fee ranges from 300-900 kyats/month by Yangon City Development Committee (YCDC). Other wastes are charged based on the amount of waste with the rate for one vehicle (3 tons’ capacity) approximately 35,000 kyats per trip. For commercial waste, the special disposal fee will be between ranging from 20,000 to 150,000 kyats per month depending on the amount of waste produced. This cost recovery policy helped the city to reduce waste disposal in many ways and successfully running a sound fiscal planning[4]. Through the above methods, garbage pollution in Myanmar has been successfully controlled.

3. Soil Remediation

The accumulation of soluble salts of magnesium, sodium, and calcium in soil constitutes salinization in arid and semi-arid climates worldwide. This salinity increase in the soil can lead to decreased plant growth and hinder the absorption of water by plants due to osmotic pressure from the soil solution[2]. Based on the soil sample of Upper Myanmar, Mandalay Division, revealed that the effective remediation for salt contaminated soil, at first, >20 cm deep of contaminated soil is needed to be mixed and ploughed to support the some degreed of liquid irrigation route, second, 7.7434 tonne/ha of local gypsum is used to soil to neutralize, third, using water ($13500m^3$/ha) to clean for undersirable compound, Final results goes to 68.59% for electrical conductivity, 60.29% for exchangeable sodium percentage and 12.03% for soil pH. On the gypsum treated soil of rice plantation could be showed better germination but no germination in salt- affected soils[18].The two industrial zone site of soil samples in Myanmar analyzed and isolated lead tolerant soil bacteria, 13 mM of Alcaligenes sp and 10mM of E.coil that stand fixed concentration of antibiotics (Kanamycin, Tetracycline, Chloramphenicol)l for individual 50 ug/ml gather with 5mN of Pb $(NO3)^2$ that shows antibiotic tolerance and lead resistant, this observation would be great outcome for bioremediation process and then provide information about lead resistant isolates with other hazardous heavy metals would be observed[14].

Conclusions

As the climate crisis accelerates, the pursuit of an environmentally sustainable landscape becomes paramount. The observation of soil pollution could serve as an awakening call to expedit the transition towards greener ecosystems. Therefore, the challenges in this issue should carefully handle and share knowledge between economic growth and environmental safeguard about environmental consequences to its own residence. In Myanmar, due to only a limited number of the environmental inverstigation about improper mining activities can cause contamination of surface noted but in near future, the research should foucus on the mining areas of environmental issue and human health because currently the research interests are chemical refining effect and geologically mapping. Mainly, it is an essential to build sustainable future for all if it can keep between environmental pollution and economic growth leading to conservation of Myanmar's economic well-being and genuine attractiveness. In agriculture pillar, Myanmar has to raise awareness on the safe apply of pesticides and biopesticides to control hazards of inorganic pesticides to affect environment and humans, on the other hand, must share how to handle pesticides and sales for strict regulations. In facts, this literature review aim to invite more research to focus on soil contaminations problems in Myanmar. By doing so, there will also be a reduction in environmental anxiety.

ACKNOWLEDGMENTS

We would like to acknowledge and offer our affection to Univeristy of Yangon, Myanmar and Prince of Songkla Univeristy, Thailand.

REFERENCES

[1] Herridge, D.F., Win. M.M., Nwe, K.M.M., Khin Lay Kyu, Win, S.S., Shwe, T., Min, Y.Y., Denton, M.D., & Cornish, P.S. (2019). The cropping systems of the entral dry zone of myanmar: productivity constraints and possible solutions,agricultural systems,Volume 169, Pages 31-40, ISSN 0308 - 521X.

[2] Goodie, A.S. (1990). Soil Salinity Causes And Controls. Techniques For Desert Reclamation.England, John Wiley And Sons, Ltd; pp 110-111.

[3] Huang, Ying & Wang, Lingyu & Wang, Wenjia & Li, Tingqiang & He, Zhenli & Yang, Xiaoe. (2018). Current Status Of Agricultural Soil Pollution By Heavy Metals In China: A Meta-Analysis. Science Of The Total nvironment. 651.10.1016/J.Scitotenv.2018.10.185.

[4] Aye, H.H., Aye, W.W., & Oo, N.W. (2020). Concentration of heavy metals in wastewater, soil and rice samples from taung in lake near mandalay industrial zone iij. myanmar acad. arts sci. 2020 vol. xviii.no.2a

[5] Htun, K. (2014). Sustainable Mining in Myanmar. Applied Environmental Research, 36(1), 25–35. https://doi.org/10.35762/AER.2014.36.1.5

[6] Oo. K.T., & Kyi, H. (2019). Asessment On Environmental Impacts Of Gold Mining In Wetthe-Phatshe Area Of Thabeikkyin Township. Yadanabon University Research Journal, Vol-10, No.1

[7] Latt, K.K., Liana, S.R., Poddar, S., & Bhaumik, A. (2023). Pesticide utilization in myanmar and effects on human health and environment. research journal of pharmacy and technology. 16(2):681-5.

[8] Kwee, Yaung & Maw, Khin & Soe, Maw. (2021). Soil quality of the tea and apple-growing sites in Mindat District, Chin state, Myanmar: A preliminary study. ZemljisteiBiljka. 70. 27-40. 10.5937/ZemBilj2101027K.

[9] Lajeunesse Connette K.J., Connette G., Bernd A., Phyo P., Aung K.H., Tun Y.L., Thein Z.M., Horning N, Leimgruber.P., Songer. M. Assessment Of Mining Extent And Expansion In Myanmar Based On Freely-Available Satellite Imagery. Remote Sensing. 2016; 8 (11):912.

[10] Leon Espira, Ther Aung, Khin Han, Pamela Jagger, And Joseph N., S. Eisenberg (2021).Determinants Of Pathogen Contamination Of The Environment In

The Greater Yangon Area, Myanmar. Environmental Science & Technology 2021 55 (24), 16465-16476.DOI: 10.1021/Acs.Est.1c02887

[11] Louise Bethany (2017). Soil Contamination: Its Causes, Effects, And Solutions. https://www.permaculturenews.Org/2017/04/03/38249/

[12] Mondal, Sudeshna. (2021). Impact Of Climate Change On Soil Fertility. 10.1007/978-3-030-76863-8_28.

[13] Münzel, T., Hahad, O., Daiber, A., & Landrigan, P. J. (2023). Soil And Water Pollution And Human Health: What Should Cardiologists Worry About?. Cardiovascular Research, 119 (2), 440–449. Https://Doi.Org/10.1093/Cvr/Cvac082

[14] May SandarKyaing, Myat Thin Khaing and KhinMaungSaing. 2019. Screening of Heavy Metal (Lead) and Antibiotics Resistant Soil Bacteria from Myanmar Industrial Sites.Int. J. Curr. Microbiol. App. Sci. 8(4): 1319-1325.

[15] Oo, T. (2019). Approach To Assessment Of Soil And Water Contamination By Mining Activities In Mandalay Region, Myanmar. International Journal Of Geomate.

[16] Pinak Ranjan Chakravarty, Saumyajit Ray, Debamitra Mitra, Jangkongam Doungel, Obja Borah Hazarika, Padam Nepal, Srimanti Sarkar, Sucheta Ghosh, Langpoklakpam Suraj Singh, Anonya Bhattacharjee, Anuja Saha(2015). JAIR Journal Of International Relations: Vol. 2, Issue 1,

[17] Swe, M. M. M., Win, M. M., Cohen, J., Phyo, A. P., Lin, H. N., Soe, K., Amorncha, P., Wah, T. T., Win, K. K. N., Ling, C., Parker, D. M., Dance, D. A. B., Ashley, E. A., & Smithuis, F. (2021). Geographical Distribution Of Burkholderia Pseudomallei In Soil In Myanmar. Plos Neglected Tropical Diseases, 15(5), E0009372.

[18] San, A.A. & Phyo, M.T. (2018). Heavy Metal Pollution of Agricultural Soils and Vegetables of Ngazun Township, Mandalay Division. Yadanabon University Research Journal. https://oar.ydbu.edu.mm/handle/123456789/269

[19] Tun, T.Z., Bonnet, S. & Gheewala, S.H. Life Cycle Assessment Of Portland Cement Production In Myanmar. Int J Life Cycle Assess 25, 2106–2121 (2020).

[20] Tun, W. E. E., Thanlyin, M., Khin, E. M., Yangon, M., & Win, S. S. (2018). Desalination And Characterization Of Salty Soils From Upper Myanmar. International Journal Of Science And Engineering Applications. Volume 7–Issue 07,115-124, ISSN:-2319–7560.

[21] Tun, A. Z., Wongsasuluk, P., & Siriwong, W. (2020). Heavy Metals In The Soils Of Placer Small-Scale Gold Mining Sites In Myanmar. Journal Of Health & Pollution, 10 (27), 200911.

[22] Win, Theint & Thu, Myat & Myat Swe, Tin & Ko, Thet & Aung, Tun & Ei, Htike & Win, Nwe & Swe, Kyi & Hlaing, Aye & Winnandar, & Khaing, Aye. (2020). Degradation Of Soil Quality In Mandalay Region Of Myanmar Due To Overuse Of Pesticides In Agriculture.

[23] Zaw, Khin & Swe, Win & Barber, A & Crow, M.J. & Nwe, Yin & Myanmar, Myo. (2017). Introduction To The Geology Of Myanmar .The Geological Society Of London. 10.13140/RG.2.2.33577.90723.

[24] Tun, A. Z., Wongsasuluk, P., & Siriwong, W. (2020). Heavy Metals In The Soils Of Placer Small-Scale Gold Mining Sites In Myanmar. Journal Of Health & Pollution, 10(27), 200911.

Techno-Science Research Journal 12 (Special Issue) 98-104

Content list available at ITC

Techno-Science Research Journal

Journal Homepage: www.ric.itc.edu.kh

Techno-Science Research Journal

Characterization of Plaster from Sambor Prei Kuk Temples, Kompong Thom, Cambodia

Manuth Ny[1*], Muoy Yi Heng[1] Phanny Yos[1,2], Tithya Keo[1], Than Heng[3], Vitharong Chan[4]

[1]*Faculty of Geo-resources and Geotechnical Engineering, Institute of Technology of Cambodia, Russian Federation Blvd., P.O. Box 86, Phnom Penh, Cambodia*
[2]*Nano-Structure and Chemical Analysis Laboratory, Institute of Technology of Cambodia, Russian Federation Blvd., P.O. Box 86, Phnom Penh, Cambodia*
[3]*National Authority for Sambor Prei Kuk, NR 6, Phum I, Sangkat Kompong Thom, Krong Stoeung Sen, Kompong Thom, Cambodia*
[4]*Department of Archaeology and Conservation, National Authority for Sambor Prei Kuk, NR 6, Phum I, Sangkat Kompong Thom, Krong Stoeung Sen, Kompong Thom, Cambodia*

Received: 22 August 2023; Accepted: 15 May 2024; Available online: August 2024

Abstract: This research was carried out with the plaster of the ancient heritage at Sambor Prei Kuk Temple which was a part of the remains of ancient Ishanapura and the capital of the Chenla Empire that flourished over much of Southeast Asia in the late 6th and early 7th centuries AD. Some part of Sambor Prei Kuk temple was damaged by conditions. To restore damaged sections of Sambor Prei Kuk temple, this research required an investigation the original of plaster's properties. This involves analyzing its physical characteristics, chemical composition, and mineral structure by employing techniques like Scanning Electron Microscopy (SEM), Optical Microscopy, and X-ray Fluorescence (XRF). Four samples were collected from some parts of the Sambor Prei Kuk temple group with different locations. As the result, analyzation under microscopy indicated that the plaster sample had a high percentage of aggregates of sand mostly quartz grain, lime, and silicate fragments within a ratio of lime/ aggregate around 1:4. The chemical composition was determined by XRF indicating the three of plaster point to use carboniferous limestone as raw material for the plaster with low magnesium content as an impurity and another one plaster point to use a natural cement that has active clay in the limestone up to 45%. SEM indicates a clear between the connection of lime binder and aggregate. The large areas of the surface and pores are filled with calcite crystals and silicate formed.

Keywords: Plasters, Scanning Electron Microscope, X-ray fluorescence, Optical Microscope, Sambor Prei Kuk Temples

1. INTRODUCTION

Cambodia has numerous ancient temples with architectural heritage. In this case, Sambor Prei Kuk Temple is an ancient temple that is a part of the remains of ancient Ishanapura "the temple in the lush forest", which was the capital of the Chenla Empire that flourished over much of Southeast Asia in the late 6th and early 7th centuries AD, and whose architectural achievements laid the foundations for those of the later Khmer Empire. The extensive Temple Zone of 840 hectares lies to the east of the remains of the moated megacity and is linked to the river Stung Sen and a possible harbor of Ishanapura by three earthen causeways between 600 and 700 measures in length.

Plaster is a structure material used for the shielding and decorative coating of walls. Plaster is typically composed of calcium carbonate, made of hydrated lime and calcite dust, bedded aggregates and occasionally mixed with white greasepaint of gypsum, calcium sulfate hemihydrate mineral [1]. The plaster materials contain bedded aggregate minerals, similar to quartz, potassium feldspar, clinopyroxene, and hematite [7].

Some part of Sambor Prei Kuk temple was damaged by some conditions like time, weather, plant growth, etc. So the study focuses on the plaster of the temple to restore those parts by investigating the physical properties of plaster, chemical composition and the structure of minerals composition that are present in the plaster sample. Moreover, the sample was collected from some parts of the temple by noting the sample names and using the GPS to set the location of the sample collection. In this case, the coordinates were important for the

* Corresponding author: Manuth Ny
Email: nymanuth0221@gmail.com

generation of the geological map of the study area (Fig. 3). In addition, the samples were collected by identifying the information on the plaster's physical properties (colors, texture...).

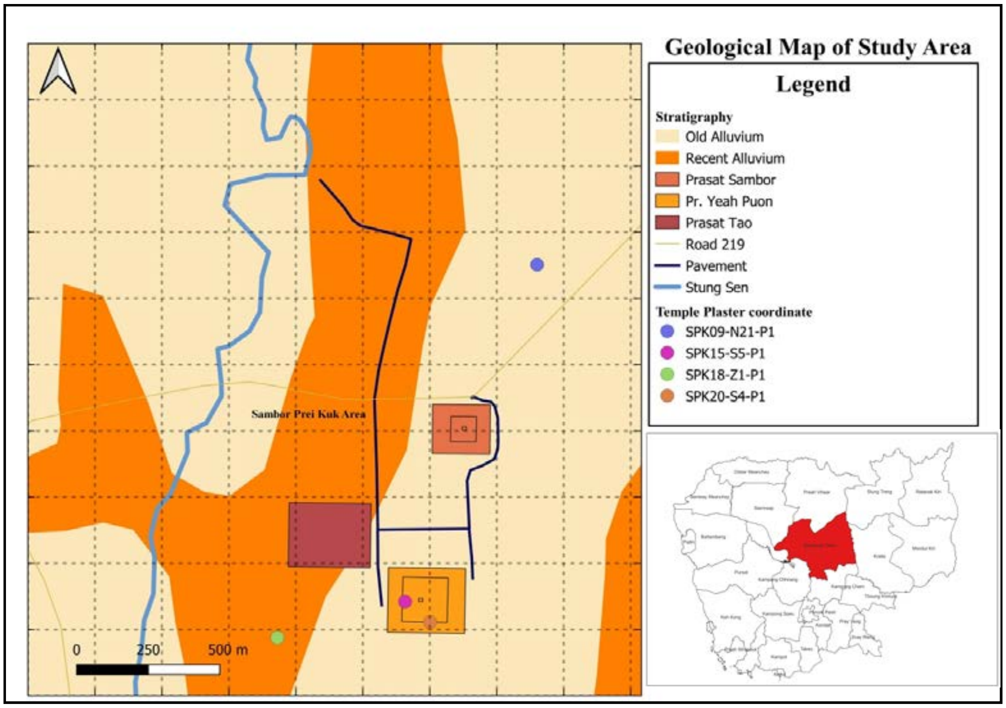

Fig. 1. Location of the study area

Fig. 2. Photograph of Sambor Prei Kuk Temple.

The physical characteristics, chemical composition, and mineral structure were observed by some techniques including Scanning Electron Microscopy (SEM), Optical Microscopy, and X-ray Fluorescence (XRF).

2. METHODOLOGY

In this study, the four plaster samples were collected from some parts of the Sambor Prei Kuk temple group which were damaged, to identify their basic physical properties, microstructural features, and mineralogical. The samples that were collected were taken to the laboratory for X-ray fluorescence (XRF) analysis to define the chemical composition. Aggregates (sand, rock fragments) and other compositions were observed by Petrography and Scanning electron microscopy (SEM).

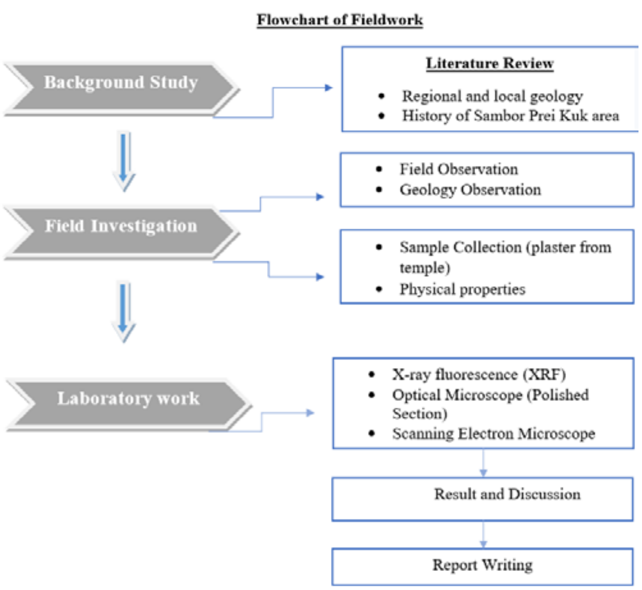

Fig. 3. Research Framework

2.1. X-ray fluorescence (XRF)

The chemical composition in plasters was determined by using an X-ray fluorescence analyzer. For sample preparation, a few grams from every sample to crushed until we obtained a < 63 µm diameter powder. After that, the powder of samples was mixed with the binding agent and pressed before measuring. In addition, another few grams of samples were taken to burn at 900 degrees Celsius to get a loss on ignition. The main aim of chemical analysis of plaster is to determine the composition of oxide concentrations such as calcium, silica, magnesium, and aluminum and sodium, iron, and potassium as the major elements through an X-ray fluorescence analyzer.

2.2. Petrography

The polished section is the removal of rock or mineral into a small piece that has been highly polished and embedded in epoxy for examination by reflected light or electron microbeam techniques. Samples were prepared in the polished section method to identify the grain size aggregates (sand, rock fragments) and other compositions in plaster samples. The composition that is present in plasters was confirmed with scanning electron microscopy (SEM) to analyze its structure.

2.3. Scanning Electron Microscopy

Scanning electron microscopy (SEM) analysis gave structural information about the plaster materials such as a binder, aggregates, and chemical composition that allowed the observation of their forms, sizes, textures, and distribution in the plasters. Samples were prepared as polished sections to note some points that wanted to be measured with scanning electron microscopy and using the rugby tape to note the specific place on the sample before measuring under scanning electron microscopy. After that, SEM will focus on the notice place and measure its structure.

3. RESULTS AND DISCUSSION

3.1. Physical Properties

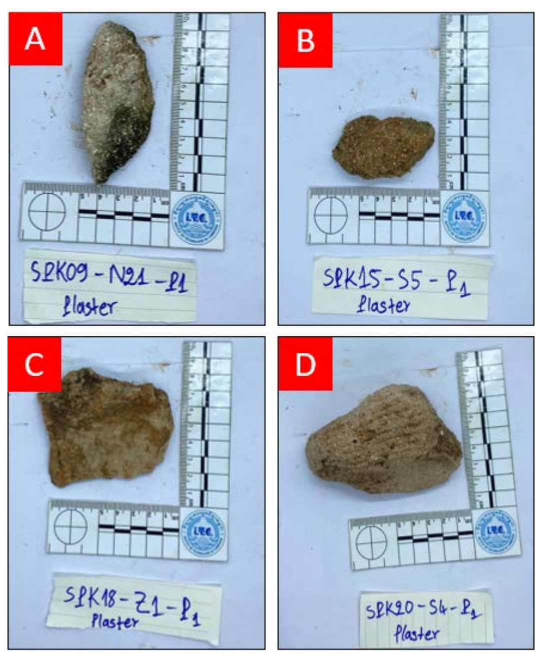

Fig. 4. Physical Properties of Plaster

The analysis of hand specimens reveals several key physical properties of the plaster samples. While color variation is evident (white for SPK09-N21-P1, yellowish for SPK15-S5-P1, white to yellowish for SPK18-Z1-P1, and white to grayish for SPK20-S4-P1), texture offers further insights. Grain size ranges from medium to coarse, within a rough, gritty, porose, and erosion surface (Fig. 4). The presence of aggregate includes quartz and rock fragments mostly from sand and binder which could be lime or gypsum. Examining the samples further, we can potentially identify other visible minerals like calcite crystals.

3.2. *Petrological analyses*

The analyzation under microscopy indicated that all plaster samples had a high percentage of aggregates of sand mostly quartz grain, lime, and silicate fragments. The boundary between aggregate and lime shows the presence of silicate as a fragment as we can see in the microscope pictures (Fig. 6). In addition, the aggregates present in all plaster samples are mostly semi-rounded, granulated, and very porous with strong connections to the lime binder. The lime/ aggregate ratios may be around 1:4 [9] considered based on the optical microscope.

3.3. *Chemical composition of the plaster*

Based on Table 1, the percentage weight of calcium oxide (CaO) is from 19.5886% in SPK18-Z1-P1 to 45.2350% in SPK09-N21-P1, while the percentage % weight of silicon dioxide (SiO_2) shows a higher from 26.4934% in SPK09-N21-P1 to 64.8465% in SPK18-Z1-P1. Sample SPK15-S5-P1, SPK18-Z1-P1, and SPK20-S4-P1 indicate that contain a great amount of mono and polycrystalline quartz and many rock fragments and, for this reason, their percentage of calcium oxide (CaO) of those three samples are lower than calcium oxide (CaO) of SPK09-N21-P1 sample [10]. In addition, these three samples have a high percentage of silicon dioxide (SiO_2) from 52.6396% to 64.8465% and the percentage weight of calcium oxide (CaO) is a lower percentage of silicon dioxide making around 20% to 30%. Anyway, magnesium oxide (MgO) varies in the range between 0.3236–1.6433%, it's pointing to the use of carboniferous limestone as raw material for the plaster with low magnesium content as an impurity [8]. The chemical observed in sample SPK09-N21-P1 is different from another sample. We can see in Table 1 shows the chemical percentage of calcium oxide (CaO) is higher than that of other samples at 45.2350% while the of silicon dioxide (SiO_2) is lower making 26.4934%. By using the Cementation Index for the various types of building lime $CI = \frac{2.8SiO2+1.1Al2O3+0.7Fe2O3}{Cao+1.4MgO}$ (Eq. 1), by using (Eq. 1), $CI = \frac{2.8(26.4934)+1.1(0.4634)+0.7(0.1814)}{45.235+1.4(0.6486)} = 1.62$, the CI value is equal to 1.62, it's between 1.1 and 1.7. Based on the description in the cementation index for the various types of building lime indicates that the value is pointing to using a natural cement in plaster that has active clay in the limestone up to 45% [5].

Table 1 **.** Chemical composition of Sabor Prei Kuk plaster (Weight Percent)

Component	SPK09-N21-P1	SPK15-S5-P1	SPK18-Z1-P1	SPK20-S4-P1
SiO_2	26.4934	57.4106	64.8465	52.6396
CaO	45.235	25.2635	19.5886	29.4967
Al_2O_3	0.4634	1.2805	0.5531	0.8998
MgO	0.6486	0.2267	1.6433	0.3236
MnO	0.0343	0.0427	0.0384	0.0173
Na_2O	0.0561	0	0.0879	0.0343
Fe_2O_3	0.1814	0.4315	0.1964	0.3273
K_2O	0.0695	0.036	0.053	0.0354
P_2O_5	0.1165	0.1056	0.1879	0.0578
TiO_2	0.0268	0.1021	0.0463	0.0699
LOI	26.5	15	12.5	16

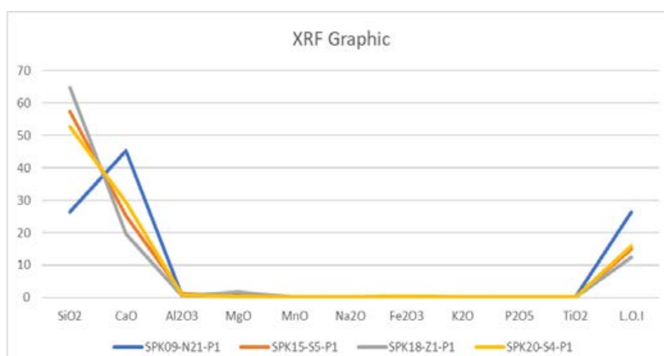

Fig. 5. Graphic of the chemical composition of Sabor Prei Kuk plaster

3.4 *Scanning Electron Microscopy*

Scanning Electron Microscopy (SEM) provides a piece of information that is very important for the characterization of plasters and microstructure that are presented in plaster. The binders are shown clearly with microstructures such as silicate, and calcite. In addition, SEM indicates a clear between the boundary of lime binder and aggregate and the binder is a connector that connects the mineral grain and mineral grain in plaster. Moreover, we can see the high percentage of quartz grain and microstructure of silicate, calcite, and clay content as shown (Fig. 7). Large areas of the surface and pores are filled with calcite crystals and silicate formed.

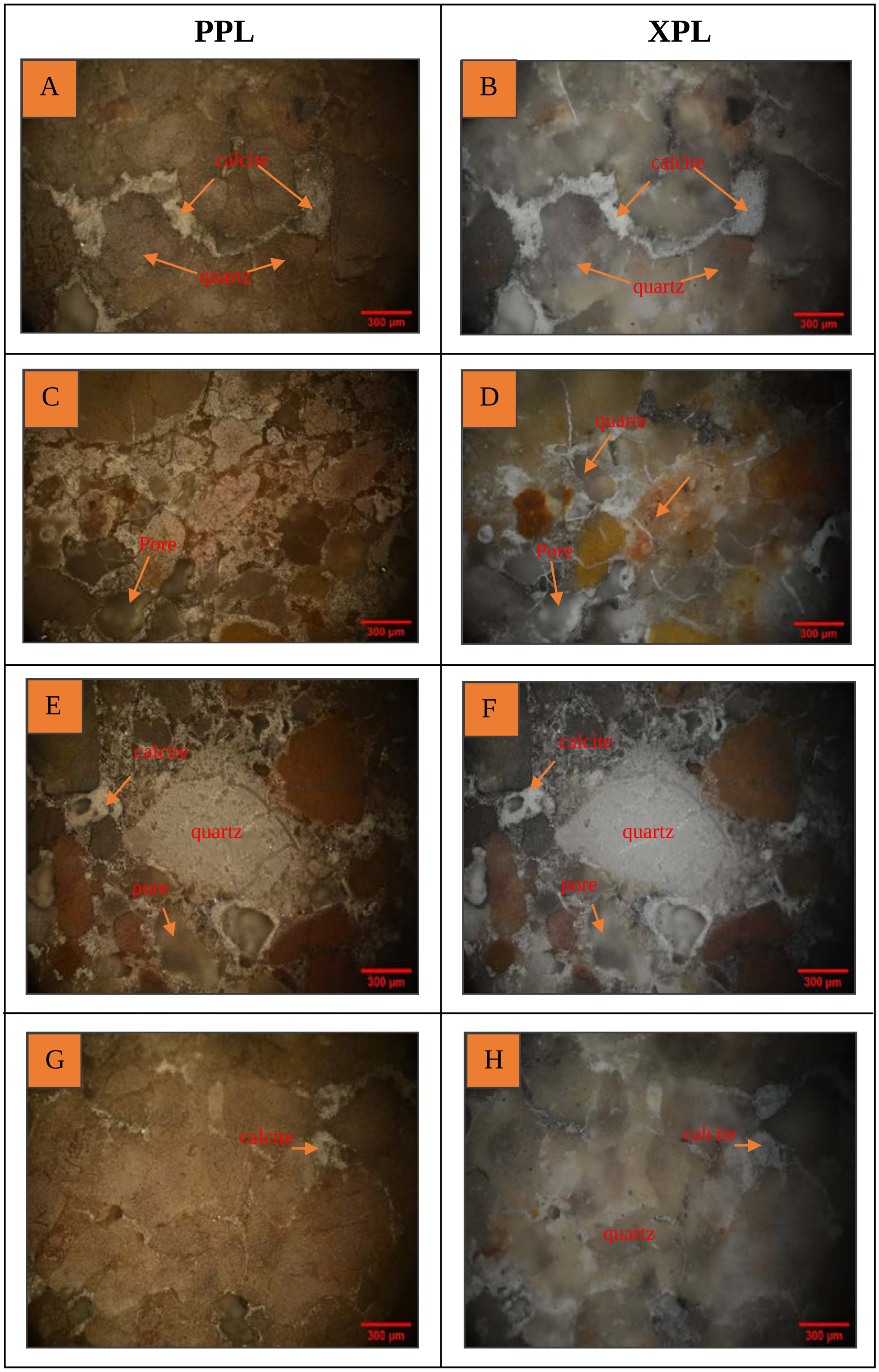

Fig. 6. Microscope picture which shows the microstructure of silicate, calcite, and a high presence of quartz that presence in plaster

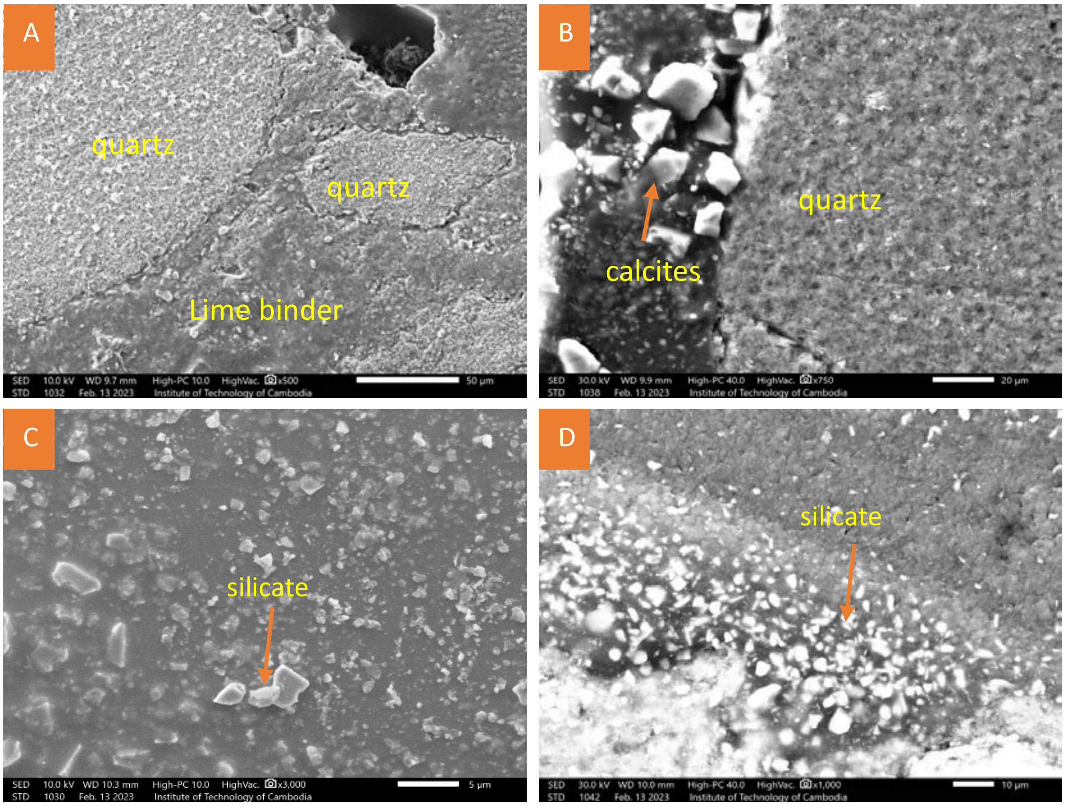

Fig. 7. Image of the plaster under SEM: A) grain size of quartz and lime binder, B, C & D) microstructure of calcites and silicates

4. CONCLUSIONS

The plaster samples exhibited a consistent composition across all four samples, dominated by a high percentage of aggregates consisting primarily of quartz sand grains. Additionally, a significant presence of lime was identified, acting as a binder to connect the aggregate particles. Furthermore, silicate fragments were observed throughout the samples. XRF analysis revealed variations in the plaster's chemical makeup. Three out of the four samples displayed a composition indicative of carboniferous limestone as the primary raw material, with a low magnesium content as an impurity. Interestingly, the fourth sample (SPK09-N21-P1) differed significantly, showing a higher percentage of calcium oxide (CaO) compared to silicon dioxide (SiO2). This suggests the potential use of a natural cement containing active clay in the limestone, possibly up to 45% based on the calculated Cementation Index. SEM analysis provided crucial insights into the microstructure of the plaster. The images clearly depicted the quartz grains and lime binder, highlighting their strong connection. Additionally, the presence of calcite crystals and silicate formations within the large surface areas and pores was evident.

ACKNOWLEDGMENTS

I would like to thank LBE-JICA and the National Authority of Sambor Prei Kuk for allowing me to do my research. Finally, I am thankful to Dr. Yos Phanny for his advice and guidance. Especially, I especially appreciate my teacher, Ms. Heng Muoy Yi for her support and correction, and thankful to my senior for his help.

REFERENCES

[1] Ali, M. F. and Elrahim, A. M. (2021). Analytical study of the blue pigment used in Ottoman house mural paintings, Cairo, Egypt. Scientific Culture, Vol. 7, No. 3, pp. 41-51. DOI: 10.5281/zenodo.4916497.

[2] Arizzi, A. and Cultrone, G. (2021) Mortars and plasters how to characterize hydraulic mortars. Archaeological and Anthropological Sciences, Vol. 13, No. 9, pp. 1–22. (Greece). Journal of Geochemical Exploration, 194, 189-197.

[3] Dana Ashkenazi, Romi Shnabel2, Achim Lichtenberger3 and Oren Tal2, chemical composition and microstructure

analysis of plaster and pigment retrieved from a decorated house wall at Seleucid Tell, 2021

[4] F. Cristiano, L. Mike, R.J. Ball, Chemical and physical characterization of three NHL 2 Binders and the relationship with the Mortar Properties. Euro-Am. Congress Rehabend 2016, 24–27 (2013)

[5] Holmes, S. & Wingate, M., 2002. Building with Lime: A Practical Introduction M. Wingate, ed., Rugby: Practical Action

[6] J. Elsen, K. Van Balen, G. Mertens, Hydraulicity in Historic Lime Mortars: A Review. In J. Válek, J.J. Hughes, & C.J.W.P. Groot, eds. Historic Mortars SE-10. RILEM Book series. Springer Netherlands, 125–139 (2012)

[7] Klempan, B., Helwig, K. and Colivicchi, F. (2017) Examination and analysis of Etruscan wall paintings at Caere, Italy. Archaeometry Vol. 59, No. 6, pp. 1082–1094.

[8] M. Singh, S. Vinodh Kumar a, Sujata A. Waghmare a, P.D. Sabale b, Aragonite–vaterite–calcite: Polymorphs of CaCO3 in 7th century CE lime plasters of Alampur group of temples, India (2016).

[9] Özlem Aslan Özkaya, Hasan Böke et al.2009, Properties of Roman bricks and mortars used in Serapis temple in the city of Pergamon.

[10] Raffaella De Luca1, Miguel Angel Cau Ontiveros2,3, Domenico Miriello1, Alessandra Pecci 1,3, Emilia Le Pera1, Andrea Bloise1 and Gino Mirocle Crisci1, Archaeometric study of mortars and plasters from the Roman City of Pollentia (Mallorca - Balearic Islands) (2013).

Techno-Science Research Journal 12 (Special Issue) 105-112

Content list available at ITC

Techno-Science Research Journal

Journal Homepage: www.ric.itc.edu.kh

Techno-Science Research Journal

Estimation of Heat Index Mapping to Support Resilient Urban Management

Thaneeya Chetiyanukornkul[1*], Yaowatat Boongla[2]

[1]*Department of Biology, Faculty of Science, Chiang Mai University, Mueang, Chiang Mai, 50200, Thailand*
[2]*Sustainable Development Technology, Faculty of Science and Technology, Thammasat University, Rangsit Campus, Pathumtani 12121, Thailand*

Received: 22 August 2023; Accepted: 15 May 2024; Available online: August 2024

Abstract: *This study examined the short-term effects of temperature on heat criteria and heat stroke in the Chiang Mai, Thailand. Chiang Mai urban communities are particularly vulnerable to climate-related health impacts due to the high incidence of highly dense population, urban heat island. Every year, Chiang Mai has the highest temperature in March and April. The purpose of this study is to build a GIS-based map that will evaluate extreme temperatures and heat index throughout the years 2020-2022. Following 2020,2021,2022, the maximum temperature was 33.4°C, 33.4°C, and 33.2°C, respectively. The dry season has the greatest influence on the metropolitan regions of Chiang Mai. The heat index mapping indicated the danger level as presented in April throughout the years 2020–2022. Furthermore, the heat index demonstrated the health risk effect of the Chiang Mai urban regions during the dry more than wet season. This study also found a relationship between heat stroke and temperature and relative humidity. According to this result, the prevalence of heat stroke is influenced by local climate. This data can help to support the policy for resilient urban management, and the authority may explore expanding green urban areas to help reduce temperature.*

Keywords: Temperature; Heat Index (HI); Heatstroke; Geographic Information System (GIS)

1. INTRODUCTION

Chiang Mai is a hub of activity, particularly in Thailand's expanding northern region.They are commonly seen as the focal points for investment, economics, administration, and social interaction quarters.Chiang Mai's scenery has changed as a result of urbanization, particularly in terms of increased urban heat.At the moment, urban green spaces are dwindling in Chiang Mai, leading to higher air temperatures[Romanello et al., 2021; Byers et al., 2018]. An urban heat island (UHI) is a region within a city or metropolitan area that is significantly hotter than its surrounding rural areas. The difference in temperature is particularly obvious at night and when the breezes are feeble [Songsome et al., 2020]. High air temperatures have been linked to higher mortality and morbidity in studies [Zhu et al., 2023; Aboubakri et al., 2023]. Currently, the number of people exposed to intense heat is expected to grow significantly with each additional unit of warming. Furthermore, evaluations at both the individual and organizational levels are critical for developing focused strategies and tailored responses to global warming.

Many studies, such as those on cardiovascular admissions [Phung et al., 2016], have examined the impact of high temperatures on health.Furthermore, according to some authors, heat stroke is classified into two types: 1) classical or nonexertional heat stroke (NEHS), and 2) exertional heat stroke (EHS). illness is nearly always referred to as heat stroke because it is the most serious health risk. It occurs when the body can no longer control its temperature: the body's temperature rises quickly, the sweating mechanism fails, and the body is unable to cool down. When heat stroke occurs, the body's temperature can quickly rise to 41°C (105.8°F) or higher. Heat stroke can result in severe disability or death if not treated immediately[Ebi et al., 2021]. The immediate repercussions of extreme weather events on human health can be severe. These might include exposure to the elements, mental health consequences, injuries incurred while attempting to flee, and even death caused by the weather event itself, such as drowning in a flood [The National Institute of Environmental Health Sciences (NIEHS), 2023]. Outdoor and indoor air pollution consist of complex mixtures of pollutants from various sources. Heat stroke is one of the side effects of

* Corresponding author:Thaneeya Chetiyanukornkul
E-mail: thaneeya.s@cmu.ac.th; Tel:+6689-7009213

extreme heat[Chunram et al., 2007]. Geographic information systems (GIS) were used in several studies to develop mapping of heat index (HI) and hazard risk[Levi Shako and Antony Wamalwa, 2014;Wu et al., 2008]. In this study, a database of temperature, relative humidity, and heat stroke cases in Chiang Mai from 2020 to 2022 was created. The purpose of this study is to build a GIS-based map to evaluate extreme temperatures and heat index (HI) from 2020 to 2022.This study investigated the relationship between heat stroke, temperature, and relative humidity.These findings underscore the necessity for public health departments to accelerate the development and enhancement of early warning systems for heatwaves and urban heat. Additionally, there is a need to strengthen health education and promotion, particularly among the vulnerable groups identified in this study.

2. METHODOLOGY

2.1 Study Site

Thailand's northern city, Chiang Mai (CM), is quickly urbanizing, resulting in a major urban heat island (UHI) impact that will undoubtedly influence regional climate, environment, and socioeconomic growth (Fig.1). Chiang Mai had a total population of about 1.7 million people and a land area of 20,107 km^2[Amnuaylojaroen et al, 2022]. The population density was 84.5 persons per square kilometer. Chiang Mai has the maximum solar intensity, longer sunny days, and the lowest precipitation and cloudiness values during the dry season (February to April). As a result, the HI effects were most likely the strongest at the time, affecting a community's environment and quality of life in Chiang Mai city [Thai Meteorological Department, 2023].

2.2 Weather Information and Heat Index

Thailand Meteorological Department provided weather data such as temperature (°C) and relative humidity (%) for the years 2020-2022 [Thai Meteorological Department, 2023].In Stedman's Heat Index [PorramesAmatayakul, 2006] was used to compute the heat index (HI) in this investigation. The heat index is a measure of how hot a person feels. As a result, we can use the heat index value for hot warning to reduce heat harm in humans. The method for analyzing use Steadman's heat index equation to estimate the heat index value with defined dry temperature ranges of 21-50 °C and relative humidity ranges of 0-100%, which are appropriate for Thailand's hot season. [National Oceanic and Atmospheric Administration, 2023], Following that, we will develop a computer program to estimate heat index values, which we will then utilize to generate heat index tables. The map was displayed using geographic information systems (GIS) visualization (Arcmap 10.8)[SupetJirakajohnkool, 2017]. The temperature mapping was built using the highest temperature data. For heat index mapping, mean relative humidity and maximum temperature data were used.

2.3 Heat Stroke Information

Data on hospital admissions were derived from the monthly count of hospital admissions owing to heat stroke diseases in Chiang Mai's hospitals (Maharaj Nakorn Chiang Mai Hospital) from January 2020 to December 2022. There are some limitations to the study. To begin with, due to data collecting constraints, we used the patient's heat stroke data from one hospital, which may not be very reliable. In the future, the number of hospitals should be more precisely quantified by gathering long-term statistics on heat stroke patients. Second, determining the cause of heat stroke is difficult.

2.4 Data Analysis

SPSS Software (version 28) was used for data analysis. SPSS is a widely used program for statistical analysis. SPSS is a popular statistical analysis tool. Pearson analysis was used in SPSS to examine the relationship between heat stroke and temperature. The monthly mean of temperature and heat stroke data was used for the years 2020-2022.

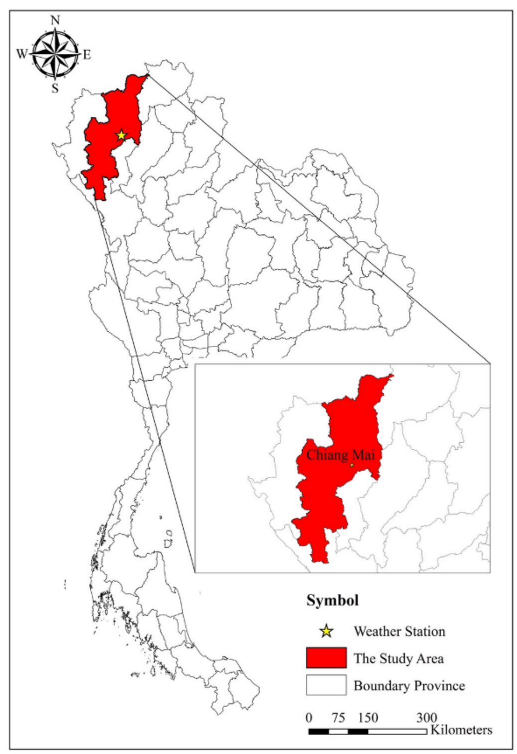

Fig.1. The study area of Chiang Mai Metropolitan Area, Thailand.

3. RESULTS AND DISCUSSION

3.1 Temperature and Relative Humidity

As can be seen in Table 1 and Fig.2 to 3, The findings suggested that the temperature in Chiang Mai city was high during the dry season, particularly in April.

Table 1. Maximum temperature and relative humidity

Monthly	2020 Temp. (°C)	2020 RH (%)	2021 Temp. (°C)	2021 RH (%)	2022 Temp. (°C)	2022 RH (%)
Jan.	32.3	63.0	30.2	67.0.	30.9	68.0
Feb.	34.2	53.0	33.1	57.0	32.6	62.0
Mar.	38.2	45.0	37.4	51.0	36.2	60.0
Apr.	38.2	49.0	34.7	66.0	35.1	65.0
May.	38	60.0	36.9	64.0	33.9	74.0
Jun.	35.4	71.0	33.8	72.0	34.9	69.0
Jul.	34.8	73.0	33.3	75.0	33.6	77.0
Aug.	32.1	81.0	33.8	75.0	32.7	80.0
Sep.	33.5	78.0	33.0	79.0	32.6	81.0
Oct.	31.8	74.0	32.6	77.0	32.4	76.0
Nov.	32.8	68.0	32.3	75.0	32.8	73.0
Dec.	30.5	68.0	29.9	70.0	30.4	72.0
Mean	34.3	65.3	33.4	69.0	33.2	71.4

The meanmaximum temperature in 2020 was 34.3 °C. The highest temperatures were recorded in March (38.2°C), April (38.2°C), and May (38°C), in that order. The coldest month was December. In 2022 and 2023 showed lower temperature than 2020, respectively. This period of extreme heat corresponds to the other findings [Chea et al., 2022; Srivanit et al., 2012]. According to the author, the monthly mean maximum temperature in Chiang Mai was highest during the dry season's summer period in April and was lowest during the winter period (November to February). While the results of the relative humidity were shown in Table 1, the monthly mean relative humidity in Chiang Mai was high in August for 2020 (81.0%) and September for 2021 (79%) and 2022 (81%), respectively. For 2020-2022, the lowest relative humidity was reported in March (45%, 51%, and 60%, respectively). Figure 4 depicted the relative humidity trend from 2020 to 2022.

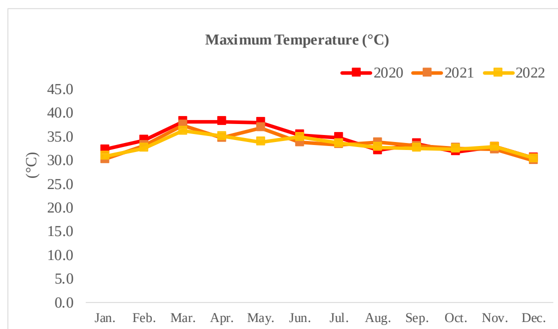

Fig.2. The maximum temperature in Chiang Mai, Thailand.

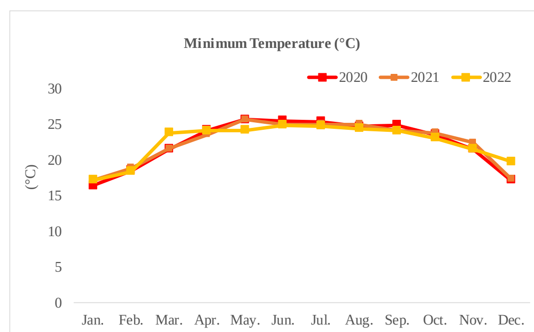

Fig.3. The minimum temperature in Chiang Mai, Thailand.

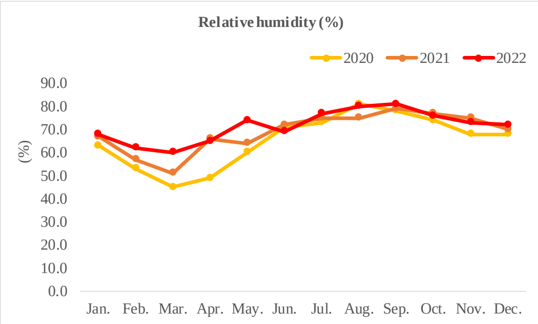

Fig.4. The monthly mean relative humidity in Chiang Mai, Thailand.

3.2 Maximum temperature and heat index (HI)

Geographic information systems (GIS) visualization (Arcmap 10.8) was used to illustrate the maximum temperature. Figures 5–7 show the maximum temperature in April for the years 2020–2022.The color was created by referring to Thailand Meteorological Department [Thai Meteorological Department, 2023].The maximum temperature map in April is colored red for 2020 and orange for 2021-2022. Other months showed in yellow and light yellow that there was less anxiety than in April.The heat index uses information on ambient temperature and relative humidity to estimate hazards during heat waves and warn about potentially hazardous situations to human health. This is especially significant during moist heat waves, when temperatures alone are insufficient to determine heat stress in the human body (Cvijanovic et al., 2023). The expanded heat index, a corrected and expanded version of the National Weather Service (NWS) heat index produced by U.S.National Oceanic and Atmospheric Administration, NOAA’s National Weather Service [National Oceanic and Atmospheric Administration, 2023], is one of several heat indices in use (Table 2). We assign five heat stress levels ('Safe,' 'Caution,' 'Extreme Caution,' 'Danger,' and 'Extreme Danger') based on the NWS graphic for various temperature and relative humidity combinations (Table 2). The heat index data revealed a warning in the caution and extreme categories. The heat index level (27-34, caution) described the possibility of tiredness from prolonged exposure and/or physical exercise. Furthermore, the heat index level with a value of 33-40 refers to heat stroke, heat cramps, or heat exhaustion that can occur with prolonged exposure and/or physical activity, as shown in Fig.8 to 10. Heat index was performaced for Chiang Mai.For 2020-2022, the heat index map in April is shaded orange. A heat index of more than 38 degrees Celsius may be harmful to human health.

3.3 The relationship between heat stroke and temperature

The relationships between temperature and data from heat stroke patients in 2020 were also plotted. As shown in Figs. 10,the patient's data recorde was low, and the total number was recorded as 7 people (R^2 = 0.0469). The correlation between the maximum temperature and the patient's data recorde was weaker (R^2 = 0.164)(11 patients) during all recored in the year 2021.Finally, the highest correlation between maximum temperature and patient data was found in 2022 (0.2345)(20 patients). Pearson Correlation (R^2) identified a relationship between temperature and heat stroke data for each year. Furthermore, the Pearson correlation (R^2) with SPSS software revealed a correlation between temperature and the number of heat stroke patients with a value of -0.123. However, the temperature is often associated with heat stroke; Shiraz Vered et al. (2020) reported that high temperatures in the summer had an effect on stroke evidence.They used data from the national stroke registry. Otani et al. (2021) applied a time-stratified case-crossover design to investigate the association of maximum/minimum air temperatures and the incidence of heat strokes. Minimum and maximum air temperatures may be linked with the incidence of heat stroke. The relationship between relative humidity and the number of heat stroke patients was 0.341 (Table 3). Due to the small number of patients' data recorded, we observed a statistically significant negative relationship between maximum temperature and heat stroke patients' data when comparing the results with relative humidity. Additional data from other hospitals may be acquired and analyzed. As a result, investigations should be conducted to study the association between temperature and the number of individuals suffering from heat stroke from diverse sources. In addition to temperature and RH, sex, age, and individual behaviors all contribute to heat stroke.Like males, they have a higher rate of heat illness than females because life expands and could be associated with individual behaviors and age [Giffort et al., 2019; Trahan et al. 2023]. Income, economics, and occupational factors have an effect on the mortality risk as present in China, where temperatures in the summer are higher than in the winter [Yan et al., 2022]. Workers who work in hot weather conditions have a high risk of health, including in the in the agricultural sector, construction, and various industries (Fatima et al 2021).

Table 2. The danger levels associated with different heat index ranges by the National Weather Service (NWS), the U.S. National Oceanic and Atmospheric Administration, and NOAA's National Weather Service

Warning	Heat Index	Impact
Safe	<26	No adverse effects expected due to heat
Caution	27.0-31.9	Fatigue possible with prolongedexposure and/or physical exercise
Extreme Caution	32.0-40.9	Heat stroke, heat cramps or heat exhaustion possible withprolonged exposure and/or physical exercise
Danger	41.0-52.9	Heat stroke, heat exhaustion like and heat strokepossible with prolonged exposure and/or physical exercise
Extreme Danger	53-92	Heat stroke highly likely
Beyond human thereshold	<93	Value beyond human resistance to heat

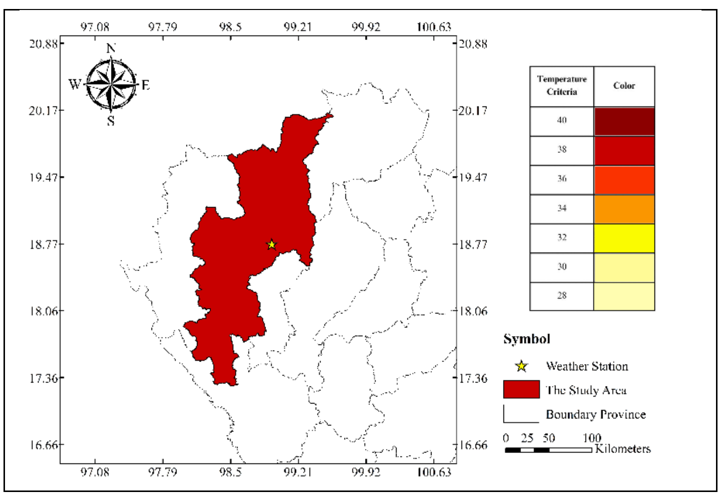

Fig.4. The maximum temperature in Chiang Mai in April 2020.

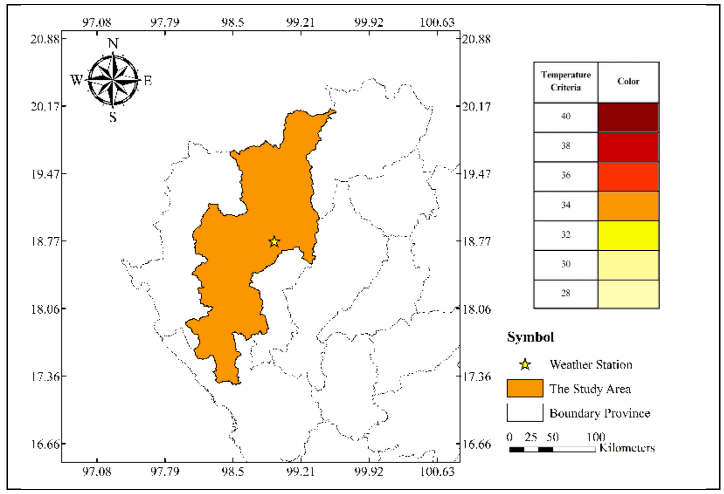

Fig.5. The maximum temperature in Chiang Mai in April 2021.

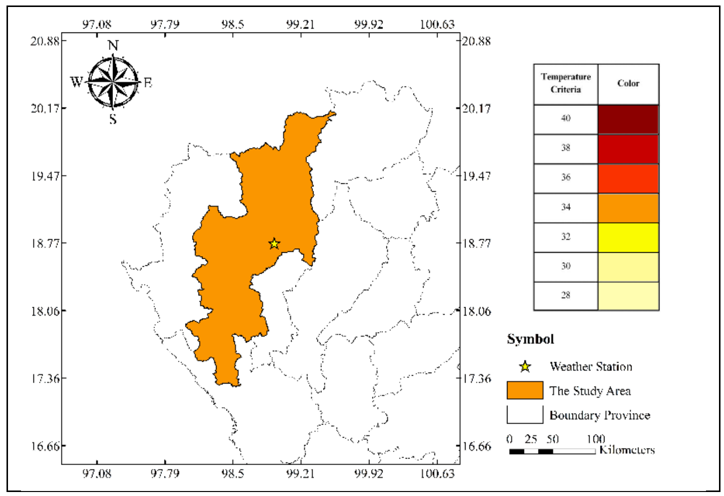

Fig.6. The maximum temperature in Chiang Mai in April 2022.

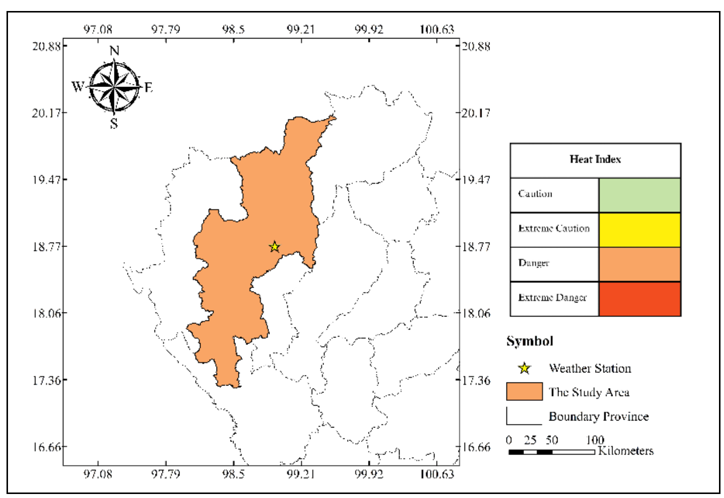

Fig.7. The heat index in Chiang Mai in April 2020.

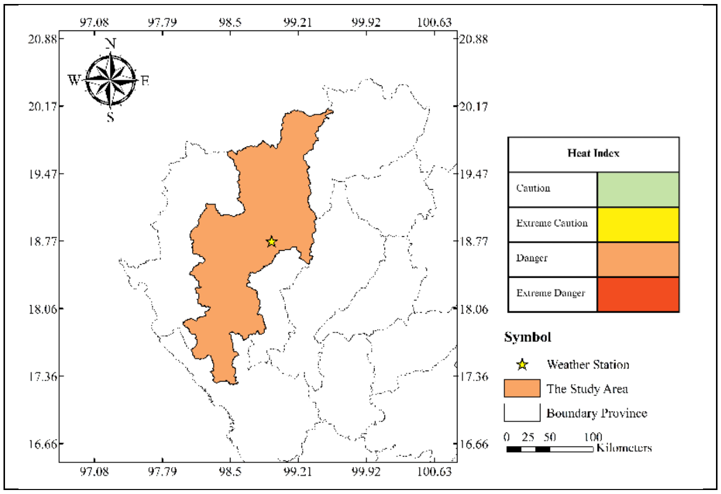

Fig.8. The heat index in Chiang Mai in April 2021.

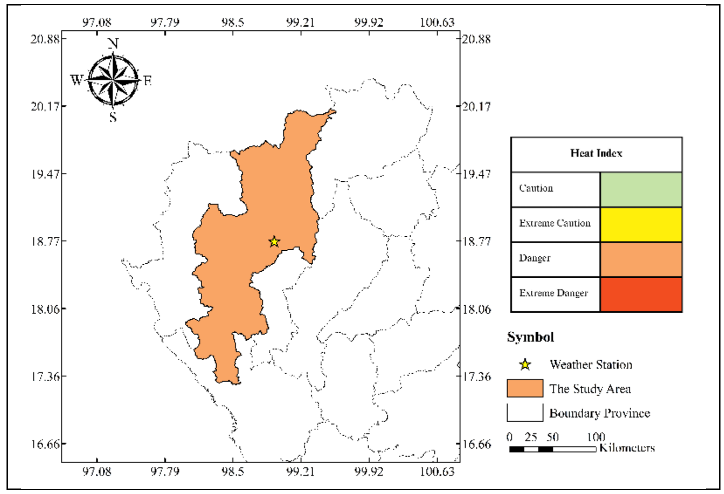

Fig.9. The heat index in Chiang Mai in April 2022.

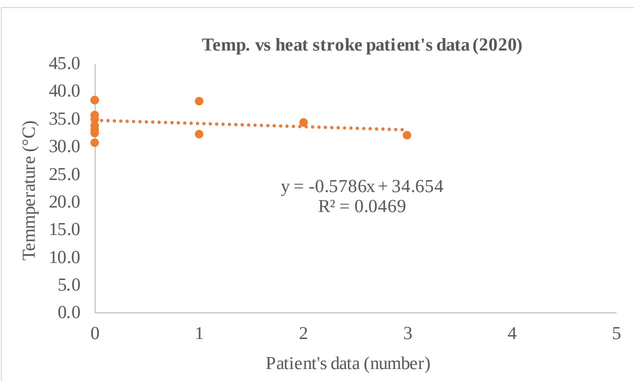

Fig.10. Correlation between maximum temperature and heat strok patient’s data in 2020.

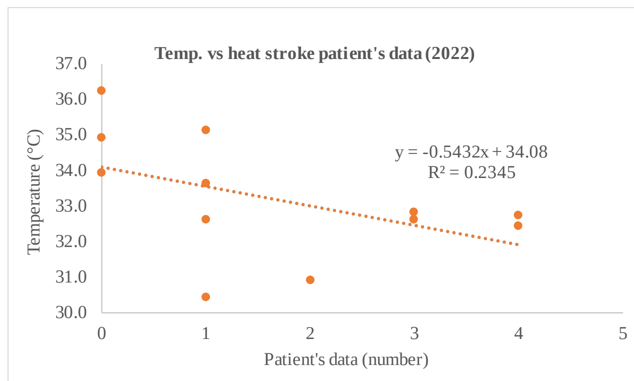

Fig.12. Correlation between maximum temperature and heat strok patient’s data in 2022.

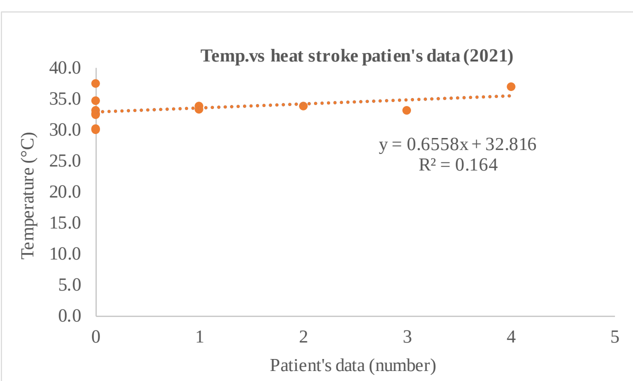

Fig.11. Correlation between maximum temperature and heat strok patient’s data in 2021.

Table 3. The Pearson Correlation Coefficient (R^2) between the number of heat stroke patients, the temperature and RH were calculated using SPSS.

R^2	Temperature (°C)	RH (%)	Patient (No.)
Temperature (°C)	1	-.587**	-.123
RH (%)	-.587**	1	.341*
Patient (No.)	-.123	.341*	1

Remark: **correlation is significant at 0.01 level; RH: relative humidity; No.: number

4. CONCLUSIONS

This study focuses on maximum temperatures and heat i ndex mapping. The maximum temperature was found at 38.2 °C for 2020. The data revealed that the maximum temperature in April was the highest. All of the annuals displayed semilary outcomes. The mean maximum temperature in 2020, 2021, and 2022 was 33.4°C, 33.4°C, and 33.2°C, respectively. The dry season has the greatest influence on the metropolitan regions of Chiang Mai due to the heat index mapping that indicates the danger level as presented in April throughout the years 2020–2022. This study also found a relationship between heat stroke and temperature and relative humidity (RH). According to this result, the prevalence of heat stroke is influenced by local climate. Based on this study, we found that it is not only temperature and RH factors that affect heat stroke; it could also be associated with other factors such as individual behavior, sex, age, income, economics, and occupational. This data can help to support the policy for resilient urban management, and the authority may explore expanding green urban areas to help reduce temperature.

ACKNOWLEDGMENTS

The authors are grateful to Chiang Mai University for the financial support, The hospital of Chiang Mai University for providing heat stroke's patient data as well as to the Thai Meteorological Department for providing weather information.

REFERENCES

[1] Romanello, M., Mcgushin, A., Di Napoli, C., Drummond, P., Hughes, N, Jamart, L., Kennard, H., Lampard, P., Solano Rodriguez, B., Arnell, N. (2021). The 2021 report of the Lancet Countdown on health and climate change: code red for a healthy future. Lancet, 398(10311):1619–1662.

[2] Byers E, Gidden M, Leclère D, Balkovic J, Burek P, Ebi K, GreveP,Grey D, Havlik P, Hillers A, et al. (2018). Global exposure and vulnerability to multi sector development and climate change hotspots. Environmental Research Letters, 13(5): 055012.

[3] Songsom, V., Suteerasak, T., Sanwang, P. (2020). The Relationship between Urban Heat Island and Tourism at Chaing Mai, Thailand based on Remote Sensing. The Journal of KMUTNB, 30(4): 678-688.

[4] Zhu, W., Yuan, C. (2023). Urban Heat Health Risk Assessment in Singapore to Support Resilient Urban Design-By Integrating Urban Heat and the Distribution of the Elderly Cities, 132, 104103.

[5] Aboubakri, O.Rezaee, R., Maleki, A., Safari, M. a Goudarzi, G., Li, G., Hassanvand, M.S. Sharafkhani, R. (2023).Temporal Change in Cold and Heat-related Burden of Mortality: an Evidence of Increasing Heat Impact in Iran. Air Quality, Atmosphere and Health. 21(2), pp.1-9.https://doi.org/10.1007/s11869-023-01414-0

[6] Phung, D., Guo, Y., Thai, P., Rutherford, S.,Wang, X., Nguyen, M., Do, C.M., Nguyen, N.H, Alam, N., Chu, C. (2016). The Effects of High Temperature on Cardiovascular Admissions in the Most Populous Tropical City in Vietnam. Environmental Pollution, 208, 33-39.

[7] Ebi, K. L., Capon, A., Berry, P., Broderick, C., de Dear, R., Havenith, G., Jay, O. (2021). Hot Weather and Heat Extremes: Health Risks. The Lancet, 398(10301), 698-708.

[8] The National Institute of Environmental Health Sciences (NIEHS).Extreme Weather Events Can Affect Human Health. Available at: Health Impacts of Extreme Weather -Climate Change and Human Health (nih.gov).

[9] Levi Shako and Antony Wamalwa (2014). GIS Applications in Heat Source Mapping in Menengai Geothermal Fiel. Proceedings 5th African Rift GeothermalConference 2014 (ARGeo-C5)27th Oct to 2nd Nov 2014, Arusha, Tanzania.

[10] Chunram, N., Vinitketkumnuen, U., Deming, R.L., Chantara, S. (2007). Indoor and Outdoor Levels of $PM_{2.5}$ from Selected Residential and Workplace Buildings in Chiang Mai. Chiang Mai Journal of Science, 34(2):219-226.

[11] Wu, K.S., Huo, X., Zhu, G.H. (2008). Relationships between Esophageal Cancer and Spatial Environment Factors by Using Geographic Information System. Science of the Total Science, 393(2-3):219-225.

[12] Amnuaylojaroen, T., Limsakul, A., Kirtsaeng, S., Parasin, N. a Surapipith, V. (2022). Effect of the Near-Future Climate Change under RCP8.5 on the Heat Stress and Associated Work Performance in Thailand. Atmosphere,13(325):1-21. https://doi.org/10.3390/atmos13020325

[13] Thai Meteorological Department Bureau.Weather Data. Availiable at: https://www.tmd.go.th/.

[14] PorramesAmatayakul. (2006). Estimating Heat Index Value Using Steadman's Method. Agro - meteorological Academic Group, Meteorological Department Bureau.

[15] Chea, K., Manomaiphiboon, K., Aman, N., Thepa, S., Junpen, A. Devkota, B. (2022). Ambient Thermal Comfort Analysis for Four Major Cities in Thailand, Cambodia, and Laos: Variability, Trend, Factor Attribution, and Large-scale Climatic Influence. ScienceAsia, 48:618-628.

[16] Srivanit, M., Hokao, K. (2012). Effect of Urban Development and Spatial Characteristic on Urban Thermal Environment in Chiang Mai Metropolitan. Lowland Technology International, 1 4(2):9-12.

[17] Cvijanovic, I., Mistry, M.N., Begg, J.D., Gasparrini, A., Rodó, X. (2023). Importance of Humidity for Characterization and Communication of Dangerous Heatwave Conditions Climate and Atmospheric Science, 6:33 ; https://doi.org/10.1038/s41612-023-00346-x.

[18] U.S. National Oceanic and Atmospheric Administration, NOAA's National Weather Service, Heat Index. Availableat:https://www.noaa.gov/jetstream/global/heat-index.

[19] Jirakajohnkool, S. (2017). Learning of Geographic Information Systems (GIS) with ArcGIS Desktop 10.5. Thammasat University Press.

[20] Vered, S., Paz, S., Negev, M., Tanne, D., Zuker, I., Weinstein, G. (2020). High Ambient Temperature in Summer and Risk of Stroke or Transient ischemic attack: A National Study in Israel. Environmental Research. 187, 109678.

[21] Otani, S.,Ishizu, S.F., Masumoto, T., Amano, H., Kurozawa, Y. (2021). The Effect of Minimum and Maximum Air Temperatures in the Summeron Heat Stroke in Japan: A Time-StratifiedCase-Crossover Study. International Journal of Environmental Research and Public Health. 18, 11-12.

[22] Gifford, R.M., Todisco, T., Stacey, M., Fujisawa, T., Allerhand, M., Woods, D.R. (2019). Risk of Heat Illness in Men and Women: a Systematic Review and Meta-analysis. Environmental Research. 171, 24–35.

[23] Trahan, A., Walshe, R., Mehta, V. (2023). Extreme Heat, Gender, and Access to Preparedness measures: An Analysis of the Heatwave Early Warning System in Ahmedabad, India. International Journal of Disaster Risk Reduction.99, 104080.

[24] Yan, M., Xie, Y., Zhu, H., Ban, J., Gong, J., Li, T. (2022). The Exceptional Heatwaves of 2017 and All-Causemortality: An Assessment of Nation Wide Health and Economic Impacts in China. Science of the Total Science, 812, 1-7.

[25] Fatima, S.H., Rothmore, P., Giles, L.C., Varghese, B.M., Bi, P. (2021). Extreme Heat and Occupational Injuries in Different Climate Zones: a Systematic Review and Meta-analysis of Epidemiological Evidence. Environment.International.148,106384

Techno-Science Research Journal 12 (Special Issue) 113-119

Content list available at ITC

Techno-Science Research Journal

Journal Homepage: www.ric.itc.edu.kh

Techno-Science Research Journal

The Study of Depositional Environment of Limestone and Shale at Phnom Thom in Banteay Meanchey Province

Sun Chhunly[1*], Eng Chandoeun[1], Heng Ratha[1,2], Chhun Chhaya[1]

[1]*Faculty of Geo-resources and Geotechnical Engineering, Institute of Technology of Cambodia, Russian Federation Blvd., P.O. Box 86, Phnom Penh, Cambodia*

[2]*Energy Tecnology and Management Unit, research and Innovation Center, Institute of Technology of Cambodia Russian Federation Blvd., P.O. Bax 86, Phnom Penh, Cambodia*

Received: 22 August 2023; Accepted: 15 May 2024; Available online: August 2024

Abstract: *The quality of the petroleum source rock is based on several factors. Among them, the depositional environment is one of the major factors controlling the preservation of the petroleum source rock. This study aims to define the depositional environment of limestone and calcareous shale at Phnom Thom in Banteay Meanchey Province through facies analysis, mineralogy, organic petrology, and the ratio of chemical elements. Petrology, X-ray fluorescence (XRF), and Scanning electron microscope (SEM) have been use in laboratory work. Facies analysis was performed after going through the fieldwork, whereas mineralogy was examined under a transmitted light microscope (thin section). The organic petrology is conducted under reflected light microscope and scanning electron microscope (SEM), whereas chemical element is derived from conducted X-ray Fluorescence (XRF). The result demonstrated that, calcareous shale samples consisted of calcite and clay mineral and less amount of quartz and organic material, whereas limestone samples composted of carbonate mud and calcite minerals. Calcareous shales are classified as clay-rich carbonate mudstone, whereas limestones are classified into wackestone and mudstone. Vitrinite, Inertinite, inertodetrinite, alginite, Micrinite and pyrite has been found in all samples. Additionally, a Scanning electron microscope (SEM) was performed to observe the presence of organic matter in high resolution. This observation will reveal details about the size, shape, and topology of biological materials on the surface. Moreover, the outcrop analysis shows about physical properties of calcareous shale and limestone facies, mineralogy, and organic petrology, which indicates a continental margin and shallow marine environment, For Ca/ (Fe +Ca) plot classifies as a marine district. The $Al_2O_3/(Al_2O_3 + Fe_2O_3)$ classifies as Overlapping area, and the Fe_2O_3 / SiO_2 with Al_2O_3 / SiO_2 classifies as continental margin. Therefore, the result of the Phnom Thom is deposited in the continental margin and shallow marine environment based on data that has been analyzed. So, Phnom Thom formation is potential for hydrocarbon source rock and good location for companies do the industry.*

Keywords: Depositional environment, Limestone, Shale, Mineral composition, Organic matter.

1. INTRODUCTION

A depositional environment is a specific place in which sediments are deposited, such as a stream channel, a lake, or the bottom of the deep ocean. They are sometimes called sedimentary environments [1]. A sedimentary environment is a part of the earth's surface that is physically, Chemically, and biologically distinct from adjacent terrains [2,3]. A sedimentary environment may be a site of erosion, non-deposition, or deposition, as a broad generalization, sub-aerial environments are typically erosional while sub-aqueous environments are mostly depositional areas [3]. The layers of sediment that accumulate in each type of depositional environment have distinctive characteristics that provide important information regarding the geologic history of an area.

Limestone is a sedimentary rock made of calcium carbonate ($CaCO_3$), usually in the form of calcite or aragonite. It may contain considerable amounts of magnesium carbonate (dolomite) as well [4]. It most commonly forms in clear, warm, shallow marine waters. It is usually an organic sedimentary rock that forms from the accumulation of shell, coral, algal and fecal debris. It can also be a chemical sedimentary rock formed by the precipitation of calcium carbonate from lake or ocean water [5]. Shale is a fine-grained, sedimentary rock formed as a

* Corresponding author : *Sun Chhunly*
E-mail:sunchhunly987@gmail.com; Tel: +855-93-917-267

result of the compaction of clay, silt, mud, and organic matter over time and is usually considered equivalent to mudstone. Shale is a laminated or fissile clastic sedimentary rock that is composed of predominance of silt and clay other minerals, especially quartz and calcite [4]. Shales were deposited in ancient seas, river deltas, lakes, and lagoons and are one of the most abundant sedimentary rock types, found at both the Earth's surface and deep underground [6].

Banteay Meanchey province is located in the far northwest part of Tonle Sap sedimentary basin, Onshore Cambodia (Figure1). Tonle Sap basin is the biggest sedimentary basin compared to six others that are located in onshore Cambodia, where an area almost more than 23,800 km^2 [7].

This study is focused on the depositional environment of limestone and shale. It has been analysis the formation of limestone and shale by mineral composition, organic matter, and depositional setting. limestone and shale are the most important source for Petroleum production and it can be making Oil and Gas production.

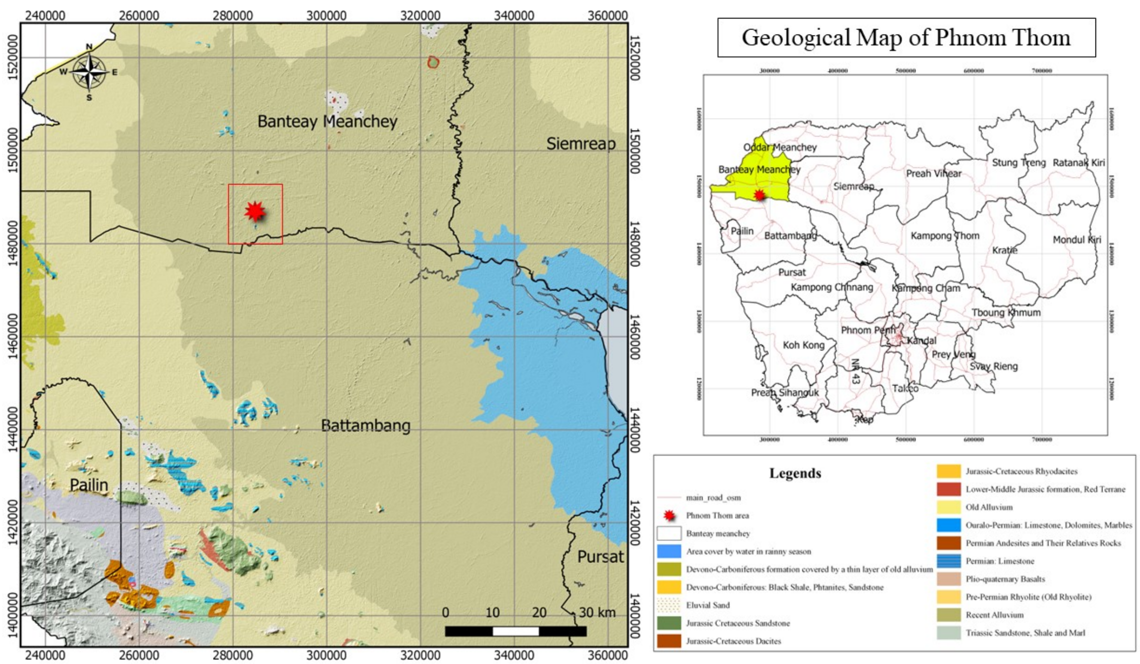

Figure 1 Geological Map

2. METHODOLOGY

2.1 Field investigation and Sample Selection

The field investigation is an important step in conducting the research study since it provides the necessary data. The two crucial methods we must use in a field investigation are the stratigraphic measurement method and the rock sample collection method. Limestone and shale were selected because they have a gray to black color with fine grain sedimentary rock to determine the depositional environment based on characteristics and organic matter in the sample. The samples that were chosen must also be current because they were obtained by hummer shattering and chiseling from the outcrop.

A total of sample that collected from the field at Phnom Thom is 11 samples (5 Limestone and 6 shale). Four method has been use in laboratory Such as Petrology (Thin section and Polish section), X-ray fluorescence (XRF), and Scanning electron Microscope (SEM).

2.2 Petrology (Thin section)

A thin section is a laboratory preparation of a rock, mineral, or even metal sample for use with a polarizing petrographic microscope in optical mineralogy and petrography. Eleven Sample were used to do thin section for analysis (5 samples are limestone and 6 samples are shale).

For this research thin section is important method that used for mineral indentified, petrographic analysisto classify rock and textural analysis to describe how a rock form. Thin section can also be stained to identify specific mineral .

2.3 Petrology (Polish Section)

Polish section is a typical technique that employs reflected light under an optical microscope to detect the type of organic present in sediments. Based on their morphology, such as color, size, shape (elongate, rounded, angular), and related minerals, the fourteen samples in the optical microscope of reflected light can be used to identify the various types of organic.

Using this method allows for identifying organic matter in the sample based on its form, color, and size using reflected light on a microscope. Using SEM method to specify the Polish section method.

2.4 X-ray fluorescence (XRF)

X-ray Fluorescence (XRF) is an analytical technique that uses the interaction of X-rays with a material to determine its elemental composition. XRF is suitable for solids, liquids and powders, and in most circumstances is non-destructive. X-ray Fluorescence (XRF) is an analytical technique that uses the interaction of X-rays with a material to determine its elemental composition. XRF is suitable for solids, liquids, and powders, and in most circumstances is non-destructive.

2.5 Scanning Electron microscope (SEM)

SEM is an analytical method that captures high-resolution images of objects from micro to nanometer scale. It produces images by scanning samples with a focused beam of electrons. The electrons interact with the atoms on the surface of the sample and collect information about the sample's topography and composition.

For sedimentary rock studying, SEM is used to identify the organic matter, mineralogy, pore size distribution, pore type, pore geometry of clay minerals or cement, and crystalline structures of other minerals.

3. RESULTS AND DISCUSSION

3.1. Thin section analysis

The eleven samples have been analyzed by petrology (thin section). The six samples are shale, and five samples are limestone. Those samples are composed of clay matrix, organic matter, calcite grain and cement, quartz, and another mineral, mostly calcite cement and calcite grain, and the percentage of those minerals is given in the comparison chart to aid in the visual estimation of the percentage.

A. Limestone

The five sample of limestone have been analysis by thin section. There are composed of carbonated mud, calcite grain, fracture calcite, a small amount of quartz grain, and the micrite cement (mud). These limestone samples are classified into mudstone according to mud-supported and grains less than 10% and wackestone is classifie by mud-supported and grain more than 10 % in limestone [8]. After that, the result has to be used a microscope for the analysis of thin sections.

Samples PTH-A5, PTH-C3, and PTH-E4 are mainly composed of calcite grain, quartz mineral (78.65%–81.43%), carbonate mud (clay mineral) (18.57%–21.35%), some organic matter, and fossils. Calcite has a fine to very fine grain, a full color, a round to subangular shape, and is covered by clay (Figure 2). Quartz mineral change color from white to gray in XPL by microscope with a medium grain and a round shape. Clay mineral (mud) is mud (particles of clay and fine silt size, less than 20 microns) (Dunham Classification) and filled between quartz grain, calcite grain, and some fossil. Fossils have a specific shape filled by calcite and some part mixed with clay, ranging from sub-round to subangular in grain shape. After I had to finish analyzing the sample under the microscope, the result showed about the mud-support is more than 10 percentage grains [8] .

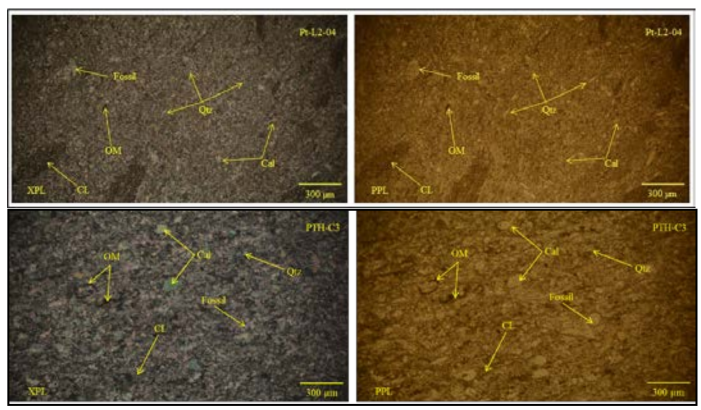

Figure 2 The Thin section of sample PTH-A5 and PTH-E4 under microscope using Plane polarized light and Cross-polarized light. Qtz: Quartz, Cal: Calcite grain, Cl: Clay mineral OM: Organic matter and Fossil.

B. Shale

The sample of calcareous shale has been analyzed. They are composed of clay matrix, organic matter, calcite grain and cement, quartz, and another mineral, mostly calcite cement and calcite grain. Particular component (silica-, carbonate-, and clay-dominated lithotypes) (Figure 3). Sample used for thin section of calcareous shale are mainly composed of calcite grain, quartz grain, organic matter, calcite veins, and clay minerals. Calcite is fine grain and has a full color in XPL and calcite is filed in veins with coarse grains or fracture of the sample. Quartz minerals are changing color from white to gray, and some of the minerals in quartz are changing from white to black under a microscope with a specific shape. Clay minerals are filled between quartz grains, calcite grains, and some fossils without a specific shape as cement. Fossils have a specific shape filled by calcite and some part mixed with clay, and they are sub-round to subangular in grain shape (Figure 3). After I had to finish analyzing the samples and plotting the data to Ternary Plot, the name of the sample is identified as clay-rich carbonate mudstone (Figure 3).

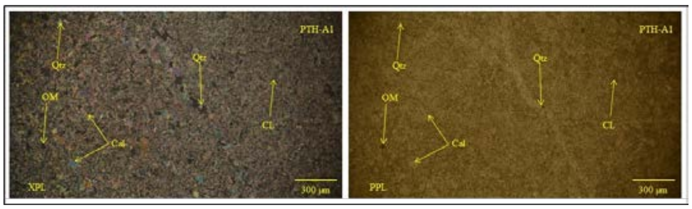

Figure 3 The Thin section of sample PTH-A1 and Pt-L3-01 under microscope using Plane polarized light and Cross-polarized light. Qtz: Quartz, Cal: Calcite grain, Cl: Clay mineral OM: Organic matter and Fossil.

After observation under microscope, the main minerals percentages for all Limestone and calcareous shale samples in Phom Thom Formations are plotted in ternary plot of shale classification to identify lithology type (Figure 4 A) [9].

It is clear to conform the name of the sample that we got from the thin section, so the result of chemically analyze the XRF date to plot the name of the rock types depends on Si, Ca, and Al, so another name is classifying as Limestone or Marly Limestone (Figure 4 B).

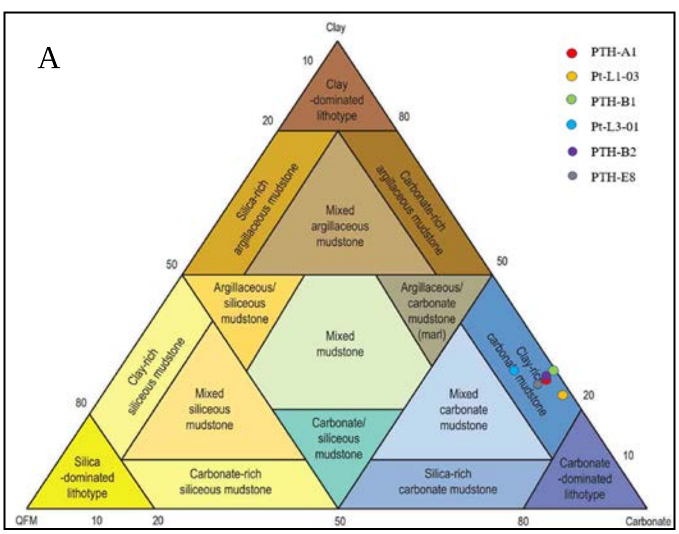

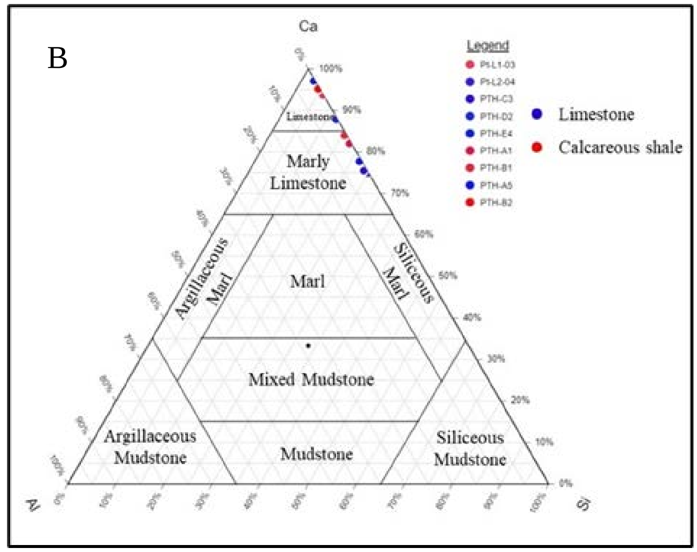

Figure 4 Ternary plot of calcareous shale samples and Ternary plot of Limestone sample Modified from Brumsack (1989) and Amendt et al. (2018).

3.2. Polish secton analysis

Vitrinite group and Inertinite group macerals were identified under incident reflected light based on their structure and reflectance color following the internationally accepted maceral classification system [10]. Additionally, fluorescence microscopy was used to investigate whether liptinite was present in the samples, which was not the case [10,11].

There are eleven samples which were selected to analysis the types of organic matter by using petrology (Polish section). Limestone and Calcareous Shale are identified as weakly to non-fluorescent with high standard deviation of liptinite reflectance that suggest presumably petroleum source rock [11]. Vitrinite, inertinite, inertodetrinite, micrinite, alginite, and pyrite have been found in these samples.

Vitrinite under a microscope, it has a shiny appearance and is derived from the cell-wall material or woody tissue of plants. which were identified by their light gray color; plant cell structures under incident white light and are also non-fluorescent (Figure 5 E).

Inertinite in the sample has elongate with yellowish white are most reflected light and poorly round (Figure 5 A and 5 B). The reflectance of the inertinite macerals begins to be exceeded by the macerals of the vitrinite group when the vitrinite and inertinite reflectance's have reached about 5%. Inertinite macerals are also characterized by their absence or lower fluorescence than vitrinite (Figure 5 B and 5 D).

Inertodetrinite is a maceral of the inertinite maceral group, occurring as discrete small inertinite fragments of varying shape. The particle size is <10 mm in the maximum dimension for compact grains and <10 mm in the minimum direction for thread-shaped fragments. In practice, particles <2 mm in diameter are referred to as micrinite [11].

Micrinite is found in some other fine-grained materials, in low-rank coals. Grey level and reflectance Pale gray to white. The reflectance is higher than that of the accompanying vitrinite but often lower than that of the other inertinite macerals (Figure 5 F). Micrinite represents especially the inertinite component of such vitrinertite that originated from resinous wood. Micrinites in limestone and shale are very small in size, with rounded to subangular grains (2 µm in diameter) [11].

Alginite can under thermal transformation at lower maturities. The lower part of the alginite is darker, and the fluorescence is more brownish than the upper part of the alginite (Figure 5 A). Alginite appears to be brown amber colored and translucent in reflected white light and oil immersion and shows strong greenish-yellow fluorescence in early mature samples.

Framboid Pyrite can be recognized throughout the investigated sample. Some of them are located within mineral matrix, while other can be also found inside the organic macerals. Framboidal pyrite occurs in some Liptinitic macerals including degraded (Figure 5 G).

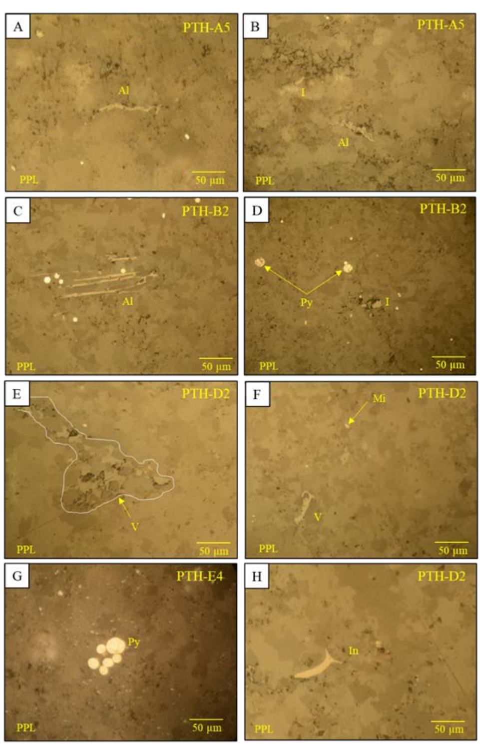

Figure 5 Photomicrographs of the Sample, shot under fluorescent light. A). Alginite (Al), B). Inertinite (I) and alginite (Al), C). Alginite (Al), D). Inertinite (I) and Pyrite framboids (Py), E). vitrinite (V), F). Vitrinite (v) and Micrinite (Mi) G). Pyrite framboids (Py) H). Inertodetrinite (In).

After getting the result from the polish section, all the organic materials that detected in the sample is potential for petroleum source rock and know about the history of the environment for source rock deposits.

3.3 X-ray Fluorescence (XRF)

X-ray fluorescence (XRF) spectroscopy is increasingly the analytical tool of choice for the direct measurement of the concentration of atomic elements in a wide range of materials. Seven sample were selected for XRF analysis (4 sample is limestone and 3 sample is calcareous shale). The chemical got from the XRF method have shown depositional environment of the sample that select to do in lab such as Ca and Mg is the chemical of calcite mineral, for Si is the chemical of quartz, etc. The range of Ca concentration is 51.8906 to 55.5685% with a mean value of 53.7295%. The range of Si concentration 1.45 to 17.27% with a mean value of 9.36%. The range of Al concentration is 0.0162 to 0.5042% with a mean value of 0.2602%. These are the most prevalent elements (Ca, Si, and Al), which is compatible with the widespread presence of quartz, pyrite, and clay minerals [11].

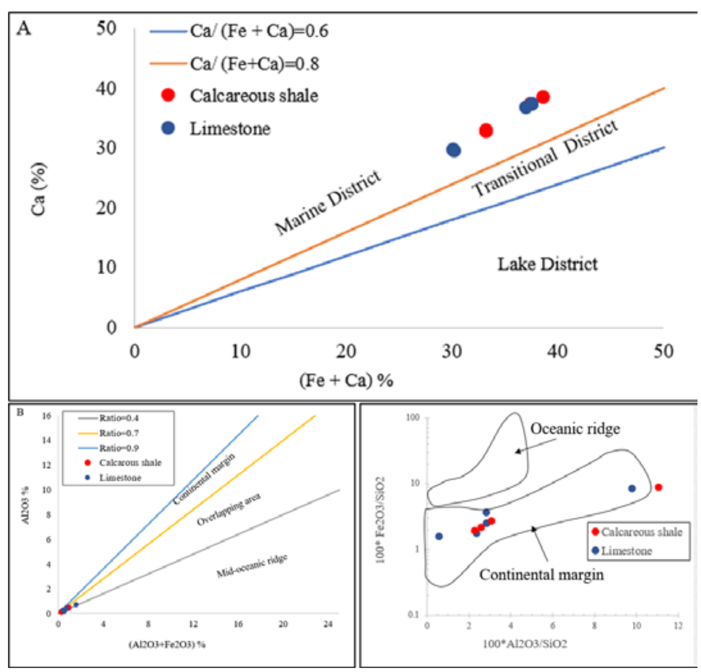

Figure 6 Plots of major and trace element in chart. The Radio Ca vs (Fe + Ca). The Radio of Al_2O_3 vs (Al_2O_3 + Fe_2O_3). The Radio of Fe_2O_3/ SiO_2 vs Al_2O_3/ SiO_2.

3.4 Scanning electron Microscope (SEM)

SEM method analyzed four samples taken from the Phnom Thom formation. The high element content like C, Ca, S, Si, O (Figure 8). The presence of Carbon (C) is show about the organic matter that is has a range value from 84.63% to 89.68%, the value of sulfide (S) is 2.19% to 6.69%, the value of Calcium (Ca) is 0.32% to 0.444% and the value of the Oxygen (O) is 2.02% to 3.27%. The organic types such as vitrinite, alginite, inertinite, and Pyrite have been found in Sample under SEM analysis. Vitrinite group maceral is generate from humie substance, are dark colored complex-composition compounds derived mostly from lignin and cellulose (Figure 7). Alginite is a liptinite maceral group, Alginite can be identified under the SEM on the basis of the distinct shape of algal bodies. Alginite can be easily identified based on their distinct shapes of algal bodies [12]. Note that alginite occurs as elongated rods perpendicular to the bedding and flattened disks parallel to the bedding [13]. It is a challenging task to confidently identify organic matter types with the SEM alone because all organic matter appears black under the SEM in backscattered electron mode due to their low density [13–15]. SEM analysis was carried out to see the appearance of organic matter with high resolution microscopically. This observation will provide information on the surface topography, shape and size of organic matter [13].

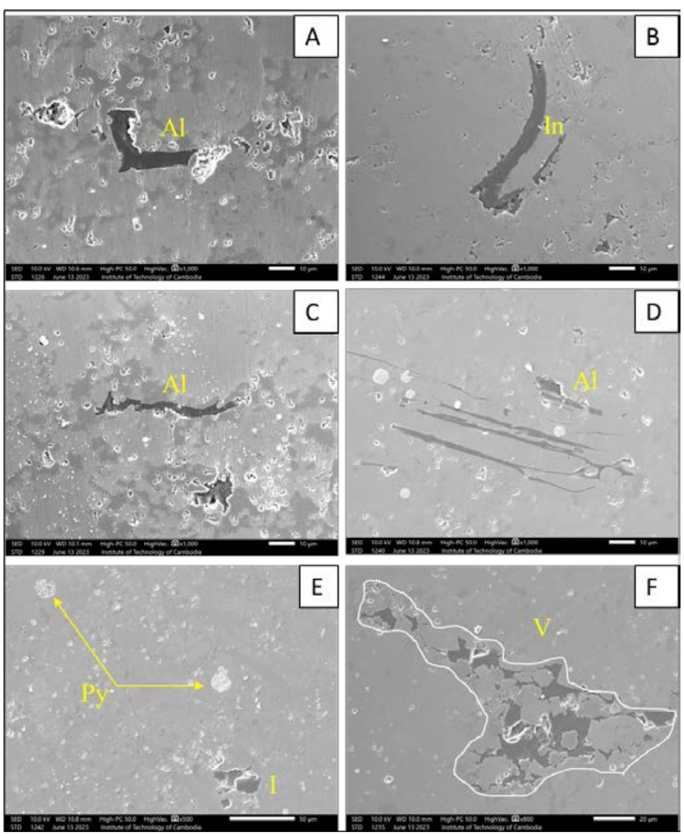

Figure 7 Scanning electron microscope result Alginite (Al), Vitrinite (V), Inertinite Pyrite Framboids (Py), Inertodetrinite (In).

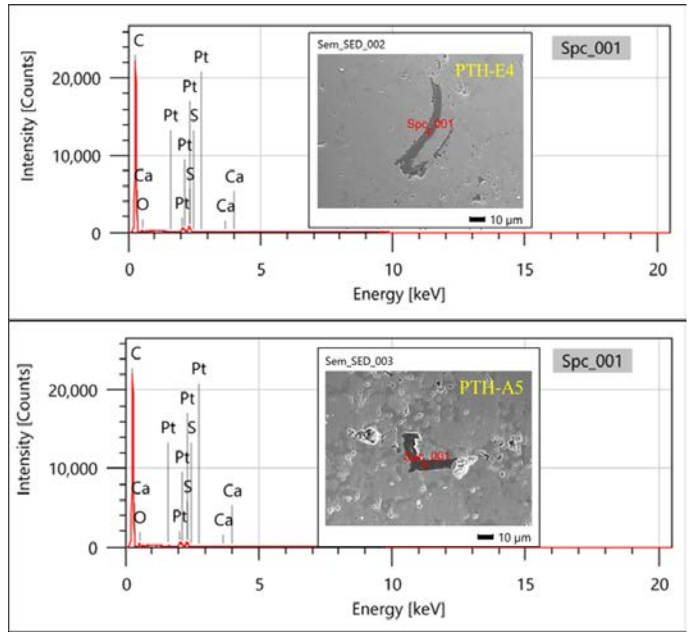

Figure 8 X-ray spectra of sample in Phnom Thom outcrop under Spektrum SEM-EDS showed that carbon content and oxygen have the dominant patterns. Moreover, its showed that high carbon content and low oxygen.

4. CONCLUSIONS

The physical characteristics of limestone and shale, organic matter types, and depositional environment have been analyzed based on field work, physical properties, and laboratory work such as petrology (thin section and polish section), X-ray fluorescence (XRF), and scanning electron microscope (SEM). limestone and calcareous shale are classified as mudstone, wackestone, (marly limestone), and clay-rich carbonate mudstone. For the organic matter types such as Vitrinite, Inertrinite,Inertodetrinite, Micrinite, alginite, and Pyrites has been found in all the samples. The depositional setting based on the Ca vs Fe + Ca radio is classify as marine district, while the Al_2O_3 Vs (Al_2O_3 + Fe_2O_3) is classifies in overlapping area. Anyway, to conform the depositional environment Fe_2O_3 / SiO_2 vs Al_2O_3 / SiO_2 is classifies as continental margin. Finally, the result of the Phnom Thom is deposit in the continental margin and shallow marine environment based on data that has been analysis from the upper. So, Phnom Thom formation is potential for hydrocarbon source rock and good located for company do the industry.

ACKNOWLEDGMENTS

First of all, I would like to express my deepest gratitude to my beloved parents and my family, who raise me well and always support me. Futhermore, I would like to thank **Laboratory-Based Education Project (LBE) of JICA** for supporting fund in this research and **Laboratory for Nanostructure and chemical analysis** for used Scanning electron microscope (SEM) analysis to support my paper research. Last but not least, I also would like to show my appreciation to my seniors for their encouragement, guidance, and motivation for me and my junior for help assisting me to do the laboratory experiments for the completion of this paper research.

REFERENCES

[1] Schaly MH. Aplicação de aprendizado de máquina na classificação de litofácies 2021.
[2] ESCAP U. ESCAP publications 1998/1999 1999.
[3] Scholle PA, Bebout DG, Moore CH. Carbonate depositional environments: AAPG Memoir 33. AAPG; 1983.
[4] He C, Ji L, Su A, Wu Y, Zhang M, Zhou S, et al. Source-rock evaluation and depositional environment of black shales in the Triassic Yanchang Formation, southern Ordos Basin, north-central China. Journal of Petroleum Science and Engineering 2019;173:899–911.
[5] Bissell HJ, Chilingar GV. Classification of sedimentary carbonate rocks. Developments in sedimentology, vol. 9, Elsevier; 1967, p. 87–168.
[6] Boggs S. Principles of sedimentology and stratigraphy 2012.
[7] Vysotsky V, Rodnikova R, Li MN. The petroleum geology of Cambodia. Journal of Petroleum Geology 1994;17:195–210.
[8] Dunham RJ. Classification of carbonate rocks according to depositional textures 1962.
[9] Gamero-Diaz H, Miller C, Lewis R. sCore: a mineralogy based classification scheme for organic mudstones, OnePetro; 2013.
[10] Sýkorová I, Pickel W, Christanis K, Wolf M, Taylor G, Flores D. Classification of huminite—ICCP System 1994. International Journal of Coal Geology 2005;62:85–106.
[11] Jahan S, Uddin A. Organic petrography and depositional environments of the upper Eocene Kopili Shale, Bengal Basin, Bangladesh. Journal of Asian Earth Sciences: X 2022;7:100092.
[12] Liu B, Schieber J, Mastalerz M. Combined SEM and reflected light petrography of organic matter in the New Albany Shale (Devonian-Mississippian) in the Illinois Basin: A perspective on organic pore development with thermal maturation. International Journal of Coal Geology 2017;184:57–72.
[13] Kwiecińska B, Pusz S, Valentine BJ. Application of electron microscopy TEM and SEM for analysis of coals, organic-rich shales and carbonaceous matter. International Journal of Coal Geology 2019;211:103203.
[14] Khatibi S, Ostadhassan M, Hackley P, Tuschel D, Abarghani A, Bubach B. Understanding organic matter heterogeneity and maturation rate by Raman spectroscopy. International Journal of Coal Geology 2019;206:46–64.
[15] Valentine BJ, Hackley PC, Hatcherian J, Yu J-J. Reflectance increase from broad beam ion milling of coals and organic-rich shales due to increased surface flatness. International Journal of Coal Geology 2019;201:86–101.

Techno-Science Research Journal 12 (Special Issue) 120-125

Content list available at ITC

Techno-Science Research Journal

Journal Homepage: www.ric.itc.edu.kh

Techno-Science Research Journal

Lithology, Hydrothermal Alteration, and Ore Mineralization of Canada Wall Porphyry Cu-Mo-Au prospect, Ratanakiri, Cambodia.

Vannak Por[1*], Sirisokha Seang[1,2], Kakda Kret[1,3], Kotaro Yonezu[4], Koichiro Watanabe[5], Jaydee Ammugauan[6], Dennis Ouellette[6], Oy Kimhouy[1], and Chea Monyneath[1]

[1] *Faculty of Geo-Resources and Geotechnical Engineering, Institute of Technology of Cambodia, Russian Federation Blvd., P.O. Box 86, Phnom Penh, Cambodia*

[2] *Materials Science and Structure Unit, Research and Innovation Center, Institute of Technology of Cambodia, Russian Federation Blvd., P.O. Box 86, Phnom Penh, Cambodia*

[3] *Angkor Resources Corp, Sangkat Boeng Keng Kong 1, Phnom Penh120102, Cambodia*

Received: 22 August 2023; Accepted: 15 May 2024; Available online: August 2024

Abstract: *The Canada Wall porphyry Cu-Mo-Au project is the mineral exploration concession of Angkor Resource Crop, which is located in the Angdongmeas district, Ratanakiri Province, Cambodia. The purpose of this research is to understand the lithology, hydrothermal alteration, and mineralization in the Canada Wall project. Based on petrography thin section and X-ray fluorescence, lithology consists of granodiorite, diorite, and andesite. Based on the petrographic thin section, there are two alteration zones in this study area phyllic and potassic alteration zones. Phyllic alteration consists of quartz+sericite+pyrite±chlorite, suggesting that host rocks were altered by the hydrothermal fluid at the temperature of approximately 200ºC to 300ºC under neutral conditions. Potassic alteration consists of quartz+K-feldspar+biotite+anhydrite+sericite±chlorite±pyrite±chalcopyrite±magneittie±molydenite. Ore minerals are composed of pyrite, sphalerite, magnetite, and chalcopyrite, which occur in veins, veinlets, and dissemination. Ore mineral styles are quartz+pyrite veinlet, quartz+pyrite+chalcopyrite+magnetite+sphalerite veinlet, quartz+molybdenite +pyrite+chalcopyrite veinlet. Geochemically, the granodiorite plots within the medium-K calc-alkaline range and shows I-type affinity.*

Keywords: Ratanakiri, Porphyry, Hydrothermal alteration, Copper-molybdenite-gold.

1. INTRODUCTION

Cambodia is situated on the Indochina Terrane in Southeast Asia which rifted northward from the northwestern part of the super-continent Gondwana during the Middle Devonian [1]. Canada Wall Porphyry Cu-Mo-Au prospect Andong is located in Meas, approximately 50 kilometers east of Banlung, the provincial capital of Ratanakiri province, within Loei Fold Belt (LFB). The LFB extends in the northern part of the belt from northern Laos through Loei province and Phetchabun province central of Thailand to Sra Kaeo in southeastern Thailand and into western Cambodia. The geological composition of the LFB primarily consists of andesitic-rhyolitic volcanic rocks from the Late Permian to the Triassic period. However, recent findings have identified older magmatic rocks from the Devonian-Carboniferous and Silurian periods. The LFB hosts a variety of mineral deposits including the Cu-Au skarn deposits, Au skarn deposits, epithermal Au deposits, and epithermal Sb-Au deposits in the area around Loei, Lobburi, Phentchabun, Nakhon Sawan, and Chachoengsao province. Those provinces occur the mineral deposits such as Pu Thap Fah Au skarn deposit, Chatree epithermal Au deposit, Phu Lon Cu-Au skarn deposit, Kusa Cu-Au Deposit, Anlong Au Deposit (Rovieng, Preah Vihear in Cambodia), and Cu porphyry deposit (Tbeang Meanchey, Preah Vihear) [2].

* Corresponding author: *POR Vannak*

Email: vannakpor206@gmail.com, Tel: +855-16921 447

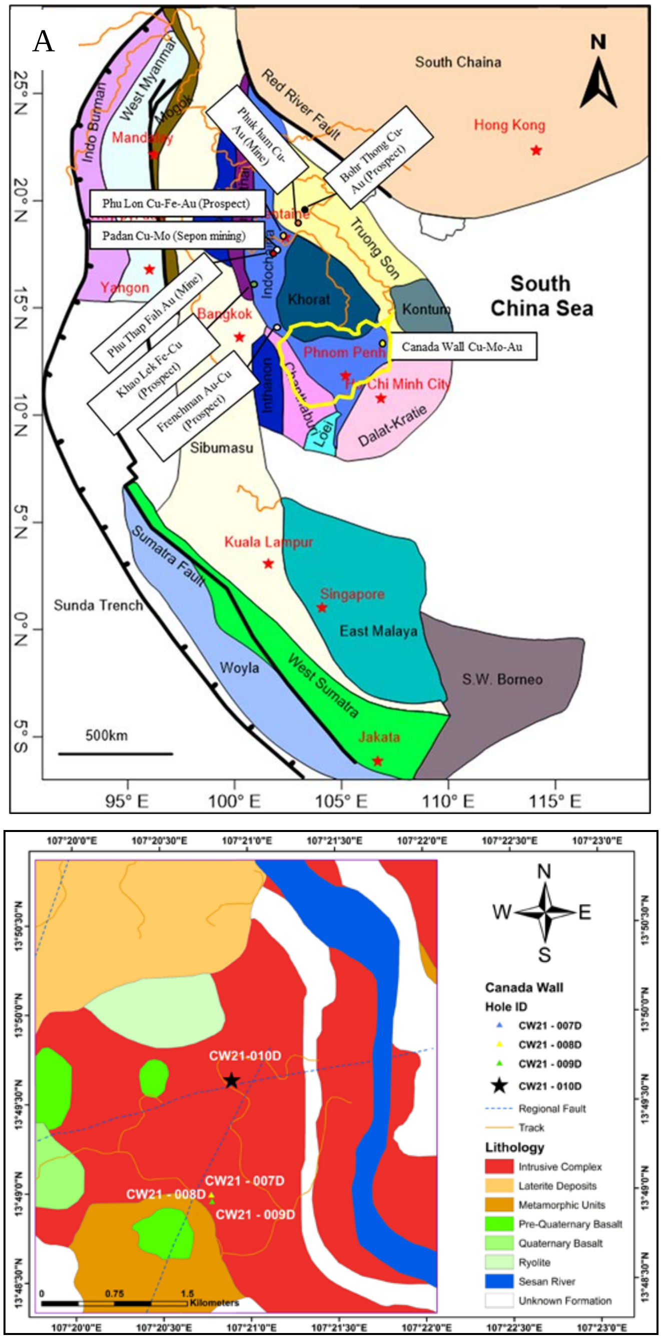

Fig. 1. (A) The regional map shows tectonic divisions of the Indochina Terrane including the mineralization belt of Cambodia, Vietnam, Laos, and Thailand [2]. (B) Location of Canada Wall Porphyry Cu-Mo-Au prospect and drill hole

2. METHODOLOGY

2.1 Research Flowchart

This study aims to study about lithology, hydrothermal alteration, and mineralization of porphyry Cu-Mo-Au deposit in Canada Wall. The study began with a literature review to understand the geology, tectonic setting, and related studies in the field. Samples were carefully selected from drill holes within the Canada Wall tenement and subsequently allocated to four distinct experiments: thin section analysis, polished section analysis, and XRF analysis.

The study starts from literature reviews such as regional studies, geological maps, previous studies, and satellite images interpreted by remote sensing. The core logging work is conducted for a week to record the geological information and sample collection. It has been divided the sample into the types of experiments fresh rock for lithology identification, altered rock for hydrothermal alteration, and ore-associated rock for ore mineralization. In the final stage, the results were interpreted (Fig. 2).

Seven (7) samples for petrographic thin sections and six (6) samples of polished sections were prepared to identify textural characteristics of the rocks, and associated ore minerals. Whole-rock major element oxides of four (4) rock samples were analyzed by X-ray fluorescence (XRF) spectroscopy. And eleven (11) core samples were conducted under and OreX-press spectrometer in terms of absorption bands of wavelength regions. All samples were analyzed at Faculty of Geo-Resources and Geotechnical Engineering, Institute of Technology of Cambodia.

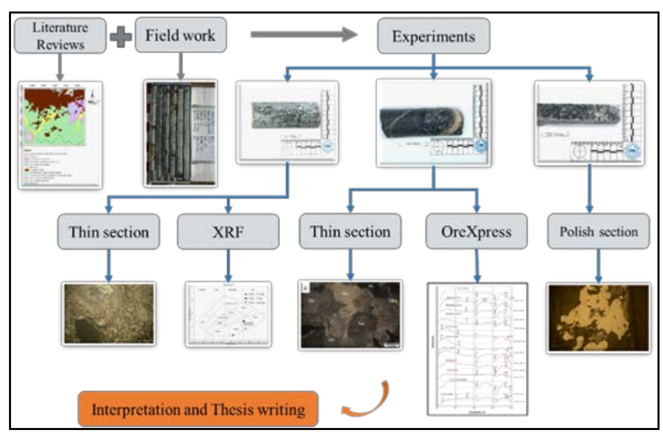

Fig. 2. Research flowchart.

3. RESULTS AND DISCUSSION

3.1. Petrographic study

The representative photographs of core samples and photomicrographs of thin sections for granodiorite and andesite porphyry recognized in this study area are shown in (Fig.3).

The granodiorite is medium to coarse-grained, dark grey, and consists of quartz, plagioclase K-feldspar, biotite, and hornblende (Fig. 3). Andesite is fine to medium-grained, dark brown. This sample comprises quartz, plagioclase, biotite, and K-feldspar. Plagioclase was partially altered to sericite (Fig. 3).

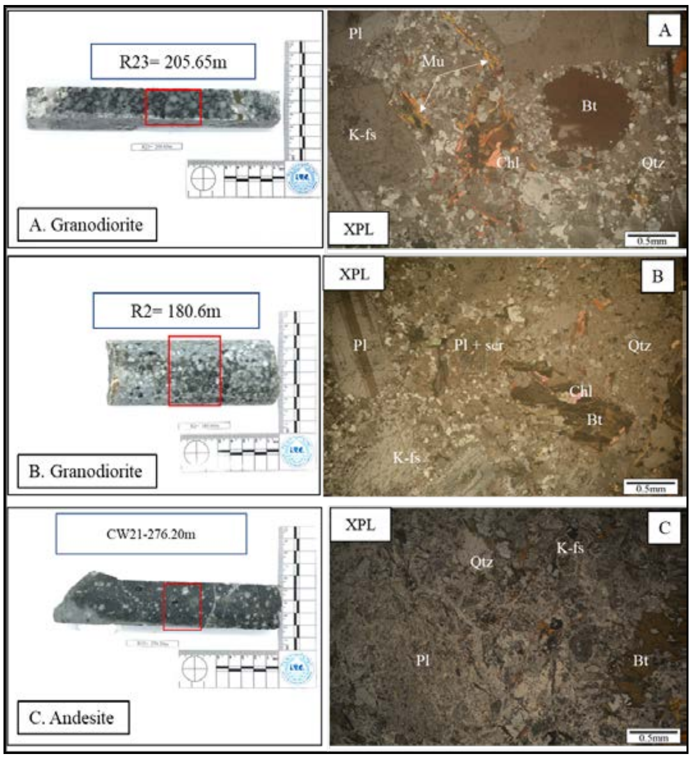

Fig. 3.Petromicrograph of granodiorite and andesite. abbreviation: Pl=plagioclase, Bt=biotite, Qtz=quartz, K-fs=k-feldspar, Chl=chlorite.

3.2. Major elements

The major element compositions from core samples are shown in Table 1. The major element In the Total-Alkali Silica (TAS) diagram (Fig. 4) [4], plutonic rock indicates that the rocks in drill hole CW-21 are classified as granodiorite (Fig. 4A). Extrusive rocks were characterized on the diagram as basaltic tracy- andesite and andesite (low silica SiO_2 content) (Fig. 4B).

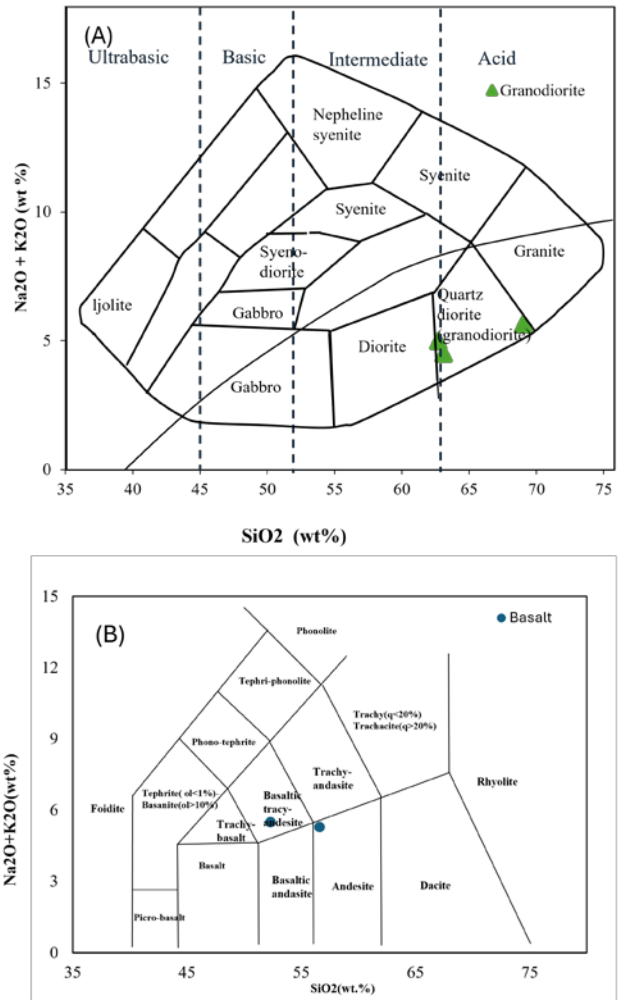

Fig. 4.(A) TAS diagram for intrusive rocks, (B) TAS diagram for Volcanic rock [4].

Intrusive rocks are medium-K calc-alkaline (Fig. 5A; [5]). Additionally, classification of rocks based on the alumina saturation index (ASI = A/CNK, $Al_2O_3/(CaO+K_2O+Na_2O)$ (Fig. 5B) indicates granodiorite are metaluminous. The plot of alumina saturation with alkalinity of the granitoid showing majority of the samples within I-type granite affinity [6,7].

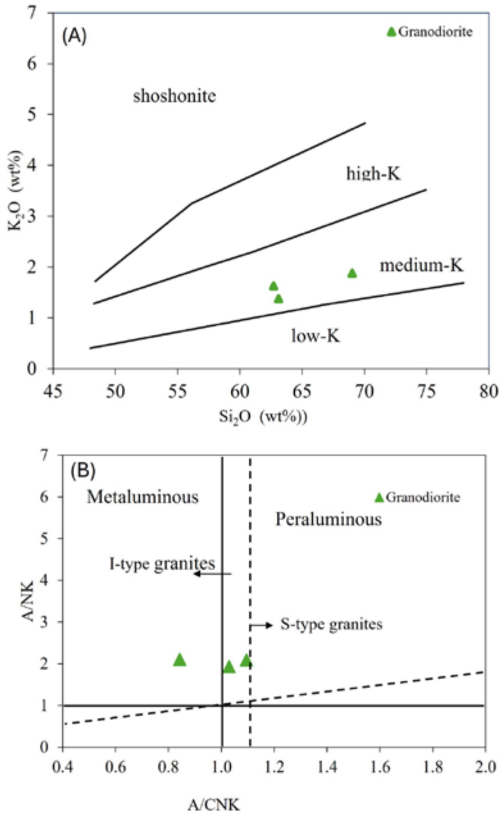

Fig. 5.(A) Diagrams showing the magma composition of intrusive rock [5]. (B) A/CNK [= molar Al_2O_3/($CaO+K_2O+Na_2O$)] versus A/NK [=molar Al_2O_3/(K_2O+Na_2O)] diagram [6,7].

Table 1 . Major elements of core samples in study area

Rock Types	Least altered Andesite	Granodio-rite	Granod-iorite	Granodiorite	Least altered Andesite
Sample ID:	47.8m	107.7m	180.7m	274.10m	310.55m
SiO2 (wt_%)	52.33	69.02	63.10	62.71	56.62
TiO2	0.91	0.28	0.26	0.26	0.42
Al2O3	15.76	15.91	13.95	15.27	18.38
Fe2O3T	7.84	2.02	3.60	3.04	5.56
MnO	0.18	0.04	0.07	0.05	0.09
MgO	6.36	1.21	1.50	1.35	2.59
CaO	4.51	3,98	5.46	3.66	5.27
Na2O	1.81	3.76	3.12	3.36	3.66
K2O	3.68	1.88	1.38	1.63	1.95
P2O5	0.38	0.03	0.17	0.21	0.41
LOI	3.21	0.76	5.16	2.95	2.30
Total	96.97	94.91	97.77	94.49	97.25
A/CNK	-	1.03	0.84	1.09	-
A/NK	-	1.94	2.11	2.09	-

3.2 Wall rocks alteration

The altered rock samples at depths of 78.35 m and 256.70 m contain alteration minerals such as sericite, quartz, and pyrite (Fig.6A-D). The veinlets and associated potassic alteration are related to granodiorite. Hydrothermal biotite and K-feldspar typically occupy the vein margins (Fig.6E, H). The fine-grained hydrothermal biotite, quartz, and K-feldspar occur as anhedral masses (Fig.6F and H).

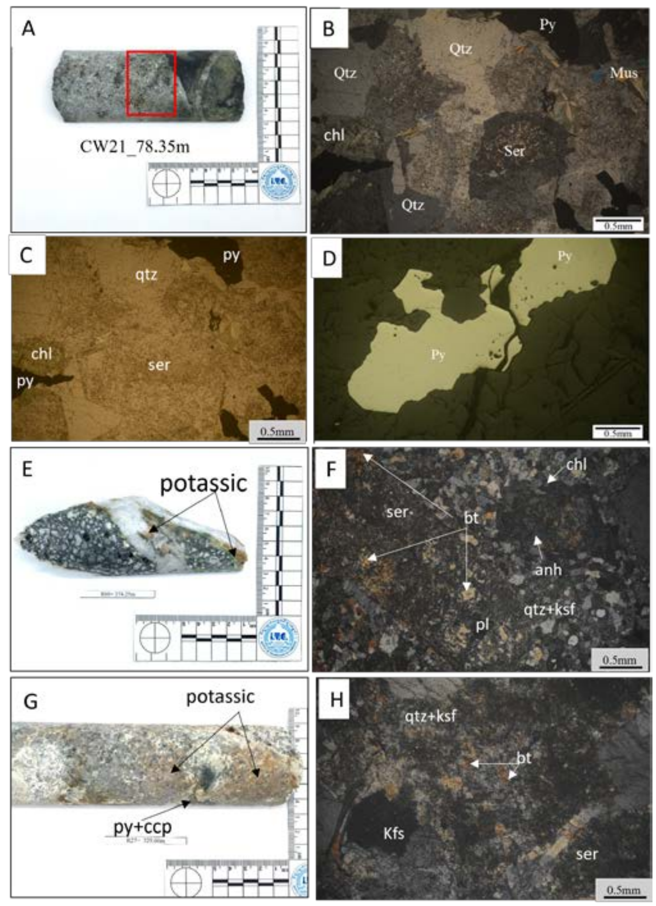

Fig.6. Representative photographs and photomicrographs of porphyry-style alteration in the study area. (A), (B), (C), and (D) granodiorite porphyry with intensive replacement by sericite-quartz-pyrite. (E), (F), (G), and (H) Replacement of granodiorite phase by potassic alteration assemblage of fine-grained quartz biotite, and an anhedral K-feldspar

Based on the OreX-press spectrometer, CW21-78.35m consists of muscovite and quartz. Muscovite is characterized by absorption features in the 1400nm and 2200nm regions [8]. The wavelength absorption bands of quartz are 750nm and 1150nm regions (Fig. 7).

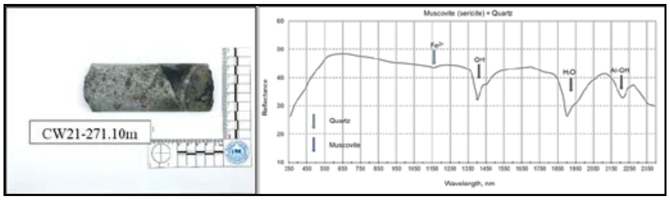

Fig. 7. Representative spectral response of common mineral in sample CW21-78.35m. The absorption bands of muscovite at wavelength 1400nm, 1900nm, and 2200 nm regions, and quartz 750nm and 1150nm regions [8].

The altered rock samples at depths of 274.50 m, 309.20 m, and 329.60 m are classified as potassic alteration. Based on the alteration minerals, this study identifies two alteration zones: phyllic and potassic alteration (Fig. 8),[9]. Phyllic alteration consists of sericite, quartz, and chlorite, suggesting that the host rocks beneath the surface were altered by hydrothermal fluids at temperatures ranging between 200°C and 350°C and under neutral pH conditions [10,11]. Potassic alteration consists of quartz, K-feldspar, biotite, anhydrite, and sericite, and includes chlorite, pyrite, chalcopyrite, magnetite, and molybdenite. Potassic alteration occurs in high-temperature phases and is located in or near the centers of porphyry intrusions [9,12].

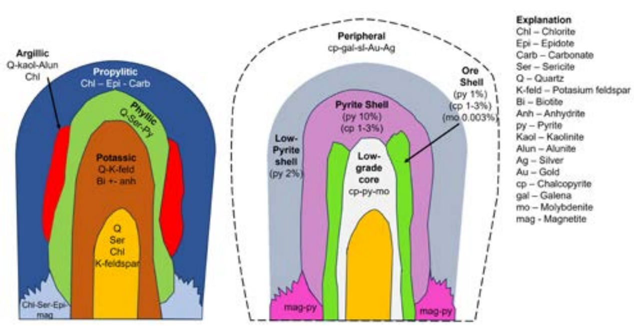

Fig. 8.Hydrothermal alteration zones associated with porphyry copper deposit [8].

3.3. Ore Mineralogy

The mineralogy includes pyrite, molybdenite, sphalerite, magnetite, and chalcopyrite. The ore minerals are disseminated in the phyllic alteration and potassic alteration, as well as in quartz veins and altered granodiorite. Gangue minerals include quartz, mica, and calcite.

Pyrite is the predominant sulfide mineral found in the study area. It occurs as vein and dissemination, associated with chalcopyrite, sphalerite, and galena (Fig. 9).

Chalcopyrite in sample demonstrated an anhedral shape in pyrite with brase-yellow and pyrite as cremation white. On the other hand, chalcopyrite is a form of gold-yellow mineral with irregular shapes, anhedral shapes, relief is medium, and has no pleochroism (Fig. 9D, F).

Sphalerite appears blackish grey under a microscope, indicating isotopism, irregular shape, and no reflectance, which occurred within pyrite, sphalerite appears as an exsolution texture (Fig. 9 B, D).

Magnetite in the sample CW21-276.2m showed grey with slight brownish and no reflectance in plane-polarized light. It has no change in brashness, is dark brown, and it's isotropic in cross-polarized light. In this sample, magnetite appears with an irregular shape and is associated with pyrite, and sphalerite (Fig. 9D).

Molybdenite has a chemical formula of MoS_2 (molybdenum disulfide). Molybdenite was found in the sample CW21-205.65m (vein) and associated with pyrite, and chalcopyrite (Fig. 9E).

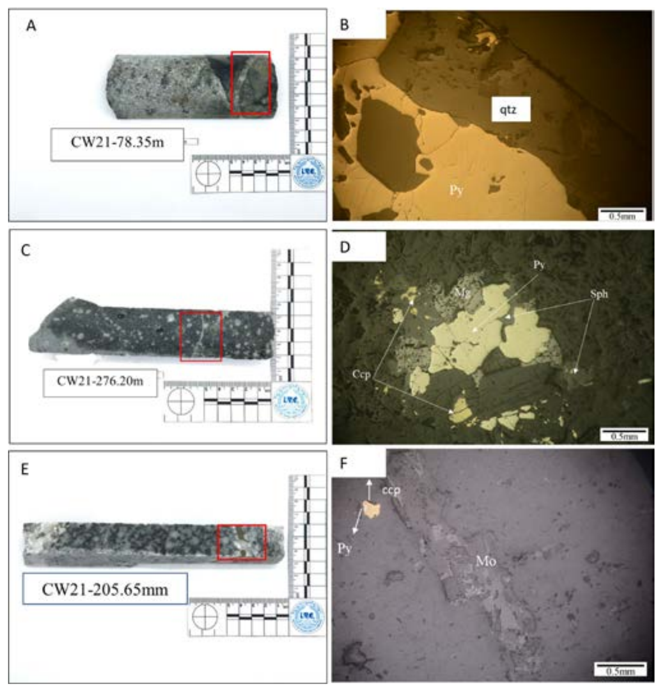

Fig. 9. (A) Representative of altered granodiorite cut by a quartz+pyrite veinlet. (B) Photomicrographs of quartz and pyrite. (C) Andesite porphyry cut by a quartz +pyrite+chalcopyrite+magnetite+sphalerite veinlet. (D) Photomicrographs of pyrite, chalcopyrite, magnetite, and sphalerite. (E) Granodiorite cut by a quartz+molybdenite +pyrite+chalcopyrite veinlet. (F) Photomicrographs of molybdenite, pyrite, and chalcopyrite.

4. CONCLUSIONS

- Common rock units in the study area (Canada Wall) are granodiorite, diorite, andesite, and mafic dyke.
- Granodiorite falls within the medium-K calc-alkaline and exhibits I-type affinity.

- There are two types of hydrothermal alteration zones: phyllic and potassic alteration zones.
- Mineralization consists of pyrite, chalcopyrite, molybdenite, magnetite, and sphalerite. The veinlet styles are quartz+pyrite veinlet, quartz+pyrite +chalcopyrite+magnetite+sphalerite veinlet, quartz+ molybdenite +pyrite+chalcopyrite veinlet.
- This research provides a comprehensive understanding of the lithology, hydrothermal alteration, and ore mineralization within the Canada Wall Porphyry Cu-Mo-Au prospect, aiding in the development of geological models for the exploration company.

ACKNOWLEDGEMENTS

I gratefully acknowledge the support of the Laboratory-Based Education (LBE) promoted by the Project for Strengthening Engineering Education and Research for Industrial Development in Cambodia, Institute of Technology of Cambodia (ITC), and Department of Geology, Ministry of Mines and Energy, Cambodia.
We extend our heartfelt gratitude to Mr. Mike Weeks, Chairman of Angkor Gold, for graciously permitting and supporting our field research in the Canada Wall Porphyry Cu-Mo-Au deposit, Ratanakiri, Cambodia.

REFERENCES

[1] Metcalfe, I. (2013). Tectonic evolution of the Malay Peninsula. Journal of Asian Earth Sciences, 76, 195-213.
[2] Zaw, K., Meffre, S., Lai, C. K., Burrett, C., Santosh, M., Graham, I., ... & Cromie, P. (2014). Tectonics and metallogeny of mainland Southeast Asia—a review and contribution. Gondwana Research, 26(1), 5-30.
[3] Le Bas, M. J., & Streckeisen, A. L. (1991). The IUGS systematics of igneous rocks. Journal of the Geological Society, 148(5), 825-833.
[4] BAS, M. L., Maitre, R. L., Streckeisen, A., Zanettin, B., & IUGS Sub commission on the Systematics of Igneous Rocks. (1986). A chemical classification of volcanic rocks based on the total alkali-silica diagram. Journal of petrology, 27(3), 745-750.
[5] Peccerillo, A., & Taylor, S. R. (1976). Geochemistry of Eocene calc-alkaline volcanic rocks from the Kastamonu area, northern Turkey. Contributions to mineralogy and petrology, 58, 63-81.
[6] Chappell, B. W., & White, A. J. R. (1992). I-and S-type granites in the Lachlan Fold Belt. Earth and Environmental Science Transactions of the Royal Society of Edinburgh, 83(1-2), 1-26.
[7] Maniar, P. D., & Piccoli, P. M. (1989). Tectonic discrimination of granitoids. Geological society of America bulletin, 101(5), 635-643.
[8] Duke, E. F. (1994). Near infrared spectra of muscovite, Tschermak substitution, and metamorphic reaction progress: Implications for remote sensing. Geology, 22(7), 621-624.
[9] Lowell, J. D., & Guilbert, J. M. (1970). Lateral and vertical alteration-mineralization zoning in porphyry ore deposits. Economic geology, 65(4), 373-408.
[10] Hedenquist, J. W., Arribas, A. N. T. O. N. I. O., & Gonzalez-Urien, E. (2000). Exploration for epithermal gold deposits.
[11] Corbett, G. J., & Leach, T. M. (1998). Southwest Pacific Rim gold-copper systems: structure, alteration, and mineralization. Society of Economic Geologists.
[12] Sillitoe, R. H. (1973). The tops and bottoms of porphyry copper deposits. Economic Geology, 68(6), 799-815.

Techno-Science Research Journal 12 (Special Issue) 126-133

Content list available at ITC

Techno-Science Research Journal

Journal Homepage: www.ric.itc.edu.kh

Techno-Science Research Journal

Petrography and Geochemistry of Basaltic Rock in Mondulkiri, and Ratanakiri Province, Northeast Cambodia

Chandara Seng[1], Sirisokha Seang[1,2*], Kakda Kret[1,2], Myo Kyaw Hlaing[3] ,Kotaro Yonezu[4], Koichiro Watanabe[4], Muhammad Irman Khalif Ahmad Aminuddin[5] ,and Reach Sam[6]

[1]*Faculty of Geo-resources and Geotechnical Engineering, Institute of Technology of Cambodia, Russian Federation Blvd., P.O. Box 86, Phnom Penh, Cambodia*

[2]*Research and Innovation Center, Institute of Technology of Cambodia, Russian Federation Blvd., P.O. Box 86, Phnom Penh, Cambodia*

[3]*Department of Geology, University of Yangon, Yangon, Kamayut 11041, Myanmar*

[4]*Department of Earth Resources Engineering, Kyushu University, Japan*

[5]*School of Materials and Mineral Resources Engineering, Universiti Sains Malaysia, Engineering Campus, 14300 Nibong Tebal, Penang, Malaysia.*

[6]*Angkor Resources Corp, Sangkat Boeng Keng Kong 1, Phnom Penh120102, Cambodia*

Received: 22 August 2023; Accepted: 15 May 2024; Available online: August 2024

Abstract: *Mondulkiri and Ratanakiri provinces are located in the northeast of Cambodia and are dominated by quaternary basalt. The basalts of Ratanakiri and Mondulkiri are the sources of zircon and olivine gemstones. This work aims to study the lithology, mineralogy, and geochemistry of basaltic rocks. Seven basaltic rock samples from Mondulkiri and six samples from Ratanakiri were chosen to represent the research area since they showed a variety of physical properties related to the different mineral compositions. According to mineralogical analysis of thin sections, the samples collected from Mondulkiri can be categorized into two groups: clinopyroxene-olivine basalt and olivine basalt. Conversely, the samples obtained from Ratanakiri are identified as olivine basalts. The olivine basalts consist of olivine phenocryst associated with albite, augite, cristobalite, and plagioclase as groundmass, and clinopyroxene-olivine basalts composed of olivine and clinopyroxene microphenocryst associated with plagioclase, augite, and cristobalite. Based on XRF results, basalts in both provinces have similar chemical characteristics and are plotted in AFM diagram (Na_2O+K_2O-MgO-FeO_{total}) within the transition between Tholeiitic and Calc-alkaline series. Nb×2 - Zr/4 - Y diagram discriminating between different types of Mid-ocean ridge basalt (MORB) and continental basalt shows that basalts in the study area are plotted in within-plate tholeiitic and alkali basalt.*

Keywords: Mondulkiri, Ratanakiri, geochemistry, petrography, basalt, Tholeiitic, Calc-alkaline

1. INTRODUCTION

Cambodia, along with Laos, the southern parts of Vietnam, and the eastern part of Thailand, is part of a larger tectonic unit called the Indochina Block. This block of continental crust has remained rigid, intact, and stable since the end of the Indonesian orogeny (210 Ma) as younger fold belts formed around its margins, resulting in extensive deformation of the older marine sedimentary basins [1,2,3].

* Corresponding author: *Sirisokha Seang*
Email: seangsirisokha@itc.edu.kh, Tel*: +855- 16308 415*

Southeast (SE) Asia serves as a significant source of gem corundum and zircon. Recent and paleo-alluvial gem deposits are found in Thailand, Cambodia, Vietnam, and Laos, forming a belt that extends over 12,000 km along the western Pacific continental margins, reaching from southern Australia in the south to eastern China and Russia in the north. All SE Asian deposits are associated with late Cenozoic (<30 Ma) intraplate alkaline basaltic volcanism, which is the result of onset of decompression melting and an extensional tectonic regime in SE Asia following the Himalayan orogeny [4,5]. In Southeast Asia, alkali basalt magmas erupted during the late Precambrian to early Cenozoic period, primarily along rifted blocks and folded terranes adjacent to the Indochina cratonic blocks, predominantly trending northward. Gem zircon and corundum xenocrysts, eroded from the host alkali basalts during the formation of lateritic soils, are concentrated into economically viable deposits through secondary processes [6].

Cenozoic basalts are widespread across SE Asia (Figure 1A), with ages ranging from 24 Ma to as recent as an eruption in 1923 off the Vietnamese coast near the island of Poulo Céci [7,8].In addition to gemstones, our focus extends to geoparks as significant natural landmarks. Geoparks represent areas where remarkable geological heritage intersects with sustainable development goals, achieved through conservation, education, interpretation, and nature-based tourism. While international geological significance is a key criterion for Geopark designation, it is not the sole qualifier. Geoparks aim to elucidate, cultivate, and celebrate the intricate connections between geological heritage and all facets of natural and cultural heritage within an area. This endeavor serves to reestablish a harmonious relationship between human society and our planet, honoring how Earth's 4,600-million-year history has profoundly influenced every aspect of human existence and societal development.

In addition to gemstones, we also prioritize the preservation of geoparks as significant natural landmarks. Geoparks represent areas where remarkable geological heritage contributes to sustainable development through conservation, education, interpretation, and nature-based tourism. While the presence of internationally significant geological features is a prerequisite for designation as a Geopark, this alone does not suffice. Geoparks aim to explore, develop, and highlight the interconnections between their geological heritage and all other facets of the area's natural and cultural legacies. They serve as a means of reestablishing the connection between human society and the planet, celebrating how Earth's 4,600-million-year history has profoundly influenced every aspect of our lives and societies [9]. For the study areas in Mondulkiri, situated at Bousra Waterfall and Dakdam Waterfall (Fig. 1B and C), and Ratanakiri, located at Kachanh Waterfall and Cha Ong Waterfall (Fig. 1D and E), to attain Geopark status, they must possess a geological heritage of international significance. Such significance may stem from exceptional natural beauty, significant contributions to scientific research, or substantial educational value.

In this study, the location of our research is covered in two provinces including Mondulkiri and Ratanakiri province of Cambodia (Fig. 1D).

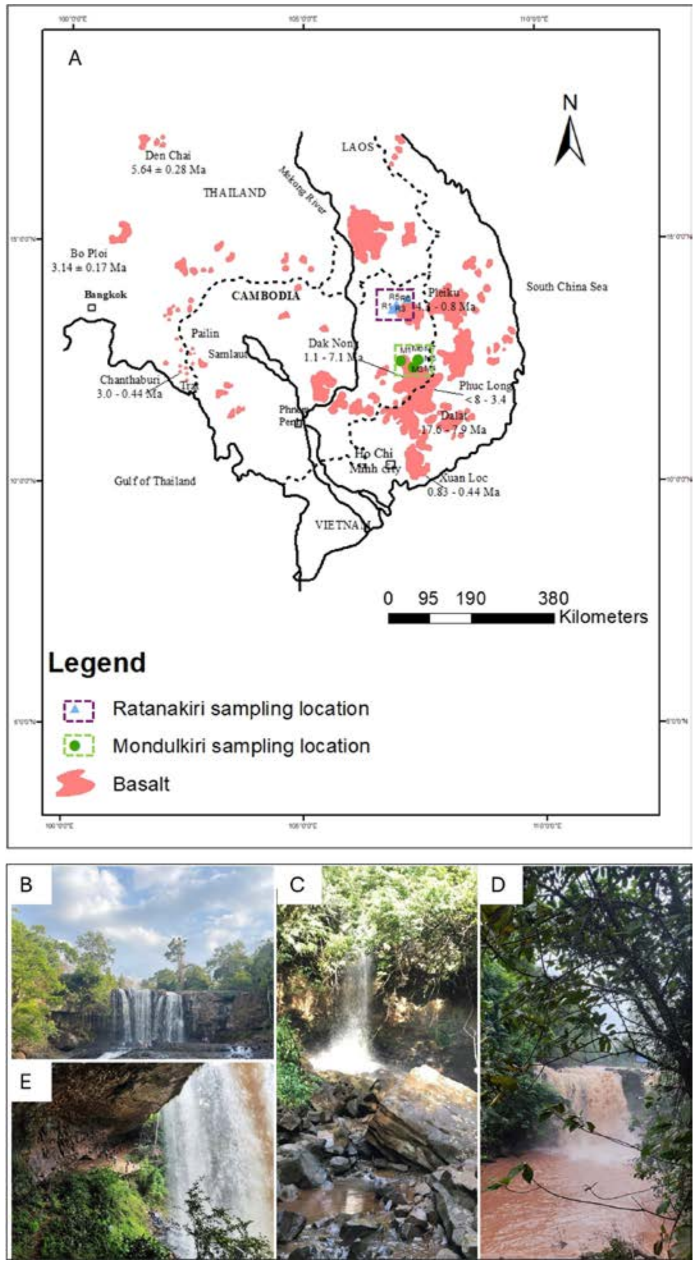

Fig. 1.(A) Basalt map in Southeast Asia with their respective age modified from [10], (B) Bousra Waterfall (C) Dakdam Waterfall, (D) Kachanh Waterfall, and (E) Cha Ong Waterfall

1.1 Geology of study area

Mondulkiri is a province in eastern Cambodia, with a total area of around 14,288 km^2. It shares borders with Kratie province to the west, Ratanakiri to the north, and Vietnam to the east and south. Mondulkiri Province is rich in deposits of minerals, mostly gold and bauxite, as a result of relatively recent tectonic and volcanic activity. In the valleys, there is a gemstone called "Peridot" which is light green and high in magnesium. Quaternary basalts are the name for the basaltic rocks found at this study location (**Fig. 2**).

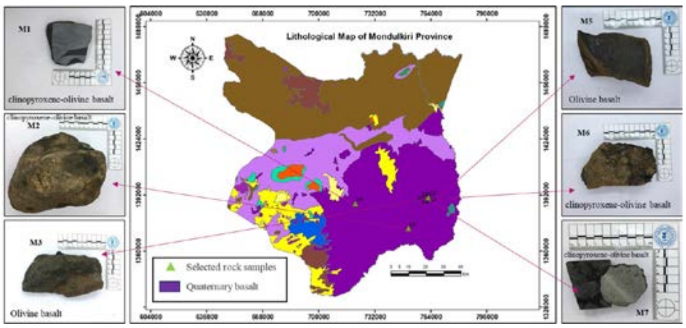

Fig. 2.Selected rock samples in Mondulkiri province

Ratanakiri is situated on the north-east plateau (approx. altitude around 200-400 m), 636 km from Phnom Penh. It borders Vietnam to the east, Laos PDR to the North, Steung Treng province to the west, and Mondulkiri to the south. The total area of Ratanakiri is about 10,782 km^2. Quaternary basaltic rocks cover approximately 10,000 km^2 of the country and overlie Quaternary alluvium and Mesozoic sediments. Two distinctly larger basaltic areas are found in Ratanakiri province and comprise the fifth largest basaltic plateau in Indochina: (1) the Bokeo plateau is located between the Sre Pok and the Sesan rivers, herein referred to as the Ratanakiri Volcanic Province (RVP), and it is host to xenocrystic gem zircon deposits and (2) the smaller, zircon-free Ban Chay plateau, northeast of Bokeo and north of the Sesan river near the Vietnamese border
Two notably expansive basaltic regions are situated within Ratanakiri province, constituting the fifth-largest basaltic plateau in Indochina. Firstly, the Bokeo plateau, positioned amidst the Sre Pok and the Sesan rivers, recognized as the Ratanakiri Volcanic Province (RVP), encompasses xenocrystic gem zircon deposits. Secondly, the smaller Ban Chay plateau, devoid of zircon, lies to the northeast of Bokeo and north of the Sesan River, in proximity to the Vietnamese border [10]. Basaltic rocks in this study were collected from an area also known as Quaternary basalts (**Fig. 3**).

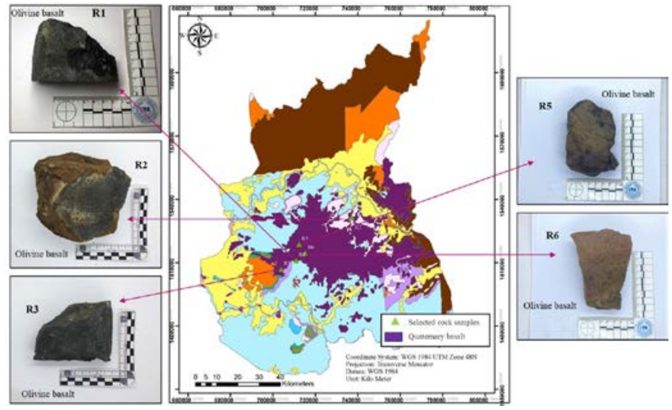

Fig. 3.Selected rock samples in Ratanakiri province

2. METHODOLOGY

Seven samples were gathered during fieldwork in Mondulkiri, while six samples were collected in Ratanakiri province to represent the rock formations in the study area. Three methods including petrography thin section, X-ray diffraction, and X-ray fluorescence, were used in this study.

2.1. Petrography analysis

Thirteen representative samples were collected from Mondulkiri and Ratanakiri provinces for petrographic analysis to identify the mineral composition and confirm the rock type. The samples were prepared for petrographic analysis under a transmitted light microscope with a standard thickness of 30 μm. The analysis was done at the Faculty of Geo-resources and Geotechnical Engineering.

2.2. X-Ray Fluorescence (XRF)

The XRF method was used to measure the main oxide elements. For the analysis, 7 grams of powdered rock from each sample was prepared for compression with a sample holder. Major oxide elements of six rock samples were analyzed using a RIGAKU XRF apparatus at the Institute of Technology of Cambodia.

2.3. X-ray diffraction (XRD)

Bulk fraction XRD analyses were conducted to identify mineral composition. The samples underwent grinding to achieve a powdered form, and then they were mounted onto a mount. The analysis was conducted by XRD in Kyushu University, Japan.

3. RESULTS AND DISCUSSION

3.1. Petrography

Based on petrography observation, plagioclase, olivine, and clinopyroxene are prevalent in the basaltic rocks in the study area. Following the analytical result, the rock samples were classified based on mineralogical assemblages and textures [11].

Sample M1 is dark-colored, fine-grained, and composed mainly of subhedral-anhedral phenocrysts of olivine (up to 1mm across), subhedral clinopyroxene (up to 0.3 mm), and elongated crystal of plagioclase (up to 0.7 mm) (Fig. 4Ci -Ai and 4-Aii).

Sample M5 is dark gray to black in color, and mainly consists of olivine (altered to iddingsite) that are enclosed by rectangular plagioclase up to 0.25 mm (Figure 4Bi & 4Bii).

Sample M6 (Fig. 4Ci & 4Cii) is brownish gray to gray in color, fine-grained, and shows phenocrysts of olivine (subhedral-anhedral) ranging from 0.2 to 0.4 mm, clinopyroxene (subhedral) about 0.4 mm, whereas the majority of the groundmass is made up of plagioclase (euhedral).

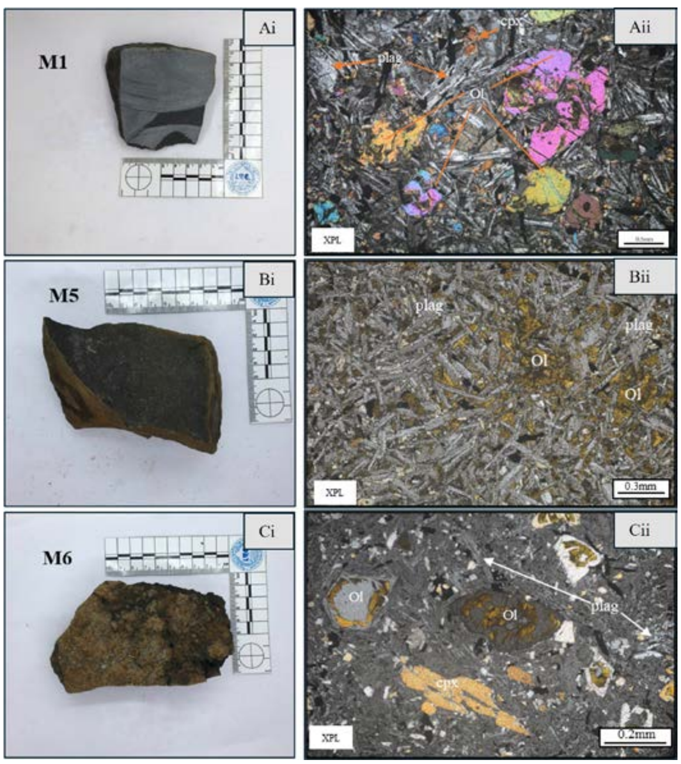

Fig. 4. Hand specimen of samples from Mondulkiri (Ai), (Bi), (Ci), and their respective photomicrographs (Aii), (Bii), (Cii) under cross-polarized light (XPL).

R1 (Figure 5-Ai) is gray to black in color and fine-grained. It shows large to medium and irregularly shaped crystals in (Fig. 5-Ai) that were identified as olivine (up to 0.3 mm) which are enclosed by a groundmass of plagioclase feldspar, and olivine (Fig. 5-Aii).

Sample R2 (Fig. 5-Bi), based on the hand-specimen observation and microscopic observation, is also a basalt. The sample is dark gray in color, fine-grained, and shows phenocrysts of olivine crystal up to 1 mm, and ehendral plagioclase up to 0.3mm (Fig. 5-Bii).

Sample R3 (Fig. 5-Ci), based on the hand-specimen observation and microscopic observation, basalt is dark gray to black in color and fine-grained and shows groundmass of plagioclase feldspar, and olivine up to 0.4 mm (Figure 5Cii).

Samples from Mondulkiri province were as olivine basalts (M3, M4, and M5) and clinopyroxene-olivine basalts (M1, M2, M6, and M7). All Samples from Ratanakiri were classified as olivine basalt. Although, Ratanakiri's samples are classified as olivine basalts. Basalts in Mondulkiri (M3, M4, M5, M7) show similar mineralogical composition with aphanitic texture. Their aphanitic texture indicates the rapid cooling of magma. However, M1 and M6 show porphyritic texture similar to all samples in Ratanakiri which suggests two stages of magma cooling. The large crystal grains, which have a diameter of 0.5 to 2 mm, were formed during the initial stage of the magma's slow cooling deep inside the crust. The lava cooled quickly in the last stage at a relatively shallower depth or when it erupted from a volcano, forming the fine grains that are often invisible to the naked eye and are known as the groundmass [11].

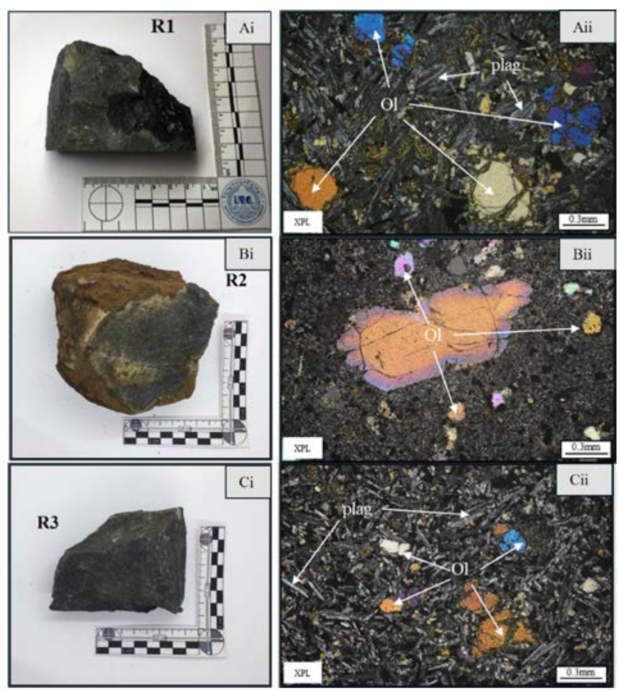

Fig. 5. Hand specimen of samples from Ratanakiri (Ai), (Ci), (Ei), and their photomicrographs (Aii), (Bii), (Cii) under cross-polarized light (XPL)

3.2 XRD analysis

Five samples were analyzed by XRD to identify mineral composition in basalts from Mondulkiri province and three samples from Ratanakiri province. The mineralogy of samples is shown in Table 1. Based on XRD analysis, these basalts mainly consist of plagioclase, olivine group, pyroxene group, quartz, cristobalite, zeolite group, chlorite, and smectite. Augite and fassaite, forsterite, and natrolite are from the pyroxene group, olivine group, and zeolite group, respectively (Fig. 6 and Fig. 7)

Table 1.Mineralogy of samples by XRD and petrography

Sample	Mineralogy by XRD	Mineralogy by Petrography Thin Section
M1	Plagioclase,Feldspar,Fassaite,Forsterite,Quartz, Critobalite	Plagioclase, Olivene, Clinopyroxene
M2	Albite, Anthophyllite, Forsterite, Fassaite	Clinopyroxene
M3	Plagioclase, Feldspar,Augite, Forsterite, Quartz	Plagioclase, Olivine
M4	Plagioclase, Feldspar,Cristobalite, Forsterite	Plagioclase, Olivine
M6	Plagioclase,Feldspar,Augite, Forsterite, Quartz, Cristobalite, Natrolite,Smectite	Plagioclase, Olivine, Clinopyroxene
R1	Anorthite, Diopside, Forsterite	Plagioclage, Olivine
R2	Plagioclase,Augite, Forsterite, Quartz, Feldspar, Cristobalite	Plagioclage, Olivine
R3	Plagioclase,Augite, Forsterite, Quartz, Feldspar, Cristobalite, smectite	Plagioclage, Olivine

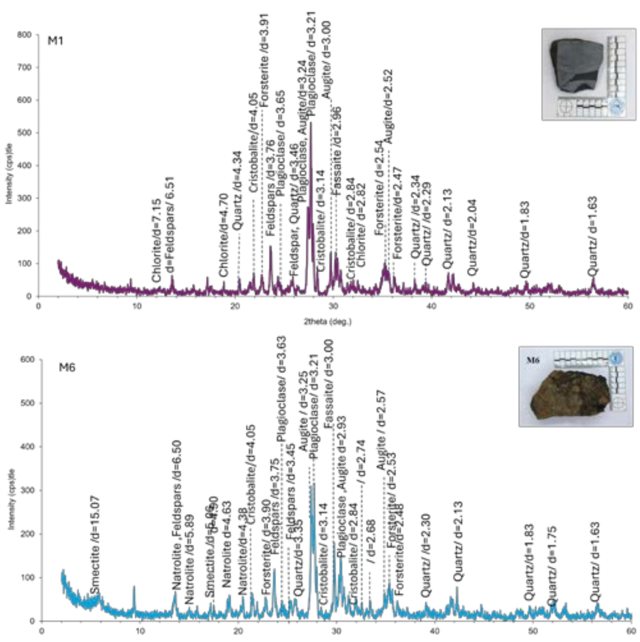

Fig. 6. Representative powder X-ray diffraction analysis diagram of samples in Mondulkiri

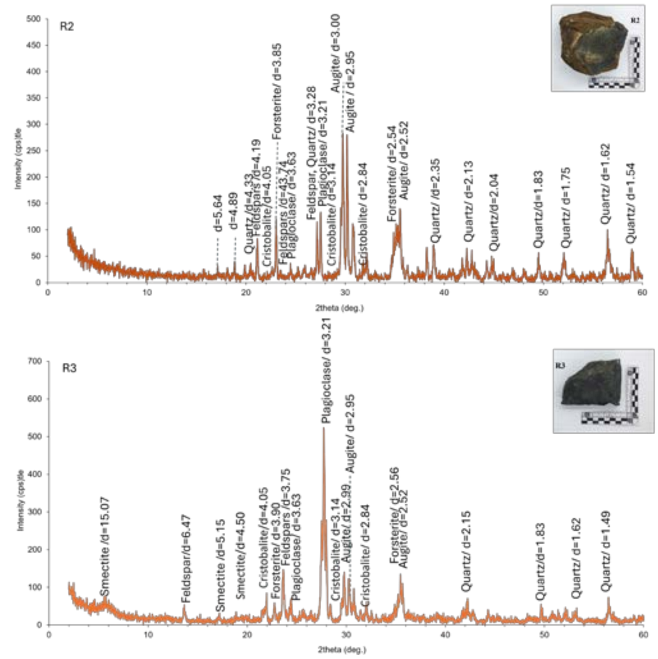

Fig. 7.Representative powder X-ray diffraction analysis diagram of samples at Ratanakiri

3.3 X-Ray Fluorescence (XRF)

Six samples of basalts from Mondulkiri and five samples from Ratanakiri province were analyzed by X-ray fluorescence analysis to get the major oxide compositions. The results of XRF analysis for samples from Mondulkiri and Ratanakiri are in Tables 2 and 3.

Table 2.Major oxide (wt.%) of basalt in Mondulkiri

	Mondulkiri					
Oxide(wt%)	M1	M2	M3	M5	M6	M7
SiO2	46.9	48.43	49.36	51.73	49.66	49.66
TiO2	2.68	2.78	2.67	1.71	1.61	1.5
Al2O3	14.2	16.77	15.02	15.88	14.67	15.15
Fe2O3	14.1	11.91	11.85	12.2	12.02	11.75
MnO	0.19	0.15	0.15	0.17	0.15	0.15
MgO	6.97	6.01	8	5.55	8.71	6
CaO	8.4	8.11	7.05	8.41	7.42	8.89
Na2O	3.03	3.19	3.07	3.32	2.99	3.08
K2O	1.62	1.95	1.75	0.39	0.95	0.38
P2O5	0.51	0.67	0.72	0.25	0.42	0.2
LOI	0.35	0.92	0.23	1.25	0.47	0.61
Total	98.95	100.89	99.87	100.86	99.07	97.37

Table 3.Major oxide (wt.%) of basalt in Ratanakiri

	Ratanakiri					
Oxide(wt%)	R1	R2	R3	R4	R5	R6
SiO2	47.38	42.19	47.87	46.97	48.32	48.41
TiO2	1.82	3.33	1.89	2.15	1.98	1.77
Al2O3	15.11	14.75	15.91	15.52	15.01	15.56
Fe2O3	12.21	12.35	11.44	11.65	11.74	12.51
MnO	0.17	0.19	0.15	0.14	0.16	0.18
MgO	8.48	9.79	7.1	7.05	6.91	5.98
CaO	8.86	8.9	8.21	8.24	8.01	8.33
Na2O	2.83	5.38	3.27	2.69	2.76	2.93
K2O	1.06	1.88	1.65	1.79	1.58	1.46
P2O5	0.48	1.15	0.67	0.66	0.53	0.4
LOI	1.3	1.05	1.53	2.79	2.7	2.4
Total	99.7	100.96	99.69	99.65	99.7	99.93

Loss on ignition (LOI) component of the samples ranges from 0.23 to 2.79 wt.%. The SiO_2, Al_2O_3, Fe_2O_3T, TiO_2, MgO, CaO and P_2O_5 concentrations range from 46.90 to 49.66 wt%, 14.20 to 16.77 wt.%, 11.85 to 14.10 wt.%, 1.50 to 2.78 wt.%, 5.55 to 8.71wt.%, 7.05 to 8.89wt.% and 0.20 to 0.72 wt.% from Mondulkiri and 46.97 to 48.41 wt% 14.75 to 15.91 wt.5, 11.44 to 12.51 wt.%, 1.77 to 3.33 wt.%, 5.98 to 9.79 wt.%, 8.01 to 8,86 wt.%, 0.40 to 1.15 wt.5 from Ratanakiri ,respectively. The total alkali concentrations from Mondulkiri and Ratanakiri are between 3.46 to 5.13 wt% and 3.89 to 4.92 wt%, respectively.

A TAS diagram for volcanic rock (Fig. 8) from [12] was used to classify rock samples from the study area. Based on this classification, all samples were classified as basalts.

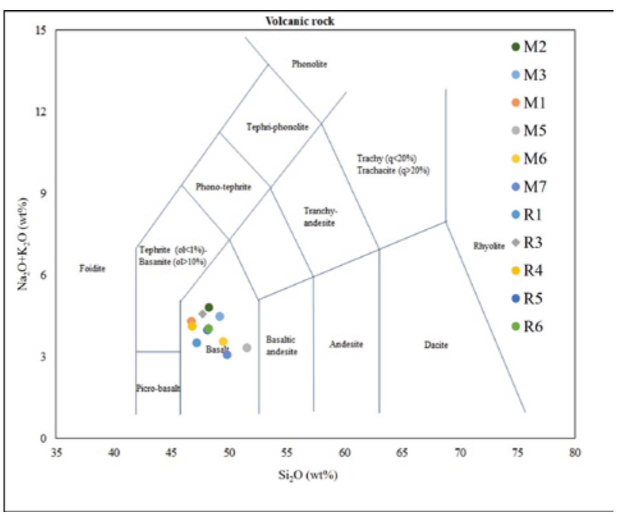

Fig. 8.TAS diagram for Volcanic rock [12]

An AFM diagram ($Na_2O + K_2O$ - MgO – FeO_{total}) [13] (Fig. 9) was used to discriminate tholeiitic and calc-alkaline series. Sample M2, M3, R2, and R3 are plotted within Calc-alkaline series, while M5, M7 were plotted within Tholeiitic. For M1, M6, R1, R4, R5, and R6 are plotted within the transition between Tholeiitic and Calc-alkaline series.

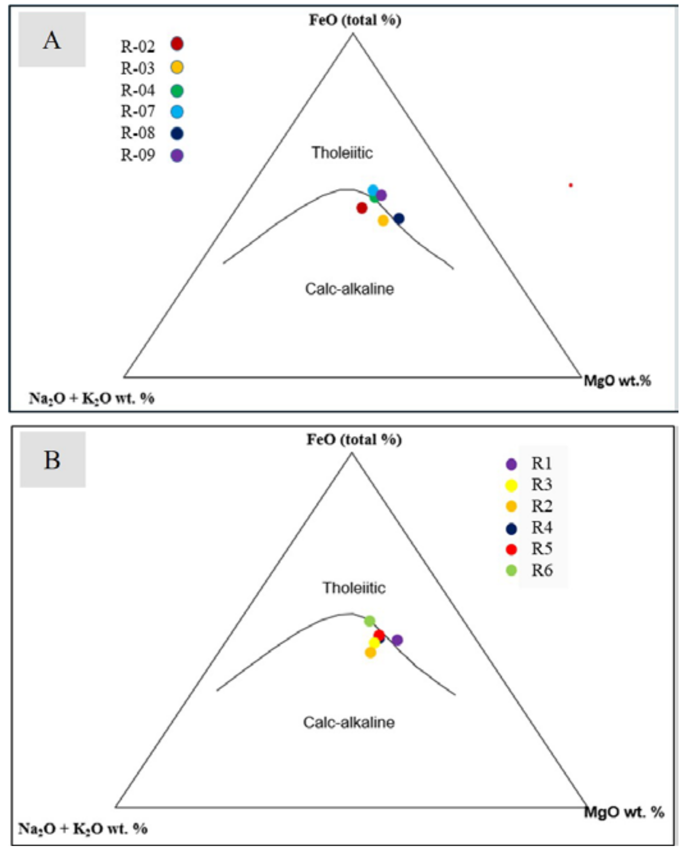

Fig. 9.The AFM diagram shows the boundary between the calc-alkaline field and the tholeiitic field [13], (A) & (B) represent results of Mondulkiri and Ratanakiri provinces, respectively

Harker diagrams of the variations in major oxide and SiO_2 contents the basaltic samples had low MnO, Na2O, P_2O_5, and K_2O contents, but they had high Al_2O_3, Fe_2O_3, TiO_2, CaO, and MgO contents (Fig. 10). The P_2O_5 concentration decreased with increasing SiO_2 content, indicating the onset of apatite crystallization. The basalt shows negative correlations of Fe_2O_3, K_2O, P_2O_5, MgO, CaO, and TiO_2 contents with SiO_2 contents. The negative correlation between CaO and SiO_2 contents, as well as the subsequent positive correlation followed by a negative correlation between Al_2O_3 and SiO_2 contents, suggests the fractional crystallization process involving clinopyroxene and plagioclase.

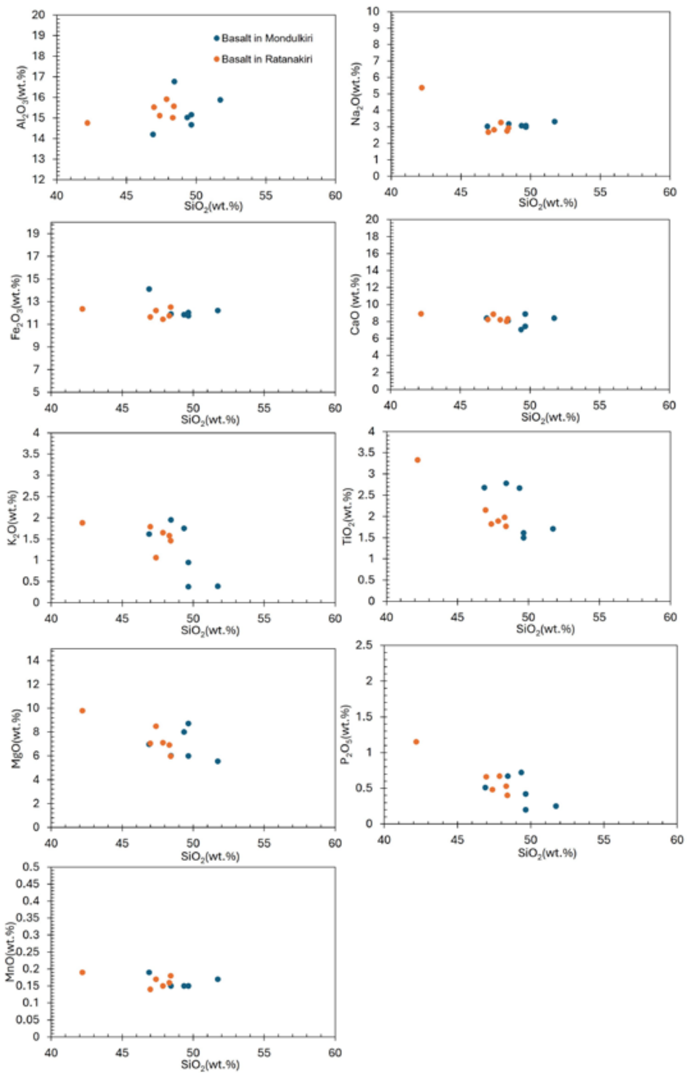

Fig. 10.Harker diagrams of the variations in major oxide and SiO2 contents[14,15]

Table 4.Summary of selected trace element (ppm) from XRF

Sample ID	Zr(ppm)	Y(ppm)	Nb(ppm)
M1	228.00	24.80	44.55
M2	235.00	26.00	36.00
M3	238.00	26.00	35.00
M5	114.00	22.00	12.00
M6	125.00	22.00	19.00
M7	102.00	19.20	11.45
R2	257.00	26.00	74.00

Nb-Zr-Y diagram [16], discriminating the types of MORB & continental tholeiites (Fig. 11), shows that the samples from Mondulkiri (M5 and M7) were plotted as within-plate tholeiitics which transitioned into within-plate alkali basalts (M1, M2, and M3). Samples from Ratanakiri (R2) were plotted as within-plate alkali basalts. The chemical properties of the Mondulkiri and Ratanakiri rocks are close to those of the basalt in Central Phetchabun, Thailand [17], which is a form of transition between Tholeiitic and alkaline basalts. In contrast, the basaltic rocks in southern Vietnam are largely Tholeiitic, with a minor contribution from alkaline basalts [18].

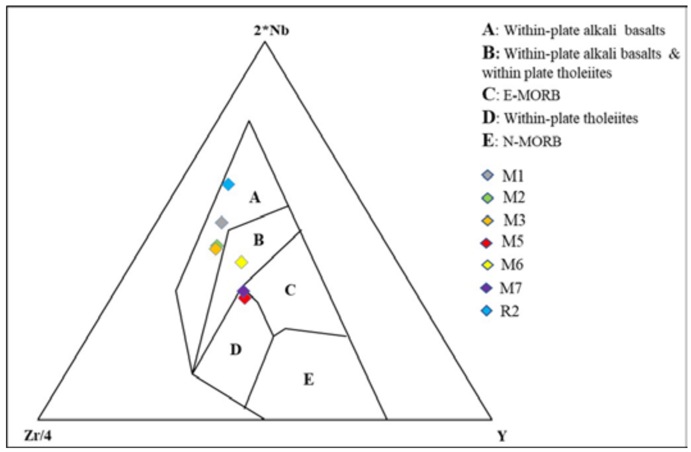

Fig. 11.Nb-Zr-Y diagram [16]

4. CONCLUSIONS

The basalts observed in the study area contain clinopyroxene and olivine as phenocrysts, along with plagioclase present as both phenocrysts and within the groundmass. Through petrographic analysis, samples from Mondulkiri were categorized into clinopyroxene-olivine basalt and olivine basalt, whereas those from Ratanakiri were identified as olivine basalts

Based on XRF results, basalts from both provinces have similar chemical characteristics and were plotted along the transition between tholeiitic and calc-alkaline series on the AFM diagram.

ACKNOWLEDGMENTS

We gratefully acknowledge the support of the Laboratory-Based Education (LBE) promoted by the Project for Strengthening Engineering Education and Research for Industrial Development in Cambodia, Institute of Technology of Cambodia (ITC), and Department of Geology, Ministry of Mines and Energy, Cambodia. We would like to express our deepest thanks to my advisor, Lecturers, seniors, and friends in the faculty for their great support.

REFERENCES

[1] Barber, A. J., Ridd, M. F., & Crow, M. J. (2011). The origin, movement, and assembly of the pre-Tertiary tectonic units of Thailand.

[2] Searle, M. P., & Morley, C. K. (2011). Tectonic and thermal evolution of Thailand in the regional context of SE Asia.

[3] Workman, D. R. (1977). Geology of Laos, Cambodia, South Vietnam, and the eastern part of Thailand.

[4] Fan, P.-F. (1995). Tectonic patterns and Cenozoic basalts in the western margin of the South China Sea.

[5] Fedorov, P. I., & Koloskov, A. V. (2005). Cenozoic volcanism of southeast Asia. PETROLOGY C/C OF PETROLOGIIA, 13(4), 352.

[6] Taylor, J. G. C., & Buravas, S. (1951). Gem deposits at Khao Ploi Waen and Bang Ka Cha, Chanthaburi Province. Geologic Reconnaissance of the Mineral Deposits of Thailand; United States Government Printing Office: Washington, WA, USA, 984, 144–148.

[7] Patte, E. Etude de l'ile des Cendres,volcan apparu au large de la côte d'Annam. Bulletin du 948 Service Géologique de l'Indochine 1925, 13, 1-19. 949 35.

[8] Saurin, E. La néotectonique de l'Indochine. Revue de géographie physique et géologie 950 dynamique 1967, 9, 143-151.

[9] UNESCO. (2015). Statutes of the International Geoscience and Geoparks Programme (IGGP).

[10] Piilonen, P. C., Sutherland, F. L., Danišík, M., Poirier, G., Valley, J. W., & Rowe, R. (2018). Zircon Xenocrysts from Cenozoic Alkaline Basalts of the Ratanakiri Volcanic Province (Cambodia), Southeast Asia—Trace Element Geochemistry, O-Hf Isotopic Composition, U-Pb and (U-Th)/He Geochronology—Revelations into the Underlying Lithospheric Mantle. Minerals, 8(12), 556.

[11] Sriwichai, M., Rachanark, B., Assavapanuvat, P., Wattanachareekul, P., Makakum, C., Watcharamai, T., Ardkham, P., Chaikam, A., Phujareanchaiwon, C., & Srisunthon, P. (2018). Preliminary Study on Petrography and Geochemistry of Basaltic Rock in Central Phetchabun, Thailand. Bulletin of Earth Sciences of Thailand, 10(1), 44–54.

[12] Bas, M. L., Maitre, R. L., Streckeisen, A., Zanettin, B., & Rocks, I. S. on the S. of I. (1986). A chemical classification of volcanic rocks based on the total alkali-silica diagram. Journal of Petrology, 27(3), 745–750.

[13] Irvine, T. N., & Baragar, W. R. A. (1971). A guide to the chemical classification of the common volcanic rocks. Canadian Journal of Earth Sciences, 8(5), 523–548.

[14] Kim, J. I., Choi, S. H., Koh, G. W., Park, J. B., & Ryu, J. S. (2019). Petrogenesis and mantle source characteristics of volcanic rocks on Jeju Island, South Korea. Lithos, 326, 476-490.

[15] Brenna, M., Cronin, S. J., Smith, I. E., Sohn, Y. K., & Maas, R. (2012). Spatio-temporal evolution of a dispersed magmatic system and its implications for volcano growth, Jeju Island Volcanic Field, Korea. Lithos, 148, 337-352.

[16] Winchester, J. A., & Floyd, P. A. (1977). Geochemical discrimination of different magma series and their differentiation products using immobile elements. Chemical Geology, 20, 325–343.

[17] Sriwichai, M., Rachanark, B., Assavapanuvat, P., Wattanachareekul, P., Makakum, C., Watcharamai, T., Ardkham, P., Chaikam, A., Phujareanchaiwon, C., & Srisunthon, P. (2018). Preliminary Study on Petrography and Geochemistry of Basaltic Rock in Central Phetchabun, Thailand. Bulletin of Earth Sciences of Thailand, 10(1), 44–54.

[18] Hoang, N., & Flower, M. (1998). Petrogenesis of Cenozoic basalts from Vietnam: Implication for origins of a 'diffuse igneous province.' Journal of Petrology, 39(3), 369–395.

Techno-Science Research Journal 12 (Special Issue) 134-139

Content list available at ITC

Techno-Science Research Journal

Journal Homepage: www.ric.itc.edu.kh

Techno-Science Research Journal

Petrographic Characteristics and Skarn-Type Gold Mineralization at the Wethey-Pheshey Area, Thabeikkyin Township, Central Myanmar

Toe Naing Oo[1*], Lucas Donny Setijadji[2], I Wayan Warmada[3]

[1]*Department of Geology, West Yangon University, Yangon, Myanmar*

[2, 3] Department of Geological Engineering, Faculty of Engineering, Gadjah Mada University, Yogyakarta, Indonesia

Received: 22 August 2023; Accepted: 15 May 2024; Available online: August 2024

Abstract: *The gold mineralization of the Wethey-Pheshey prospect area is located in the Mogok Metamorphic Belt, which is one of the largest gold belts in Myanmar. The prospect area's lithology is recognized by the occurrence of Lower Paleozoic metamorphic rocks and Middle Miocene granitic rocks of the Mogok Metamorphic Belt. This study aims to investigate the geology, characteristics of mineralogy, and genetic type of gold skarn mineralization in the research area. Detailed geological mapping and field observation were conducted to identify the geological framework as well as delineate metamorphic and granitic rock distributions. Laboratory analyses, including petrography and ore microscopy to characterize the skarn-type gold mineralization. The petrographic characteristics of the metamorphic and granitic rocks were conducted using a polarizing microscope. Meanwhile, polished sections of ore samples were studies under a reflected-light microscopes study to recognize the ore mineral assemblages. XRD analysis was conducted to reveal the skarn-type alteration minerals. The skarn-type gold mineralization occurs along the contact zone between marble and granitic rocks. The skarn-type alteration minerals include amphibole, garnet, chlorite, epidote, diopside, calcite and fosterite. The principal ore minerals in the mineralized ore veins are pyrite, sphalerite, galena, chalcopyrite and native gold. The results of the nature and characteristics of host rocks, alteration and mineralization styles, ore and gangue mineralogy and gold mineralization in the Wethey-Pheshey prospect area area classified as intrusion-related to skarn-type gold mineralization.*

Keywords: Gold-mineralization; Mogok Metamorphic Belt; Petrography; Skarn-type; Wethey-Pheshey

1. INTRODUCTION

The Wethey-Pheshey prospect area is one of the essential gold deposits from central Myanmar. It is located in Thabeikkyin Township, Mandalay Region (Fig.1). Gold exploration has been carried out not only in small-scale local gold mine production but also abundant in artisanal mining operations in the research area for three decades. This area is a segment of the Mogok Metamorphic Belt [1] which is one of the distinct geological units and metallogenic provinces in Myanmar. Based on previous studies [2,3,4] the Mogok Metamorphic Belt of gold deposit in central Myanmar is considered as mesothermal 'orogenic gold' as well as epithermal gold deposit and skarn mineralization types. The predominant rock units cropped out in this area are metamorphic and igneous rocks. They include diopside marble, calc-silicate rocks, phlogopite marble and white marble, and biotite microgranite. The high-grade metamorphic mineral assemblages within the metamorphic rocks indicate that the area has undergone high-grade regional metamorphism related to the subduction tectonic setting. Skarn-type gold mineralization occurs in white marble and diopside marble belonging to the Mogok Metamorphic Belt in the study area. Skarn mineralization is generally found along the contact between intrusion and carbonate rocks (marble) and dominated by calc-silicate mineral assemblages, such as garnet, diopside, epidote, chlorite and pyroxene, is recognized as a relatively simple rock type that is described by its mineralogy [5,6].

The Wethey-Pheshey area is recognized by extensive hydrothermal alteration. Altered rocks are occupied in the metamorphic and igneous rocks of the Lower Paleozoic and Middle Miocene age and rock types include diopside marble, phlogopite marble, white marble and biotite granite. Hydrothermal alteration types associated with skarn-type gold mineralization in the Wethey-Pheshey prospect area comprises

* Corresponding author: Toe Naing Oo
E-mail:toenaingoo.geol84@gmai.com, Tel: +959448327577;
Fax: +855-23-880-369

calc-silicate alteration, propylitization, sericitization (argillitization) and hematization [4]. However, the skarn-type gold mineralization in the Wethey-Pheshey area has not been studied systematically. Therefore, the current research work has interpreted information about, petrographic characteristics, ore mineral assemblages and characteristics of skarn-type gold mineralization in the Wethey-Pheshey area.

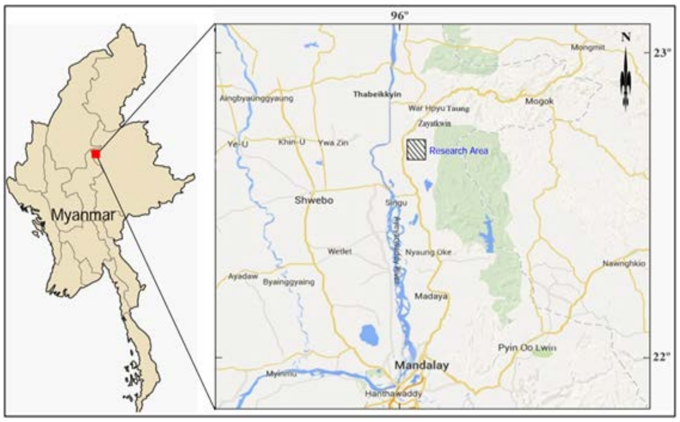

Fig.1. Location map of the study area.

2. GEOLOGIC SETTING

The Mogok Metamorphic Belt (MMB) is one of the most important mineral belts as well as distinct geological units in Myanmar which trends generally N-S in direction with large-scale folding. It is situated between the West Myanmar (Central Belt) to the west and the Shan plateau to the east (Fig.2). The well-known dextral Sagaing strike-slip Fault [7] behaves as the western boundary of the Mogok Metamorphic Belt. This belt is also the southern part of Himalayan syntaxis at the western margin of the Shan-Thai block. Along the northeastern margin of the India plate, the plate boundary marked from the Paleogene suture zone to Neogene Sagaing Fault, whereas the West Myanmar microplate has entertained some of the northward movement of India [8]. Therefore, it has been pointed out that the Mogok Metamorphic Belt was formed not only by collision in the Late Mesozoic but also by strike-slip movement in the Early Triassic [9]. This belt is characterized by the presence of gneisses, marbles, quartzite and calc-silicate rocks of Paleozoic to Mesozoic ages that were intruded by plutonic rocks such as biotite granite and syenite of Eocene to Miocene ages. To the east, Shan Plateau is a topographic high with an average elevation of about 1,000m and it mainly consists of carbonate and continental sedimentary rocks of Paleozoic to Mesozoic ages. The western margin of the Mogok Metamorphic Belt is brought together with the Central Belt which is filled with Eocene to Pliocene-Quaternary ages sediments (Fig.2)

3. METHODS

Representative ore and host rock samples were mainly collected from the ore pile on the surface, resulting from the mining excavation. Some host rock samples were collected from outcrops at and near the mining area. About thirty marble samples were collected from the Wethey-Pheshey area. Of these, 15 samples were prepared for thin sections and studied under a polarizing microscope in order to determine the mineralogical composition and textural characteristics. In addition, 5 samples were carefully selected for ore microscopy. Polished sections as well as polished thin sections of ores samples were made for selected samples and examined under the refracted light microscope for petrographic study. This study was conducted in Kyushu University, Japan. Furthermore, 10 alteration samples were also identified by XRD. This study was carried out at the Department of Geological Engineering, Gadjah Mada University, Yogyakarta, Indonesia.

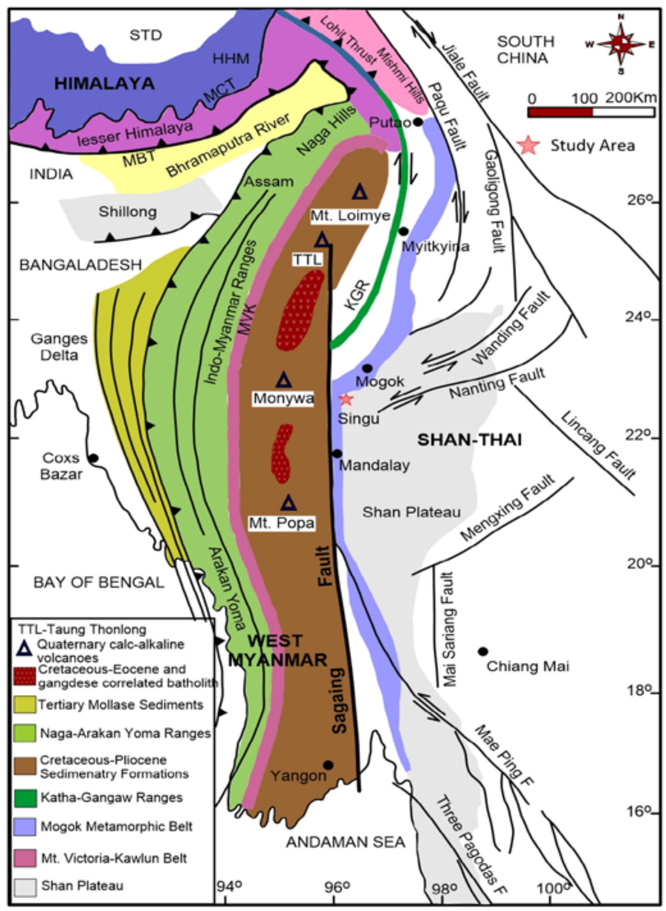

Fig.2. Simplified geologic map (modified from [10,11,12] illustrating the Mogok Metamorphic Belt and major geological units in Myanmar.

4. RESULTS AND DISCUSSION

4.1 Local Geology

The local geology of the research area is characterized by the occurrences of metamorphic and igneous rocks (Fig.3). Metamorphic rocks are extensively formed in the eastern and western parts of the research area such as a variety of marbles, calc-silicate rock, and gneiss. They are basically related to regional metamorphism and also related to contact metamorphism. The metamorphic rocks include a variety of marbles such as white marble, phlogopite marble, diopside marble, graphite marble, calc-silicate rocks, and gneiss which are widely distributed in the research area (Fig. 4).

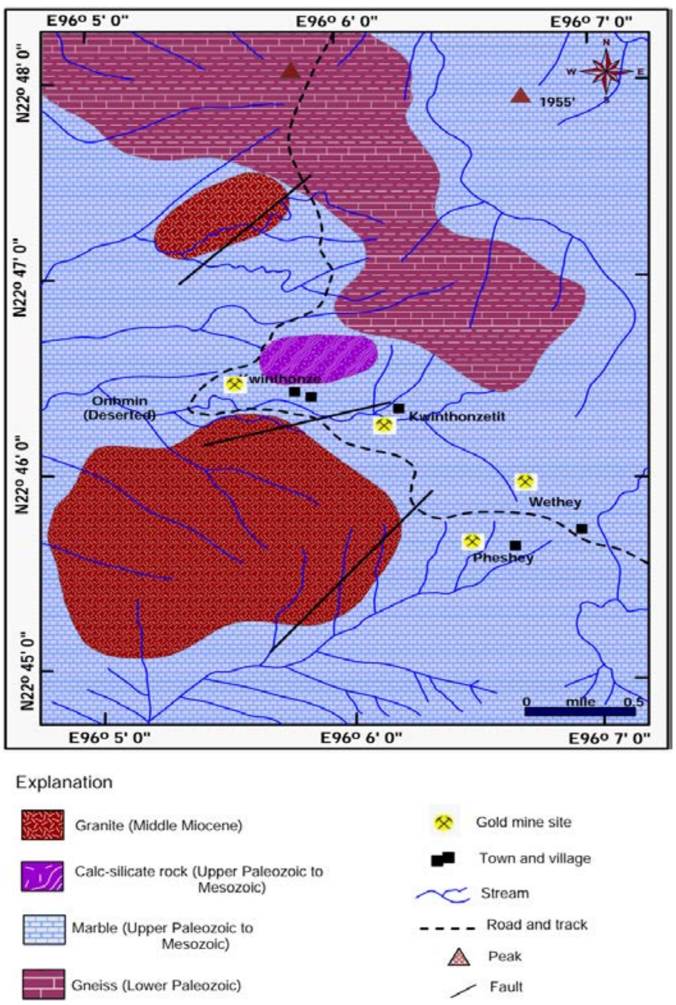

Fig.3. Geological map of the Wethey-Pheshey area.

The geological ages of these rock units are recognized as most probably Late Paleozoic to Mesozoic [3] . Metamorphic rocks are intruded by granite (Kabaing granite). Stratigraphically, gneiss is the oldest rock unit, and it is widely observed in the northern part of the research area. The igneous rock unit cropped out in the research area is mainly comprised of biotite microgranite. The igneous rock is the Eocene to Middle Miocene as a result of the dating of biotite microgranite [1]. In the middle part of the research area, a variety of plutonic igneous rocks are exposed either intrusive bodies or veins. A geological map of the Wethey-Pheshey area is shown in Fig.3. Photographs taken in the field of mineralized host rocks at the Wethey-Pheshey prospect are illustrated in Fig.4.

Fig.4. Photographs showing (a) diopside marble, (b) brass color of phlogopite marble, (c) disseminated graphite mineral in the white marble, (d) calc-silicate rock with drag fold and ridge and furrow structures, (e) nature of banded gneiss, (f) massive exposure of biotite granite from the Wethey-Pheshey area.

4.2 Petrographic Characteristics

In this study, phlogopite is one of the component minerals in phlogopite. It is found in a tabular form with a brass brown color and shows slight pleochroism (Fig.5a,b). It shows a distinct set of perfect basal cleavage. Some phlogophite flanks are bent, crenulated, and display wavy extinction due to later deformation processes. Graphite is also an important mineral in this unit which occurs as disseminated scales as well as tabular masses with a dark color (Fig.5c,d). It shows black color with metallic luster under reflected light. This mineral is found as a fissure or vein-filling mineral. Sometimes, forsterite mineral is also observed in the diopside marble unit. Mineral grains are mostly subrounded or idioblastic aggregates with conspicuous high reflective indices. Sizes are ranged from 0.5mm to 1.5mm in diameter. Intense chemical alteration is pronounced along the fracture. Between crossed Nicol (X.P.L), it shows second-order bright. Diopside occurs as rounded idioblastic to xenoblastic crystal with pale green to dark green color (Fig.5e,f). Size is ranged from 0.4 to 0.7 mm in diameter where large grains are randomly oriented. It is characterized by the occurrence of sub-rounded form, high relief, pale green to greenish pink color (Fig.5e,f). In general, the crystal grains display transverse fractures of crack probably as a result of the deformation process during and after the crystal growth. Petrographically, garnets are observed as medium-coarse-grained, subhedral to euhedral crystals. Garnet forms at high temperatures and pressure, so they typically occur in their crystals form as rounded dodecahedrons (twelve-sided) or twenty-four-sided trapezohedron (Fig.5e,f). Forsterite is mostly found as individual spots of subhedral crystals. The form of forsterites is polygonal and has a fracture and no cleavage. The low relief and second order bright (Fig.g,h).

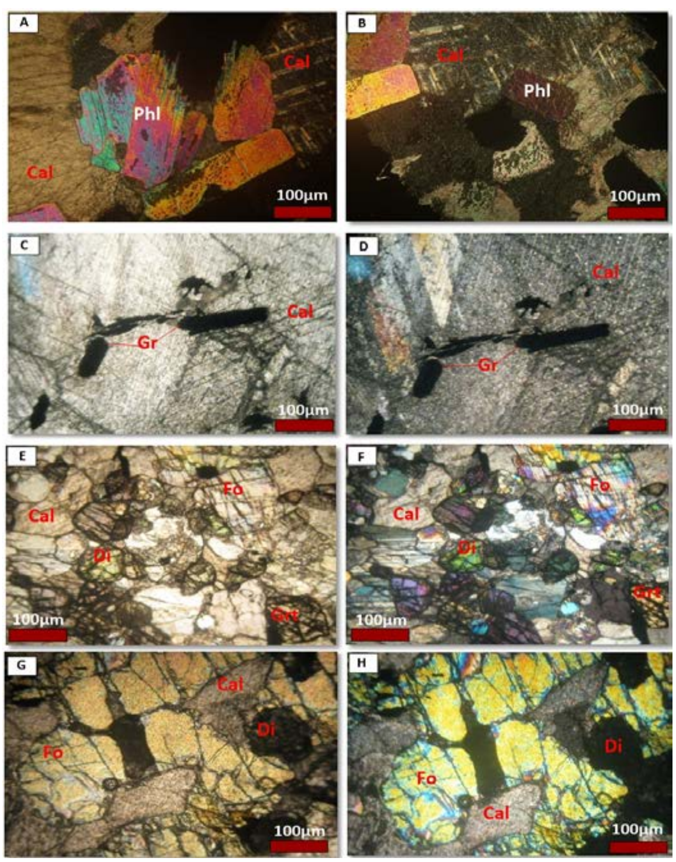

Fig.5. Photomicrograph of a representative marble host rocks showing (a,b) pink color of phlogopite and euhedral calcite with two sets of rhombohedral cleavage, (c,d) elongated dark color of graphite and euhedral calcite with two sets of cleavage, (e,f) diopside occurs as rounded idioblastic to xenoblastic crystal with pale green to dark green color, (g,h) subrounded or polygonal shape of fosterite and diopside. Cal: calcite, Phl: phlogopite, Gr: graphite, Grt: garnet, Di: diopside, Fo: forsterite.

4.3 Skarn Alteration

Based on the petrographic characteristics and XRD analysis, skarn (Calc-silicate) alterations in the Wethey-Pheshey area include silification, garnetification, pyroxinization and chloritization. Silification is the typical alteration in the skarn zone. Prograde skarn alteration is dominated by garnet and amphibole. Chloritization occurs as retrograde alteration related to skarn mineralization in the Wethey-Pheshey area. The result of the bulk rock powder XRD analysis, quartz is characterized by diffraction peaks at 4.25, 3.34, 2.45, 2.28, and 1.81Å (Fig.6a-d). Cordierite shows the basal spacing of diffraction peaks at 8.4, 3.12, and 3.0Å (Fig 6a). Amphibole has the major diffraction peaks at 4.17, 3.3, 3.12, and 2.57Å (Fig.6b) and chlorite is recognized by its major diffraction peaks at 14.4, 7.1, 4.72, 3.54Å, 14.4-14.8, 7.1, 4.75, and 3.54 Å (Fig.6c,d). Pyrite has the d-spacing at 3.12, 2.70, 2.42, 2.20 and 1.63Å whereas chalcopyrite is identified by its basal spacing of diffraction peaks at 3.02Å (Fig.6a,b,d).

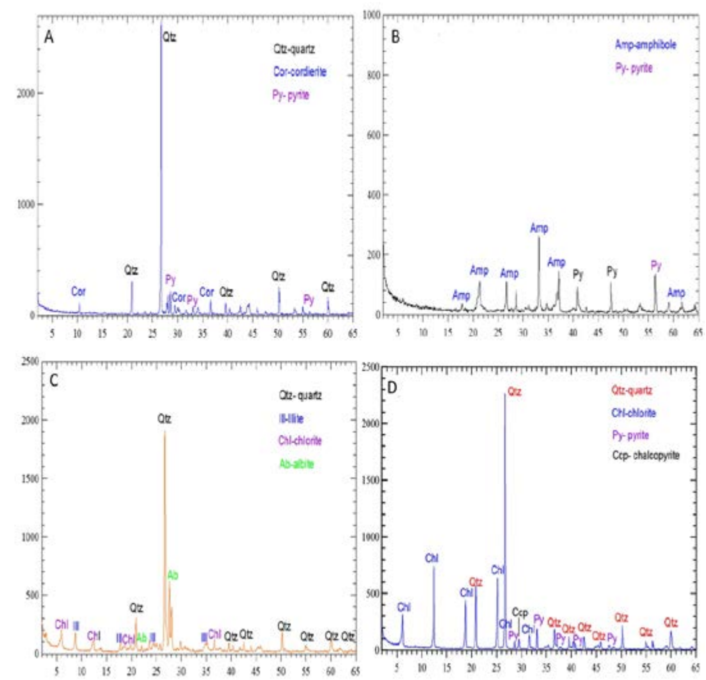

Fig.6. X-ray diffractograms of skarn alteration mineral assemblages from the Wethey-Pheshey area. Abbreviations: Qtz: quartz, Chl: chlorite, Amp: amphibole, Cor: cordierite, Al: albite, Ilt: Illite, Py: pyrite, Ccp: chalcopyrite.

4.4 Mineralization Characteristics

Gold skarn-type mineralisation in the Mogok Metamorphic Belt of the Wethey-Pheshey prospect, Thabeikkyin Township, central Myanmar is mainly hosted in white marble and diopside rocks unit (Fig.7). The principal mineralization is developed in the form of dissemination as well as fracture-filling veins (Fig.7). These veins are generally confined and belong to fractures and shear zones which are trending N-S, and NE-SW with steep dipping of about 65° to nearly vertical. These structural trends might be controlled by the movement of the Sagaing Fault system. Mineralisation is associated with alterations characterized by skarn alteration, (quartz, calcite, pyrite), argillic alteration, (illite, illite/smectite, quartz, sericite, chlorite) and propylitic alteration (chlorite, epidote, quartz, pyrite) and hematization [4]. Pyrite, chalcopyrite, galena, and sphalerite sulfide are the major primary sulfide minerals. Pyrite is the visible sulfides of the ore in marble (Fig.7c,d). The ore mineralization zone is generally capped by the oxidized zone of iron oxides. Iron oxides such as goethite and hematite are observed as supergene-oxidized ores.

The common primary ore minerals in mineralization veins include pyrite, sphalerite, galena, chalcopyrite, and native gold. On the other hand, hematite as well as goethite, are found as late supergene minerals reflecting the oxidation of primary sulfides [4]. Pyrite is the most abundant sulfide mineral in the ore body, formed over the entire period of mineralization as fine-grained massive aggregates to large euhedral grains (Fig.8). Native gold occurs as free grains or locked in the euhedral pyrite and it is intimately associated with chalcopyrite and galena (Fig.8a,b).

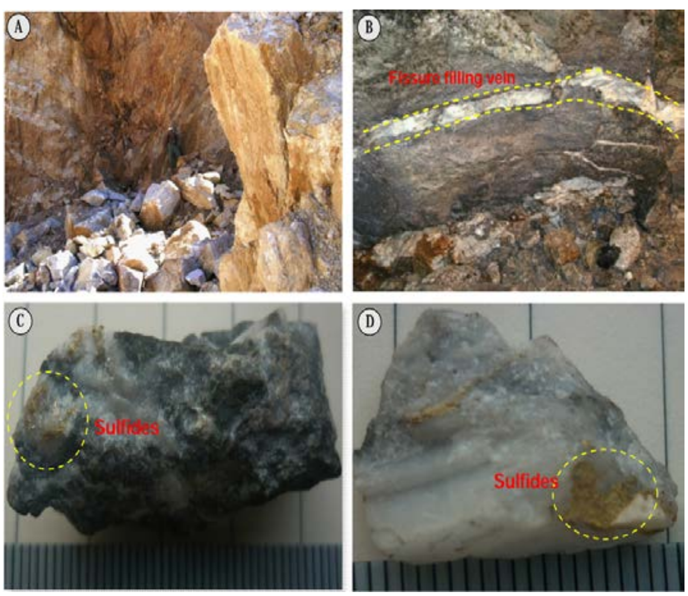

Fig.7. Photographs showing (a) Open pit mining near (Future mine), (b) Fissure filling vein in marble hosted (c) Samples of gold-bearing sulfide ore in diopside marble, (d) Gold-bearing sulfide ore in white marble from the Wethey-Pheshey area.

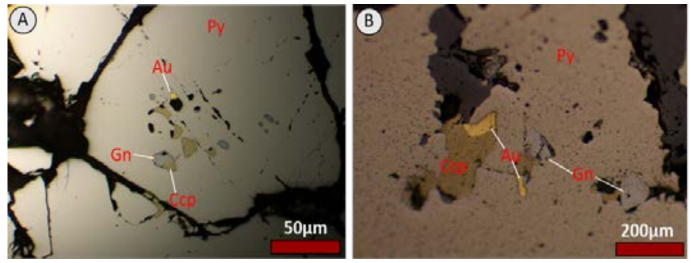

Fig.8. Reflected light photomicrographs of (a) native gold mineral grains occurring in the euhedral pyrite crystal (b) fine to medium native gold grain found in contact between chalcopyrite and pyrite in the ore sample of the Wethey-Pheshey area. Au: native gold, Py: pyrite, Ccp: chalcopyrite, Gn: galena, Sp: Sphalerite.

5. CONCLUSIONS

Gold skarn-type mineralization is occurred in the Wethey-Pheshey prospect area, Thabeikkyin Township, Mandalay region, Myanmar. It is mainly hosted by diopside and white marble which are intruded by granite. The skarn-type gold mineralization in the study area may have been apparently controlled by faults in the regional structure, especially a well-known dextral Sagaing strike-slip fault. Hydrothermal alteration types associated with gold skarn mineralization include skarn alteration silification, garnetification, pyroxinization and chloritization. The skarn alteration mineral assemblage is characterized by the presence of chlorite, diopside, cordierite, calcite, forsterite and scapolite. In the research area, skarn-type gold mineralization styles found as replacements as well as open space filling and disseminated natures in marble units that are intruded by granite. Gold intimately observed as primary in host rock marble as sulfides (pyrite, chalcopyrite, galena and sphalerite)-quartz veins and gold-bearing sulfide carbonated (marble) veins and in the ambient wall rock alteration zone in the underground mine section and in secondary enrichment gossans zone. Common ore minerals and genesis of gold skarn-type mineralization in the Wethey-Pheshey prospect area comprise chalcopyrite, galena, sphalerite, pyrite, and native gold. Data combination of available data from the host rocks/associated rocks, types of alteration, mineralization style, ore and gangue mineralogy, the ore mineralizations in the Wethey-Pheshey area is identified as intrusion-related to gold skarn type mineralization.

ACKNOWLEDGEMENTS

We sincerely thank Gold Winner (Future Mine) for the permission to collect host rocks and ore samples as well as for the support during the fieldwork. The authors want to express deepest gratitude to AUN/SEED-Net for providing financial support to conduct this research. We also would like to thank the two anonymous reviewers for their critical reading of the manuscript and providing valuable comments and suggestions, which greatly improve this paper.

REFERENCES

[1] Searle, D.L., & Haq, B.T, (1964). The Mogok Belt of Burma and Its Relationship to the Himalayan Orogeny, In: Proceedings of the International Geological Congress, Vol. 22, pp. 132–161.

[2] Myint, T.A., Than, T.N., and Min, A. (2014). Precious and Base Metal Mineralization in Kwinthonze-Nweyon area, Singu and Thabeikkyin Townships, Mandalay Region, Myanmar, Proceedings of Sundaland Resources 2014 MGEI Annual Convention, pp. 343–354.

[3] Thein, M,L., Myint, O., Kyi, S., and Win, H,M., (1990). Geology and Stratigraphy of the Metamorphosed Early Palaeozoic Rocks of the Mogok-ThabeikkyinSingu-Mandalay Areas, Research paper Session II in Communication of Diamond Jubilee, p. 2-3.

[4] Oo, T.N., Setijadji, L.D., Warmada, I.W and Oo, T.T. (2016). Geochemistry, Hydrothermal alteration and Ore mineralogy of Skarn Mineralization at Wethey-Pheshey area, Thabeikkyin Township, Mandalay Region, Myanmar, Journal of Applied Geology, Vol. 1(2), pp. 53–62.

[5] Einaudi, M. T., Meinert, L. D., and Newberry, R. J. (1981). Skarn deposits:E CON.G EOL.75th ANNIV. Vol. 5, p. 317-391.

[6] Meinert, L.D. (1997). Application of skarn deposit zonation models to mineral exploration. Exploration Mining Geo/ogy, 6, (2), 185-208.

[7] Swe, W. (1972). Strike-slip faulting in the central belt of Burma, In: N.S. Haile, ed., Regional Conference on the Geology of Southeast Asia, Kuala Lumpur. Annex to Geological Society of Malaysia Newsletter, Vol. 34, p. 59.

[8] Barley, M.E., Pickard, A.L., Zaw, K., Rak, P. and Doyle, M.G. (2003). Jurassic to Miocene magmatism and metamorphism in the Mogok metamorphic belt and the India-Eurasia collision in Myanmar, Tectonics, Vol. 22, No. 3, pp. 1-14.

[9] Mitchell, A.H.G. (1979). Guides to metal provinces in the Central Himalaya collision belt; the value of regional stratigraphic correlations and tectonic analogies, Memoir of the Geological Society of China, Vol. 3, pp. 167-194.

[10] Mitchell, A.H,G., Htay, M.T., Htun, K.M., Win, M.N., Oo, T. and Hlaing, T. (2007). Rock Relationships in the Mogok Metamorphic Belt, Tatkon to Mandalay, Central Myanmar, Journal of Asian Earth Sciences, V.29, pp 891-910.

[11] Searle, M.P., Noble, S.R., Cottle, J.M., Waters, D.J., Mitchell, A.H.G., Hlaing, T. and Horstwood, M.S.A. (2007). Tectonic Evolution of the Mogok Metamorphic Belt, Burma (Myanmar) Constrained by U-Th-Pb Dating of Metamorphic and Magmatic Rocks, Tectonics, Vol. 26, TC2083.

[12] Lee, H.Y., Chung, S.L. and Yang, H.M. (2016). Late Cenozoic Volcanism in Central Myanmar: Geochemical Characteristics and Geodynamic Significance. Lithos, 245, 174-190.

Techno-Science Research Journal 12 (Special Issue) 140-145

I.T.C

Content list available at ITC

Techno-Science Research Journal

Journal Homepage: www.ric.itc.edu.kh

Techno-Science Research Journal

Geology, Mineralogy and Lead-Zinc-Silver Mineralization at Yadanatheingi Area, Naungcho Township, Northern Shan State, Myanmar

Moe Min Soe[1*]

[1]*Department of Geology, West Yangon University, Yangon, Myanmar*

Received: 23 August 2023; Accepted: 15 May 2024; Available online: August 2024

Abstract: *The research area is located about 60 km north of Mandalay in the Yadanatheingi mine area,Nyaungcho Township, Northern Shan State Myanmar. The investigated area lies within the Sino-Burman Ranges. It represents the largest tectonic units in Myanmar. It is mainly composed of the Palaeozoic and Mesozoic sediments. Stratigraphically, the research area consists of the rock units ranging from the Precambrian to Palaeozoic in age. The investigated area is mainly composed of the succession of four stratigraphic rock units. The four stratigraphic rock units from oldest to youngest are: Chaung Magyi Group of greywackes, shale and siltstone, Pangyun Formation consists of sandstone with coarse purple conglomerates, Naungkangyi Group consists of muddy limestone and Shan Dolomite Group of Devonian dolomite. The area can be divided into four physiographical units: the Mankyin Upland, the Yadanatheingi Fold Belt, the Kalagwe Syncline and Nankashwe Scarplands. The purposes of the research area are to investigate the geology, mineralization and ore mineralogy. The investigation involves literature review, field observation and laboratory work. Geological data were transferred to 1:63360 scale topographic base map. Laboratory work involves ore microscopy and AAS (Atomic Absorption Spectrometer) analysis. The Yadanatheingi area is producing lead, zinc, silver and copper deposit. The lead, zinc, silver and copper mineralization occur within the Chaung Magyi Group and the iron, nickel and cobalt mineralization was found in adjacent rocks of the Pangyun Formation. The ore minerals include galena, pyrite, sphalerite, chalcopyrite, cobaltite and pentlandite. The gangue minerals are barite, siderite, quartz and calcite. Rock alteration features were observed at the research area. The sericitization, silicification, chloritization and pyritization are more distinct. Ore microscope study indicated that there were two main stages of the mineralization. On the basis of the present mineralogical investigation, the mineralization of the research area is of epigenetic origin and formed by the hydrothermal solution mainly at a mesothermal range.*

Keywords: Sino-Burman Ranges; Chaung Magyi Group; Pangyun Formation; Yadanatheingi Fold Belt; Kalagwe Syncline

1. INTRODUCTION

The research area is located about 60 km north of Mandalay in the Yadanatheingi mine area, Nyaungcho Township, Northern Shan State. It lies between the latitude 22 d30′ 00″ N and the longitude 96 d24′53″ E. The research area is approximately 45 square kilometers in extent. The research area falls on Myanmar topographic map No. 93B/6 and 93B/10.

The research area can be reached by Pyin Oo Lwin-Mogok motor road or by railway up to Hsum Hsai Station. The purposes of the research are to investigate the geology, mineralization and ore mineralogy.

Topographically, the area is a mountainous region and has rugged terrain with steep slopes. In some places, a rolling hill range is intervened by the typically lowlands. The highest point is 1200 m from the above sea level. General elevation in this area is 1100 m above sea level.

In the research area, the northeastern parts have parallel trellis pattern and in the south-western parts have fine to coarse dendritic pattern. Most of the stream flows from the northwest to the southeast direction.

The research area lies within the Sino-Burman Ranges. It represents the largest tectonic units in Myanmar. The research area physiographically lies on the margin of the Shan Scarp region. The area can be divided into the four physiographic units: Mankyin Uplands, Yadanatheingi Fold Belt, Kalagwe Syncline and Nankashwe Scarplands [5].

* Corresponding author: Moe Min Soe

E-mail: moemins893@ gmail.com Tel: +9595170496

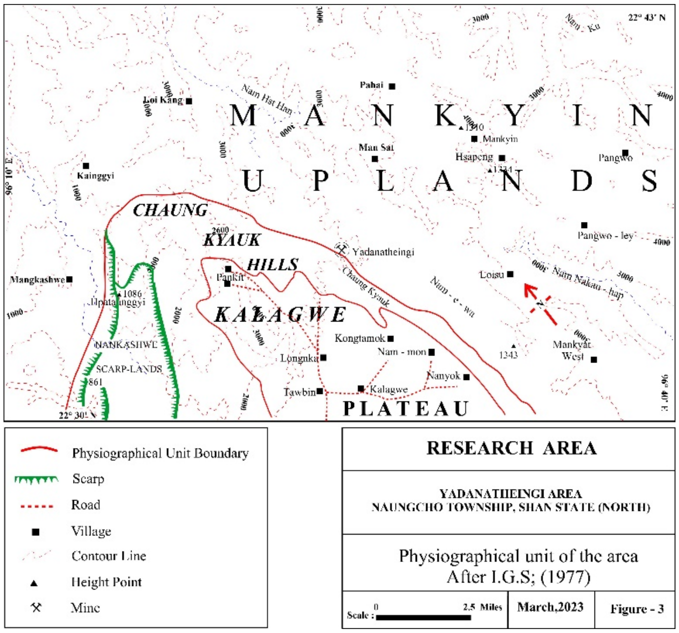

Fig.1 Physiographical Units Map of the Research Area (Modified After [5])

It is mainly composed of the Palaeozoic and Mesozoic sediments. The region lies within the Eastern Highlands near the western margin of the Shan Plateau. The plateau consists largely of a thick folded succession of the Late Precambrian greywackes and mudstones, overlain by Cambrian volcanic rocks and by folded Palaeozoic clastic and carbonate succession.

Regionally, it is covered with the Palaeozoic rocks ranging from the Precambrian to Permo-Carboniferous in age. In the present research area, the Palaeozoic rock units are extensively exposed. Stratigraphically, the investigated area is mainly composed of the succession of four stratigraphic rock units. The four stratigraphic rock units from oldest to youngest are: Chaung Magyi Group, Pangyun Formation, Naungkangyi Group and Shan Dolomite Group [5,6].

1.1 Chaung Magyi Group

It is the dominant stratigraphic unit in this research area. The main rock types are greywackes, shales and siltstones. The Chaung Magyi Group forms a very thick succession of flysch type sediments. The age of the Chaung Magyi Group is Late Precambrian.

1.2 Pangyun Formation

The Pangyun Formation consists of a series of predominantly clastic sediments, largely interbedded purple and white sandstones with coarse purple conglomerates and volcanoclastic rocks, green siltstones and cross-bedded quartzites.

The unconformity between the Chaung Magyi Group and Pangyun Formation is distinct in the west of the Yadanatheingi area. The Pangyun Formation is Cambrian in age.

1.3 Naungkangyi Group

The Naungkangyi Group consists of interbedded ripple marked muddy limestone and calcareous grey and red shales. The Pangyun Formation is overlain by the fossiliferous sandstones, siltstones and muddy limestones of the Ordovician Naungkangyi Group. The age of the Naungkangyi Group is Ordovician.

1.4 Shan Dolomite Group

In the area, Shan Dolomite Group mainly consists of the Devonian dolomite and dolomitic limestone of the Permo-Carboniferous limestone. The Shan Dolomite Group unconformably overlies the Ordovician Naungkangyi Group.

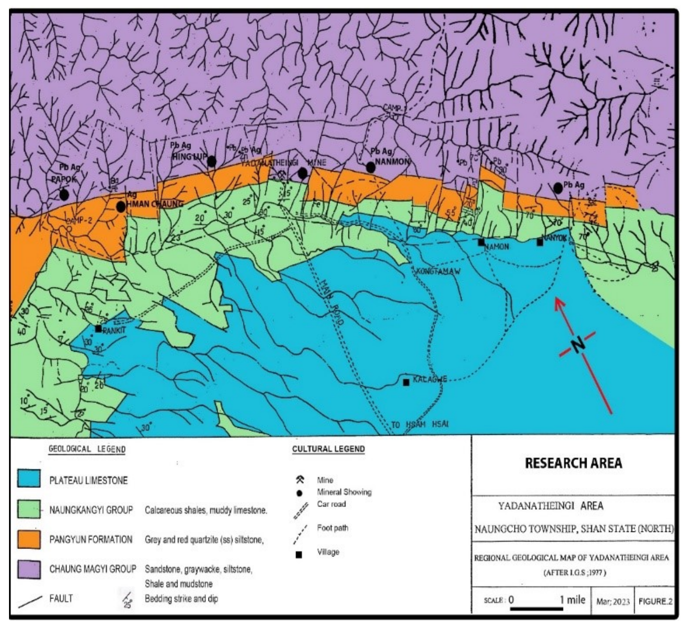

Fig 2 Geological Map of the Research Area (Modified After[5])

2. METHODOLOGY

Methods of investigation involves literature review, field observation and laboratory work. Geological data were transferred to 1: 63360 scale topographic base maps. Laboratory work involves ore microscopy and AAS (Atomic Absorption Spectrometer) analysis. The soil and rock geochemical were studies in the research area. Soil samples were collected systematically from the research area. The 50 soil samples were dried and sieves to 80 mesh. The rock samples were collected random from either the measured traverse lines or from definite known points on the general traverses. AAS analysis were made to determine average metal contents and component elements. Representative ore and host rock samples were mainly collected from the Yadanatheingi mine area. About fourteen ore samples were collected from the Yadanatheingi mine area. Of these, 10 samples were prepared for polished section and studied under reflected microscope in order to determine the mineralogical composition and textural characteristics. All laboratory analyses were conducted at the Applied Geological Department, Yangon University, Myanmar.

3. RESULTS AND DISCUSSION

3.1 Host Lithology

The research area includes the western part of the Yadanatheingi area. There are three main rocks types in the research area: Chaung Magyi Group, Pangyun Formation and Naungkangyi Group. The lead, zinc, silver and copper mineralization occur within the Chaung Magyi Group. The iron, nickel and cobalt mineralization was found in adjacent rocks of the Pangyun Formation.

The lead, zinc, silver and copper mineralization were largely found in brecciated zone along some bedding planes within the Chaung Magyi Group. The iron, nickel and cobalt mineralization is hosted in sandstone unit of the Pangyun Formation.

Fig. 3 Photograph showing argentiferous galena ore in Pangyun Formation

Fig.4 Photograph showing massive galena ore in Chaung Magyi Group

3.2 Ore Mineralogy

The ores from the Yadanatheingi area are dominant Pb -Ba (lead -barium) throughout the entire belt. One important characteristic is that the ores are highly argentiferous. The Pb:Ag ratio of the ores is generally around one unit of lead (1% Pb) to one troy ounce of silver and occasionally the silver values can be higher.

The silver-bearing minerals can be divided into two classes: the sulphides and the sulphosalts. The first category silver-bearing minerals are galena, argentite and polybasite.

3.2.1 Galena (PbS)

Galena is the most widespread and the main sulphide mineral in the research area. Massive galena ore investigated under the reflected light shows almost always numerous gangue fragments (mostly barite, siderite and quartz) and minor rock fragments. Galena containing appreciable silver values is said to be argentiferous, where silver probably occurs in solid solution and this mineral with characteristic triangular pits can be readily identified under the ore microscope [3].

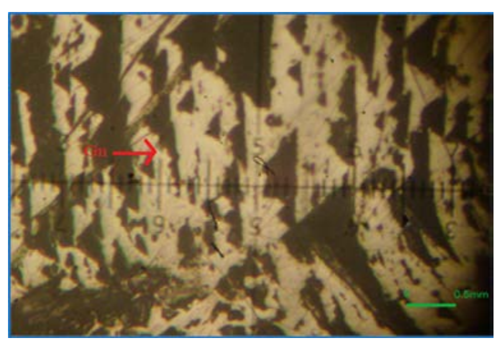

Fig.5 Photomicrograph showing massive galena ore (Gn) with numerous triangular pits (Polished Section)

3.2.2 *Pyrargyrite ($Ag_3 SbS_3$) – Proustite ($Ag_3 As S_3$)*

These silver-bearing minerals are also called the "Ruby Silver" because of the ruby red colour [8]. Pyrargyrite is distinguished from proustite by darker red colour and tests of antimony. Proustite shows lamellar twining is more common with galena-siderite ores of the lower levels of the Yadanatheingi mine [6].

Pyrargyrite commonly replace and also form mutual boundaries with galena while proustite, intergrowth with pyrite and galena replacing the two sulphides and it is also seen in the gangue.

Fig.6 Photomicrograph showing anhedral pyrargyrite (Pyra) (Polished Section)

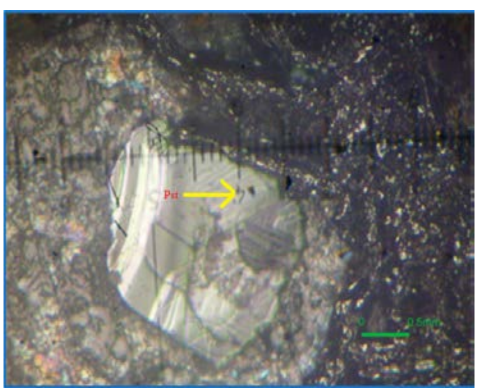

Fig.7.Photomicrograph showing anhedral of Proustite (Pu) shows lamellar twinning (Polished Section)

3.2.3 *Tetrahedrite (Cu_3SbS_3) -Tennantite (Cu_3AsS_3)*

These sulphosalts of copper are commonly seen in the galena-siderite ores as euhedral grains in the siderite is association with galena and chalcopyrite.

The tetrahedrite-tennantite are end members of a solid solution series displaying complete diadochy of arsenic for antimony [2].

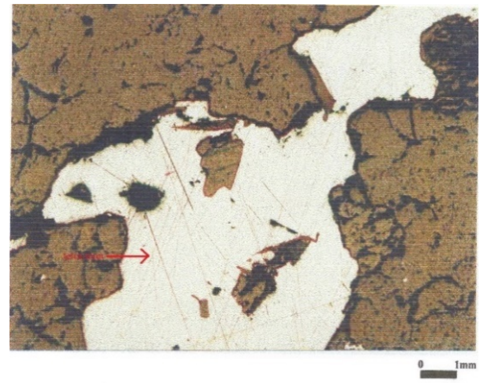

Fig.8 Photomicrograph showing grey tetrahedrite-tennantite (Tetra-ten) (Polished Section).

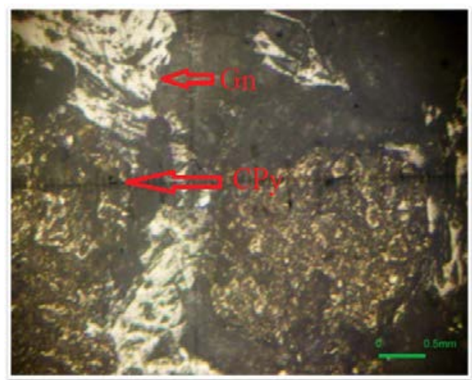

Fig.9 Photomicrograph showing chalcopyrite (CPy) and galena (Gn) showing mutual boundary (Polished Section)

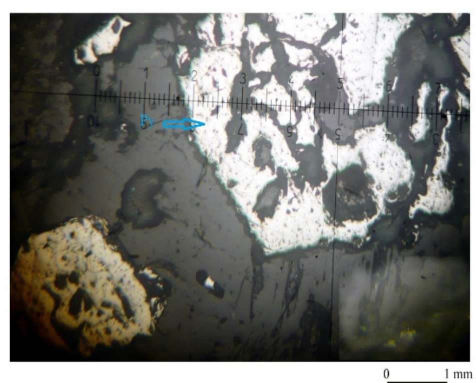

Fig.10 Photomicrograph showing massive pyrite (Py) (Polished Section)

3.3 *Alteration of Host Rocks*

Rocks alteration features were observed at the research area. Some alteration characters could be recognized in the field but others were obviously observed in polished-section only with the microscope. The following alteration characters were observed: sericitization, chloritization and pyritization. Near the ore bodies, bleaching of the rocks and the staining with iron are the most distinctive features of the alteration in this research area.

Fig.11 Photograph showing rock alteration with staining iron near ore body in the Yadanatheingi area

3.4 Controlling of Mineralization

The controlling factors of mineralization in the research area are structural controls and the relation with the shear zones and fractures. The nickels, cobalt and iron mineralization are confined to a narrow zone of the shearing in Pangyun Formation. This zone of shearing is more or less parallel to the structural trend of Chaung Magyi Group rocks.

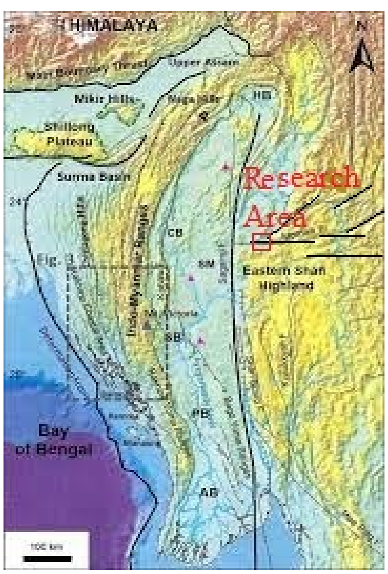

Fig.12 Physiographic Feature Map of Myamar showing Geological Structures of the Research Area (Modified After [4])

3.5 Assay Results

The minimum and maximum contents of lead in the individual soil samples are 90 ppm and 170 ppm. The minimum and maximum contents of silver in the individual soil samples are 0.38 ppm and 3.24 ppm. The minimum and maximum contents of zinc in the individual soil samples are 65 ppm and 130 ppm. The minimum and maximum contents of copper in the individual soil samples are 105 ppm and 150 ppm. The minimum and maximum contents of cobalt in the individual soil samples are 15 ppm and 35 ppm.

The rock geochemical assay results of the research area give 70 ppm to 100 ppm of Co and 46 ppm to 138 ppm of Ni. The high silver values in the ores are evident from assay results of ore samples. The No.1 vein at Yadanatheingi mine yielded 20% Pb and 900 g/t Ag.

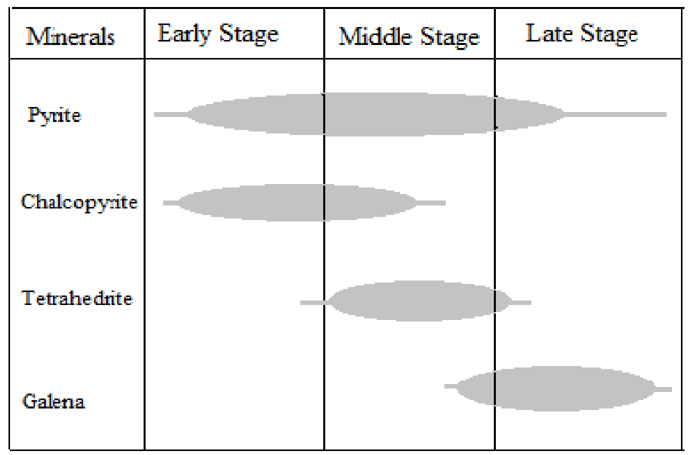

Fig.13 Paragenetic sequence diagram of the research area

4. CONCLUSION

The present study was directed towards geochemical and mineralogical investigation of the ore deposit to contribute geochemical and mineralogical information of the mineralization at Yadanatheingi area.

Stratigraphically, the lead, zinc, silver and copper mineralization were found in metasediment of the Chaung Magyi Group and iron, nickel and cobalt mineralization was found in adjacent rocks of the Pangyun Formation.

Geochemical surveys using the rock chip and soil sampling were useful tools in locating the mineralization. The No.1 vein at the Yadanatheingi mine yield 20% Pb and over 900 g/t Ag. Ore microscopic study indicated that there were two main stages of the mineralization. The first mineralization might take place in pre-existing Chaung Magyi sediment. The ores carry low zinc and copper as chalcopyrite. The dominant gangue minerals are barite, quartz and siderite. After the deposition of these minerals, intense shearing took place with the mineralization of more complex sulphosalt and sulphide minerals. On the basis of the present mineralogical investigation, the mineralization of the research area is of epigenetic origin and formed by the hydrothermal solution mainly at a mesothermal range.

It is concluded that the present research has confirmed the high values of silver in the ores, contributed by both silver bearing sulphides and sulphosalts. The sulphides are more abundant and important than the sulphosalts. These minerals are distributed over the entire length of the Yadanatheingi area which can now be considered as an important resource for silver.

ACKNOWLEDGMENTS

The researcher wishes to express sincere gratitude to Associate Professor Dr Toe Naing Oo, West Yangon University for his encouragements to do this research.

REFERENCES

[1] Amos, B.J, (1975). Stratigraphy of some of the Upper Palaeozoic and Mesozoic Carbonate of Eastern Highland, Burma. Vol. 4, p 49-70.

[2] Barnes, H.L, (1977). Geochemistry of Hydrothermal Ore Deposits. John Wily& Sons, New York.

[3] Edwards, A.B, (1965). Texture of the Ore Minerals and their significance. The Aus. MM & Met, Australia.

[4] GIAC (2001). Geodynamic of India-Asia collision the tectonic of Myanmar.

[5] Mitchell, et al,(1977).Geology and exploration geochemistry of the Yadanatheingi and Kyaukme- Longtawkno area, Northern Shan State. Burma, IGS London.

[6] Sein Tin, (1980). Mineralogical Investigation of the ore minerals at Yadanatheingi mine, Northern Shan State Burma. MSc thesis Department of Geology, Rangoon Arts and Science University.

[7] Soe Win, (1968). Progress report on Yadanatheingi exploration, Myanmar Bawdwin Corporation.

[8] Uytenbogaardt, W and Bruke, E.A.J, (1971). Table for Microscopic Identification of Ore Minerals.

Techno-Science Research Journal 12 (Special Issue) 146-151

Content list available at ITC

Techno-Science Research Journal

Journal Homepage: www.ric.itc.edu.kh

Techno-Science Research Journal

The sandstones of the Angkor monuments, and their supply sources and transport routes

Etsuo Uchida[1*]

[1] *Department of Resources and Environmental Engineering, Faculty of Science and Engineering, Waseda University, Ohkubo 3-4-1, Shinjuku, Tokyo 169-8555, Japan*

Received: 12 August 2023; Accepted: 15 May 2024; Available online: August 2024

Abstract: *The Angkor monuments were built by the Khmer people from the 9th to the 15th century, and were registered on the World Heritage List of UNESCO in 1992. The Angkor monuments are mainly constructed of sandstone and laterite. Three types of sandstones were used: gray to yellowish-brown sandstone, greenish graywacke, and red siliceous sandstone. Among these, gray to yellowish-brown sandstone is most important and used in almost all of the buildings. There is no difference in the constituent minerals and chemical composition of this sandstone among the temples. However, its magnetic susceptibility varies over time, which can be used to estimate the construction period and sequence of the temples. Additionally, the shape of the stone blocks, the orientation of the bedding plane, and the stacking method vary from one period to another, which can also be used to estimate the construction period of the temples. Gray to yellowish-brown sandstone is quarried from the southeastern foothill of the Kulen Mountain, located about 35 km northeast of the Angkor capital, and there are many traces of quarrying there. It is believed that the stone blocks were transported from the Kulen Mountain to the Angkor capital through canals and rivers. On the other hand, greenish graywacke is a valuable stone material, found to be used at Ta Keo temple and for devine statues. Greenish graywacke is deduced to have been supplied from Sandan and Trapeang Tuol Kruos villages in Kratie Province, which are located along the Mekong River about 220 km east of the royal capital of Angkor. It is highly likely that greenish graywacke blocks were transported from these villages to the Angkor area through the Mekong River and the Tonle Sap River.*

Keywords: Angkor monuments; sandstone; supply source; transport route

1. INTRODUCTION

The majority of Angkor monuments are densely located in the north of the Tonle Sap Lake. The monuments were built by the Khmer people between the 9th and 15th centuries to dedicate to the Hinduist and Buddhist deities. In 1992, the Angkor monuments were registered on the World Heritage List of UNESCO.

The monuments built by the Khmer people during this period are collectively called Khmer monuments. They are distributed not only in Cambodia but also in Thailand and Laos. Representative Khmer monuments in Cambodia include the Angkor monuments, the Koh Ker monuments, the Great Preah Khan monuments, the Preah Vihear temple and the Banteay Chhmar temple. In this paper, the stones used to construct the monuments in Angkor region will be investigated.

Figure 1 is a map showing the distribution of major Angkor temples [1].

2. METHODS

Magnetic susceptibilities were measured by using a portable magnetic susceptibility meter (SM30, ZH Instruments, Brno, Czech Republic) on the flat surfaces of sandstone blocks. Chemical composition analysis was performed by using a portable X-ray fluorescence analyzer (Type DP-4000-C, Innov-X Systems Delta Premium, Waltham, MA, USA). Measurements were performed in soil mode for a total measurement time of around 1 min.

* Corresponding author: Etsuo Uchida

E-mail: weuchida@waseda.jp; Tel: +81-3-5286-3318

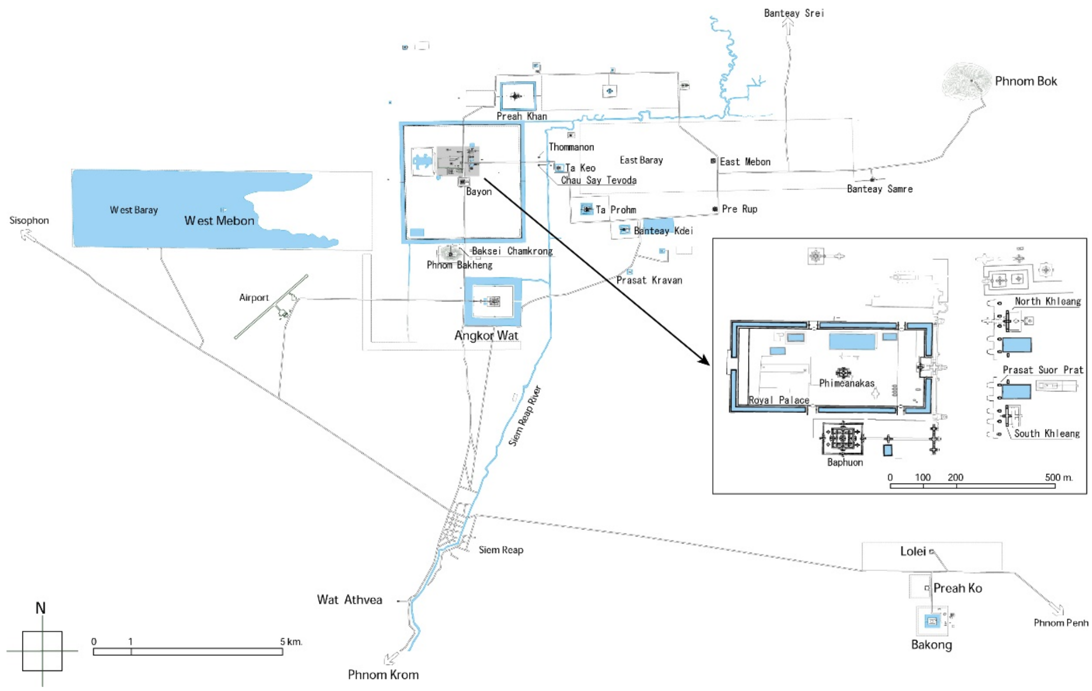

Fig. 1. Map of the Angkor monuments, showing the distribution of the representative temples (modified after Uchida et al. [1]).

3. CONSTRUCTION MATERIALS

In Angkor region the majority of monuments were constructed of sandstone and laterite [2-4], but bricks were also used in general until the 10th century.

Three types of sandstones were used in the construction of the Angkor monuments: gray to yellowish-brown sandstone, greenish graywacke, and red siliceous sandstone. Among these, the most important one is the gray to yellowish-brown sandstone. This sandstone was used in almost all temples. Greenish graywacke was used only in the five sanctuaries of the Ta Keo temple. In addition, greenish graywacke was used for statues and Linga/Yoni, which are symbols of Hinduism. Red siliceous sandstone is the main construction material used for the construction of Banteay Srei temple.

The sandstones used for the construction of the Angkor monuments were all supplied from the Khorat Group of Triassic to Cretaceous. In Thailand, the Khorat Group is subdivided into nine formations [5]. It is considered that the greenish graywacke was supplied from the Huai Hin Lat Formation of Triassic, the gray to yellowish-brown sandstone from the Phu Kradung Formation of Jurassic to Cretaceous, and the red siliceous sandstone from the Sao Khua Formation of Cretaceous [6]

3.1 Gray to yellowish-brown sandstone

Figures 2a and 2b show the photomicrographs of gray to yellowish-brown sandstone under a polarizing microscope [2]. It is a fine-grained sandstone. A particle size is around 0.2 mm. The main constituent materials are quartz, plagioclase, K-feldspar, rock fragments, biotite, and muscovite. There is no difference in the constituent materials between the sandstones used to construct the Angkor temples. The whole-rock chemical composition of gray to yellowish-brown sandstones collected from the temples selected for this study were determined. Even including trace elements, no differences were found [2].

However, we revealed that the magnetic susceptibility of the gray to yellowish-brown sandstone was different depending on the construction period [2]. The difference in magnetic susceptibility is thought to be proportional to the amount of magnetite in the sandstone.

Figure 3 shows the grouping of the temples based on magnetic susceptibility of gray to yellowish-brown sandstone. The earlier temples are arranged from bottom to top. By analyzing this result, it was deduced that the gray to yellowish-brown sandstone of the Angkor monuments was supplied from seven quarrying areas [1-2]. Some temples indicate that the sandstone was supplied from multiple quarries.

Figure 4 is a plan of the Bayon temple [7]. This figure is color-coded by average magnetic susceptibility. The sandstone of the central tower and inner gallery in the central part of the Bayon temple shows a low magnetic susceptibility of around 1.0×10^{-3} SI units. On the other hand, the sandstone of the outer galleries and lower terrace show a magnetic susceptibility of around 1.7×10^{-3} SI units. The highest magnetic susceptibility of around 2.2×10^{-3} SI units is shown by the sandstone of the upper terrace and the northern and southern libraries. This fact suggests that the temple was built in the order of the areas marked in yellow, red, and blue.

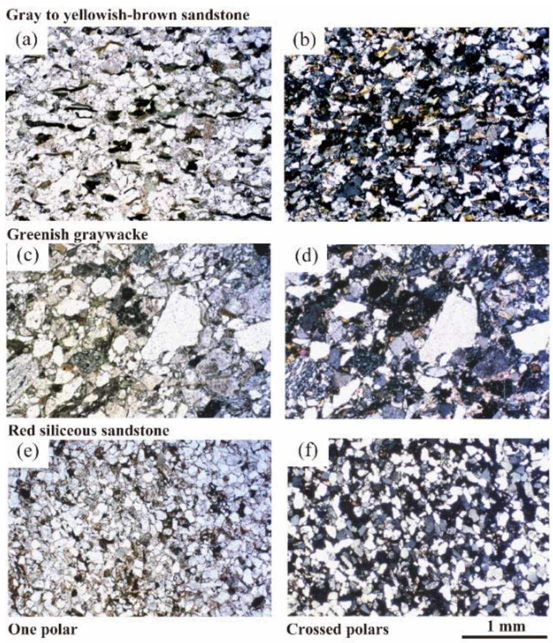

Fig. 2. Photomicrographs under a polarizing microscope presented in plain on the left and cross polarized on the right, of gray to yellowish-brown sandstone (upper), greenish graywacke (middle), and red siliceous sandstone (bottom) [2].

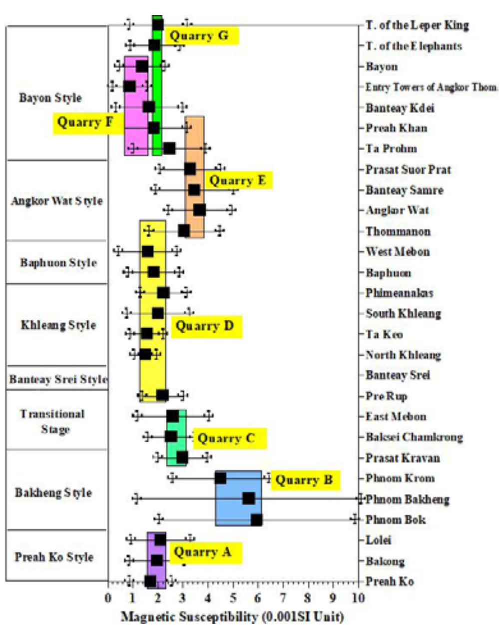

Fig. 3. Magnetic susceptibilities of gray to yellowish-brown sandstones used in the Angkor monuments. The temples of earlier periods start from the bottom. The standard deviation (1σ) is also shown in the figure (modified after Uchida et al. [2]).

The Bayon temple is located at the center of Angkor Thom. It is surrounded by a 12 km long wall built of laterite. The wall has five sandstone gates and four sandstone buildings called Prasat Chrung at each corner. The average magnetic susceptibility of these sandstone buildings is around 1.0×10^{-3} SI units. This suggests that the surrounding wall was constructed when the central part of the Bayon temple was built.

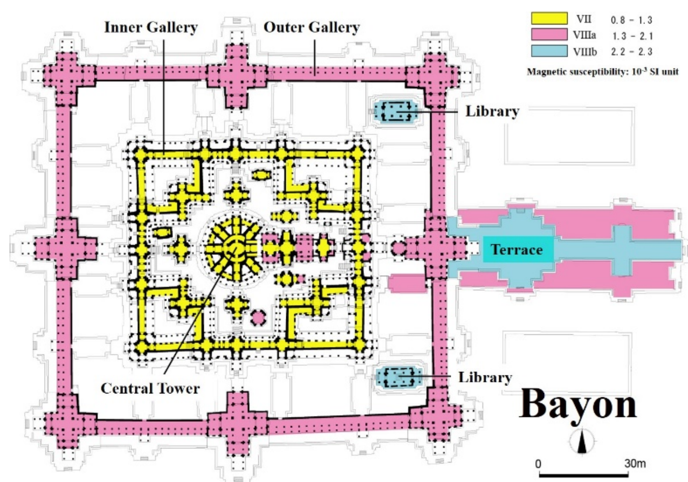

Fig. 4. The construction sequence of the Bayon temple deduced from the magnetic susceptibilities of the sandstones. Three stages can be distinguished [6].

3.1.1 Characteristics of stone blocks

Figure 5 shows major characteristics of stone blocks [8].

Until the Baphuon style period, the stone blocks have square ends. In the Angkor Wat style period, the stone blocks have either square or rectangular ends. In the Bayon style period, stone blocks have rectangular ends. Before the Bayon style period, the size and shape of the stone blocks is almost uniform, but they became irregular in the Bayon style period. Before the Bayon style period, the stone blocks show a successive bed joint, but in the Bayon style period, they show a non-successive bed joint. Until the Baphuon style period, the orientation of the bedding plane is random, but in and after the Angkor Wat style period, it became mostly horizontal. The construction period can be estimated from these characteristics (Fig.5)

3.1.2 Supply source of the gray to yellowish-brown sandstone

It has long been known that the gray to yellowish-brown sandstone was supplied from the southeastern foothill of the Kulen Mountain [9-12]. It is located about 35 km northeast of the Angkor monuments. However, detailed information on sandstone quarries was not available. Therefore, we conducted a field investigation for over one month in total at the southeastern foothill of the Kulen Mountain.

Figure 6 is a topographic map showing the location of sandstone quarries. We found traces of quarries at 145 sites in total [13-14]. We could identify the seven sandstone quarrying areas, judging from the magnetic susceptibility and stone block size, particularly step height.

Figure 7 shows the large-scale quarry, No. 45, which is supposed to be a quarry in the Bayon style period because of their low magnetic susceptibility and low step height.

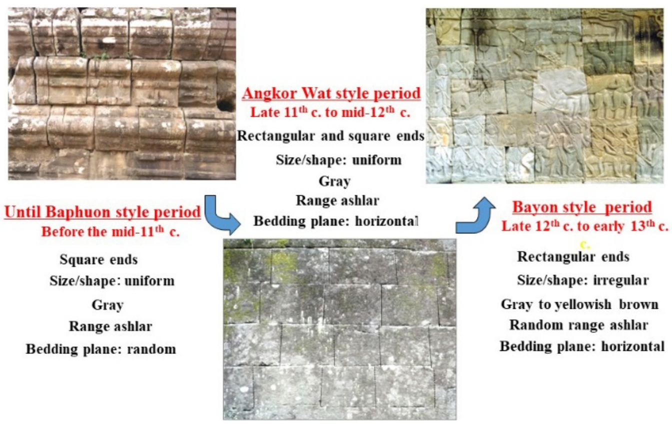

Fig.5. Summary of characteristics of the sandstone and laterite blocks used in the Angkor monuments.

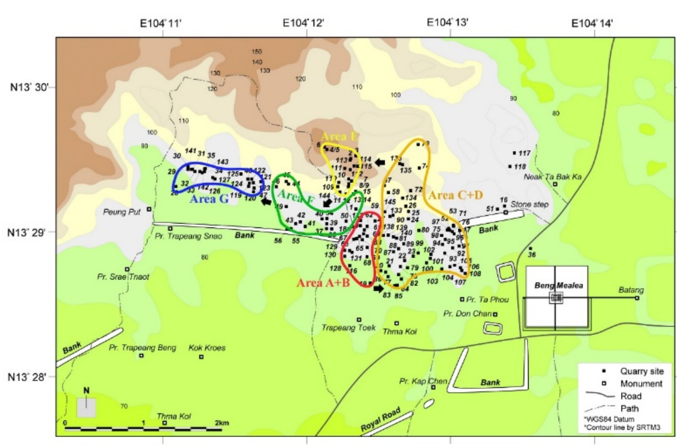

Fig. 6. Topographic map showing distribution of gray to yellowish-brown sandstone quarries during the Angkor period at the southeastern foothill of the Kulen Mountain (modified after Uchida et al. [14]).

3.1.3 Transport route of the gray to yellowish-brown sandstone

We found canals and rivers connecting the Kulen Mountain to the Royal Capital of Angkor (Fig. 8) [13]. The photographs of the canal are shown in Fig. 8.

Fig. 7. Photograph of the gray to yellowish-brown sandstone quarry, no.45 in Fig. 6.

Fig. 8. Transport route of gray to yellowish-brown sandstone blocks, connecting the quarrying sites at the southeastern foothill of the Kulen Mountain to the Angkor area, shown with a red line [13].

3.2 Greenish greywacke

Greenish graywacke is used only for five sanctuaries on the top of the Ta Keo temple. In addition, this sandstone is used for statues and Linga/Yoni, which are symbols of Hinduism.

Figures 2c and 2d show photomicrographs of greenish graywacke. The constituent materials are similar to those of gray to yellowish-brown sandstone. However, the detrital grains are angular and poorly sorted.

3.2.1 Supply source of the greenish graywacke

Carò and Douglas [15] found greenish greywacke blocks in Sandan and Trapeang Tuol Kruos villages in Kratie Province. They are located about 220km southeast of Siem Reap.

Figure 9 shows greenish graywacke blocks in Sandan and Trapeang Tuol Kruos villages. However, Carò and Douglas [15] did not carry out any measurement such as chemical composition and magnetic susceptibility of the greenish graywacke. Therefore, we conducted a series of investigations by using these measurements [16].

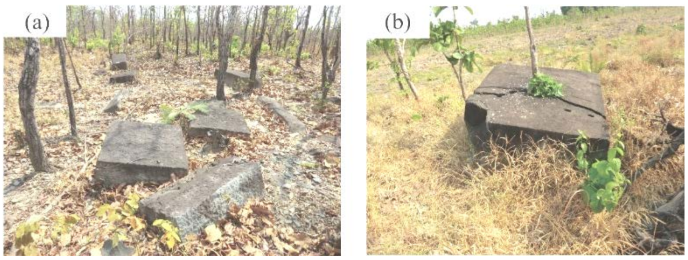

Fig. 9. Photographs of (a) greenish graywacke cut stones scattered in Sandan village, and (b) an unfinished pedestal made of greenish graywacke found in Trapeang Tuol Kruos village [16].

Figure 10 shows results for magnetic susceptibility and Rb content measurements [16]. Greenish graywacke blocks in the Ta Keo temple and those in Sandan village show similar magnetic susceptibility and Rb content. Therefore, we concluded that the greenish greywacke blocks in the Ta Keo temple were supplied from Sandan village [16].

Greenish graywacke for statues and Linga/Yoni shows relatively high magnetic susceptibility and low Rb content. These characteristics are similar to those of greenish graywacke in Trapeang Tuol Kruos village. Therefore, we consider that greenish graywacke for statue and Linga/Yoni may be supplied from Trapeang Tuol Kruos village [16].

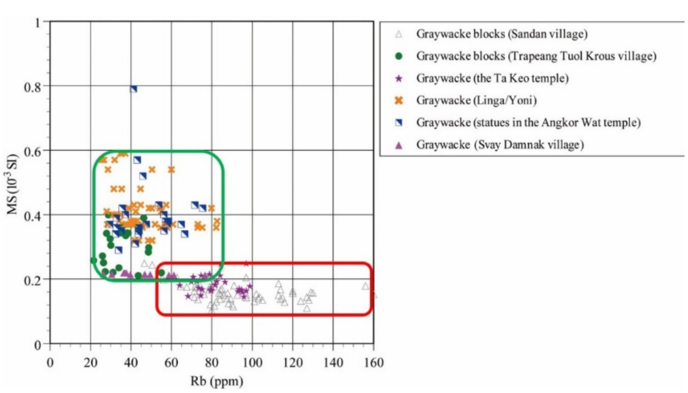

Fig. 10. Magnetic susceptibility vs. Rb content diagram for the greenish graywacke used in the Angkor monuments and also in Sandan, Trapeang Tuol Kruos, and Svay Damnak villages [16].

3.2.2 Transport route of the greenish graywacke

The straight-line distance from these villages to the Angkor area is about 220 km. There is no Royal Road connecting these areas. Therefore, the use of the Mekong River is considered as a possible transport route of greenish graywacke blocks. Sandan and Trapeang Tuol Kruos villages are located near the Mekong River (Fig. 11) [16]. There is the Tonle Sap Lake to the south of the Angkor monuments. The Tonle Sap Lake is connected to the Mekong River via the Tonle Sap River. In the rainy season, the water level of the Mekong River rises, and water flows back into the Tonle Sap Lake. Therefore, it is highly likely that greenish graywacke blocks could be easily transported by water by going down the Mekong River and then by going up the Tonle Sap River in the rainy season.

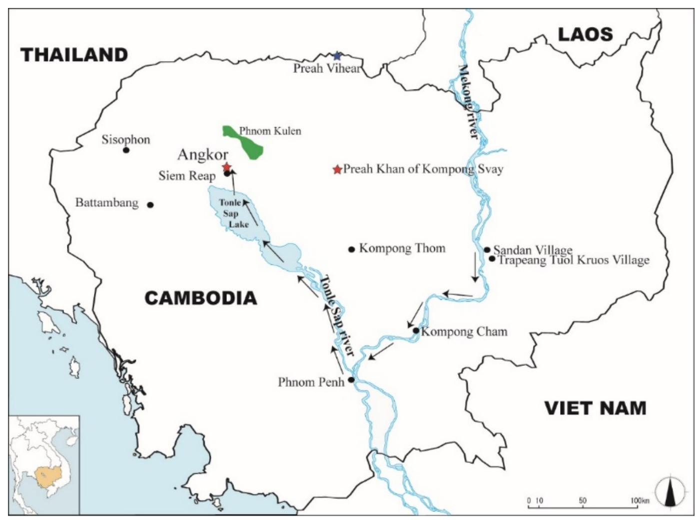

Fig. 11. A map showing the transport route network of greenish graywacke from Kratie Province to the Angkor area, using the Mekong and Tonle Sap rivers [16].

4. CONCLUSIONS

(1) The major construction materials for the Angkor monuments are sandstone, laterite, and brick.
(2) Three types of sandstone were used for the Angkor monuments: gray to yellowish-brown sandstone, greenish greywacke, and red siliceous sandstone.
(3) The magnetic susceptibility is useful to distinguish gray to yellowish-brown sandstone and to estimate the construction period and sequence.
(4) Characteristics of sandstone and laterite blocks changed over time, and are useful to explain the construction period.

(5) Gray to yellowish-brown sandstone blocks were supplied from the southeastern foothill of the Kulen Mountain and transported by using canals and rivers.
(6) Greenish greywacke was used for the construction of the sanctuaries on the top of the Ta Keo temple. In addition, this stone was used for Ling/Yoni and devine statues.
(7) Greenish greywacke was supplied from Sandan and Trapeang Tuol Kruos villages, located 220 km, southeast of the Royal Capital of Angkor.
(8) Greenish greywacke was transported through water ways, using the Mekong River and the Tonle Sap River to the Angkor area.

ACKNOWLEDGMENTS

This research was conducted with the permission of the Authority for Protection and Management of Angkor and the Region of Siem Reap (APSARA National Authority), Cambodia. We received various supports from members of the Japanese Government Team for Safeguarding Angkor for the field survey. This research was financially supported in part by Grants-in-Aids for Scientific Research of Japan Society for the Promotion of Science and Waseda University Grants for Special Research Projects.

REFERENCES

[1] Uchida, E., Cunin, O., Suda, C., Ueno, A., Nakagawa, T. (2007) Consideration on the construction process and the sandstone quarries during Angkor period based on the magnetic susceptibility. J. Archaeol. Sci., 34, 924-935.

[2] Uchida, E., Ogawa, Y., Nakagawa, T. (1998) The stone materials of the Angkor monuments, Cambodia. The magnetic susceptibility and the orientation of the bedding plane of the sandstone. J. Min. Pet. Econ. Geol., 93,411-426.

[3] Uchida, E., Maeda, N., Nakagawa, T. (1999) The laterites of the Angkor monuments, Cambodia. The grouping of the monuments on the basis of the laterites. Jour. Min. Pet. Econ. Geol., 94,162-175.

[4] Uchida, E., Ogawa, Y., Maeda, N., Nakagawa, T. (1999) Deterioration of stone materials in the Angkor monuments, Cambodia. Eng. Geology, 55,101-112.

[5] Meesook, A. (2011) 8. Cretaceous. Eds: Ridd, M.F., Barber, A.J., Crow, M.J. The Geology of Thailand, The Geological Society London, 169-184.

[6] Uchida, E., Ito, K., Shimizu, N. (2010) Provenance of the sandstone used in the construction of the Khmer monuments in Thailand. Archaeometry, 52, 550-574.

[7] Uchida, E., Cunin, O., Shimoda, I., Suda, C., Nakagawa, T. (2003) The construction process of the Angkor monuments elucidated by the magnetic susceptibility of sandstone. Archaeometry, 45, 221-232.

[8] Uchida, E., Suda, C., Ueno, A., Shimoda, I., Nakagawa, T. (2005) Estimation of the construction period of Prasat Suor Prat in the Angkor monuments, Cambodia, based on the characteristics of its stone materials and the radioactive carbon age of charcoal fragments. J. Archaeol. Sci., 32, 1339-1345.

[9] Garnier, F. (1873) Voyage d'exploration en Indochine, effectué pendant les année 1866 et 1868, Paris

[10] Saurin, E. (1954) Quelques remarques sur le grès d'Angkor. Bulletin de l'École Française d'Extrême-Orient, vol. 46, pp. 619-634.

[11] Delvert, J. (1963) Recherches sur l'érosion des grès des monuments d'Angkor. In: Bulletin de l'École Française d'Extrême-Orient, vol. 51, pp. 453-534

[12] Carò, F., Im, S. (2012) Khmer sandstone quarries of Kulen Mountain and Koh Ker: a petrographic and geochemical study. J. Archaeol. Sci. 39, 1455–1466.

[13] Uchida, E., Shimoda, I., Shimoda, M. (2013) Consideration of the construction period of the Khmer temples along the East Royal Road to Preah Khan of Kompong Svay and the provenance of sandstone blocks based on their magnetic susceptibility. Archaeol. Discovery, 1, 37-48.

[14] Uchida, E., Watanabe, R., Murasugi, M., Sakurai, Y., Shimoda, I. (2020) The sandstone quarries of the Angkor monuments in the southeastern foothills of Kulen Mountain. Archaeol. Discovery, 8, 207–227.

[15] Carò, F., Douglas, J.G. (2013) Nature and provenance of the sandstone used for Bayon style sculptures produced during the reign of Jayavarman VII. J. Archaeol. Sci. 40, 723–734.

[16] Uchida, E., Watanabe, R., Cheng, R., Nakamura, Y., Takeyama, T. (2021) Non-destructive in-situ classification of sandstones used in the Angkor monuments of Cambodia using a portable X-ray fluorescence analyzer and magnetic susceptibility meter. Jour. Archael. Sci.: Reports, 39, 103137.

Techno-Science Research Journal 12 (Special Issue) 152-155

Content list available at ITC

Techno-Science Research Journal

Journal Homepage: www.ric.itc.edu.kh

Techno-Science Research Journal

Laterization Origin of Heritage Rampart of Sambor Prei Kuk Area, KompongThom Province, Cambodia

Mengsean Heng[1*], Muoy Yi Heng[1] ,Phanny Yos[1,2], Tithya Keo[1], Than Heng [3],Vitharong Chan [4]

[1]*Faculty of Geo-resources and Geotechnical Engineering, Institute of Technology of Cambodia, Russian Federation Blvd., P.O. Box 86, Phnom Penh, Cambodia*

[2]*Nano-Structure and Chemical Analysis Laboratory, Institute of Technology of Cambodia, Russian Federation Blvd., P.O. Box 86, Phnom Penh, Cambodia*

[3]*National Authority For Sombor Prei Kuk, NR 6, Phum I, Sangkat Kompong Thom, Krong Stoeung Sen, Kompong Thom, Cambodia*

[4]*Department of Archaeology and Conservation, National Authority For Sombor Prei Kuk, NR 6, Phum I, Sangkat Kompong Thom, Krong Stoeung Sen,Kompong Thom, Cambodia*

Received: 22 August 2023; Accepted: 15 May 2024; Available online: August 2024

Abstract:. *Magnetic susceptibility is a significant variable in magnetism. It plays the same role as density dose in gravity interpretation. Although instruments are available for measuring the susceptibility of the formation, there is also significant variation, even for particle rock, and wide overlap between different types, such as sedimentary rock, which has the lowest average susceptibility.Widespread rhyolitic volcanism on the peninsula during Triassic, especially in the middle and late Triassic times. The sorts of magnetic minerals were studied based on magnetic susceptibility measurements on laterite rock temples. The inter-association and paragenesis of amorphous and crystalline variations of iron oxide minerals (hematite, goethite), which are further affected by deposition inputs and changes in porosity, are described in detail by ore microscopy. The study aims to identify the lateralization origin, which may reveal the laterite's origin. Magnetic susceptibility and main chemical makeup were use to plot the laterite ternary diagram's. The samples were delivered to the GGE laboratory for chemical investigation, the magnetic susceptibility of the fifteen nearby locations by Kappameter KT series. The main chemical constituents, including SiO_2, Al_2O_3, Fe_2O_3, and others, is used to gauge the degree of laterization. The final result showed that the laterite in the temples of Sambor Prei Kuk had varied laterization weak to moderate, and data on magnetic susceptibilities suggested that the sedimentary rock was the source of the phenomenon. In conclusion, there is a laterite in Prasat Sambor Prei Kuk, which is said to have been created by a weathering of the sedimentary rock.*

Keywords: : Laterization, Magnetic Susceptibility

1. INTRODUCTION

The SPK temple was inscribed on the World Heritage List in 2017. This ancient political center was during the Pre-Angkorian Chenla Kingdom (late 6th to 9th century). The laterite rock is a used to build temple fences. We investigate the surroundings of the ancient temple walls to determine the physical properties and chemical composition to rebuild the damaged temples. Additionally, they are essential parameters concerning clay due to chemical reactivity, mechanical strength, and durability. Schulman's (1981) chemical classification of laterite was accepted by Herbillon and Nahon (1988). It is independent of genetic interpretation and applies equally to unconsolidated materials such as hard or soft iron crusts. The blocks laterites sample to investigate are from Prasat Sombor, Prasat Tao, Prasat Yeai Pouen, and Quarry measured by Magnetic susceptibility (Kappameter of KT series) to define magnetic types of rock. Magnetic susceptibility

* Corresponding author: Heng Mengsean
E-mail:mengseanheng36@gmail.com; Tel: +855-11 798 702

was measured on laterite rock temple to determine types and among magnetic minerals and selection samples to do in the laboratory.[1] [6]

2. METHODOLOGY

Fifteen samples were collected, one of which of them from quarry (Fig2.d). In this study, the following methods were undertaken from hand specimens to confirm magnetic susceptibility at the field. All samples were analyed by X-ray fluorescence (XRF) to define the laterization of of rock weathering. The mostly of laterite rock are similary depend on magnetic value at field and physical properties. There are three samples to do the Polish section depend on the types of magnetic values of low, medium and high, also based on the physical of laterite rock (color, texture). These laterites are interpreted to be formed by the weathering of sandstone andconglomerate (Figure1).[4]

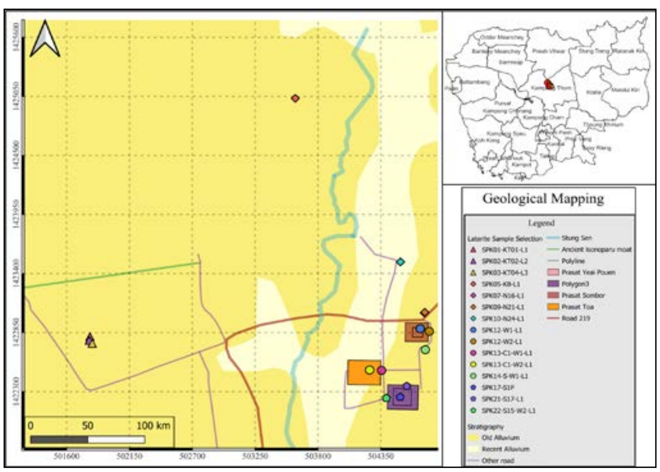

Fig. 1. Mapping of Laterite samples selection

3. RESULTS AND DISCUSSION

3.1) Magnetic Susceptibility of rock magnetism

The magnetic susceptibility of sandstones is attributed to a slight magnetite contain in the sandstone. However , magnetite was absent in the laterite because there were oxidizing conditions. Also, they remain of hematite and goethite, which are low as a two- or three-order relative of magnetite (cf., Carmichael,1982). As a result of our fieldwork, 15 alternative temple locations have been investigated. The average magnetic susceptibility of laterite rock at the temples ranged from 0.629(10^{-3})SI at Prasat Yeai Poun (Fig.4, Aand B) to 1.772(10^{-3})SI at Tropang Kre (Quarry)(Table1). Based on magnetic susceptibility data compared to the yellowish porous laterite from the Angkor monument, it may be concluded that laterization in the area may Laterization from the weathering. [2]

3.2) Laterite Description

The reddish, yellowish, and dark brown laterite rocks make up the Sombor Prie Kuk temple. We can divide the physical characteristics of laterite based on hand specimen into two categories. Pebble grains and highly porous laterization (massive rock) with a reddish color characterize the texture of laminar flow of hematite and goethite weathering (Figure2). Additionally, the hand specimen for SPK04-TPK exhibits reddish to yellowish and dark brown hematite with a poorly sorted conglomerate texture of iron oxidation(Figure2,d). The ratio of hematite (red), goethite (yellow), and kaolinite (white) determines the color of laterites. [6]

3.3) Microscopy observation

According to a summary of microscopy analyses, SPK01-KT01-L1 has been eroded by iron oxide, such as hematite (reddish color), and SPK04-TPK-L1 (Figure 2c) shows goethite, which is orange to yellowish (Figure2.b). The majority of the quartz was found in the laterite. Even in laterite that experienced strong laterization, there are moderate amounts of orange quartz sand with angular and irregular grain forms that are thought to be of detrital origin and not a subsequent product.[3]

Table 1: Magnetic susceptibility of laterite at SPK

Site	ID	Average of Mag.Sus ($10^{-3} mm/cm^3$)
SAMBOR PREI KUK ANCIENT TEMPLES AREA	SPK01-KT01-L1	0.767
	SPK02-KT02-L2	0.848
	SPK03-KT04-L3	1.145
	SPK04-TPK	**1.772**
	SPK05-K8-L1	0.948
	SPK07-N16-L1	1.125
	SPK09-N21-L1	0.898
	SPK10-N24-L1	1.109
	SPK12-W1-L1	0.832
	SPK12-W2-L1	0.629
	SPK13-C1-W1-L1	0.906
	SPK13-C1-W2-L1	0.788
	SPK14-S-W1-L1	0.758
	SPK17-S1P	1.100
	SPK21-S17-L1	0.634
	SPK22-S15-W2-L1	0.948

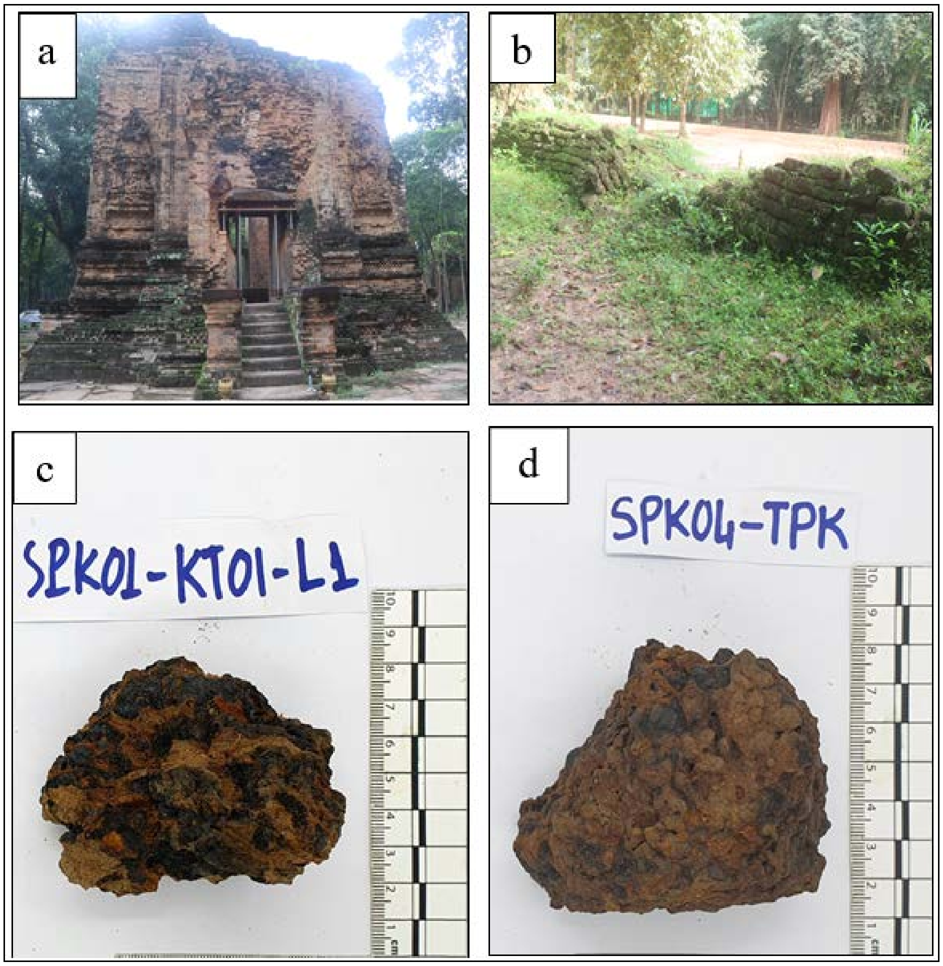

Fig. 1. (a) and (b) is location study at Sombor Prei Kuk laterite temple.(c) and (d) lateritic hand specimen sample.

3.4) Bulk Chemical composition

X-ray fluorescence (XRF) uses the bulk chemical composition to classify the condition of laterization. Nine elements of chemistry were analyzed, but we focused on three elements: Si, Al, and Fe oxides. The result, silica (Si), was recorded as the highest dry weight percentage in the range of 16.65% to 57.10%. The second highest is ferum (Fe) in the range of 21.91% to 58.97%, followed by aluminum (Al) in the range of 8.34% to 16.47%(Table 2). The final result was then represented on Schellman's Ternary diagram (Fig.3). Most of the laterite appears to have failed between weak and moderate lateralization. E. Uchida discovered that the laterites of These laterites experienced weak to moderate lateralization, in contrast to the sandstone and conglomerate weathering that was supposed to build the the Angkor. [5] Thus, the weathering of sedimentary rock may produce laterite from the Sambor Prei Kuk Area. [4]

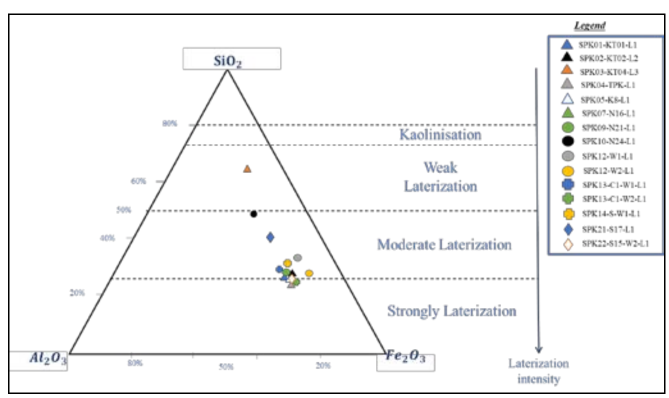

Schellman's diagram of define condition of Laterization in rock

Table 2: Quantification of major elements in samples using XRF analysis

Sample name	Result XRF		
	SiO_2	Al_2O_3	Fe_2O_3
SPK01-KT01-L1	20.86	14.18	43.57
SPK02-KT02-L2	23.47	13.88	47.83
SPK03-KT04-L3	57.15	10.29	21.91
SPK04-TPK-L1	16.65	16.47	51.88
SPK05-K8-L1	20.96	13.74	45.06
SPK07-N16-L1	21.78	14.52	49.48
SPK09-N21-L1	24.35	14.55	49.48
SPK10-N24-L1	43.78	14.55	29.13
SPK12-W1-L1	37.08	8.34	39.27
SPK12-W2-L1	17.08	9.76	58.97
SPK13-C1-W1-L1	23.53	16.35	42.23
SPK13-C1-W2-L1	21.59	14.00	49.24
SPK14-S-W1-L1	26.89	13.02	44.45
SPK21-S17-L1	33.89	13.19	34.75
SPK22-S15-W2-L1	22.60	15.22	48.91

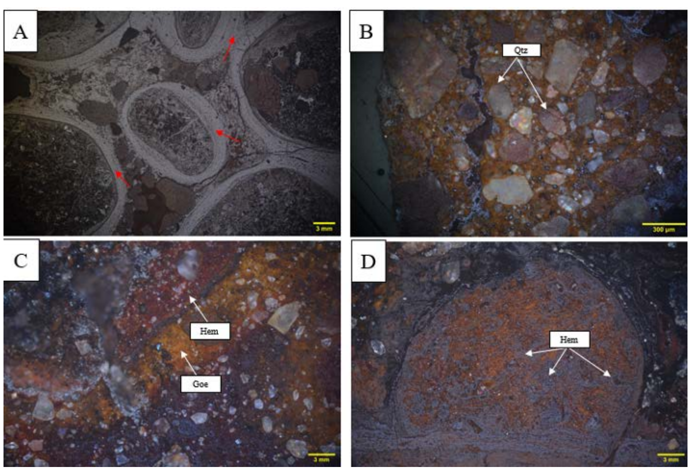

Fig. 2. Photomicroscope showing Hem: Hematite, Qtz: Qaurtz and Goe: Goethite, A) Conglomerate sandstone of hematite/goethite red arrow, B) Primary quartz with angular, rounded and irregular shape, C) Hematite and goethite weathering, D) Vesicula of hematite

4. CONCLUSIONS

- According to the results and observation from both field investigation, the SBK laterite ranges in weak to strong laterization, which may indicate the leaching from the original rocks, while the concentration of iron and aluminum increases.
- Studies on the magnetic susceptibility of SBK laterite conducted in the field may demonstrate that these rocks result from sedimentary rock weathering. SBK Laterite was predicted to form as a result of sedimentary rock weathering.
- Most laterite samples consist of hematite, Kaolinite, and quartz with reddish, yellowish, and dark brown laterite rocks.

ACKNOWLEDGMENTS

The General National Authority Sambor Prei Kuk, JICA_LBE, provided financing for the project, which the authors are grateful for. The authors acknowledge the scientists from the Institute of Technology of Cambodia's Center for Materials Research for their work with XRF and Petrography Microscopy.

REFERENCES

[1] Bourman, R. P., & Ollier, C. D. (2002). A critique of the Schellmann definition and classification of ‘laterite’. Catena, 47(2), 117-131

[2] Girard, J. P., Freyssinet, P., & Morillon, A. C. (2002). Oxygen isotope study of Cayenne duricrust paleosurfaces: implications for past climate and laterization processes over French Guiana. Chemical Geology, 191(4), 329-343.

[3] Swanson, C. O.(1923).The origin, distribution and Composition of laterite. Joural of the American Ceramic Soiety,6(12),1248-1260.

[4] Uchida, E., Tsuda, K., & Shimoda, I. (2014). Construction sequence of the Koh Ker monuments in Cambodia deduced from the chemical composition and magnetic susceptibility of its laterites. Heritage Science, 2(1), 1-11.

[5] Etsuo Ta, Noriyuki Maeda, & Takeshi Nakagawa (1999).

[6] 田悦生, 前田則行, & 中川武. (1999). The laterites of the Angkor monuments, Cambodia. The grouping of the monuments on the basis of the laterites. 岩鉱, 94(5), 162-175

Techno-Science Research Journal 12 (Special Issue) 156-162

Content list available at ITC

Techno-Science Research Journal

Journal Homepage: www.ric.itc.edu.kh

Techno-Science Research Journal

Oxidative Precipitation of Arsenic (III) with Iron (II) in Synthetic Groundwater using Diffused Aerator

Andy Theam[1], Saret Bun[2*], Phaly Ham[2,3], Rathborey Chan[2]

[1]*Department of Chemistry, Faculty of Science, Royal University of Phnom Penh, Phnom Penh 12156, Cambodia*
[2]*Water and Environmental Engineering, Faculty of Hydrology and Water Resources Engineering Institute of Technology of Cambodia, Phnom Penh 12156, Cambodia*
[3]*Water and Environment Research Unit, Research and Innovative Center Institute of Technology of Cambodia, Phnom Penh 12156, Cambodia*

Received: 21 August 2023; Accepted: 15 May 2024; Available online: August 2024

Abstract:. *The oxidation of Fe (II) might affect arsenite (As (III)) removal through co-oxidation and adsorption onto ferric hydroxide particle, a product results from Fe (II) oxidation. Many studies have investigated for iron (Fe) and arsenic (As) treatment methods, the simultaneous reduction of iron and arsenic has not widely studied by using aeration process. Therefore, this study aimed to investigate the effect of iron co-presence on arsenic removal in air diffused reactor towards optimizing the treatment operation and process. Five influent parameters, i.e., gas flow (1 – 3 L/min), initial pH (6.5 – 7.5), initial Fe (II) concentration (0 – 20 mg/L), and additional ferric hydroxide particle (α-FeOOH) (0 – 20mg/L), were examined in terms of As (III) removal efficiency. The experiments were conducted in 2-liter bubble column with a rigid stone air sparger at the bottom. Dissolved oxygen and pH meters were connected and monitored throughout the experiment. The results revealed that initial pH, initial Fe (II) concentration, operating time, and air flow are significant factors affect As (III) removal efficiency, except iron hydroxide factor. The removal efficiency of As (III) increases from 4% to 91% after increase initial pH from 6.5 to 7.5. A rapid rise was observed after changing from acidic to neutral condition. Hence, As (III) could be removed to more than 75% at circumneutral pH. As (III) removal without Fe (II) co-presence found approximately 15%, while increasing up to 80% in average after providing presence of ferrous iron 10 mg/L. However, it could find a slight change to 83% after increasing up to 20 mg/L of Fe (II) concentration. The optimum values for each factor were established based on the optimization plot such as initial pH ≈ 7.12, initial Fe (II) concentration ≈ 17.5. mg/L, gas flow rate ≈ 2 L/min, and operating time ≈ 40 minutes. In overall, it can be stated that the performance of As (III) removal is greater at higher pH values under identical operating conditions. Higher values of operating time and ferric hydroxide led to improve arsenic removal, except higher gas flow rate slightly decreases removal efficiency.*

Keywords: Arsenic; Co-oxidation; Diffused reactor; Groundwater; Iron

1. INTRODUCTION

Groundwater is frequently utilized for agriculture and domestic use [1]. More than 50% of the population relies on it for drinking water during the dry season, with the proportion rising in rural areas where surface water is inaccessible [2]. Groundwater is acceptable with their clean and clear appearance, however, iron and arsenic, are frequently found within groundwater. These substances are known as toxic substance which can harm to consumers. Phan et al. [3] found that some rural Cambodians who reside in arsenic-polluted area have already noticed to arsenic adverse effect.

WHO and United Stated Environmental Protection Agency (USEPA) set the drinking water standard guideline to less than 10 µg/L for arsenic. To comply with WHO standard guidelines, several treatment technologies were documented such as adsorption [4], coagulation-flocculation [5], electrochemical [6], ions exchange [7], membrane technology [8], and oxidation-filtration [9-10]. These methods have been

* Corresponding author: Saret Bun
E-mail: saret@itc.edu.kh; Tel: +855-68-721-111

frequently employed, but they have some disadvantages, including high operating and waste treatment costs, high chemical consumption, and produce amount of sludge production [10]. Oxidation can be done through aeration process is commonly applied to remove some pollutants load in wastewater treatment [11], and also dissolved metals in groundwater [12]. This method is simple, affordable, and sustainable use for rural area.

To remove arsenic effectively, As (III) must be converted to As (V) and followed by other treatment technologies. Arsenic oxidation through the aeration process has also been mentioned, but the oxidation rate was sluggish. The oxidation process of ferrous iron converting to ferric hydroxide particle might partially oxidize As (III) to As (V), according to literature [13]. Thus, iron co-presence is crucial to enhancing the oxidation rate for arsenic. Indeed, the adsorption process of arsenic onto ferric hydroxide has also been discussed in several publications [15-16]. Even though many researchers have investigated iron and arsenic treatment methods, the simultaneous reduction of iron and arsenic has yet to be thoroughly investigated on aerated oxidation by air. Therefore, this study aimed to investigate the effect of iron co-presence on arsenic removal by aeration process. Furthermore, five influent parameters, including supplied gas flow rate, fixed initial pH, initial concentration of ferrous iron, and initial ferric hydroxide particle were examined.

2. METHODOLOGY

2.1 Experimental set-up and procedure

The experiments were conducted in the beaker which can contain 2 L of total working volume, as illustrated in Fig.1. A rigid stone air sparger was connected with a compressed air pump and put at bottom of the reactor. pH and DO meters were connected and monitored throughout the experiment. DO and pH sensors were placed to the top of beaker for monitoring purpose. Gas flow rate was controlled by using gas flow meter.

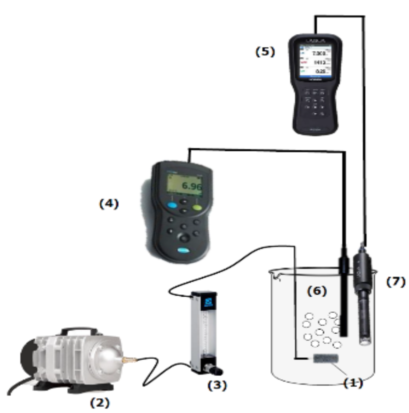

(1). Rigid stone air sparger
(2) Compressed air pump
(3) Gas flow meter
(4) Multi-meter
(5) Multi-meter
(6) DO probe
(7) pH probe

Fig. 1. Experimental set-up as batch experiment

Batch experiment was conducted in this study. Synthetic groundwater must be freshly prepared from de-aerated tap water using sodium sulfite $NaSO_3$ (Merck) to remove dissolved oxygen to lower than 0.1mg/L before adding other chemicals. The variations of Fe (II) and Fe (III) concentration were prepared by adding ferrous sulphate heptahydrate $FeSO_4.7H_2O$ (Merck) and ferric hydroxide particle (α-FeOOH) (Alfa Aesar), respectively. As (III) was prepared from sodium meta-arsenite $NaAsO_2$ (KEMAUS). The pH condition was adjusted by using 1 M of HCl and NaOH. As an additional investigated parameter, sampling time varied depending on the experimental design. Fe (II), As (III) concentration, the change of pH and dissolved oxygen were all measured throughout the process. Dissolved oxygen and pH of water sample were monitored by using DO sensor (HACH Intellica LDO) and pH sensor (Horiba PH100s), respectively. Gas flow rate was controlled by using gas flow meter (KOFLOC RK1250).

2.2 Analytical methods

The concentration of Fe (II) were measured by using 1,10-phenanthroline colorimetric method, followed standard method [15]. UV-Vis spectrophotometer (model Shimadzu 1280-UV Spectrophotometer) were used to measure the colour intensity with wavelength 510 nm. Since the removal of As (III) was the main focus of this investigation. As a result, before analysis, arsenic speciation must be distinguished. Using the disposable cartridge, As (V) and As (III) species was separated from water samples[16]. A few drops of 65% nitric acid were used to acidify the filtered sample, which was then refrigerated for further analysis. Water sample was delivered to the Laboratory of Nanostructure and Chemical Analysis under Faculty of Geo-resources and Geotechnical Engineering (GGE). Microwave Plasma Atomic Emission Spectroscopy (Model Agilent 4210 MP-AES) was used to determine the arsenic concentration in the water sample, with a lower detection limit of 1.4 µg/L [17].

2.3 Removal efficiency

Experimental performance was evaluated in terms of pollutant removal efficiency as expressed in Eq. 1 below, where C is concentration.

$$\text{Removal (\%)} = [(C_{initial} - C_{final})/C_{initial}] \times 100 \quad \text{(Eq. 1)}$$

2.4 Experimental design and statistical analysis

Central Composite Design for Response Surface Methodology (CCD-RSM) was used for experimental design and analysis in factor optimization. In this study, Design of Experiment (DOE) of Minitab 19 computer software was used to define the design of experimental conditions and analysis. Analysis of Variance (ANOVA) was also used as statistical analysis of experimental result. It should be noted that single and square term in ANOVA was used to compare mean value and also relationship between factors and response, respectively. The experimental condition was constructed in three levels for five factors, as expressed in Table 1. The basic design of each factor's range was based on the initial experiment.

Table 1. Factors and factor levels for optimization study

Factors	Units	Factor Levels		
		-1	0	+1
Initial pH (pH_o)	-	6.5	7.0	7.5
Initial Ferrous concentration $[Fe^{2+}]_o$	mg/L	0	10	20
Additional ferric hydroxide (α-FeOOH)	mg/L	0	10	20
Gas flow rate (Qg)	L/min	1	2	3
Time (T)	min	0	20	40

It should be mentioned the figure from Minitab software has its limitation in that it only depicts the fitted curve of actual data points.

3. RESULTS AND DISCUSSION

This section aimed to examine influent factors on the As (III) removal. The statistical analysis of variance (ANOVA) was used as the main analysis approach. Regarding to the findings, the initial pH, initial Fe (II) concentration, operation time, and air flow rate significantly affected As (III) removal with single terms (p-values<0.05). While, ferric hydroxide was found insignificant effect on As (III) removal on both single and square term (p-value <0.05). In overall, it can be concluded that initial pH, initial concentration of ferrous iron, gas flow rate, and operation time were the significant factors influent on As (III) removal, except ferric hydroxide. This can be due to inadequate of additional ferric hydroxide for increasing removal performance. Most studies on the arsenic adsorption use adsorbent concentration up to g/L [18] compare to this study used mg/L. This relates to conversion of Fe (II) concentration to Fe (III) due to stoichiometric of reaction. The trend and pattern of each investigated factors on As (III) treatment performance would therefore analysed in the following section.

After obtaining the experimental result designed by full design of response surface methodology with three levels and single replication, the optimization process was studied. Fig 2. illustrates the main effective plot of each factor on As (III) removal. Except for the operation time factor, which was given in a linear line with the factor levels, each variable's pattern was shaped such a curve. Initial pH and initial Fe (II) iron concentration, and gas flow rate were showed in concave curve, while additional ferric hydroxide was presented in convex plot.

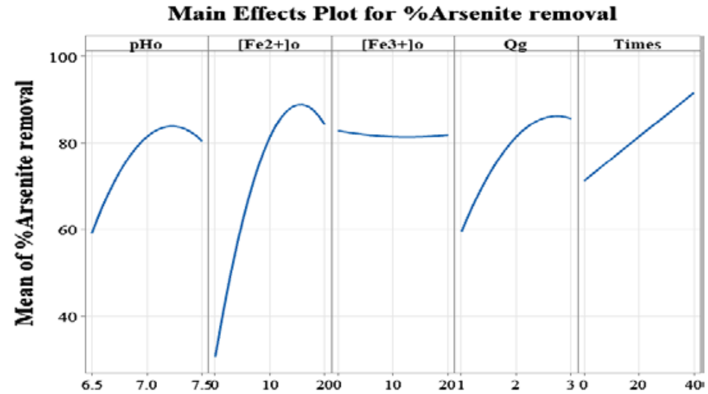

Fig.2. Optimized plot of each variable on As (III) removal

3.1 Effect of initial pH

Higher removal efficiency increases with increasing pH from 6.5 to 7.0. However, increasing from 7.0 to 7.5 resulted a moderate decrease in average of treatment efficiency due to some experimental conditions, designed in low level of Fe (II) concentration ($[Fe(II)]_o$ ~ 0 mg/L). Therefore, a slight decrease in average of As(III) removal should be due to some conditions designed without Fe (II) co-presence. The removal efficiency varied between 4% and 91% as a result of the initial pH being changed from 6.5 to 7.5. It increased rapidly when the initial pH increased from 6.5 to 7.0, but slightly declined as the initial pH kept increasing from 7.0 to 7.5 as illustrated in Fig.3. The elimination of As (III) may be increased to more than 75% around circumneutral pH. It should be emphasized that the main effective plot (see in Fig.2) was constructed using the mean value of the removal efficiency of As (III).

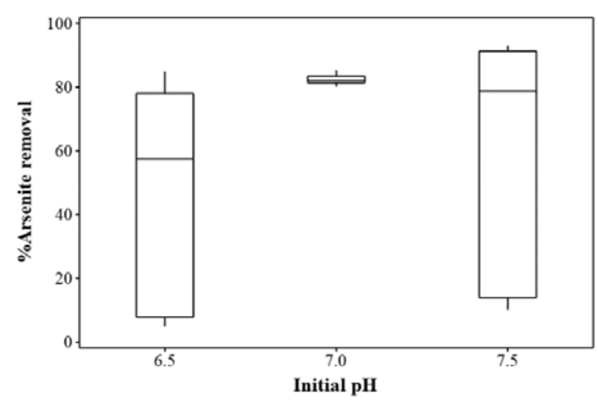

Fig.3. Boxplot of a relative effect of pH on As (III) removal efficiency

The reduction of As (III) may be increased to more than 75% around circumneutral pH as illustrated in Fig.4. It evident that the effect of initial pH, increasing from 6.5 to 7.0, or equivalent to the actual pH change from 6.87 to 7.38, is a significantly influent on As (III) removal. After keeping an initial pH increases from 7.0 to 7.5, or an actual pH increase from 7.38 to 7.72, the removal efficiency is reversely reduced.

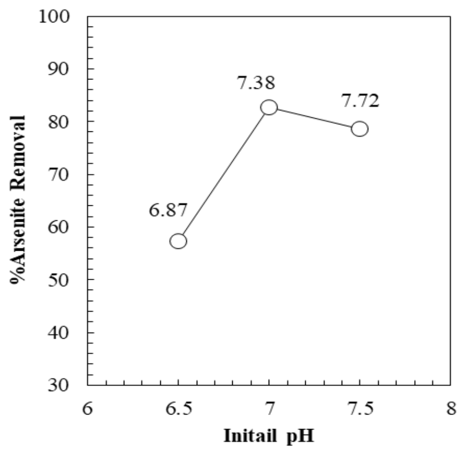

Fig.4. Comparison of As (III) removal at different initial pH (actual pH) under the condition: $[Fe(II)]_o$ ~ 10 mg/L, $[Fe(OH)_3]$ ~ 10 mg/L, Qg ~ 2 L/min, and 20 minutes

Higher initial pH could increase Fe (II) oxidation rate, but it could also provide an impact on As (III) oxidation. At higher initial pH, the rate of iron oxidation was completed rapidly. Thus, As (III) is not further oxidized when Fe (II) oxidation is completed [19]. Detailed elucidation would be discussed in the effect of Fe (II) iron with section below. Additionally, pH was also an important parameter in the arsenic adsorption process because the variation of proton concentration can strongly modify the chemical speciation of arsenic as well as a surface charge of sorbents. Hu et al. [20] reported that As (III) removal by adsorption onto goethite (α-FeOOH) arise with increasing pH from 3.1 to 7.0, and remains the same afterward from 7.0 to 9.5. Therefore, it can be concluded that significant removal performance could be observed around the neutral condition.

3.2 Effect of initial ferrous iron

The boxplot for all experimental conditions at different initial concentrations of Fe (II) iron was illustrated in Fig.5. As (III) removal without ferrous iron co-presence provided from approximately 14.77% in mean value for arsenic removal efficiency while, the removal performance could increase up to approximately 80% in mean value after providing the presence of Fe (II) 10 mg/L. Nevertheless, performance found a slightly change to 83% in mean value after increasing ferrous iron by 20 mg/L.

Arsenic co-precipitation with naturally occurring Fe(II) is the most straightforward arsenic removal method without chemical addition [13].

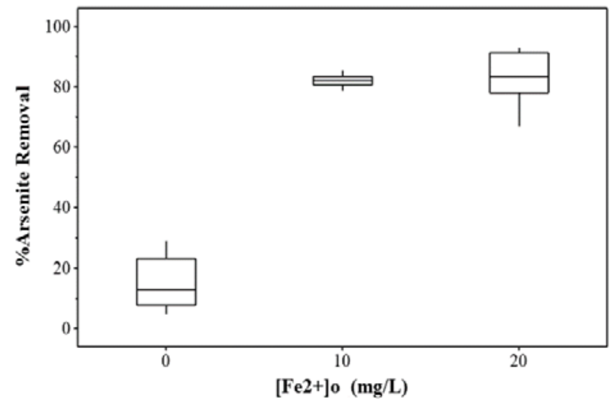

Fig.5. Boxplot of relative effect of initial Fe (II) concentration As (III) removal efficiency

Without presence of Fe (II) iron, As (III) removal was reduced through adsorption onto goethite particle. The results found 14.77% for removal with initial pH of 6.5 and an increase to 57.39% for the initial pH 7.0. However, for initial pH 7.5 the removal efficiency was decreased to 13.7%. This can explain due to the surface charge of ferric hydroxide particle and the structure of As (III). In this part, main mechanism is only adsorption process. At neutral pH, surface of goethite (α-FeOOH) is in positively charge (pH_{zpc}= 7.2) [21] which could benefit for As (III) adsorption. Subsequently, anionic As (III) species predominate at more alkaline pH values and the surface of the solid is negatively charged, the interaction between arsenic and the minerals is more challenging [22].

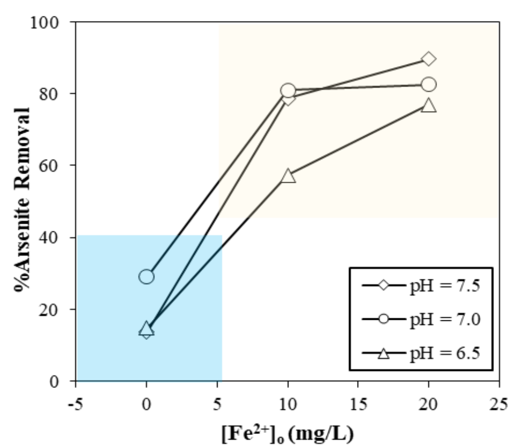

Fig.6. Comparison of mean As (III) removal at different ferrous initial concentration and initial pH (data label presents actual pH)

Fig.6. has been shown that when Fe (II) concentration increases, As (III) removal also increases. Removal performance revealed that the mean value of removal efficiency was approximately the same for 10 mg/L, at initial pH 7.0 and 7.5, except for initial pH 6.5. This can be explained due to slow oxidation process for Fe (II) iron to produce oxidant. As (III) removal straightly increased with increasing of initial ferrous iron in higher initial pH. The oxidation of As (III) must occur by reactive oxygen species (O_2^-, H_2O_2, OH^-), or other oxidizing intermediates that are formed as intermediates during the reduction of O_2 with Fe (II) [19]. The co-presence of Fe (II) and Fe (III) is beneficial for arsenic removal. Since Fe (II) can lead As (III) to undergo oxidation to As (V), ferric hydroxide particle from Fe (II) oxidation could also provide adsorption behaviour in order to increase the removal performance [23,24]. Therefore, higher ferrous iron could provide higher As (III) removal.

3.3 Effect of other parameters

Based on the factorial analysis, the other significant factors are operating time, air flow rate. As expected, the effective trend of operating time linearly increased with As (III) removal. Between 20 and 40 minutes, it could achieve higher than 75% removal efficiency. Therefore, it can be concluded that within 40 minutes operating time, the arsenic could be removed up to 84%. Gas flow rate also pronounce a substantial effect on arsenic removal according to factorial analysis. Increasing gas flow effect on two aspect including dissolved oxygen concentration and mixing condition of aquatic solution.

When Fe (II) is not presented, As (III) may be removed by 29% adsorption onto ferric hydroxide particles, according to one operating condition. Therefore, adsorption is a crucial step in the elimination of arsenic without iron co-present.

3.4 Summary of optimum level

The effects of process parameters and the optimal level for removing As (III) from aqueous solutions were attempted to be summed up in this section. The initial pH, the initial concentration of ferrous iron, the operating time, and the gas flow rate were all significant factors in single terms, except iron hydroxide was found insignificant effect according to the factorial analysis using the statistical analysis of variance (ANOVA) developed by CCD-RSM. This implies that it is required to analyse and optimize all previously investigated parameters in order to maximize removal efficiency. It was evident that As (III) removal performance improves with pH value, and that its considerable removal performance could be noticed in neutral and alkaline conditions, although pH was found to be present in the main effective plot's optimum curve. Finally, it is suggested that the aquatic pH be prepared at a level at least higher than 7.0 to obtain high arsenic removal.

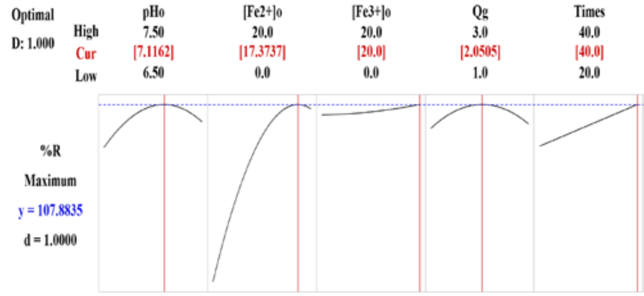

Fig.7. Optimization plot of each variable to maximize As (III) removal.

The optimum of each factor was established based on the optimization plot as shown in Fig.7, i.e., initial pH ≈ 7.12, initial ferrous iron concentration ≈ 17.47 mg/L, initial iron hydroxide concentration ≈ 20 mg/L, gas flow rate ≈ 2 L/min, and operating time ≈ 40 minutes. Table.2 provides a summary of the examined range (factor level) and optimal condition for each factor. It finally recommends that the actual aquatic pH should be prepare at least higher than 7.

Table 2. Summary of factor levels studied and optimum conditions

Factors	pH_0	$[Fe(II)]_0$	$[Fe(OH)_3]_0$	Qg	Time
	[-]	[mg/L]	[mg/L]	[L/min]	[min]
Studied ranges	Min	6.50	0	0	1
	Max	7.50	20	20	3
Optimum level		7.12	17.37	20	2

4. CONCLUSIONS

A key approach for dealing with arsenic removal should be the study of arsenic removal with iron co-presence by aeration. Therefore, this current research aimed investigate the effect of oxidative Fe (II) co-presence on arsenic removal. The results found that relative influence of Fe (II) co-presence on the removal of As (III) in batch conditions were also examined. The removal efficiency could range between 4% to 91% with initial pH changed from 6.5 to 7.5. A rapid change was observed to more than 75% of removal efficiency when changing acidic to neutral condition. Additionally, 15% less As (III) was removed when Fe (II) was absent. The removal efficiency was enhanced by up to 80% when Fe (II) was increased to 10 mg/L. However, minor variation was noticed after increasing the Fe (II) concentration to 20 mg/L. The initial pH, the initial concentration of ferrous iron, the operating time, and the air flow are all significant factors in single terms, except iron hydroxide was found insignificant effect according to the factorial analysis using the statistical analysis of variance (ANOVA) developed by CCD-RSM. The optimum values for each factor were established based on the optimization plot, i.e., initial pH ≈ 7.12, initial ferrous iron concentration ≈ 17.47. mg/L, initial iron hydroxide concentration ≈ 20 mg/L, gas flow rate ≈ 2 L/min, and operating time ≈ 40 minutes. Since Fe (II) is easily oxidized by aeration process and may provide beneficial substances which could possibly to enhance arsenic removal from water by using existing natural pollutants in groundwater.

ACKNOWLEDGMENTS

This study was funded by Laboratory-Based Education (LBE) Project of Japan International Cooperation Agency (JICA) in Institute of Technology of Cambodia (ITC).

REFERENCES

[1] R. Johnston, M. Roberts, T. Try, and S. De Silva, "Groundwater for Irrigation in Cambodia," *International Water Management Institute*, no. June, 2013, [Online]. Available: http://www.iwmi.cgiar.org/Publications/issue_briefs/cambodia/issue_brief_03-groundwater_for_irrigation_in_cambodia.pdf

[2] ODC, "Groundwater," *Open Development Cambodia*, 2016. https://opendevelopmentcambodia.net/topics/groundwater/ (accessed Aug. 04, 2023).

[3] K. Phan *et al.*, "Health risk assessment of inorganic arsenic intake of Cambodia residents through groundwater drinking pathway," *Water Research*, vol. 44, no. 19, pp. 5777–5788, 2010, doi: https://doi.org/10.1016/j.watres.2010.06.021.

[4] J. G. Hering, P.-Y. Chen, J. A. Wilkie, M. Elimelech, and S. Liang, "Arsenic removal by ferric chloride," *Journal AWWA*, vol. 88, no. 4, pp. 155–167, Apr. 1996, doi: https://doi.org/10.1002/j.1551-8833.1996.tb06541.x.

[5] V. Pallier, G. Feuillade-Cathalifaud, B. Serpaud, and J.-C. Bollinger, "Effect of organic matter on arsenic removal during coagulation/flocculation treatment," *Journal of Colloid and Interface Science*, vol. 342, no. 1, pp. 26–32, 2010, doi: https://doi.org/10.1016/j.jcis.2009.09.068.

[6] J. F. Martínez-Villafañe, C. Montero-Ocampo, and A. M. García-Lara, "Energy and electrode consumption analysis of electrocoagulation for the removal of arsenic from underground water," *Journal of Hazardous Materials*, vol. 172, no. 2, pp. 1617–1622, 2009, doi: https://doi.org/10.1016/j.jhazmat.2009.08.044.

[7] A. Ortega, I. Oliva, K. E. Contreras, I. González, M. R. Cruz-Díaz, and E. P. Rivero, "Arsenic removal from water by hybrid electro-regenerated anion exchange resin/electrodialysis process," *Separation and Purification Technology*, vol. 184, pp. 319–326, 2017, doi: https://doi.org/10.1016/j.seppur.2017.04.050.

[8] C. M. Nguyen, S. Bang, J. Cho, and K.-W. Kim, "Performance and mechanism of arsenic removal from water by a nanofiltration membrane," *Desalination*, vol. 245, no. 1, pp. 82–94, 2009, doi: https://doi.org/10.1016/j.desal.2008.04.047.

[9] M.-J. Kim and J. Nriagu, "Oxidation of arsenite in groundwater using ozone and oxygen," *Science of The Total Environment*, vol. 247, no. 1, pp. 71–79, 2000, doi: https://doi.org/10.1016/S0048-9697(99)00470-2.

[10] B. Shao, Y. Guan, Z. Tian, X. Guan, and D. Wu, "Advantages of aeration in arsenic removal and arsenite oxidation by structural Fe(II) hydroxides in aqueous solution," *Colloids and Surfaces A: Physicochemical and Engineering Aspects*, vol. 506, pp. 703–710, 2016, doi: https://doi.org/10.1016/j.colsurfa.2016.07.049.

[11] G. Skouteris, G. Rodriguez-Garcia, S. F. Reinecke, and U. Hampel, "The use of pure oxygen for aeration in aerobic wastewater treatment: A review of its potential and limitations," *Bioresource Technology*, vol. 312, p. 123595, 2020, doi: https://doi.org/10.1016/j.biortech.2020.123595.

[12] G. T. Charles Crittenden,David W. Hand, R. Rhodes Trussell, Kerry J. Howe, "MWH's Water Treatment Principles and Design," in *Removal of Selected Constituents*, 2012, p. 1548.

[13] L. C. Roberts, S. J. Hug, T. Ruettimann, M. M. Billah, A. W. Khan, and M. T. Rahman, "Arsenic Removal with Iron(II) and Iron(III) in Waters with High Silicate and Phosphate Concentrations," *Environmental Science & Technology*, vol. 38, no. 1, pp. 307–315, Jan. 2004, doi: 10.1021/es0343205.

[14] W. Driehaus, M. Jekel, and U. Hildebrandt, "Granular ferric hydroxide—a new adsorbent for the removal of arsenic from natural water," *Journal of Water Supply: Research and Technology-Aqua*, vol. 47, no. 1, pp. 30–35, Feb. 1998, doi: 10.2166/aqua.1998.0005.

[15] APHA, "3500-Fe B. Phenantroline Method," in *Standard Methods for the Examination of Water and Wastewater*, A. D. E. Lenore S.Clesceri, Arnold E. Greenberg, Ed., 20th ed.American Publich Health Association, 1999, pp. 472–477.

[16] W. W. Xiaoguang Meng, "SPECIATION OF ARSENIC BY DISPOSABLE CARTRIDGES," in *Third International Conference on Arsenic Exposure and Health Effects*, 1998.

[17] R. A. S. Rodolfo Lorençatto, Debora Nascimento Monção, "High Throughput, Multi-Element Analysis of Effluents by MP-AES," 2020. Accessed: Mar. 08, 2023. [Online]. Available: https://www.agilent.com/cs/library/applications/application_multielement_effluents_4210_mp-aes_5994-1746en_us_agilent.pdf

[18] M. Gallegos-Garcia, K. Ramírez-Muñiz, and S. Song, "Arsenic Removal from Water by Adsorption Using Iron Oxide Minerals as Adsorbents: A Review," *Mineral Processing and Extractive Metallurgy Review*, vol. 33, no. 5, pp. 301–315, Sep. 2012, doi: 10.1080/08827508.2011.584219.

[19] S. J. Hug and O. Leupin, "Iron-Catalyzed Oxidation of Arsenic(III) by Oxygen and by Hydrogen Peroxide: pH-Dependent Formation of Oxidants in the Fenton Reaction," *Environmental Science & Technology*, vol. 37, no. 12, pp. 2734–2742, Jun. 2003, doi: 10.1021/es026208x.

[20] J.-L. Hu, X.-S. Yang, T. Liu, L.-N. Shao, and W. Zhang, "Adsorption characteristic of As(III) on goethite waste generated from hydrometallurgy of zinc," *Water Science and Technology*, vol. 75, no. 12, pp. 2747–2754, Mar. 2017, doi: 10.2166/wst.2017.101.

[21] S. Dultz, H. Steinke, R. Mikutta, S. K. Woche, and G. Guggenberger, "Impact of organic matter types on surface charge and aggregation of goethite," *Colloids and Surfaces A: Physicochemical and Engineering Aspects*, vol. 554, pp. 156–168, 2018, doi: https://doi.org/10.1016/j.colsurfa.2018.06.040.

[22] J. Giménez, M. Martínez, J. de Pablo, M. Rovira, and L. Duro, "Arsenic sorption onto natural hematite, magnetite, and goethite," *Journal of Hazardous Materials*, vol. 141, no. 3, pp. 575–580, 2007, doi: https://doi.org/10.1016/j.jhazmat.2006.07.020.

[23] C. M. van Genuchten and A. Ahmad, "Groundwater As Removal by As(III), Fe(II), and Mn(II) Co-Oxidation: Contrasting As Removal Pathways with O2, NaOCl, and KMnO4," *Environmental Science & Technology*, vol. 54, no. 23, pp. 15454–15464, Dec. 2020, doi: 10.1021/acs.est.0c05424.

[24] L. Wang and D. E. Giammar, "Effects of pH, dissolved oxygen, and aqueous ferrous iron on the adsorption of arsenic to lepidocrocite," *Journal of Colloid and Interface Science*, vol. 448, pp. 331–338, 2015, doi: https://doi.org/10.1016/j.jcis.2015.02.047.

Techno-Science Research Journal 12 (Special Issue) 163-171

Content list available at ITC

Techno-Science Research Journal

Journal Homepage: www.ric.itc.edu.kh

Groundwater Quality Assessment Towards Sand Filter Modification for a Rural Community of Cambodia

Kimlay Ngorn[1], Saret Bun[1*], Phaly Ham[1,2], Rathborey Chan[1]

[1] *Water and Environmental Engineering, Faculty of Hydrology and Water Resources Engineering, Institute of Technology of Cambodia, Russian Federation Blvd., P.O. Box 86, Phnom Penh, Cambodia*

[2] *Water and Environmental Research Unit, Research and Innovation Center, Institute of Technology of Cambodia, Phnom Penh 12156, Cambodia*

Received: 22 August 2023; Accepted: 15 May 2024; Available online: August 2024

Abstract: *In Cambodia, groundwater is utilized significantly in rural areas, and half of the population relies on it as their drinking water source. Unfortunately, high levels of arsenic (As), iron (Fe), manganese (Mn), and total dissolved solids (TDS) commonly found in the groundwater of Cambodia. Long-term exposure to those contaminants will pose a health risk to the consumer. This study focuses on groundwater quality assessment and the modification of sand filter for household water use. The study was conducted in Prasat commune of S'ang district, Kandal province, where groundwater is the main source of drinking water. As a result, it was found that As, turbidity, and Fe exceeded the permissible limits of drinking water quality standard. By using the water quality index (WQI) technique, up to 40% of the groundwater in this commune was not suitable for consumption or drinking purposes. The modification of the sand filter was employed by adding commercial activated carbon in order to remove Fe and As. Before this modification, various depths (18.4 cm as low, 36.6 cm as medium, and 55.0 cm as high depths) and sand diameter (1 – 0.6 mm and 0.3 – 0.5 mm) were studied in order to improve the removal performance. An acrylic tank comprising a dimension of 20 cm × 20 cm and 70 cm height with a combination of sand, coarse sand, and gravel was used. As a result, the optimized depth and size of sand for Fe and As removal were 55 cm with a sand size of 0.3–0.5 mm, which can remove Fe and As up to 95% and 50%, respectively. Furthermore, the effect of the co-presence of Fe was also examined for arsenic removal. The removal efficiency was improved up to 90% with an As:Fe ratio of 3:100. By adding activated carbon, As can be removed by up to 95% at a depth of 18.4 cm. The activated carbon should be placed at the top of the sand layer in order to get a high-performance result. The finding is important as an alternative technique instead of the conventional sand filter that cannot remove arsenic from water. Moreover, the commercial activated carbon nowadays can be found in the local market with low cost.*

Keywords: Commercial activated carbon; Groundwater quality; Rural community; Sand filter; Water quality index

1. INTRODUCTION

In Cambodia, groundwater is mostly used by people in rural areas when surface water is not available (e.g. due to contaminants, no pipe water available, and the distance of surface water sources). Groundwater has supplied around 53% of the population's drinking water in the dry season and the proportion increased in rural areas [1]. Furthermore, high levels of contamination, including arsenic, iron, manganese, fluoride, and total dissolve solids, have been observed in groundwater in certain areas [2,3]. Especially arsenic and iron are frequently detectable in groundwater. The high concentration of arsenic was found along the Mekong River deltas. According to the study by Berg et al.[4], the main sources of arsenic pollution in the Mekong River Deltas are natural weathering of arsenic-containing minerals, agricultural practices such as the use of arsenic-containing pesticides and fertilizers, and aquaculture activities.

In terms of treatment, 23% of households in rural areas do not treated their drinking water and are unaware of their groundwater quality. In addition, thousands of Cambodian families have utilized bio-sand filter (BFS) to purify

* Corresponding author: Saret Bun

E-mail: saret@itc.edu.kh; Tel: +855-68-721-111

contaminated water due to its cost-effectiveness and efficieny in removing impurities from water, making it ideal for the Cambodian region. According to study conducted by Ngai et al. [5], a bio- sand filter has capacity of removing up to 80% of remove arsenic and iron. However, the sand media is not a complete solution for the removal of arsenic, and some individuals believe that activated carbon may be a more effective option for effective option for elimination this toxic chemical. To address this concern, the aim of this investigation is to evaluate the physical and chemical attributes of groundwater to enhance the performance of sand filter as household water treatment units. The assessment involves collecting and analyzing samples of groundwater from different locations to identify potential contaminants. Additionally, the water quality index method has been used in order to represent the quality of groundwater in this study area. Groundwater assessment is an important first step in determining the need for bio-sand modification in a rural community to make the groundwater safe for consumption. The modification is to ensure that the size and depth of sand media used in water treatment processes is effective in removing contaminants and producing safe drinking water for communities. The people living in this impacted area would also benefit from the information collected, which could be used to identify possible sources of contamination and create plans to stop contamination in the future.

2. METHODOLOGY

2.1 Study Area

Prasat is a rural commune in district of S'ang, Kandal province, located about 54 km from Phnom Penh, the capital city of Cambodia. Geographically, Prasat is located 11°17'26.5'' latitude and 105°9'22.9'' longitude with coverage area of 84.71 km^2. The population of this commune is approximately 5430 in 2019 and the population density is 64.10/km^2. Administratively, this commune exists 5 villages including Lek Mouy Village, Lek Pi Village, Lek Bei Village, Lek Boun Village and Lek Pram Village as shown in Figure. 1. Each village has different number of sources and haft of people in this commune use groundwater (hand dug well and electric well) for consumption. The study area was selected due to the report of IRD [6] was evaluated the arsenic concentration were observe within this commune which associated with the iron concentration and turbidity. But the insufficient number of sample were collected in this commune to adequately characterize groundwater conditions.

2.2 Groundwater Sampling

The grab sampling technique was employed since it provided more representative sampling for groundwater. In order to evaluate the water quality in this research area and analyze the water for physical and chemical parameters, twelve water well samples were taken. The sampling site was shown in Figure 4 along with the spacial map of water quality index value. The selection is based on the number of residents in the village who rely on groundwater for daily needs and the sample's accessibility.The twelve water samples were sampled from Lek Pram, Lek Pi, and Lek Bei villages. Onsite measurements included pH, temperature, electrical conductivity, dissolved oxygen, salinity, ORP, and TDS. Chemical parameters were collected for laboratory analysis. Samples were stored at 4°C to prevent contamination.

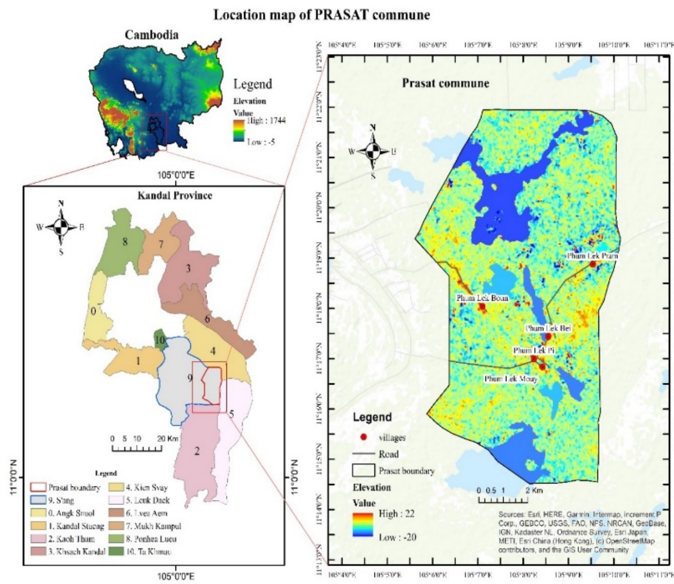

Fig. 1. Location of the study area

2.3 Water Quality Index Method

The study of water quality index method was attemped in order to evalute the quality of groundwater in Prasat commune whether it was suitable for drinking purpose or not. Ten water quality parameters have been selected including pH, turbidity, electrical conductivity (EC), oxygen reduction potential (ORP), total dissolved solid (TDS), arsenic (As), iron, fluoride, chloride, and total hardness. The calculation of water quality index was followed four steps as:

Step 1: Assigned the weight (AWi) of those ten parameters which ranging from 1 to 5 depending on their perceived effect on primary health. These assigned weights were based on the study by Ramakrishnaiah, C. et al. [7] , Dwivedi, S. et al. [8], Karakaya, N. et al. [9], Pesce, S. et al. [10], and Alobaidy, A. et al. [11].

Step 2: Secondly, calculate the relative weight (RW) by using the following:

$$RW=\frac{AW_i}{\sum_{i=1}^{n} AW_i} \qquad \text{(Eq. 1)}$$

where:
RW = relative weight
AW = assigned weight of each parameter
N = number of parameters

Step 3: Thirdly, calculate the quality rating scale (Q_i) for all parameters except pH and DO.
Quality rating scale of each parameter were calculated by:

$$Q_i=\frac{V_i}{S_i}\times 100 \qquad \text{(Eq. 2)}$$

Quality rating scale for pH and DO were calculated by:

$$Q_{pH,DO}=\frac{V_i-I_i}{S_i-I_i} \qquad \text{(Eq. 3)}$$

Where, I_i= the Ideal value which is considered as 7.0 for pH and 14.6 for DO.

Table 1. The calculation of relative weight for each parameters

Parameter	Unit	WHO standard	Assigned Weight (AW_i)	Relative Weight (RW_i)
pH	-	6.5-8.5	4	0.129
EC	µS/cm	1600	2	0.065
TDS	mg/L	800	4	0.129
ORP	mV	700	1	0.032
Turbidity	NTU	5	2	0.065
Arsenic	mg/L	0.01	5	0.161
Iron	mg/L	0.3	4	0.129
Fluoride	mg/L	1.5	4	0.129
Chloride	mg/L	250	3	0.097
Hardness	mg/L	300	2	0.065
	Total:		31	1

Step 4: Finally, calculation the sub-indices (SI_i) for each parameter. Then, computing the water quality index (WQI) by following the below:

$$SI_i=RW\times Q_i \qquad \text{(Eq. 4)}$$

$$WQI=\sum_{i=1}^{n} SI_i \qquad \text{(Eq. 5)}$$

The computed WQI values are classified into five types from “excellent water” to “unsuitable for drinking” [7].

Table 2. Water quality index classification [12]

WQI value	Water quality
<50	Excellent
50-100	Good water
100-200	Poor water
200-300	Very poor water
>300	Water unsuitable for drinking purpose

2.4 Filter Design

The filter design for this study was designed followed by CAWST [13]. The bench scale column filter had 750 mm depth with 5cm standing water and 200mm filter dimension as shown in Figure 2. The column test was installed using transparent material (acrylic tank) in order to observation the clogging, adjustment of the height of media and can be seen clearly when the tank performance. A diffuser was also designed in order to distribute the flow of water across the surface of the sand bed. This allows for more effective filtration of the water, as it ensures that all areas of the sand bed are used to filter out impurities. One acrylic tank was set up for this study with observation on three difference depth and two difference diameters of fine sand in order to find the best performance of removal of the filter. Additionally, the filter media was arranged with gravel at the bottom, coarse sand in the middle, and fine sand at the top.

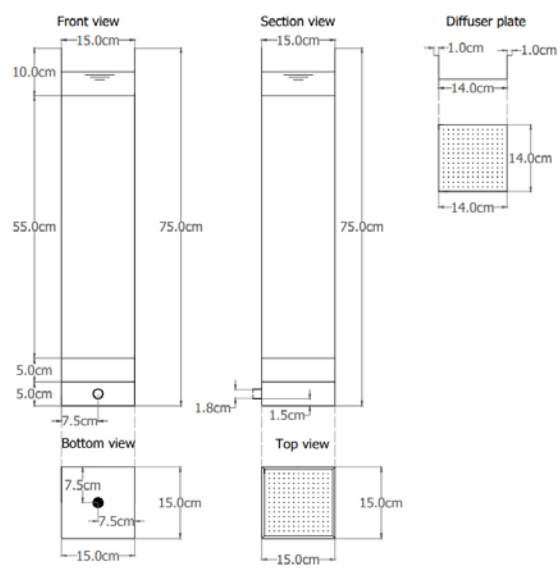

Fig. 2. The schematic design for sand filter

2.5 Media Preparation

The selection and preparation of the filtration medium is an essential process for the treatment efficiency of the filter tank. The river sand was used as the medium in this study. However, the river sand is usually contaminated with pathogens which can come from the human and animal excreta and contain organic material. Therefore, the river sand was disinfected and organic material removed by take in the oven at 105℃ for 4 to 5 hours. The sand medium was classified into: gravel with paticle size of 6mm, coarse sand with particle size of 2mm. The finer sand was sapareted into two particle (particle size 1-0.6 mm and 0.5-0.3mm).

The commercial granular activated carbon from Coconut shell was added in order to enhance arsenic removal efficiency by creating a large internal surface area with small pores for adsorption. In Cambodia commercial activated carbon can be purchased from various suppliers such as Mall, chemical supply companies etc.

2.6 Experimental Procedure

The bench scale or filter column was conducted in the laboratory with difference study condition in order to find the optimization of depth and size of media to remove contaminants. Based on the findings of the study area's groundwater quality, synthetic water was used in the experiment, followed by the highest concentrations of iron and arsenic. Initially,to prepare the source of iron, $FeCl_3.6H_2O$ were weighted by using the microbalance for low, moderate and high iron concentration. The gram of $FeCl_3.6H_2O$ was dissolved in 20 L of tap water and mixed thoroughly with the fixed of pH 7. Similarly, to prepare source of arsenic, micropipette was used to transport solution $NaASO_2$ and mixed with 20 L of tap water. The study included four conditions: (i). The Effect of depth and size medium on iron removal by study on the different filter depth of shallow depth (18.4cm), medium depth (36.6cm), and high depth (55cm) with the two different sizes of medium; finner sand (0.6mm- 1mm) and larger sand (0.3mm-0.5mm); (ii). The evaluated arsenic removal under optimum condition found; (iii). The effect of additional of iron co-presence on arsenic removal with the ratio of As/Fe; (iv). The effect of additional commercial activated carbon on arsenic removal which focuse on the four depth of activated carbon as shown in Figure. 3.

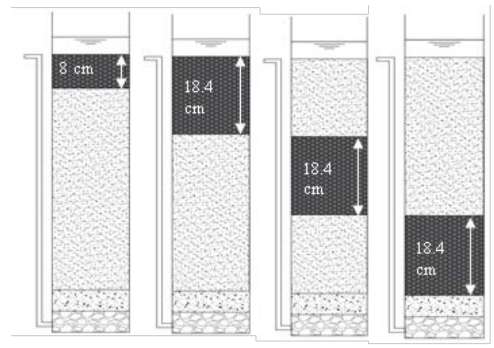

Fig. 3. The experimental study on the differences condition of activated carbon on arsenic removal.

3. RESULTS AND DISCUSSION

3.1 Raw Charicteristic of Groundwater

Groundwater quality in Prasat commune was analyzed for physical and chemical parameters from 12 sampling sites and compared to WHO and Cambodian national standards (MRD), as shown in Table 3. The comparision of raw charicteristic of groundwater in Prasat commune with WHO and national standard (MRD) guideline.

The basic water quality parameters pH, ORP, EC, DO, salinity, and TDS were all measured together. The pH ranged from 6.8 to 7.9, with a mean of 7.3 ± 0.3, indicating that the water samples were slightly base. The average TDS value of 348.9 ± 126.78 mg/L indicates the salinity and mineral soluble in groundwater. The electrical conductivity (EC) was found to range between 767.8 ± 175.86 µs/cm. The higher of EC in water indicates the higher concentration of ions in water. Based on these findings, no well exceeds the

Table 3. The comparision of raw characteristic of groundwater in Prasat with WHO and National standard MRD guidline

Parameter	Unit	Min	Mean	Max	Std	WHO Standard	MRD Standard
pH	-	6.8	7.3	7.9	0.3	6.5-8.5	6.5-8.5
ORP	mV	129.4	146.9	161.2	8.12	700	-
DO	mg/L	1.8	3.4	5.8	1.2	-	-
EC	µS/cm	559	767.8	1107	175.86	1600	-
Salinity	%	0.005	0.042	0.066	0.02	-	-
TDS	mg/L	46.5	348.9	552	126.78	800	800
Arsenic	mg/L	0.003	0.079	0.25	0.11	0.01	0.03
Iron	mg/L	0	0.8	3.4	1.03	0.3	0.3
Fluoride	mg/L	0.2	0.6	0.8	0.17	1.5	1.5
Chloride	mg/L	4	54.7	106.5	32.62	250	250
Total Hardness	mg/L	43.2	220	345.6	73.29	300	400
Turbidity	NTU	0.7	5.9	29.5	8.42	5	8

permissible level of standard for both WHO and national drinking water guidelines for pH, EC, TDS, and ORP. However, the mean turbidity value was 5.9 ± 8.42 NTU, which exceeded the WHO maximum level.
The high turbidity of raw well water has potential to undermine the confidence of the consumer [14]. The mean values for DO and salinity were 3.4 ± 1.2 mg/L and 0.042% ± 0.02%, respectively. There is no standard permissible level for salinity and DO. However high salinity in water may affect the taste and indicate the ion in water such as sodium (Na), Chloride (Cl), magnesium (Mg), calcium (Ca), and sulfate (SO_4). The measurement of dissolve oxygen (DO) in groundwater control the valence state of trace metal element in water [15], as lower DO will not be sufficient to dissolve iron [16].

Furthermore, the chemical parameter including arsenic, iron, hardness, chloride and fluoride was observe. The mean concentration of arsenic in the analytic was 0.079 ± 0.11 mg/L, which exceeded the WHO and national standards for arsenic in drinking water. The maximum arsenic concentration was 0.25 mg/l.

3.2 Water Quality Index

In this study the computed WQI values was categorized into five types from “excellent water” to “unsuitable water for drinking”. This index was determined in order to evaluate the quality of water in Prasat commune whether it is suitable for drinking purpose or not. The WQI using the following ten parameters including pH, arsenic, iron, chloride, fluoride, turbidity, electrical conductivity (EC), total dissolve solid (TDS), and total hardness. In the assessment using WQI method, 50 % of wells sources found of good water quality, 8% were of poor quality, 17% were of very poor quality, and 25% were of unsuitable for drinking purpose

The WQI value from the above calculation was input in Arcgis to represent the quality of groundwater in this study area. By using the spatial interpolation method (IDW) the map of groundwater was illustrated in the Figure 4.2. below. The spatial map indicated the recent groundwater in this study area was analyze in term of physical and chemical parameter. As the result, most of the well’s water in Lek Mouy village, Lek pi village and Lek Bei village was good and can be used for drinking purposes. The groundwater in those three villages is mostly affected by turbidity which makes a few wells in these villages have poor water quality. However, the groundwater quality in Lek Pram village was unsuitable for drinking purposes. The major contributing parameters to the unsuitable well in this village are the high concentrations of arsenic, iron, and arsenic as shown in the study of correlation between WQI and water quality parameter.

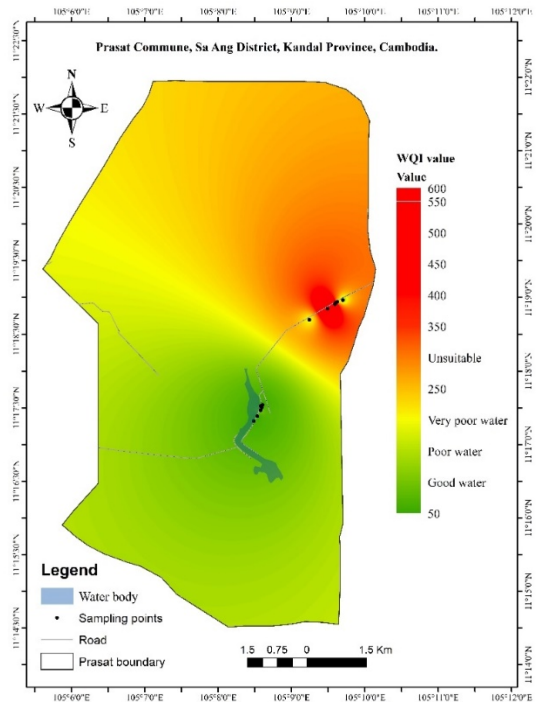

Fig. 4. The spatial distribution of groundwater quality index and sampling site in Prasat commune

3.3 The Performance of Iron Removal using Sand Filter

3.3.1 Effect of Sand Diameter

The effect of sand diameter on the iron removal was study in sand diameter between 0.5mm to 0.3mm (finner sand) and between 1mm to 0.6mm (larger sand) with the sampling time in range of 0 minute to 200 minutes by using the initial concentration of low concentration (range: 2mg/L – 3mg/L), medium (range: 4mg/L- 7mg/L) and high (8mg/L – 13 mg/L) differently at pH around 7. Initially, iron reduction in an average of 97.54 % for finner sand and 95.65 % for larger sand. The minimum removal efficiency of the finner sand was 92.8% and larger sand was 85.7%. Additionally, the maximum removal efficiency was 99.95% and 99.93% for finner and larger sand, respectively. The results in Figure. 5., showed that both sand diameters had a significant on iron removal effectively below the standard of drinking water (0.3 mg/L of total iron). However, the sand with smaller diameter can remove iron more effectively than larger diameter. The diameter of sand particles plays a importance role in the effectiveness of iron removal through sand filtration follow the process called adsorption (onto each other and on to sand) and filtration (trapping between pores). The higher removal efficiency observed with sand media range from(0.5mm-0.3mm) attributed to its smaller pore size which can attracted to the surface of sand particle. They can become trapped in the filter bed as water flows through it.

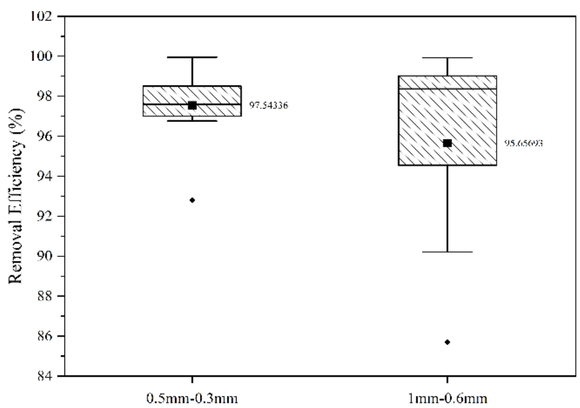

Fig. 5. The effect of sand diameter on iron removal

3.3.2 Effect of Depth Filter

The three-depth sand filter was observed for the iron removal. The observations on the depth of the filter are classified as low depth (18.4cm), medium depth (36.6 cm), and high depth (55cm). Figure. 6 showed the efficiency of iron removal followed by the lowest depth ranged from 85% to 99%, with an average of 94.5% ± 5.3%. Medium depth ranged from 92% to 98% with an average of 96% ± 2.5% and high depth ranged from 97% to 99% with an average of 99.14% ±1.02%. As a result, those three depths were significant in remove iron in state of ferric up to 80%. However, the high depth was better at adsorbing ferric than the medium and low depths. This due to the high depth can provide more contact time between the water source and the sand particles, leading to better adsorption and trapping of iron particle through physical process. The lower depth may easy in leaching which can reduce the removal efficiency.

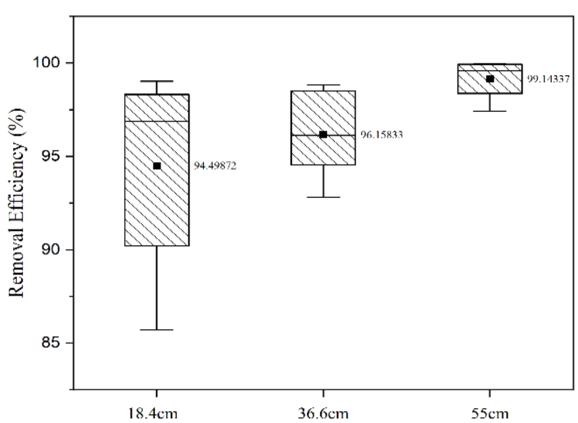

Fig. 6. The effect of sand depth on iron removal

3.4 Asrsenic Removal under Optimum Conditon Found

In this study the initial concentration of arsenic was 0.3 mg/L or 300 ppb with fixed pH around 7. Initially, for the first influent the arsenic was reduce to 0.2 mg/L with removal efficiency of 33.33 %. After, 20 minutes the removal efficiency was increase to 50%. At 40 minute and 60 minutes the removal rate was steady as shown in Figure 7. Then increase slightly to the maximum value of 76.66% at 100 minutes and 120 minutes with effluent concentration of 0.07 mg/L or 70 ppb. Even the removal efficiency was above 50% but the sand filter was not reduced arsenic below the national standard of 0.03 mg/L or 30 ppb. The sand filter can remove arsenic from water through a process called adsorption. This is a process where the arsenic molecules are attracted to the surface of the particles. Arsenic ions in water can adsorb onto the surface of the sand particles due to electrostatic and chemical interactions [19].

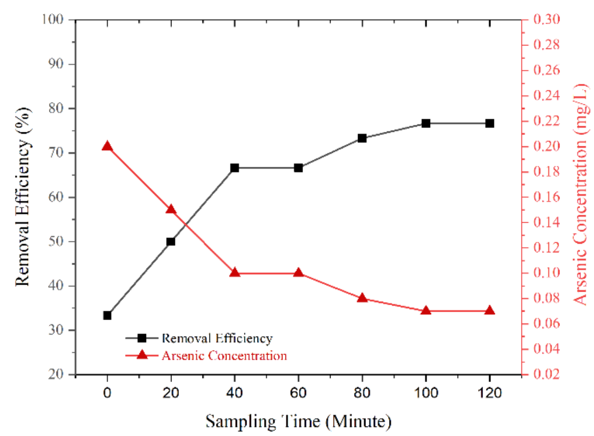

Fig. 7. The effect of sand depth on arsenic removal

3.5 Effect of Additional Iron Co-presence on arsenic Removal

The presence of iron in water also has an effect on arsenic removal. When dissolved iron (ferrous) is exposed to oxygen, it forms Fe (III) (ferric), and arsenic can be removed when this precipitate then co-precipitation with As can occur [4,20,21]. The ferric co-precipitation with arsenic was effective to remove arsenic ions at pH higher than 4 [18]. In this study, two conditions for adding proportions of Fe and As were studied. Both conditions had an As/Fe (by mass) ratio of 3/50 and an As/Fe ratio of 3/100 with the fixed pH at 7. This means the As concentration in mg/L is divided by the Fe concentration in mg/L. The result of those two conditions showed that an As/Fe ratio of 50 was needed to reduce the As concentration from 66.7% to 83.3% with an effluent concentration of 0.05 mg/L, or 50 ppb. By increasing the As/Fe ratio to 3/100, the removal efficiency was up to 96% with an effluent concentration of arsenic below 0.03 mg/L. The result in Figure 8 was shown that the ratio of 50 had an effect on the arsenic removal. Moreover, by increasing a ratio to 100, arsenic removal was enhanced to reach the national standard. The ferric iron can remove arsenic through a process called precipitation, when arsenic-containing water passes through a sand filter, the arsenic molecules can react with the iron in the sand to form ferric hydroxide. This is a solid that can then precipitate out of the water, carrying the arsenic molecules with it.

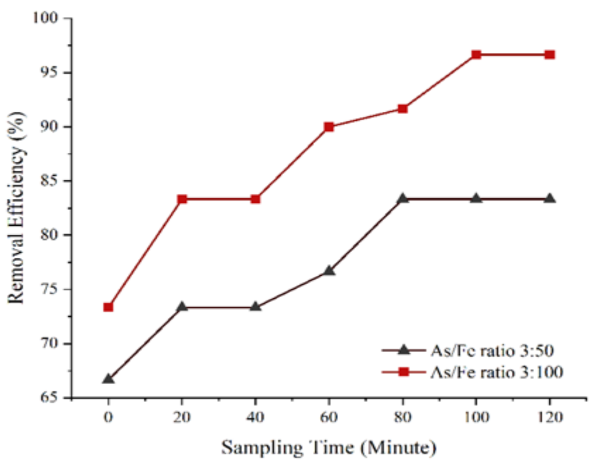

Fig. 8. The effect of iron co-presence on arsenic removal

3.6 Effect of additional commercial activated carbon on arsenic removal

3.6.1 Effect of Activated Carbon Quantity

The amount of additional activated carbon was also observed in this part with the placed of 8cm depth and 18.4 cm depth. The initial concentration was 0.3 mg/L of As (III), firstly better absorbed by the activated carbon with the 8 cm depth, up 96% after 40 minutes of sampling. The removal declined from 96% to 66% after an hour. The removal efficiency was consistently 66% between 100 and 120 minutes. However, the activated carbon with depth of 18.4 cm was better for arsenic absorption. The first effluent with removal efficiency of 66.67% then increase to 91.67 % at 20 minutes. At 40 minute the removal was increase slightly to 95% and steadily at 60 minutes until 120 minutes as shown in figure 9. It was observed that there is no decline rate for 18.4 cm depth of AC. As the result the quantity of AC was affected on the arsenic removal. In this study the depth of AC at 18.4cm is better than depth of 8 cm due to its porous material with a large surface area. The surface area of activated carbon is created by the presence of micropores, which are very small pores that are typically less than 2 nm in diameter [22]. These micropores provide a large number of active sites for the absorption of arsenic. The amount of arsenic that can be adsorbed by activated carbon is directly proportional to the surface area of the activated carbon. The mechanism of activated adsorb contaminant. This means that a larger amount of activated carbon will have a larger surface area and will be able to adsorb more arsenic. Arsenic is more likely to be adsorbed by activated carbon with micropores that are the same size as the arsenic molecules. For these reasons, a large amount of activated carbon is better for arsenic absorption. This is because a larger amount of activated carbon will have a larger surface area and a narrower pore size distribution, which will allow it to adsorb more arsenic.

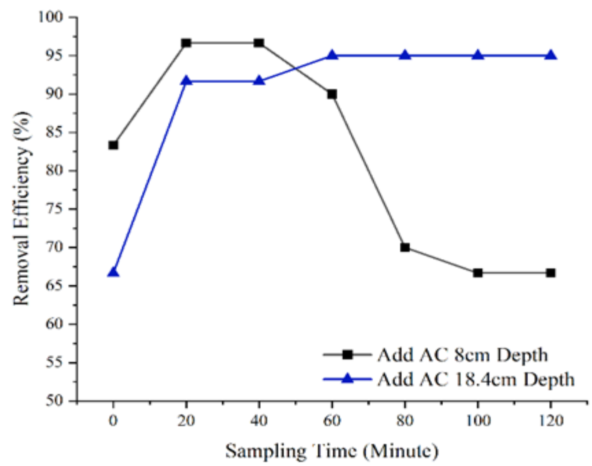

Fig. 9. The effect of activated carbon quantity on arsenic removal

3.6.2 Effect of Activated Carbon placement

The placement was divided in to 3 places: on top, middle and bottom of sand layer as with the depth of 18.4 cm of AC. From 60 minutes of sampling time, the activated carbon on top of the sand layer removed arsenic up to 95% with a concentration of 0.015 mg/L. The same depth of activated carbon was then placed in the middle of the sand layer. As shown in Figure 10, the removal efficiency of the first effluent was 41.67%, then dropped to 33.33% after 20 minutes, and finally increased to 76.67% with a concentration of 0.07 mg/L after 1 hour. This may due to more and more arsenic is adsorbed onto the activated carbon, its capacity to adsorb additional arsenic decreases, causing a decline in efficiency. However, over time, the activated carbon can become "recharged" as it releases previously adsorbed arsenic and adsorbs new arsenic, leading to an increase in efficiency once again. The removal efficiency of AC placed at the bottom of the sand filter was shown to be only 23% (0.23 mg/L) for the first effluent and increased to 56% with effluent concentration of 0.13 mg/L at sampling time of 120 minutes. With these three experiments, among the three depths, the best place to put activated carbon in a sand filter is on top of the sand layer. This codition allows the water to pass through the sand layer for physical filtration before moving on to the activated carbon layer for chemical filtration and can adsorb arsenic more better. Placing the activated carbon between the sand layers or at the bottom of the sand layer may result in clogging, blocking the pore size of activated carbon and reduce the capacity of adsorbent.

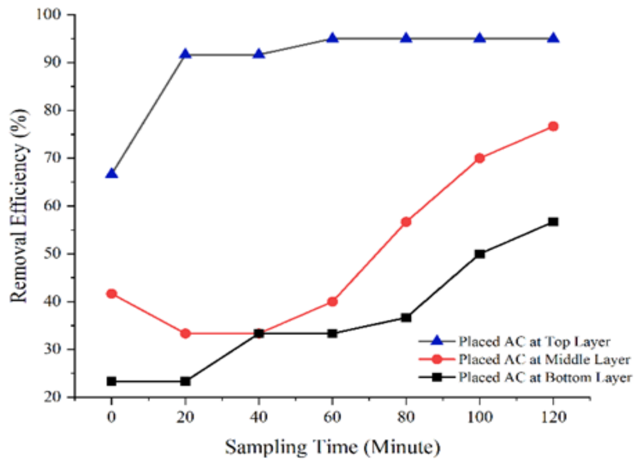

Fig. 10. The effect of arsenic removal by activated carbon media placement.

4. CONCLUSIONS

The groundwater sample were selected and physicochemical parameters measured compared with WHO and MRD standards. The bio-sand filter was chosen for its affordability and suitability in rural Cambodia. The filter was modified with commercial activated carbon and observed for size and depth improvements. Groundwater assessment in Prasat commune revealed high concentrations of turbidity, arsenic, and iron, exceeding national and WHO standards. Water quality index (WQI) showed 50% good, 17% poor, 8% very poor, and 25% unsuitable. In terms of the treatment process, a bio-sand filter has the ability to remove iron up to 85%, but in a ferric state. The filter with a sand depth of 55 cm and a diameter of 0.3–0.5 mm can remove iron up to 90%. For arsenic removal, the initial concentration was 0.3 mg/L; if the water contains ferric at 10 mg/L, then the arsenic can be removed up to 90%. The modification of the sand filter was employed by adding commercial activated carbon. It is recommended to use activated carbon at a depth of 18.4 cm and to place it on top of a sand layer. After one hour of performance, the removal efficiency for this condition reached 96% for arsenic removal.

Even the optimization of depth and diameter of sand and activated carbon media was found for arsenic and iron removal but it does not make sure that the sand filter can always remove these contaminants over a long time period. Hence, it is important for the further research to assess the ability of the filter to remove contaminants by sampling the effluent throughout the day and over longer periods of time. Additionally, studying yhe durability of activated carbon for arsenic with filter efficiency should be undertaken. If soluble ferrous iron is present in groundwater, aeration should be performed prior to its passage through the bio-sand filter.

ACKNOWLEDGMENTS

Authors would like to acknowledge WE-LAB and Laboratory-Based Education (LBE) Project of JICA in Institute of Technology of Cambodia (ITC).

REFERENCES

[1] Johnston, R., Roberts, M., Try, T., & De Silva, S. (2013). Groundwater for Irrigation in Cambodia. International Water Management Institute, June.

[2] JICA. (2013). Profile on Environmental and Social Considerations in Cambodia. Jica, Japan International Cooperation Agency, 324.

[3] Fredericks, D. 2004. Situation analysis: arsenic contamination of groundwater in Cambodia. Report, January 2004. Phnom Penh, Cambodia: UNICEF.

[4] Berg, M., Luzi, S., Giger, W., Trang, P. T. K., Viet, P. H., & Stüben, D. (2007). Response to comment on “Arsenic removal from groundwater by household sand filters: Comparative field study, model calculations, and health benefits”. Environmental Science and Technology, 41(3), 1053.

[5] Ngai, T. K. K., Shrestha, R. R., Dangol, B., Maharjan, M., & Murcott, S. E. (2007). Design for sustainable development - Household drinking water filter for arsenic and pathogen treatment in Nepal. Journal of Environmental Science and Health - Part A Toxic/Hazardous Substances and Environmental Engineering, 42(12), 1879–1888.

[6] RDI. (2007). GROUNDWATER QUALITY ANALYSIS REPORT Kandal - S’ang - Prasat (N/A). 5915(June 2008).

[7] Ramakrishnaiah, C. R., Sadashivaiah, C., & Ranganna, G. (2009). Assessment of water quality index for the groundwater i n Tumkur taluk, Karnataka state, India. E-Journal of Chemistry, 6(2), 523–530.

[8] Dwivedi, S. L., & Pathak, V. (2007). A preliminary assignment of water quality index to Mandakini River, Chitrakoot. In Indian Journal of Environmental Protection (Vol. 27, Issue 11, pp. 1036–1038).

[9] Pesce, S. F., & Wunderlin, D. A. (2000). Use of Water Quality Indices To Verify the Córdoba City (Argentina) on Suquía River. Wat. Res., 34(11), 2915–2926.

[10] Alobaidy, A. H. M. J., Abid, H. S., & Maulood, B. K. (2010). Application of Water Quality Index for Assessment of Dokan Lake Ecosystem, Kurdistan Region, Iraq. Journal of Water Resource and Protection, 02(09), 792–798.

[11] Karakaya, N., & Evrendilek, F. (2010). Water quality time series for Big Melen stream (Turkey): Its decomposition analysis and comparison to upstream. Environmental Monitoring and Assessment, 165(1–4), 125–136.

[12] WHO. (2017). Biochemical aspects. In Proceedings of the Royal Society of Medicine (Vol. 55, pp. 1023–1024).

[13] CAWST. (2009). Biosand filter manual design, construction, installation, operation and maintenance. Centre for Affordable Water and Sanitation Technology, September, 129.

[14] Herschy, R. W. (2012). Water quality for drinking: WHO guidelines. In Encyclopedia of Earth Sciences Series (pp. 876–883).

[15] Long, R. S. and A. (1988). Dissolvedoxygeningroundwater.

[16] Kowalski, K. P., & Søgaard, E. G. (2014). Implementation of zero-valent iron (ZVI) into drinking water supply - Role of the ZVI and biological processes. Chemosphere, 117(1), 108–114.

[17] Al., L. L. et. (2008). Modelling arsenic hazard in Cambodia: a geostatistical approach using ancillary data. Applied Geochemistry, 23, 3010-3018.

[18] Nur, T., Loganathan, P., Ahmed, M. B., Johir, M. A. H., Nguyen, T. V., & Vigneswaran, S. (2019). Removing arsenic from water by coprecipitation with iron: Effect of arsenic and iron concentrations and adsorbent incorporation. Chemosphere, 226, 431–438.

[19] Crittenden, J. C., Trussell, R. R., Hand, D. W., Howe, K. J., & Tchobanoglous, G. (2012). MWH's Water Treatment: Principles and Design: Third Edition. MWH's Water Treatment: Principles and Design: Third Edition.

[20] Smith, K., Li, Z., Chen, B., Liang, H., Zhang, X., Xu, R., Li, Z., Dai, H., Wei, C., & Liu, S. (2017). Comparison of sand-based water filters for point-of-use arsenic removal in China. Chemosphere, 168, 155–162.

[21] Leupin, O. X., Hug, S. J., & Badruzzaman, A. B. M. (2005). Arsenic removal from Bangladesh tube well water with filter columns containing zerovalent iron filings and sand. Environmental Science and Technology, 39(20), 8032–8037.

[22] Stevenson, D. G. (1997). Water Treatment Unit Processes. In Water Treatment Unit Processes.

Techno-Science Research Journal 12 (Special Issue) 172-180

Content list available at ITC

Techno-Science Research Journal

Journal Homepage: www.ric.itc.edu.kh

Techno-Science Research Journal

Seismic Hazard Assessment of Magway City, Magway Region, Myanmar

Pyi Soe Thein[1*], Subagyo Pramumijoyo[2], Naing Tun Lin[3], Aye Ko[3] ,Thet Htar Su Wai[3]

[1,3]*Department of Geology, University of Magway, Magway 04012, Myanmar*
[2]*Faculty of Engineering, Geological Engineering Department, Gadjah Mada University, Yogyakarta 55281 , Indonesia*

Received: 6 August 2023; Accepted: 15 May 2024; Available online: August 2024

Abstract: *Magway city, the second largest city of Myanmar's seven division, lies very closed to the dextral Sagaing fault and Gwegyo thrust. In the historical record, several earthquakes happened in and around Magway region from the beginning of the year of 1400. Among them the most distinct event is the Taungdwingyi earthquake struck on September 22, 2003. Its epicenter is centred southeast of the nearby town of Taungdwingyi, at least 50 km from the Sagaing Fault. The earthquake occurred due to shallow strike-slip faulting. The source fault is located along the eastern foothills of the Pego Yoma range, and adjacent to the Sagaing Fault. The magnitude of this event is about 6.6 and caused around 7 death tolls, 42 casualties in Taungdwingyi. Accordingly, the seismic hazard assessment is carried out by using the deterministic seismic hazard assessment in Magway City. This research mainly focuses on results of geo-resistivity survey at 30 sites and data from the 7 boreholes for determination of sediment thickness characteristics and seismic hazard assessment in Magway City, Magway region. The subsurface profiles, predominant periods, shear wave velocity structures and information about sediment thickness or depth of engineering bed rock were evaluated based on data from boreholes, geo-resistivity survey and laboratory results, combining with inversion and the magnification program. On the other hand, the seismic hazard assessment of Magway city accounts for seven themes – geological and geomorphological, basement or bedrock, factor of safety for soil stability, shear wave velocity, predominant periods, and surface consistent peak ground acceleration. Strong ground motion was generated by empirical stochastic green's function computer code based on the USGS epicenter of September 22, 2003 earthquake, magnitude Mw 6.6, focal depth 10 km and used as bedrock motions in seismic response analysis. The three broad qualitative hazard classifications – 'low', 'moderate', and 'strong' could be applied in both the cases, albeit with different implications to peak ground acceleration variations. The peak ground acceleration becomes more than 0.40 g in some areas, which causes severe damage for buildings in high probability. The seismic hazards gradually decrease to the east, therefore the eastern part of Magway city presents the minimum seismic hazard zone. These developed seismic hazard map offer better representation of the local specific seismic hazard assessment in Magway City, Myanmar.*

Keywords: boreholes, geo-resistivity survey, shear wave velocity, peak ground acceleration, deterministic seismic hazard assessment;

1. INTRODUCTION

Over the past three decades, urbanization in Myanmar has been rapidly increasing. In most cities throughout the country, this urbanization took place with minimal consideration of building codes, sound construction and urban planning practices. In addition, the impact of potential future nature disaster events was never considered. As a result, many of Myanmar's urban cities developed in the proximity of active seismic sources and are at risk of experiencing earthquake events. These seismic sources include the Sagaing, Kyaukkyan faults and Gwegyo thrust which are known to have produced significant earthquakes in the past. A strong earthquake striking a major city such as Yangon, Bago, Naypyitaw, Meikhtila, Taunggyi, Mandalay, Sagaing, Taungdwingyi will likely result in widespread destruction and have disastrous consequences for the nation as a whole. However, the amount of damage and its geographic distribution were previously unknown. This project was designed to identify possible seismic sources in Magway City, and then to develop national seismic hazard map. These national seismic hazard map would in turn identify an area or a city where a detailed seismic risk assessment study would be carried out. Magway, a highly populated city and a commerce hub in the central region of Myanmar, was chosen as a pilot city for study because of its

[*] Corresponding author: Pyi Soe Thein
E-mail: u.pyisoethein@gmail.com; Tel: +959-79-672-2811; Fax: +959-25-718-7188

close proximity to the Gwegyo thrust and the Sagaing fault. In this study, we investigate the mechanical properties and geometry of the Magway City using different and independent field data. The main goal of the new measurements was the determination of the shear-wave velocities and peak ground acceleration throughout the Magway City, since they are very important parameters for site response analysis. The new field surveys reported here are Standard Peneration Test (SPT) measurements, geo-resistivity profiles that had not been previously analyzed, and additional in-situ and laboratory geotechnical investigations. The synthesis of these information resulted in a 3D soil model adequate to site response analysis, wave propagation and strong ground motion interpretation.

2. STUDY AREA

Magway is located in the central dry zone of Myanmar by the Irrawaddy river at 20.146° North and 94.938° East. It sits at 30 meters (98 feet) above the mean sea level. The study area in this project includes 15 wards of Magway City, covering an area of 37.46 km^2. The study area is shown in Figure 1. Although the study area was planned for the 15 central wards, some of the areas were restricted for security reasons.

Fig.1. Location map of Magway City

3. SEISMICITY

Using the earthquake catalog of USGS (1963 – 2012)[1], we observed the nature of the seismicity of Myanmar by plotting the epicenters of the previous earthquakes (Figure 2). This is especially to differentiate the Benioff zone seismicity (i.e. the interplate earthquakes) and crustal seismicity (i.e. intraplate earthquakes). When four classes of shallow (<35km) focus, intermediate (35 – 70km) and deep (70 – 150km) and very deep (>150km) focus earthquakes are categorized, we found that all of these categorized seismicity is consistent with the India – Eurasia subduction system, in the west of Myanmar. The shallow focus earthquakes in the central and eastern part of the region comprise the crustal faults, the dextral Sagaing fault which passes through the central portion of Myanmar, trending NS with the total length of about 1200 km [2,3]. The other crustal faults involve Kyaukkyan fault, Nam Pun fault, Shweli fault, Moemeik fault, and Namma fault, etc. Myanmar has experienced several high magnitude earthquakes. Many of these events had a magnitude of 7 or greater and resulted in severe damages and significant causalities.

3.1Putao Earthquake (1906)

The Putao earthquake was a violent earthquake which shocked the northern part of Myanmar region on 31 August 1906. The estimated magnitude of this earthquake was 7 on the Richter scale. The epicenter was estimated to be located at about 58 kilometers southwest of Puta in Myitkyina district of northern Myanmar.

3.2 Innwa Earthquake (1839)

The Innwa earthquake occurred at about 4 am on 23 March 1839. Its epicenter was estimated at 22° North and 96° East with the maximum intensity of XI (Modified Mercali Intensity Scale). The shock was accompanied by a tremendous roar and lasted about 20 seconds. While damage was experienced in neighbouring areas such as Amarapura, Innwa sustained extensive destruction. It is estimated that about 300 to 400 people were killed in the event [4].

3.3 Maymyo Earthquake (1912)

A disastrous intraplate earthquake occurred in 1912 at 97°E and 21°N with a moment magnitude of 8.0. Damage was severe in Maymyo (Pyin Oo Lwin). Railways lines were bent where they crossed the fault and massive landslides occurred. They were aftershocks for six months following the event.

3.4 Bago Earthquake (1930)

The Bago (Pegu) earthquake of 5 May 1930, which caused widespread destruction of the town, is considered as a disaster of the first magnitude by Chhibber.[4]. It killed some 500 people in Bago and the other 50 in Yangon, some 30 miles southwest of the epicenter which is about 30 miles south of Bago, all in the flat coastal plain [5].

3.5 Pyay Earthquake (1858)

The Pyay earthquake was a destructive event that occurre on 24 August 1858. The shock was most severe near Thayetmyo and Pyay. Houses were rocked considerably and most of the pagodas were badly damaged with their tops falling down.

3.6 Kyaukse Earthquake (1931)

Occurring on 19 August 1931, the Kyaukse earthquake was strong enough to cause minor cracking to buildings in Mandalay and to knock light articles over in Kalaw.

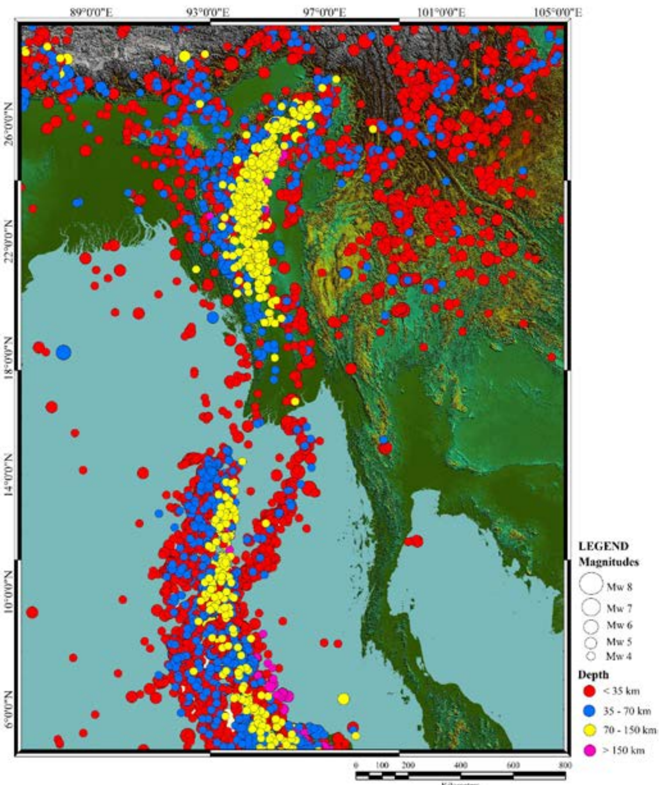

Fig.2. Seismicity map of Myanmar

3.7 Sagaing Eathquake (1956)

The epicenter of the Sagaing earthquake was at 24.6°N and 99°E near Sagaing in central Myanmar with the depth between 8 and 10 km. It occurred at 15:07 hours GMT on 16 July 1956 and had a magnitude of 7.0 on a Richter scale. The earthquake was destructive in Upper Myanmar causing property damage at Mandalay and damaging 80% of the houses in Sagaing (22 km from Mandalay) as well as causing up to 50 causalties and 50 injuries [4].

3.8 Bagan Eathquake (1975)

The Bagan earthquake on 8 July 1975 was the most memorable in recent Myanmar history. It had a magnitude of 6.8, but its destruction horrified the people of Myanmar. The epicenter lies at latitude 21.48° N and longitude 94.70°E which is located in the northern part of Tankgyi Taung. It was a deep focus earthquake, however, the macroseismic intensity map conducted by Department of Meterology and Hydrology indicated that the highest intensity was around the Gwecho Fault. Tremors of three aftershocks with moderate intensity were felt in Bagan and its surrounding area.

3.9 Taungdwingyi Earthquake (2003)

The Taungdwingyi earthquake occurred on 22nd September 2003. It had a magnitude of 6.6 and the epicenter lies at latitude 19.86° N and longitude 95.72°E. Fortunately it occurred in the midnight, so most of the community centers and school buildings were empty, and that reduced causality in the affected area (7 death and 43 injured). The location of the epicenter was at the western boundary of the Bago Yoma anticlinorium and the alluvial plain composing of the water-saturated silts and sandy loam. Scientists believe that the earthquake, showing a transpressional nature in its USGS fault plane solution, occurred after buried southern extension of Gwegyo thrust, which is strikingly exposed near Mt. Popa Volcano north of the present location [6]. Large crack opened across the line. Embankments of the line were dropped some inches. Large cracks appeared in the ground and from which water and sand were ejected forming heaps of sand.

4. REGIONAL GEOLOGY

The development of the regional shear-wave velocity (Vs^{30}) models is performed with consideration for the varying surficial geology of the region as well as for the stratigraphy underlying the surficial deposits. The 1:1,000,000 scale geologic map shows the various surficial geologic deposits in the area [7]. The upper Miocene - Pliocene of Irrawaddy Formation was shown in Figure 3. Sediments overlie most rock deposits in the area and few outcrops can be identified around the Magway region.

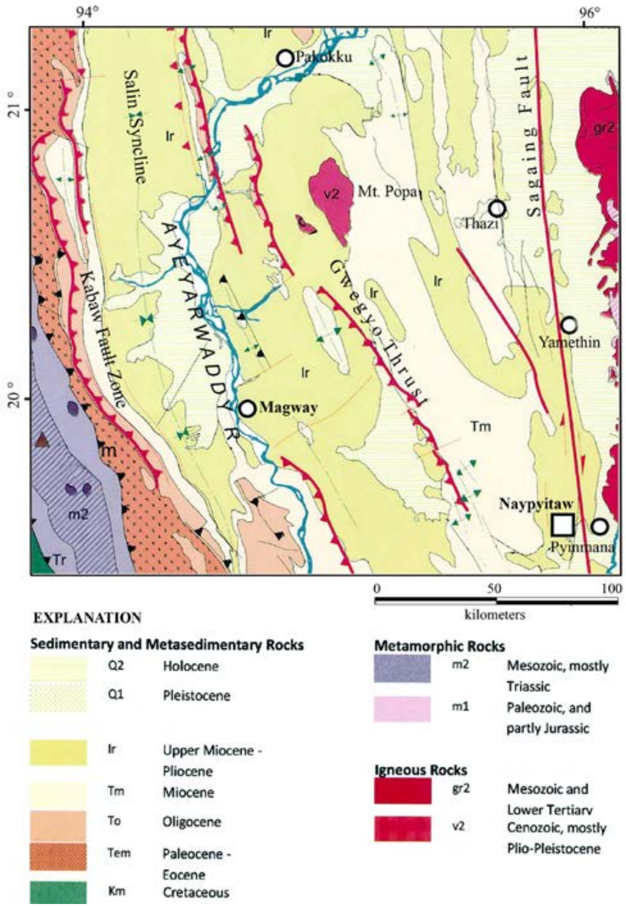

Fig.3. Regional geological map of Magway region [7].

5. METHODOLOGY

The study used a guided method to meet the set objectives, which included literature review, analysis of borehole data from SPT Tests, soil data analysis and geophysical (geo-resistivity) method. From the seven borehole completing records, borehole logs were used to identify the weathered and fractured zones and guided the calibration of the geotechnical layers. The thirty geo-resistivity profiles using PQWT-TC300 equipment were performed targeting all the underground structure established from the data (Figure 4). This was performed to reveal the layout of the stratigraphy to a maximum depth of 300 m. The imageries such as aerial photographs and digital elevation model were used for the generation of stereo-pairs in order to generate geomorphological map of the valley. The available spatial data was organized in access and imported to Global mapper and ArcGIS 10.5. The necessary analysis was carried out for the generation of ArcGIS 10.5 layer models, lithological cross section, fence diagram etc, respectively. Finally, empirical stochastic green's function was based on the strong ground motion prediction and therefore it was quite appropriate for this research. Flow chart of the research methodology is shown in figure 5.

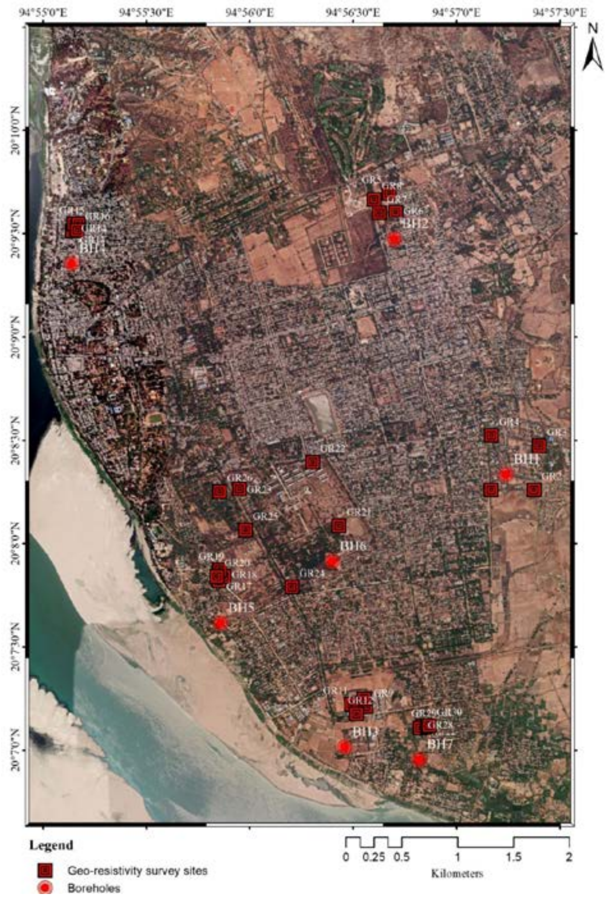

Fig.4. Location map of geo-resistivity sites and boreholes in Magway City

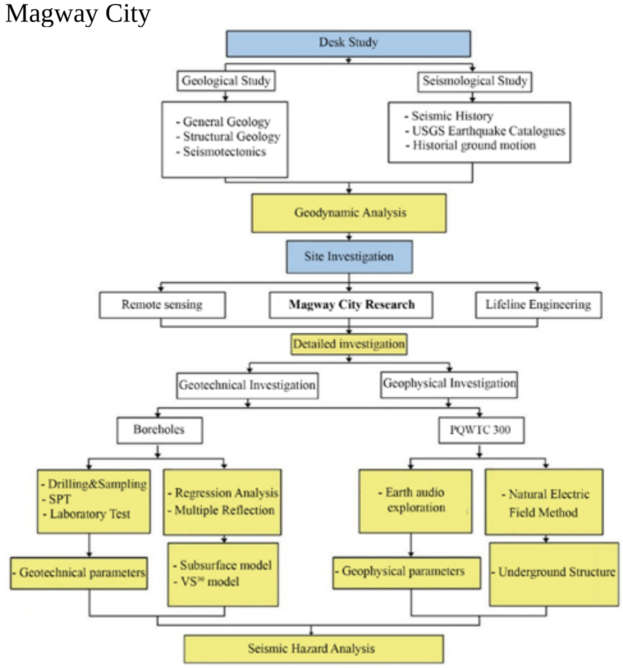

Fig.5. Flow chart of research methodology

6. RESULTS AND DISCUSSION

6.1 Geotechnical Results

Engineering soil properties are crucial for estimating the shear wave velocity and conducting soil response analysis. In this research, detailed engineering soil investigation was performed by "Tay Zar Aung, Geotechnical Engineering and Service Company" at 7 locations in the Magway City. The depth of each borehole was 12 meter which is the maximum depth possible with equipment used by a company in the local area. Standard penetration test (SPT) is one of the most widely used tools to predict the soil properties. Since the majority of empirical equations of soil properties are related to SPT N-value, it is beneficial to find the best correlation between SPT and N-values. In this study, the multiple reflection analysis and multiple regression (MR) are used to predict the correlation between SPT and N-values. To achieve this goal, seven borehole data were calculated at various depths. Three parameters including depth, N-value and shear wave velocity were chosen as the input of the seismic response analyses. Geotechnical properties of subsurface layer at Magway Education Degree College, borehole no.2 is shown in table 1. The available borehole data included total depths, soil information and N values (Figure 6 to 8). The subsurface soil profiles and soil types are determined according to United State Soil Classification (USCS) system [8,9], based on grain size analysis, Atterberg's limits test and drill logs.

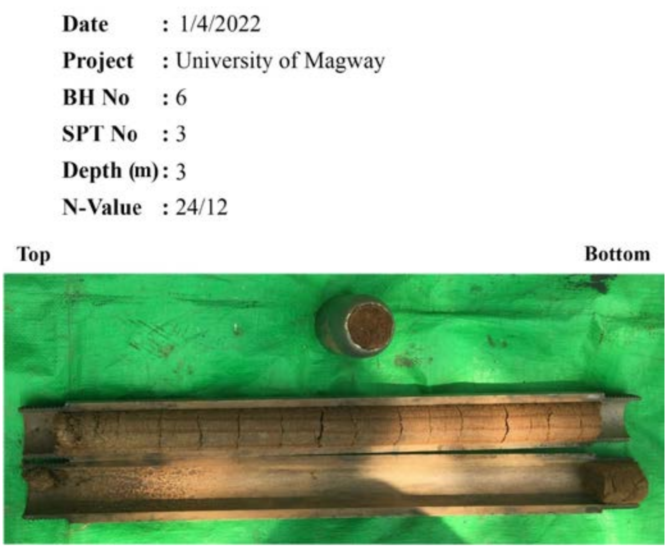

Fig.6. Borehole log No.6, University of Magway at Magway City

Table 1. Geotechnical properties of each subsurface layer at borehole No.2, Magway Education Degree College

Layers No.	Depth (m)	N values	Remarks
1	0-0.9	21	stiff silty clay
2	0.9-2.1	14	stiff silty clay
3	2.1-3.3	24	stiff silty clay
4	3.3-4.5	30	stiff silty clay
5	4.5-6.0	34	hard silty clay

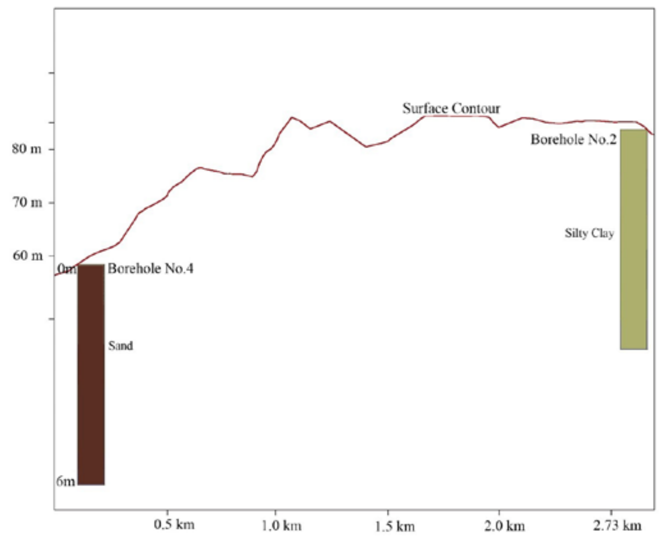

Fig.7. Geological logs along profile borehole No.4 to No.2

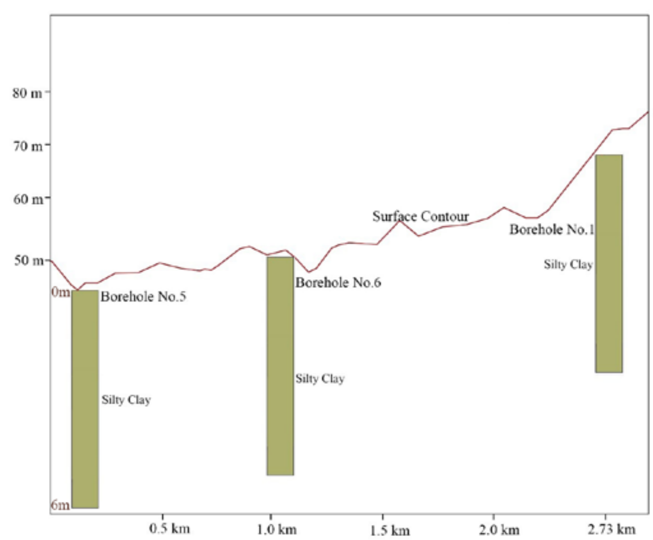

Fig.8. Geological logs along profile borehole No.5 and No.6 to No.1

6.2 Geophysical Results

The geophysical measurement was carried out in the month of June 2022. The sites of 30 were selected based on a combination of factors such as borehole logs present and physical manifestations on the ground, in areas revealing faulting zones from digital elevation model. A total of 30 profiles were investigated using PQWT-TC300 series equipment.

The results of the profile measurements reflected lateral changes in resistivity, corresponding to variations in lithology and thickness of formations at a fixed depth along the profile. Our model shows excellent correlation with the surface geology and reveals the basin geometry, Geo-resistivity profile data is normally interpreted qualitatively (Figure 9).

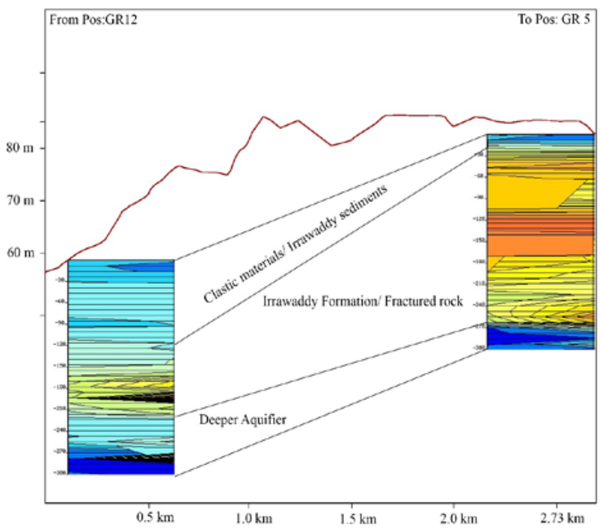

Fig.9. Geo-resistivity profile result along GR 12 to GR 5

7 Modeling of Vs^{30}

In Magway City, Vs$_{30}$ is important because it is a measure of the average shear wave velocity in the top 30 meters below the surface, which is crucial for earthquake site effects and ground response analysis. Vs30 data is used to assess the capacity of soil and determine seismicity hazard in an area, which is crucial for regional planning and development. Most of the borehole data contains N-values to a depth of 12 meter. Shear wave velocities from the bottom depth of boreholes to a depth of 30 m were obtain from the multiple reflection analysis. The multiple reflection analysis was used to calculate the transfer function, which expresses the relation between the period and the corresponding magnification factor. Calculation of predominant period by using boring data and the ground model profile is done according to the multiple reflection analysis. The governing equation is

$$\frac{\delta^2\mu}{\delta t^2} = G\,\frac{\delta^2\mu}{\delta Z^2} + \eta\,\frac{\delta^3\mu}{\delta Z^2\delta t} \qquad \text{(Eq.1)}$$

in which μis the displacement of horizontal S-wave (SH), Z the direction of wave propagation (up-down), t the time, ρ the density, G the shear modulus and η the coefficient of visco-elasticity. The soil damping is considered by giving the complex value to the shear modulus and solving equation.1). The damping constant is 5% of critical damping for each layer [10]. It is here estimated the predominant period by calculating transfer function of model ground based on the electrical resistivity and borehole data. The multiple reflection analysis is the linear analysis, however, above H/V ratio results also obtained as linear vibration phenomena. Therefore, this method was adopted for the determination of ground motion parameter. Distinct peaks express the characteristics of the layers for which the shear wave velocity is quite different. The shorter and longer periods are corresponding to a shallow and a deep soil layer or hard and soft soil. Figure. 10 reflects an effect of different soil characteristics, respectively. Although the predominant period does not always indicate the characteristics of an individual layer because typically the actual shaking mode of the ground is complex, it was assumed that the long and short periods reflected information from each layer. If each value of the predominant period obtained is considered to be a realization of a stochastic random field [11]. Space interpolation is conducted by ordinary Kriging technique [12].

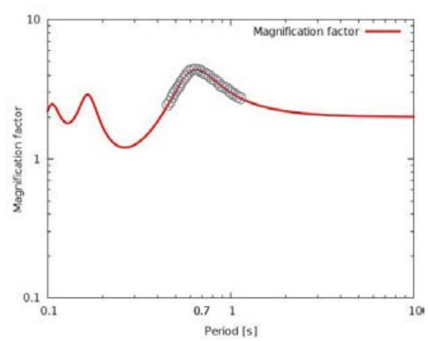

(a)

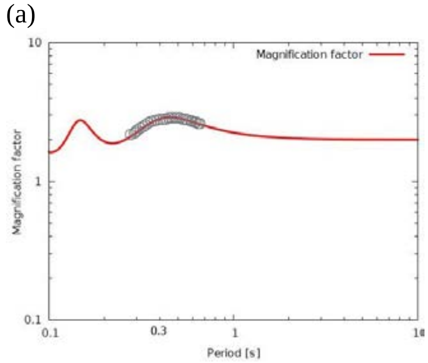

(b)

Predominant period appears in (a)a shorter period and (b) a longer period

Fig.10. Example of the predominant periods

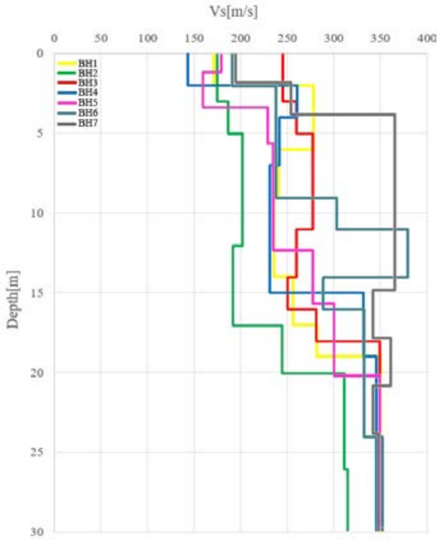

Fig.11. The evaluated Vs and depth profiles at Magway City

The geological data with multiple reflection result is used to develop surfaces describing the distribution of time-averaged shear wave velocity, Vs^{30}, across the urban area in Magway City. Target profile depths of 5, 10, 20. 30 m were considered to allow for an assessment of the distributions of soil stiffness with depth across the region. Vs^{30} values are computed for each target depth, as (Eq.2) [13]. The evaluated subsurface profiles are shown in the following Figure 11.

$$Vs^{30}=\frac{\sum d_i}{\sum t_i}=\frac{\sum d_i}{\sum(\frac{d_i}{vs_i})} \qquad \text{(Eq.2)}$$

where v_{si} is shear wave velocity, d_i thickness of i layer and t_i one way travel time in ith layer. Vs^{30} structures could be obtained at borehole measurements, however, the ground profiles are not uniquely determined.

8 PEAK GROUND ACCELERATION (PGA)

Peak Ground Acceleration, PGA, is commonly used to describe ground motion because of their natural relationship to inertial force induced in certain types of structures are closely related to it. Based on acceleration histories of response analysis, PGA values are determined. The most commonly used measure of amplitude of a particular ground motion is peak ground acceleration, PGA. It is the absolute value of horizontal acceleration. The vertical acceleration has received less attention in earthquake engineering than horizontal one because of the margin of safety against gravity induced static vertical forces.

Peak ground acceleration and amplification characteristics in Magway City had been computed by using synthetic waveforms of 2003 Taungdwingyi earthquake as input bedrock motion below the alluvium sediments. The Irikura's computer code was used to generate synthetic waveforms, mainly based on epicentral distance, magnitude and focal depth of earthquake. The USGS epicenter, magnitude Mw 6.6 and focal depth 10 km are used for calculation of the strong ground motion where borehole at 7 sites and geo-resistivity measurements at 30 sites were conducted and interpolated kringing sites in Magway City. In this study, ground model is constructed by combining two layers model and average seismic bed rock model.

The PGA value is generally ranging from less than 0.05 g to greater than 0.40 g in Magway City. Strong zone, especially around central part of Myohaung, Sonhtana,Ywathit Pwekyo, Myoma-Ohbo, Zeleso, Sashwekin and western part of Aungmyitta wards show very high PGA values are greater than 0.40 g. Moderate zone, especially around central part of Theingargiri, western part of Myintha, eastern part of Pyidawtha, Kantha, western part of Aungmingala, central part of Mingangyi and Aungmyitta wards show moderate PGA values are 0.10 to 0.25 g. Low zone, especially around Aungyadana, Aungchantha, eastern part of Aungmingala, Mingangyi and Aungmyitta wards show that low PGA values are less than 0.05 g. Based on the site response analyses considering various depths of engineering bedrock, for peak ground acceleration vales with seismic microzonation map is proposed for the seismic hazard assessment of Magway City (Figure 12).

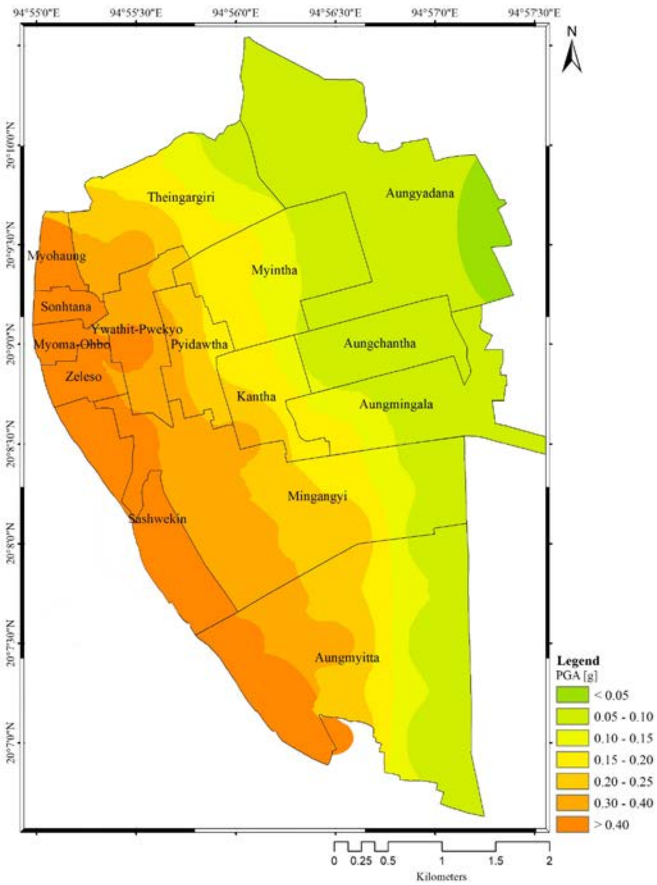

Fig.12. Peak Ground Acceleration (PGA) map of Magway City

9 CONCLUSIONS

In this research, a total of 7 boreholes and 30 geo-resistivity results were analyzed and plotted in ArcGIS 10.5 to get the spatial maps showing the sedimentary layered media and shear wave velocity maps of Magway City. Most of the site condition represents very dense, stiff and soft soil, with the average shear wave velocity Vs^{30} values range from 150 to 400 m/s. Our preferred shear wave velocity model provides a preliminary community velocity model for the Magway City, which can be used for a variety of seismological and geological applications and investigations. According to the Empirical Stochastic Green's Function calculation, the highest seismic zone comprises the western marginal part of Magway city and decreasing towards the east. Peak ground acceleration maps obtained in this research are very useful especially for urban land use planning, retrofitting the various sorts of building after assessing the vulnerability, in designing the future construction of the various sorts of structures and earthquake preparedness, thereby reducing earthquake risk in Magway.

ACKNOWLEDGMENTS

This research was supported by the University of Magway, Ministry of Education, Myanmar. The acknowledgement is extended to rector Dr. Khin Maung Oo and pro-rectors of Dr. Than Aung Htwe and Dr Cho Cho Lwin, University of Magway for their kind permission for the submission of this research paper. We would also like to acknowledge Professor Dr. Junji Kiyono, Department of Urban Management, Graduate School of Engineering, Kyoto University for providing his invaluable support. We would also like to thank the Tay Zar Aung, Geotechnical Engineering and Service Company for providing geotechnical data of the Magway City. Managing director Mr Kyaw Khant (Robust Trust Company) provided geophysical data of the study area and his deserve special acknowledgement.

REFERENCES

[1] U.S. Geological Survey (2012). Digital earthquake catalogue-downloaded

[2] Myint Thein, Kyaw Tint, and Aye Ko Aung (1991). On the Lateral Displacement of the Sagaing Fault, Georeports, Vol. 1, No. 1, p.23-34.

[3] Win Swe (1970). Rift-features at the Sagaing-Tagaung Ridge, Abstract, Burma Research Congr., Rangoon, 101.

[4] Chibber, H.L., (1934). The Geology of Burma, Macmilland Com. & Limited, London, P538.

[5] Maung Thein, Than Myint, Soe Thura Tun, & Tint Lwin Swe. (2009). Earthquake and tsunami hazard in Myanmar. Journal of Earthquake and Tsunami, 3, 43–57.

[6] Soe Thura Tun, Min Swe, Tin Maung Nyunt and Win Naing, 2003. September 22 (2003). Earthquake in the Taungdwingyi Area, western Central Myanmar. Abstract, School Family Day Seminar, University of Yangon.

[7] Myanmar Geoscience Society (2014). Geological map of Burma, Partly based on Geological Map of the Socialist Republic of the Union of Burma (1977 ((Scale 1:1,000,000).

[8] Craig, R. F. (1991). Soil Mechanics, CHAPMAN & HALL, 2-6 Boundary Row, London SE1 8HN.

[9] Bernard R, W., Jason T D and Thomas S. (2012). Guidelines for Estimation of Shear Wave Velocity Profiles, Pacific earthquake engineering research center, PEER Report 2012/08.

[10] Pyi Soe Thein, J. Kiyono, Tun Tun Win, Than Than Nu and Day Wa Aung, (2015). Seismic Microzonation of Mandalay City, Myanmar. Journal of Geological Resources and Engineering, David Publishing.

[11] Pyi.Soe.Thein,S.Pramumijoyo.,K.S.Brotopuspito.,W. Wilopo ., J.Kiyono and , A. Setianto (2013). Investigation of Subsurface Soil Structure by Microtremor Observation at Palu, Indonesia, The 6th ASEAN Civil Engineering Conference (ACEC) & ASEAN Environmental Engineering Conference (AEEC), Civil and Environmental Engineering for ASEAN Community, Bangok, Thailand,, p.C-6

[12] Kiyono, J. and Suzuki, M. (1996). Conditional Simulation of Stochastic Waves by Using Kalman Filter and Kriging Techniques, Proc. of the 11th World Conference on Earthquake Engineering, Acapulco, Mexico, Paper No.1620.

[13] Ohta, Y. and Goto, N. (1976). Estimation of s-wave velocity in terms of characteristic indices of soil, Butsuri-Tanko, 29(4): 34-41

Techno-Science Research Journal 12 (Special Issue) 181-187

Content list available at ITC

Techno-Science Research Journal

Journal Homepage: www.ric.itc.edu.kh

Techno-Science Research Journal

Electrical Resistivity Tomography Survey Data in Drought Prone Areas Case Study: Buriram Province, Thailand

Naruemol Saoanunt [1*], Narongdet Yongsukkasam[2]

[1] *Department of Mining and Materials Engineering, Faculty of Engineering, Prince of Songkla University, Songkla 90110, Thailand*
[2]*Department of Civil Engineering Technology, Faculty of Industrial Technology, Buriram Rajabhat University, Buriram 31000, Thailand*

Received: 14 August 2023; Accepted: 15 May 2024; Available online: August 2024

Abstract: *Electrical Resistivity Tomography (ERT) investigation was conducted in four drought-prone districts areas in Buriram, Thailand, with the aim of assessing the potential of groundwater as a reserve water source for household, landuse and agricultural use in the dry season through the implementation of the Schlumberger array configuration. An electrical resistivity survey instrument was used to generate a 2D resistivity model of the electrical resistance profiles or pseudo section profiles. The survey instrument included more than 50 electrodes, enabling the investigation of the profile to a depth of up to 50 m from the ground surface. The resistivity values obtained from the field data were recorded and converted using RES2DINV.EXE software. The data were analyzed by comparing them with the geological information of the site and referencing the the observation data from geological boreholes. The results of the measured survey indicated that groundwater in the arid areas of Buriram Province is found at shallow depths around 15-20 m from surface and deposited in layers of sedimentary such as gravel, sand, sandstone and clay, and it remained relatively stable over a 2-year period with the water level being measured by an electric water level probe in all seasons of Northeast Thailand.*

Keywords: ERT; Drought-prone; Groundwater; Electrical Resistivity Survey; Reserve Water Source

1. INTRODUCTION

In Northeast Thailand, the issue of drought has increasing become a significant concern for residents, agricultural and industrial sectors. Specially in the province of Buriram, including the districts of Mueang Buriram, Ban Dan, and Huai Rat, the severity of the issue has been exacerbated over the years, resulting in detrimental impacts on water consumption, agricultural productivity, and industry operations. Department of Disaster Prevention and Mitigation of Buriram province officially declared the affected areas as drought disaster areas, subsequently providing immediate assistance to the affected residents from 2017 to 2036. In addition to this, the consumption of groundwater in the area has been hampered by salt water, resulting in adverse consequences for the people in the area (Satarugsa P., 2011; Satarugsa et al., 2008;). Nonetheless, it is worth noting that groundwater represents a valuable natural resource that can be desalinated and leveraged to mitigate water scarcity in both the short and long term (http://www.dgr.go.th). However, the sustainable utilization of groundwater resources requires a careful approach based on academic data in order to prevent potential environmental impacts such as subsidence and groundwater contamination. Effective geophysical survey data on this area is lacking. While some parts of Buriram Province have good-quality surface and groundwater, it is often insufficient for consumption during the dry season (DGR, 2018). Hence, researchers acknowledge the significance of conducting research to establish a geographic information database system of groundwater resources by applying geophysical surveying technology, Electrical Resistivity Tomography (ERT) (Ayolabi et al., 2014; Loke M.H., 2000; Satriania A., Lopertea A., and Soldovierib F., 2015; Safaa F. Y., Janmaizatulriah J., and Mazidah M., 2018). ERT is an accepted method for effectively planning groundwater management (Hany et al., 2017; Gómez-Ortiz D. and Martín-Crespo T., 2012).

* Corresponding author: Naruemol Saoanunt
E-mail: naruemol.sao@psu.ac.th; Tel: +667-428-7314; Fax: +667-455-8834

2. ERT METHODS

2.1 Electrical Resistivity Tomography (ERT)

Electrical Resistivity Tomography (ERT) methods is a popular method for groundwater survey due to its high accuracy and non-invasive nature, which does not cause damage to the soil layer or the underground rock system (Safaa et al., 2018). ERT results can be used to assess groundwater characteristics in gravel-sand layers, rock fractures, or cavities in the rock. The method enables the calculation of groundwater depth, thickness, and quality, which can be determined by interpreting resistivity data obtained from field measurements. This information can help identify whether the groundwater is fresh, brackish, or saline. ERT is also a quick and straightforward method for interpreting information using the electric discharge current (I). This method involves directing a direct current into the ground through current electrodes (C1, C2), which then circulates in all directions as a spherical (half-sphere) pattern within the soil. During the ERT process, some parts of the current flow towards the opposite polarity, causing the voltage between the two current terminals. The measurement of the voltage (V) generated through the potential electrodes (P1, P2) calculates the resistance as shown in Equation (1).

$$V = IR \text{ or } R = V/I \qquad \text{(Eq. 1)}$$

When V is voltage (unit is millivolt)
I is current (unit is milliampere)
R is resistance (unit is ohm)

There are various types of electrodes configurations available for the Resistivity Method. In this research, Schlumberger configuration was used to calculate the electrical resistivity. The schlumberger array is commonly used for vertical electric sounding (VES) for groundwater and earth materials. VES using the schlumberger any provides better resolution, and take less time to deploy than the wenner array (Loke M.H., 2000, Hany et al., 2017, Safaa et al., 2018) An array configuration where 4 electrodes are placed in line around a common midpoint. Two outer electrodes, A and B, are current electrode, and the two inner electrodes, M and N, are potential electrodes placed close together. With the schlumberger array, for each mearsurement the current electrodes A and B are moved outward to a greater separation thoughout the exploration. While the potential electrodes M and N stay in the same position util the observed voltage become M and N are moved outward to a new spacing. The resistivity give a resistance value, R = V/I, so in practice the apparent resistivity value is calculated by

$$p_a = kR \qquad \text{(Eq. 2)}$$

where k is the geometric factor which depends on the four electrodes. It is important to note that this value is not the actual resistivity of soil or rock. It represents the apparent resistivity, which is the resistivity of a homogeneous soil providing the same resistance of the same electrode arrangement. The relationship between Apparent Resistivity and True Resistivity is complex. Therefore, the interpreting inversion method is used to interpret resistivity data using computer-based methodology (Loke M.H., 1999). Table 1 presents Resistivity for some common earth materials; however the in-situ Resistivity is strongly influenced by porosity, fracture density, saturation, salinity and temperature of ground water. Sedimentary rocks typically contain more water than igneous rocks, and unconsolidated sediments and soils typically contain the most water.

2.2 Field Exploration Equipment Data Collection and Interpretation

The Geomative GD-10 Series was the geophysical survey instrument for measuring resistivity in this study. Its purposes were to investigate groundwater and assess the resistance of soil or rock in study areas including three districts of Buriram province: Ban Dan, Huai Rat, and Mueang Buriram. Electrical Resistivity Tomography (ERT) techniques were utilized to simulate the subsurface structure, locate features, and determine the extent of subsurface disconformities.

Table 1 Graphical Plot of the Resistivity Values of Different Types of Materials (after Loke M.H. [8])

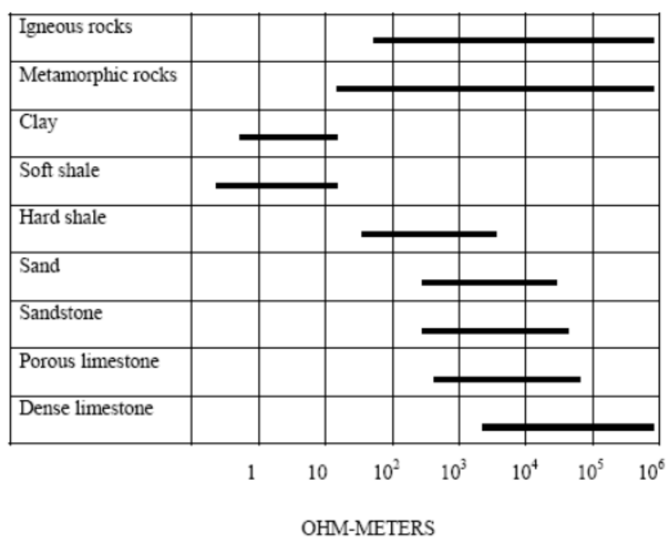

2.3 Data Collection and Interpretation

RES2DINV is (2-D) resistivity inversion model for the subsurface from electrical imaging survey data. It is capable of measuring the electrical resistance and utilizes Gauss-Newton's least squares inversion method (Sasaki, 1992) to construct a 2D model of soil or from the Apparent Resistivity.

RES2DINV automatically selects the optimal inversion parameter for the data set. Nevertheless, users have the ability to edit the inversion parameter and adjust the smoothing filter to emphasize electrical resistance patterns, such as vertical, horizontal, or diagonal features. RES2DINV can be optimized to generate models with smooth boundaries, such as Chemical Plumes, or irregular boundaries, such as Fracture Zones. In addition, it has the capability to integrate resistance data from boreholes and other sources to limit the inversion process of recognized boundaries where there are sudden changes in electrical resistance, which can then be incorporated into the inversion model. The borehole data of this study were used to compared and confirmed the accuracy of the data obtained from the ERT explorations.

This program has been extensively employed to simulate 2D and 3D models of subsurface geology (Castilho and Maia, 2008; Loke M.H., 2000), investigate disconformities (Henry et al., 2017; Araffa et al., 2014), survey groundwater resources (Satriani et al., 2012; Ayolabi et al., 2009), explore holes, ventricles, and underground salt layers (Gómez-Ortiz and Martín-Crespo, 2012). The interpretation data of the findings that were generated through the inversion method are presented in the form of a 2D model. Electric current flows through materials via conduction. The conductivity occurs in materials such as metals and semiconductors. The study of conductivity in saturated materials that utilized engineering methods by Loke M.H. (1977) demonstrated that the free electrons flow through the material and the conductivity arises from the movement of ions such as Na+ and Cl-. The conductivity of a material plays an important role in the interpretation of resistance data.

3. GEOPHYSICAL SURVEY RESULTS

The results of groundwater surveys in the study area were obtained using geophysical techniques that involved the use of an electrical resistance instrument. This paper presents the outcomes of the survey point location of resistivity apparent data. The results and interpretation outcomes were as follows.

Location 1, coordinates N15°01'24.8" E103°13'22.6", Khok Lek Subdistrict, Huai Rat District, Buriram Province, the data was processed using inversion modeling in RES2DINV software, as a 2D model as shown in Figure 1(a). The length of the area was 300 m. The electrode spacing was 5 m. The maximum depth that could be measured was 50 m. The error of interpretation was 2.5%. This error is usually due to variations in field survey data processed by the RES2DINV software. The results from this study area were as follows.

Layer 1 Electrical resistivity 1-8 Ohm-m at depths from the surface to 20 m, it could be identified as soil or zone of saturation.

Layer 2 Electrical resistivity 10-17 Ohm-m at a depth of 20-30 m, it could be identified as sedimentary rocks.

Layer 3 Electrical resistivity 20-50 Ohm-m at a depth of 30-50 m, it could be identified as a sedimentary aquifer.

Location 2, coordinates N14°47'46" E103°28'0", Mueang Fang Subdistrict, Mueang District, Buriram Province, the total length of the survey was presented, along with the soil layer, and the orientation of the groundwater, including the boundaries, thickness, and depth as shown in the 2D model (Figure 1(b)). Regarding the survey point location 1, Muang Fang sub-district, the total length of the survey was 374 m, the maximum depth was 55 m, and the error was 5.2%. The results of data interpretation were summarized as follows:

Layer 1 Electrical resistivity 30-100 Ohm-m at a depth from the surface up to 3 m, it could be identified as a top soil.

Layer 2 Electrical resistivity 1-10 ohm-m at depths 3-20 m indicated that it was a soil or sedimentary aquifer.

Layer 3 Electrical resistivity 20-40 Ohm-m. At depths of 20-50 m, it could be identified as sedimentary rock that accumulates or confines an aquifer.

Location 3, coordinates N15°06'22.5" E103°09'38.5", Ban Dan Subdistrict, Ban Dan District Buriram Province, the total length of the survey was 264 m, the maximum depth was 55 m, and the error was 3.5%, as a 2D model as shown in Figure 1(c). The data interpretation was summarized as follows.

Layer 1 Electrical resistivity 30-173 ohm-m at depths from the soil surface up to 5 m. It could be identified as a layer of soil and layer of soil reclamation because the resistivity was different significantly.

Layer 2 Electrical resistivity 3-15 ohm-m, at a depth of 5-20 m, it could be identified as a sedimentary or aquifer.

Layer 3 Electrical resistivity 30-55 ohm-m, at depths of 20-55 m, it could be identified as a sedimentary rock with a zone of saturation.

4. EXPLORATION AND WATER LEVEL IN THE OBSERVATION WELLS

The drilling exploration was conducted following a geophysical survey that measured conductivity in the field. This was done to investigate the accuracy of the resistivity interpretation and to monitor and measure groundwater levels in the study area. Due to the COVID-19 situation, the city has locked-down preventive measures, the survey drilling operations were limited to a single area in Muang Fang Sub-district, Muang District. The drilling was conducted from the surface to a depth of 50 m, with a 101.6 mm (4 in.) diameter drill bit. The location of the exploration well is shown in Figure 2.

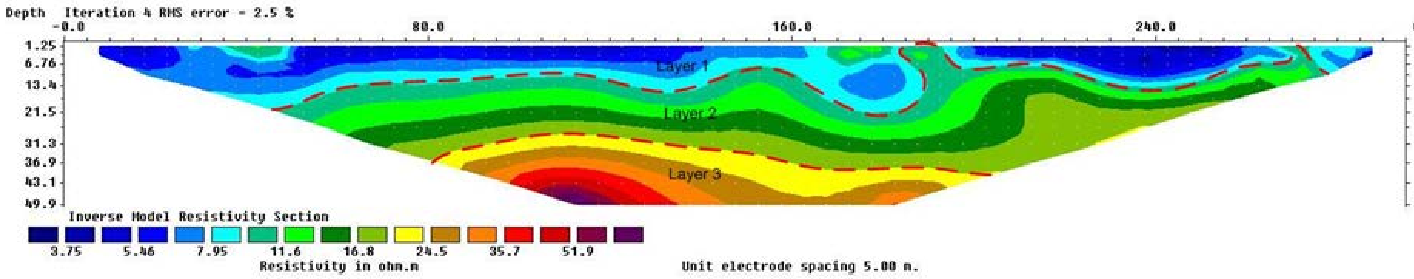

(a)

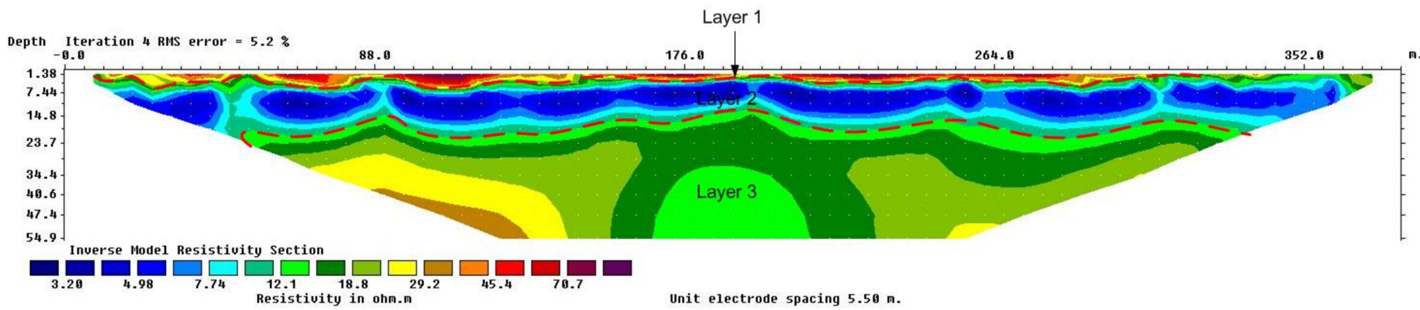

(b)

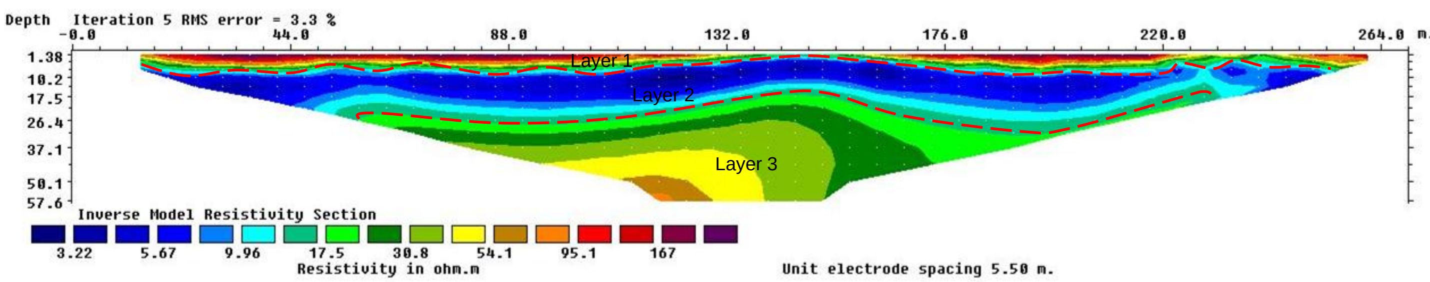

Fig.1. Resistivity 2D model of (a) Location 1 Khok Lek Subdistrict, Huai Rat District (b) Location 2 Mueang Fang Subdistrict, Mueang District and (c) Location 3 Ban Dan Subdistrict, Ban Dan District Buriram Province Thailand.

4.1 Explorations

At a depth of 2.5 m from the surface, the exploration revealed a layer of soil consisting of sediments (clastic rocks) such as gravel, sand and clay. From a depth of 2.5 m to 30 meters, the soil consisted of clay contaminated with gravel sediment (Clastics rock), appearing as light brown and not solidified. Groundwater was found accumulating at a depth of 30 m to 50 m. The characteristics of this layer were brown to dark brown mixed with Greenwich gray sandstone and there was groundwater retention at this depth. The drilling exploration results indicated that groundwater in the aquifer consists of sand, gravel, clay, and red-brown sandstone with an average depth ranging from 2.5 to 50 m. The amount of water in the well was 33 m^3/hr, indicating that the groundwater is suitable for utilization.

4.2 Water level in observation wells Explorations

The measurement of water level in 5 observation wells in Muang Fang Sub-district, Mueang District, Buriram Province has a borehole depth of 50 m from the surface and a borehole diameter of 101.6 mm. The water level in the well, measured from the surface, is presented in Figure 3. The groundwater level was monitored from June 2021 to May 2022. There was little variation in the groundwater levels during this

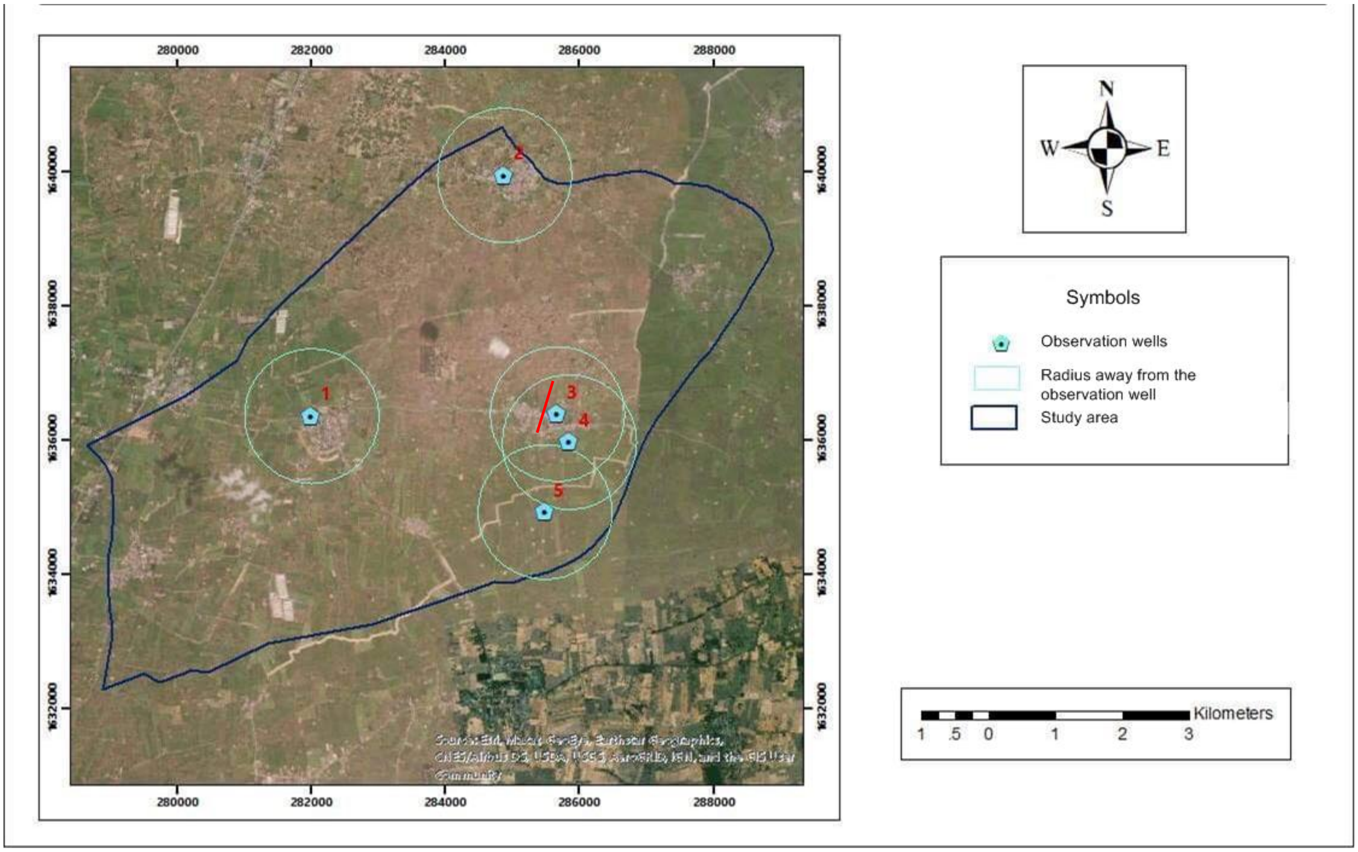

Fig.2. Survey line (red line) and Location of the 5 exploration wells in the study area

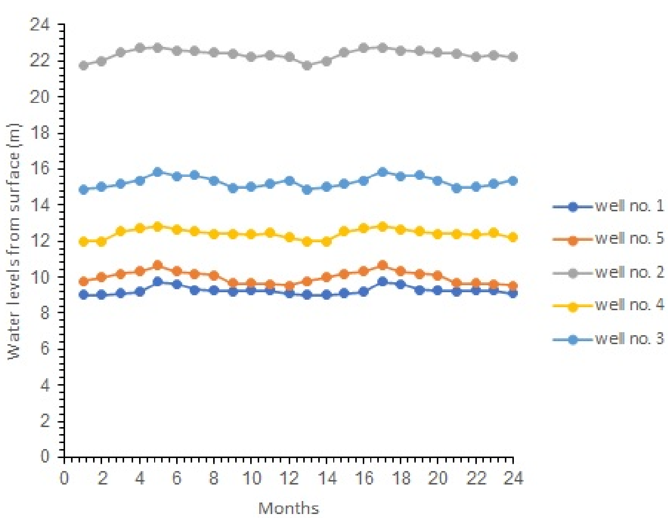

Fig.3. Measured water level in 24 months (2 years) for each observation wells in Muang Fang Sub-district, Muang District.

study period. This is because the accumulated average rainfall was very high, resulting in a high water and moisture retention rate in the year of data collection (2021-2022).

5. DISCUSSIONS AND CONCLUSIONS

This section pertains to the reliability of groundwater exploration using geophysical surveying, electrical resistivity tomography (ERT). The study evaluates the adequacy of the survey results and measurements of groundwater levels on the site. Additionally, the study compares the results from this investigation with those of previous research.

Geophysical surveying techniques, specifically ERT, are utilized to estimate the conductivity and resistivity of soil, rock, and groundwater levels in drought areas of Buriram Province. The aim of this study is to investigate underground water sources and determine locations for utilizing groundwater sources for household and agricultural purposes. The data of this exploration is processed and simulated in a 2D model using inversion modeling. The results of the ERT survey are clearly displayed in both vertical (depth) and horizontal (width) orientations. The survey results indicate the presence of sedimentary and sedimentary rock formations containing underground water at depths ranging from 2 to 55 m in the three investigated areas, which is consistent with Buriram Provincial Geological Survey data of the Department of Mineral Resources in 2010. Unlike the borehole monitoring data, water was found at a depth of ~9-22 m. This is due to the moisture content that the instrument was able to measure close to the surface. But the actual accumulated water level is in this depth range (~9-22 m). They are rocks of the Korat group that are unconsolidated. The findings also correspond to the resistivity of the material proposed by Loke M.H. (1999). The limitation of the survey at this depth is due to its inability to investigate beyond this level, which can be attributed to the distance between the electrodes placement, affecting the vertical signal transmission and electrical resistance measurement. The survey results indicate that no aquiclude was found at this depth, as a result, the maximum depth measurement is only around 55 m, which is consistent with the findings of previous studies by Satarugsa et al. (2008), Satarugsa P. (2011) and Loke M.H. (2010). These studies utilized geophysical surveys to measure electrical resistance and compared different types of terminals to align with the survey purposes. Observation wells were utilized to measure changes in groundwater level during June to September. The data was obtained by measuring the water level in five observation wells located at depths of 40-50 m below the surface in Muang Fang Sub-District, Muang Buriram District. During the study period, a slight stable in the water level was observed in all five observation wells.

However, it is possible that the COVID-19 pandemic may have contributed to this, as the research team was unable to conduct additional measurements in the area due to delays caused by the pandemic. Based on changing the groundwater level of this study. This area can be used for groundwater to household or agricultural work without affecting the subsidence due to the reduction of the groundwater level. The ground water level can be interpreted from all three 2D resistivity profiles or layers (> 5 ohm-m). This finding aligns with the information of the Department of Mineral Resources, DMR (2010) that groundwater levels at depths of 15-40 m from the upper water level of the Korat group can be safely utilized without affecting the environment in Buriram Province. If groundwater is extracted from a greater depth, there is a higher risk of encountering saltwater due to the melting of salt rock.

ACKNOWLEDGMENTS

The authers would like to thank Department of Civil Engineering Technology, Faculty of Industrial Technology, Buriram Rajabhat University and Department of Mining and Materials engineering, Faculty of Engineering, Prince of Songkla University to provide the necessary equipment to success this research.

REFERENCES

[1] Department of Mineral Resources (DMR). (2020). Zone classification for geological and mineral resource management Buriram Province. Bangkok, Thailand. [2021-01-25]. https://data.dmr.go.th.

[2] Department of Groundwater Resources (DGR). (2018). 20-year Strategy of Groundwater Management in Thailand (2017–2036).Thailand.[2019-12-22]. http://www.dgr.go.th.

[3] Araffa, S. A. S., Atya, M. A., Mohamed, A. M. E., Mohamed, M. G. A., Soliman, Z. M. M., Mesbah, H. S. U., and Shaaba, M.H. M. (2014). Subsurface investigation on Quarter 27 of May15th city, Cairo, Egypt using electrical resistivitytomography and shallow seismic refractiontechniques. National Research Institute of Astronomy and Geophysics Journal of Astronomy and Geophysics, 3, 170–183.

[4] Ayolabi, E. A., Folorunso, A. F., Eleyinmi, A. F., and Anuyah, E. O. (2009). Applications of 1D and 2D Electrical Resistivity Methods to Map Aquifers in a Complex Geologic Terrain of Foursquare Camp, Ajebo, Southwestern Nigeria. The Pacific Journal of Science and Technology, 10(2).

[5] Gómez-Ortiz, D. and Martín-Crespo, T. (2012). Assessing the risk of subsidence of a sinkhole collapse using ground penetrating radar and electrical resistivity tomography. Engineering Geology, 149, 1-12.

[6] Hany S. M., Essam A. M., Mamdouh M. S. and Khamis K. (2017). Joint application of Geoelectrical Resistivity and Ground PenetratingRadar techniques for the study of hyper-saturated zones. Case study in Egypt. National Research Institute of Astronomy and Geophysics Journal of Astronomy and Geophysics, 6, 256 - 266.

[7] Loke M.H. 2000. Topographic modelling in resistivity imaging inversion. In 62nd EAGE Conference & Technical Exhibition Extended Abstracts, D-2.

[8] Loke M.H. 1999. Time-lapse resistivity imaging inversion. In Proceedings of the 5th Meeting of the Environmental and Engineering Geophysical Society European Section, Em1.

[9] Loke M.H., Acworth, I. and Dahlin, T. 2003. A comparison of smooth and blocky inversion methods in 2D electrical imaging surveys. Exploration Geophysics, 34, 182-187.

[10] Loke M.H., Wilkinson, P. and Chambers, J. 2010. Fast computation of optimized electrode arrays for

2D resistivity surveys. Computers & Geosciences, 36: 1414-1426.

[11] Safaa F. Y., Janmaizatulriah J., and Mazidah M. 2018. Geophysical measurement for estimation of groundwater hydraulic properties. Data in brief, 21: 907 – 910.

[12] Sasaki Y. (1992). Resolution of resistivity tomography inferred from numerical simulation. Geophysical Prospecting, 40: 453-464.

[13] Satriania A., Lopertea A., and Soldovierib F. 2015. Integrated geophysical techniques for sustainable management of water resource. A case study of local dry bean versus commercial common bean cultivars. Agricultural Water Management, 162: 57-66.

[14] Satarugsa, P., Srisuk, K, Seangchomphu, and Youngmee, W. 2008. Mapping of salinity distribution in an unconfined aquifer overlying rock salt bodies with and electromagnetic survey. In: Xu Yixian and Xia Jianghai (eds), Proceeding of the 3rd International Conference on Near-surface geophysics and human activity, 15-20 June 2008: Wuhan, China, pp. 282-287.

[15] Satarugsa, P. 2011. The lessons learnt from geophysical investigation of sinkholes in rock salt in Thailand. In: Satarugsa, P, Phamchote, S., Khomkarn, K and Lertsirivorakul, R. (eds). Proceedings on International Conference on Geology, Geotechnology and Mineral Resources of Indochina (GEOINDO 2011), 1-3 December 2011: Khon Kaen,Thailand.

Techno-Science Research Journal 12 (Special Issue) 188-194

Content list available at ITC

Techno-Science Research Journal

Journal Homepage: www.ric.itc.edu.kh

Techno-Science Research Journal

Interpolation Maps of Geotechnical Subsoil Property in Boeng Keng Kang, Phnom Penh, Cambodia

Oudom Sokly[1], Sophea Boeut[1*], Sainglong Kaing[1], Peou Sieng[1,2], Veasna Sok[1], Rithysak Chan Ran[1], Hong Nong[1]

[1]*Faculty of Georesources and Geotechnical Engineering, Institute of Technology of Cambodia, Russian Federation Blvd., P.O. Box 86, Phnom Penh, Cambodia*
[2]*Research and Design Enterprise, No.17, St. 558, P.O.Box 2002, Phnom Penh, Cambodia*

Received: 21 August 2023; Accepted: 15 May 2024; Available online: August 2024

Abstract: Khan Boeng Keng Kang is one of the most developing districts in Phnom Penh City, Cambodia. The existing geotechnical data became important for feasibility studies and potential area research for both residential and commercial projects. Geotechnical soil data have been managed from individual borehole data with a total number of 67 boreholes into maps of different soil layers, from ground level to the 20-meter depth, with a 5-meter interval. Classified into four layers, two interpolation methods, Inverse Distance Weighted (IDW) and Kriging were applied. The selective drill hole data was obtained from 2012 and 2022, conducting the maps of the number of soil penetration tests (N-SPT), Water Content, Dry Density, and Elastic Modulus. The maps were then validated with other five-selected boreholes to represent the entire area. The validation process revealed that the N-SPT maps, created using both IDW and Kriging methods, demonstrated an accuracy of 67% and 58%, respectively. For water content, the IDW and Kriging interpolation methods yielded accuracy rates of 55% and 80%, respectively. Similarly, the dry density maps produced using these two methods achieved accuracies of 68% and 90%. The elastic modulus maps, generated using IDW and Kriging, displayed accuracy rates of 73% and 75%, respectively. Both the IDW and Kriging interpolation methods yielded validated results with an accuracy exceeding 65% for all the geotechnical parameters studied.

Keywords: IDW; Kriging; subsoil properties; Boeng Keng Kang, Phnom Penh

1. INTRODUCTION

With the steady expansion of both the agricultural and industrial sectors, soil quality has continued to deteriorate in the developing world [1–3]. Phnom Penh is the capital and largest city in Cambodia. Phnom Penh is also the country's economic, cultural, and political center, with a large population. Based on previous data investigations, Phnom Penh city is a good geotechnical area [4].

Engineering data, particularly those utilized by geotechnical engineers, are expensive, challenging to acquire, and challenging to interpret. The soil parameters are time-consuming and costly to determine due to the variety of layers at every location on the site. Engineers have always worked hard to manually draft diagrams and sketch maps to predict the variations in soil and its qualities. The majority of these outdated techniques are laborious and expensive [5]. Existing data sources in the form of hard, electronic, and paper copies, such as maps, site investigation reports, and even photos, can be integrated in less time using the GIS digital mapping platform as a tool to improve efficiency and effectiveness [6]. In fact, this research used a simple and affordable platform based on GIS technology and creates digital soil maps based on themes relevant to the soil, such as its SPT value, water content, dry density, and elastic modulus.

However, the research area covered 3.9 km^2 in Khan Boeung Keng Kang, Phnom Penh (Fig. 1). Research and Design Enterprise (RDE), which conducted the investigation from 2012 to 2022, provided the soil investigation data

* Corresponding author: *Sophea Boeut*
E-mail: boeurtsophea@gmail.com; Tel: +855-81-790-829;
Fax: +855-23-880-369

(secondary data) for this project. Borehole data were collected from 67 different sites in Khan Boeng Keng Kang.

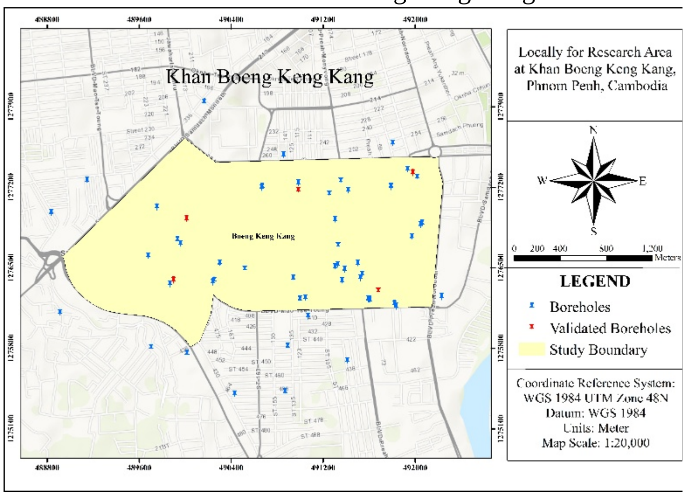

Fig. 1 Location of the study area in Boeng Keng Kang

To cover all the geotechnical properties of soil (i.e., the physical and mechanical qualities), collecting of huge data with a vast region is important. This can provide the basic data for geotechnical engineers for the suitable foundation design for a preliminary design stage. With the aid of such a digital map, geotechnical engineers will be able to gain an idea, gather important details about the soil layers, and decide the type of footing for preliminary research and even feasibility studies [6]. In this research, the IDW and Kriging interpolation methods were used, and the covered depth was approximately 20 m below ground level. Multiple types of soil properties were digitalized into ArcMap for interpolation map processing and reproduced. This research mapping, georeferenced to the WGS 1984 coordinate system, was projected on the Universal Transverse Mercator (UTM) Zone 48N. The WGS 1984 is a coordinate system mainly used in navigation tools [7]. The Universal Transverse Mercator (UTM) is a projection coordinate system and can also be called a Cartesian coordinate system [8], while 49N indicates the location where this research was conducted.

2. METHODOLOGY

Relevant secondary data were obtained from the RDE, soil investigation firm. Based on soil boring records, geotechnical study was collected between 2012 and 2022. The data utilized in this study were acquired, categorized, and examined before being input into the GIS environment. The second step was data preparation for the GIS software (ArcMap). All 67 study boreholes were analyzed and prepared in Excel sheet, before input as spatial data into ArcMap, 5 boreholes were kept for validations. The depth range of the research study was 0 to 20 m underground. The last stage was database creation and analysis of the result. The distribution of the soil properties (N-SPT, water content, dry density, and elastic modulus) layer can be made using the interpolation method. IDW and Kriging interpolation were important choices for this research.

The Inverse distance weighted (IDW), which integrates multivariate statistical analysis with GIS, is one of the most popular deterministic interpolation techniques in soil research [9]. IDW assumes a value for an attribute *z* at any unsampled point as a distance weighted average of sampled points lying within a defined neighborhood around that un-sampled point [10]. This method uses a semi-variogram that represents spatial differences and values between all data samples [11].

According to Wang (2019) [12], the formula of the Inverse Distance Weighting (IDW) algorithm is as follows:

$$\hat{Z}(x_0, y_0) = \sum_{i=1}^{n} \lambda_i Z(x_i, y_i) \qquad \text{(Eq.1)}$$

$$\lambda_i = (1/d_i)/(\sum_{k=0}^{n}(1/d_i)) \qquad \text{(Eq.2)}$$

$$d_i = \sqrt{(x_i - x_0)^2 + (y_i - y_0)^2} \qquad \text{(Eq.3)}$$

Where:

$\hat{Z}(x_0, y_0)$ = is the predicted value at an unknown point

$Z(x_i, y_i)$ = given value of the surrounding known sample points

λ_i = the weight of the sample point for the estimated point,

d_i = the distance from the sample point to the predicted point.

The interpolation in ordinary kriging starts with the construction of a variogram from the scatter point set to be interpolated. Once the model variogram is determined, it is used to compute the weights used in the Kriging [10]. Then, the Kriging interpolation formula is as follows:

$$Z^* = \sum_{i=1}^{n} \lambda_i Z_i \qquad \text{(Eq.4)}$$

Where:

Z^* = the predicted value at an unknown point

λ_i = the weight of each point

Z_i = is the value whose location and data are already known

n = the number of data points of the neighborhood

The weight, λ_i, is derived from the kriging equation of the covariance matrix structure, which minimizes the error variance. The covariance values according to the lag distance are obtained through variogram modelling [13].

Some borehole data points were not used in interpolation, keeping as the data validation. The result from interpolated was then compared with the remaining boreholes to check the degree of accuracy.

3. RESULTS AND DISCUSSION

A standard penetration test (SPT) is the most common method of geotechnical in situ testing [14]. This method provides a variety of correlations between the measured blow count (N-value) and properties of the tested materials, such as soil properties and the parameters of the foundation design. Measurement of the N-value is variability and uncertainty, which depend on the theoretical input energy and the actual hammer energy in the sample [15].

The ranges of the SPT blow Fig. 2 obtained from IDW interpolation increasing according to depth. Fig. 2(a) and (b) showed the distribution of SPT blows varies from less than 10 blows to 30 blows from depth 0 to 10 m. Western part of depth 0 to 5 m covered by range of N-SPT around 15 blows. Depth 5 to 10 m, Western part consisted of no more than 30 blows. Fig. 2(c) and (d), similarly consisted of less than 10 blows to greater than 50 blows of N-SPT.

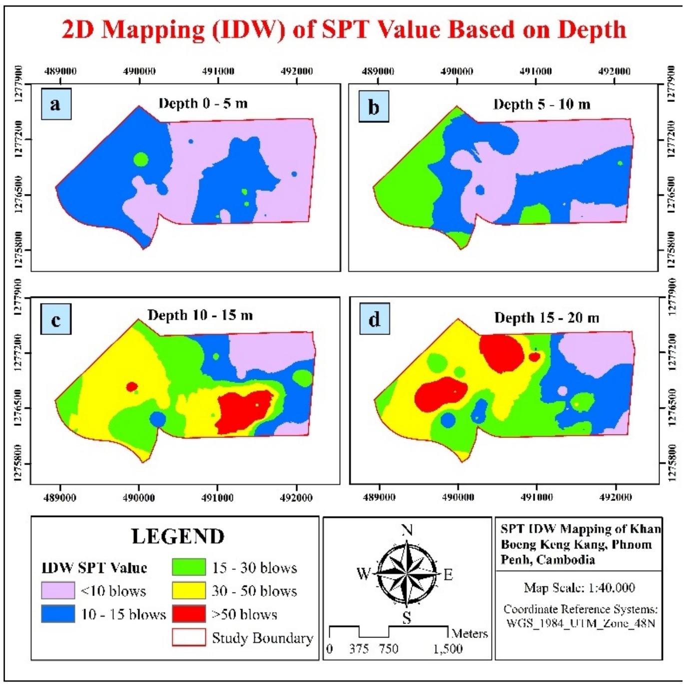

Fig. 2. 2D Mapping (IDW) of N-SPT according to the depth of (a) 0-5 m, (b) 5-10 m, (c) 10-15 m, and (d) 15-20 m

It was noticeable from Fig. 3 that the use of Kriging interpolation, illustrating the changes of the N-SPT blows unlike IDW methods. Fig. 3(a), N-SPT is lower than 10 blows covering the whole boundary. Fig. 3(b) shows the distribution of N-SPT over the study area, varying less than 10 to 30 blows, presenting the depth of 5-10 m. Yet, the distribution mostly shows the N-value of less than 15, except for a small portion of the west part arising of N-value up to 30 blows. Fig. 3(c) shows the value of SPT reaching 30 blows, considering one-third of the regions spreading at the west. The east side shows of low N-value, lower than 15 blows. The depth of 15-20 m (Fig. 3(d)), shows higher N-value of greater than 30 up to 50 blows at the North-West whilst the South-East part consist of SPT value less than 30 blows but not smaller than 10 blows. This reveals the occurrence of stiff soil. However, there are some locations that consisted of an N-SPT value between 10 and 50 blows.

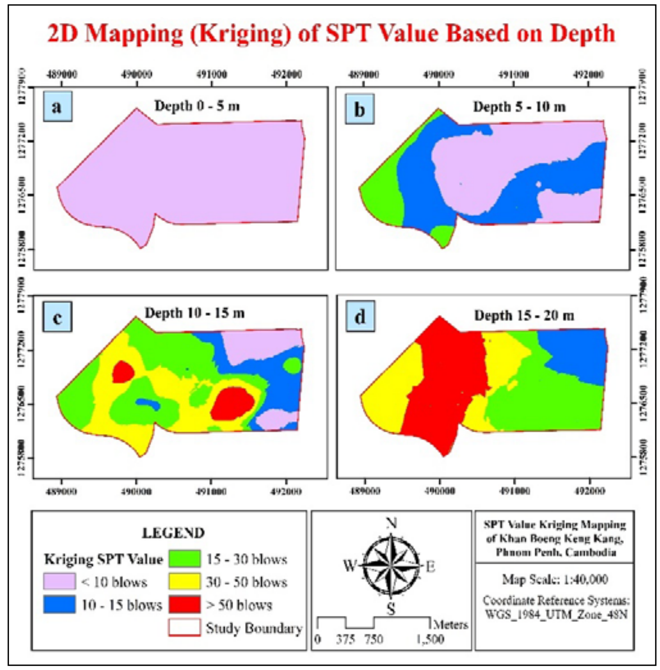

Fig. 3. 2D Mapping (Kriging) of N-SPT according to the depth of (a) 0-5 m, (b) 5-10 m, (c) 10-15 m, and (d) 15-20 m

After generated and analyzed the mapping, the remaining 5 borehole which keep for validation have use for validating and get the result in table below. Validation of IDW tends to be a better result than Kriging for N-SPT. This is providing the similar prediction according to Al Ani et al. (2014), stated the better maps attaining of geotechnical maps in Australia [16]. The IDW is not correlated to the prediction autocorrelation, yet it predicts based on the impacted distance and controlling the influence of the known data to the prediction zone. The correlation might decrease its influence due to the increase in distance.

Table 1. SPT validation result of IDW and Kriging method

Depth	IDW (Validation %)	Kriging (Validation %)
0 – 5 m	100	100
5 – 10 m	80	60
10 – 15 m	40	40
15 – 20 m	50	50
Overall	68	58

Once soil layer is found below the water level, it will obviously be fully saturated [6]. Fig. 4 shows the value of water content data from borehole data obtained from the project in Khan Boeng Keng Kang. The depth of the study was from the surface, 0 m, to the depth of 20 m below the surface. Colors variation denoted the classification of value of water content by IDW method. Fig. 4(a), (b) and (c) shows the distribution of water content varies from 15 % to higher than 30 %. Mostly, between 15 to 20 % covered the boundary within depth 0 to 15 m. Fig. 4(a), more than 30 % of water content value existed in the Southern part. Fig. 4(b) and (c), reveal a water content value greater than 30 %, similarly, presenting in North-East part and South-East part. Fig. 4(d), consisted of water content values not much different from other depth, it just exists less than 10 % of water content in the northern part. In the western part, the water content varies mainly from 25 % to 30 %. And it was seen to have higher than 30 % in the eastern part near the border of the research boundary.

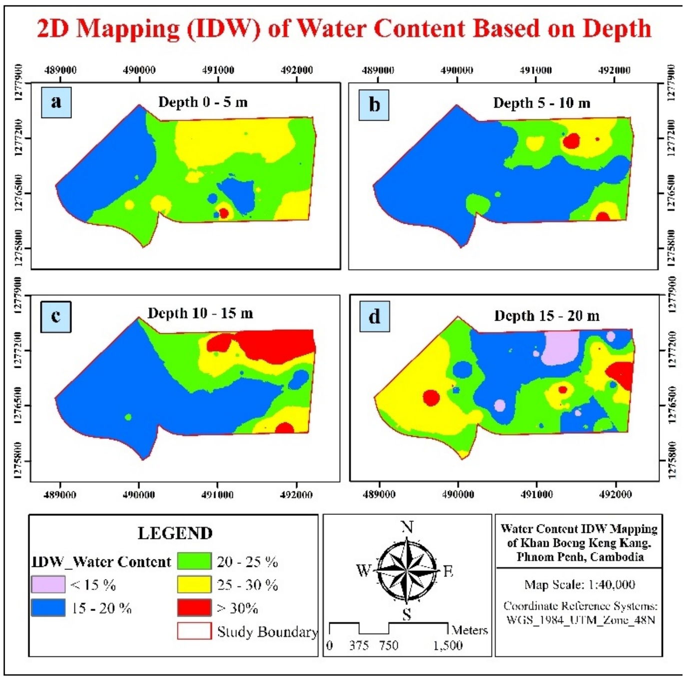

Fig. 4. 2D Mapping (IDW) of water content according to the depth of (a) 0-5 m, (b) 5-10 m, (c) 10-15 m, and (d) 15-20 m

The value of water content from Kriging interpolation was demonstrated into 4 different depths as shown in Fig. 5. In the past, most of the Khan Boeng Keng Kang location was covered with water. Therefore, the soil in this area is shown to have a high percentage of water content. Figs. 5(a), (b), and (c), denoted that from 0 to 15 m, the range of water content obtained from the interpolation map varies from 10% to 30 %. Depth 0 to 5 m, most of the area covered by 20 % and 30%, representing the western part and the eastern part, respectively. It can be seen at depths of 10 m to 15 m, the natural moisture content varies between 15% and 20% existing in the western part and more than 25 % occurring in the eastern part. However, 15 % to 20 % of natural moisture content value covered the whole boundary in depth of 15 m to 20 m, as we can observe from the interpolation map in Fig. 5(d).

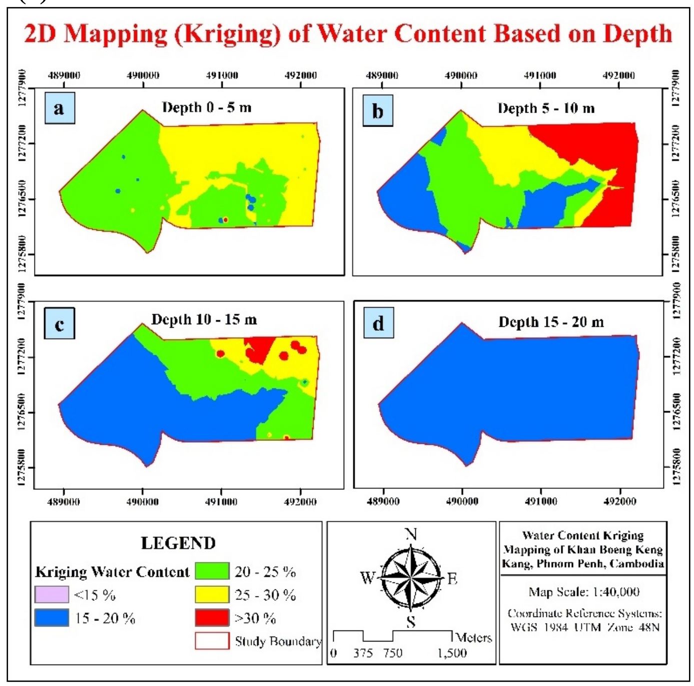

Fig. 5. 2D mapping (Kriging) of the water content according to the depth of (a) 0-5 m, (b) 5-10 m, (c) 10-15 m and (d) 15-20 m

Similarly, validation between IDW and Kriging interpolation of water content was used to determine and see the difference of accuracy of the interpolation methods above.

Table 2. Water content validation result of IDW and Kriging method

Depth	IDW (Validation %)	Kriging (Validation %)
0 – 5 m	40	40
5 – 10 m	40	100
10 – 15 m	60	80
15 – 20 m	80	100
Overall	55	80

The predicted value of dry density by the IDW method, increasing along with the study depths (Fig. 6). Figure 6(a), shows a GIS interpolation map of dry density, varies less than 1.5 g/cm^3 to 1.7 g/cm^3 at depth 0 to 5 m underground. The area in the western part consisted of a dry density value between 1.6 g/cm^3 and 1.7 g/cm^3. More, Figure 6(b), showed a similar value of dry density which ranged between less than 1.5 g/cm^3 to more than 1.8 g/cm^3. On the other hand, the dry density value at depths of 10 m to 15 m consisted of value not higher than 1.8 g/cm^3 in the study boundary. Clearly, there were some areas in the south-west, denoted values of the dry density ranging from 1.7 g/cm^3 to 1.8 g/cm^3. This reveals the occurrence of soil which contained low water content percentage. Figure 6(d), dry density value not unlike from Figure 6(b), but value less than 1.5 g/cm^3 was lacking.

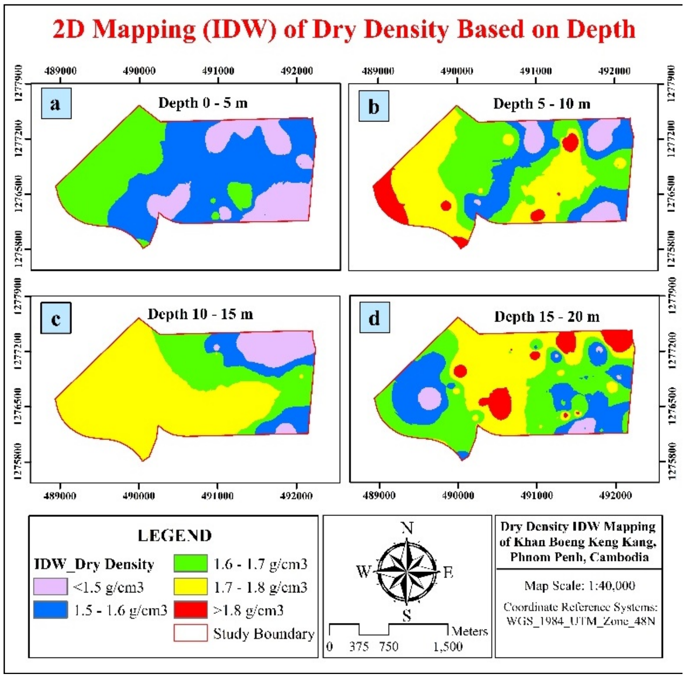

Fig. 6. 2D mapping (IDW) of dry density according to the depth of (a) 0-5 m, (b) 5-10 m, (c) 10-15 m and (d) 15-20 m

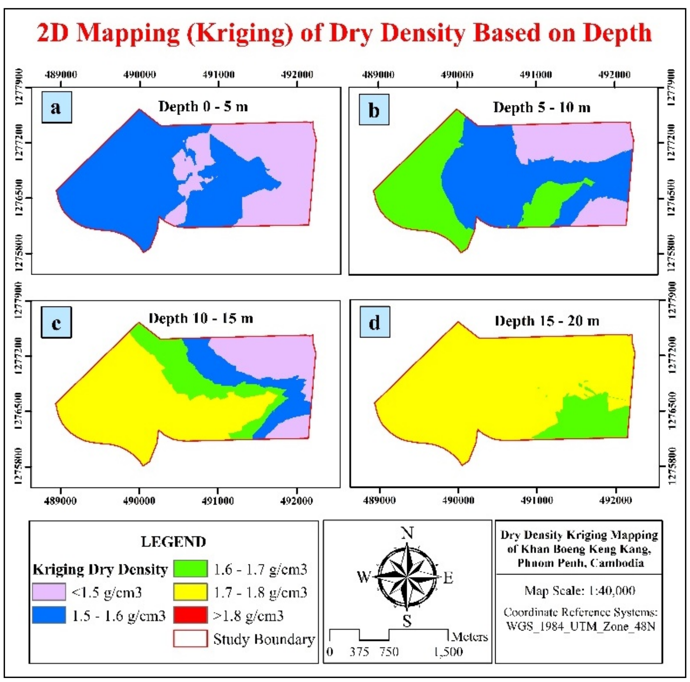

Fig. 7. 2D mapping (Kriging) of dry density according to the depth of (a) 0-5 m, (b) 5-10 m, (c) 10-15 m and (d) 15-20 m

Despite that, Fig. 7 showed the dry density over the research boundary. Colors variation illustrated the result of value of dry density based on different colors, varies from less than 1.5 g/cm^3 to greater than 1.8 g/cm^3.

Table 3. Dry density validation result of IDW and Kriging method

Depth	IDW (Validation %)	Kriging (Validation %)
0 – 5 m	100	100
5 – 10 m	40	60
10 – 15 m	80	100
15 – 20 m	50	100
Overall	68	90

The elastic modulus value increases with depth in Khan Boeng Keng Kang. The IDW method predicted that the elastic modulus value would vary from 10 MPa to 30 MPa at depths of 0 to 10 m, as shown in Fig. 8(a) and (b). However, at the depths of 5m to 10m, the maximum value was 50 MPa, which is in the Western part of the study area. Fig. 8(c) showed the changes in the elastic modulus of the soil. The elastic modulus value fluctuates from less than 10 MPa to 70 MPa. Fig. 8(d) shows that the elastic modulus varies from 10 MPa to 70 MPa. This clearly indicates that stiff soil exists at depths of 15 to 20 m.

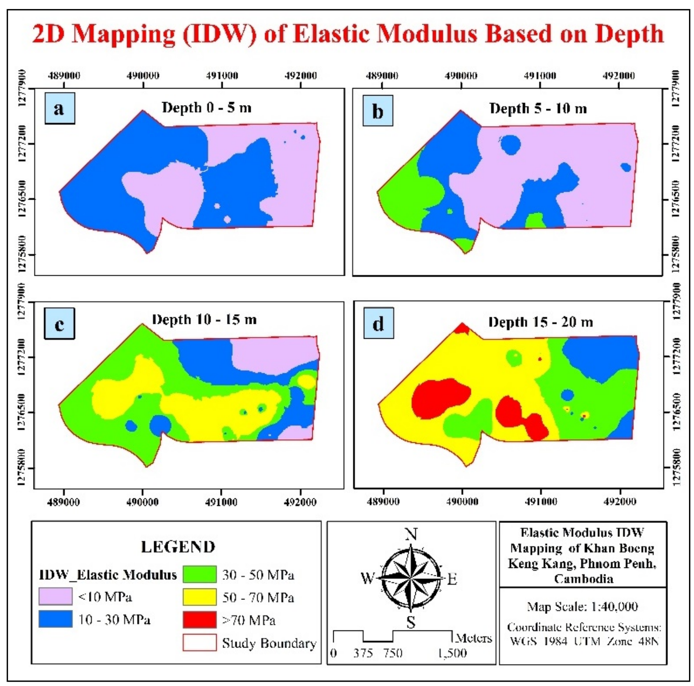

Fig. 8. 2D mapping (IDW) of the elastic modulus according to the depth of (a) 0-5 m, (b) 5-10 m, (c) 10-15 m and (d) 15-20 m

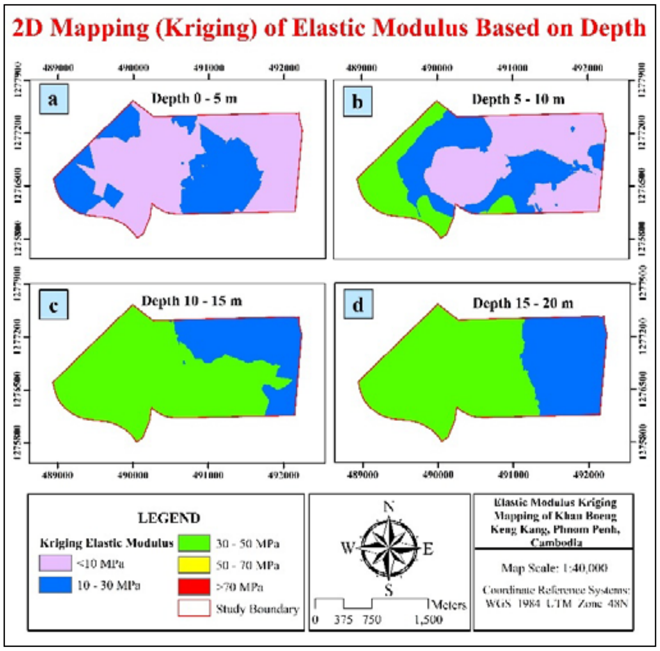

Fig. 9. 2D mapping (kriging) of the elastic modulus according to the depth of (a) 0-5 m,(b) 5-10 m,(c) 10-15 m and (d)15-20m

The interpolation by kriging method is shown in Fig. 9. At the depths of 0 to 10 m, the elastic modulus value varies from less than 10 MPa to 50 MPa utmost the whole research boundary, (Fig. 9(a) and (b)), except the Western and Eastern parts which demonstrate the elastic modulus of 10 MPa to 50 MPa (Fig. 9(c) and (d)).

The reliability of soil property interpolation results has been the question, and researchers have advised against using interpolation techniques for mapping purposes without validation [17,18]. This is because the accuracy varies depending on the method used and the characteristics of the data. To determine the best interpolation method for a particular application, it is important to perform validation using a subset of the data that was not used to create the interpolation map.

In this study, we compared the performance of two interpolation methods, inverse distance weighting (IDW) and kriging, for mapping the elastic modulus of soil (Table 4). After creating interpolation maps of the elastic modulus using both methods, we validated the results using the remaining borehole data. The validation results showed that kriging was better in percentage of validation in terms of the elastic modulus interpolation method for this data set.

Table 4. Elastic modulus validation result of IDW and Kriging method

Depth	IDW (Validation %)	Kriging (Validation %)
0 – 5 m	100	60
5 – 10 m	80	80
10 – 15 m	60	60
15 – 20 m	50	100
Overall	73	75

4. CONCLUSION

This study is part of preliminary research on creating geotechnical interpolation maps for the most crucial subsurface soil properties in Khan Boeng Keng Kang, Phnom Penh. IDW and Kriging techniques produced drastically different results for N-SPT, water content, dry density, and elastic modulus. Kriging underestimated the interpolated values, while IDW overestimated them. In other words, Kriging produced values that were smaller than their true values, while IDW produced values that were higher. To determine which method was more accurate, validation was carried out. The results showed that Kriging was the better interpolation method for most of the soil properties studied.

These interpolation methods at which the prediction maps of some geotechnical properties in this study area are beneficial for geotechnical use in footing and foundation design. They can also help consultants, investigators, and clients to identify and avoid potential problems during feasibility studies of future developments. In some cases, in-situ validation tests may be recommended to confirm the accuracy of the interpolation results, especially if there is any uncertainty.

ACKNOWLEDGMENTS

The secondary data in this research project was provided by Research Design and Enterprise (RDE) and funded support by JICA - LBE.

REFERENCES

[1] Soffianian A, Madani ES, Arabi M. Risk assessment of heavy metal soil pollution through principal components analysis and false color composition in Hamadan Province, Iran. Environ Syst Res 2014;3:1–14.

[2] Othman Z, Wahid MA, Latib FWM, Derahman A, Muhamad NS, Khalid K, et al. Risk mapping on heavy metal and nutrients after flood event on Pahang River using interpolation distance weighted (IDW) approach. Magnesium 2006;2:0–757.

[3] Akopyan K, Petrosyan V, Grigoryan R, Melkomian DM. Assessment of residential soil contamination with arsenic and lead in mining and smelting towns of northern Armenia. J Geochem Explor 2018;184:97–109.

[4] Touch Somphors. Three Dimensional Geological Modeling of Phnom Penh Subsoils. Chulalongkorn University, 2011.

[5] Khatri S, Suman S. Mapping of soil geotechnical properties using gis. Geotech GEOENVIRONMENTAL Eng ICGGE 2019.

[6] Asad H. A, Mohammed J, Saleem HD. Digital maps of mechanical geotechnical parameters using GIS. Cogent Eng 2020;7:1779563.

[7] Musayev I, Gojamanov M. Geodetic Errors Arising from the Differences Between Sk-42 and Wgs-84 Coordinate Systems when Implemented in Modern Weapons Systems. Konya J Eng Sci 2021;9:306–13.

[8] Sayed BH, George LE. Flat Model for Representing Contiguous UTM Coordinates over Iraq Territory. Iraqi J Sci 2020:908–19.

[9] Saha A, Bhaskar Sen Gupta, Sandhya Patidar, Nadia Martínez-Villegas. Optimal GIS interpolation techniques and multivariate statistical approach to study the soil-trace metal(loid)s distribution patterns in the agricultural surface soil of Matehuala, Mexico. J Hazard Mater Adv 2023. https://doi.org/10.1016/j.hazadv.2023.100243.

[10] Ibrahim DrAM, Nasser RHA. Comparison between Inverse Distance Weighted (IDW) and Kriging. Int J Sci Res IJSR 2017;6. https://doi.org/10.21275/ART20177562.

[11] Abdullah F, Yulianto E, Riyanto A, others. Pseudo 3D seismic using kriging interpolation. J. Phys. Conf. Ser., vol. 1725, IOP Publishing; 2021, p. 012075.

[12] Wang P, Feng Z, Tang Y, Zhang Y. A fingerprint database reconstruction method based on ordinary kriging algorithm for indoor localization. 2019 Int. Conf. Intell. Transp. Big Data Smart City ICITBS, IEEE; 2019, p. 224–7.

[13] Mingi K, Han-saem K, Choong-ki C. A Three-Dimensional Geotechnical Spatial Modeling Method for Borehole Dataset Using Optimization of Geostatistical Approaches. KSCE J Civ Eng 2020. https://doi.org/DOI 10.1007/s12205-020-1379-1.

[14] Braja MD. Principles of Foundation Engineering. Eighth Edition. 2016, 2012 Cengage Learning; 2014.

[15] ASTM D1586-11. Standard Test Method for Standard Penetration Test (SPT) and Split-Barrel Sampling of Soils. Annu Book ASTM Stand 2008.

[16] Al-Ani H, Oh E, Chai G, Al-Uzairy BN. GIS-interpolated geotechnical zonation maps in surfers paradise, australia. 6th Int. Conf. Adv. Geogr. Inf. Syst. Appl. Serv. GEO-Process. 2014 Spain Barc., vol. 142, 2014, p. 148.

[17] Childs C. Interpolating surfaces in ArcGIS spatial analyst. ArcUser July-Sept 2004;3235:32–5.

[18] Goovaerts P. Geostatistics for natural resources evaluation. Applied Geostatistics; 1997.

Techno-Science Research Journal 12 (Special Issue) 195-199

Content list available at ITC

Techno-Science Research Journal

Journal Homepage: www.ric.itc.edu.kh

Techno-Science Research Journal

Subsurface Soil Mapping of Geotechnical Properties Using IDW in Khan Tuol Kouk, Phnom Penh Capital City, Cambodia

Chanrithi Sak Ran[1], Sainglong Kaing[1*], Sophea Boeut[1], Peou Sieng[1,2], Hong Nong[1], Oudom Sokly[1], Veasna Sok[1], Mony Norn[1] and, Vicheka Van[1]

[1]*Faculty of Geo-resources and Geotechnical Engineering, Institute of Technology of Cambodia, Russian Federation Blvd., P.O. Box 86, Phnom Penh, Cambodia*

[2]*Research and Design Enterprise (RDE),Khan Toul kouk, Phnom Penh, Cambodia*

Received: 22 August 2023; Accepted: 15 May 2024; Available online: August 2024

Abstract: *The establishment of a geodatabase of geological studies and subsurface soil mapping is beneficial for the initial evaluation of engineering projects in Khan Tuol Kouk, Phnom Penh. This study aimed to produce some soil parameter maps in accordance with the N-SPT value and Plastic Index. Data from a total of 43 boreholes from 2012 to 2020 provided by RDE were used to map the soil characteristics maps. N-SPT value and Plasticity Index maps were created in the ArcGIS, a tool in Geographic Information System (GIS) using IDW interpolation method. The soil layer was divided into five groups based on the viscosity and density of clay and sand. The results shew that soils at the depth of deeper than 10 meters contained N-SPT values below 15 blows, soil depths between 10 to 20 meters consisted N-SPT values of 15 to 50 blows, and soils greater than 20 meters contained N-SPT values greater than 50 blows. This result was validated with four other boreholes and the overall results showed that the accuracy was over 40%. The results of plasticity index showed that soils of depth below 10 meters was apparent a plastic index value between 10% to 20% and 20% to 40%, while soils between 10 and 20 meters esisted a plastic index value between 5%-10% to 20%-40%. Thus, the validation result from the-four boreholes provided the overall accuracy of greater than 55%.*

Keywords: Soil property, Mapping, Plasticity Index, SPT, Phnom Penh

1. INTRODUCTION

Subsurface mapping is the establishment of a geodatabase for geological studies and subsurface soil mapping, which is useful and facilitates the initial evaluation of engineering projects can be defined as a geological map depicting geodatabase or features below the Earth surface, and describes the objectives and scope of this research will focus on mapping the subsurface based on the result from soil properties investigation that were collected at different site in Khan Tuol Kouk. All the soil data reports are secondary data from Research & Design Enterprise soil laboratory. In this research, data depth from 0 m to 25 m was selected to do the spatial analysis by using the Inverse Distance Weighting interpolation technique consisting of N-SPT and Plasticity Index through each layer. Therefore, the problem of this research is that getting more data by soil investigation is very costly and time-consuming this means that the research is to reduce and help for prediction of soil investigation as an apparent condition on soil data and is still limited in terms of quality and quantity for soil distribution.

In this study, all soil data of borelog was collected from 2012 to 2020. Besides that, all soil data that gathered for this study are already tested from RDE soil laboratory as well by following the Geotechnical Engineering Properties. There are 39 boreholes were being used for interpolation purpose furthermore, another 4 boreholes were kept for the validation purpose as well were shown in Fig 1.

Phnom Penh, the vibrant capital city of Cambodia, is divided into various administrative districts known as "khan." One such khan is Tuol Kouk, which is located in the northwest quadrant of the city. Khan Tuol Kouk is a bustling district that offers a unique blend of residential, commercial, and educational facilities, making it a popular choice among locals and

* Corresponding author: Sainglong Kaing
E-mail: skaing@itc.edu.kh; Tel: +855-11-812-001;
Fax: +855-11-812-001

expatriates. Khan Tuol Kouk is known for its modern infrastructure and development, featuring a wide range of amenities and services. The district boasts numerous shopping malls, supermarkets, restaurants, and cafes, providing residents with ample opportunities for leisure and entertainment. After boundary changes, its population has decreased to 145,570 [6]. Khan Tuol Kouk has a relatively high population density. The district's population density stands at approximately 11,679 people per square kilometer. This density is attributed to the district's increasing urbanization and the concentration of residential and commercial developments in a limited area.

On the other hand, Khan Tuol Kouk is a thriving district within Phnom Penh, Cambodia, characterized by a growing economy, a rising population, and a high population density. The district's favorable location, improved infrastructure, and diverse range of amenities have contributed to its development and attractiveness to businesses and residents alike [8]. In this research, the study area has an area of 7.99 km^2 starting from coordinating approximately 487000E to 490500E and 1276500N to 1281500N. This district is subdivided into 10 sangkats and 143 villages [9]. Which was located in the northern part of the city known for its commercial and residential areas moreover, it has a coordinate system (UTM 48P 489517 1280600; E 104.90385, N 11.5844).

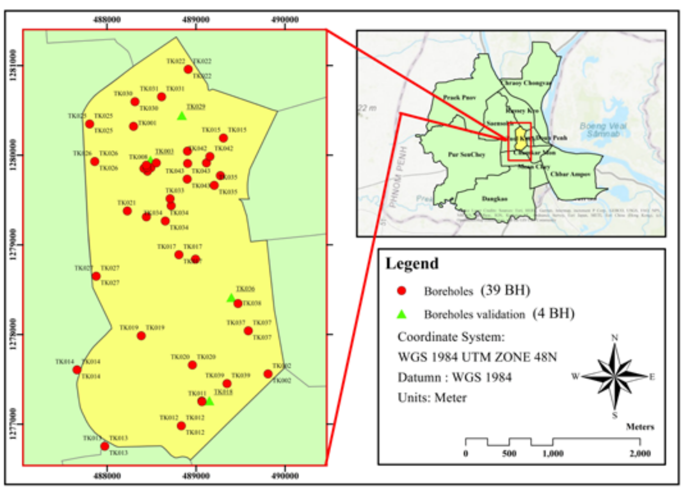

Fig 1. Location of the study area

2. METHODOLOGY

2.1 Inverse Distance Weighting (IDW)

Inverse Distance Weighting (IDW) interpolation is a commonly used method in geographic information systems (GIS) and remote sensing for estimating values at unobserved locations based on known data points. It is particularly useful when dealing with data that exhibits spatial autocorrelation, where values closer to each other tend to be more similar. One of the advantages of IDW interpolation is its simplicity and ease of implementation. It does not require complex algorithms or assumptions about the underlying data distribution. However, it is important to note that IDW interpolation tends to smooth out abrupt changes in the data and may give more importance to outliers [5]. All interpolation methods have been developed based on the theory that points closer to each other have more correlations and similarities than those farther. The IDW method generally assumes that the degree of relatedness and similarity between neighbors is proportional to the distance between them, which can be defined as the inverse function of the distance of each point to neighboring points. Note that the definition of the adjacent radius and the associated power of the inverse distance function are considered important points in this method. The power parameter “p” value has the most impact on how accurate the inverse distance interpolator is. Furthermore, the size of the neighbourhood and the number of neighbours have an impact on how accurate the results are. [3,1]

$$Z_0 = \frac{\sum_{i=1}^{N} z_i . d_i^{-n}}{\sum_{i=1}^{N} d_i^{-n}} \qquad (1)$$

where:

Z_0 = The estimation value of variable z in point I.
z_i = The sample value in point I.
d_i = The distance of sample point to estimated point.
N = The coefficient that determines weigh based on a distance.
n = The total number of predictions for each validation case.

2.2 Standard Penetration Test (SPT)

SPT is used for calculating the static and dynamic parameters of coarse-grained soils, including internal friction angle (ϕ'), relative density (D_r), bearing capacity, and settlement, soil shear wave velocity (v_s), and liquefaction potential. The SPT has been used to estimate engineering characteristics including undrained compressive strength (q_u), undrained shear strength (S_u), and coefficient of volume compressibility (m_v) in fine-grained soils even though it was initially designed for coarse-grained soils. Its application for fine-grained soils is still being examined [10]. SPT is performed in a borehole by repeatedly striking a standard (split spoon) sampler with a hammer that weighs 63.5 kg (140 lb.) and the hammer falling through 762mm (30 in.). The split spoon is connected to the hammer via rods, which are manipulated at the top of the borehole. The split spoon is lowered to the bottom of the hole, penetrated 450mm (18 in.) into the ground, and the blows are measured, typically every

76mm (3 in.) of penetration. The number of blows needed to drive the split spoon for the last 300mm (1 ft) of penetration is known as the penetration resistance (N) (Clayton 95) [7].

2.3 Plasticity Index (PI)

The plasticity index is the fundamental index of soil in the sense that it is used to classify fine-grained soils through the plasticity chart. The significance of the plasticity chart lies in the fact that it identifies plasticity as the two-dimensional property. The plasticity chart is widely used to differentiate between clays and silts and to further subgroup them according to the degree of their compressibility. Plasticity is an inherent property of fine-grained soil. Conventionally, plasticity of soil is represented through an index called the Plasticity Index, (PI). The plasticity index is the magnitude of the water content range over which the soil remains plastic. It is numerically equal to the difference between the liquid and the plastic limit water contents of the soil [11].

3. RESULTS AND DISCUSSION

3.1 N-SPT Interpolation

The IDW interpolation value of N-SPT are covered Khan Tuol kouk which is obtained from IDW interpolation established into 5 different thickness as shown in Fig 2 was generated the value in every depths were defined such as:

- For *Depth 1* (0 to 5 m): the range of N-SPT value is lower than 10 blows are cover up some part of the area and the highest value is from 10 to 15 was nearly cover up all the area.

- For *Depth 2* (5 to 10 m): N-SPT value from 10 to 15 blows is still much to cover up the area. There were 30 to 50 blows of SPT in the middle and surrounded by 15 to 30 blows.

- For *Depth 3 to Depth 4* (10 to 20 m): the N-SPT value mostly covered of 15 to 30 blows, except that of the utmost-north of the study area which was showing the value of between 30-50 blows

- For *Depth 5* (20 to 25 m): There existed over 50 blows of N-SPT value.

From this result of the IDW map, soil in this region appears soft soil from level zero to 10 m deep. Yet, the soil N-SPT increased as it reached the depth of 10 to 20 m representing medium consistency. Soil of deeper than 20 m presenting higher N-SPT presenting high consistency soil with the value of SPT exceeding 50 blows. The interpolation map of N-SPT by IDW showed the increase in N-value with the deeper depth of soil. The map demonstration in Fig 3 was to summarize the N-SPT value proposed in layer-3D-likewise map.

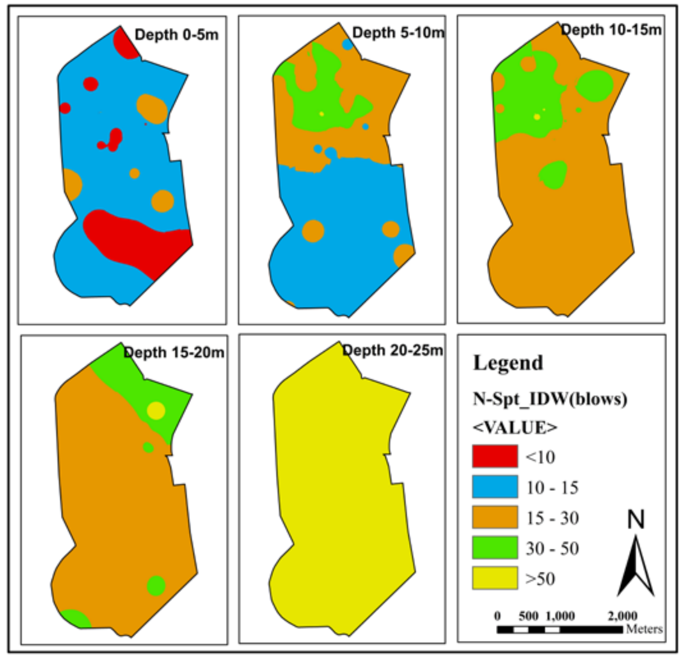

Fig 2. N-SPT value interpolation

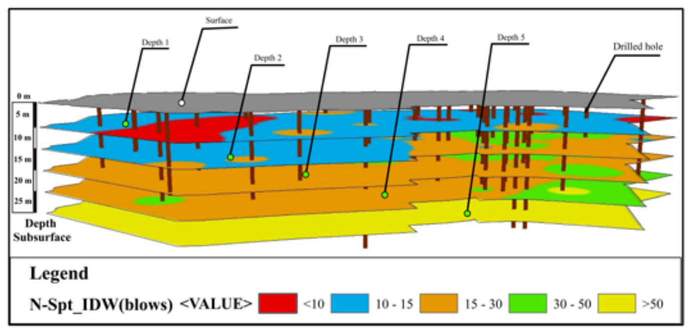

Fig 3. N-SPT (IDW) interpolation shown in 3D

Table 1. N-SPT value for validation

BH-ID	TK003	TK018	TK029	TK036
Depth (m)	Borelog (blows)	Borelog (blows)	Borelog (blows)	Borelog (blows)
0 - 5	11	6	12	30
5 - 10	27	10	14	26
10 - 15	36	16	39	41
15 - 20	56	68	39	-
20 - 25	55	-	-	-

Table 2. N-SPT value from IDW interpolation

BH-ID Depth (m)	TK003 IDW (blows)	TK018 IDW (blows)	TK029 IDW (blows)	TK036 IDW (blows)
0 - 5	10 - 15	<10	15 - 30	15 - 30
5 - 10	30 - 50	10 - 15	15 - 30	10 - 15
10 - 15	30 - 50	15 - 30	15 - 30	15 - 30
15 - 20	15 - 30	15 - 30	30 - 50	-
20 - 25	>50	-	-	-

Table 3. N-SPT result comparison between Validation value with Interpolation value

BH-ID	TK003	TK018	TK029	TK036
Score	2/5	3/4	1/4	1/3
Pecentage	40%	75%	25%	33%
Overall	**43.33%**			

To a certain the result from the interpolation *N-SPT* mapping, four boreholes were selected for the validation (Table 1); the result of the validation in comparing to that of the interpolated map showed the degree of accuracy greater than 40% (Table 2) Some validated data presented of less than 40%, some showed approximately 40% and greater. This might be due to the limitation of the number of borehole data in the predicted zone.

3.2 Plasticity Index Interpolation

The IDW interpolation value of Plasticity Index are cover the Khan Tuol kouk which is obtained from IDW interpolation is established into 4 different thickness as shown in Fig 4 was generated the value in every depths were defined such as:

- For *Depth 1* (0 to 5 m): From 0 to 5 m depth, the range of PI value from 5% to 10% are cover up some part of the area and PI value from 10% to 20% was nearly cover up all the area.

- For *Depth 2* (5 to 10 m): *PI* value from 10% to 20% blows is still much to cover up the area and *PI* value from 20% to 40% were attend as well.

- For *Depth 3* (10 to 15 m): From 10 to 15m depth, PI value 20% to 40% were attend but it is just a little zone surrounded by PI value from 10% to 20%.

- For *Depth 4* (15 to 20 m): From 15 to 20m depth, PI value from 5% till 40% were deposited all over the area.

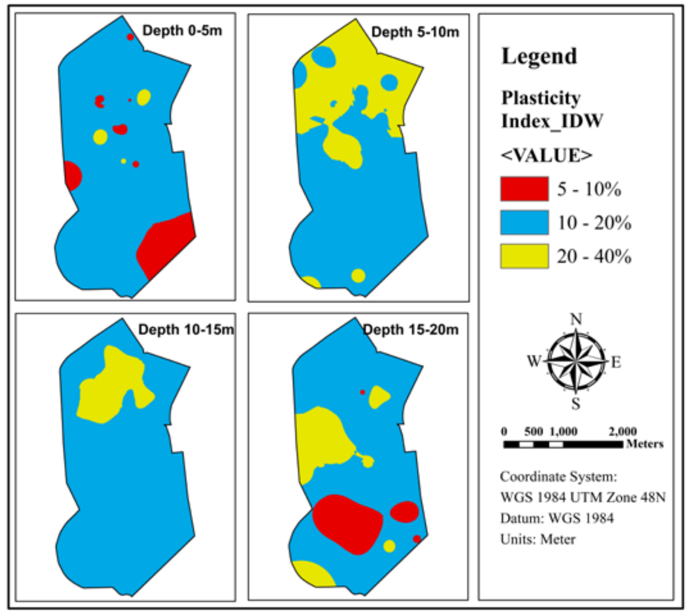

Fig 4. Plasticity Index (PI) value interpolation by IDW

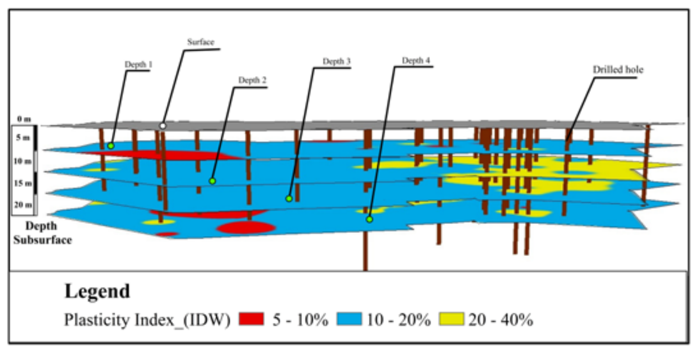

Fig 5. Plasticity Index (IDW) interpolation shown in 3D

Table 4. Plasticity Index (PI) value for validation

BH-ID Depth (m)	TK003 Borelog (%)	TK018 Borelog (%)	TK029 Borelog (%)	TK036 Borelog (%)
0 - 5	13.12	17.01	18.75	16.93
5 - 10	21.46	15.31	18.71	6.88
10 - 15	28.28	8.56	34.94	10.83

Table 5. Plasticity Index value from IDW interpolation

BH-ID Depth (m)	TK003 IDW (%)	TK018 IDW (%)	TK029 IDW (%)	TK036 IDW (%)
0 - 5	10 - 20	5 - 10	10 - 20	10 - 20
5 - 10	20 - 40	10 - 20	20 - 40	10 - 20
10 - 15	20 - 40	10 - 20	20 - 40	10 - 20

Table 6. Plasticity Index result comparison between Validation value with Interpolation value

BH-ID	TK003	TK018	TK029	TK036
Score	3/3	1/3	2/3	1/3
Pecentage	100%	33%	67%	33%
Overall	**58.33%**			

The soil becomes cohesionless after the verified result using IDW interpolation *PIasticity Index* (PI) mapping assumes every layer looks like it has low plasticity the most, which indicates the amount of clay is actually less deposited. However, validation data showed to be more than 55% suitable with those 4 boreholes data.

4. CONCLUSIONS

The subsoil investigation map of both N-SPT and Plasticity index was observed from 43 boreholes in Khan Tuol Kouk, Phnom Penh. The outcome of the research enhanced the creation of a digital database of some subsoil parameters rather than collectively in paper-based or other Portable Document Format which is difficult for primary site investigation. As a result, both N-SPT and plasticity index maps in comparing to the validation data seemed in high corporation with the overall accuracy of around 50%. This primary result would provide the key information before any starting of geotechnical technique in addition, Plasticity Index was performed quite well as well it is useful with results from soil investigation properties for comparison purposed.

Thus, all the analyst results and mapping of soil properties are useful for future research and study on subsurface conditions in Khan Tuol Kouk associated with civil engineering requirements and helpful for geotechnical research.

ACKNOWLEDGEMENTS

The project research was obtaining the secondary data from Research and Design Enterprise (RDE) and funded support by LBE-ITC.

REFERENCES

[1] Agung Setianto & Tamia Triandini (2013). Comparison of kriging and Inverse Distance Weighted (IDW) interpolation Methods in lineament extraction and Analysis, Geological Engineering Department, Faculty of Engineering, Universitas Gadjah Mada, Yogyakarta, Indonesia

[2] Burmister. (1949). Principles and techniques of soil identification. In: Proceedings of annual highway research board meeting, National Research Council, Washington, DC, 29, pp 402–433.

[3] Burrough, P.A., McDonnell, R.A. (1998) Creating continuous surfaces from point data. In: Burrough, P.A., Goodchild, M.F., McDonnell, R.A., Switzer, P.,Worboys, M. (Eds.), Principles of Geographic Information Systems. Oxford University Press, Oxford, UK.

[4] Chen, F. (. (1999). Soil engineering: testing, design, and remediation ISBN 0-8493-2294-4 (alk. paper) 1. Soil mechanics. 2. Engineering geology. 3. Foundations. 4. Soil remediation.

[5] Cressie, Noel A. C. (2015). Statistics for spatial data revised edition / Noel A. C. Cressie.p. cm.-(Wiley series in probability and mathematical statistics. Applied probability and statistics section).

[6] General Population Census of the Kingdom of Cambodia 2019 – Final Results. National Institute of Statistics. Ministry of Planning. 26 January 2021.

[7] Hara, A., Ohta, T., Niwa, M., Tanaka, S., and Banno, T. (1974) “Shear modulus and shear strength of cohesive soils,” Soils and Foundation., 14(3), 1-12.

[8] Phnom Penh City Hall. (2021). General Information Introduction,Retrievedfromhttp://phnompenh.gov.kh/en/phnom-penh-info/general-info/

[9] Phnom Penh Khan Toul Kouk. Realestate.com.kh, https://www.realestate.com.kh/locations/phnompenh/phnom-penh-khan-toul-kouk/.Accessed-11/Sept/2021.

[10] Sirvikaya, O. (2009) “Comparison of Artificial Neural Networks Models with Correlative Works on Undrained Shear Strength,” Eurasian Soil Science, Vol. 42, No. 13, pp. 1487–1496 Pleiades Publishing, Ltd.

[11] Sridharan, A., Nagaraj, H. B., and Prakash, K., “Determination of the Plasticity Index from Flow Index,” Geotechnical Testing Journal, GTJODJ, Vol. 22, No. 2, June1999,pp.169–175.

Techno-Science Research Journal 12 (Special Issue) 200-207

Content list available at ITC

Techno-Science Research Journal

Journal Homepage: www.ric.itc.edu.kh

Techno-Science Research Journal

Estimation of Surface Temperature and Mineral Alterations using Landsat-8 OLI Image. A case study Te Teuk Pus Hotspring, Kampong Speu Province, Cambodia.

Theary Mork[1*], Kakda Kret[1,2], Sirisokha Seang[1,3]

[1]Faculty of Geo-resources and Geotechnical Engineering, Institute of Technology of Cambodia, Russian Federation Blvd., P.O. Box 86, Phnom Penh, Cambodia

[2] Energy Technology and Management Unit, Research and Innovation Center, Institute of Technology of Cambodia, Russian Federation Blvd., P.O. Box 86, Phnom Penh 120404, Cambodia

[3] Materials Science and Structure Unit, Research and Innovation Center, Institute of Technology of Cambodia, Russian Federation Blvd., P.O. Box 86, Phnom Penh 120404, Cambodia

Received: 22 August 2023; Accepted: 15 May 2024; Available online: August 2024

Abstract: *we applied the single-window Algorithm (SWA) to Landsat-8 to obtain a Land Surface Temperature (LST) that we used to investigate the distribution of temperature on the surface in the Te Teuk Pus geothermal field, in southwest Cambodia. We first estimated the emissivity with the help of the proportion of vegetation technique. Then, we estimated LST using the estimated emissivity. As a result, LST was high in the Te Teuk Pus hydrothermal area (33.45-39.24 ° C) due to active hot fluid in this area, while LST was low in the thick vegetation cover regions. Furthermore, the temperature ranges from 15.4° C to 39.24 ° C. The area around the Te Teuk Pus is mostly high vegetation for emissivity, contributing to a high land surface emissivity result (i.e., 0.986-0.99). As the single-window algorithm uses both OLI (i.e., band 4 and band 5) and thermal infrared (TIR) (i.e., band 10). The colour composite and band ratio were used to map hydrothermal alteration. We further analyzed lineament and lineament density maps using ASTER GDEM for a possible zone of structural weakness related to potential areas of the geothermal field in the study area. The LST results indicated that the areas of thermal anomalies are well correlated with the development of faulted structures. Our results show good spatial agreement with anomaly areas compared to the geothermal field area, suggesting that TIR remote sensing provides an effective way of mapping and quantifying surface features to facilitate the exploration and assessment of geothermal resources in Cambodia.*

Keywords: LST, Alteration, SWA, and Landsat-8 (OLI)

1. INTRODUCTION

The distribution of land surface temperatures (LST), thermal anomalies, and alteration is useful for identifying climate change and hydrothermal fluid temperature. The Landsat-8 OLI is processed using a variety of single-window algorithms (SWA). Hence, a new possibility area has been suggested for future comprehensive study. Meanwhile, the normalized difference vegetation index threshold method for emissivity retrieval, the split-window algorithm for LST (Mia et al., 2019). The presence of clay minerals on the surface can help determine predicted clay minerals in their temperature range(Primayudha et al., 2021).

[*] Corresponding author: *Theary Mork*
E-mail: thearymork2k@gmail.com; Tel: +855-88-773-1166

Normalized Indifference Vegetation Index (NDVI) is a new technique that assists in evaluating vegetation cover change. To adapt and alleviate the effects of global climate change, vegetation is important for supplying many ecosystem services and goods. The relationships between climate and vegetation at the landscape level have been studied using spectral vegetation index data (Ridwan et al., 2018).

Alteration is the reflection of the response of pre-existing, rock-forming minerals to physical and chemical conditions different than those, under which they originally formed, especially by the action of hydrothermal fluids (Banerjee et al., 2019).

1.1 Study Area

The study area is located at Te Teuk Pus Hotspring, Sangke Sap Commune, Oral District, Kampong Speu province. It is the first place in Cambodia to have hot spring water. These are data from satellite images such as Landsat-8 (OLI) shown below

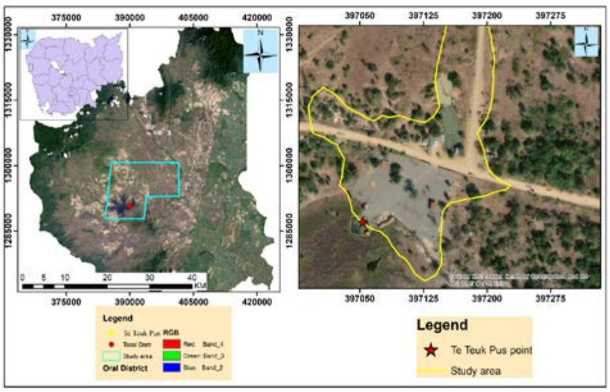

Fig.1. The study area in located Te Teuk Pus Hot Spring.

2. GEOLOGYCAL SETTING

Cambodia is located in Indochina's southernmost craton. Granitic magmatism in this area is governed by tectonics, namely the Indosinian orogeny. A granitic intrusion in Cambodia has been related to a series of suturing and collisions between allochthonous fragments from Gondwanaland (Classification, 1900).

2.1 Assessing Water of Te Teuk Pus Hot Spring

The objective of the current study is to investigate the water quality and potential of the hotspring. Eleven Te Teuk Pus water samples were taken, and the Hanna COD, Multiparameter photometer HI 83099, and Hach DR 1900 Spectrophotometer were used to examine the results (TableTable). According to analytical findings, the Te Teuk Pus hot spring has an average temperature of 47.83 °C and a temperature range of 43.67 ˚C to 63.00 ˚C. To reduce public health issues and leisure activities related to tourists, further research on thermally tolerant bacteria should be conducted. The WHO'S drinking water quality guideline (DWQG) regulation limit is exceeded by the mean PH (9.02) of the hot spring. The temperature of Hotspring water is quite lower than those of China, Vietnam, and Thailand.

Table 1 Summary of physicochemical properties of the Hot Spring water (Seng, Chheng Y, 2019.).

Physicochemical	Mean	SD	Min	Max
Tem (˚C)	**47.83**	**5.87**	**43.67**	**63:00**
PH	9.02	0.23	8.84	9.22
ORP (mV)	-	78.52	-305.1	-24.93
TDS (mg^{-1})	79.13	1.69	292.03	296.9
EC (μs cm^{-1})	294.5	8.81	572.53	604.47
Salinity (%)	3	0.03	1.1	1.2
Turbidity (NTU)	589.5	0.20	0	0.67
	1			
	1.11			
	0.06			

Drinking Water Quality Guideline (DWQG), Cambodian Drinking Water Quality Standard (CDWQS), and Standard deviation (SD).

3. METHODOLOGY

3.1 processing steps Satellite Image

OLI band data were converted to TOA planetary reflectance using reflectance rescaling coefficients provided in the image metadata files.

$$TOA=ML*Q_{cal}+AL-O_i \qquad \text{(Eq. 1)}$$

where:

TOA = Top atmospheric spectral radiance

ML = Radiance multiplicative Band

Q_{cal} = Quantized and calibrated standard product pixel values

O_i = Correction value for band 10

The TIRS band data were converted from spectral radiance to brightness temperature using the thermal constants provided in the image in the metadata file.

$$BT = \frac{K_2}{Ln\left(\frac{K_1}{L_\lambda}+1\right)} \qquad \text{(Eq.2)}$$

Where:

K1&K2= the band number 10 (K_1 = 774.8853, K_2 =1321.0789)

Convert degree Kelvin (K) to degrees Celsius

$$C = K - 273.15 \quad \text{(Eq.3)}$$

NDVI has provided an estimate of the presence of vegetation cover.

$$\text{NDVI} = \frac{\text{NIR} - \text{RED}}{\text{NIR} + \text{RED}} \quad \text{(Eq.4)}$$

Where:

RED = DN values of the red band, (band 4)
NIR = DN values from the Near-Infrared band, (band 5)

Calculate the Proportion of Vegetation (PV) an area covered by predefined vegetation or soil cover types.

$$PV = \left[\frac{NDVI - NDVI_{min}}{NDVI_{max} + NDVI_{min}}\right]^2$$

(Eq.5)

Calculation of Land Surface Emissivity (LSE), which is a measurement of the capacity of a material to radiate energy

$$E = 0.004 * PV + 0.986$$

(Eq.6)

Calculation of Land Surface Temperature (LST)

$$LST = \frac{BT}{\left(1 + \left(\frac{\lambda * BT}{C_2}\right) * Ln(E)\right)} \quad \text{(Eq.7)}$$

Where;

λ = wavelength of the emitted radiance (11.5 µm for band 10 in Landsat-8 OLI)

C_2= h × c/s = 1.4388 × 10^{-2} m K

h = Planck's constant = 6.626 × 10^{-34} Js
c = velocity of light = 2.998 × 10^{8} m/s.
s = Boltzmann constant = 1.38 × 10^{-23} J/K

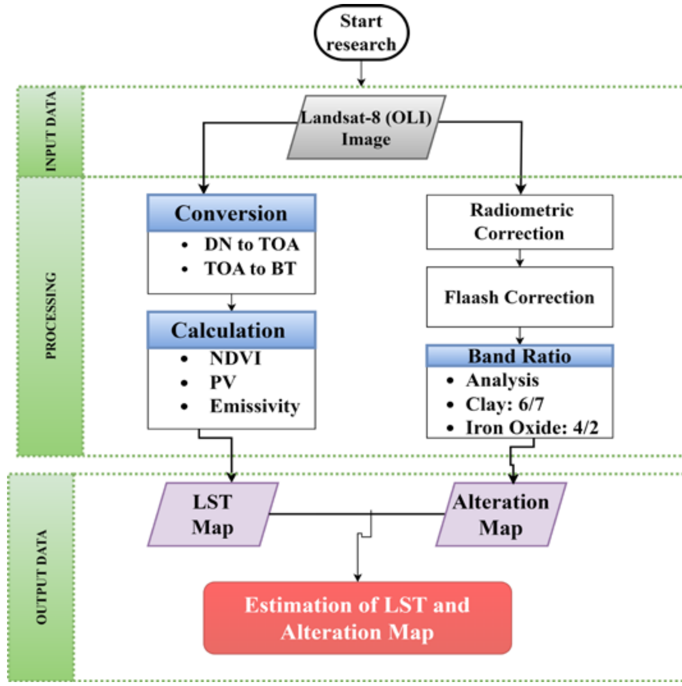

Fig.2. Research flowchart.

4. RESULTS AND DISCUSSION

4.1 Normalized Difference Vegetation Index (NDVI)

The Normalized Difference Vegetation Index (NDVI) provides results that are comparable to those of the LST. The Te Teuk Pus Hot Spring is largely surrounded by low vegetation and a lack of greenery can raise the temperature increase significantly every year during the dry season. NDVI map shows high values (i.e., -1 to 1). The result of the NDVI map shows the change in value from 2017 to 2019. In the years 2017 and 2019, the NDVI map shows high values (i.e., -0.227 to 0.393) and (i.e., -0.123 to 0.572) where the area is under the forest cover region. The value below 0 represents a water body, and the value > 0.40 represents vegetation.

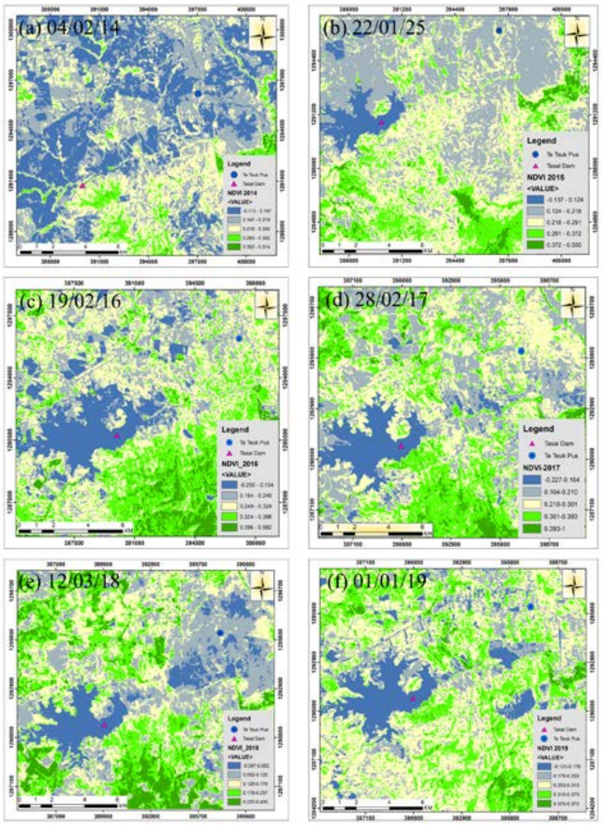

Fig.3. NDVI map.

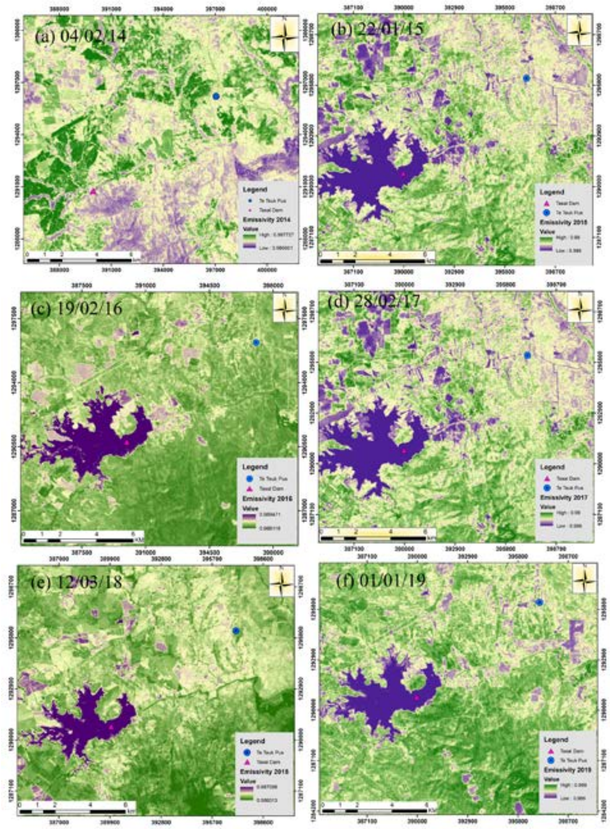

Fig.4. Emissivity map.

4.2 Land surface emissivity estimation (LSE)

The NDVI is able to be changed in order to show changes in emissivity, which reflects temperature of the soil in areas with little or no vegetation. Emissivity exhibits a high value (0.989) around areas with high vegetation cover and a low value (0.986) around areas with vegetation or bodies of water. When calculating LST, emissivity is a crucial factor to consider because it affects how much thermal radiation a surface emits.
The acceptable range of emissivity is 0 to 1.

4.3 Land Surface Temperature (LST)

The temperature of the water at Te Teuk Pus Hot Spring is higher than in other areas, and the results were shown (31.45-36.24 °C). It high temperature is indicated around the area where there is low vegetation cover. Estimated LST values revealed that in 2017, The temperature lies in the range of 33 -36°C, range value in 2019 has show around (32-36 °C) cover most of Te Teuk Pus hot Spring area and built up areas, field investigation should be conducted for validation with selected hydrothermal field and anomaly area using Google earth engine for calculating LST.

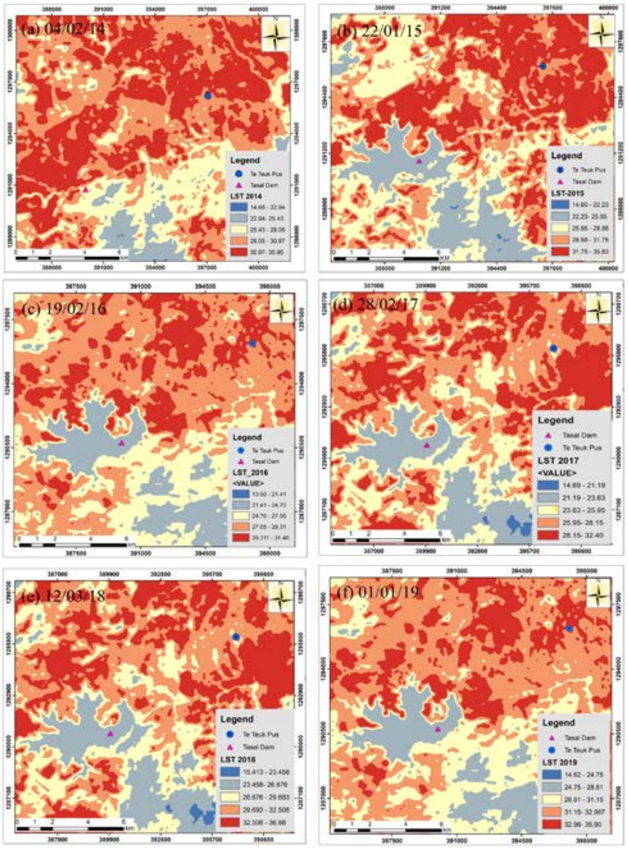

Fig.5. LST map.

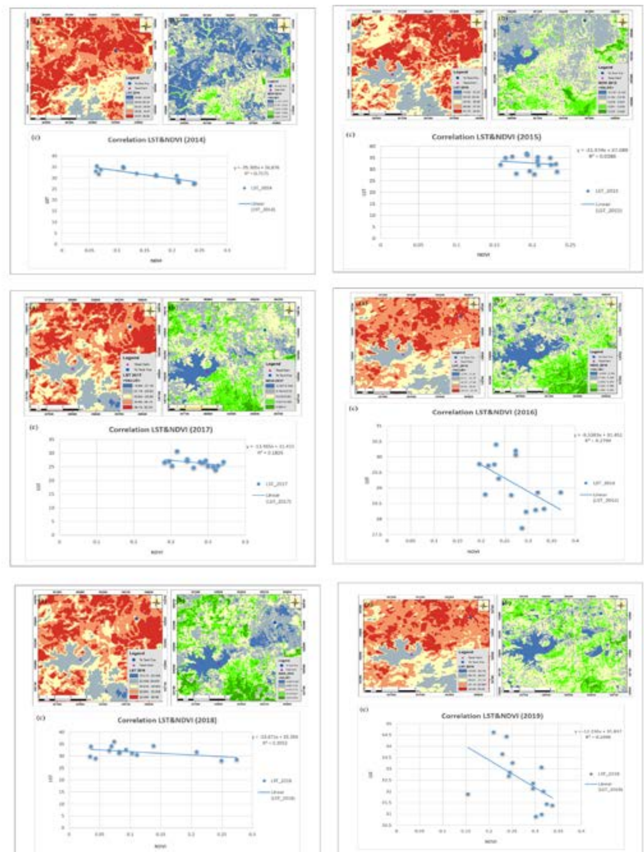

Fig. 6 Correlation NDVI and LST Map Te Teuk Pus Hot Spring.

4.4 Correlation of NDVI and LST

Normalized Difference Vegetation Index (NDVI) has been computed and their relationships with Land surface temperature (LST) in each season were examined. NDVI is very sensitive to changes and variations of NDVI might cause changes in land surface temperature. The relationship between NDVI and LST changed from season to season, but without obvious regularity. Correlation analysis has been done to find out the relationship between LST and NDVI which has shown a strong negative correlation has shown i.e.R^2 = 0.7575 in February 2014, R^2 = 0.0286 in January 2015, R^2 = 0.2799 in February 2016, R^2 = 0.1805 in February 2017, R^2 = 0.2052in February 2018, and R^2 = 0.2998 in February 2019. The strong negative correlation of NDVI with LST indicates that healthy green vegetation lowers surface temperature.

4.5 Alteration of clay and iron map

Clay and iron minerals are products of the activities of hydrothermal fluid; diffraction analysis shows clay and iron minerals, dominant the fluid temperature range in the Te Teuk Pus Hot Spring. Data interpretation shows the highest temperature zonation within the range 120–280 °C, range 180–260 °C zonation, and range 180–280 °C zonation. Temperature zonation obtained by using clay mineral association.

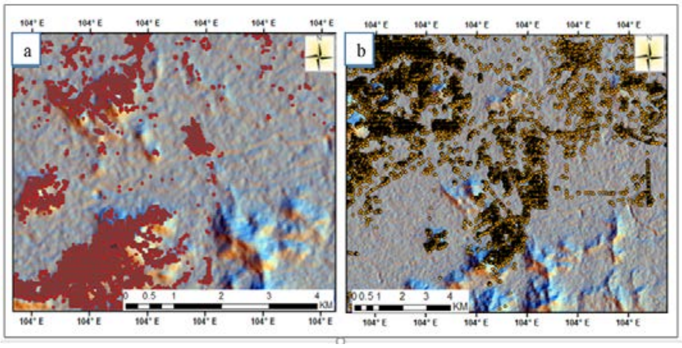

Fig. 6. Land-8 band radio alteration (a) clay and (b) iron.

4.6 Lineament Mapping

The analyst results we used tools on ArcGIS software, the ASTER GDEM data display the data of extra representative images. The first phase called for performing the hillshade method using ASTER GDEM knowledge with four different sun angle input values of 0°, 45°, 90°, and 135°; the input value for sun altitude, however, remained the same at 45°. Lineament information is largely provided in the research area's southwest and northeast. Depicted linear structures such as faults, faults, valleys, mountain peaks, and other distinctive features that occur in this area using the relief-shading approach.

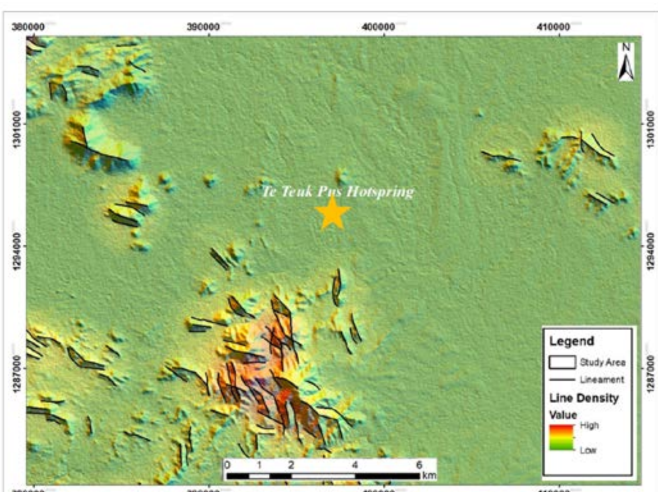

Fig.6. Lineament map Te Teuk Pus Hot Spring.

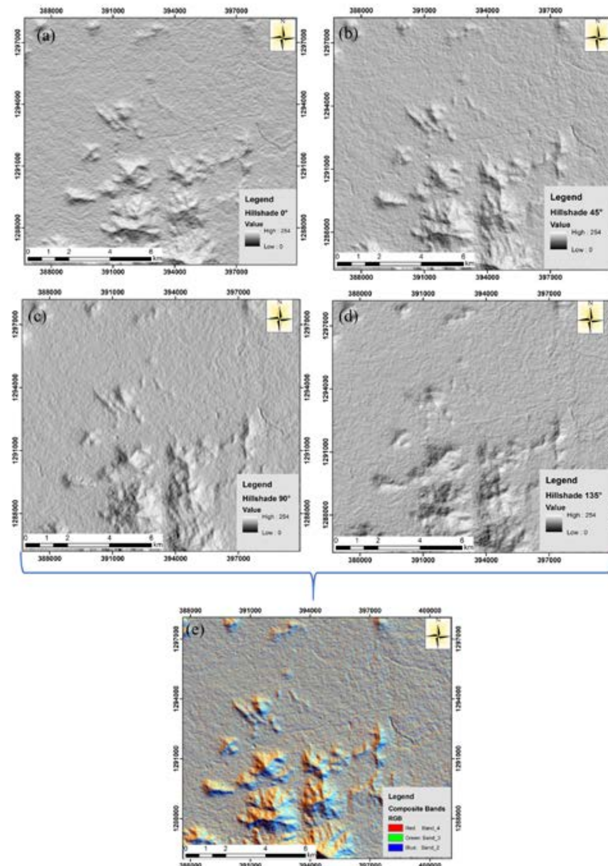

Fig.7. The image of (a) hillshade 0°, (b) hillshade 45°, (c) hillshade 90°, (d) hillshade 135°, (e) overlapping all hillshade in Te Teuk Pus Hot Spring.

5. CONCLUSIONS

The potential for using free Landsat -8 OLI and TIRS sensor bands from the USGS to estimate LST distribution in order to examine temperature change in Te Teuk Pus Hot Spring. Methods based on the Single Window Algorithm (SWA) are used to determine the LST that related with clay and iron alteration to conducted mineral in the surface can help to determine the hydrothermal fluid temperature at Te Teuk Pus Hot Spring. The results of alteration mapping, lineament (i.e., faults), and lineament density of clay and iron oxide showing the potential. Structural lineaments have revealed a variety of NE-SW, NW-SE, N-S, and trends related to rocks related to local faults. The results of Landsat-8 OLI data image analysis correlation between LST and NDVI increased during the years 2014 to 2019. The temperature and the strong negative correlation of NDVI with LST indicates that healthy green vegetation lowers the surface temperature.

ACKNOWLEDGMENTS

We would like to express sincere gratitude to all those who assisted us with this research and provided us with valuable recommendations. The international conferences on EraGET 2023 provided funding for this effort.

We want to use this occasion to say how grateful we as a community appreciate.

REFERENCES

[1] Aeronautics, N. (2007). Landsat. Van Nostrand's Scientific Encyclopedia, 3–6.

[2] Ali, M. (2007). The Exploitation of Remote Sensing Products to Improve Water Quality Monitoring in the Nile Delta. August 2007, 51.

[3] Amusuk, D. J., Hashim, M., Pour, A. B., & Musa, S. I. (2016). Utilization of landsat-8 data for lithological mapping of basement rocks of plateau state north central Nigeria. International Archives of the Photogrammetry, Remote Sensing and Spatial Information Sciences - ISPRS Archives, 42(4W1), 335–337. https://doi.org/10.5194/isprs-archives-XLII-4-W1-335-2016

[4] Barbier, E. (2002). Geothermal energy technology and current status: An overview. Renewable and Sustainable Energy Reviews, 6(1–2), 3–65.

[5] Barrie, C. T. (2012). Volcanogenic Massive Sulfide Occurrence Model. Economic Geology, 107(5), 1073–1073. https://doi.org/10.2113/econgeo.107.5.1073

[6] Carter, A., Roques, D., Bristow, C., & Kinny, P. (2001). Understanding mesozoic accretion in Southeast Asia: Significance of triassic thermotectonism. https://doi.org/10.1130/0091-7613(2001)029<0211:UMAISA>2.0.CO;2

[7] Chen, Y., Yang, K., He, J., Qin, J., Shi, J., Du, J., & He, Q. (2011). Improving land surface temperature modeling for dry land of China. Journal of Geophysical Research Atmospheres, 116(20), 1–15. https://doi.org/10.1029/2011JD015921

[8] Cheng, R., Uchida, E., Katayose, M., Yarimizu, K., Shin, K. C., Kong, S., & Nakano, T. (2019). Petrogenesis and tectonic setting of Late Paleozoic to Late Mesozoic igneous rocks in Cambodia. https://doi.org/10.1016/j.jseaes.2019.104046

[9] Classification, T. P. (1900). Chapter 1 Overview of the Position. 57, 1–11.
Czubski, K. (2018). Comparison of ASTER GDEM and SRTM DEM in the Pieniny National Park. November. https://doi.org/10.13140/RG.2.2.33139.99360

[10] D'Allestro, P., & Parente, C. (2015). Gis application for ndvi calculation using landsat 8 oli images. International Journal of Applied Engineering Research, 10(21), 42099–42102.

[11] Finster, M., Clark, C., Schroeder, J., & Martino, L. (2015). Geothermal produced fluids: Characteristics, treatment technologies, and management options. Renewable and Sustainable Energy Reviews, 50, 952–966. https://doi.org/10.1016/j.rser.2015.05.059

[12] Kalma, J. D., McVicar, T. R., & McCabe, M. F. (2008). Estimating land surface evaporation: A review of methods using remotely sensed surface temperature data. Surveys in Geophysics, 29(4–5), 421–469. https://doi.org/10.1007/s10712-008-9037-z

[13] LaBerge, J. M., & Andriole, K. P. (2003). Digital Image Processing: A Primer for JVIR AuthorsandReaders.Part3:DigitalImageEditing.https://doi.org/10.1097/01.RVI.0000106744.94154.B3

[14] Ly, S., Seang, S., Kret, K., Kimhouy, O., & Ammugauan, J. (2021). Preliminary study on lithology , hydrothermal alteration and soil / rock geochemistry for gold and copper at Area 6 , Phnom Sro Ngam Tenement , Preliminary study on lithology , hydrothermal alteration and soil / rock geochemistry for gold and copper at Ar. March 2022.

[15] Ahmed, N. (2016). Application of NDVI in Vegetation Monitoring Using GIS and Remote Sensing in Northern Ethiopian Highlands. Abyss. J. Sci. Technol, 1(1), 12–17. http://wujournals.com/data/documents/Article-3-Mr.-Nurhussen-Revised.pdf

[16] Banerjee, K., Jain, M. K., Jeyaseelan, A. T., & Panda, S. (2019). Landsat 8 OLI data for identification of hydrothermal alteration zone in Singhbhum Shear Zone using successive band depth difference technique - A new image processing approach. Current Science, 116(10), 1639–1647. https://doi.org/10.18520/cs/v116/i10/1639-1647

[17] Classification, T. P. (1900). Chapter 1 Overview of the Position. 57, 1–11.

[18] Mia, M. B., Fujimitsu, Y., & Nishijima, J. (2019). Exploration of hydrothermal alteration and monitoring of thermal activity using multi-source satellite images: A case study of the recently active Kirishima volcano complex on Kyushu Island, Japan. Geothermics, 79(January), 26–45. https://doi.org/10.1016/j.geothermics.2019.01.006

[19] Primayudha, F., Sahdarani, D. N., Kadja, G. T. M., & Supriyanto. (2021). The relationship of volcanic facies and temperature range derived from the associated clay mineral in Gunung Endut, Banten. Journal of Physics: Conference Series, 1725(1). https://doi.org/10.1088/1742-6596/1725/1/012073

[20] Ridwan, M. A., Radzi, N. A. M., Ahmad, W. S. H. M. W., Mustafa, I. S., Din, N. M., Jalil, Y. E., & Isa, A. M. (2018). Applications of Landsat-8 Data : a Survey. 7, 436–441.

[21] Vu, T. A., Tuyen, D. Van, Anh, T. T., Toan, D. Van, & Phong*, L. H. (2017). Identification of geothermal reservoir from exploration data in the Bang hot spring area, Central [27]Vietnam. Vietnam Journal of Earth Sciences, 39(3). https://doi.org/10.15625/0866-7187/39/3/10590

[22] Subregion, G. M., Subregion, G. M., River, M., River, R., Mekong, T., Mesozoic, U., Plateau, K., River, C. P., Nam, V., River, R., & Pdr, L. (n.d.). No Title. 77–152.

[23] Sukojo, B. M., & Mardiana, R. (2017). Geothermal Potential Analysis Using Landsat 8 and Sentinel 2 (Case Study: Mount Ijen). IOP Conference Series: Earth and Environmental Science, 98(1). https://doi.org/10.1088/1755-1315/98/1/012025

[24] Sun, F., Yao, Y., & Li, G. (2020). Literature review on a U-shaped closed loop geothermal energy development system. Energy Sources, Part A: Recovery, Utilization and Environmental Effects, 42(22), 2794–2806. https://doi.org/10.1080/15567036.2019.1618

[25] Tanjung, F. H., Dhianaufal, Rahmadhani, A. U., Sihombing, F. M. H., Sahdarani, D. N., & Supriyanto, S. (2020). Lineament mapping using remote sensing and correlation on surface manifestation distribution in Gunung Endut, Banten Province, Indonesia. IOP Conference Series: Earth and Environmental Science, 538(1). https://doi.org/10.1088/1755-1315/538/1/012051

[26] Teck, V., Poortinga, A., Riano, C., Dahal, K., Legaspi, R. M. B., Ann, V., & Chea, R. (2023). Land use and land cover change implications on agriculture and natural resource management of Koah Nheaek, Mondulkiri province, Cambodia. Remote Sensing Applications: Society and Environment, 29(November 2022), 100895. https://doi.org/10.1016/j.rsase.2022.100895

[27] Waghmare, B., & Suryawanshi, M. (2017). A Review- Remote Sensing. International Journal of Engineering Research and Applications, 07(06), 52–54. https://doi.org/10.9790/9622-0706025254

[28] Wood, S. H., & Singharajwarapan, F. S. (2014). Geothermal systems of Northern Thailand and their association with faults active during the quaternary. Transactions - Geothermal Resources Council, 38(January), 607–615.

[29] Yang, I., & Acharya, T. D. (2015). Exploring Landsat 8. International Journal of IT, Engineering and Applied Sciences Research, 4(4), 8. https://www.researchgate.net/profile/Tri-Acharya/publication/311901147_Exploring_Landsat_8/links/589c0de6458515e5f4549e58/Exploring-Landsat-8.pdf%0Ahttp://earthobservatory.nasa.gov/IOTD/

Techno-Science Research Journal 12 (Special Issue) 208-214

Content list available at ITC

Techno-Science Research Journal

Journal Homepage: www.ric.itc.edu.kh

Techno-Science Research Journal

Subsurface Soil Mapping of Geotechnical Engineering Properties in Khan Prampir Makara, Phnom Penh, Cambodia

Veasna Sok[1], Sophea Boeut[1*], Sainglong Kaing[1], Pov Sieng[1,2], Oudom Sokly[1], Hong Nong[1], Rithysak Chan Rorn[1], Mony Norn[1], Vichaka Van[1], Engsong Srong[1], Bunrong Sovann[1]

[1] *Faculty of Georesources and Geotechnical Engineering, Institute of Technology of Cambodia, Russian Federation Blvd., P.O. Box 86, Phnom Penh, Cambodia*

[2] *Research and Design Enterprise, No.17, St. 558, P.O.Box 2002, Phnom Penh, Cambodia*

Received: 22 August 2023; Accepted: 15 May 2024; Available online: August 2024

Abstract: *Khan Prampir Makara is one of the most developed districts in Phnom Penh. Such a growing district does not have a subsoil property map, which could make a preliminary study easier. The 26-borehole soil data was collected from Research and Design Enterprise (RDE) for this study. The purpose of this study is to produce a kriging interpolation map of geotechnical parameters such as N-SPT, natural moisture content, and plasticity index at a depth of 25 m below the surface with an interval of 5 m. For conducting a soil property map, ArcGIS was chosen as the software for producing a geotechnical property map via the Kriging interpolation technique. Based on the results of the spatial distribution map, the value of the N-SPT showed an increase in depth and an increase in the number of blows. At a depth of 0 to 15 m, the soil in Khan Prampir Makara in the east is very soft; from the middle of the district to the west, the soil in this area is medium stiff or hard. From 15 to 25 m in depth, the consistency of the soil in the whole district is very stiff or hard. For the natural moisture content, at depth of 0 to 10 m, the soil in the east of Khan Prampir Makara is very wet. From the middle of the district to the west, the moisture content of the soil is medium. At depths of 10 to 25 m, the moisture content of the soil in the east is medium, while in the west the moisture content of the soil in this area is very dry. For the plasticity index, at depths of 0 to 5 m and 15 to 20 m, almost the whole area in this district demonstrates a soil with medium plasticity. At depths of 5 to 10 m, 10 to 15 m, and 20 to 25 m, it indicates that the soil in the west of the district has low plasticity, while in the east, the plasticity of the soil in this area is high. The validation result shows that the N-SPT map was closed to more than 50 %; the natural moisture content and the plasticity index maps indicate that the accuracy was more than 45 % the same. This kriging interpolation map is useful as a preliminary study in geotechnical and civil engineering design.*

Keywords: Kriging; spatial distribution, geotechnical property map,Phnom Penh.

1. INTRODUCTION

The construction is increasing, and urbanization is expanding the city. The rapid urbanization and development in Phnom Penh have forced the city to spatially expand to encompass surrounding suburban areas [7]. The expansion of the city and the creation of additional districts added further to the population growth [2]. Prampir Makara District is the smallest district in Phnom Penh, Cambodia, as shown in Fig. 1. The district is subdivided into 8 arrondissements and 33 groups. The district has an area of 2.22 squar kilometer. According to the Phnom Penh Municipality, it has a population of 91,895 with a population density of 44,395 people per squar kilometer. Soil properties play a vital role in the field of geotechnical engineering and field of civil engineering. With the help of a proper geodatabase, geotechnical engineering works are done easier [3]. The growth rate of construction increases dramatically these days in this district, yet, there is not subsoil property map for the the preliminary study in the geotechnical engineering sector. Additionally, there is not enough information on the geotechnical engineering property map of subsoil in Khan

* Corresponding author: *Boeut Sophea*
E-mail:boeurtsophea@gmail.com; Tel: +855-81-790-829
Fax: +855-23-880-369

Prampir Makara. As a substitute, a measure of the soil properties of the representative sample at selected locations and then predicting other values in all other locations using the GIS Kriging interpolation tool can save cost and time [1].

Consequently, the study focused on the subsoil properties of Khan Prampir Makara based on some borehole data. In addition, this research work will use geotechnical properties in Khan Prampir Makara to map a spatial distribution map of subsurface soil by layers using ArcGIS via the Kriging Interpolation method. This project consists of 26 boreholes obtained from the RDE laboratory in the period from 2012 to 2019, and we kept three boreholes for validation (Fig. 2).

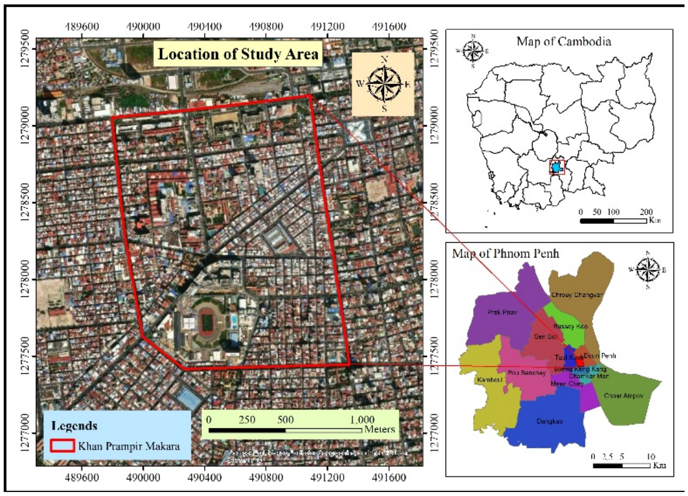

Fig. 1. Location Map of the Study Area

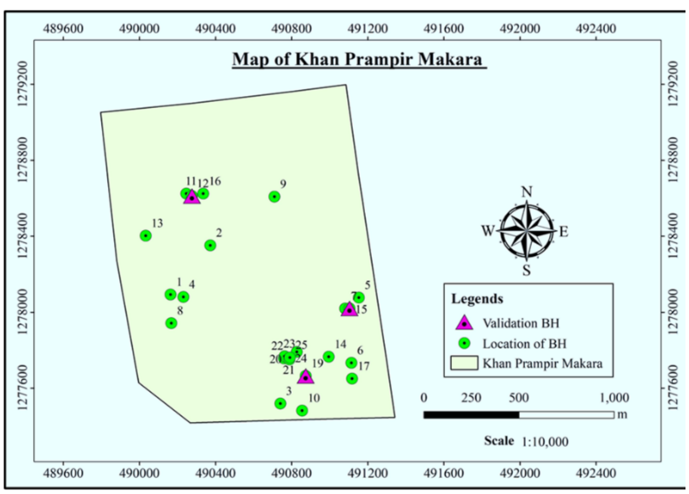

Fig. 2. Studied Boreholes location in Khan Prampir Makara

2. METHODOLOGY

2.1 Interpolation analyst

The interpolation analyst provides a set of tools that allow models that use spatial soil parameters data and point coordinates to be constructed by using ArcMap. The available geotechnical parameter is spatially interpolated using GIS to provide information the whole area. The geospatial interpolation technique is applied to the dataset to interpolate the data for the uninvestigated location. On the other hand, the geostatistical method such as the kriging method and its variant is very effective across a wide area for interpolating spatial information. Among the various available geospatial techniques, this approach employs the kriging method of geostatistical analysis. The kriging technique incorporates the effect of both the distance and direction or degree of variation. The fundamental equation for expressing the kriging method of spatial interpolation is given [4]. It assume that:

$$Z^{*} = \sum_{i=1}^{n} z_i \lambda_i \qquad \text{(Eq.1)}$$

Where:
Z^* = the estimated value at the unsampled location
z_i = the value of know data
λ_i = the kriging weight

2.2 Ordinary kriging

The Ordinary Kriging method is used to estimate the value of the unsampled locations by incorporating the spatial variability into the random variable. Ordinary Kriging is a type of Kriging which is most widely when the first and second order moments are constant values, satisfying the second order stationarity [5]. Ordinary kriging assumes the model:

$$Z(s) = \mu + \varepsilon(s) \qquad \text{(Eq.2)}$$

Where:
μ = an unknown constant
$Z(s)$ = the variable of interest
$\varepsilon(s)$ = autocorrelated errors form
s = indicate the location

2.3. Validation

This procedure is conducted to check the degree of accuracy of kriging interpolation map. Some boreholes was selected for the validation process to compare with the interpolation analysis using the Kriging method on some soil property such as N-SPT, natural moisture content, and plasticity index. The process included:

1. The arragangment of three boreholes for validation on N-SPT, natural moisture content, and plasticity index (Fig. 2).

2. Import all boreholes into the spatial distribution map of soil property, notify validation borehole (three boreholes), and then capture the value based on the range in each soil property map of an exact point of each validated borehole.
3. Tabulate the value obtained from maps, then put on a new sheet and compare it with the actual value from the bore log based on each depth.
4. Giving the score to boreholes based on how many values are in the range of each borehole (i.e., 2/5, 3/5) because we consist of five depths. Then calculate the percentage correct through each depth and find the overall percentage that is corrected for the N-SPT map, the natural moisture content map and the plasticity index map.

3. RESULTS AND DISCUSSION

Fig. 3 shows the distribution of N-SPT over the study area. The color variation shown in the map denotes the result of each layers; each color indicates a range of N-SPT values (blows). There are five classes of color ranges, such as red, orange, light green, sky blue, and blue (Table 1). Fig. 3(a) and (b) show the consistency of N-SPT at depths of 0 to 5 m and 5 to 10 m, respectively. From the north part of the Prampir Makra district to the middle, soil in this area is very soft, which shows that the number of blows is less than 10 blows in the red color. In the middle of the district, the soil consistancy in this area is still weak, which indicates by the orange color of the number of blows, ranging from 10 to 15 blows. And the west and northwest of the district soil in Khan Prampir Makara changed from weak to medium consistancy, which is in intervals of 15 to 30 blows. Fig. 3(c) demonstrates soil in Khan Prampir Makara at a depth of 10 to 15 m. In the south-east of this district, the consistency of soil is very soft, highlighted in orange ranging from 10 to 15 blows. In the middle of the district, the consistency of the soil is high, in the range of 30 to 50 blows. Directly, from the middle of the district to the west, most soil consistancy in Prampir Makara is in the medium range of 15 to 30 blows, which indicates a light green color. Fig. 3(d) shows the N-SPT at depth of 15 to 20 m, indicating that soil consistancy in the north of the district is very hard or dense. Numberically, the number of blows is greater than 50. In the middle district to the south, soil in Khan Prampir Makara changes from high to medium, which decreases the number of blows, ranging from 30 to 50 blows highlighted in sky blue and 15 to 30 blows highlighted in light green. Fig. 3(e) shows the N-SPT at depths of 20 to 25 m. The north of the district soil consistancy in this area is very high, which is greater than 50 blows, highlighted in blue, and from the north to the middle of the district, mostly in the rest, is still high ranging from 30 to 50 blows. Lastly, in the west-south, soil consistency in this area is in the medium range of 15 to 30 blows, which is highlighted in light green.

According to the result, the value of N-SPT showed an increase in depth and an increase in the number of blows.

Table 1. Classes of N-SPT value with colors

Color Classes	N-SPT (blows)
Red	< 10
Orange	10 - 20
Light green	20 - 30
Sky blue	30 - 50
Blue	>50

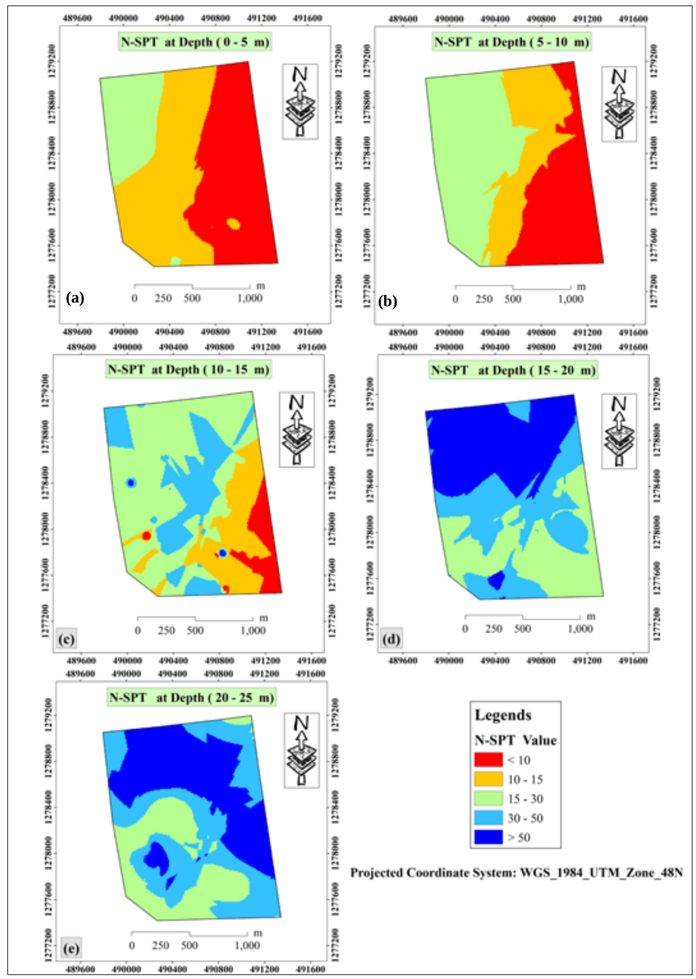

Fig. 3. Spatial distribution map of the N-SPT of (a) 0 to 5 m; (b) 5 to 10 m; (c) 10 to 15 m; (d) 15 to 20m; and (e) 20 to 25 m

For the natural moisture content, it divides into five classes, which vary in colors such as green, blue, purple, orange, and brown (Table 2). Fig. 4(a) shows the distribution of the natural moisture content in the study area of Khan Prampir Makara. The color variation denotes a range percent of natural moisture content; 1st layer depth from 0 to 5 m; the blue color indicates a low moisture content, which is known as a dry condition range about 15% to 20%; the pink color range from 20% to 25%, which shows moderate moisture content between wet and dry conditions; the yellow color consists of a range of 25% to 30%, which is a high moisture content in wet conditions; and the brown color is the same in wet condition, with a high moisture content consists of a range more than 30%. Fig. 4(b), color variation denotes the result of moisture content in the 2nd layer depth from 5 to 10 m; as observed, it is similar to the 1st layer. The blue color indicates a low moisture content range of 15% to 20%; the pink color ranges from 20% to 25%, which is moderate moisture content between wet and dry conditions; the yellow color is high moisture content with a percentage range of 25% to 30%; and the brown color in the 2nd layer is more than 30%, which is high moisture content. In Fig. 4(c), the moisture content is starting decrease a little bit from high to low, which is from wet to dry conditions. The distribution colors in the 3rd layer indicate the zone of high and low moisture content; the light green color shows a very low moisture content, which is very dry condition; the percentage is less than 15%; similar to the 1st and 2nd layers, the blue color indicates a low moisture content, which is known as a dry condition ranging from 15% to 20%; the pink color rangeing from 20% to 25%, which shows a moderate moisture content between wet and dry conditions; the yellow color consists of a range of 25% to 30%, which is high moisture content in wet condition; the brown color is the same in wet condition; the high moisture content consists of a range of more than 30%.In Fig. 4(d), the moisture content decreases from high to low, which is from wet to very dry conditions, respectively. There are only two colors in the 4th layer, whose depth is from 15 to 20 m. The light green color shows a very low moisture content, which is a very dry condition; the percentage is less than 15%, which is in the blue color, the same, indicates a low moisture content ranging from 15% to 20%. Fig. 4(e) showed the last layer at the depth from 20 to 25 m; in this depth, some zones are a little bit in wet condition, and mostly this layer is in dry condition. It consists of three colors: the light green color is very low in moisture content and exists in a range of less than 15%; the blue color and the pink color indicate a low level of moisture content, which is in the dry condition range; and the pink color shows a moderate level of moisture content, which is between wet and dry conditions and ranges from 15% to 20% and 20% to 25%, respectively.

Table 2. Classes of natural moisture content value

Color classes	W (%)	Condition
Green	<15	Very dry
Blue	15 - 20	Dry
Purple	20 - 25	Moderate
Orange	25 - 30	Wet
Brown	>30	Very wet

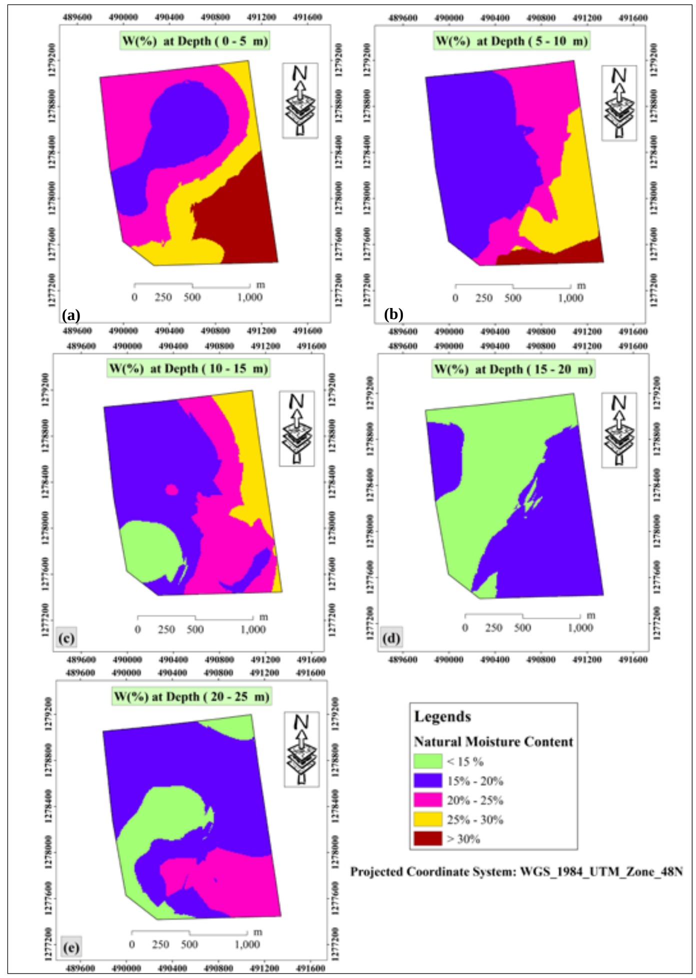

Fig. 4. Spatial distribution map of the natural moisture content of (a) 0 to 5 m; (b) 5 to 10 m; (c) 10 to 15 m; (d) 15 to 20 m; and (e) 20 to 25 m

For the plasticity index, the colors classes is divided into three colors such as, red, yellow, and green. Fig. 5(a) shows the distribution of the plasticity index over the study area. The various color ranges indicate the amount of plasticity index present in Khan Prampir Makara. Based on the range of the plasticity index [6], the 1st layer, depth from 0 to 5 m, the yellow color shows ranges of PI from 7 to 17, indicates medium plasticity and cohesiveness; the green color indicates a value of PI greater than 17, which shows a high plasticity and cohesiveness in the soil. In Fig. 5(b), it is the 2nd layer, which has a depth of 5 to 10 m and consists of three-color classes: the red color, whose range of PI is less than 7, indicates a low level of plasticity and partly cohesive soil, whereas the yellow color consists of a range of PI 7 to 17, which is medium plasticity with cohesive soil, and the green color shows the range of PI is more than 17, which is a high level of plasticity and cohesive soil. In Fig. 5(c), it is the 3rd layer with a depth of 10 to 15 m, and there are two color classes.

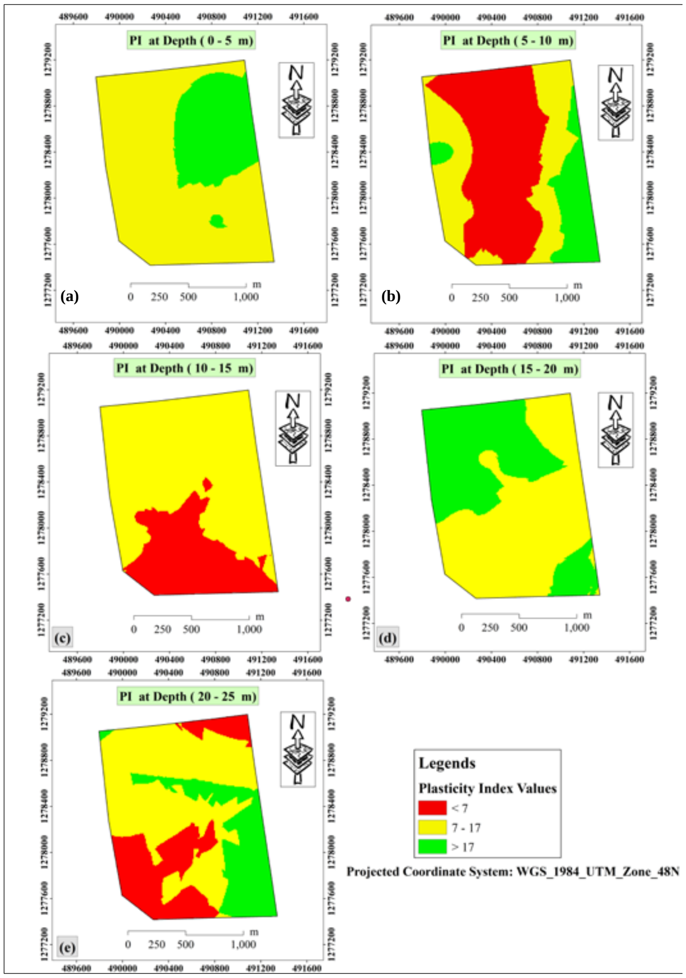

Fig. 5. Spatail distribution map of the plasticity index (a) 0 to 5 m; (b) 5 to 10 m; (c) 10 to 15 m; (d) 15 to 20 m; and (e) 20 to 25 m

The red color shows a low plasticity of the soil; the range of PI value is less than 7, and the yellow color indicates the range of PI value between 7 to 17, which demonstrates a medium plasticity with cohesiveness. In Fig. 5(d), it is the 4th layer; the depth starts from 15 to 20 m; the yellow color ranges between 7 to 17, and the green color consists of a range of PI greater than 17. Basically, it is high plasticity and cohesiveness in the soil in this zone. In Fig. 5(e), depth from 20 to 25 m, the red color ranging less than 7, which indicates a low level of plasticity and partly cohesive soil at the south-west and north-east of Khan Prampir Makara, whereas the yellow color consists of ranges 7 to 17, which shows a medium level of plasticity with cohesiveness of soil, and the green color shows the range of PI is more than 17, which is a high level of plasticity and cohesive soil in the south-east of Khan Prampir Makara.

Table 3. Classes of plasticity index value

Color classes	PI	Plasticity
Red	< 7	Low plastic
yellow	7 - 17	Medium plastic
Green	> 17	High plastic

3.4. Validation of N-SPT map

From the validation result of these three boreholes, the overall percentage of the N-SPT map was closed to more than 50 %; (Table 4).

Table 4. Validation of N-SPT between bore log value and kriging value

BH-ID	Depth (m)	Bore Log (blows)	Kriging (blows)	Score	%
	0 – 5	8*	15 - 30		
	5 – 10	23	15 - 30		
12	10 – 15	30	15 - 30	3/5	60%
	15 – 20	40*	>50		
	20 – 25	67	>50		
	0 – 5	6	<10		
	5 – 10	9	<10		
15	10 – 15	14*	<10	3/5	60%
	15 – 20	37	30 - 50		
	20 – 25	40*	>50		
	0 – 5	6	<10		
	5 – 10	6	< 10		
19	10 – 15	28*	10 - 15	2/5	40%
	15 – 20	58*	15 - 30		
	20 – 25	32*	15 - 30		
Overall					53%

Noted: (*) is not in the range

3.5. Validation of natural moisture content map

From the validation result of these three boreholes, the overall percentage of the natural moisture content map that we can truthfully say was more than 45% (Table 5).

3.6. Validation of plasticity index map

From the validation result of these three boreholes, the overall percentage of the plasticity index map that we can truthfully say was more than 45% (Table 6).

Table 5. Validation of natural moisture content between bore log and kriging value

BH-ID	Depth (m)	Bore Log (%)	Kriging (%)	Score	%
12	0 – 5	17.26	15 - 20	2/5	40%
	5 – 10	14.16*	15 - 20		
	10 – 15	9.51	15 - 20		
	15 – 20	12.18	<15		
	20 – 25	9.40*	15 - 20		
15	0 – 5	30.54	>30	3/5	60%
	5 – 10	28.31	25 - 30		
	10 – 15	17.63*	20 - 25		
	15 – 20	12.34*	15 - 20		
	20 – 25	16.37	15 - 20		
19	0 – 5	27.75*	>30	2/5	40%
	5 – 10	75.30	25 - 30		
	10 – 15	19.48	20 - 25		
	15 – 20	20.53	15 - 20		
	20 – 25	17.95*	20 - 25		
Overall					47%

Table 6. Validation of plasticity index between bore log value and kriging value

BH-ID	Depth (m)	Bore Log	Kriging	Score	%
12	0 – 5	0.95*	7 - 17	2/5	40%
	5 – 10	13.49*	<7		
	10 – 15	12.96	7 - 17		
	15 – 20	16.80*	>17		
	20 – 25	16.63	7 - 17		
15	0 – 5	12.16	7 - 17	4/5	80%
	5 – 10	11.78*	>17		
	10 – 15	11.66	7 - 17		
	15 – 20	13.35	7 - 17		
	20 – 25	17.39	>17		
19	0 – 5	4.82*	7 - 17	1/5	20%
	5 – 10	21.13*	7 - 17		
	10 – 15	24.35	<7		
	15 – 20	11.71	7 - 17		
	20 – 25	5.98*	7 - 17		
Overall					47%

Noted: (*) is not in the range

The measurement of the accuracy of these interpolated map was the validated of the non map generated boreholes. In overall, the accuracy was closed to 50% for most parameters in the maps which consided as the medium degree of accuracy. The degree of accuracy might be comprehend various aspects including the number of input data, human error during the *in-situ* data collection and laboratory experiment as well as the equipment used during the task. In this case, the limitation of borehole data might be the main concern in the accuracy due to unmanageable of borehole point selection. Another component might be the error during laboratory experiment for some parameters or the secondary data interpretation for some parameters, for example, modulus of elasticity as the secondary interpretation in the raw data file and moisture content data as error in the laboratory testing. To the researchers, this primary map results are possibly the baseline for the site investigation especially, the N-SPT value mapping. This would probably providing the estimated depth for the on site drilling.

4. CONCLUSIONS

This research study focuses on the subsoil mapping of geotechnical engineering properties in Khan Prampir Makara. The geotechnical engineering properties of the subsoils present in the Khan Prampir Makara regions were estimated to create a database, and these properties were represented within the N-SPT, natural moisture content and plasticity index maps using Geographic Information Systems (GIS) by interpolation analysts using Kriging techniques. The result obtained from the interpolation analyst consisting of three kriging maps, such as the N-SPT map, the natural moisture content map, and the plasticity index map, varies in depths: 0 to 5 m, 5 to 10 m, 10 to 15 m, 15 to 20 m and 20 to 25 m. Meanwhile, these three-interpolation maps have been validated, and as a result, the N-SPT kriging map, the accuracy was closed to 50%, and the natural moisture content and the plasticity index kriging map's overall validation percentage can be truthful at more than 45 % the same. Geotechnical engineers can run more queries in varied combinations regarding soil properties map, which can help in decision-making process. The geotechnical maps produced give a concept on the soil properties over the specified study area as a preliminary study before construction, and it is also possible to reduce borehole drilling for soil investigation.

ACKNOWLEDGMENTS

The research was funded by JICA under LBE-ITC project funding and the secondary borehole data was obtained from the Research and Design Enterprise (RDE).

REFERENCES

[1] Adam, J., Saleh, S., Olowosulu, A. T., Ashara, A. H., & Srividhya, S. (2018). Mapping of Soil Properties Using Geographical Information System (GIS): A Case Study of Hassan Usman Katsina Polytechnic. Open Journal of Civil Engineering, 2018, 8, 544-554. https://doi.org/10.4236/ojce.2018.84039

[2] JICA. (2014). THE PROJECT FOR COMPREHENSIVE URBAN TRANSPORT PLAN IN PHNOM PENH CAPITAL CITY (PPUTMP).
[3] Jyothi, J., H, M., Jayakrishnan, K., S, S., & S, G. A. (2022). SOIL MAPPING USING GIS. International Research Journal of Engineering and Technology (IRJET), 09(07).
[4] Khan, M. S., Park, J., & Seo, J. (2021). Geotechnical Property Modeling and Construction Safety Zoning Based on GIS and BIM Integration. Appl. Sci. 2021, 11, 4004. https://doi.org/10.3390/app11094004
[5] Miller, J., Franklin, J., & Aspinall, R. (2007). Incorporating spatial dependence in predictive vegetation models. ELSEVIER ScienceDirect. https://doi.org/10.1016/j.ecolmodel.2006.12.012
[6] Prakash, S., & Jain, P. K. (1979). Engineering Soil Testing. Nem Chand & Bros, 1992.
[7] Yin, S., Kikutake, N., Xinyuan, L., Sarah, Caldwell, J., Erik, L., B., Judy, & Ou,Narya, O. (2017). Urban development in Phnom Penh, World Bank Group.

Techno-Science Research Journal 12 (Special Issue) 215-222

Content list available at ITC

Techno-Science Research Journal

Journal Homepage: www.ric.itc.edu.kh

Techno-Science Research Journal

Using Near- Surface Seismic Refraction Tomography and Multichannel Analysis of Surface Waves for Geotechnical Evaluation of Soil Properties Compared with Bore-Hole Data

Rathreaksmey CHAN[1*], Chandoeun Eng[1], Kimhouy Oy[1], Mouy Yi Heng[2], Phanny Yos[1,2], and Sopheap Por[1]

[1]*Faculty of Geo-resources and Geotechnical Engineering, Institute of Technology of Cambodia, Russian Federation Blvd., P.O. Box 86, Phnom Penh, Cambodia*
[2]*Research and Innovation Center, Institute of Technology of Cambodia, Russian Federation Bld, P.O. Box 86, Phnom Penh, Cambodia.*

Received: 22 August 2023; Accepted: 15 May 2024; Available online: August 2024

Abstract: *Characterization of subsurface soil and evaluating its properties are essential components of geotechnical site investigations. This study focues on the implimentation of seismic refraction tomography (SRT) and multichannel analysis of surface waves (MASW) to map soil layers and estimate engineering parameters at factory construction project in Samrong Thom commune, Kien Svay district, Kandal province. Two SRT and MASW lines were acquired with 24-channel seismographs equipped with 4.5 Hz geophones. Each line was set up with a 2 m between geophones, covering a total distance of approximately 48 m. The SRT technique allowed for mapping of subsoil layers through 2D profile of P-wave (Vp). MASW provides a quantitative parameter, specifically the 1D shear wave velocity (Vs), which describes the dynamic properties of soils. The results from both seismic lines revealed the presence of four distinct subsoil layers in the depth range of 0.0 to 20 m. These layers were identified as follows: very soft clay (Vp range: 190 to 490 m/s; Vs range: 100 to 170 m/s), soft clay (Vp range: 500 to 920 m/s; Vs range: 180 to 230 m/s), medium dense silty sand (Vp range: 930 to 1240 m/s; Vs range: 240 to 300 m/s), and medium dense to dense silty sand (Vp range: 1240 to 1450 m/s; Vs range: 310 to 350 m/s). Furthermore, these four soil layers were grouped into two categories: the upper layer consisting of soft and very soft clay, and the lower layer comprising of medium and very dense silty sand. This categorization facilitated the estimation of engineering parameters such as Poisson's ratio, density, stress ratio, concentration index, material index, and density gradient. By utilizing seismic velocities (Vp and Vs), these estimated engineering parameters were employed to assess the stiffness and distribution of subsurface materials, and evaluate the geotechnical engineering characteristics relevant to the construction site. The seismic velocity values, engineering consolidation, and strength parameters indidates the presence of two distinct layers in the field study: the upper layers (very soft and soft clay) and the lower layer (medium dense to very dense silty sand). These findings suggest the presence of weak and sliglhly competent soils based on a low concentration index (ranging from 3.17 to 3.14), high stress ratio (ranging from 0.7 to 0.87), low material index (ranging from -0.72 to -0.86), and high Poisson's ratio (ranging from 0.432 to 0.465).*

Keywords: Geotechnical site investigation, seismic refraction tomography, multichannel analysis of surface waves

1. INTRODUCTION

Over the past decade, construction activities in Cambodia, especially Phnom Penh City have witnessed significant acceleration, with a focus on residential, educational, and institutional, and bridges. High-rise residential buildings, factories, boreys, hotels, commercial buildings, and office buildings have attracted considerable investiments from both foreign investors and local development companies. To ensure quality construction, geotechnical investigations, including standard penetration test (SPT) and various laboratory tests such as Atterberg limits, moisture contents, and quick undrained triaxial tests, are typically conducted to understand the engineering characteristics and bearing capacity of the subsurface geomaterials in construction site. These investigations often involve expensive borehole drilling, which can be time-consuming, and provide limited information, particularly for large study areas. To address these challenges, geophysical approaches, specially seismic methods, offere

* Corresponding author: ENG Chandoeun
E-mail: chandoeun.eng@itc.edu.kh;*Tel: +855-71-990-0760*

indirect means to characterize the subsurface, reduce number of boreholes, lower cost, and enable coverage of larger areas compared to direct surveys.

Geophysics methods, including seismic refraction tomography (SRT) and multichannel analysis of surface waves (MASW), are widely employed in civil engineering as well as the geotechnical studies (soil properties, foundations), environmental assessments (landfills, geohazards), and hydrological investigations. These methods provide non-invasive means of subsurface exploration and data collection, allowing for efficient soil investigations. SRT and MASW are two geophysical techniques commonly ultilized to assess subsurface conditions. These methods are capable of detecting subsurface features over large distances and at greater depths, making them cost-effective and time-saving. By observing physical phenomena such as seismic reflection, seismic refraction, electrical resistivity, magnetic properties, and gravity, geophysics methods aim to interpret subsurface characteristics. SRT and MASW, in particular, have emerged as valuable tools in the past few decades for solving engineering problems, offering more affordable alternatives to other geophysical methods while providing broader horizontal coverage. These techniques enable volumetric measurements and the creation of 1D and 2D images of the underground. Previous studies have successfully applied SRT and MASW for geotechnical site investigations. For example, Shahandashti et al. (2021) employed SRT for shallow subsurface investigations, Mohammed et al. (2020) deployed shallow seismic refraction and MASW for soil characterization for foundation, Al-Saigh et al. (2014) and Sarkar et al. (2021) applied SRT and MASW for geotechnical site investigation, Anbazhangan & Sitharam (2006) used MASW to map subsoil layers and evaluate their properties, Vanli et al. (2020) mapped landslide area using shallow seismic methods, and Yordkayhun et al. (2014) deployed seismic refraction and MASW to estimate SPT-N values.

In this field study, we apply SRT and MASW for geotechnical site investigation in a factory building project located in Kandal Province, Cambodia (Figure 1). The SRT method allows for the mapping of subsoil layers through 2D profiles of P-wave velocity (Vp), while MASW provides a quantitative parameter, namely the 1D shear wave velocity (Vs), which characterizes the dynamic properties of soils. Additionally, the geophysical data obtained in this study is utilized to estimate geotechnical engineering parameters relevant to the construction project. By employing geophysical and seismic methods, we aim to characterize the subsurface indirectly, reducing the need for extensive borehole drilling while maintaining cost-effectiveness and enabling coverage of larger study areas.

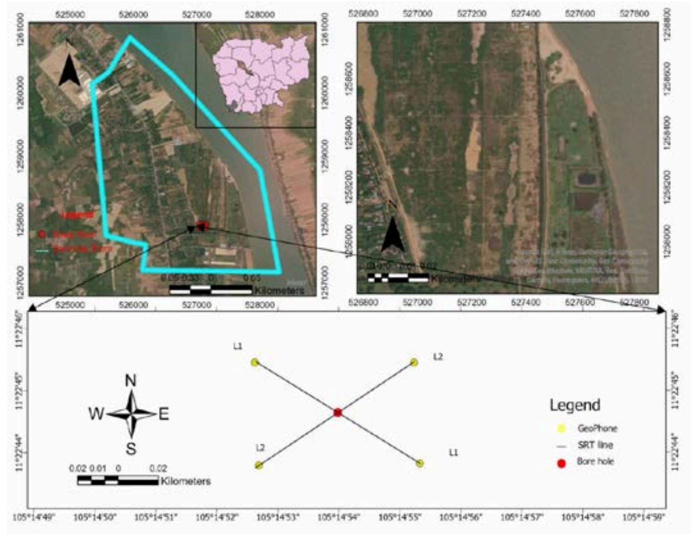

Figure 1: The location of study area. Two black lines indicates seismic laines, which cross cut the borehole (red circle).

2. MATERIALS AND METHODS

A geophysical survey, incorporating seismic refraction tomography (SRT) and multichannel analysis of surface waves (MASW), was conducted to investigate the subsurface soil characteristics and identify potential geotechnical challenges for the factory construction project in Kandal province.

2.1. Seismic Refraction Tomography (SRT)

Seismic refraction tomography (SRT) is a geophysical method used to interpret seismic refraction data. The main purpose is to estimate the P-wave acoustic velocity of near-surface soils. The basic principle of SRT involves measuring the travel times of seismic waves that are refracted at the interfaces between the subsurface layers of different velocities. Seismic energy generated at the surface radiates outward in all directions. Some waves may travel directly through the upper layer (direct arrivals), while others may travel down to and along higher velovity layers before reflecting back up (refracted arrivals) (Kesarwani et al., 2012). SRT indicates that the subsurface can be considered as continuous media, where the first break recorded do not strictly depend on materials or refractors with a high contrast of velocitites (Rucker, 2000; Imani et al., 2021). SRT is well-suited for characterizing areas with strong gradients in lateral velocities. It can also be applied in high precipitation zones to provide the subsoil images based on seismic velocity increasing at greater depths. The seismic data is recorded on a seismograph and travel-time versus distances curves and then drawn. These curves are used to calculate velocities of the overburden and refractor layers (Rucker, 2000; Imani et al., 2021). The refraction tomography method uses a gridded, inversion technique to determine the velocity of individual 2D blocks (pixels) within a profile, rather than modeling velocity as distinct layers. This can allow refraction tomography to more accurately model and provide better resolution of complex subsurface velocity structures compared to traditional approaches (Redpath 1973; Al-Heety and Shanshai, 2016).

2.2. Multichannel Analysis of Surface Waves (MASW)

Multichannel analysis of sureface waves (MASW) is one of the most important surface wave methods and first introduced by Park et al. (1999). It is a technique for estimating the share-wave velocity (Vs) profile of subsurface layers by analyzing the dispersive properties of Rayleigh waves. In the active MASW method, surface waves (ground roll) can be readily generated using a swept vibration source or an impact source like a sledgehammer. The maximum depth of penetration is determined by the longest wavelength of the generated surface waves, which depends on the power of the source. Shear wave velocity is related to the stiffness of the medium the waves travel through. As the result, MASW method has become a popular and widely used tool for determining variations in ground stiffness with depth, as well as estimating the Vs velocities for applications of near-surface geology, environment, and engineering (Ibrahim, 2014).

2.3. Data Acquisition

SRT and MASW profiles were conducted for the study area to estimate P and S-waves velocities. During data collection the geophones of frequency 4.5 Hz was used for the MASW and SRT survey. In the SRT and MASW surveys, we used 24 geophones for each method. The receivers (geophones) spacing was 2 m and the source offset (source produced by strike plate and sledgehammer) to the first and last geophones offset was 6 m. Seismograph model DAQLink 4 was used to obtain the raw data from the field survey. Two lines were surveyed for SRT and MASW methods. Seismic lines were laid out in a way to intersect the borehole (Figure 1 and 2). Each line extends for a total length of 52 m.

A sledgehammer (8 Kg) striking a metal strike was used to generate the seismic waves. A total of 10 stacks were made per geophone shot point, which enhanced the signal-to-noise ratio. Moreover, the study area is located far from any noise source such as traffic, machinery, daily human activities, and other factors which enhanced the seismic resolution.

2.4 Engineering Parameter

No construction material has more variable engineering and physical parameters than the ground's soil. To evaluate the subsurface competence for construction, several shallow soil engineering parameters were calculated, including the Concentration Index *(C_i)*, the Material Index *(V)*, the Density

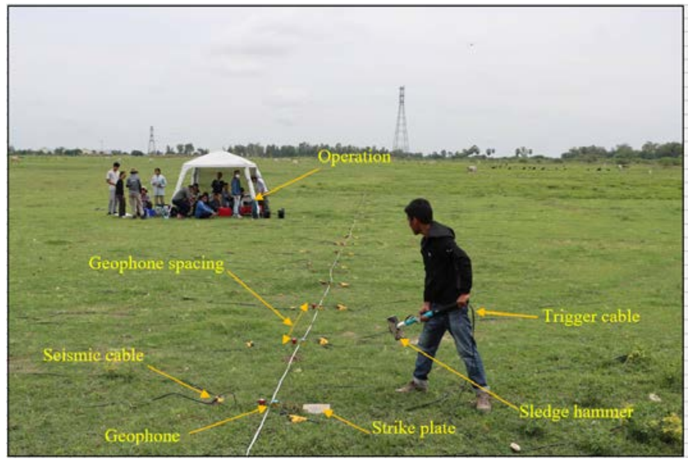

Figure 2: SRT and MASW surveys

Gradient *(D_i)*, and the Stress Ratio *(S_i)*. These four parameters are integrated to select the most appropriate site for construction (Khalil and Hanafy, 2008).

The values of P-wave velocity *(Vp)*, S-wave velocity *(Vs)*, density *(ρ)*, Poisson's Ratio *(σ)*, were required to calculate these parameters. Both P- and S-wave velocities are obtained from the SRT and MASW profiles, respectively.

2.4.1 Elastic modulus parameter

The dynamic elastic modulus, such as Poisson's ratio *(σ)* , and Density *(ρ)* , of near-surface geological materials are measures of the materials strength of different types of stress loadings (Abudeif et al., 2017) . In this study, we present an account of elastic modulus that is summarized in Table 1 to enable evaluation of the geotechnical competency of the suggested site.

Table 1: List of equations used to calculate geotechnical engineering parameters.

Elastic Modulus	Used equation	Reference
Poisson's Ratio	$\sigma = \frac{1}{2}\left[1 - \frac{1}{\left(\frac{V_p}{V_s}\right)^2 - 1}\right]$	(Rao et al., 2009), (Khalil & Hanafy, 2016)
Density	$\rho = \alpha V_p^{0.25}$	(Ahmed, 2020), (Abudeif et al., 2019)

2.4.2 Poisson ratio

In terms of P and S-wave velocities, Poisson's ratio is calculated by the following:

$$\sigma = \frac{1}{2}\left[1 - \frac{1}{\left(\frac{V_p}{V_s}\right)^2 - 1}\right] \qquad \textbf{Eq. 1}$$

Where: σ: Poisson's ratio
Vp : Primary wave velocity (m/s)
Vs : Shear wave velocity (m/s)

2.4.3 Density

Density can be calculated by the following:

$$\rho = \alpha V_p^{0.25} \qquad \textbf{Eq. 2}$$

Where:
σ: Density (g/cm^3)
α: is a constant equal to 0.31 when the density is given in g/cm^3
Vp : P- wave velocity (m/s)

2.4.4 Geotechnical engineering parameter

The computation of engineering parameters for subsurface material in a construction site is very important before foundation design. The geotechnical parameters are calculated using shallow geophysical methods to give a better understanding of the engineering condition of the subsurface in the study area. The following sections list the equations used to calculate each of the geotechnical parameters that are summarized in Table 2**.**

Table 2: List of equations used to calculate geotechnical engineering parameters.

Geotechnical Engineering Parameter	Used Formula	Reference
Stress Ratio	$S_i = 1 - 2\left(\frac{V_s^2}{V_p^2}\right)$	(Al-Saigh & Al-Heety, 2013), (Khalil & Hanafy, 2008)
Material Index	$V = \frac{3 - \left(\frac{V_p}{V_s}\right)^2}{\left(\frac{V_p}{V_s}\right)^2 - 1} = 1 - 4\sigma$	(Al-Saigh & Al-Heety, 2013), (Khalil & Hanafy, 2008)
Concentration index	$C_i = \frac{3 - 4\left(\frac{V_s^2}{V_p^2}\right)}{1 - 2\left(\frac{V_s^2}{V_p^2}\right)}$	(Al-Saigh & Al-Heety, 2013), (Khalil & Hanafy, 2008)
Density Gradient	$D_i = \left(\frac{3}{V_p^2}\right) - \left(\frac{1-\sigma}{1+\sigma}\right)$	(Al-Saigh & Al-Heety, 2013), (Khalil & Hanafy, 2008)

2.4.5 Stress ratio

Stress ratio generally forms under high fluid pressure and will have low differential pressure and therefore abnormally low seismic velocities. The propagation velocity of seismic waves is proportional to the differential pressure between sedimentary overburden and the pore-filling fluids. During excess pressure caused by a stress change, a consolidation settlement occurs. By the end of the consolidation process, the excess pressure is nearly zero and the stress change will have gone from a total stress to an effective stress state (Bowles, 1997).

The stress ratio can be calculated by using P and S-wave velocity as follow:

$$S_i = 1 - 2\left(\frac{V_s^2}{V_p^2}\right) \qquad \textbf{Eq. 3}$$

Where: S_i: Stress ratio
V_p: Primary wave velocity (m/s)
V_s: Shear wave velocity (m/s)

The following remarks are noted:

- S_i tends to be higher for finer soils than coarser ones
- S_i will be larger for loose cohesionless soils
- S_i tends to decrease with an increase in overburden pressure
- S_i will be larger when the soil is over-consolidated.

2.4.6 Material index

The material index defines the material quality for foundation purposes. It is an indicator of the degree of competence of a material and is based on the elastic modulus (Table 3). It is influenced by the material composition, degree of consolidation, fracturing, jointing, and presence or absence of fluid in pore spaces, thus, affecting the wave velocity. The material index is given by:

$$V = \frac{3 - \left(\frac{V_p}{V_s}\right)^2}{\left(\frac{V_p}{V_s}\right)^2 - 1} = 1 - 4\sigma \qquad \textbf{Eq. 4}$$

Where: V: Material index
σ: Poisson's ratio

Table 3: Soil description according to Poisson's ratio and Material index based on (Abudeif A. M.-H., 2019; Ahmed, 2020; Khalil, 2008).

Soil description parameter	Incompetent to slightly competent	Fairly to Moderately competent	Competent materials	Very competent materials
Poisson's Ratio	0.41-0.49	0.35-0.27	0.25-0.16	0.12-0.03
Material Index	(-0.5) -(-1)	(-0.5) -(0.0)	0.0-0.5	>0.5

2.4.7 Concentration index

The Concentration Index is an engineering parameter indicating the degree of material concentration or impaction (competence) for foundation and other civil engineering purposes (Table 4). The main factors that control the concentration index are the elastic modulus of the materials and the depth-pressure distribution (Bowles, 1997).

The concentration index can be defined in terms of P- and S-wave velocities as follow:

$$C_i = \frac{3 - 4\left(\frac{V_s^2}{V_p^2}\right)}{1 - 2\left(\frac{V_s^2}{V_p^2}\right)} \qquad \textbf{Eq. 5}$$

Where: C_i: Concentration index
Vp: Primary wave velocity (m/s)
Vs: Shear wave velocity (m/s)

2.4.8 Density gradient

The density gradient can be found as follow:

$$D_i = \left(\frac{3}{V_p^2}\right) - \left(\frac{1-\sigma}{1+\sigma}\right) \qquad \textbf{Eq. 6}$$

Where: D_i: Density gradient
σ: Poisson's ratio
Vp: Primary wave velocity

Table 4: Ranges of concentration index and stress ratio correspondent to the soil competent degree based on (Abudeif A. M.-H., 2019; Khalil, 2008; Ahmed, 2020).

Soil description parameter	Weak		Fair		Good
	Incompetent		Fairly competent		Competent
	Very soft	Soft	Fairly competent	Moderate competent	Competent
Concentration Index	3.5-4.0	4.0-4.5	4.5-5.0	5.0-5.5	5.5-6.0
Stress Ratio	0.7-0.61	0.61-0.52	0.52-0.43	0.43-0.34	0.34-0.25

3. RESULTS AND DISCUSSION

The seismic refraction tomography (SRT) and multichannel analysis of surface waves (MASW) were carried out with two lines, SE -NW and NE -SW directions, which cross cut the borehole (Figure 1). The soil layers and soil properties were captured with 2D SRT profiling and 1D MASW (Figure 3 and 4). The seismic velocities (Vp and Vs) were used to estimate the engineering parameters and characterize the soil stiffness.

3.1 Characterization of Soil Layers

Seismic P -wave velocity of seismic refraction tomography for two profiles was produced as 2D velocity -depth profiles, indicating the subsurface geology with seismic wave propagation to a depth of up to 20 m, a horizontal extension of 60 m and offset of 12 m. The seismic velocity (Vp; Line 1 and 2) showed that the subsurface of the study area was divided into four layers, such as (1) very soft clay, (2) stiff soft clay, (3) medium dense silty sand, and (4) medium dense to dense silty sand (Figure 3 and 4).

The interpreted four soil layers from seismic velocities is consistent with soil profile obtained from borehole data (Figure 4). Layer 1, very soft clay, was indicated with P-wave velocity ~100 -490 m/s and a vertical interval from the surface to a

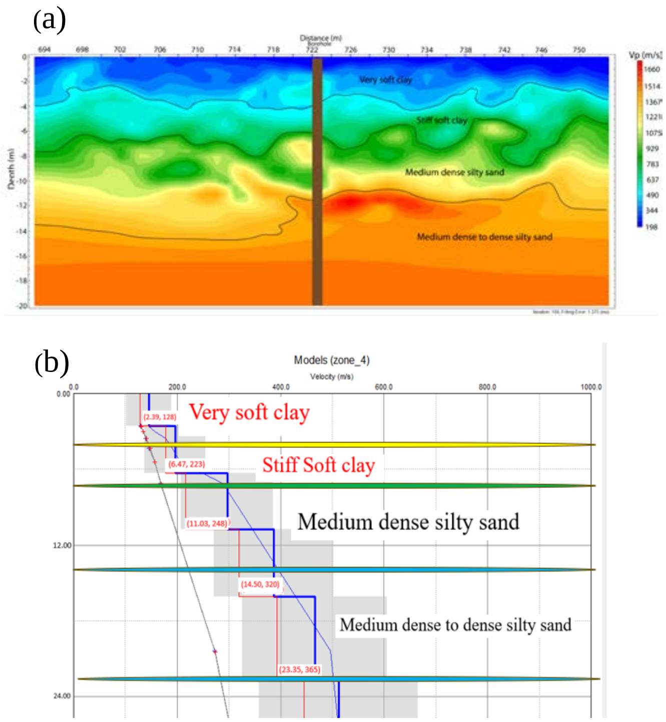

Figure 3: (A) 2D seismic refraction tomography profile of line 1. (B) 1D shear wave velocity-depth profile of Line 1 survey obrained from MASW.

depth of 4.5 m (Figure 3 and 4). This type of soil was also identified from shear wave velocity (Vs) with a velocity range of ~100 -180 m/s (Figure 3b). In this case, the borehole data showed a low N -value ~6 for this very soft clay (Figure 4) . Layer 2, stiff soft clay, was indicated based on the P-wave velocity range ~500 -920 m/s and shear wave velocity ~185 - 230 m/s. This layer appeared with vertical interval from 4.5 - 7.5 m depth on the profile of Line 1. In addition, the borehole data showed an N -value 10- 19 for this stiff soft clay (Figure 4). Layer 3, medium dense silty sand, showed with the P-wave velocity range of 920- 1240 m/s and shear wave velocity range of 240-300 m/s. This high seismic velocity is due the soil being more compacted with depth. The thickness of this soil layer is about 7.5-13.5 m. The borehole data showed an N -value 15-32 for medium dense silty sand (Figure 4). Layer 4, medium dense to dense silty sand, was indicated with a seismic velocity range of ~1240 -1450 m/s for P-wave velocity, while the shear wave velocity ranged ~310-350 m/s. This layer was observed from the interval thickness between 13 -20 m. The borehole data showed an N -value ~36 for medium dense to dense silty sand (Momoh, 2020; Figure 4).

3.2 Elastic and Geotechnical Parameter Estimation from Seismic Velocity

Table 6: Borehole No. 2 (BH-02)

Test Number	Depth (m)		Thickness (m)	Unified Soil Classification System (USCS)	SPT's hammer blows
No.	From	To		Unified Soil Classification System(USCS)	N
	m	m	m		
0	0.00	1.50	1.50	Soft to Medium Stiff Lean CLAY (CL), Brown	-
1	1.50	3.00	1.50		6
2	3.00	4.50	1.50	Soft to Medium Stiff Silty CLAY (CL-ML), Grey	3
3	4.50	6.00	1.50		3
4	6.00	7.50	1.50		8
5	7.50	9.00	1.50	Medium Dense Silty SAND (SM), Grey	10
6	9.00	10.50	1.50		19
7	10.50	12.00	1.50		18
8	12.00	13.50	1.50		18
9	13.50	15.00	1.50		15
10	15.00	16.50	1.50		19
11	16.50	18.00	1.50	Medium Dense to Dense Silty SAND (SM), Grey	15
12	18.00	19.50	1.50		25
13	19.50	21.00	1.50		32

Figure 4: Summary of soil properties obtained from standard Penetration Test (SPT).

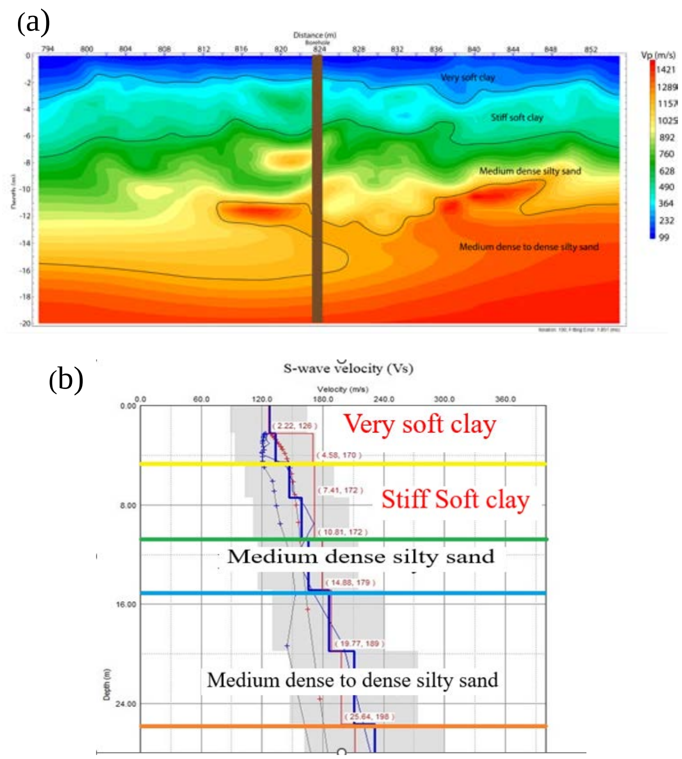

Figure 5: (A) 2D seismic refraction tomography profile of line 2. (B) 1D shear wave velocity-depth profile of Line 2 survey obrained from MASW.

No building materials have higher changeable engineering and ecstatic properties than subsurface soil and they have strong variations in vertical and lateral directions (Mohammed et al., 2020). To check suitability of subsurface materials for construction, parameters such as Poisson's ratio, Density, Concentration index, Stress ratio, Material index, and Density gradient were determined using P- and shear wave velocities. To estimate these parameters, the four soil layers were grouped into two groups (Table 5), such as (1) upper layer (very soft and soft clay) and (2) lower layer (medium and very dense silty sand).

a. Poisson's Ratio *(σ)*

Poisson's Ratio *(σ)* values for the upper (very soft and soft clay) ranged and lower (medium and very dense silty sand) layer ranged from 0.432 to 0.468 is characterized by relative high Poisson's Ratio, which indicates incompetent to slightly competent soil. Weak materials possess higher Poisson's ratio (Table 5).

b. Density *(ρ)*

Density *(ρ)* value for the upper layer (very soft and soft clay) is 1.45 g/cm3 and lower layer (medium and very dense silty sand) is 1.85 g/cm^3 (Table 5).

c. Concentration Index *(C_i)* and Stress Ratio *(S_i)*

The upper (very soft and soft clay) and lower (medium and very dense silty sand) layers was characterized as weak incompetent soil by low Concentration Index *(C_i)* with a range between 3.317 to 3.315 and Stress Ratio *(S_i)* with a range between 0.7 to 0.87 (Table 5).

d. Material Index *(V)*

Rendering to. Calculated Material Index *(V)* values for the upper (very soft and soft clay) and lower (medium and very dense silty sand) layer with a range between with a range between -0.72 to -0.86 indicated to incompetent to slightly competent soil (Table 5).

e. Density Gradient *(D_i)*

The calculated Density Gradient *(D_i)* for the upper (very soft and soft clay) layer is characterized by relative low-Density Gradient where lower (medium dense and very dense silty sand) layer reveals values characterized by relative high-Density Gradient with a range between -0.39 to -0.365 (Table 5).

Table 5: The calculated Engineering parameters of the soil layer.

V_p m/s	V_s m/s	ρ g/cm^3	σ	C_i	S_i	V	D_i
Upper layer							
490	170	1.45	0.432	3.317	0.7	-0.72	-0.39
Lower layer							
1400	357	1.85	0.468	3.315	0.87	-0.86	-0.365

4. CONCLUSION

The investigation the geotechnical site for factory construction at Kandal Province were successfully mapped subsurface information using seismic refraction tomography (SRT) and multichannel analysis of surface waves (MASW). The main findings of this study are:

- From seismic velocities, the soil layers were identified as four layers and grouped into two main groups such as (1) upper layer (layer 1: very soft clay was indicated with P-wave velocity ~100 -490 m/s and S-wave velocity ~ 100-180 m/s, layer 2: stiff soft clay was indicated with P-wave velocity ~500-920 m/s and S-wave velocity ~180-230 m/s), (2) lower layer (layer 3: medium dense silty sand was indicated with P-wave velocity ~925 -1240 m/s and S-wave velocity 240-300 m/s, layer 4: medium dense to dense silty sand was indicated with P-wave velocity ~1240 -1450 m/s and S-wave velocity ~310- 350 m/s).
- The engineering parameters such as Poisson's ratio *(σ)*, Density *(ρ)*, Concentration index (C_i), Stress ratio (S_i), Material index *(V)*, and Density gradient (D_i) were calculated to investigate the stiffness for two main group layers (upper and lower layers). The upper layers (very soft and stiff soft clay) and the lower layer (medium dense to medium dense to dense silty sand) indicated to the weak incompetent soil and incompetent to slightly competent soil according to low Concentration index (3.17 to 3.15), high Stress ratio (0.7 to 0.87), low Material index (-0.647 to -0.897), and high Poisson's ratio (0.432 to 0.468). Moreover, these two main layers was indicated with Density value (1.45 g/cm3 for upper layer to 1.85 g/cm3 for lower layer) and Density gradient value (-0.39 for upper layer to -0.365 for lower layer).

ACKNOWLEDGMENTS

We would like to thank to the projects that was funded by the Cambodia Higher Education Improvement Project (Credit No.

6221-KH). We thank to Advanced Geotechnical Lab & Consultant Co., Ltd (AGLC) for providing the borehole data and facilitating us for field survey.

REFERENCES

Abudeif, A. M. (2017). Abudeif, A. M., Raef, A. E., Abdel Moneim, A. A., Mohammed, M. A., & Farrag, A. F. (2017). Dynamic geotechnical properties evaluation of a candidate nuclear power plant site (NPP): P- and S-waves seismic refraction technique, North Western Coast, Egypt. S.

Abudeif, A. M.-H. (2019). Abudeif, A. M., Fat-Helbary, R. E., Mohammed, M. A., Alkhashab, H. M., & Masoud, M. M. (2019). Geotechnical engineering evaluation of soil utilizing 2D multichannel analysis of surface waves (MASW)technique in New Akhmim city, Sohag, Upper Egypt. Journal .

Ahmed, U. (. (2020). Ahmed, U. (2020). Estimation of near-surface geotechnical parameters using seismic measurements at phase || site, Ahmadu Bello University Zaria, North-western Nigeria Aeromagnetic Investigation of geologic Structures associated with gold mineralization al.

Al-Saigh, N. H., & JaddoaAl-Heety, A. (2014). Seismic refraction tomography and MASW survey for geotechnical evaluation of soil for the teaching hospital project at Mosul University. Journal of Zankoy Sulaimani-Part A (JZS-A), 16(1), 1.

Anbazhagan, P. and Sitharam, T.G., (2006). Evaluation of dynamic properties and ground profiles using MASW: correlation between Vs and N60. In Proceedings of 13th Symposium on Earthquake Engineering, Indian Institute of Technology, Roorkee, December (pp. 18-20).

Awang, H. N. (2016). Awang, H., Nazly, M., & Mohamad, N. (2016). InCIEC 2015. InCIEC 2015.

Bowles, J. E. (1997). Foundation Analysis and Design International Fifth Edition. In Civil Engineering Materials.

Ibrahim, R. K. A. R. (2014). Using Seismic Refraction Method to Investigate The Shallow Geologic Structures at Ayer Hangat Area, Langkawi, Malaysia. August, 14–32. https://doi.org/10.13140/RG.2.1.4834.8000

Imani, P., Abd EL-Raouf, A., & Tian, G. (2021). Landslide investigation using Seismic Refraction Tomography method: a review. Annals of Geophysics, 64(6), SE657-SE657.

Khalil, M. H. (2008). Khalil, M. H., & Hanafy, S. M. (2008). Engineering applications of seismic refraction method: A field example at Wadi Wardan, Northeast Gulf of Suez, Sinai, Egypt. Journal of Applied Geophysics, 65(3–4), 132–141.

Kearey, P. &. (1991). Kearey, P., & Brooks, M. (1991). An introduction to geophysical exploration. 2nd edition. In An introduction to geophysical exploration. 2nd edition.

Kesarwani, A., Sharma, A., & Jain, C. (2012). MASW versus refraction seismic method in terms of acquisition and processing of data and the accuracy of estimation of velocity profiles. In 9th Biennial International Conference & Exposition on Petroleum Geophysics, Hyderabad (Vol. 5).

Khalil, M. H. (2008). Khalil, M. H., & Hanafy, S. M. (2008). Engineering applications of seismic refraction method: A field example at Wadi Wardan, Northeast Gulf of Suez, Sinai, Egypt. Journal of Applied Geophysics, 65(3–4), 132–141. https://doi.org/10.1016/j.jappgeo.2008.06.

Mohammed, M. A.-a. (2020). Mohammed, M. A., Abudeif, A. M., & Abd el-aal, A. K. (2020). Engineering geotechnical evaluation of soil for foundation purposes using shallow seismic refraction and MASW in 15th Mayo, Egypt. Journal of African Earth Sciences, 162(October 2019), 103721. h.

Momoh, K. O. (2020). Estimation of near-surface geotechnical parameters using seismic measurements at phase || site, Ahmadu Bello University Zaria, North-western Nigeria. Global Journal of Earth and Environmental Science,, 5(1), 1-10.

Park, C. B. (2006). Park, C. B., & Miller, R. D. (2006). Roadside passive MASW. 19th Symposium on the Application of Geophysics to Engineering and Environmental Problems, SAGEEP 2006: Geophysical Applications for Environmental and Engineering Hazzards - Advances and Constrai.

Park, C. B., Miller, R. D., & Xia, J. (1999). Multichannel analysis of surface waves. Geophysics, 64(3), 800–808. https://doi.org/10.1190/1.1444590

Rucker, M.L., 2000. Applying the seismic refraction technique to exploration for transportation facilities. Geophysics, 1, pp.1-3.

Sarkar, R., Kolathayar, S., Drukpa, D., Choki, K., Rai, S., Tshering, S. T., & Yuden, K. (2021). Near-surface seismic refraction tomography and MASW for site characterization in Phuentsholing, Bhutan Himalaya. SN Applied Sciences, 3, 1-18.

Shahandashti, M. H. (2021). Advanced Geophysical Tools for Geotechnical Analysis.

Vanlı Senkaya, G., Senkaya, M., Karsli, H., & Güney, R. (2020). Integrated shallow seismic imaging of a settlement located in a historical landslide area. Bulletin of Engineering Geology and the Environment, 79, 1781-1796.

Yordkayhun, S., Sujitapan, C. and Chalermyanont, T., (2014). Joint analysis of shear wave velocity from SH-wave refraction and MASW techniques for SPT-N estimation. Songklanakarin Journal of Science & Technology, 36(3).

Techno-Science Research Journal 12 (Special Issue) 223-229

Content list available at ITC

Techno-Science Research Journal

Journal Homepage: www.ric.itc.edu.kh

Techno-Science Research Journal

Experimental and Numerical Study of Tyfo® FibrAnchors Inserting to Concrete Cylinder Confined by Glass Fiber Reinforcing Polymer

Lymeng Ty [1*], Narith Prok[2] , Sovann Sathya Rath[2], Sovanvichet Lim[2] , Wee Keong Ong[3]

[1]*Maiterial and structural Engineering, Institute of Technology of Cambodia, Russian Federation Blvd., P.O. Box 86, Phnom Penh, Cambodia*

[2] *Research and Innovation Center, Institute of Technology of Cambodia, Russian Federation Blvd., P.O. Box 86, Phnom Penh, Cambodia*

[3]*Assistant General Manager, Fyfe Asia Pte Ltd, 6 Clementi Loop #02-20, Singapore 129814.*

Received: 22 August 2023; Accepted: 15 May 2024; Available online: August 2024

Abstract: *Fiber-reinforced polymer (FRP) materials have a wide range of applications and are widely used in construction, such as strengthening and repairing structures. When the structure was strengthened by FRP, anchors could be applied to delay the debonding of the FRP. The mechanical anchor system is to prevent or postpone debonding, which occurs after externally bonded FRP detaches from the RC substrate due to the low tensile strength of concrete. The importance of using mechanical anchorage systems to enhance the strength of FRP in cases where debonding or insufficient development length is an issue. However, there is not enough research data on anchorage to fully incorporate FRP anchorage systems. The objective of this research is to conduct experimental and numerical simulations. This include optimum embedment depths and diameters for fiber anchors inserting into concrete specimens confined by Glass fiber-reinforced polymer (GFRP) and formulating an equation for the correlation obtained from test results.The experimental results demonstrated that the mode of failure and pullout resistance of Tyfo® Fibr anchors are significantly influenced by the diameter and embedment depth of the anchors. The pullout capacity increases with the increase in anchor diameter and embedment depth.*

Keywords: FRP **,** GFRP, Anchor, Debonding, Pullout, Strengthening.

1. Introduction

Fiber-reinforced polymers (FRP) are materials composed of a combination of a polymer matrix and reinforcing fibers. FRP materials have a wide range of applications and are widely used in construction, such as to strengthening and repairing structures. When the structure was strengthened by FRP, anchors could be applied to delay the debonding of FRP. The primary function of anchor systems is to prevent or postpone debonding, which occurs after externally bonded FRP detaches from the RC substrate due to the low tensile strength of concrete. Anchors systems are also used to provide a load transfer mechanism at critical locations of structural members or, in some cases, provide a ductile failure mode for the structural member instead of the typical sudden, brittle failure modes of FRP debonding and rupture.

A major problem with FRP strengthening is debonding failure, which occurs when the FRP is no longer adhered to the member due to a crack or separation of the fiber matrix and bond interface resulting from increased strain in the strip. An anchor system that can delay debonding failure is therefore of the utmost importance in order to improve the efficiency, reliability, and safety of FRP strengthening. Anchors made from FRP, known as FRP anchors, are an attractive form of anchorage as they are non-corrosive and can be applied to a wide variety of structural elements. The *ACI Committee 440* [1] mentioned the importance of using mechanical anchorage systems to enhance the strength of FRP in cases where debonding or insufficient development length is an issue. There is not enough research data on anchorage to fully incorporate FRP anchorage systems[2]. However, there are some research

[*] Corresponding author: TY Lymeng
E-mail: ty_lymeng@itc.edu.kh; Tel: +855-88-819-5455;

papers have been conducted on FRP anchor such as Kim and Smith [3][4][5], Eligehausen et al. [6][7], and Ozbakkaloglu et al. [8].

The purpose of this research is to provide experimental data to quantify the efficiency of the FRP anchors, and to study the effect of key parameters on failure modes and pullout capacity of FRP anchors. In addition, equations for predicting pullout resistance of Tyfo® Fibr anchor and corresponding mode of failure are also established which can be used in design. A numerical model is also developed to fully understand the mechanism of the embedded fiber anchor under pullout test and also to compare with the test results.

2. Experimental Method

A total of 74 specimens of Tyfo® Fibr anchors made from glass fiber were used in this experiment to understand the failure mechanism and the ultimate failure load. These FRP anchors were embedded in concrete cylinders of 150 mm diameter and 300mm height with the compressive strength 30 MPa. The diameter of FRP anchor was 10 mm, 12 mm, 15 mm, 20 mm, and 25 mm with embedment depth of 100 mm, 150 mm, 200 mm, and 250 mm. The summary of number of specimens for each case is shown in Table 2.1.

Table 2.1 Summary of Test Specimens

Embedment depth (mm)	Anchors's diameter (mm)				
	10	12	15	20	25
50	—	—	—	—	—
100	4	4	4	—	—
150	4	4	4	4	—
200	4	4	4	4	4
250	4	4	4	4	4

2.1 Specimen

The detail of specimen is represented in Fig 2.1. The concrete cylinder was wrapped with GFRP to prevent the splitting of concrete specimen which enable the embedded FRP anchor to fully reach their ultimate capacity. Each anchor varies in diameter and embedment depth while having the same free length of 200 mm.

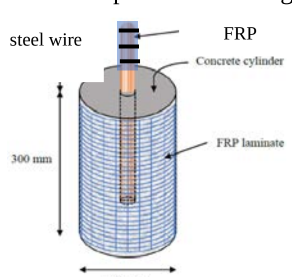

Figure 2.1 Specimen Details

2.2 Material and Property

2.2.1 Tyfo® Fibr Anchor

Anchors used in the experiment were provided by Fyfe Asia Pte Ltd. They are called Tyfo® SEH Composite Anchors, which are made of uni-directional reinforcing glass fiber bundles combined with Tyfo® S Epoxy. Tyfo® SEH Composite Anchors is presented in Fig.2.2. Typical mechanical properties of the Tyfo® SEH Anchors are shown as well in Table 2.2.

Figure 2.2 Tyfo® SEH Composite Anchors

Table 2.2 Properties of Tyfo® SEH Composite Anchors

	Tensile Strength (MPa)	Tensile Modulus (GPa)	Ultimate Elongation (%)
Dry fiber	3240	72.4	4.5
Composite anchor			
Test value	575	26.1	2.2
Design value	460	20.9	1.76

2.2.2 Tyfo® Epoxy

Tyfo® S Epoxy, provided by Fyfe Asia Pte Ltd., was used in the experiment. Typical properties of epoxy specified by the manufacturer are presented in Table 2.3. The Tyfo® S Epoxy is a low viscosity, high strength, two-component epoxy matrix that is usually used in practice as a chemical adhesive for bonding applications.

Table 2.3 Properties of Tyfo® S Epoxy Tested at Temperature 21°C

Tensile Strength	72.4MPa
Tensile Modulus	3.18GPa
Elongation Percent	5.00%
Compressive Strength	86.2MPa
Compressive Modulus	3.2GPa
Flexural Strength	123.4MPa
Flexural Modulus	3.12GPa

2.2.3 FRP Laminate

Laminate used in the experiment is Tyfo® SEH-25A Composite which is comprised of Tyfo® S Epoxy and Tyfo® SEH-25A reinforcing fabric. The typical properties of the laminate are presented in Table 2.4.

Figure 2.3 Tyfo® SEH-25A Reinforcing Fabric

Table 2.4 Properties of Composite Laminate Glass Fiber

Property composite laminate	**Test Value**	**Design Value**
Tensile Strength in primary fiber direction	521MPa	417MPa
Tensile Modulus	26.1GPa	20.9GPa
Elongation at break	2.00%	1.76%
Tensile Strength in 90° to primary direction	25.8MPa	20.7MPa
Laminate Thickness	0.50mm	0.50mm

2.3 Installation of Anchor

A hole with corresponding diameter as FRP anchor to be installed was drilled vertically through the centroid of cylinder sectional area as shown in Fig 2.4. Then these holes were cleaned with the compressed air to ensure that there was no dust nor debris before anchor installation can be started. A dried and cleaned hole ensures a tight bonding between concrete surface and anchor by the means of epoxy. After anchor installation, the specimen was cured for 1 day before wrapping the FRP laminate over the top part of anchor with steel wire as its improvement as.

Figure 2.4 The Drilling Process and Cleaning Hole

Figure 2.5 Installation Process of Anchor

2.4 Test Set Up and Procedure

After the anchors were cured, a pullout test was conducted on the specimens. The specimens were tested using a 400kN capacity universal testing machine as shown in Fig 2.6. Each specimen was held in place between two steel plates, one with a hole of 100mm in diameter where the free end of anchor was inserted into the top wedge grips of the machine and the other one was welded to a steel bolt of large diameter to provide fixity when gripped to the bottom wedge grips of the machine, as illustrated in Fig.2.6.

Figure 2.6 Testing Machine with Tyfo® SEH Anchors

After testing 74 specimens, it was found that the pullout load of each Tyfo® SHE Anchor recorded from the testing machine was based on the maximum load sustained before failure. Fig 2.7 show two fiber achors after testing that failed in different modes of failure.

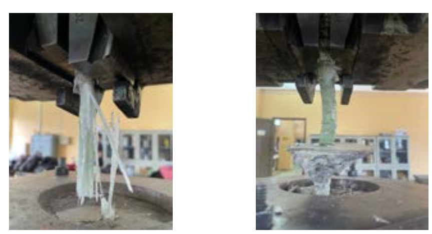

Figure 2.7 Observed Failure Modes

3. Results and Discussion

3.1 Combined Cone-Bond Failure (CB)

The CB failure mode occurred at depth embedment of 50mm with anchor diameter 10mm, 12mm, and 15mm. For anchor diameter 20mm, the CB failure mode occurred for all cases of embedment depths tested, while for anchor diameter 25mm, it occurred at embedment depth 50 mm to 150 mm. By assuming uniform distribution of bond stress along the embedment depth of anchor [7].

$$\tau = \frac{F_u}{\pi d h_{emb}} \qquad \text{Ep.1}$$

where F_u=pullout load; d=diameter of anchor; and h_{emb}=embedment length of anchor.

3.2. Anchor Rupture Failure

Anchor ruptures mode (RF) were observed on specimens of small anchor diameter (10mm, 12mm and 15mm) at embedment depths from 100mm to 250mm. RF failure occurs when the tensile strength of anchor is lower than the bond strength between anchor and concrete. This indicates that the embedment depth of the anchor is sufficient to prevent different concrete failures and the anchor consequently reaches its tensile capacity. The theoretical capacity of an anchor can be calculated using the following equation.

$$F_{FRP} = f_{FRP}\, A_{FRP} \qquad \text{Eq.2}$$

where f_{FRP} = 575 MPa is the design tensile strength of FRP anchor; and $A_{FRP} = \pi d^2/4$ is the sectional area of anchor

3.3 Effect of Anchor Embedment Depth

The pullout load increased with the increase in embedment depth, especially in the case of CB and RF as show in Fig 3.1. This was clearly indicated in the test results of 20mm and 25mm anchor diameters where most of the specimens failed in CB. In addition, for anchor diameter of 10mm,12mm and15mm, rupture starts at embedment depth of 150mm which is why only slight variations in the failure loads was observed at embedment depth deeper. This was perhaps due to the poor alignment of fibers during anchor installation with embedment depth deeper than 150 mm. which led to low tension capacity of anchors. The variation of anchor rupture failure loads of specimens having the same anchor diameter was observed as well in the experiments conducted by Kim and Smith [6] and Ozbakkaloglu and Saatcioglu [8].

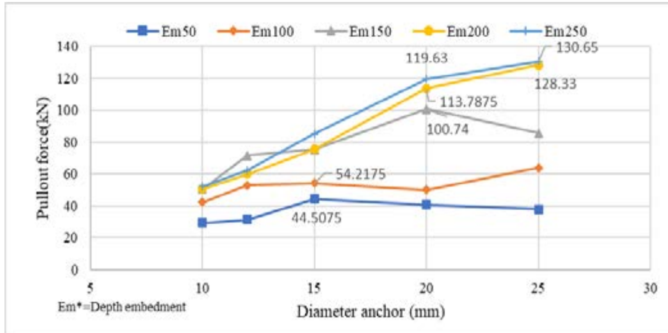

Figure 3.1. Variation of Pullout Load with Anchor Diameter and Embedment Depth

3.4 Pullout Resistance of a Single FRP Anchor Focusing on Predicting Failure Mode

Based on the experimental results, when focusing on predicting failure mode, the model describing the pullout resistance of a single FRP anchor is given as:

$N_u = \min(N_{cb}, N_{rf})$		Eq.3a
$N_{cb}=13.53\pi d h_{emb}$	For d=10mm,12mm and 25mm	Eq.3b
$N_{cb}=8.35\pi d h_{emb}$	For d=20mm and 25mm	Eq.3c
$N_{rf}=1A_{FRP}F_{FRP}$	For d=10mm and 12mm	Eq.3d
$N_{rf}=0.77A_{FRP}F_{FRP}$	For d=15mm	Eq.3e
$N_{rf}=0.69A_{FRP}F_{FRP}$	For d=20mm	Eq.3f
$N_{rf}=0.46A_{FRP}F_{FRP}$	For d=25mm	Eq.3g

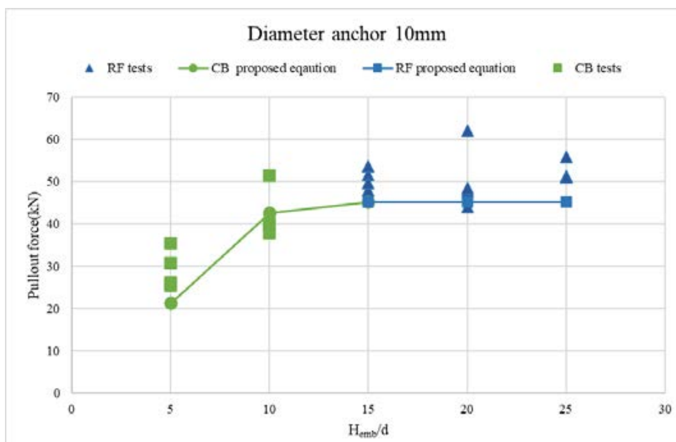

Figure 3.2 Relationship Between Pullout Force and H_{emb}/d (Embedment Depth/Diameter) for Anchor Diameter 10mm

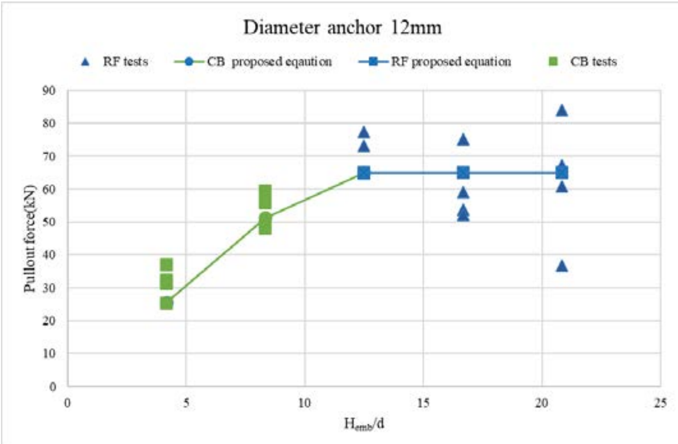

Figure 3.3 Relationship Between Pullout Force and Hemb/d (Embedment Depth/Diameter) for Anchor Diameter 12mm

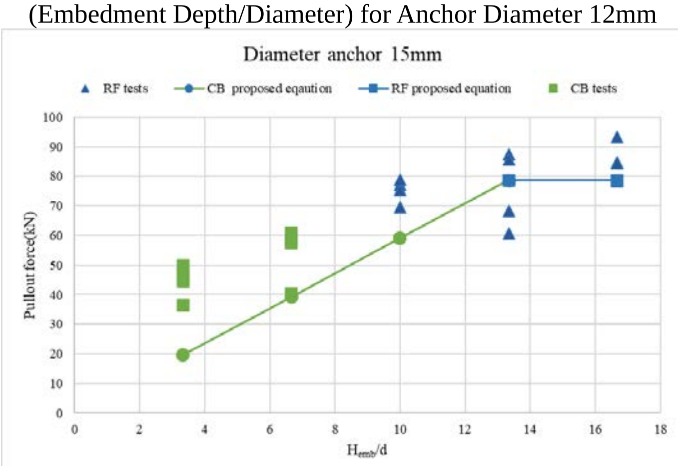

Figure 3.4 Relationship Between Pullout Force and Hemb/d (Embedment depth/Diameter) for Anchor Diameter 15mm

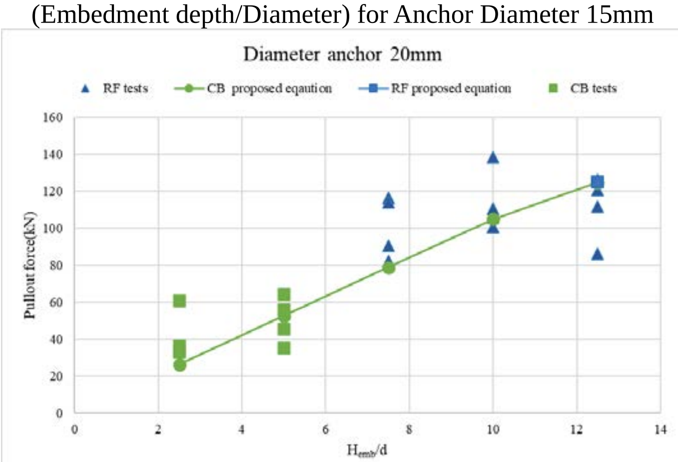

Figure 3.5 Relationship Between Pullout Force and Hemb/d (Embedment Depth/Diameter) for Anchor Diameter 20mm

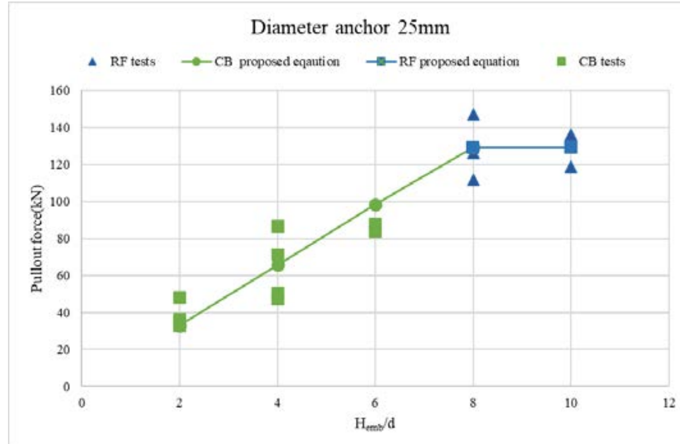

Figure 3.6 Relationship Between Pullout Force and Hemb/d (Embedment Depth/Diameter) for Anchor Diameter 25mm

4. Numerical Simulation

4.1 Modeling

First, a quarter of 3D deformable solid for a concrete cylinder of diameter 75mm. the top surface of the concrete according to the diameter of the anchor, assuming an epoxy thickness of 0.2mm. Then partition the cell according to the sketched surface. Then, a quarter of 3D deformable wire for FRP laminate of radius 75mm. was defined the material to each component (concrete, FRP anchor, epoxy, and FRP laminate) was assigned.

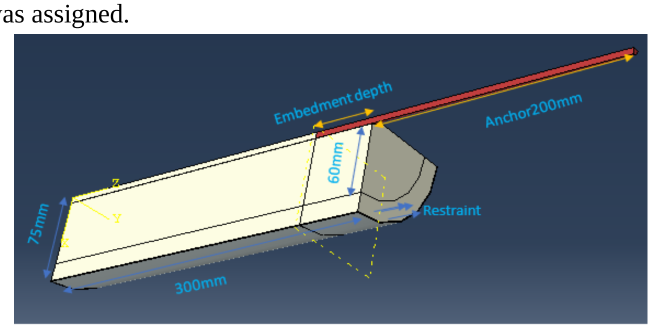

Figure 4.1 Details of the Model

The static general procedure was used in this simulation. A constant stress was applied at the free end of FRP anchor. For load apply displacement 8mm since the anchor failure in strain 0.021 and top of anchor have length 200mm so the displacement anchor and concrete failure around 8mm. The boundary condition was followed as the experimental test.

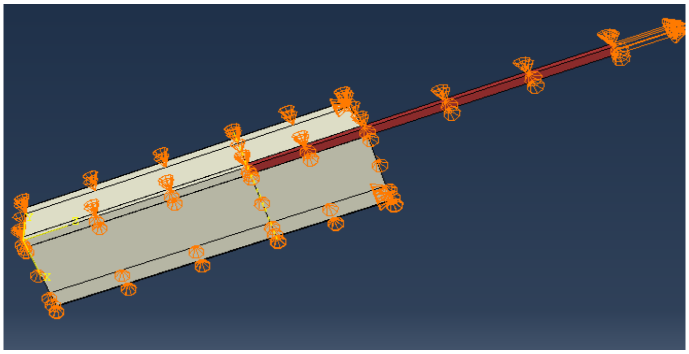

Figure 4.2. Loading and Boundary Condition of the Model

Structured meshing was applied in this modeling. Mesh of each part are shown in Fig4.3. Concrete was assigned the element type of standard stress with element deletion option set to YES. For FRP anchor and epoxy, the assigned element type was standard stress with default setting for element deletion. FRP laminate was assigned the standard element type.

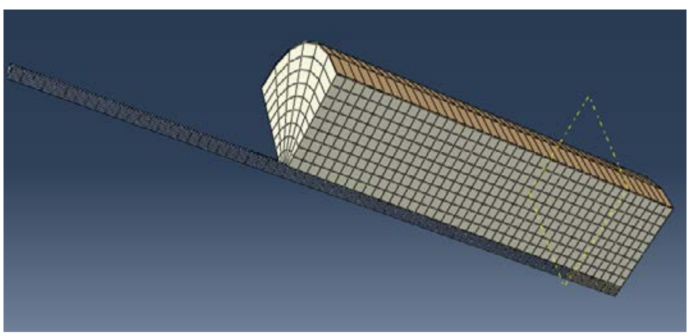

Figure 4.3. Mesh of Concrete, FRP Anchor, Epoxy Layer and FRP Laminate.

4.2 Results of Numerical Simulation

Results of 25 series of specimen of different anchor diameters (10mm, 12mm, 15mm, 20mm and 25mm) and embedment depths (50mm, 100mm, 150mm, 200mm and 250mm) are shown in Fig4.4 to Fig 4.8.The force at failure of anchor were considered when the concrete damage was reached, hence the concrete elements were broken down.

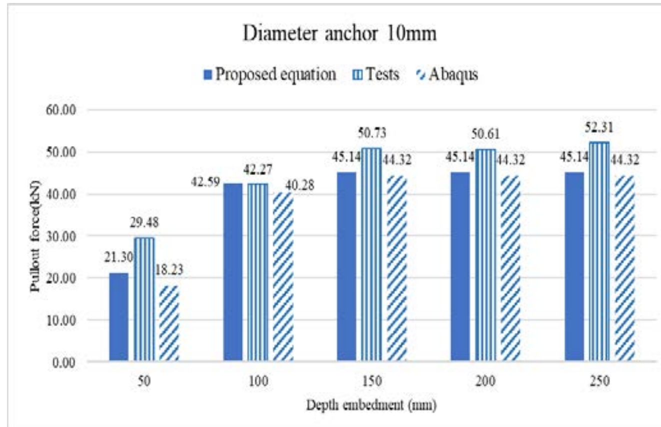

Figure 4.4 Pullout Force Failure and Average Pullout Force From Test Result for Anchor Diameter 10mm

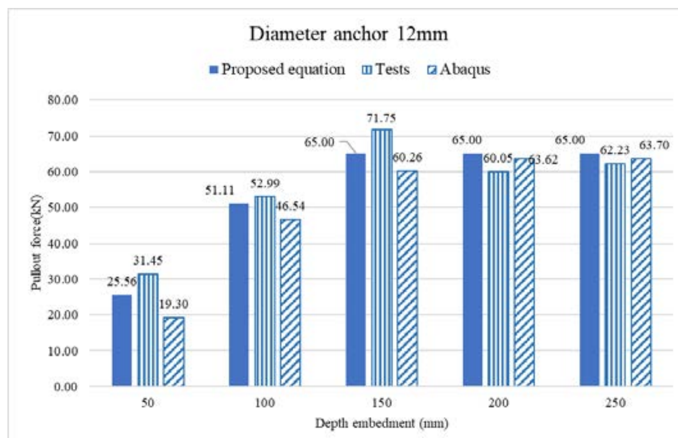

Figure 4.5 Pullout Force Failure and Average Pullout Force from Test Result for Anchor Diameter 12mm

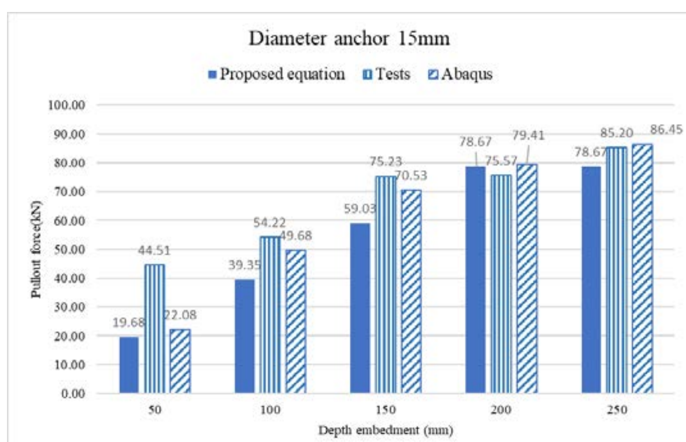

Figure 4.6 Pullout Force Failure and Average Pullout Force from Test Result for Anchor Diameter 15mm

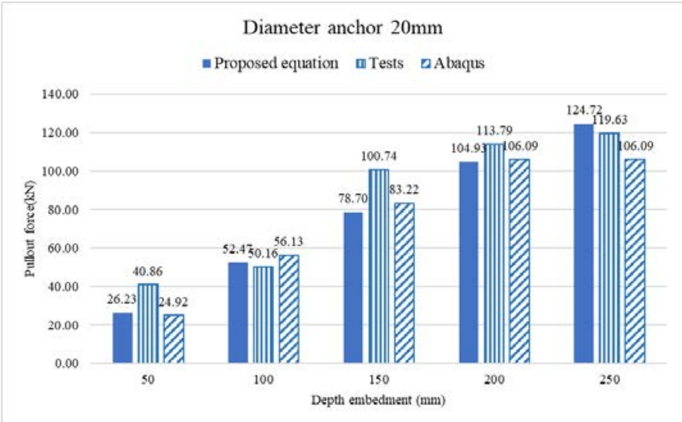

Figure 4.7 Pullout Force Failure and Average Pullout Force From test Result for Anchor Diameter 20mm

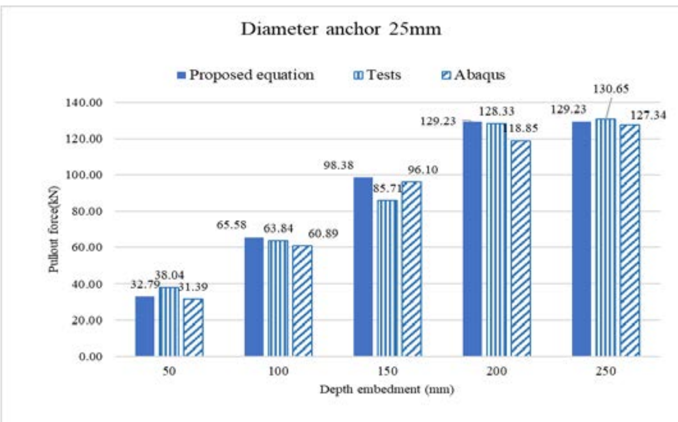

Figure 4.8 Pullout Force Failure and Average Pullout Force From Test Result for Anchor Diameter 25mm

5 Conclusion

According to the results of experimental, analytical, and numerical study in this paper, the following conclusion can be drawn:

- The optimum embedment depth is 150mm for diameter anchors 10mm to 20 mm, but for diameter anchors 25 mm, the optimum embedment depth is 200mm.
- From a depth embedment depth of 150mm, the pullout capacity of the anchor depends on the anchor diameter (10 mm, 12 mm, 15 mm, and 20mm).
- Tyfo® Fibr Anchor pullout strength increases with an increase in embedment depth and is ultimately limited by anchor rupture strength. Therefore, it can be used to delay or prevent debonding failure of externally bonded FRP strengthening system.
- The proposed equation provides the acceptable pullout capacity of Tyfo®FibrAnchors and good anticipation of failure mode compared to experimental result and numerical simulation.

ACKNOWLEDGMENTS

The author express gratitude to the Faculty of Civil Engineering at the Institute of Technology of Cambodia for providing laboratory and technical support. Funding and composite materials provided by the Fyfe Asia Pte Ltd company are gratefully acknowledged.

REFERENCES

[1] ACI 440 2R-17: Guide for the Design and Construction of Externally Bonded FRP Systems for Strengthening Concrete Structures.
[2] Ceroni et al., 2008: Debonding strength and anchorage devices for reinforced concrete elements strengthened with FRP sheets. Pages 429-441
[3] Kim, S.J., Smith, S.T., 2007. Pull-out tests on FRP anchors. International Institute for FRP in Construction for Asia-Pacific Region (APFIS)
[4] Kim, S.J., Smith, S.T., 2009. Behavior of handmade FRP anchors under tensile load in uncracked concrete. Adv. Struct. Eng. 12, pp. 845–865.
[5] Kim, S.J., Smith, S.T., M. ASCE, 2010. Pullout Strength Models for FRP Anchors in Uncracked Concrete. Journal of Composites for Construction, ASCE, pp. 406–2414.
[6] R. Eligehausen, R.A. Cook, J. Appl. (2006). *Behavior and design of adhesive bonded anchors*. ACI Struct. J., 103(6), pp. 822–831.
[7] R. Elighehausen, E.P. Popov, V. Betero. (1983). *Local bond stress-slip relationships of deformed bar under generalized excitations*. Rep. No. UCB/EERC-83/23, Earthquake Engineering, Research Center, Berkeley, Calif.
[8] T. Ozbakkaloglu, M. Saatcioglu. (2009). *Tensile behav-ior of FRP anchors in concrete*. Journal of Composites for Construction, ASCE, Vol. 13, No. 2, pp. 82–92.

Techno-Science Research Journal 12 (Special Issue) 230-237

Content list available at ITC

Techno-Science Research Journal

Journal Homepage: www.ric.itc.edu.kh

Techno-Science Research Journal

Experimental and Numerical Study of Tyfo® FibrAnchors Embedded in Low Compressive Strength Concrete Cylinder

Mengla An[1*], Narith Prok[2], Sovann Sathya Rath[2], Sovanvichet Lim[2], Wee Keong Ong[3]

[1]*Materials Science and Structure, Institute of Technology of Cambodia, Russian Federation Blvd., P.O. Box 86, Phnom Penh, Cambodia*

[2]*Research and Innovation Center, Institute of Technology of Cambodia, Russian Federation Blvd., P.O. Box 86, Phnom Penh, Cambodia*

[3]*Assistant General Manager, Fyfe Asia Pte Ltd, 6 Clementi Loop #02-20, Singapore 129814*

Received: 22 August 2023; Accepted: 15 May 2024; Available online: August 2024

Abstract: *The developing construction industry demands constant research and innovation of new technologies to meet specific needs. One such of these technologies is strengthening using fiber reinforcement polymer (FRP). FRP is a high-strength composite material bonded to a structure's surface member for retrofitting and strengthening purposes. However, premature debonding remains a significant challenge when using FRP to strengthen structures, caused by failure at the adhesive concrete interface with the fiber anchor. This research aims to investigate the bond behavior of confined fiber polymer and fiber anchors in low-strength concrete cylinders under pullout test. The study utilizes a total of 58 concrete cylinders with varying fiber anchor embedded depths and diameters. The experiments and numerical simulations using ABAQUS aim to enhance the understanding of the behavior and properties of fiber anchors. This research aims to investigate the effect of confinement on the bond behavior of fiber polymer and fiber anchor, identify the optimum embedment depth and diameter of the fiber anchor, and determine the bond interface's failure mechanism. This research will contribute to the development of more effective and reliable techniques for using fiber anchors in strengthening and retrofitting low-strength concrete structures. The results of this research will provide more comprehensive understanding of the performance of fiber anchors under different conditions, including anchor diameter and embedment depth.*

Keywords: FRP, Fiber anchor, bond behavior, pullout test, confinement

1. INTRODUCTION

FRP is a composite material with high strength, commonly used for retrofitting and strengthening existing structures. However, one of the main challenges encountered when employing FRP is the transfer of shear loads. This challenge can be mitigated by incorporating fiber anchors, which enhance the strength and durability of the material.

A significant issue associated with FRP strengthening is premature debonding, which arises due to failure at the adhesive concrete interface with the fiber anchor. Previous studies by K. Soputhih [5], have identified several shortcomings in the testing setup employed for concrete cylinders, leading to suboptimal performance and inaccurate results regarding debonding failure. Hence, this research aims to address these limitations and provide a comprehensive investigation into the bond behavior of confined fiber polymer and fiber anchors within low-strength concrete cylinders under pullout tests.

The research will involve conducting experiments and numerical simulations using ABAQUS. In addition the objectives of this research are :

- To improve the test setup
- To identify the diameter and optimum embedment depth of the fiber anchor
- To understand the variation of bonding failure
- To discuss the results of testing experimental with numerical simulation

* Corresponding author: AN Mengla

E-mail: anmengla@gmail.com; Tel: +855-68-493-118

2. Experimental procedure

Conducting experimental study at laboratory is very important to understand the condition and precise measurement which can lead to more accurate and reliable results. The total number of 58 specimens (including 6 for trail test) of concrete cylinder were inserted with FRP anchor wrapping with FRP laminate at its top end. The adhesive used in this experiment was Tyfo® S epoxy. The experiment focused on the effect of two parameters, embedment depth and anchor diameter. With the aim of focusing on aging concrete structures, a low compressive strength of concrete of 20 MPa is the target while the average value of compressive strength of overall concrete specimens obtained in this experiment was 20.5 MPa [2]. The concrete cylinder specimens used in the experiment had a dimension of 150x300mm, and each anchor had a varying diameter and embedment depth, but a constant free length of 200 mm. The concrete cylinder were wrapped with 1 layer of FRP laminate with 15cm overlap length.

In order to enhance the test setup from previous studies [5], it is necessary to conduct trial tests. The method of embedding the FRP anchor has been revised, whereby a hole is created at the top of the anchor for ease of conducting pullout tests. After the initial results were deemed unacceptable, additional trial tests were conducted to improve the methodology. One approach involved using a pipe to wrap the FRP anchor at the top. The detailed specimen of these two trail tests is shown in Fig. 2.1.

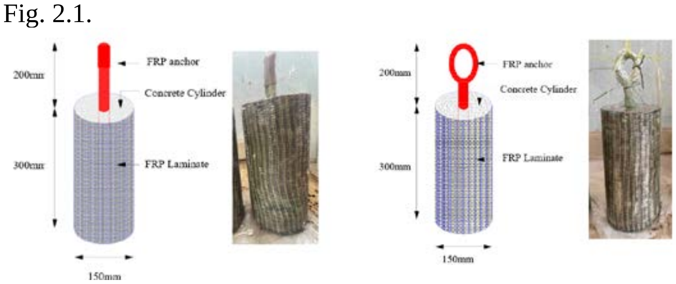

Figure 2.1. Detail sample of cylinder Pilot test 1 & 2

Following the trial tests, the results obtained by wrapping the FRP laminate at the top of the surface,as shown in Fig.2.2, were satisfactory for the purpose of the experimental study. And the wrapping the FRP laminate 80x300 mm were wrapped at the top of FRP anchor and improve with steel wire. The comparison on pullout force obtained from these Pilot tests is shown in Fig. 2.3.

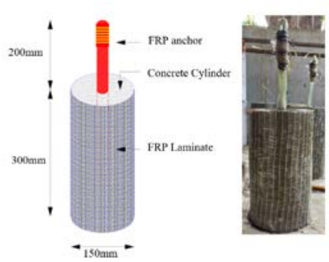

Figure 2.2. Detail specimen for experimental study

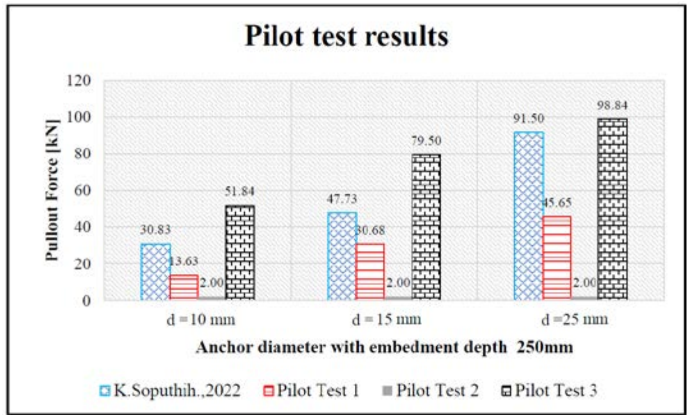

Figure2.3. Result of pilot test

After considering the positive outcome of the third test results, the pullout forces of third test is higher than K.soputhith test, pilot test 1&2. we made the decision to implement this approach. The number of specimens used for each anchor, categorized by embedment depth and diameter is shown in Table 2.1.

Table 2.1. Summary of experimental specimens

Number of specimens					
Embedment depth [mm]	Anchor diameter [mm]				
	10	12	15	20	25
50	-	-	-	-	-
100	4	4	4	-	-
150	4	4	4	-	-
200	4	4	4	-	-
250	4+2	4	4+2	-	4+2
Total	58 (Including 6 trial test)				

2.1 Material and property

2.1.1. Concrete

In accordance with ASTM Standards [4], the laboratory designed the concrete used in the experiment to have a compressive strength of 20 MPa, as indicated in Table 2.2.The Portland composite cement, specifically the locally available Camel brand was used in this study. All concrete cylinders used , casted, and cured at the laboratory for 28 days before starting preparation the specimen. The mix design of concrete is shown in Table 2.2.

Compressive strength [MPa]	Sand [kN/m^3]	Gravel [kg]	Cement [kg]	Water [kg]
20	776	1036	335	209.5

Table 2.2. Concrete mix design per $1m^3$

2.1.2. Epoxy

The epoxy used in this research is Tyfo® S Epoxy, provided by Fyfe Asia Pte Ltd [3]. The manufacturer has provided specific properties of the epoxy, which are listed in Table 2.3. Tyfo ® S Epoxy is a common material used in civil engineering applications for bonding and strengthening purposes. It is known for its high strength and durability, as well as its ability to adhere to a variety of surfaces. In this study, the Tyfo® S Epoxy was likely used to bond the FRP Anchors to the concrete substrate, creating a strong reinforced connection.

Table2.3. Properties of Tyfo® S Epoxy

Properties of epoxy material	
Tensile Strength	72.4 MPa
Tensile Modulus	3.18 GPa
Elongation Percent	5.0 %
Compressive Strength	86.2 MPa
Compressive Modulus	3.2 GPa
Flexural Strength	123.4 MPa
Flexural Modulus	3.12 GPa

2.1.3. FRP anchor

The FRP anchor used in the research study is the Tyfo® SEH as shown in figure 2.4, which was provided by Fyfe Asia Pte Ltd. The manufacturer has provided detailed specifications of the FRP anchor, including its mechanical properties as shown in Table 2.4. These properties are important to consider when using the FRP anchor in construction or retrofitting projects, as they can impact the strength and durability of the structure [3].

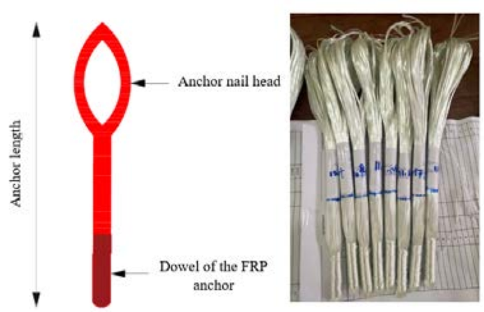

Figure2.4. Tyfo® SEH Anchors

Table 2.4. Properties Tyfo® SEH CompositeAnchor

	Tensile Strength [MPa]	Tensile Modulus [GPa]	Ultimate Elongation [%]
Dry fiber			
	3240	72.4	4.5
Composite anchor			
Test Value	575	26.1	2.2
Design Value	460	20.9	1.76

2.1.4. FRP Laminate

The Tyfo® SEH-25A composite comprises two primary components, Tyfo® S Epoxy and Tyfo® SEH-25A reinforcing fabric as shown in Fig. 2.5. The reinforcing fabric, Tyfo® SEH-25A, is a uni- directional glass fabric that is custom-woven for use in the Tyfo® Fibrwrap system. When combined with the Tyfo® epoxy material, the Tyfo® SEH-25A fabric enhances the composite's strength and ductility [3]. The properties of Tyfo® SEH-25A is shown in Table 2.5.

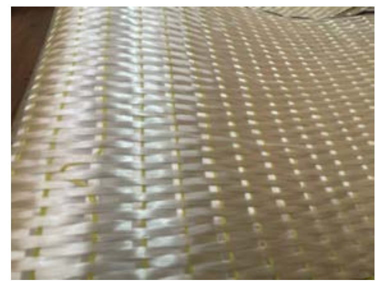

Figure 2.5 Tyfo® SEH -25A reinforcing fibric

2.3 Preparation experimental specimen

The flowchart shown in Fig. 2.6 and Fig. 2.7 describes about the preparation process. The specimen preparation is shown in Fig. 2.8.

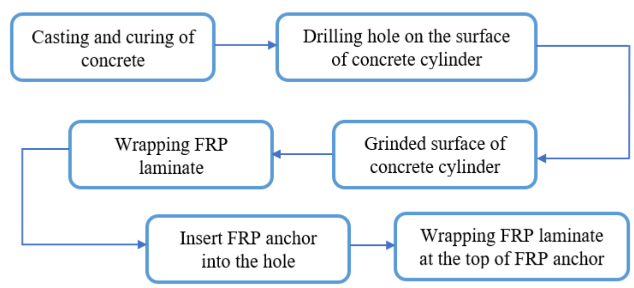

Figure 2.6. Flowchart for preparation sample poullout test

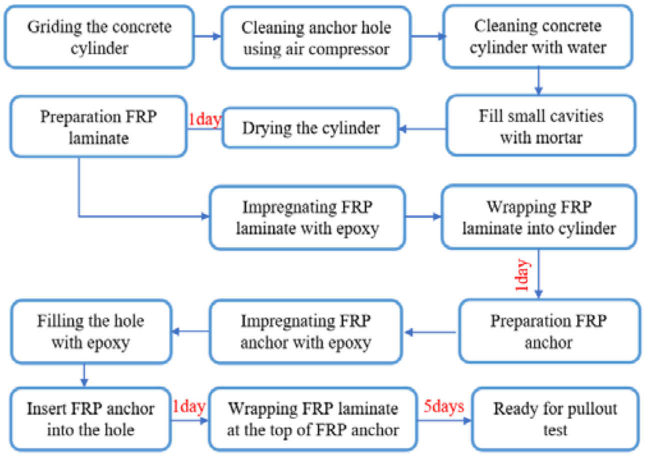

Figure 2.7. Wrapping FRP laminate and Insert anchor

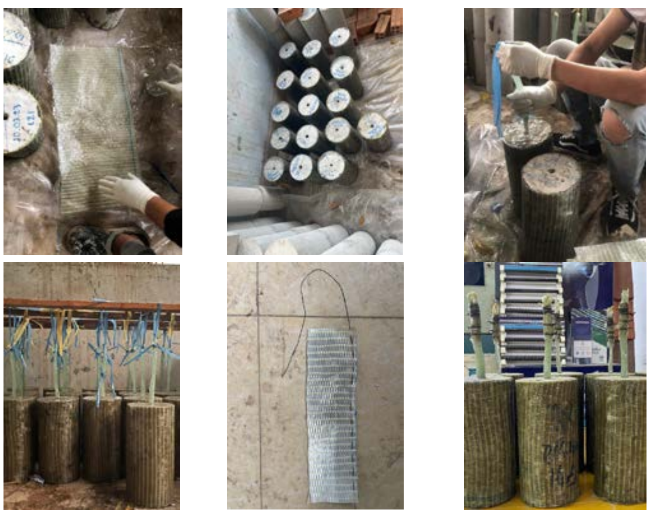

Figure 2.8. Specimen preparation

2.4. Process of pullout test

In the testing set up used for this experiment, each specimens were securely held in place between two steel plates as shown in Fig. 2.9. The particular setup of the specimens were subjected to a consistent and stable testing environment, which allowed for accurate and reliable data to be obtained from the pullout test. The use of steel plates on either side of the specimen ensured that the anchor was held securely in place during the test, preventing any slippage or undesired movement that could have affected the results.

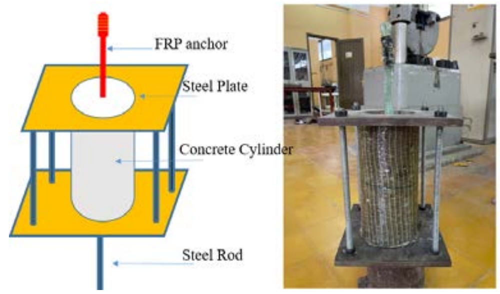

Figure 2.9. Preparation of specimen for testing

After preparing the sample with steel formwork, the next steps in the pullout test procedure involve placing the specimen into the pullout machine and holding the wedge grips during the test as shown in Fig. 2.10. A loading rate of 10N/s was applied in this experiment.

Figure 2.10. The process of pullout test

2.5. Failure mode of specimens

Under pullout test, the specimens exhibited different failure modes such as the concrete cone failure (CC), combined cone-bond failure (CB) and anchor rupture failure (RF). The tested specimens with CB and RF failure mode is shown in Fig. 2.11.

Figure 2.11. Failure mode of specimens

3. RESULTS AND DISCUSSION

3.1.Combined cone-bond failure (CB)

Combined cone-bond failures were observed on specimens of various anchor diameters and embedment depths. CB failures occurred at embedment depth of 100mm for anchors of diameters 10mm, 12mm and 15mm. Anchors of diameter 25mm failed in CB at all embedment depths [8].

3.2.Anchor Rupture (RF)

Anchor ruptures failure mode occurred at smaller anchor diameters (10mm, 12mm, and 15mm) at embedment depths falling within the range of 100mm to 250mm. RF failure occurred when the tensile strength of the anchor was smaller than the bond strength between the anchor and the concrete. This signifies that the anchor's embedment depth is sufficient to prevent various concrete failures and that the anchor has reached its tensile capability [8].

3.3. Effect of bond strength on anchor

The average uniform bond stress was calculated for each anchor diameter at various embedment depths. The results indicate that the average bond strength of FRP anchors tends to decrease as the anchor diameter increases. This trend suggests that larger anchor diameters may result in reduced bond performance between the FRP anchor and the substrate material.

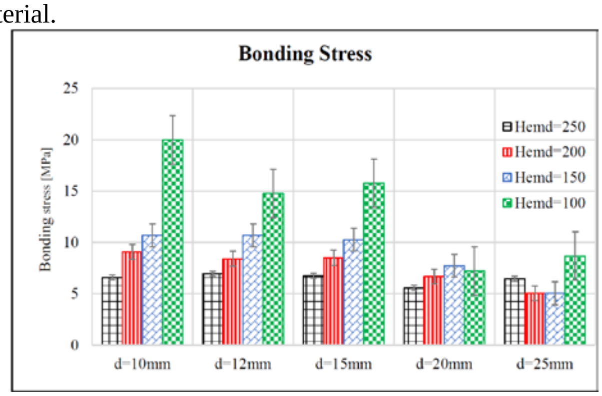

Figure 3.1. Effect of bonding stress

3.4. Effect of anchor hole diameter

Based on the data presented in Fig 3.2, several noteworthy observations can be made:

- For anchor diameters of 10mm, 12mm, and 15mm, the pullout force decreases gradually up to an embedment depth of 200mm. After reaching this point, the pullout force increase slightly. Therefore, the optimal embedment depth for achieving the highest pullout force seems to be at 200mm for these specific anchor diameters [2].
- For the anchor diameters of 20mm and 25mm, it is observed that the pullout load consistently increases as the embedment depth increases. This suggests that the optimum point for achieving the highest pullout load may be at an embedment depth of 250mm for these specific anchor diameters [2].

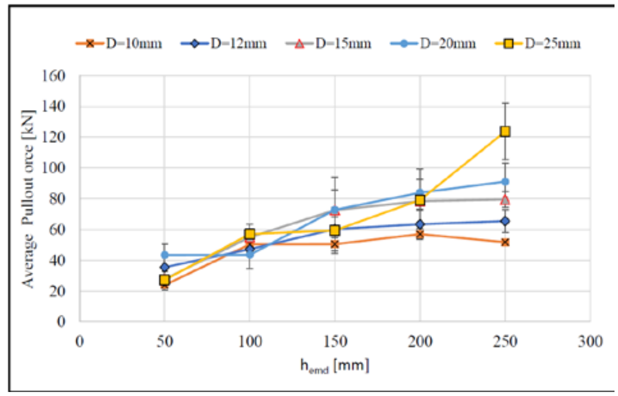

Figure 3.2. Effect of anchor hole diameter

3.5. Analysis of the Test Data Experimental

The examination of the test data utilizing the models proposed revealed disparate specimen preparation techniques as well as the utilization of the same model form K.Soputhih [5]. However, the results obtained from previous research were unsatisfactory primarily due to its limited applicability within a specific range. The limitations of previous reserch became apparent as it was found to have a restricted range of applicability. Due to these limitations, it was decided to focus solely on the best-fit models.

The pullout resistance of a single FRP anchor when focusing on failure load can be calculated from the following equations [5,6,7,8] :

$$N_U = \min(N_{CC}, N_{CB}, N_{RF})$$

Where $N_{CC} = 16.044 \cdot h_{emd}^{1.5}\sqrt{f_c'}$ (concrete-cone) (Eq.1)

$N_{CB} = 8.399 \cdot \pi d h_{emd}$ (combined cone-bond) (Eq.2)

$N_{RF} = 0.607 A_{FRP} f_{FRP}, d > 15mm$

$N_{RF} = 0.785 A_{FRP} f_{FRP}, d \leq 15mm$ (anchor rupture) (Eq.3)

The pullout resistance of the model versus test result are presented in figure 3.3 to 3.7. The ranges of test parameters are anchor diameter $10mm \leq d \leq 25mm$ with embedment depth $50mm \leq h_{emd} \leq 250mm$.

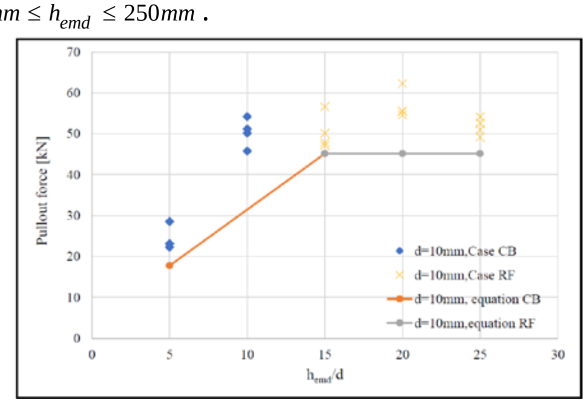

Figure3.3. Each failure mode with a 10mm anchor diameter

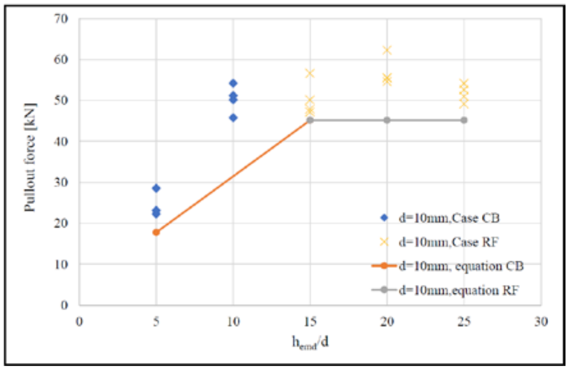

Figure3.4. Each failure mode with a 12mm anchor diameter

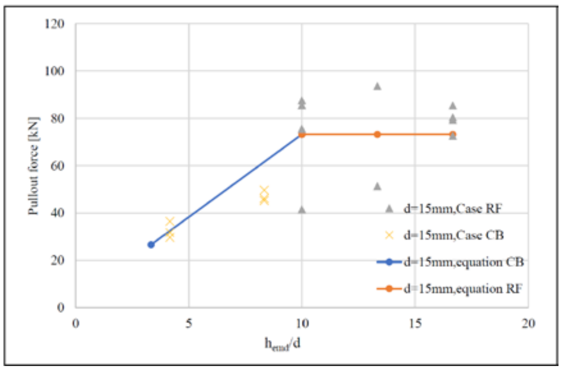

Figure3.5. Each failure mode with a 15mm anchor diameter

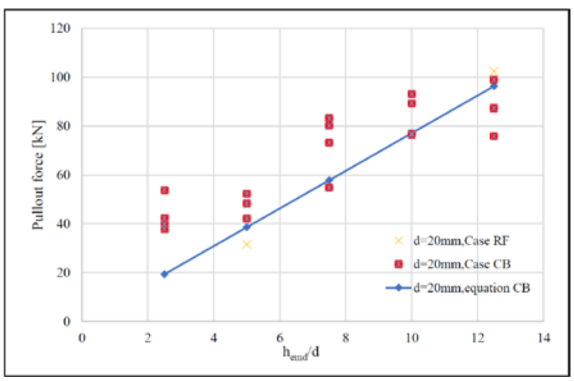

Figure3.6. Each failure mode with a 20mm anchor diameter

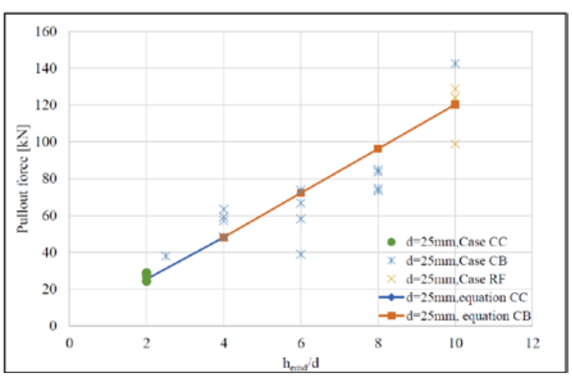

Figure3.7. Each failure mode with a 25mm anchor diameter

4. NUMERICAL SIMULATION

4.1. Modeling procedure

To model the samples in Abaqus,the following step was follow as shown below [1]:

- Create a new model in Abaqus/CAE
- Define the geometry of the specimens by creating appropriate parts for component (concrete, FRP anchor, epoxy, and FRP laminate)
- Assign the respective material properties to each component. Specify the material properties for concrete, FRP anchor, epoxy, and FRP laminate based on the specific materials used in study.
- Generate meshes for each component of the specimens.
- Apply appropriate boundary conditions to the model.
- Set up the analysis steps. Define the loading conditions, such as displacement or load increments,
- Run the analysis and monitor the response of the specimens.

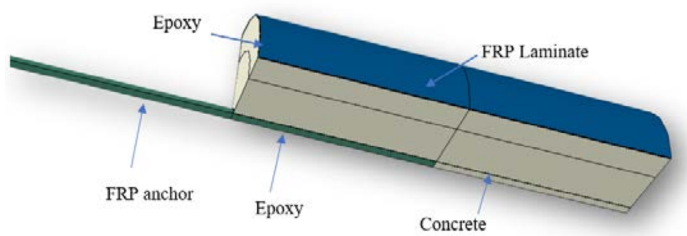

Figure 3.8. Modeling specimens

4.2. Results of analysis

The analysis model results were obtained for a total of 25 series of specimens, each characterized by different combinations of anchor diameter and embedment depth. The ranges of the tested parameters were specified as follows:

- Anchor Diameter (d): 10mm ≤ d ≤ 25mm
- Embedment Depth (h): 50mm ≤ h ≤ 250mm

The comparison of results obtained by ABAQUS modeling and experimental test for each anchor diameter is shown in Fig. 3.9 through Fig. 3.13.

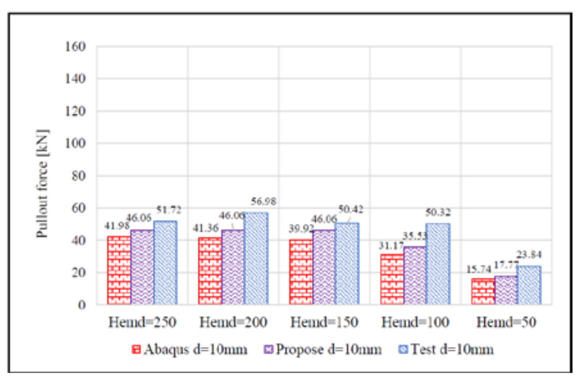

Figure3.9. Pullout force obtained from ABAQUS versus test for anchor diameter 10mm

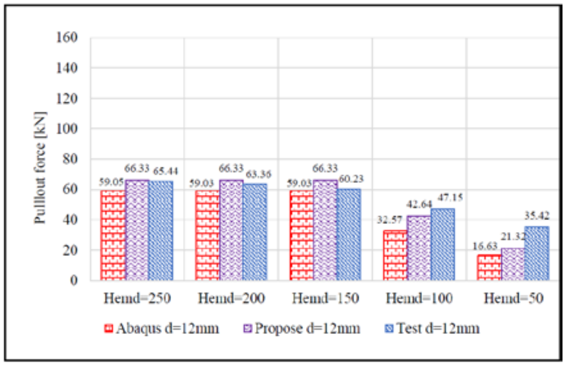

Figure3.10. Pullout force obtained from ABAQUS versus test for anchor diameter 12mm

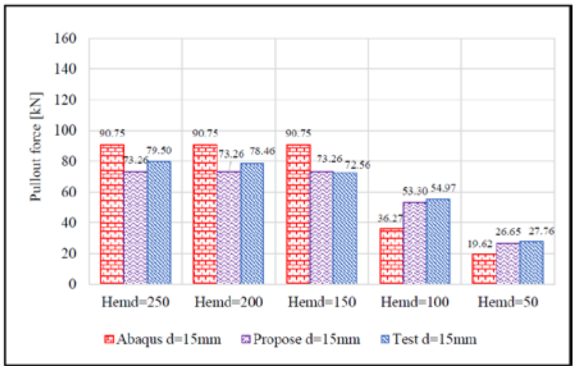

Figure3.11. Pullout force obtained from ABAQUS versus test for anchor diameter 15mm

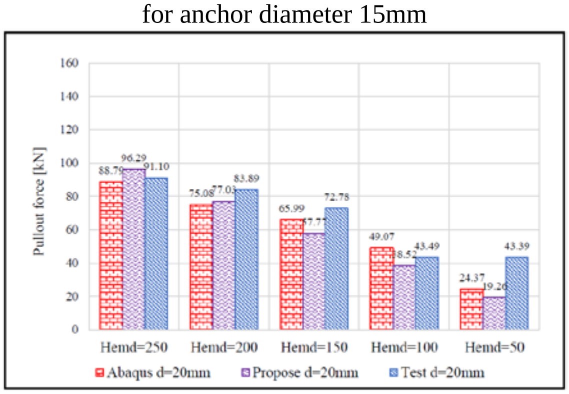

Figure3.12. Pullout force obtained from ABAQUS versus test for anchor diameter 20mm

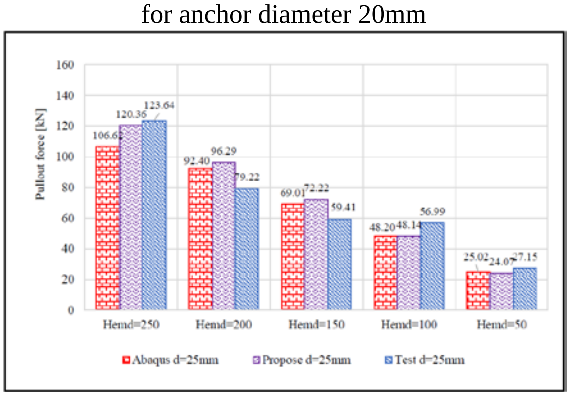

Figure3.12. Pullout force obtained from ABAQUS versus test for anchor diameter 25mm

5. CONCLUSIONS

Based on the test results presented in this study, the following conclusion can be drawn [2]:

- The pullout strength of FRP anchor is increased with increasing of embedment depth. However, the ultimate limit of the pullout strength is determined by rupture strength of FRP anchor.
- The average bond stress is decreased with increasing of FRP anchor diameter and embedment depth.
- The failure mode is RF when anchor diameter is smaller than 15mm and embedment depth is greater or equal to 150mm. While the failure mode is primarily in CB when the embedment depth is smaller than 150mm.
- The failure mode is mostly in CB when anchor diameter is 20mm and 25mm.
- The proposed equation is demonstrated an acceptable result compared to experimental and numerical simulation data for both pullout capacity and failure mode.
- The optimal depth is 200mm for anchor diameter from 10mm to 15mm. While optimal depth is 250mm for anchor diameter from 20mm to 25mm.

ACKNOWLEDGMENTS

The author express gratitude to the Faculty of Civil Engineering at the Institute of Technology of Cambodia for providing laboratory and technical support. Funding and composite materials provided by the Fyfe Asia Pte Ltd company are gratefully acknowledged.

REFERENCES

[1] Abaqus Analysis User's Guide 6.14
[2] AN Mengla .,2023 Experimental and numerical study of Tyfo® Fibr anchors Embedded in low compressive strength concrete cylinder
[3] AEGION, 2015. Tyfo ® S Saturant Epoxy 1–2.
[4] K. Soputhuthith.,2022 Experimental and numerical study on performance of Tyfo® Fibr anchors under axial tension
[5] Kim S.J., Smith, S.T., 2009. Behavior of handmade FRP anchors under tensile load in uncracked concrete. Adv. Struct. Eng. 12, pp. 845–865.
[6] Ozbakkaloglu, T. and Saatcioglu, M., 2009. Tensile behavior of FRP anchors in concrete, Journal of Composites for Construction, ASCE, Vol. 13, No. 2, pp. 82–92.
[7] Perumalsamy, B.L.G.R., Antonio, N.N., James, G.C.P., 2009. FRP Composites for Reinforced and Prestressed
[8] Smith, S.T., and Teng, J.G., 2003. "Shear-bending interaction in debonding failures of FRP-plated RC

beams", Advances in Structural Engineering, Vol. 6, No. 3, pp. 183–199.

[9] Teng, J. G., Smith, S. T., Yao, J., Chen, J. F., 2003. Intermediate crack-induced debonding in RC beams and slabs. Construction and Building Materials, 17(6–7), pp. 447–462.

Techno-Science Research Journal 12 (Special Issue) 238-245

Content list available at ITC

Techno-Science Research Journal

Journal Homepage: www.ric.itc.edu.kh

Techno-Science Research Journal

An Investigation of External Pressure Coefficient for Low-Rise Building: A Comparison between CFD and ASCE7-22 Models for Cambodia Wind

Rittyvirak Thai[1], Piseth Doung[1,2*]

[1] *Faculty of Civil Engineering, Institute of Technology of Cambodia, Russian Federation Blvd., P.O. Box 86, Phnom Penh, Cambodia*
[2] *Research and Innovation Center, Institute of Technology of Cambodia, Russian Federation Blvd., P.O. Box 86, Phnom Penh, Cambodia*

Received: 22 August 2023; Accepted: 15 May 2024; Available online: August 2024

Abstract: *For wind loading, the external pressure coefficients (C_p) on the walls of low-rise buildings are an important factor in the structural design process. These coefficients affect the wind-induced lateral load, which results in different structural responses. Hence, the assessment of external pressure coefficients is necessary. This study aims to compare the coefficient of pressure on the wall surfaces of low-rise buildings adopting two approaches: Computational Fluid Dynamics (CFD) and ASCE7-22, which specify wind in Cambodia. The study examined the external coefficients of pressure on both main directions of the building, considering the difference between a rectangular plan with a gable roof type building. Firstly, commercial CFD software, Rwin2.02, was used to simulate the wind profile characteristics around the building and to calculate the coefficients of external pressure. Secondly, a table of the Wall Pressure Coefficient, C_p in ASCE7-22 was used to compare the coefficients of external pressure provided by the CFD approach. The investigation results showed that the pressure coefficient values estimated by ASCE7-22 were higher than those obtained from CFD simulations. The differences were higher for the wall surfaces exposed to the windward directions of the building configuration. Moreover, ASCE7-22 overly predicts the pressure values when compared with CFD with the angular dependency of the pressure coefficient on the orientation of the wind flow.*

Keywords: External Coefficient of pressure, Low-rise building, Lateral load.

1. INTRODUCTION

The external coefficient pressure (C_p) of a low-rise steel building is a measure of the wind load that the building is subjected to. It is a dimensionless value that is multiplied by the wind pressure to determine the actual wind load. The external C_p varies depending on the shape and orientation of the building, as well as the wind speed. In general, the external C_p is higher on the windward side of the building and lower on the leeward side. The external C_p is also higher for taller buildings than for shorter ones. The external C_p is an important factor in the design of low-rise buildings because it is used to determine the strength and size of the structural members that are needed to resist the wind load.

Computational fluid dynamics (CFD) is a numerical method that can be used to simulate the flow of wind around buildings. CFD simulations can provide more accurate predictions of C_p than empirical equations, and they can be used to study the effects of different building shapes, sizes, and orientations of wind loads.

Currently, there is no specific wind load code for engineers to design the structure for the wind effect in Cambodia. Moreover, Matthew et al. [1] reported that ASCE 7-22 standard provides a good prediction of C_p based on wind tunnel test results compiled 5 decades ago. However, it would not be accurate for all building types and wind conditions.

This study investigates the accuracy and efficiency of CFD simulations for predicting the coefficient of pressure on the wall surfaces of low-rise buildings with gable roofs in Cambodia, as compared to the ASCE7-22 wind loading provisions.

* Corresponding author: Piseth Doung
E-mail: piseth@itc.edu.kh; Tel: +855-12-472-517

2. METHODOLOGY

In this study, the numerical simulation of the wind tunnel for gable roof low-rise steel building structure by RWIN 2.02 commercial software was investigated based on steady flow- RANS k-ε [1] modeling on the horizontal plane terrain at level Z=0. The objective is to obtain the value of the external C_p and to investigate the effects of the building's height, roof angle, and orientation on the external C_p.

2.1 Selection of a turbulence model

The turbulence intensity is an important factor to consider in CFD simulations of low-rise buildings. This is because turbulence can affect the distribution of wind pressure on the building, and it can also affect the flow around the building. If the turbulence intensity is not correctly represented in the CFD simulation, the results may not be accurate. Therefore, it is important to use a turbulence model that is appropriate for the specific application.

In a study by Aly Mousaad Aly et al. [2], the research concluded that “Increase in large-scale turbulence content in incident flow allows vortices to attain maturity, and as a result higher peak pressures can be reproduced”.

Table 1. Types of CFD simulations [3].

Type of CFD simulation	Action
Reynolds-averaged Navier-Stokes (RANS) simulations. These are the most common type of CFD simulation. They are relatively computationally inexpensive and can be used to simulate a wide range of flows. However, they do not accurately capture the small-scale turbulent structures that can be important in some applications.	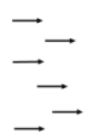
Large eddy simulation (LES) simulations. LES simulations are more computationally expensive than RANS simulations, but they can provide more accurate results for turbulent flows. They do this by directly simulating the large-scale turbulent structures while modeling the smaller-scale structures using a turbulence model.	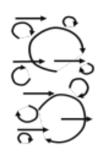
Direct numerical simulation (DNS) simulations. DNS simulations are the most accurate type of CFD simulation. They directly simulate all of the scales of turbulence, without using a turbulence model. However, they are also the most computationally expensive type of CFD simulation.	

2.2 Define the building geometry

The ratio of W/L is set to be a parameter in determining the wind loads on a building. Buildings with a larger W/L ratio experience higher wind loads than buildings with a smaller W/L ratio. Based on the literature review of Hatem [4] written that the experimental building study investigated by Stathopoulos (1979), the size of buildings mostly are small buildings with a small ratio of width over the length (W/L). Therefore, in this study, the sizes of the buildings chosen are the large warehouse with a great ratio of W/L, as shown in Table 1.

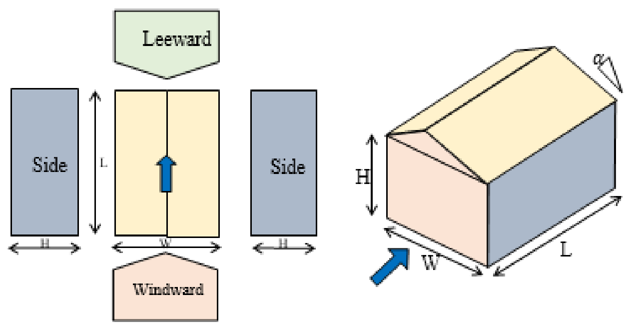

Fig.1. The definition of the dimension and wall name

Table 2. The size of the model building in CFD simulation

Building No	W (m)	L (m)	H (m)	Roof Angle α (Degree)
1	30	130	12.5	5°
2	35	70	15	20°
3	40	60	17.5	25°
4	35	140	12.5	7°
5	35	75	15	22.5°
6	40	65	17.5	27°
7	25	110	12.5	15°
8	30	65	15	23°
9	20	40	17.5	27°

2.3 Set the boundary conditions

To compare the external coefficient pressure walls of ASCE7-22 with the external coefficient pressure obtained from CFD simulation results, the atmospheric boundary layer (ABL) environments are used to define in simulation.

The building for the numerical simulation is a gable-roof low-rise structure with length (L) and width (W) as listed in Table 3 following the concept study of Tominaga et al. [5]. The building is considered in the open terrain exposure. This study considered the steady flow, the turbulence model RANS k-ε modeling on the horizontal plane terrain level Z=0 at the base of the building, under the basic design wind speed value 35m/s in Phnom Penh, Cambodia for a return period of 50 years [6]. The dimension of the wind tunnel simulation varies due to the size and orientation of the building which can be seen in Table 3 below.

Table 3. The dimension of the wind tunnel [7]

Size	w+	W	w-	d-	d	d+	h	h+
Value	2.5W	W	2.5W	2.5L	L	2.5L	H	5H

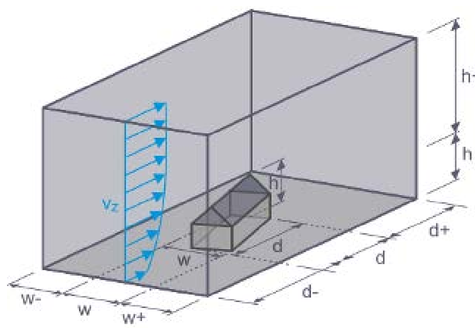

Fig.2. Schematic depiction of the wind tunnel in Rwin 2. [8]

Wind profile by power law can be described in the following equations [4].

$$\frac{u}{u_r} = \left(\frac{z}{z_r}\right)^{\alpha} \qquad \text{(Eq. 1)}$$

where:

u = the wind speed (m/s) at height z (m)
u_r = the known wind speed (m/s)at reference height z (m)
z = the height (m) of the wind speed u
z_r = the reference height (m) of the wind speed u_r
α = empirically derived coefficient (0.14) [9]

$$I_z = c\left(\frac{10}{z}\right)^{d} \qquad \text{(Eq.2)}$$

where:
c & d = variables related to the exposure category at reference height 10m
z = the desired height

Table 4. Turbulence Intensity of profile parameters

Terrain Category	Cambodia	
	c	d
A	0.40	1/6
B	0.30	1/6
C	0.25	1/6

Table 5. Wind profile in wind tunnel simulation based on basic wind speed [6].

H (m)	(U_z/U_G)	I(z)
0.0	0.000	0.700
2.0	0.795	0.523
7.0	0.950	0.424
12.0	1.026	0.388
17.0	1.079	0.366
22.0	1.119	0.351
27.0	1.152	0.339
32.0	1.181	0.330
37.0	1.206	0.322
42.0	1.228	0.315
47.0	1.247	0.309
52.0	1.266	0.304
57.0	1.282	0.299
62.0	1.298	0.295
67.0	1.312	0.291
72.0	1.326	0.288
77.0	1.339	0.285
82.0	1.351	0.282
87.0	1.362	0.279

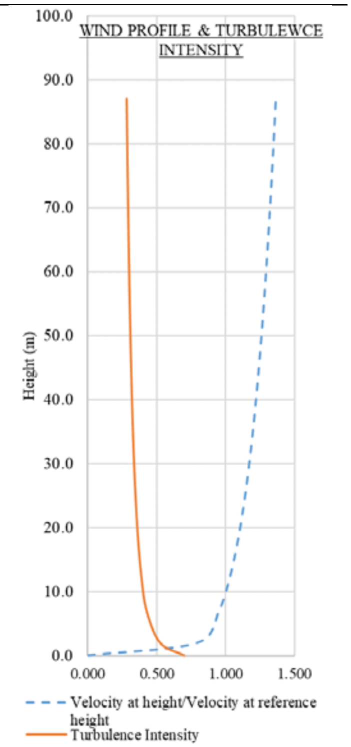

Table 5. above shows the approaching wind profile of longitudinal mean wind speed (U_z/U_G) and turbulence intensity I(z) using Eq.1 & Eq.2. The value of turbulence intensity also decreased with height above the ground, but not as rapidly as the wind speed.

2.4 Simulation Performance

The CFD simulations were performed using the Rwin2.02 software. The simulations were set up using a Reynolds-averaged Navier-Stokes (RANS) solver with the k-ε turbulence model. The mesh density is 20% (The cells size= 0.65m) which produces 129 705 cells.

To determine the wind external pressure coefficient distribution in the CFD simulation in this research. The following process of work is repeated:

Step 1: Creating a model in RFEM6 (RFEM 6 is a structural analysis software that can be used to create 3D models of buildings. The model created in RFEM 6 can then be imported into Rwin 2.02 for the CFD simulation).

Step 2: Defining zone name on the wall in Rwin 2.02

Step 3: Defining the boundary condition (The inlet boundary condition specifies the wind speed, direction, and turbulence intensity).

Step 4: Meshing and Running the simulation.

Step 5: Data evaluation.

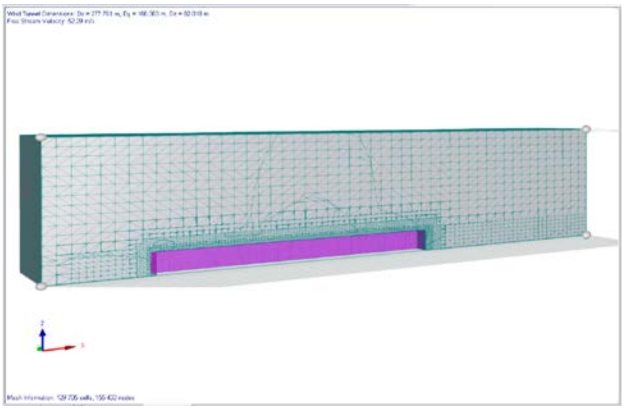

Fig.3. Section of mesh simulation of model-1 along the wind flow direction 0 º

3. RESULTS AND DISCUSSION

The results of the external C_p obtain from simulations are discussed thoroughly in this section.

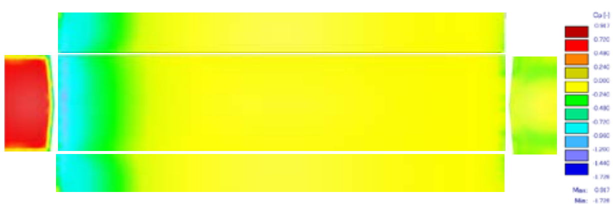

Fig.4a. Skewness contours of External Cp (Model-1, α=0º)

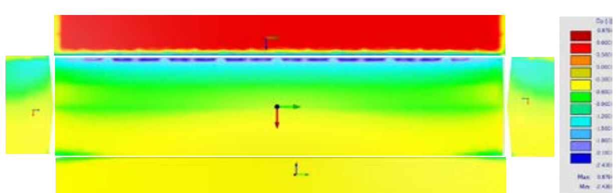

Fig.4b. Skewness contours of External Cp (Model-1, α=90º)

The external pressure patterns of the leeward walls in simulations showed the peak pressure located at the middle area of the leeward wall. Moreover, the local external pressure of windward and leeward walls are highest for wind direction which is perpendicular to the ridge of the roof.

It can be found that the lower pressure, suction force dominates due to the airflow separation and creation of a low-pressure zone behind the building. Peak suction typically occurs near the center and upper portions of the wall.

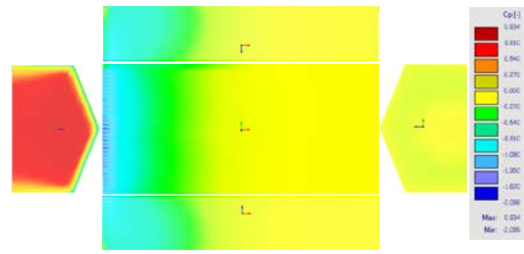

Fig.5a. Skewness contours of External Cp (Model-2, α=0º)

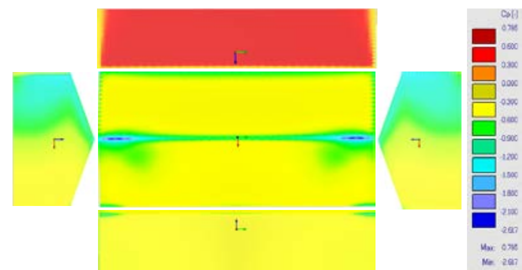

Fig.5b. Skewness contours of External Cp (Model-2, α=90º)

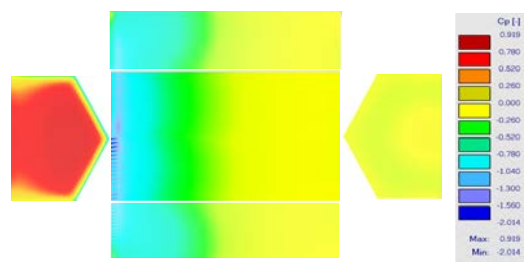

Fig.6a. Skewness contours of External Cp (Model-3, α=0º)

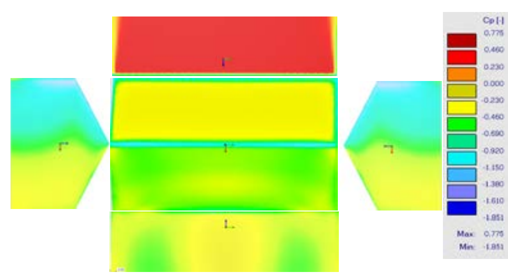

Fig.6b. Skewness contours of External Cp (Model-3, α=90º)

As seen from the figure, the external pressure on the windward walls for the wind direction parallel to the ridge is always greater than the result obtained from the wind direction normal to the ridge.

The greater area of the windward is the obstacle for the flow streamline. After the wind hits the obstacle, its velocity decreases to zero and its molecules need to flow to the side wall. This phenomena makes a layer of air which becomes a membrane to decrease the velocity of the wind of the next streamline.

Fig.7a. Skewness contours of External Cp (Model-4, α=0^o)

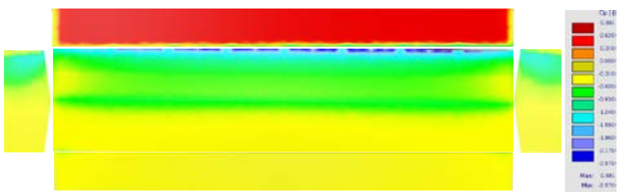

Fig.7b. Skewness contours of External Cp (Model-4, α=90^o)

For the whole side wall, the external pressure is negative. In addition, the side wall tends to get the suction at the upper streamline near the windward wall and then the lower streamline near the leeward wall. However, it will have some error as the average value of the external pressure of each wall isused in the data comparison.

The external pressure on the side wall is slightly changed in the vertical direction but its distribution is noticeably changed in the horizontal direction along the wall.

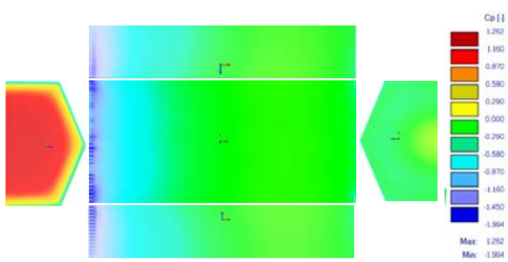

Fig.8a. Skewness contours of External Cp (Model-5, α=0^o)

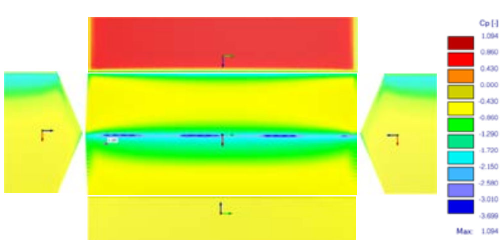

Fig.8b. Skewness contours of External Cp (Model-5, α=90^o)

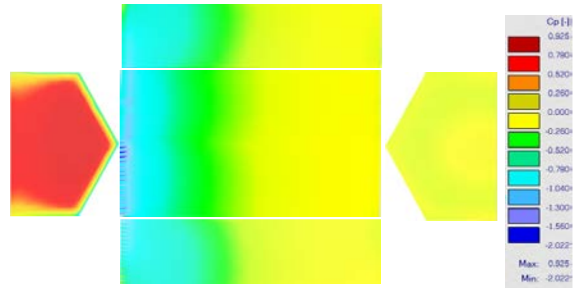

Fig.9a. Skewness contours of External Cp (Model-6, α=0^o)

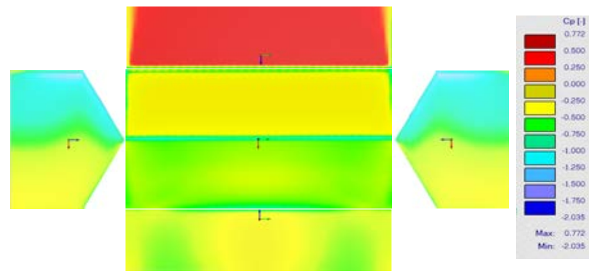

Fig.9b. Skewness contours of External Cp (Model-6, α=90^o)

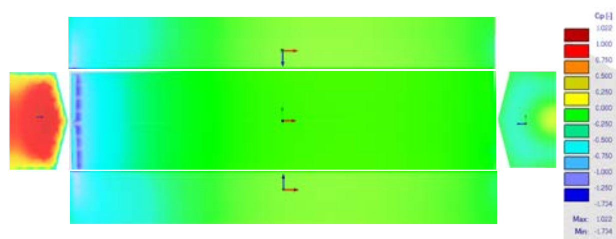

Fig.10a. Skewness contours of External Cp (Model-7, α=0^o)

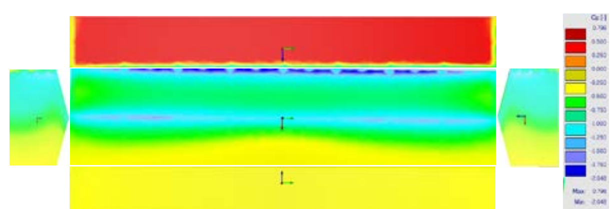

Fig.10b. Skewness contours of External Cp (Model-7,α=90^o)

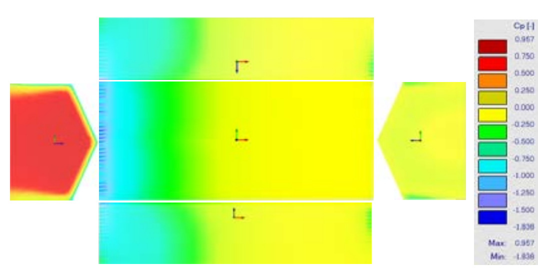

Fig.11a. Skewness contours of External Cp (Model-8, α=0^o)

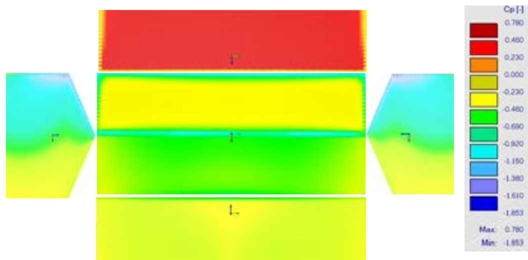

Fig.11b. Skewness contours of External Cp (Model-8,α=90º)

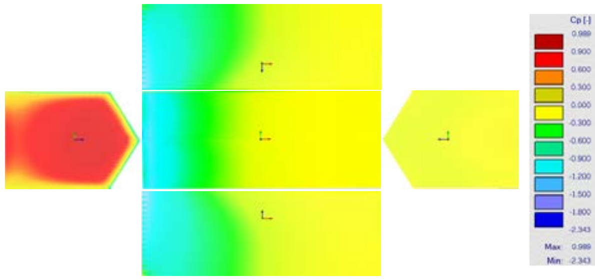

Fig.12a. Skewness contours of External Cp (Model-9, α=0º)

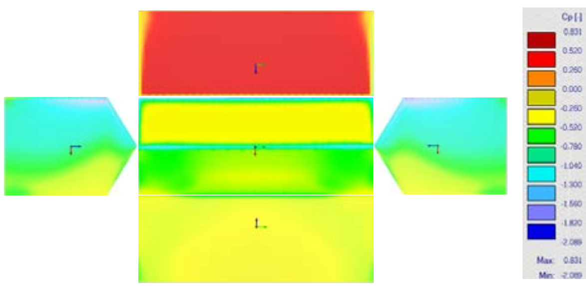

Fig.12b. Skewness contours of External Cp (Model-9,α=90º)

Figures 4a to 12b illustrated the external coefficient pressure distribution on the entire building. As shown, the external pressure coefficient value on the windward wall is not always positive over the entire area of the walls. At the corner between the windward wall and the side wall, there was a slight suction effect caused by the stagnation point on the windward wall.

The results of the CFD studies of external coefficient pressure on low-rise buildings have shown that the external coefficient pressure could vary significantly depending on the shape and orientation of the buildings. The buildings' walls that were perpendicular to the wind direction also tended to experience higher external coefficient pressure than the walls that were parallel to the wind direction. Furthermore, the height of the building and the angle of the roof also had a significant effect on external pressure, as seen in model 5 which produced greater results of windward external pressure.

Table 6. The external C_p of each model

No	Angle of Attack	Ratio (L/B)	Windward (C_p)	Leeward (C_p)	Sidewall (C_p)
1	0	4.33	0.61	-0.224	-0.179
	90	0.23	0.623	-0.32	-0.641
2	0	2.00	0.652	-0.192	-0.316
	90	0.50	0.653	-0.414	-0.671
3	0	1.50	0.645	-0.185	-0.391
	90	0.67	0.633	-0.409	-0.64
4	0	4.00	0.605	-0.233	-0.183
	90	0.25	0.645	-0.283	-0.583
5	0	2.14	0.894	-0.2	-0.365
	90	0.47	0.866	-0.305	-0.667
6	0	1.63	0.64	-0.176	-0.379
	90	0.62	0.628	-0.448	-0.666
7	0	4.40	0.682	-0.217	-0.192
	90	0.23	0.623	-0.29	-0.694
8	0	2.17	0.66	-0.176	-0.328
	90	0.46	0.655	-0.429	-0.681
9	0	2.00	0.687	-0.178	-0.407
	90	0.50	0.635	-0.401	-0.801

Table 7. The External Wall pressure coefficient, C_p [10].

Surface	L/B	Cp
Windward wall	All values	0.8
Leeward wall	0-1	-0.5
	2	-0.3
	≥4	-0.2
Sidewall		-0.7

With the result obtained from simulation in Table 6. And Table 7. We can make a comparation External C_p graph of each wall as below:

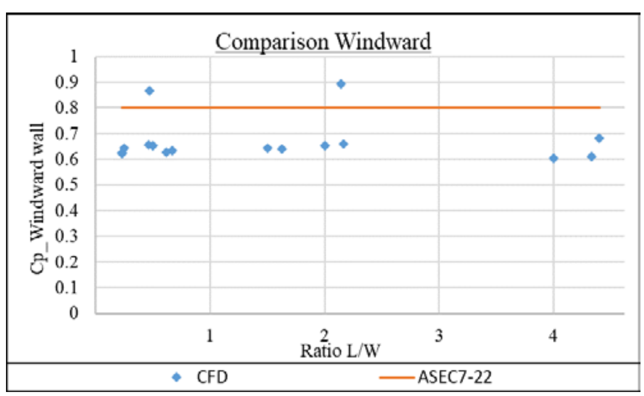

Fig.22. The comparison of windward wall C_p

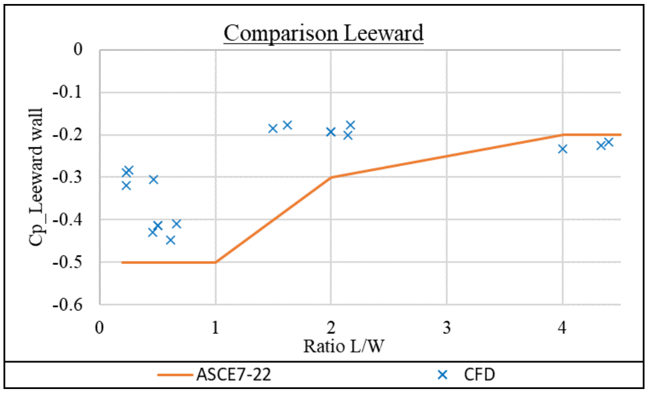

Fig.23. The comparison of leeward wall C_p

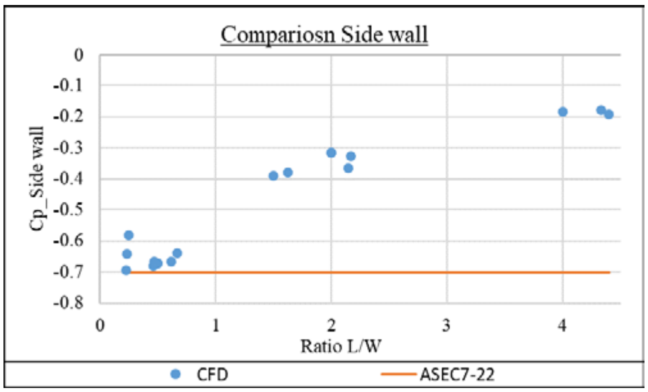

Fig.24. The comparison of the side wall C_p

The results of CFD simulations and ASCE7-22 can be compared to assess the accuracy of each method. In general, CFD simulations tended to produce less value of external coefficient pressures than ASCE7-22. This is because CFD simulations accounted for factors that are not included in ASCE7-22, such as wind turbulence and surface roughness. However, it is important to note that the CFD simulations were not always accurate due to a number of factors, including the complexity of the structure, the turbulence intensity of the wind, and the mesh resolution.

A comparison of the results obtained from CFD and ASCE7-22 can be described as follows:

- For the external windward pressure coefficients the value of C_p obtained from CFD is less than ASCE7-22 except for model 5 with a ratio L/W =75/35 and a roof angle of 22.5º.
- For the external leeward pressure coefficient, the C_p value from ASCE7-22 is overestimated comparing to CFD, except for the model with a ratio L/W > 4.
- For the external sidwall pressure coefficient, the C_p value from ASCE7-22 also overestimates compared to CFD.
- The application of the CFD technique had the potential to obtain external pressure for complex structures that are not in the domain of ASCE7-22 or other load codes. However, the accuracy of results strongly and effectively depends on the data input, as described in the paper.

4. CONCLUSIONS

The investigation has shown that the external coefficient pressure of the building can be evaluated using both the CFD simulations and ASCE7-22. It was worth noting that each approach has its limitations. The CFD simulations may not always be correct due to data input. Moreover, it was sometimes computationally costly and time-consuming. Although in Cambodia, ASCE7-22 is commonly used to calculate the wind pressure, applying this standard to low-rise buildings in Cambodia needs to be further investigated since the results of this study show that there are a few external coefficient pressures that are higher than ASCE 7-22 recommended.

In general, it is recommended to evaluate the external coefficient pressure of structures using a mix of CFD simulations and ASCE7-22, if possible. This action would produce more accurate results.

Moreover, this study also found that the CFD simulation was not necessary for the rectangular low-rise building, and ASCE7-22 can be used to obtain the external coefficient pressure (C_p).

ACKNOWLEDGMENTS

The work was funded by Cambodia Higher Education Improvement Project (Credit No. 6221-KH). The authors would like also to express their gratitude to Dlubal (Structural Analysis and Design Software) for supporting the trial version of RWIN2 (Wind tunnel simulation).

REFERENCES

[1] Matthew L., G., Brian M., P., Dat, D., & Bilal M., A. (2017). Wind-Pressure Coefficients on Low-Rise Building Enclosures Using Modern Wind-Tunnel Data and Voronoi Diagrams. *ascelibrary.org*.

[2] Aly, M. A., Faiaz, K., & Hamzeh, G.-Z. (2020). Aerodynamics of Low-Rise Buildings: Challenges and Recent Advances in Experimental and Computational Methods.

[3] Y. Abu-Zidan, P. Mendis , T. Gunawardena, D. Mohotti, & S. Fernando. (2022). Wind Design of Tall Buildings: The State of the Art. *Electronic Journal of Structural Engineering*.

[4] Hatem, A. (2015). *Wind Pressures On Flat Roof Edges And Corners Of Large Low Buildings.* Montréal, Canada.

[5] Tominaga, Y., Shin-ichi, A., Takuya, K., & Yuki, A. (2014). Airflow around isolated gable-roof buildings with different roof pitches: Wind tunnel experiments and CFD simulations. *Building and Environment, 84*(2015), 204-213.

[6] Lin, C. (2022). Basic Wind Speed Analysis and Development for the Design of the Design of Buildings in Cambodia. *Master Thesis. Institut of Technology of Cambodia*.

[7] Fouad, S. N., Mahmoud, H. G., & Nasr, E. N. (2017). Comparative study of international codes wind loads and CFD results for low-rise buildings. *Alexandria Engineering Journal*.

[8] RWIN2. (2022). *Dlubal Software, Inc.*

[9] John, A. D., Roy, A. K., & Gairola, A. (2012). Wind Loads on Wall of Low-Rise Building. *6th National Conference on Wind Engineering (NCWE)*, (pp. 449-456). New Delhi.

[10] ASCE 7. (2022). Minimum Design Loads and Associated Criteria for Buildings and Other Structures. *Virginia: American Society of Civil Engineers*.

Techno-Science Research Journal 12 (Special Issue) 246-252

Content list available at ITC

Techno-Science Research Journal

Journal Homepage: www.ric.itc.edu.kh

Experimental study on the improvement of bolted connection of glass structure by using ion-exchange

Socheata CHANN [1], Raveth HIN [1*], Jean-Christophe SANGLEBOEUF [2]

[1] Research and Innovation Center, Institute of Technology of Cambodia, Russian Federation Blvd., P.O. Box 86, Phnom Penh, Cambodia

[2] Institute of Physics of Rennes, University of Rennes 1, UMR CNRS 6251, F-35042 Rennes, France

Received: 22 August 2023; Accepted: 15 May 2024; Available online: August 2024

Abstract: *The glazing system is widely used in high-rise building due to its lightweight advantages compared to the conventional masonry. In such an application, the structural design of point-fixing system involves mainly the connection between glass and frame, which potentially increases the bearing capacity of system while reducing the weight. Hence, this work aims to improve bolted connection strength of window glass panel by introducing surface compressive stresses via an ion-exchange process. The study covers some parameters related to the glass sample and characteristics of assembly. A hole was drilled on both sides of Soda-Lime Silicate (SLS) Glass panels, measuring 5.80mm and 9.80mm in thickness, using tungsten carbide drill bits of varying diameters. The assembly was carried out with the intermediate insert materials of 3D printed Polylactic acid (PLA) and Thermoplastic polyurethane (TPU) filaments, placed between the contact of steel bolt and glass hole. In-plan loading test was performed to determine the failure load and evaluate the maximum stress distribution around the hole. The ion-exchanged glass increases the failure load from 2 to 3 times compared to annealed glass. With ANOVA analysis, the other influence parameters are bolt diameter, insert materials thickness, and clearance of contact. On the other hand, there is no significant effect on maximum principal stress of different insert materials between Polylactic acid and Thermoplastic polyurethane.*

Keywords: Ion-exchange; Soda-lime silicate glass (SLS); Insert material; In-plan loading; Bolted connection

1. INTRODUCTION

Glass is commonly used in civil engineering for building covers such as windows, cladding, façade, and so on because of its transparency, which allows for a large clearance for the building. Not long ago, the usage of glass materials in the last decade for not only architectural elements but also structural elements such as staircases, canopies. floors, and small pedestrian bridge. This represents a special challenge because of the glass's brittleness [7].

To be a primary structural element, glass needs to sustain safely with high load and the glass connections must be able to transfer the load to other elements of building. In the design of such structures made of tempered flat glass, connections cannot be avoided, especially when large spans and the loads are transferred via compound point-supports or bolts of steel to the glass drill hole.

A proper layer or bushing material, such as aluminum or plastic, must be used to avoid any contact between steel and glass. Moreover, the kind of the support, the geometry of the components, the quality of the glass edges and surfaces as well as the interlayer material influence the stress distribution around the drill hole [6].

The main problem of structural use of glass panels lies in the difficulty of transferring the load from the glazing system to the main building structure. The aim of this work is to develop strength of bolt connection of soda-lime glass by improving compression stress on the surface through chemical strengthening using a pure potassium nitrate salt (KNO_3) [8]. This study investigated several strategies of specimens, including the types of glass (Soda-Lime Silicate and tempered glass by chemical tempering); diameter of bolt and bushing material (Polylactic acid and Thermoplastic polyurethane). Moreover, this experiment will focus on the failure load

* Corresponding author: HIN Raveth
E-mail: raveth.hin@itc.edu.kh;
Tel: +855-12-321-684

capacity and maximum stress distribution around the drill hole by study on influences of different types of glass, glass's thickness, diameter of hole and insert materials.

2. METHODOLOGY

Before the strengthening process, sample preparation is highlighted as a possible step in chemical tempering. Additionally, mechanical testing using in-plane loading is recommended, along with various methods from the existing literature that could be incorporated into the experimental setup. The processes are illustrated in Fig. 2.1.

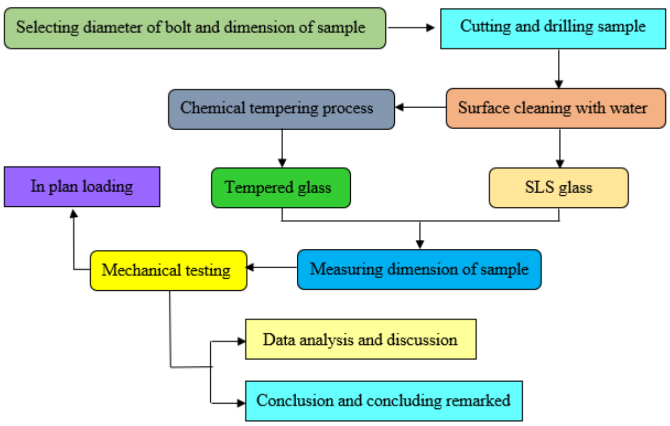

Fig.2.1: Schematic representation of the experimental procedure

2.1 Sample Preparation

SLS glass with nominal thicknesses of 5.80 mm and 9.80 mm called glass 5.80 and glass 9.80, respectively from a commercial source was used for the research. As mentioned before SLS is the main product of all commercial glasses, cheap price, strong chemical durability, and good transmission in the visible field that are the reasons why this material was used in this work. Initially, glass sheets provided in plate of size 120cmx30cm were used in this work. Then, glass sheets were manually cut into 360 specimens (40% unusable specimens) of 300mmx150mm for each glass thickness with two holes of diameter of 10mm, 12mm and 16mm drilled along the center axis [5].

In order to maintain the contamination of the surface at a minimum and increase the contact area as a result of improving the efficiency of the IE process, glass specimens were cleaned with water by gently swabbing and taking care to avoid any damage on glass surfaces before strengthening [2, 9]. The step for cleaning of the specimens was repeated after the IE process to remove the salt bath residues from the glass surfaces by water and dried them at room temperature.

a.) Cutting b.) Drilling c.) Cleaning

Fig.2.2: Sample preparation

2.2 Chemical Tempering Process

The IE process was performed in an electrical furnace (CS-0610). The EI process was conducted at different temperatures and times using pure potassium nitrate (99.0% purity) because small differences in the composition of potassium nitrate have different strengthening effects on EI efficiency [1, 4]. Since the conventional IE process was conducted at molten bath (KNO_3) temperatures of from 370 to 550 °C within a given process time, thus in this work, the process was realized at temperature 435 °C determined as being under the glass transition temperature within process time 8 hours [3].

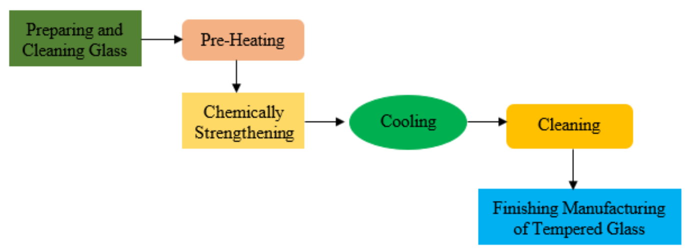

Fig.2.3: Schematic representation of chemical tempering process

Fig.2.4: Melting KNO_3

Fig.2.5: Pre-heating glass

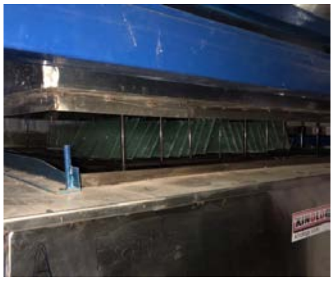

Fig.2.6: Immersing glass fully melted potassium salt

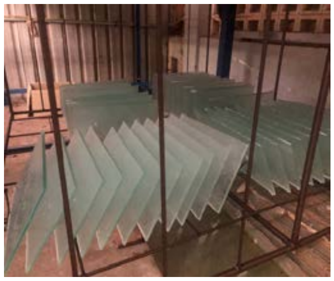

Fig.2.7: Taking chemically into tempered glass from molten

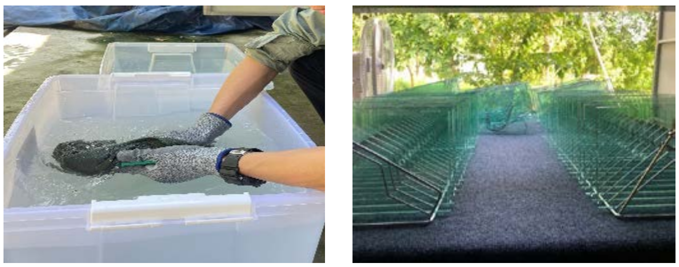

Fig.2.8: Cleaning chemically tempered glass specimens after chemical strengthening

2.3 Mechanical Testing: In-Plan Loading

To test, a digital meter with 0.01mm precision was used for the edges and thickness measurement after tempering and glass surfaces were taped with adhesive plastic tape to ensure well be safe when glass specimens broke during the test. For narrative simplicity, specimens were given notations representing nominal thickness, diameter of bolt, insert material type, treatment, and number in the last term, for instance “G5.8-D10-PLA-Unstr./1” represents the specimen number 1 with a nominal thickness of 5.8mm with two holes of diameter of 10mm including PLA for inserting material and unstrengthening. After that, specimens were grouped and kept in box divided by cleaned paper at the interface between specimen and specimen.

Fig.2.9: Measurements, taping with plastic and labeling

The glass panels are connected with bolts at splice plates. Between the glass drill hole and the steel bolt, different bushing materials are integrated. The bushings are produced in a way that there is no clearance between steel bolt and bushing. Electromechanical Universal Testing Machine Series LFM-TOP-50 was used in this experiment. At the lower edge the panels are fixed with a clamping strip. To receive a clamping, screws are used which are tightened with torque.

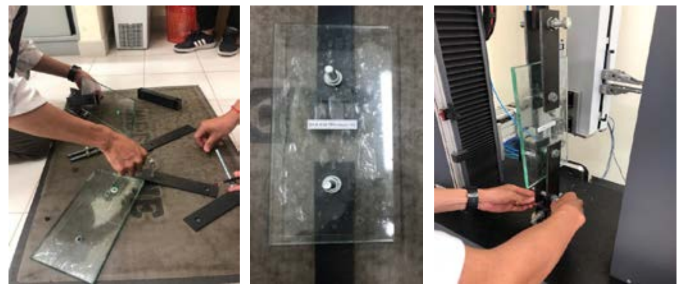

Fig.2.10: Setting up the in-plan bolted connection test

Tensile force is applied to the glass specimens by bolts through the drilled holes of the specimens. The load is applied on the specimen with constant velocity 1 mm/min until maximum load is reached [6]. The tests were performed in laboratory air (temperature ≃ 23°C). During the test performance the displacement and failure force of specimen were recorded.

Fig.2.11: Universal testing machine

The maximum principal stress was determined from the maximum failure force P as below [6]:

$$\sigma_{\theta\max} = K_{tn} \cdot \sigma_N \qquad \text{(Eq. 1)}$$

$$K_{tn} = 12.882 - 52.714 \cdot \left(\frac{a}{c}\right) + 89.762 \cdot \left(\frac{a}{c}\right)^2 - 51.667 \cdot \left(\frac{a}{c}\right)^3 \quad \text{(Eq. 2)}$$

$$\sigma_N = \frac{P}{2bt} \frac{\sqrt{1-\left(\frac{a}{c}\right)^2}}{1-\left(\frac{a}{c}\right)} \frac{1-\left(\frac{c}{2b}\right)}{1-\left(\frac{c}{2b}\right)\left[2-\sqrt{1-\left(\frac{a}{c}\right)^2}\right]} \quad \text{(Eq. 3)}$$

Where,

K_{tn} = stress concentration factor
σ_N = nominal stress
a = radius of hole
b = semi-width of panel
c = the shorter distance between panel edge and hole center

3. RESULTS AND DISCUSSION

3.1 Preliminary Study Results

The results of in-plane loading test on 15 samples in each case for the preliminary study of the effect of unstrengthened and strengthen without insert material and with insert material are summarized in Fig.3.1 and Table 3.1. The remarkable feature of the results is that the average of the failure load after the chemical tempering process was increased about twice compared to unstrengthened glass without insert materials. Moreover, when we put a bushing material between steel bolt and glass hole, the average of ultimate load becomes larger at least two times more compared to strengthened glass without insert materials. The direct contact between the steel bolt and the glass hole leads to a considerable variation in failure load, with standard deviations (Std.) of 0.21 and 0.41 observed for the unstrengthened and strengthened samples, respectively. Thus, it could be seen that the glass bolting with insert material have significant effective than without insert material.

Table 3.1: Summary of failure load measured on unstrengthened and strengthened sample for preliminary study of effect of insert material for glass 9.80

Glass Type	Average [kN]	Min. [kN]	Max. [kN]	Std. [kN]
Unstrengthened glass9.8 without Insert Material	1.56	1.24	1.89	0.21
Strengthened glass9.8 without Insert Material	2.38	2.03	3.02	0.41
Unstrengthened glass9.8 with Insert Material	2.62	2.51	2.73	0.07
Strengthened glass9.8 with Insert Material (TPU)	4.78	4.22	5.33	0.35

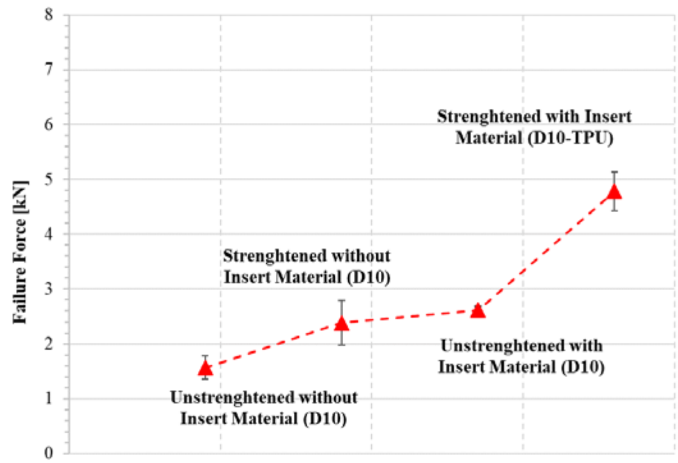

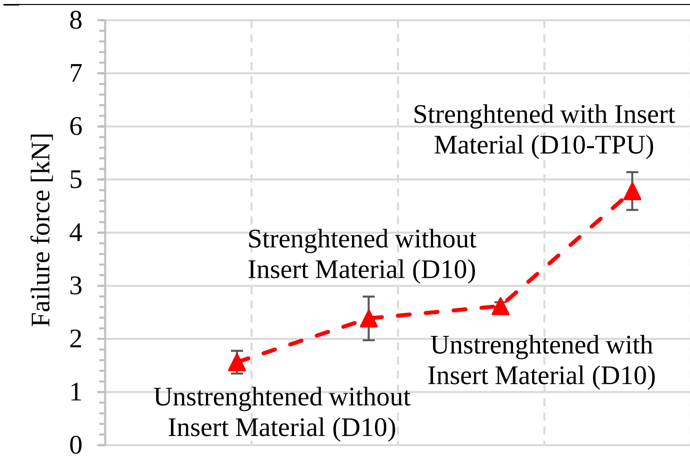

Fig.3.1: Summary of failure load of preliminary study (glass 9.80)

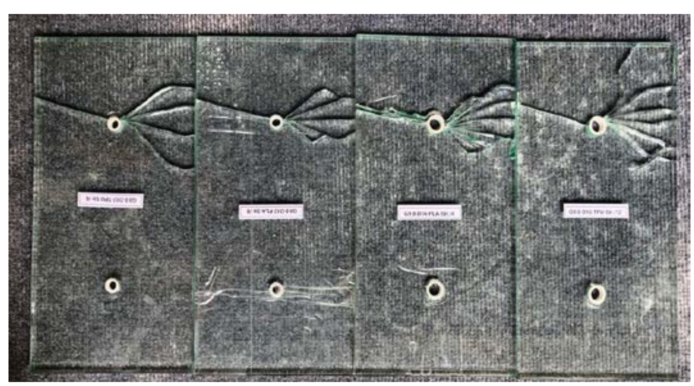

(a) (b) (c) (d)

Fig.3.2: Sample after testing (a) G9.8-D12-TPU-Str, (b) G9.8-D12-PLA-Str, (c) G9.8-D16-PLA-Str, (d) G9.8-D16-TPU-Str

3.2 Failure Load and Assessment

To further investigate the effect of glass types, diameter of hole and type of insert material on ultimate load and maximum stress distribution around the hole, the SLS glass with nominal thickness 5.8mm and 9.8mm were carried out under various conditions. These values were obtained from analyzing results of In-Plane loading test which is suitable for tensile test.

To assist in interpreting the results of the experiments, it was helpful to construct a graph of the average responses at each treatment combination as shown in Fig.3.3. The average failure load of unstrengthened glass with insert material PLA for diameter of hole 10mm, 12mm and 16mm were 1.41 kN, 1.89 kN and 2.25 kN respectively. In contrast, these values were increased around twice or over for strengthened glass. Similarly, the ultimate load of strengthened glass was improved nearly two times or more compared to unstrengthened glass with TPU insert material. Therefore, tempered glass by chemical tempering has significant effect on ultimate load for in-plane loading test. Moreover, the bigger diameter of hole provided higher load capacity as well.

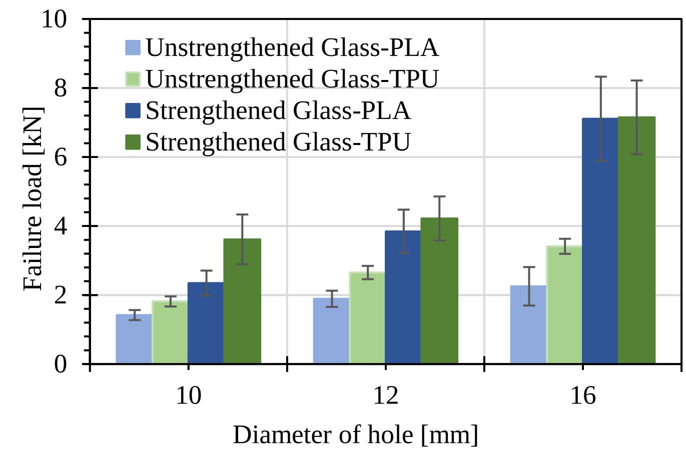

Fig.3.3: Failure load-diameter of hole for glass thickness 5.8mm

According to the graph in Fig.3.4, the average failure load of unstregthened glass with nominal thickness 9.8mm for drilling hole 10mm, 12mm and 16mm including PLA-bushings

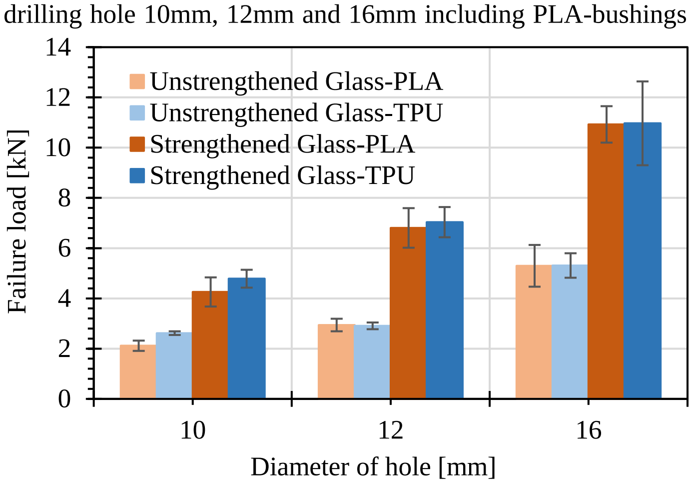

material were 2.11 kN, 2.94 kN and 5.29 kN, respectively. But, when we replaced unstrengthened glass to strengthened glass with the same parameters, the average of ultimate load has changed to 4.25 kN, 6.80 kN and 10.92 kN. Thus, both PLA and TPU that are inserted in the hole of strengthened glass have 2 times larger in ultimate load compared to unstrengthened glass. A remark from obtained results, ultimate load increased gradually with rising diameter of hole for all glass types.

Fig.3.4: Failure load-diameter of hole for glass thickness 9.8mm

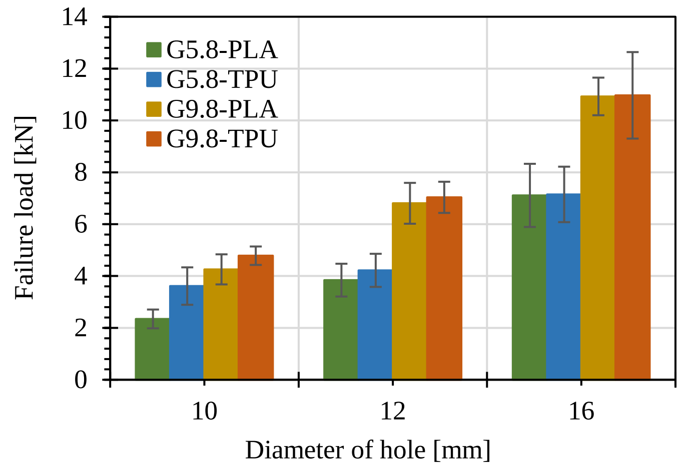

Fig.3.5: Failure load-diameter of hole for strengthened glass

To help demonstrate the results of the tests, a graph showing the average failure load for each treatment combination was created as shown in Fig.3.5. The average failure load of strengthened glass with nominal thickness 9.8mm with insert material PLA for diameter of hole 10mm, 12mm and 16mm were 4.25 kN, 6.80 kN and 10.92 kN respectively. On the other hand, if we replaced PLA by TPU with the same parameters, the average ultimate load has changed to 4.78 kN, 7.03 kN and 10.96 kN for diameter of hole 10mm, 12mm and 16mm respectively. Therefore, the average failure load of strengthened glass thickness 9.8mm with insert material PLA for all diameter of hole is slightly different from insert material with TPU. Similarly, for tempered glass with nominal thickness 5.8mm, both PLA and TPU have a little different in the ultimate load for all diameter of hole except diameter of drilled hole 10mm was different so far. Based on ANOVA, we observed that there is no significant effect on the failure load for in-plan loading test of different insert materials between PLA and TPU. But when we have a large bolt diameter it has high stiffness at the connected area because slenderness effect of the bolt is neglected. Obviously, glass plates also have a large hole so influence between glass width and hole should be considered. Therefore, this section investigates the influence of bolt diameter without insert material and increasing Young's Modulus of bolt. Based on force diagram in Fig.3.3, Fig.3.4 and Fig.3.5, there are three different bolt diameters plotted. The results show that higher bolt diameter provide higher load capacity under the same thickness of glass and insert material type.

3.3 Stresses Load and Assessment

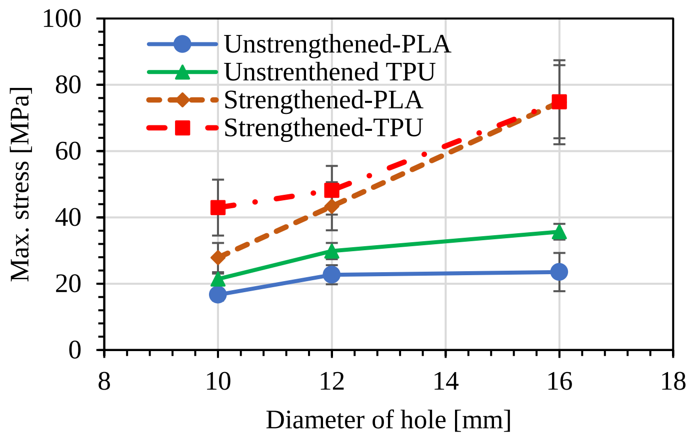

Fig.3.6: Maximum stress-diameter of hole for glass thickness 5.8mm

According to the chart in Fig.3.6, the average of maximum stress distribution around the hole of unstrengthened glass with nominal thickness 5.8mm with dimeter of hole 10mm, 12mm and 16mm including PLA-bushings were 16.65 MPa, 22.69 MPa and 23.50 MPa, respectively. By contrast, if we use strengthened with the same parameters, the average of maximum stress was shown at 27.88 MPa, 43.36 MPa and 74.73 MPa. This value showed that there was increased around 2 times between unstrengthened glass and strengthened glass in average of failure load. However, TPU-bushings material has a slightly larger load capacity in both types of glass. Moreover, the bigger diameter of hole provided higher load capacity as well. According to Maniatis & Parke, 2006 [6], further investigation is performed to validate the FE modeling technique presented that if the ratio of drill hole radius a and panel width b lies in the range of $0.1<a/b<0.2$ the stresses increase enormously or tend to infinity. An interesting aspect is that for values $a/b>0.2$ the stresses decrease until a minimum is reached between $a/b=0.5$ and the value rises again from 0.5 afterward. The main reason of the influence is the amount of stress distribution which may occurs in fluence of panel width and the distance between hole and panel edge.

The graph in Fig.3.7 illustrates the maximum stress of different hole diameters with another insert material of two types of glass with nominal thickness 9.8mm. The average maximum stress distribution around the hole of unstrengthened glass with nominal thickness 9.8mm with dimeter of hole 10mm, 12mm and 16mm including PLA-bushings were 14.98 MPa, 19.80 MPa and 32.85 MPa, respectively. By contrast, if we use strengthened with the same parameters, the average maximum stress was shown 30.04 MPa, 45.82 MPa and 67.66 MPa. As a result, these values were increased about 2 times between unstrengthened glass and chemically strengthened glass. Therefore, we can conclude that strengthening has a significant effect on maximum stress around the hole.

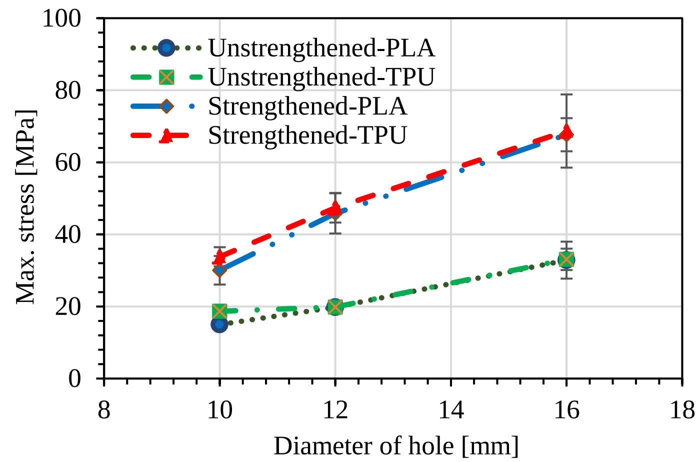

Fig.3.7: Maximum stress-diameter of hole for glass thickness 9.8mm

To explain the results of the tests, a graph illustrating the average responses for each treatment combination was generated as shown in Fig.3.8. The average maximum stress distribution around the hole of strengthened glass with nominal thickness 5.8mm with dimeter of hole 10mm, 12mm and 16mm including PLA-bushings were 27.88 MPa, 43.36 MPa and 74.73 MPa, respectively. Moreover, when the nominal thickness 5.8mmm was replaced by 9.8mm, it showed that the average maximum stress distribution near a hole were 30.04 MPa, 45.82 MPa and 67.66 MPa with different hole diameters 10mm, 12mm and 16mm respectively. We can see that there is a slightly different stress for both glass thickness. Similarly, it is the same with TPU also. Therefore, in this study, glass

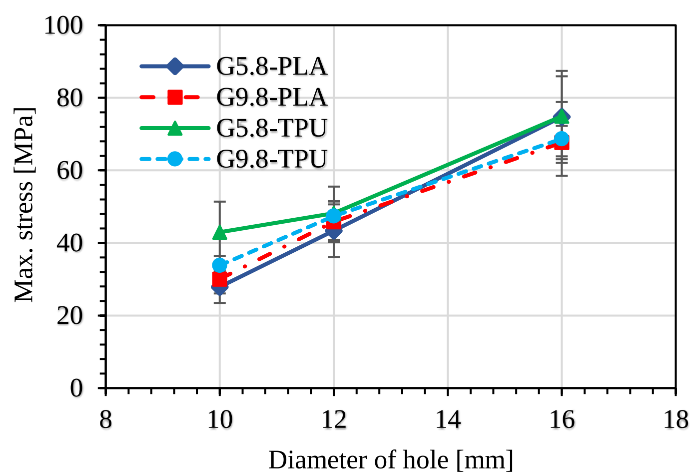

thickness and bushings material does not have a significant effect on the maximum stress distribution around the hole.

Fig.3.8: Maximum stress-diameter of hole for strengthened glass

4. CONCLUSIONS

This work within this thesis contributed to investigate in-plane load pinned joint in unstrengthened glass and chemically strengthened glass under identifying influence of variation of glass thickness, diameter of hole and insert material type. The entire problem was simulated by conducting experiments and using statistical analysis to evaluate and compare results. The results, ultimate load, maximum stress around the hole and its relationships with diameter of hole, insert material types and glass types were observed and compared. The key findings were discussed, and those observations as well as conclusion can be made as below:

- ❖ Influence of different glass types

Glass is a brittle material that typically fails in an abrupt and disastrous way. Due to its brittleness nature, reinforcement of mechanical properties of glass is highly necessary. Among methods of strengthening glass, chemical tempering or also called ion exchange strengthening is considered as the most effective technique. Compressive stress in surfaces of chemically tempered glass is bigger than that of thermally tempered glass, it indicates that strength of chemically tempered glass is stronger. According to the experiment, the maximum stress around a hole of chemically strengthened glass was increased at least 2 times compared to unstrengthened glass (SLS) for both glass thickness and all diameter of hole.

- ❖ Influence of different insert materials

The assumption that different bushing materials (PLA and TPU) have a considerable influence on the magnitude of maximum stresses distribution around the hole. The value of the maximum stress only differs slightly despite the different insert materials (PLA, TPU). The maximum stresses for both material combinations have approximately identical values. However, the difference of load capacity in these insert materials we obtain that insert TPU has a slightly larger than the PLA-bushings. Moreover, the PLA-bushings with a thickness 2mm, have only linear elastic deformations occur until a load reached a maximum at room temperature ≃ 23℃. By contrast, the TPU-bushings with a thickness 2mm, have significant plastic deformations occur until ultimate load at room temperature ≃ 23℃.

- ❖ Influence of different diameter of bolt

The diameter of bolt is also very important for influence of stress distribution around the hole. The bolt with larger diameter provides a higher load capacity. Furthermore, the contact clearance is another dominant factor to be investigated.

ACKNOWLEDGMENTS

The work was funded by Cambodia Higher Education Improvement Project (Credit No. 6221-KH).

REFERENCES

[1] Araujo, R. (2004). Thermodynamics of ion exchange. Journal of Non-Crystalline Solids, 349(1–3), 230–233. https://doi.org/10.1016/j.jnoncrysol.2004.08.147

[2] Atılgan, S., Özben, N., Sökmen, İ., Wondraczek, L., & Akman, S. (2020). Effect of surface cleaning prior to chemical strengthening process of glass. International Journal of Applied Glass Science, 11(4), 720–729. https://doi.org/10.1111/ijag.15479

[3] Güzel, A. S., Sarıgüzel, M., Özdemir Yanık, M. C., Günay, E., Usta, M., & Öztürk, Y. (2020). Enhancing mechanical endurance of chemical-tempered thin soda-lime silicate float glass by ion exchange. Journal of the Australian Ceramic Society, 56(1), 185–201. https://doi.org/10.1007/s41779-019-00375-x

[4] Gy, R. (2008). Ion exchange for glass strengthening. In Materials Science and Engineering B: Solid-State Materials for Advanced Technology (Vol. 149, Issue 2, pp. 159–165). https://doi.org/10.1016/j.mseb.2007.11.029

[5] Hin, R., Cheng, K., Han, V., Bernard, F., Seang, C., Keryvin, V., & Sanglebœuf, J. C. (2020). Flexural strength improvement for structural glass: A numerical study. IOP Conference Series: Materials Science and Engineering, 849(1). https://doi.org/10.1088/1757-899X/849/1/012083

[6] Maniatis, I., & Parke, G. A. R. (2006). Numerical and Experimental Investigations on the Stress Distribution of Bolted Glass Connections under In-Plane Loads.

[7] Nielsen, J. Henrik., & Danmarks Tekniske Universitet. DTU Byg. (2009). Tempered glass: bolted connections and related problems: PhD Thesis. DTU Civil Engineering, Technical University of Denmark.

[8] Sglavo, V. M., Quaranta, A., Allodi, V., & Mariotto, G. (2014). Analysis of the surface structure of soda lime silicate glass after chemical strengthening in different KNO3 salt baths. Journal of Non-Crystalline Solids, 401, 105–109. https://doi.org/10.1016/j.jnoncrysol.2014.01.026

[9] Varshneya, A. K. (2010). Chemical Strengthening of Glass: Lessons Learned and Yet To Be Learned. International Journal of Applied Glass Science, 1(2), 131–142. https://doi.org/10.1111/j.2041-1294.2010.00010.x

Techno-Science Research Journal 12 (Special Issue) 253-258

Content list available at ITC

Techno-Science Research Journal

Journal Homepage: www.ric.itc.edu.kh

Techno-Science Research Journal

Mineral and Chemical Characteristics of Ancient brick of Sambor Prei Kuk Temple, Kompong Thom, Cambodia

Ya Phall[1*], Muoy Yi Heng[1], Phanny Yos[1], Than Heng[2], Vitharong Chan[3]

[1]*Faculty of Geo-resources and Geotechnical Engineering, Institute of Technology of Cambodia, Russian Federation Blvd., P.O. Box 86, Phnom Penh, Cambodia*
[2]*National Authority of Sambor Prei Kuk, NR 6, Phum I, Sangkat Kompong Thom, Krong Stoeung Sen, Kompong Thom, Cambodia*
[3]*Department of Archaeology and Conservation, National Authority of Sambor Prei Kuk, NR 6, Phum I, Sangkat Kompong Thom, Krong Stoeung Sen, Kompong Thom, Cambodia*

Received: 22 August 2023; Accepted: 15 May 2024; Available online: August 2024

Abstract*: This article presents the results of material characterization studies conducted on historical brick samples from the heritage site of Sambor Prei Kuk temple, Kampong Thom, Cambodia. According to history, the location corresponds to the ancient city of Isanapura, which served as the capital of the Chenla kingdom and was documented in the 7th century CE. The Sambor Prei Kuk Archaeological Site is in the Stung Sen River's floodplain and adjacent upland. The upland surface is gently undulated and has lower flat regions and higher areas covered with forest (upland I) (uplands II and III). More than 90% of the medium- to fine-grained sand found in the uplands surrounding Sambor Prei Kuk is made high of quartz grains that are irregularly shaped, nearly translucent, and colorless. Several analyses were carried out to determine their fundamental physical properties, mineralogical, and raw material compositions, using handheld X-ray fluorescence, X-ray fluorescence (XRF), Petrography analysis, and scanning electron microscopy (SEM) provided images indicative of the material characteristics.*

Keywords: Mineral characteristics, Lime, Clay, Ancient Brick

1. INTRODUCTION

Cambodia is renowned for having many old temples scattered throughout its several districts. The Sambor Prei Kuk Archaeological Site is in the central province of Kampong Thom. Sambor Prei Kuk is one of Cambodia's most significant pre-Angkorean sites (about the 7th to 8th centuries CE), even though many Angkorean structures have already been studied. According to legend, the location corresponds to the ancient city of Isanapura, which served as the capital of the Chenla kingdom and was documented in the 7th century CE.

Bricks have been used to construct buildings in Sambor Prie Kuk temple for thousands of years. The use of clay bricks has increased due to the availability of clay as a raw material and advancements in fire technologies. Bricks with good mechanical and physical properties have been created as a result. The chemical and mineral composition of the raw materials utilized significantly impacts other properties like porosity and firing temperature.

The physical characteristics of the bricks are impacted by the presence of some elements (particularly their valence). (e.g., color) The raw clay's mineral and chemical composition, firing temperature, and kiln environment all affect the color of fired clay bricks. For instance, bricks with a high iron concentration are pink, but bricks with a high lime content are white or yellow. The majority of bricks burn in various shades of red. The hue changes from dark red to purple, then, as the temperature rises, to brown or grey at about 1300 °C.

This paper uses a variety of methods to explore the physical, chemical, mining-alogical, and petrographical properties of old bricks such as hand specimens; X-ray fluorescence (XRF) to define the composition of bricks; and Optical properties of a polish section of brick samples was used before making SEM.

[*] Corresponding author: Ya Phall
E-mail: phalya68@gmail.com

A scanning electron microscope is a tool that uses a stream of aligned electrons to sweep the sample's surface line by line and create its images. Studies employing a scanning electron microscope have made it possible to compare the microstructure's functional characteristics[3,7,8].

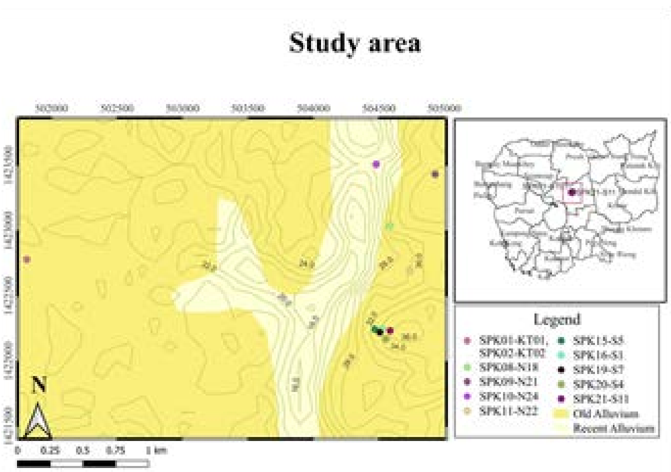

Fig.1. Mapping of bricks Sample selection

Fig. 2. A schematic map of the temple site and an image of one of the temples.

2. METHODOLOGY

In their study, brick samples were collected from the walls of the Sambor Prie Kok temple for identification basic of physical properties, mineralogical, chemical compositions, X-ray fluorescence(XRF) , Scanning Electron Microscope(SEM)

3. RESULTS AND DISCUSSION

3.1 Physical Properties

SPK11-N22-B1	Colorless, but burned inside, coarse grain and porous	
SPK11-N22-B2	Red, pink, grey, yellowish, Smooth, coarse grain, and porous	
SPK02-KT02B3	Colorless, yellowish, smooth, coarse grain, and porous	

Fig.3.list of sample analysed.

Red bricks were used to construct most of the temples, typically burnt at modest temperatures (less than 850°C). Due to the presence of atmospheric and biological depositions, it is dark in color. The inside surfaces were reddish-orange because they weren't exposed to the outside environment [4,5].

3.2 Optical Properties

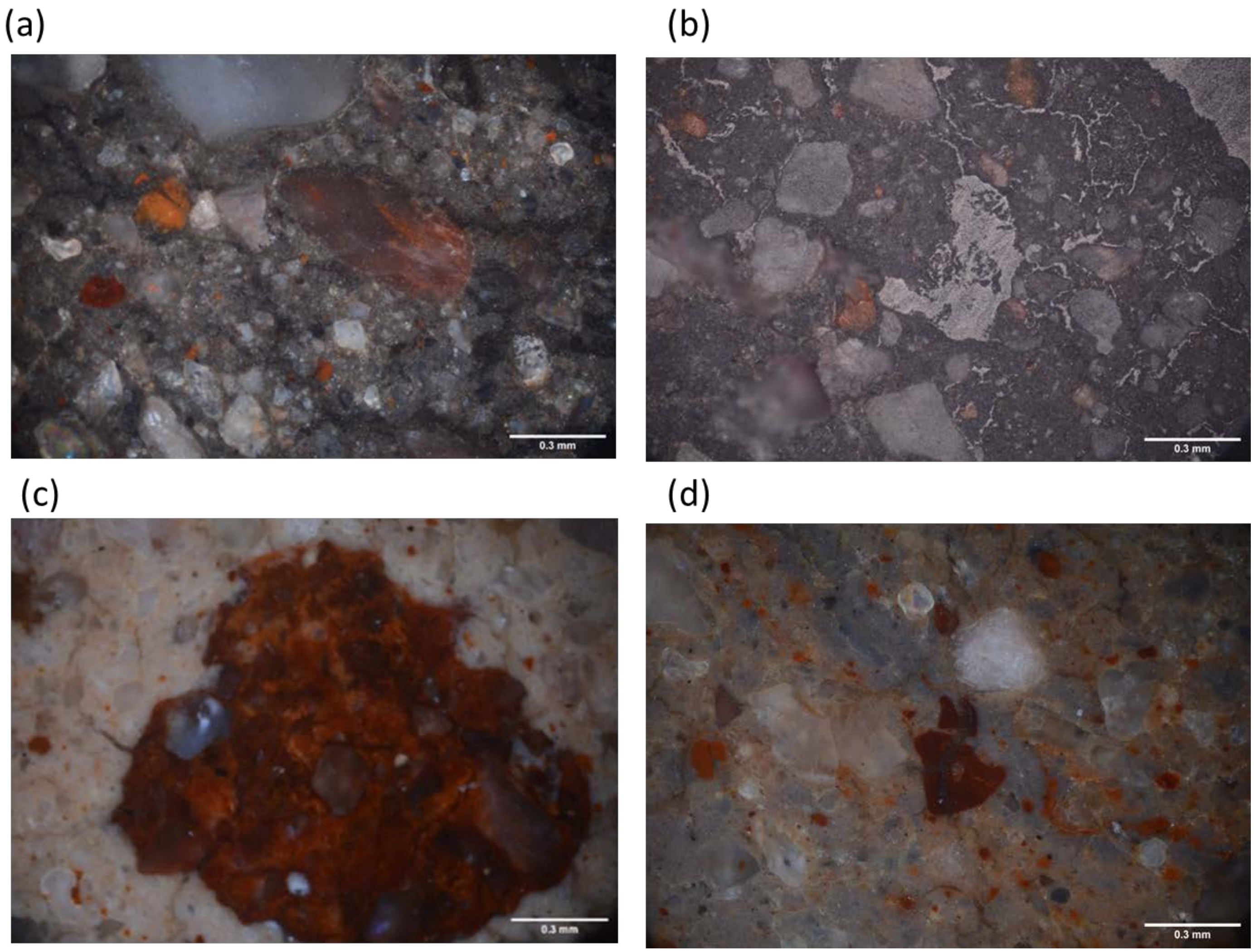

Fig.3. Microphotographs showing microtextures of bricks.

Figure 3. shows the visual features, such as color and texture of the studied brick samples. The color of the samples ranges from light to dark reddish to yellowish-brown depending on the firing temperature and the placement of the bricks in the kiln. The polished bricks' surface may be viewed under a stereomicroscope and has a variety of colors, from light brown to reddish brown. The texture of samples differs fromcoarse-grained (fig c, d) [6].

3.3 The chemical compositions

The chemical makeup of the gathered bricks is the main topic of the current study. LOI was calculated by heating the samples in an electric furnace to 900C. Crushed samples were used for the X-ray fluorescence chemical analysis. Al_2O_3, CaO, Fe_2O_3, K_2O, MgO, Na_2O, P_2O_5, SiO_2, SO_3, and TiO_2 were the main substances examined.

Sample ID	SiO_2	Al_2O_3	Fe_2O_3	K_2O	TiO_2	SO_3	P_2O_5	CaO	Na_2O	ZrO_2	MgO	MnO	LOI
SPK02-KT02-B1	65.7191	20.325	2.0352	0.7731	0.5715	0.2321	0.1076	0.0662	0.0359	0.0309	0.0265	0.0229	10
SPK02-KT02-B2	76.1163	13.155	2.9239	0.0684	1.7651	0.0481	0.0868	0.4288	0.0613	0.0683	0.0799	0.1446	5
SPK02-KT02-B3	65.7932	20.897	2.6341	1.436	0.6672	0.0508	0.0633	0.2558	0.2164	0.0291	0.1318	0.1544	7.5
SPK08-N18-B1	85.2187	9.7556	0.8627	0.0477	0.818	0.0413	0.1077	0.0255	0.0222	0.0487	0.0214	0.0086	3
SPK08-N18-B2	87.6232	7.5057	0.5564	0.1102	0.85	0.0262	0.0787	0.0636	0	0.0748	0.0671	0.0138	3
SPK09-N21-B1	81.0331	13.441	1.7184	0.8289	0.7446	0.1123	0.0929	0.1655	0.0753	0.0473	0.1716	0.0114	1.5
SPK09-N21-B2	80.5657	12.12	1.7863	0.0967	1.5749	0.0561	0.0656	0.0306	0	0.0652	0.088	0.0083	3.5
SPK10-N24-B1	74.5209	18.702	1.6718	0.0665	3.546	0.0354	0.164	0.0395	0	0.093	0.0761	0.0174	1
SPK10-N24-B2	65.8375	18.484	5.5714	0.786	1.1917	0.0454	0.1321	0.255	0.1339	0.049	0.4118	0.0299	7
SPK11-N22-B1	65.583	19.711	3.5209	1.7969	0.6255	0.0455	0.1245	1.0299	0.1432	0.0214	0.2529	0.0263	7
SPK11-N22-B2	70.0832	18.157	2.6891	2.3402	0.4443	0.1274	0.1601	0.0821	0.1796	0.0417	0.0424	0.0547	5.5
SPK16-S1-B1	77.0657	13.702	2.0015	1.2852	0.6587	0.0388	0.1248	0.1249	0.1371	0.0531	0.1966	0.0175	4.5
SPK16-S1-B2	80.4167	12.275	2.2906	0.6719	0.6974	0.0407	0.0812	0.1078	0.1039	0.0519	0.1984	0.0171	3
SPK20-S4-B1	52.063	14.709	3.0699	0.3731	1.2779	0.0328	0.0914	0.0668	0.0561	0.0443	0.1432	0.0187	28
SPK20-S4-B2	74.0596	18.372	4.3516	0.2957	1.7841	0.0194	0.0761	0.0466	0	0.0521	0.372	0.0135	0.5
SPK23-S3-B1	58.3966	21.754	7.1037	0.4851	1.6302	0.0534	0.0553	0.178	0.0346	0.0472	0.1528	0.0121	10
SPK23-S3-B2	73.5582	16.332	1.2134	0.1413	1.4537	0.0368	0.0776	0.0373	0	0.0635	0.0322	0.0088	7

Fig4: Results of the XRF elemental data of the brick sample with composition. The chemical element names attached to the oxygen forming the oxides are the following: Silicon (Si), Aluminum (Al), Iron (Fe), and Calcium (Ca). Loss On Ignition (LOI) is a chemical compound that is volatile.

The lowest LOI content was observed in bricks SPK20-S4-B2 and SPK10-N24-B1, with 0.5 and 1%, respectively, which can be related to their high firing temperature and higher Kaolinitic content. All brick samples had low levels of CaO and Na_2O, albeit the first two could have been contaminated by lime mortars and soluble salts. The greater Al_2O_3 (20.325, 20.897, 21.754%) in SPK02-KT02-B1, SPK02-KT02-B3, and SPK23-S3-B1 can be attributed to Al-rich Kaolinitic clays, which highlighted the careful selection of locally-sourced raw materials on those materials (the Sambor PreiKuk region is highly rich in Kaolin deposits). Bricks CaO (0.2558, 0.1655, 0.255,0.1249, 0.1078, 0.178%) in samples SPK02-KT02-B3, SPK09-N21-B1, SPK10-N24-B2, SPK16-S1-B1, SPK16-S1-B2, SPK23-S3-B1 and MgO (0.1318, 0.1716, 0.4118, 0.1432, 0.1528 %) in SPK02-KT02-B3, SPK09-N21-B1, SPK10-N24-B2, SPK20-S4-B1, SPK23-S3-B1 The higher MgO content samples may be the result of the application of Mg-enriched clays (non-pure Kaolin) to increase mortars plasticity (pure Kaolins are low plastic clay). The lowest LOI content was observed in bricks.

SPK20-S4-B2, SPK10-N24-B1, SPK09-N21-B1, and, with 0.5,1,1.5%, respectively, which can be related to their high firing temperature and higher Kaolinitic content. The amount of Fe_2O_3 in brick samples ranging from 5.5714 to 7.1037% did not differ significantly either, while a substantially greater content might have been the result of adding Fe_2O_3 to make brick fire easier by boosting the thermal storage capacity. Since the variability mean of SiO_2 (52.07%) exhibits low variance, the chemical makeup of the raw clay utilized to make bricks is comparatively uniform. All brick samples included low CaO, Na_2O, and TiO_2 levels, albeit the first two may have been contaminated by soluble lime mortars [6].

3.4 Characteristics of brick

SEM analysis was used to assess the bricks' microstructural characteristics and elemental compositions. The analysis findings reveal that the bricks have high concentrations of SiO_2, Al_2O_3, and Fe_2O_3 and low concentrations of CaO. Their low calcium content suggests that calcium-poor clays from locally accessible raw material sources should be used[1].

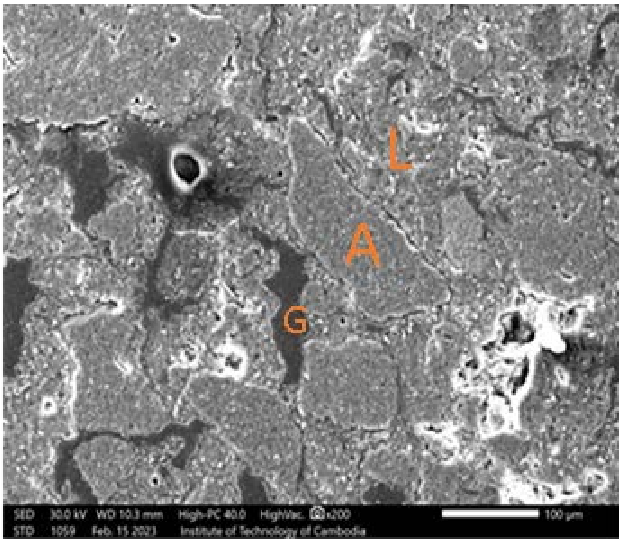

Fig3. Image of a waste-fired brick particle (Grog:G) in the brick matrix. agregates and lime(A:Agregate, L:lime)

(a)

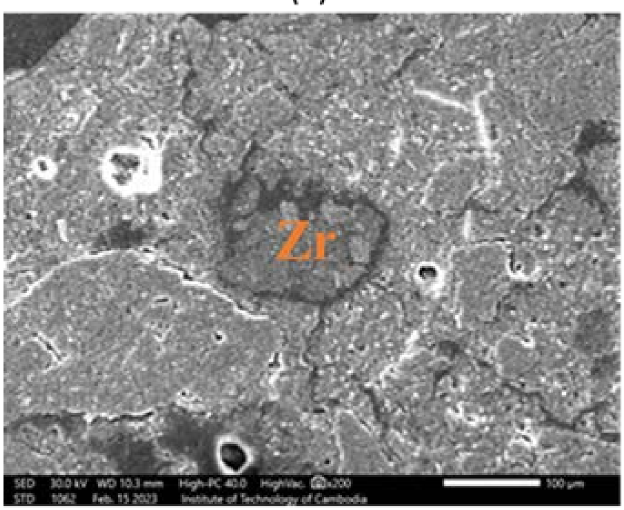

(b)

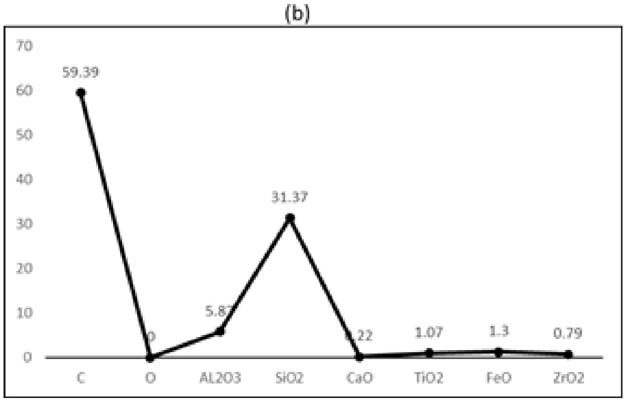

Fig.4. Image (a) and EDX spectrum (b) of a tiny zircon(zirconium silicate: Z) particle in the brick matrix

Small shards of fractured brick (grog) and trace amounts of metal compounds such as titanium oxide and zirconium silicate were visible in the bricks' microstructural features (Figure 3). The presence of grog particles in the brick's raw materials can be interpreted as a way to minimize the addition of water, which speeds up extrusion but slows down the drying phases of brick manufacture (Figure 4) [8]. Before the discovery of cement, lime bricks, which were made by combining lime and aggregate, were the most fundamental and widely used binding medium in the construction of buildings (Fig 3). The spaces between the aggregates are filled by lime, and the aggregates and lime adhere better. After a minimum of three years of settling, this mixture was used. In the mortars and plasters of many structures, baked ceramic materials such as bricks and tiles were also utilized as an artificial pozzolan [2].

4. CONCLUSIONS

Representative samples of brick-structured historic buildingswere investigated using physical properties optical microscopy (OM), X-ray fluorescence(XRF) ,Scanning Electron Microscope(SEM). Red bricks were used to construct the majority of the temples, and they were typically burnt at modest temperatures. The color of the samples ranges from light to dark reddish to yellowish-brown depending on the firing temperature and the placement of the bricks in the kiln. The lowest LOI content was observed in bricks with 0.5 and 1%, respectively, which can be related to their high firing temperature and higher Kaolinitic content. All brick samples had low levels of CaO and Na2O, albeit the first two could have been contaminated by lime mortars and soluble salts. The greater Al2O3 can be attributed to Al-rich Kaolinitic clays, which highlighted the careful selection of locally-sourced raw materials on those materials (the Sambor Prei Kuk region is highly rich in Kaolin deposits). The spaces between the aggregates are filled by lime, and the aggregates and lime adhere to one another better. After a minimum of three years of settling, this mixture was used. In the mortars and plasters of many structures, baked ceramic materials such as bricks and tiles were also utilized as an artificial pozzolan.

ACKNOWLEDGMENTS

The authors are grateful to The General National authorithy Sambor Prei Kuk, JICA_LBE for funding the project.The authors thank the researchers of the Centre for Materials Research at the Institute of Technology of Cambodia for Petrography Microscopy ,XRF and SEM analyses during the experimental stage of this study.

.

REFERENCES

[1] Properties of Roman bricks and mortars used in Serapis templein the city of Pergamon Özlem Aslan Özkaya, Hasan Böke⁎ Architectural Restoration Department, İzmir Institute of Technology, 35430 İzmir, Turkey

[2] Archaeological and Chemical Investigation on Mortars and Bricks from a Necropolis in Braga, Northwest of Portugal. Ana Fragata 1,* , Carla Candeias 1 , Jorge Ribeiro 2, Cristina Braga 2, Luís Fontes 2, Ana Velosa 3and Fernando Rocha

[3] Impact of modification of sand-lime mass with organic compounds onthe microstructure and mechanical features of silicate bricks Ryszard Dachowski, Anna Stepien Kielce University of Technology, Department of civil and environmental engineering, Al. 1000-lecia P.P.7, 25-317 Kielce, Poland

[4] Chemical Characterisation of the Organic Materials Used for the Constructionof the Temples and Buildings in Mỹ Sơn (Vietnam) from the Champa Kingdom

[5] Characterization of historic bricks and binder at Vat Phou World Heritage Site in Lao PDR and selection of compatible replacement units for restoration
Swathy Manohar*, Shivangi Shukla, Arun Menon and Manu Santhanam
Department of Civil Engineering, Indian Institute of Technology Madras, Chennai 600 036, India

[6] Mineralogical, physical and chemical characteristics of historic brick-made structures A. A. El-Midany1 & H. M. Mahmoud2. Received: 2 November 2014 /Accepted: 29 September 2015 /Published online: 5 October 2015 Springer-Verlag Wien 2015

[7] Estimated Construction Order of the Major Shrines of Sambor Prei Kuk Based on an Analysis of Bricks